THE UNIVERSITY OF OKLAHOMA

GRADUATE COLLEGE

INTERPRETATION OF HORIZONTAL WELL PERFORMANCE IN MULTI-LAYER RESERVOIRS BY THE BOUNDARY ELEMENT METHOD

A DISSERTATION

SUBMITTED TO THE GRADUATE FACULTY

in partial fulfillment of the requirements for the

degree of

DOCTOR OF PHILOSOPHY

by

KITTIPHONG JONGKITTINARUKORN

Norman, Oklahoma

1998

UMI Number: 9839791

INTERPRETATION OF HORIZONTAL WELL PERFORMANCE

IN MULTI-LAYER RESERVOIRS

BY THE BOUNDARY ELEMENT METHOD

A DISSERTATION APPROVED

FOR THE SCHOOL OF PETROLEUM AND GEOLOGICAL ENGINEERING

BY

ACKNOWLEDGMENTS

I would like to express my sincere appreciation to Dr. Tiab for his guidance and encouragement throughout my Ph.D. program. Thanks also to Dr. Anuj Gupta, Dr Samuel Osisanya, Dr. Subhash Shah, and Dr. Luther W. White for serving as members of my dissertation committee.

In particular, special thanks to my friends Pornpun Eamhame, Vicharn Puntoornvanich, Boonyarach Kitiyanun, Sirirut Vanichiyaboon, Nopawan Ratasuk, Freddy Escobar, Balkrishna Gadiyar, Xianhong Yang, Wei Wang, Zahid Bhatti, Sarfraz Jokhio, Ahmed Almarouqi, and Hyun Cho who provide guidance, supports, assistance, and discussions.

I am also indebted to Mr. Michael D. Tuttle, of the Silicon Graphics Computer Systems, who provided the computer times and assistance. Without his sincere help, this dissertation must be postponed.

I dedicate this work to my parents who gave me this wonderful life, my brothers, my sisters, and my cousins who provide love and supports.

ABSTRACT

Pressure transient analysis for horizontal wells has gained a lot of attention recently due to the increasing number of horizontal wells. Interpretation of horizontal well test data is much more difficult than for a vertical well. Due to heterogeneity, application of single-layer models fails to interpret the reservoir properties. Numerical methods are essential for a horizontal well in multi-layer reservoir with complicated wellbore configuration and boundary conditions.

This dissertation presents a boundary element method for solving pressure transient behavior of multi-layer reservoirs. Two types of boundary conditions, Dirichlet and Neumann, can be handled by the proposed technique. The boundary element method yields several advantages over the conventional finite-different and finite-element methods; including the reduction of the dimension of the problem by one, yielding more accurate results by using the analytical solutions of the governing equations as the weighting functions, no gird orientation and numerical dispersion effects, and flexibility of handling complex geometries and boundary conditions.

The developed algorithm is successfully applied to some simple cases with known analytical solutions including a finite linear aquifer, a horizontal well in closed reservoir, and a horizontal well in a multi-layer reservoir.

The developed algorithm is applied to generate the dimensionless pressure and the dimensionless pressure derivative for a horizontal well in eight different systems whose analytical solutions are not available. These cases include (1) a horizontal well in a two-

layer reservoir, (2) a horizontal well in a two-layer reservoir with gas-cap drive, (3) a horizontal well in a two-layer reservoir with bottom-water drive, (4) a horizontal well in a two-layer reservoir with gas-cap and bottom-water drives, (5) a horizontal well intersecting a two-layer reservoir, (6) a snake-shape horizontal well in a two-layer reservoir, (7) a horizontal well intersecting a three-layer reservoir, and (8) a vertical well intersecting a two-layer reservoir without cross flow. Their transient behaviors are studied in this work.

The step-by-step procedures for calculating reservoir parameters are developed in this work. The direct synthesis is applied to interpret pressure transient behavior of a horizontal well in complicated systems without type-curve matching. The conventional log-log, semi-log, and the Cartesian plots are used in this work. The procedure is illustrated by numerical examples.

TABLE OF CONTENTS

LIST OF TABLES

LIST OF FIGURES

Chapter 1

INTRODUCTION

1.1) Horizontal Well Application

Horizontal wells were first used to enhance contact area in the early part of 1940's as reported by Renney (1941). Due to its high cost, this completion technology was considered only when hydraulic fracturing from a vertical well was not practical. Horizontal well technology has gained a lot of attention in petroleum industry today. The current technology can drill a deeper and longer horizontal well. Several successful field cases (Higgin (1953), Eastman (1954), Perrine (1955), Roemershauser and Hawkins (1955), Landrum and Crawford (1955), Colamasi and Canne (1963), and Stormont (1983)) have been documented in the literature. The horizontal well technology was applied recently in both Western Europe and North America (Bezgire and Morkiw (1979), Killough and Foster (1979), Pitt (1980), Moore (1980), Stramp (1980), Cawvey (1981), Anon (1981), Astier et al. (1981), Jourdan and Baron (1981), Wash (1981), Holbert (1981), Stiegler (1982), Loxam (1982), Anon (1982), Pugh (1982), Giger and Jourdan (1983), Anon (1983), Wittrisch and Jordan (1983), Jordan and Baron (1984), Reiss et al. (1984), Giannesini (1984), Giger and Reiss (1984)). Experts predict that the number of horizontal wells will rise considerably in the next century and this technology will be applied increasingly to initial reservoir development.

The main purpose of a horizontal well is to enhance reservoir contact and well productivity. Horizontal wells can be applied in the following areas (Joshi, 1991):

(1) In reservoir with water and gas coning problems; they can be used to r coning problems by minimizing drawdown while maintaining production.

(2) In naturally fractured reservoirs; they are used to intersect fractures.

(3) In tight gas reservoir; they can be used to enhance the production in lo reservoirs.

(4) In EOR applications; they provide high sweep efficiency, low injectio larger contact area, and higher grow injectivity.

(5) To over come the drilling and drilling related cost problems.

(6) In offshore and in environmentally sensitive area, the number of wells by drill long horizontal wells. In term of productivity, one horizontal wel to several vertical wells.

Pressure transient analysis for horizontal wells has gained a lot of recently due to the increasing number of horizontal wells. Horizontal wel initially analyzed with the technique designed for vertical wells. Renney i an article on drilling horizontal wells in 1941. After that, many articles w on pressure transient analysis of a horizontal well (Giger el al. (1984), G Clonts and Ramey (1986), Karcher (1986), Goode and Thambynayagam Reiss(1987), Sherrard et al. (1987), King and Ertekin (1988), Joshi (1988 (1988), Ozkan and Raghavan (1989), Rosa and Carvalho (1989), Babu ar Ozkan and Raghavan (1990), Odeh and Babu (1990), Abbaszadeh and H Suzuki (1990), Lichtenberger (1990), Rosenzweig (1990), Kuchuk et al. (et al. (1991), Goode and Kuchuk (1991), Goode and Wilkinson (1991), S

1-26, Kuchuk, and Jongkittinarukorn and Tiab (1996)). All of these papers deal with a single-layer homogeneous reservoir. Field experience indicates that interpretation of horizontal well test data is much more difficult than for a vertical well. Several factors including the wellbore storage effect, 3D flow geometry, partial penetration and boundary effects, and lack of radial system make it difficult to interpret.

Mattar and Santo (1995) have summarized the available horizontal well-test models and divided them into two categories as the followings.

(1) The segmental analysis

This technique identifies and analyses individual flow regimes; wellbore storage dominated flow, vertical radial flow, horizontal linear flow, horizontal radial flow, and boundary dominated flow. Goode and Thambynayagam (1987), Daviau et al. (1988), and Odeh and Babu (1989) models are in this class. The advantages of the segmental analysis are:

- It is similar to the methods used for vertical well testing,
- Identifying each flow regimes gives an engineer a qualitative feeling for the degree of reliability of the parameter calculated.

This approach also yields several limitations such as:

- Individual flow regimes are not readily identified,
- It may be difficult to know whether it is the vertical-radial or the horizontal-radial flow if only one radial flow regime is observed,
- Due to different percentage deviation allowed, different model yields different durations of flow regimes,

- These models were derived for drawdown. Application of these techniques to build-up test results in errors due to relatively short flow periods,
- This approach is limited to simple reservoir models,
- Different values of reservoir parameters may be obtained for analyzing different flow regimes.

(2) The integrated model

The analytical solution is used to generate the synthetic pressures which are then compared to the corresponding measured pressures. The variables are modified by history matching. The models in this category includes Ozkan et al. (1987), Carvalho and Rosa (1988), Kuchuk et al. (1990), and Thompson et al. (1991). This technique offers several advantages including:

- It can analyze all of the data regardless of whether it belongs to a specific flow regime or a transition,
- The effect of each parameter can be easily determined,
- This approach can be applied over any portion or sequence of flows.

These approach yields several serious drawbacks including

- It is computationally intensive,
- Different acceptable matches can be obtained with totally different models,
- The match based on the pressure and on the pressure derivative can be different,
- Different best-fit techniques can result in different models,
- A search for global match is impractical,

- The physical meanings of flow through porous media are masked by the mathematics of computation.

Joshi (1991) pointed out that horizontal wellbore are rarely horizontal but rather snake-like with many variations in the vertical plane. Different wellbore portions will observe different pressure response. While some portion of the well may observe the bottom-boundary effect earlier than the remaining portion of the well, some portion of the well may observe the top-boundary effect earlier. The influence of the pressure along the horizontal wellbore is not well known. Due to the different chronological deposition environment, a reservoir always has a variation in properties in the vertical direction. Figure 1.1 shows the horizontal well profile in multilayer reservoir. Therefore, the pressure distribution along the wellbore is three-dimensional in nature and susceptible to irregularities in geometry and properties of layers. The combination of horizontal-well profile and layering effects make a horizontal well-test data difficult to interpret.

Due to heterogeneity, application of single-layer models fails to interpret the system properties. A more realistic three-dimensional model is essential for analysis of horizontal well performance. There is only one paper dealing with pressure transient analysis in layered reservoirs. Kuchuk and Habashy (1996) used the reflection and transmission concept of electromagnetic to solve the diffusivity equation in three dimensional layered reservoirs, where heterogeneity is present in only the vertical direction. It is clear from their works that estimation of parameters of individual layers is difficult. A multi-layer reservoir with large variation in layer permeability should not be treated as an equivalent single-layer reservoir with average properties. They have also shown that the conventional Horner method does not work for a horizontal well in layered reservoirs. Their model has several limitations including:

- the horizontal well is parallel in the y direction and completed in only one layer.
- the system is infinite in horizontal directions.
- each layer has a uniform thickness.

Analytical models are preferred to numerical models because of their accuracy and continuity. But they can be applied only for some ideal situations leading to the limited number of existing solution procedures. Some simple boundary shapes can be generated by the principle of superposition. This technique becomes too tedious for calculations at long time when the infinite number of image wells is required and consequently yields considerable computational efforts. Therefore, numerical models are essential for a horizontal well in multilayer reservoirs. They can be used to solve more realistic and complicated reservoir systems. However, analytical models may be used to validate numerical models.

1.2) Literature Reviews of Numerical Methods

Finite-different method (FDM) is the most popular in petroleum engineering. Because of it simplicity, this method has been applied to solve fluid flow through porous media problem for both transient and pseudo-steady state flows. The performance of a horizontal well is usually calculated by finite-different simulators (Papatzakos et al. (1989), Bendakhlia and Aziz (1989), Economides et al. (1990), Stone et al. (1989), Rosenzweig et al. (1990)) utilizing a standard cartesian grid that does take into account the flow geometry around the well and yields numerical uncertainty. The second most used method is finite element (FEM). Both of these techniques have several drawbacks including

1. Grid orientation effects,
2. Numerical dispersion,
3. Wellbore and boundary representations.

Boundary-element method (BEM) has emerged as a powerful alternative to finite elements and finite difference methods particularly in cases where accuracy is required due to problems such as infinite domain and irregular boundaries. The BEM is concerning with the numerical solution of integral equation and has been applied in a variety of engineering problems. This technique yields several advantages over the FEM and FDM including

- <u>The reduction of the dimensionality of problem by one</u>

  Thus, it only requires discretization of the boundary rather than the whole domain, illustrated in Fig. (1.2). Meshes can be easily generated and changed. In addition, smaller systems of equations and reduction in the data are required to solve a problem.,

- <u>More accurate results</u>

  The BEM yields more accurate results than the FEM and FDM because the weighting functions used by this method are analytical solutions of the governing equations.

- <u>No grid orientation and numerical dispersion effects</u>

Since the domain discretization is not required, the problem is determined by the governing differential equation, and is not restricted by the grid system. Discretization errors are introduced only at the boundary. Therefore, grid orientation effects related to the domain discretization can be removed. The BEM is an integral method which is a smoothing technique compared to FEM and FDM which tend to accentuate the errors when evaluating derivatives. Thus the numerical dispersion is minimized yielding much more accurate solutions.

- Better problem representation.

  It offers flexibility of handling complex geometries and boundary conditions. In stead of wellbore pressure, the producing-block pressure is evaluated in FEM and FDM. The BEM can directly calculate well drainage boundary pressure without making such an assumptions.

Kellog (1953) first developed this technique in the potential theory. With the arrival of the digital computer, the application of this method expanded tremendously during the 1970's in eleastodynamics, heat transfer, fluid mechanics, and groundwater hydrology. Since then, many researches (Liu and Ligget, Brebbia and Walker, Lennon et al., Lafe et al., Numbere, Liggett and Liu, Connor and Brebbia, Masukawa) have been conducted to solve various engineering problems.

Numbere and Tiab (1988) applied the BEM to generate streamlines for homogeneous and sectionally homogeneous reservoirs having irregular boundaries. They summarized that the BEM offers several advantages including

- the ability to handle handle homogeneous as well as nonhomogeneous (zoned) porous media.
- the ability to handle all shapes of boundaries - regular or irregular.
- all kinds of boundary conditions - Neumann. Dirichlet, or mixed.
- the elimination of trial-and-error procedures or the personal judgment of the user.
- the accuracy and reliability of the solution in the interior of the domain of interest.

Masukawa and Horne (1988) presented the application of the boundary integral method (BIM) to fluid displacement problems to demonstrate its usefulness in reservoir simulation. They developed a method to solve two-dimensional, piston-like displacement for incompressible fluids. They noted that the method has the following advantages.

- The results are accurate because the solution does not suffer the grid orientation effects and numerical dispersion.
- The method can handle any combination of Dirichlet- and Neumann-type boundary conditions and complex geometries.
- Both time and storage area of a computer can be saved because the technique using only a boundary grid reduces the domain of interest by one.
- Velocity and flow potential at any point in the domain can be solved by the method.

Kikani and Horne (1988, 1992) developed accurate solutions for transient flow of fluid in homogeneous arbitrary-shape systems with a variety of constant and/or time-dependent boundary conditions. Two techniques, the real space and Laplace transform solutions, were presented in their works. Kikani and Horne (1989) also applied their techniques in streamline generation, isochrones for steady-state single-phase flow problems, and well testing to some field examples. For multi-well situations with arbitrarily shaped boundaries and a variety of boundary conditions, their technique can be used to solve for front tracking in the steady-state case quickly and effectively.

The Laplace domain boundary-element method (BEM) was developed by Kikani and Horne (1993) to calculate transient pressure in a piecewise homogenous porous media with arbitrary geometry of each region. Each region can have different rock and fluid properties. The technique can be applied to solve for impermeable barriers of any shape, sizes, and orientations, including large pressure-support sources and fluid-injection problems showing composite behavior.

Sato and Horne (1993) developed a perturbation boundary element method (BEM) for both steady-state flow and transient-flow problems in heterogeneous media. The BEM gives the perturbation series with the complete solution for the original governing equation. Their model can be applied to track streamlines and displacing-fluid fronts. They also applied the technique to solve transient-flow problems.

Brunch (1991) has applied the FDM, FEM, and BEM to solve groundwater flow problems. He recommended that BEM is the most suitable, since it allows the most efficient handling of free surfaces, infinite flow domains and singularities. Besides, the BEM yields more accurate results than the other methods because the weighting functions used by this method are analytical solutions of the governing equations. He illustrated the technique by solving the fluid flow problems for both transient and steady state periods.

Koh and Tiab (1993) developed a versatile boundary-element algorithm for solving transient and steady state problems in isotropic or anisotropic reservoirs. First, the governing equations and the boundary conditions were transformed into the Laplace domain. Then the integral equation was formed using a weighted residual approach. The boundary is discretized using isoparametric linear triangular elements. The Gaussian quadratures were utilized to evaluate the integral equation. The solution from the Laplace domain was inverted to real space domain by the well-known Stehfest algorithm. Six problems with known analytical solutions were modeled by the proposed algorithm. Excellent agreement between the numerical and analytical solutions were observed. They also illustrated the algorithm by modelling (1) a vertical well with partial completion and (2) a tortuous Horizontal well. Their algorithm can handle

- reservoirs of arbitrary shapes,
- finite-radius wellbore of arbitrary geometry,
- any combination of Dirichlet and Neumann boundary conditions.

The technique can be used to solve a wide variety of three-dimensional horizontal well problems. But the reservoir must be homogeneous. Thus, their algorithm cannot be applied to solve for a horizontal well in multi-layer reservoir.

1.3) Objectives of Study

This study has three objectives:

1. To develop the three-dimensional diffusivity equation for fluid flow through multi-layer reservoir,

2. To develop a boundary element method for the formulated problem.
3. To simulate the performance of a horizontal well performance in a single-layer, two-layer and multi-layer reservoirs.

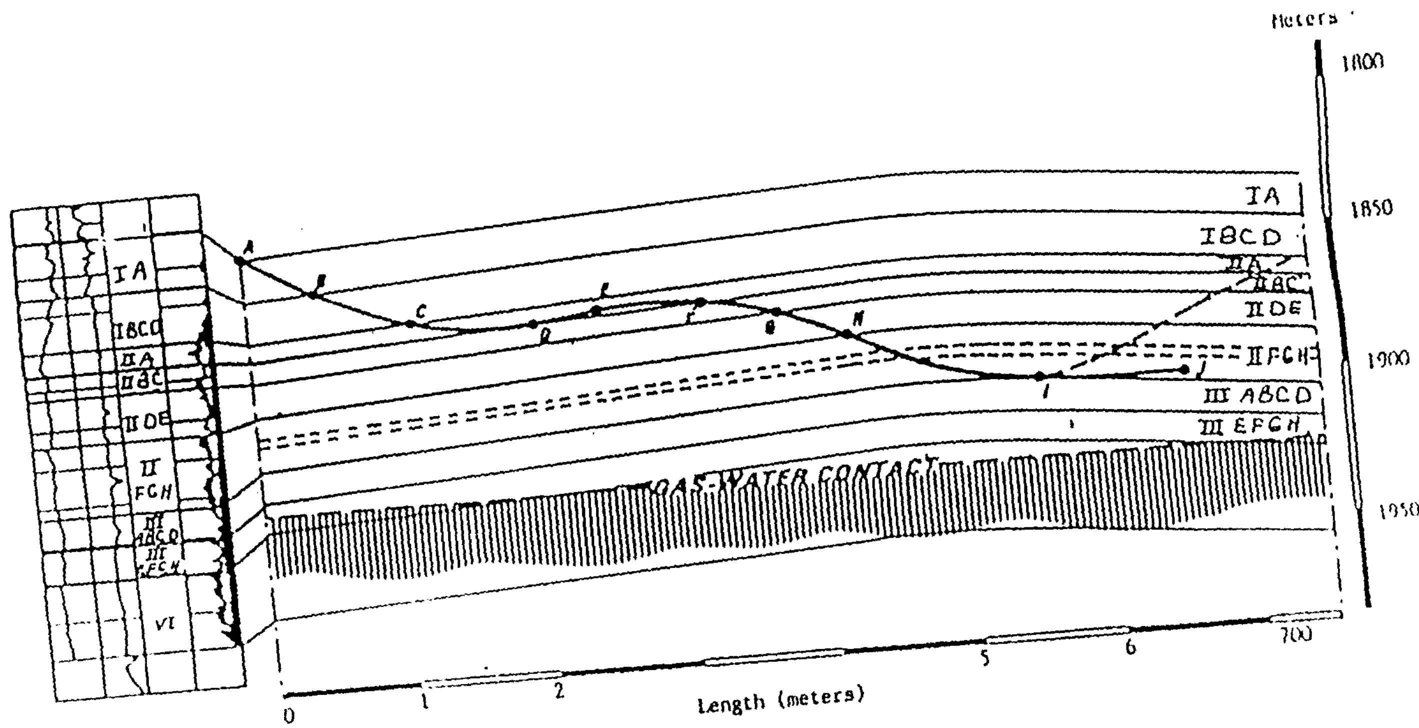

Figure 1.1 Horizontal Well Profile (After Fritz et. al.)

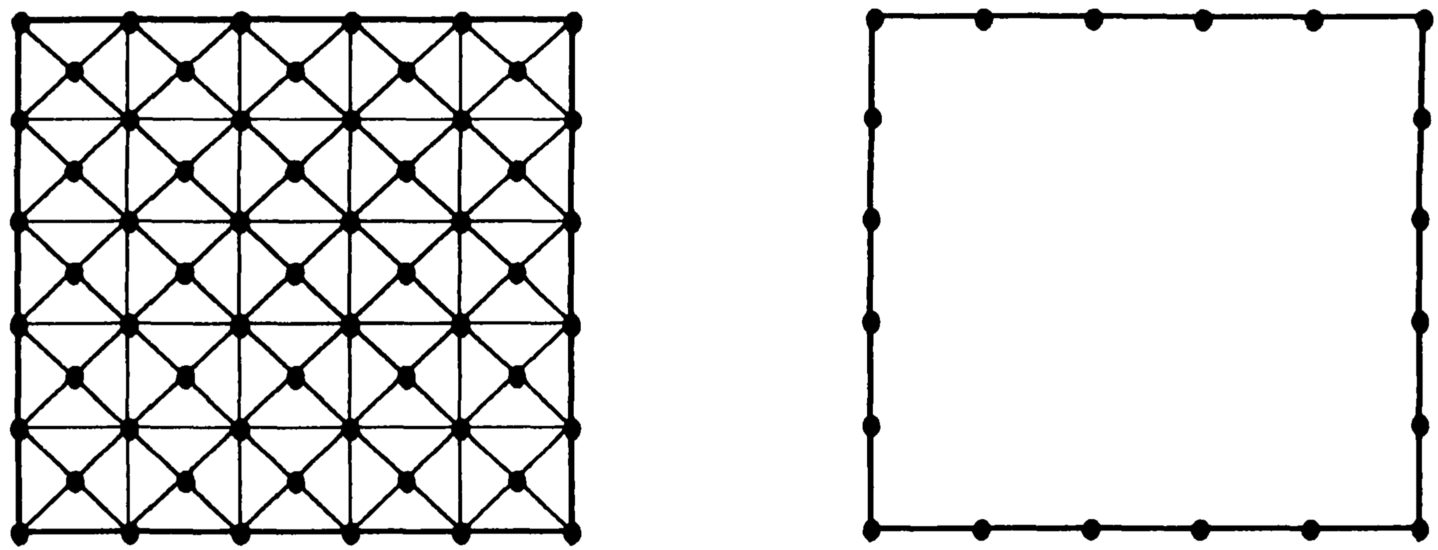

(a) Finite-element mesh (b) Boundary-element mesh

Figure 1.2 Finite-Element versus Boundary-Element Meshes

Chapter 2

A HORIZONTAL WELL

IN SINGLE-LAYER HOMOGENEOUS RESERVOIR

This chapter presents a review of the solutions for a horizontal well in a single-layer homogeneous reservoir. Both analytical and numerical solutions will be considered here. The analytical method reviewed in this study was developed by Jongkittinarukorn and Tiab (1996) and Thompsons et al. (1991). The numerical method is the boundary-element method developed by Koh (1993).

2.1 ANALYTICAL SOLUTION

Several mathematical models have been proposed in the literature to calculate pressure response at a horizontal well. Most of these models requires tremendous amounts of time to evaluate the pressure response.

Jongkittinarukorn and Tiab (1996) considered a horizontal well drilled in a box-shaped drainage volume, parallel to the y direction. Type curve matching techniques of pressure and pressure derivative to determine several reservoir parameters are presented in their works. A new techniques, known as direct synthesis, for interpreting the pressure behavior of a horizontal well without type-curve matching is presented. Characteristic points are obtained at intersections of various straight line portions of the pressure and pressure derivative curves, slopes and starting times of these straight lines. These points, slopes and times are then used with appropriate equations to solve directly for reservoir characteristics. A step-by-step procedure for calculating these parameters without type-curve matching is included in this paper. The productivity index equation is derived from the conventional pseudo steady state equation for a vertical well in a bounded reservoir.

The dimensions of the reservoir are: length (x direction) = a, width (y direction) = b, thickness (z direction) = h. The following assumptions are made:

(1) The boundaries of the drainage volume are sealed in x and y direction,

(2) The reservoir is homogeneous, and anisotropic with principle permeabilities k_x, k_y, k_z in x, y, and z directions respectively,

(3) A single-phase fluid with slightly compressible,

(4) The viscosity (μ) and formation volume factor (B) are constant,

(5) The initial pressure is uniform and is equal to P_i, and

(6) Gravity effects are neglected.

In this study, a horizontal well is considered to be a partially penetrating vertical well in a closed rectangular reservoir. A horizontal well can be considered to be a vertical well because gravity effect is neglected. First, the physical model is rotated 90^0 such that the well (in y direction) is vertical and x and z directions are on a horizontal plane. Then we remove all of the boundaries in x and z directions which will be taken into account later by using principle of superposition. There are three flow regimes:

(1) radial flow around the open interval (L),

(2) transition period during which the flow develop vertically yielding a spherical flow regime for centrally located open interval or a hemispherical flow for an open interval near the top or bottom boundary, and

(3) second radial flow over the entire formation thickness (b).

For a horizontal well in anisotropic reservoir, the following dimensionless terms are defined as:

$$P_D = \frac{\sqrt{k_x k_z}\, b(P_i - P_{wf})}{141.2 qB\mu} \tag{2.1}$$

$$t_D = \frac{0.0002637\sqrt{k_x k_z}\, t}{\phi\mu c_t \left[r_{wh}\right]^2} \tag{2.2}$$

$$t_{DA} = \frac{0.0002637\sqrt{k_x k_z}\, t}{\phi\mu c_t A} \tag{2.3}$$

$$r_D = \frac{r}{r_{wh}} \tag{2.4}$$

$$r_{wh} = \frac{r_w}{2}\left[\sqrt[4]{\frac{k_z}{k_x}} + \sqrt[4]{\frac{k_x}{k_z}}\right] \tag{2.5}$$

$$A = ah \tag{2.6}$$

$$r = \left[\frac{(x - x_o)^2}{\sqrt{k_x / k_z}} + \frac{(z - z_o)^2}{\sqrt{k_z / k_x}}\right]^{1/2} \tag{2.7}$$

$$X_D = 2x_o/a \tag{2.8}$$

$$Z_D = 2z_o/h \tag{2.9}$$

For a constant rate of production, assuming the reservoir is radially infinite, the pressure response at the wellbore is given by Streltsova (1981) as:

$$P_D = -\frac{1}{2}Ei(-\frac{1}{4t_D}) + s_p(t_D, r_{DD}) + \frac{s}{(L/b)} \tag{2.10}$$

where the pseudo-skin factor due to partial penetration is:

$$s_p(t_D, r_{DD}) = \frac{1}{\pi^2 b_p^{'2}} \sum_{n=1}^{\infty} \frac{1}{n^2}[\sin(n\pi b_2^{'}) - \sin(n\pi b_1^{'})]^2 W(u,\beta) \tag{2.11}$$

$$W(u,\beta) = \int_u^{\infty} \frac{1}{x} \exp(-x - \frac{\beta^2}{4x})dx \tag{2.12}$$

$$b_1^{'} = y_1/b \tag{2.13}$$

$$b_2^{'} = y_2/b \tag{2.14}$$

$$b_p^{'} = L/b = b_2^{'} - b_1^{'} \tag{2.15}$$

$$\beta = n\pi r_{DD} \tag{2.16}$$

$$u = \frac{r_D^2}{4t_D} \tag{2.17}$$

and

$$r_{DD} = \frac{r_{wh}}{b}\sqrt{\frac{k_y}{\sqrt{k_x k_z}}} \tag{2.18}$$

In order to determine the pressure response at a horizontal well in a closed boundary system, the principle of superposition in space is employed to account for four boundaries in both x and z directions. Therefore, the dimensionless pressure at the wellbore is:

$$P_D = P_{wD} + \sum_{i=1}^{\infty} P_{Di}$$

$$= -\frac{1}{2}Ei(-\frac{1}{4t_D}) + s_p(t_D, r_{DD}) + \frac{s}{(L/b)} + \sum_{i=1}^{\infty}\left(-Ei(-\frac{r_{Di}^2}{4t_D}) + s_p(t_D, r_{DDi})\right) \tag{2.19}$$

Since the radius of the partial-penetration influence is a function of reservoir length in y direction which is usually assumed to be a very big number compared to the formation thickness in z direction. Therefore, we need to include the pseudo skin at the image well. The radius of investigation of pseudo skin (s_p) is much larger than that of the Ei 's function. The pressure derivative of the above equation is:

$$P_D' = \frac{1}{2t_D}\exp\left[\frac{-1}{4t_D}\right] + \frac{d s_p}{d t_D} + \sum_{i=1}^{n}\left(\frac{1}{2t_D}\exp\left[\frac{-r_{Di}^2}{4t_D}\right] + \frac{d s_{pi}}{d t_D}\right) \tag{2.20}$$

Thompson et al. (1991) proposed an efficient algorithm for computing the bounded reservoir horizontal well pressure response with minimal computational effort. Their model is considered in this study and will be used to compare with the numerical solution.

A horizontal well with wellbore length L_w, shown Fig. 2.1, is drilled in closed box-shaped system with dimension $L_x*L_y*L_z$. The wellbore is located at ($x', y_1<y'<y_1+L_w, z'$). The reservoir under isothermal condition is assumed to have a slightly compressible fluid with constant viscosity. For a constant production rate, the pressure response is

$$P(x,y,z) = P_i - \int_0^t \frac{5.615q}{L_w \phi c_t} \Delta P_x \Delta P_y \Delta P_z d\tau \tag{2.21}$$

where (x,y,z) is any point within the reservoir except a well axis. For small value of τ, the instantaneous point source pressure drop is calculated as

$$\Delta P_x = \frac{1}{2\sqrt{\eta_x \pi\tau}} \sum_{n=-\infty}^{\infty} \sum_{i=1}^{2} \exp\left[-\frac{\left(x'+\{-1\}^i x-2nL_x\right)^2}{4\eta_x\tau}\right] \tag{2.22}$$

$$\Delta P_y = \frac{1}{2}\sum_{m=-\infty}^{\infty}\sum_{i=1}^{2}\left[\operatorname{erf}\left(\frac{L_w + 2y_1 + \{-1\}^i y - 2mL_y}{2\sqrt{\eta_y \tau}}\right) - \operatorname{erf}\left(\frac{y_1 - \{-1\}^i y - 2mL_y}{2\sqrt{\eta_y \tau}}\right)\right] \tag{2.23}$$

$$\Delta P_z = \frac{1}{2\sqrt{\eta_z \pi \tau}}\sum_{l=-\infty}^{\infty}\sum_{i=1}^{2}\exp\left[-\frac{\left(z' + \{-1\}^i z - 2nL_z\right)^2}{4\eta_z \tau}\right] \tag{2.24}$$

where the directional diffusivities are:

$$\eta_i = \frac{0.00633\, k_i}{\phi \mu c_t} \qquad \text{for } i = x,\ y, \text{ and } z \tag{2.25}$$

For large values of τ, Eqs. (2.23) - (2.25) can be replaced by the following equations, respectively.

$$\Delta P_x = \frac{1}{L_x} + \frac{2}{L_x}\sum_{n=1}^{\infty}\left[\cos\left(\frac{n\pi x}{L_x}\right)\cos\left(\frac{n\pi x'}{L_x}\right)\exp\left(\frac{-n^2\pi^2\eta_x \tau}{L_x^2}\right)\right] \tag{2.26}$$

$$\Delta P_y = \frac{L_w}{L_y} + \frac{4}{\pi}\sum_{m=1}^{\infty}\left[\frac{1}{m}\cos\left(\frac{m\pi\{L_w + 2y_1\}}{2L_y}\right)\sin\left(\frac{m\pi L_w}{2L_y}\right)\cos\left(\frac{m\pi y}{L_y}\right)\exp\left(\frac{-m^2\pi^2\eta_y \tau}{L_y^2}\right)\right] \tag{2.27}$$

$$\Delta P_z = \frac{1}{L_z} + \frac{2}{L_z}\sum_{l=1}^{\infty}\left[\cos\left(\frac{l\pi z}{L_z}\right)\cos\left(\frac{l\pi z'}{L_z}\right)\exp\left(\frac{-l^2\pi^2\eta_z \tau}{L_z^2}\right)\right] \tag{2.28}$$

Table 2.1 shows the criterion based on the minimum number of terms required for convergence between Eqs. (2.22) - (2.24) and (2.26) - (2.28). The small arbitrary tolerance is $\varepsilon \approx 10^{-12}$. In order to generate the pressure response, a point close to the well axis must be chosen since Eq. (2.21) is invalid on the well axis, due to its singularity.

The drawback of this model is the use of the line-source solution which assumes the wellbore radius approaches zero. Thus, the result for this model is invalid at very early time of production.

Clonts and Ramey (1986), Ozkan, Raghavan, and Joshi (1989), and Daviau et. al. (1988) developed the pressure response at the wellbore assuming that there is no pressure drop with the horizontal well. Their model is shown in Fig. 2.2. The dimensionless pressure response is

$$P_D(x_D, y_D, z_D, z_{wD}, L_D, t_D) = \frac{\sqrt{\pi}}{4}\sqrt{\frac{k_h}{k_v}}\int_0^{t_D}\left[\operatorname{erf}\left(\frac{\sqrt{\frac{k_h}{k_x}}+x_D}{2\sqrt{\tau}}\right)+\operatorname{erf}\left(\frac{\sqrt{\frac{k_h}{k_x}}-x_D}{2\sqrt{\tau}}\right)\right]*\left[\exp\left(-\frac{y_D^2}{4\tau}\right)\right]$$

$$\left[1+2\sum_{n=1}^{\infty}\exp(-n^2\pi^2L_D^2\tau)\cos(n\pi z_D)\cos(n\pi z_{wD})\right]\frac{d\tau}{\sqrt{\tau}} \tag{2.29}$$

where

$$P_D = \frac{k_h h(P_i - P)}{141.2qB\mu} \tag{2.30}$$

$$t_D = \frac{0.001055k_h t}{\phi\mu c_t L^2} \tag{2.31}$$

$$L_D = \frac{L}{2h}\sqrt{\frac{k_v}{k_h}} \tag{2.32}$$

$$x_D = \frac{2x}{L}\sqrt{\frac{k_h}{k_x}} \tag{2.33}$$

$$y_D = \frac{2y}{L}\sqrt{\frac{k_h}{k_v}} \tag{2.34}$$

$$z_D = \frac{z}{h} \tag{2.35}$$

$$z_{wD} = \frac{z_w}{h} \tag{2.36}$$

$$r_{wD} = \frac{2r_w}{L}\sqrt{\frac{k_h}{k_v}} \tag{2.37}$$

$$k_h = \sqrt{k_x k_y} \tag{2.38}$$

Goode and Thambynayagam (1987) indicated that a horizontal well may exhibit four regimes depending upon the reservoir geometries and the well properties. These four flow regimes are shown in Fig. 2.3.

Early-Time Radial Flow

This flow regime corresponds to the vertical radial flow perpendicular to the wellbore. The pressure drop at the wellbore is expressed as

$$P_i - P_{wf} = \frac{162.6qB\mu}{\sqrt{k_v k_y}L}\left[\log\left(\frac{\sqrt{k_v k_y}t}{\phi\mu c_t r_w^2}\right) - 3.23 + 0.868s\right] \tag{2.39}$$

The permeability and the skin can be calculated as

$$\sqrt{k_v k_y} = \frac{162.6qB\mu}{m_1 L} \tag{2.40}$$

$$s = 1.151\left[\frac{P_i - P_{1hr}}{m_1} - \log\left(\frac{\sqrt{k_v k_y}}{\phi\mu c_t r_w^2}\right) + 3.23\right]$$

where m_1 is the slope of the semi-log plot of P versus t and P_{1hr} is the pressure obtained by extrapolating the semi-log straight line to t = 1 hour. When the pressure disturbance reaches the top or bottom boundary, this flow regime is ended. The length of this flow regime is:

$$t_{e1} = \frac{190 d_z^{2.095} r_w^{0.095} \phi \mu c_t}{k_z} \qquad (2.41)$$

where d_z is the distance from the wellbore to the closest boundary.

Early-Time Linear Flow

Once the pressure transient reaches the top and bottom boundaries, the early-time linear flow regime may develop if the well is relatively long compared to the formation thickness. The pressure drop during this period can be expressed as

$$P_i - P_{wf} = \frac{8.128 qB\mu}{Lh} \sqrt{\frac{t}{\phi \mu c_t k_y}} + \frac{141.2 qB\mu}{L\sqrt{k_y k_z}} (s_z + s) \qquad (2.42)$$

where the pseudo-skin in z-direction is given as

$$s_z = \ln\left(\frac{h}{r_w}\right) + 0.25 \ln\left(\frac{k_y}{k_z}\right) - \ln\left(\sin\frac{180 z_w}{h}\right) - 1.838 \qquad (2.43)$$

The product of permeability and wellbore length square can be calculated as:

$$L^2 k_y = \left(\frac{8.128 qB}{h m_2}\right)^2 \frac{\mu}{\phi c_t} \qquad (2.44)$$

where m_2 is the slope of the straight line on the plot of ΔP versus $t^{0.5}$. The mechanical skin can be calculated as

$$s = \Delta P(t=0)\frac{L\sqrt{k_x k_y}}{141.2qB\mu} - s_z \tag{2.45}$$

where $\Delta P(t=0)$ is the value of the pressure drop at $t^{0.5} = 0$. This flow regime is ended at

$$t_{e2} = \frac{20.8\phi\mu c_t L^2}{k_x} \tag{2.46}$$

Pseudo-Radial Flow

This flow regime starts at

$$t_{s3} = \frac{1230 L^2 \phi\mu c_t}{k_x} \tag{2.47}$$

When the pressure disturbance reaches one of the outer boundaries, this flow period is ended. This flow regime may not develop if the top or bottom boundary is flowing boundary. The pressure response is expressed as

$$P_i - P_{wf} = \frac{162.6qB\mu}{\sqrt{k_x k_y}h}\left[\log\left(\frac{k_x t}{\phi\mu c_t L^2}\right) - 2.023\right] + \frac{141.2qB\mu}{L\sqrt{k_x k_y}}(s_z + s) \tag{2.48}$$

The equivalent horizontal permeability can be calculated as

$$\sqrt{k_x k_y} = \frac{162.6qB\mu}{m_3 h} \tag{2.49}$$

where m_3 is the slope of the semi-log straight line. The skin factor is

$$s = \frac{1.151L}{h}\sqrt{\frac{k_y}{k_x}}\left[\frac{P_i - P_{1.hr}}{m_3} - \log\left(\frac{k_x}{\phi\mu c_t L^2}\right) + 2.023\right] - s_z \tag{2.50}$$

Late-Time Linear Flow

This flow regime develops when the radius of investigation reaches the lateral boundaries. The pressure drop during this period is expressed as

$$P_i - P_{wf} = \frac{8.128qB}{2x_e h}\sqrt{\frac{\mu t}{k_x \phi c_t}} + \frac{141.2qB\mu}{L\sqrt{k_y k_z}}(s_x + s_z + s) \tag{2.51}$$

where x_e is the half width of the reservoir.

Equation	Minimum Number of Terms	Equation	Minimum Number of Terms
(2.2)	$1+\frac{\sqrt{-\sqrt{\frac{k_x}{k_y}\tau}\ln\left(2\varepsilon\sqrt{\pi\tau\sqrt{\frac{k_x}{k_y}}}\right)}}{2L_x/L_w}$	(2.6)	$\frac{2L_x}{\pi L_w}\sqrt{\frac{-\ln\left(\varepsilon\frac{2L_x}{L_w}\right)}{\tau\sqrt{\frac{k_x}{k_y}}}}$
(2.3)	$1+\frac{10\sqrt{\tau\sqrt{\frac{k_y}{k_x}}}}{2L_y/L_w}$	(2.7)	$\frac{20L_y}{\pi L_w}\sqrt{\frac{1}{\tau}\sqrt{\frac{k_x}{k_y}}}$
(2.4)	$1+\frac{\sqrt{-\sqrt{\frac{k_x k_z}{k_y k_x}\tau}\ln\left(2\varepsilon\sqrt{\pi\tau\sqrt{\frac{k_x k_z}{k_y k_x}}}\right)}}{2L_z/L_w}$	(2.8)	$\frac{2L_z}{L_w}\sqrt{\frac{-\ln(2\varepsilon L_z/L_w)}{\sqrt{\frac{k_x k_z}{k_y k_x}\tau}}}$

Table 2.1 Minimum Number of Terms Required for Convergence

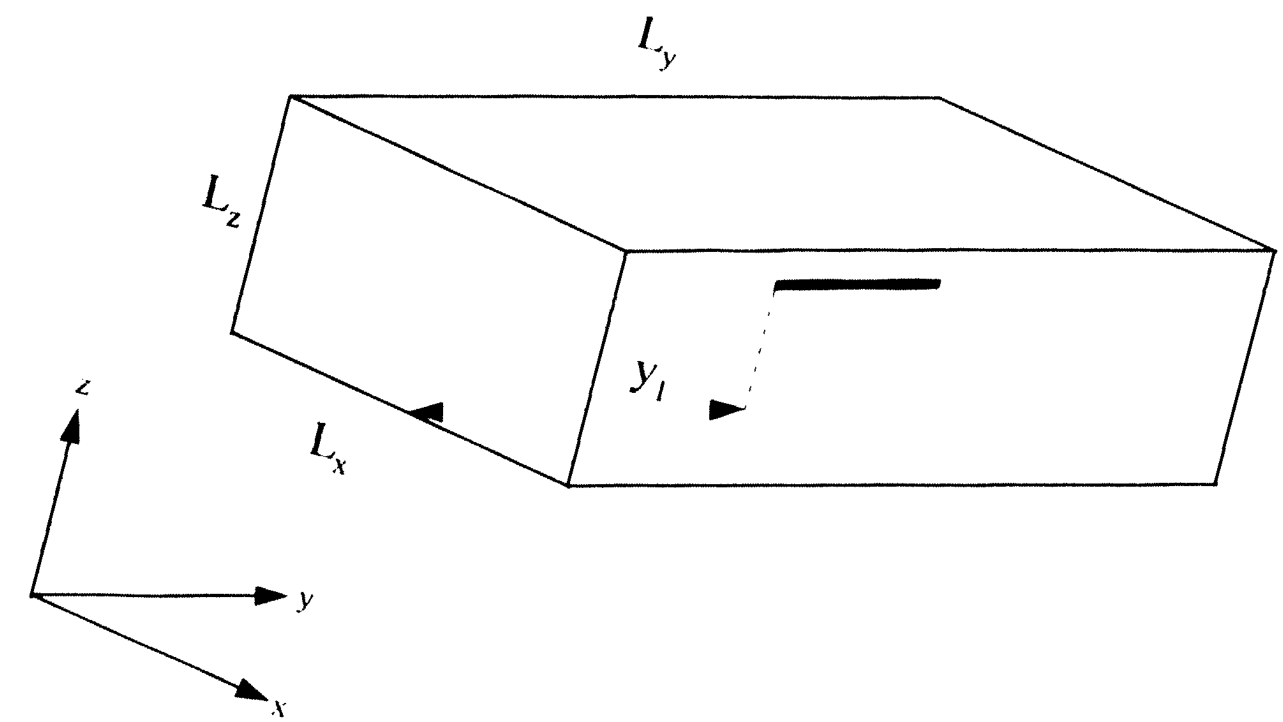

Figure 2.1 A Horizontal Well of Thompson et. al. (1991)

in a Bounded Reservoir

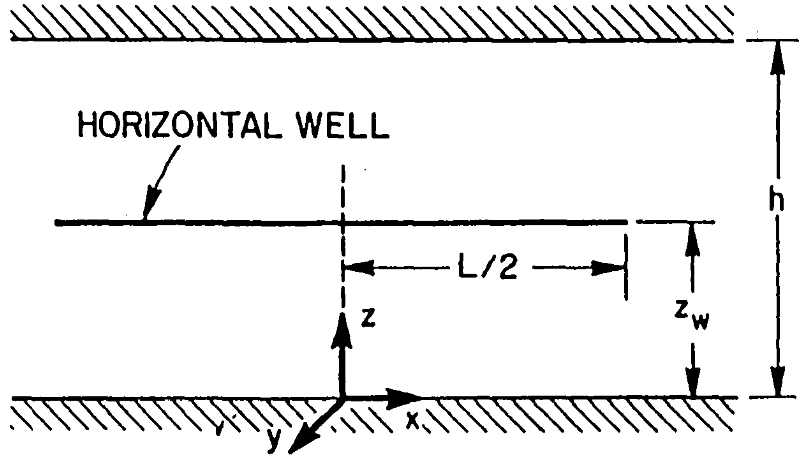

Figure 2.2 A Horizontal Well Model of Clonts and Ramey (1986), Ozkan, Raghavan, and Joshi (1989), and Daviau et. al. (1988)

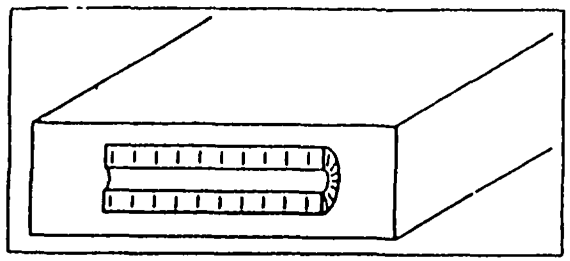

(a) Early-time radial flow

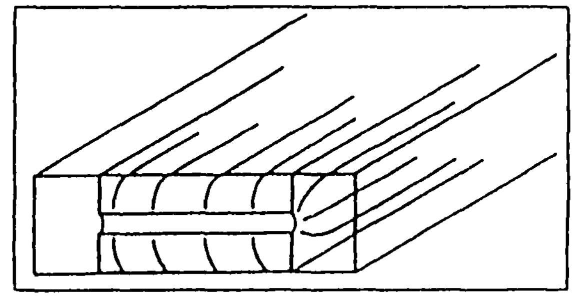

(b) Early-time linear flow

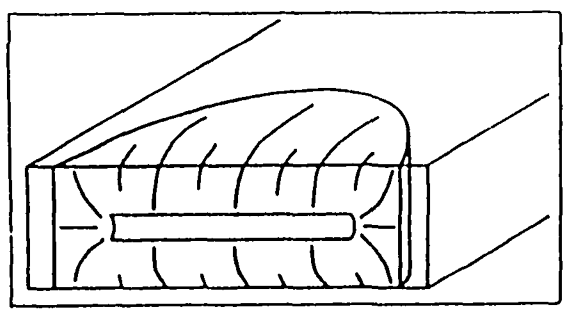

(c) Pseudo-radial flow

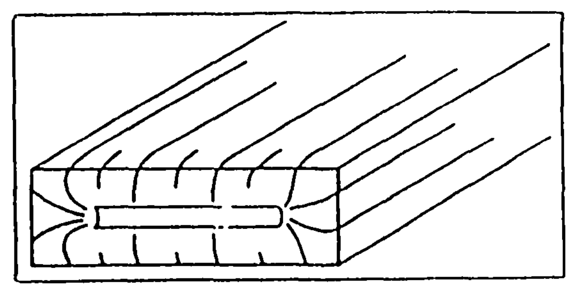

(d) Late-time linear flow

Figure 2.3 Flow Regimes in A Horizontal Well (after Goode and Thambynayagam, 1987)

2.2 NUMERICAL SOLUTION

2.2.1) A Governing Differential Equation for Homogeneous Reservoir

The continuity equation of isothermal flow of a single-phase fluid through a homogeneous porous material can be derived by considering a small element shown in Fig. 2.2. The mass balance of this element has the following form.

$$\{\text{rate of accumulation of mass}\} = \{\text{rate of mass flow in}\} - \{\text{rate of mass flow out}\} \quad (2.52)$$

where

$$\{\text{ rate of accumulation of mass }\} = \frac{\rho\phi|_{t+\Delta t} - \rho\phi|_t}{\Delta t} \Delta x_1 \Delta x_2 \Delta x_3 \quad (2.53)$$

$$\{\text{ rate of mass flow in }\} = \rho u_{x1} + \rho u_{x2} + \rho u_{x3} \quad (2.54)$$

and

$$\{\text{ rate of mass flow out }\} = \rho u_{x1} + \Delta(\rho u_{x1}) + \rho u_{x2} + \Delta(\rho u_{x2}) + \rho u_{x3} + \Delta(\rho u_{x3}) \quad (2.55)$$

Substitute Eqs. (2.53) - (2.55) into (2.52) and rearrange as:

$$-\frac{\rho\phi|_{t+\Delta t} - \rho\phi|_t}{\Delta t} \Delta x_1 \Delta x_2 \Delta x_3 = \Delta(\rho u_{x1}) + \Delta(\rho u_{x2}) + \Delta(\rho u_{x3}) \quad (2.56)$$

Divide Eq. (2.56) by $\Delta x_1 \Delta x_2 \Delta x_3$ and take the limit as $\Delta x_1 \Delta x_2 \Delta x_3$ and $\Delta t \rightarrow 0$ yielding in

:

$$\frac{\partial(\rho u_{x1})}{\partial x_1} + \frac{\partial(\rho u_{x2})}{\partial x_2} + \frac{\partial(\rho u_{x3})}{\partial x_3} = -\frac{\partial(\rho\phi)}{\partial t}$$

$$= \vec{\nabla} \bullet (\rho\bar{u}) \quad (2.57)$$

If we assume that x_1 and x_2 are horizontal so that gravity force is only on x_3 direction, a flow potential is defined as

$$\psi = gx_3 + \int_{P_0}^{P} \frac{dP}{\rho(P)} \tag{2.58}$$

The general darcy's law representing the relationship between the volumetric flux and the gradient of flow potential is

$$u_i = -\frac{\rho}{\mu}\left(k_{i1}\frac{\partial\psi}{\partial x_1} + k_{i2}\frac{\partial\psi}{\partial x_2} + k_{i3}\frac{\partial\psi}{\partial x_3}\right) \text{ for } i = 1, 2, \text{ and } 3 \tag{2.59}$$

which can be written in matrix form as

$$\vec{u} = \begin{Bmatrix} u_1 \\ u_2 \\ u_3 \end{Bmatrix} = -\frac{\rho}{\mu}\begin{bmatrix} k_{11} & k_{12} & k_{13} \\ k_{21} & k_{22} & k_{23} \\ k_{31} & k_{32} & k_{33} \end{bmatrix}\begin{Bmatrix} \dfrac{\partial\psi}{\partial x_1} \\ \dfrac{\partial\psi}{\partial x_2} \\ \dfrac{\partial\psi}{\partial x_3} \end{Bmatrix}$$

$$= -\frac{\rho}{\mu}\bar{K}\bar{\nabla}\psi \tag{2.60}$$

The direction of x_1, x_2, and x_3 can be selected such that the permeability tensor, $\overleftrightarrow{K}$, becomes a diagonal matrix. This direction is called the principal axes of the porous medium. Let 's denote this new axes by X, Y, and Z. Then the permeability tensor becomes

$$\bar{K} = \begin{bmatrix} k_X & 0 & 0 \\ 0 & k_Y & 0 \\ 0 & 0 & k_Z \end{bmatrix} \tag{2.61}$$

where k_x, k_y, and k_z are the principal permeabilities in x, y, and z directions, respectively. Neglecting gravity effects, substitute Eq. (2.60) into (2.57) resulting in

$$\vec{\nabla} \bullet \left(\frac{\rho}{\mu} \vec{K} \vec{\nabla} P \right) = \frac{\partial(\rho\phi)}{\partial t} \tag{2.62}$$

For a slightly compressible fluid with constant compressibility, c_t, the density can be expressed as:

$$\rho = \rho_0 \exp\{c_t(P - P_0)\} \tag{2.63}$$

where ρ_0 is the density at P_0. If we assume that ϕ and μ are constant, introduce Eq. (2.63) into (2.62) yields

$$k_X \frac{\partial^2 P}{\partial X^2} + k_Y \frac{\partial^2 P}{\partial Y^2} + k_Z \frac{\partial^2 P}{\partial Z^2} = \phi \mu c_t \frac{\partial P}{\partial t} \tag{2.64}$$

Define the contracted coordinate as

$$x = X, \tag{2.65}$$

$$y = Y \sqrt{\frac{k_X}{k_Y}}, \tag{2.66}$$

and

$$z = z \sqrt{\frac{k_X}{k_Z}} \tag{2.67}$$

Introducing Eqs. (2.65) - (2.67) into Eq. (2.64) yields

$$\frac{\partial^2 P}{\partial x^2} + \frac{\partial^2 P}{\partial y^2} + \frac{\partial^2 P}{\partial z^2} = \frac{\phi \mu c}{k_x} \frac{\partial P}{\partial t} \tag{2.68}$$

Define dimensionless space variables, pressure and time as

$$x_D = \frac{x}{\sqrt{A}}, \tag{2.69}$$

$$y_D = \frac{y}{\sqrt{A}},\tag{2.70}$$

and $$z_D = \frac{z}{\sqrt{A}}\tag{2.71}$$

$$P_D = \frac{(P_{ini} - P)}{\tilde{P}}\tag{2.72}$$

$$t_D = \frac{k_x t}{\phi \mu c_t A}\tag{2.73}$$

where P_i is the initial porous medium pressure. A and $\tilde{P}$ are normalizing factors with dimensions of $[L^2]$ and $[F / L^2]$, respectively. Substitute Eqs. (2.72) - (2.73) into Eq. (2.68) yields the diffusivity equation.

$$\frac{\partial^2 P_D}{\partial x_D^2} + \frac{\partial^2 P_D}{\partial y_D^2} + \frac{\partial^2 P_D}{\partial z_D^2} = \frac{\partial P_D}{\partial t_D}$$

$$= \nabla^2 P_D\tag{2.74}$$

The reservoir. initially, has a uniform pressure condition which can be expressed in dimensionless form as

$$P_D(x_D, y_D, z_D, 0) = 0 \quad \text{at } t_D = 0\tag{2.75}$$

Two types of boundary conditions are considered in fluid through porous media. The first type is Dirichlet, a constant-pressure boundary condition, where the pressure at the boundary is assumed to be constant.

$$P_D = \hat{P}_D\tag{2.76}$$

where $\hat{P}_D$ is the prescribed value of P_D.

The second type is Neumann, flow or no-flow boundary condition, where the flux is prescribed.

$$P'_D = \frac{\partial P_D}{\partial n}$$

$$= \vec{\nabla} P_D \bullet \vec{n}$$

$$= \hat{P}'_D \tag{2.77}$$

where $\vec{n}$ is the unit outward normal vector at the boundary and $\hat{P}'_D$ is the assigned value of P'_D.

2.2.2) Boundary Element Algorithm

Koh (1993) developed a boundary-element algorithm for modeling 3-D fluid flow through homogeneous porous media for both transient and steady states. The Laplace transform is applied to remove the time variable. Introducing Laplace transform to Eqs. (2.51) - (2.54) yields

$$\frac{\partial^2 \bar{P}_D}{\partial x_D^2} + \frac{\partial^2 \bar{P}_D}{\partial y_D^2} + \frac{\partial^2 \bar{P}_D}{\partial z_D^2} = s\bar{P}_D \tag{2.78}$$

$$\bar{P}_D = \frac{\hat{P}_D}{s} \tag{2.79}$$

$$\bar{P}'_D = \frac{P'_D}{s} \tag{2.80}$$

Eq. (2.78) is a three-dimensional Helmholtz equation for the diffusivity equation, where s is a transform parameter and $\bar{P}_D$ represent P_D in Laplace domain.

A combination of a weighted residual technique and an integration by parts is the fundamental integral statements of the boundary element method. This process reduces the order of the continuity required for the $\overline{p}_D$. Apply this technique to the solution of a three-dimensional Helmholtz equation for the diffusivity equation, Eq. 2.78, as

$$\int_{\Omega}\left(\frac{\partial^2 W}{\partial x_D^2}+\frac{\partial^2 W}{\partial y_D^2}+\frac{\partial^2 W}{\partial z_D^2}-sW\right)\overline{p}_D\, d\Omega \;+\; \int_{\Gamma}\left(W\frac{\partial \overline{P}_D}{\partial n}-\overline{P}_D\frac{\partial W}{\partial n}\right)d\Gamma = 0 \qquad (2.81)$$

where Ω is the domain of porous media, W is a weighting function, and Γ is the boundary of the porous media.

The free space Green's function, $\overline{G}$, is chosen as the weighting function where

$$\overline{G}(r_D,s) = \frac{\exp\left(-r_D\sqrt{s}\right)}{4\pi r_D}$$

$$= W \qquad (2.82)$$

where r_D is the dimensionless distance between the field point (x_D, y_D, z_D) and the source point $\left(x_D^o, y_D^o, z_D^o\right)$. Substitute the free space Green's function, $\overline{G}$, into Eq. (2.81) and rearrange as

$$\overline{P}_D(r_D,s) = \int_{\Gamma}\left(\overline{G}\frac{\partial \overline{P}_D}{\partial n}-\overline{P}_D\frac{\partial \overline{G}}{\partial n}\right)d\Gamma \qquad (2.83)$$

which is only valid when the source point $\left(x_D^o, y_D^o, z_D^o\right)$ is in the domain of interest, Ω. This equation was modified by Koh (1993) to handle the situation when the source point is on the boundary yielding the boundary integral equation.

$$\omega\,\overline{P}_D(r_D,s) = \int_{\Gamma}\frac{e^{-\sqrt{s}r_D}}{r_D}\left[\overline{P}'_D+\frac{d_{Dn}}{r_D}\left(\sqrt{s}+\frac{1}{r_D}\right)\overline{P}_D\right]d\Gamma \qquad (2.84)$$

where

$$\omega = 4\pi \qquad \text{for } \left(x_D^o, y_D^o, z_D^o\right) \in \Omega \tag{2.85}$$

$$\omega = \omega_0 \qquad \text{for } \left(x_D^o, y_D^o, z_D^o\right) \in \Gamma \tag{2.86}$$

where ω_0 is the solid angle subtended at the boundary source point by its immediate neighborhood within the domain. The normal dimensionless distance from the source point to the field point is expressed as

$$d_{Dn} = \vec{r}_D \bullet \vec{n} \tag{2.87}$$

where $\vec{r}_D$ is a vector from the source point to the field point and $\vec{n}$ is a unit outward normal vector at the boundary.

The numerical method is necessary to evaluate the boundary integral equation, Eq. (2.84). Thus, the boundary (Γ) is discretized into several elements. The isoparametric linear triangular elements are chosen by Koh (1993). The discretized form of the boundary integral equation, Eq. (2.84), for source point i on the boundary is

$$\omega_0^i \overline{P}_D^i = \sum_{j=1}^{N_e} \int_{\Gamma_j} \frac{e^{-\sqrt{s}r_D}}{r_D}\left[\overline{P}'_D + \frac{d_{Dn}}{r_D}\left(\sqrt{s} + \frac{1}{r_D}\right)\overline{P}_D\right] d\Gamma \qquad \text{for } i = 1, 2, \ldots, N_n \tag{2.88}$$

where N_e and N_n is the number of elements and number of nodes, respectively, on the boundary (Γ). Eq. (2.88) can be expressed in matrix form as

$$[H]\,\{\overline{P}_D\} = [G]\,\{\overline{P}'_D\} \tag{2.89}$$

where [H] and [G] are $N_n \times N_n$ matrices and $\{\overline{P}_D\}$ and $\{\overline{P}'_D\}$ are vectors of length N_n for $\overline{P}_D$ and $\overline{P}'_D$, respectively. The above equations can be solved once the N_n boundary conditions are prescribed.

Once all values of $\overline{P}_D$ and $\overline{P}'_D$ on the boundary are know, the value of $\overline{P}_D$ at any point i in the domain Ω can be calculated from Eq. (2.88) by locating a source point at the point i.

$$4\pi \overline{P}^i_D = \sum_{j=1}^{N_e} \int_{\Gamma_j} \frac{e^{-\sqrt{s}r_D}}{r_D} \left[\overline{P}'_D + \frac{d_{Dn}}{r_D} \left(\sqrt{s} + \frac{1}{r_D} \right) \overline{P}_D \right] d\Gamma \tag{2.90}$$

The solutions $(\overline{P}_D)$ to Eqs. (2.88) and (2.90) are in Laplace domain. Stehfest's algorithm is chose to invert the solutions to the real space solutions (P_D). Koh (1993) recommended to use the number of summation terms (N_s) to be 8 which yields reasonably accurate results. The value of P_D at any point in the domain can be calculated as

$$P_{Di}(t_D) = \frac{\ln 2}{t_D} \sum_{k=1}^{8} V_k \overline{P}_{Di}(s(k)) \tag{2.91}$$

where

$$V_k = (-1)^{4+k} \sum_{m=\mathrm{int}\left[\frac{1}{2}(k+1)\right]}^{\min(k,4)} \frac{m^4(2m)!}{(4-m)!m!(m-1)!(k-m)!(2m-k)!} \tag{2.92}$$

and the transform parameter is expressed as

$$s(k) = \frac{\ln 2}{t_D} k \tag{2.93}$$

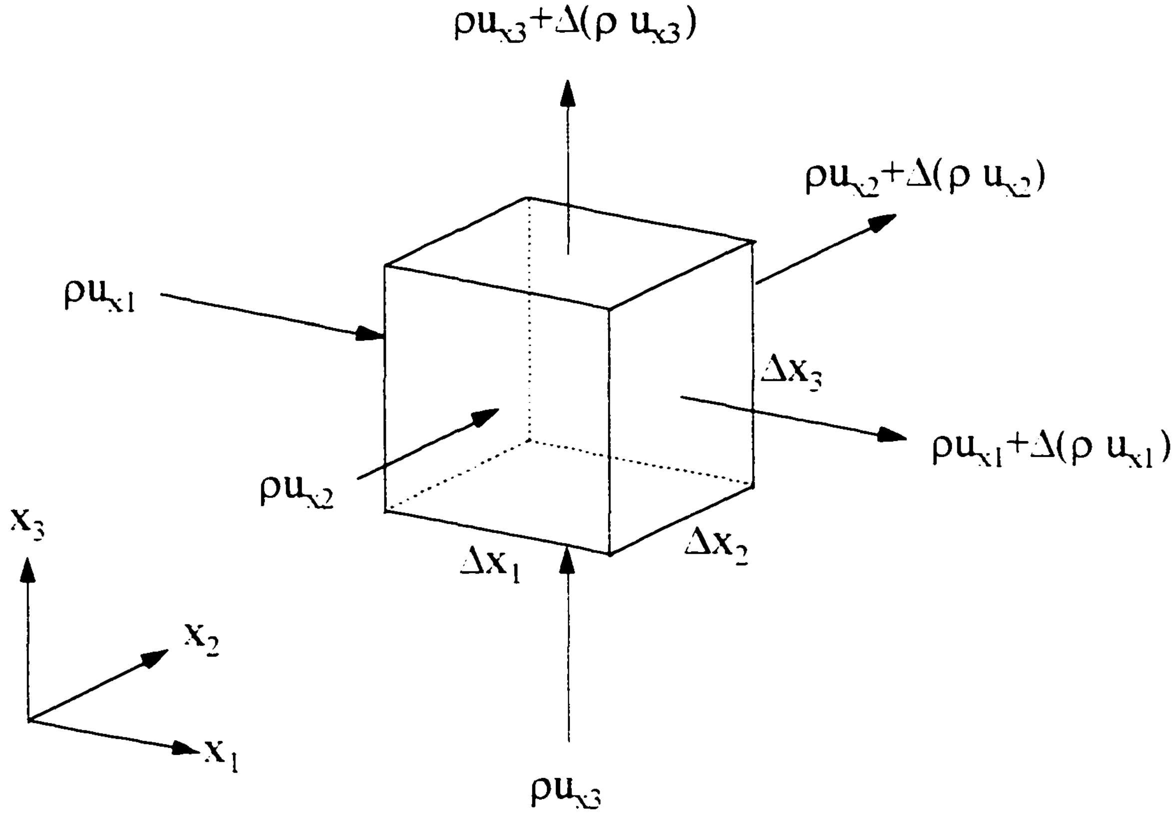

Figure 2.4 A Small Element of Homogeneous Porous Material

Used for Mass Balance Equation

Chapter 3

A HORIZONTAL WELL IN MULTI-LAYER RESERVOIR

3.1 ANALYTICAL SOLUTION

The only analytical solution available in the literature for a horizontal well in multi-layer reservoir with cross flow was proposed by Kuchuk and Habashy (1996). A reservoir consisting of n layers, shown in Fig. 3.1, is infinite in x and y direction and is layered in the z direction. A horizontal well is completed in layer k. The fluid in each layer is assumed to have slightly compressibility and constant viscosity. The pressure response at the wellbore is

$$P_D = 2\int_0^{t_D} g_w(r_{wD}, \tau)d\tau \tag{3.1}$$

where

$$P_D = \frac{2\sqrt{(k_x k_z)_k}\, L_w}{141.2 q \mu_k}(P_i - P_w) \tag{3.2}$$

$$t_D = \frac{0.0002637(k_x)_k}{(\phi\mu c_t)_k L_w^2} t \tag{3.3}$$

$$r_{wD} = \frac{r_w}{2 L_w}\left[\sqrt{\left(\frac{k_x}{k_y}\right)_k} + \sqrt{\left(\frac{k_y}{k_z}\right)_k}\right] \tag{3.4}$$

$g_w(r_{wD}, t_D)$ is an impulse response for a horizontal well and L_w is a half open length of the wellbore. The subscript k denotes the properties of the source layer. Eq. (3.1) can be expressed in the Laplace domain as

$$\bar{P}_D = 2\frac{\bar{g}_w(r_{wD}, s)}{s} \tag{3.5}$$

where s is the transform parameter. The dimensionless impulse wellbore response is

$$\bar{g}_w(r_{wD}, s) = \bar{g}_{wu}(r_{wD}, s) + \frac{4}{\pi^2}\int_0^\infty \int_0^\infty \left(\frac{\sin^2(\alpha)}{\alpha^2}\bar{\bar{G}}_h(s, \alpha, \beta)\right) d\alpha d\beta \tag{3.6}$$

where the unbounded horizontal wellbore solution is given as

$$\bar{g}_{wu}(r_{wD}, s) = \frac{1}{2}\left[\frac{K_0(r_{wD}\sqrt{s})}{r_{wD}\sqrt{s}K_1(r_{wD}\sqrt{s})} - \frac{1-\exp(-2\sqrt{s})}{2\sqrt{s}} - E_1(2\sqrt{s}) \right] \tag{3.7}$$

and the homogeneous solution is given as

$$\bar{\bar{G}}_h(s, \alpha, \beta) = \frac{\pi}{4\upsilon_k}\frac{1}{\left[1-(\zeta_u)_k(\zeta_d)_k \exp(-2\upsilon_k h_{Dk})\right]}$$

$$* \left\{\left[1+(\zeta_d)_k \exp(-2\upsilon_k z_{wD})\right](\zeta_u)_k \exp(-2\upsilon_k z_{sD})\right.$$

$$\left. +\left[1+(\zeta_u)_k \exp(-2\upsilon_k z_{sD})\right](\zeta_d)_k \exp(-2\upsilon_k z_{wD})\right\} \tag{3.8}$$

where

$$\upsilon_i = \sqrt{\frac{\left[\alpha^2+(\lambda_y)_i\beta^2+s/\kappa_i\right]}{(\lambda_z)_i}} \tag{3.9}$$

$$\kappa_i = \left(\frac{k_x}{\phi\mu c_t}\right)_i \Big/ \left(\frac{k_x}{\phi\mu c_t}\right)_k \tag{3.10}$$

$$h_{Dk} = \sqrt{\left(\frac{k_x}{k_z}\right)_k} \frac{h_k}{L_w} \tag{3.11}$$

$$z_{wD} = \sqrt{\left(\frac{k_x}{k_z}\right)_k} \frac{z_w}{L_w} \tag{3.12}$$

$$z_{sD} = \sqrt{\left(\frac{k_x}{k_z}\right)_k} \frac{z_s}{L_w} \tag{3.13}$$

An upgoing global reflection coefficient is

$$(\zeta_u)_i = \frac{R_{i,i-1} + (\zeta_u)_{i-1} \exp(-2\upsilon_{i-1} h_{D,i-1})}{1 + R_{i,i-1} (\zeta_u)_{i-1} \exp(-2\upsilon_{i-1} h_{D,i-1})} \qquad \text{for } i = 1, 2, \ldots, k \tag{3.14}$$

For the top layer.

$$(\zeta_u)_1 = 1 \qquad \text{for a no-flow boundary}$$

$$= -1 \qquad \text{for a constant-pressure boundary} \tag{3.15}$$

An downgoing global reflection coefficient has the same relation as the upgoing global reflection coefficient. The local reflection coefficient in Eq. (3.14) is

$$R_{i,i-1} = \frac{\upsilon_i - \gamma_{i-1,i} \upsilon_{i-1}}{\upsilon_i + \gamma_{i-1,i} \upsilon_{i-1}} \tag{3.16}$$

where

$$\gamma_{i-1,i} = \frac{(k_z/\mu)_{i-1}}{(k_z/\mu)_i} \tag{3.17}$$

The local reflection coefficient equals 1 if the (i-1) th layer is a no-flow boundary and equals -1 if it is a constant-pressure boundary

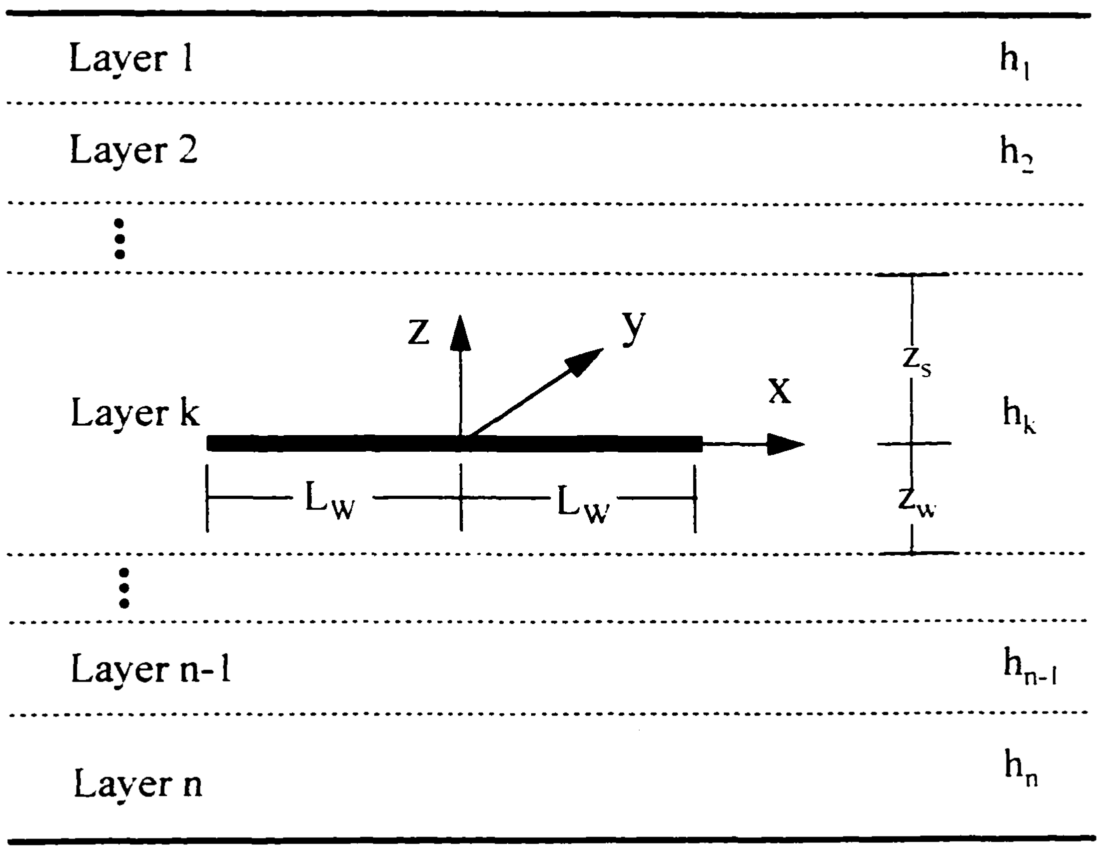

Figure 3.1 Horizontal well model by Kuchuk and Habashy

3.2 NUMERICAL SOLUTION

3.2.1) Subregions Technique for Anisotropic Layered Reservoirs

In chapter 2. the boundary element algorithm have been formulated for a homogeneous porous reservoir. In realistic. reservoirs are not homogeneous and layered due the depositional environment. These problems can be solved by using the previous formulation of boundary element algorithm and some continuity or compatibility conditions.

Let 's consider an n-layer reservoir. shown in Fig. 3.2. with crossflow where the reservoir is layered in the z direction. The reservoir is bounded in x and y directions. Each layer can have different rock and fluid properties with the following assumptions.

(1) the system is under isothermal condition.

(2) homogeneous and anisotropic with principle permeabilities k_{xi}, k_{yi}, and k_{zi}.

(3) a single-phase fluid with slightly compressible.

(4) the viscosity (μ) and formation volume factor (B) are constant.

(5) the initial pressure is uniform and equals to P_{ini}, and

(6) the gravity effects are neglected.

First. the reservoir is diviled into several layers. Each layer can be considered as a homogeneous porous medium. The system of equations formulated for each homogeneous layer plus the continuity conditions over the interface boundaries create a system that can be solved when the boundary conditions are prescribed.

The diffusivity equation for layer i is:

$$\frac{\partial^2 P_{Di}}{\partial x_D^2}+\frac{\partial^2 P_{Di}}{\partial y_D^2}+\frac{\partial^2 P_{Di}}{\partial z_D^2}=\frac{(k_x/\phi)_1}{(k_x/\phi)_i}\frac{\partial P_{Di}}{\partial t_D} \qquad \text{in } \Omega_i \quad \text{for } i = 1, 2, \ldots, n \tag{3.18}$$

with the Dirichlet boundary condition

$$P_{Di} = \hat{P}_D \qquad \text{on } \Gamma_{i,1} \qquad \text{for } i = 1, 2, \ldots, n \tag{3.19}$$

and the Neumann boundary condition

$$P'_D = \hat{P}_D \qquad \text{on } \Gamma_{i,2} \qquad \text{for } i = 1, 2, \ldots, n \tag{3.20}$$

where

$$\Gamma_i = \Gamma_{i,1} + \Gamma_{i,2} \qquad \text{for } i = 1, 2, \ldots, n \tag{3.21}$$

Define the normalizing factors as the followings.

$$A = r_{ws}^2 \tag{3.22}$$

$$\tilde{p} = \frac{141.2qB\mu}{k_{x,1}L_{ws}} \tag{3.23}$$

where r_{ws} and L_{ws} is a wellbore radius and wellbore length, respectively, in the lowest layer containing a wellbore. Thus, the dimensionless quantities, in field units, become

$$P_{Di} = \frac{k_{x,1}L_{ws}}{141.2qB\mu}(P_{ini} - P_i) \qquad \text{for } i = 1, 2, \ldots, n \tag{3.24}$$

$$t_D = \frac{0.0002637k_{x,1}}{\phi_1 \mu c_t r_{ws}^2}t \tag{3.25}$$

The wellbore condition considered in this study is

(1) The pressure is constant along the wellbore which can be expressed as

$$P_D(x_D, y_D, z_D, t_D) = P_{wD}(t_D) \tag{3.26}$$

(2) The flow rate is constant.

$$q = \int_0^{L_w}\int_0^{2\pi}(u_r r_w)d\theta dl \qquad (3.27)$$

which can be discretized as

$$q = 2\pi r_w L_w * \sum_{i=1}^{m}(w_i u_{r,i}) \qquad (3.28)$$

where w_i is a fraction of wellbore area covered by node i. Hence,

$$0 \le w_i \le 1 \qquad \text{for } i = 1, 2, \ldots, n \qquad (3.29)$$

$$\sum_{i=1}^{m} w_i = 1 \qquad (3.30)$$

The value of $u_{r,i}$ can be calculated by using the equation, (A.40), derived in Appendix A which expresses the value of radial velocity in term of normal dimensionless pressure derivative.

Consider an interface boundary between layers i and i+1, shown in Fig. 3.3. Two compatibility conditions are required at the interface boundary. First, the potential is continuous across the interface, $\Gamma_{i,i+1}$, which can be expressed as

$$P_i = P_{i+1} \qquad \text{on } \Gamma_{i,i+1} \qquad \text{for } i = 1, 2, \ldots, n-1 \qquad (3.31)$$

or in dimensionless form as

$$(P_D)_i = (P_D)_{i+1} \qquad \text{on } \Gamma_{i,i+1} \qquad \text{for } i = 1, 2, \ldots, n-1 \qquad (3.32)$$

Second, the amount of fluid flowing out of layer 'i' across any small area, ΔA, must equal the amount of fluid flowing into layer 'i+1'.

$$u_{n,i} * \Delta A = u_{n,i+1} * \Delta A \qquad \text{for } i = 1, 2, \ldots, n-1 \qquad (3.33)$$

which can be expressed in term of the normal derivative as

$$k_{x,i}\frac{\partial P_i}{\partial n}\Delta A = k_{x,i-1}\frac{\partial P_{i-1}}{\partial n}\Delta A \qquad \text{for } i = 1, 2, \ldots, n-1 \tag{3.34}$$

Eq. (3.34) can be written in term of dimensionless pressure gradient as

$$k_{x,i}\vec{\nabla} P_{Di} = k_{x,i-1}\vec{\nabla} P_{Di-1} \qquad \text{for } i = 1, 2, \ldots, n-1 \tag{3.35}$$

Along the interface boundary, the unit outward normal vector is

$$\bar{n}_i = -\bar{n}_{i-1} = \bar{n} \qquad \text{for } i = 1, 2, \ldots, n-1 \tag{3.36}$$

Multiply Eq. (3.36) by Eq. (3.34) and rearrange as

$$k_{x,i}P'_{Di} + k_{x,i+1}P'_{Di+1} = 0 \qquad \text{on } \Gamma_{i,i+1} \qquad \text{for } i = 1, 2, \ldots, n-1 \tag{3.37}$$

Apply Laplace transform to Eqs. (3.18) - (3.20), (3.26), and (3.37) yields, respectively,

$$\frac{\partial^2 \bar{P}_{Di}}{\partial x_D^2} + \frac{\partial^2 \bar{P}_{Di}}{\partial y_D^2} + \frac{\partial^2 \bar{P}_{Di}}{\partial z_D^2} = \frac{(k_x/\phi)_1}{(k_x/\phi)_i} s\bar{P}_{Di}$$

$$\text{for } (x_D, y_D, z_D) \in \Omega_i \qquad \text{for } i = 1, 2, \ldots, n \tag{3.38}$$

$$\bar{P}_{Di} = \frac{\hat{P}_{Di}}{s} \qquad \text{on } \Gamma_{i1} \qquad \text{for } i = 1, 2, \ldots, n \tag{3.39}$$

$$\bar{P}'_{Di} = \frac{\hat{P}_{Di}}{s} \qquad \text{on } \Gamma_{i2} \qquad \text{for } i = 1, 2, \ldots, n \tag{3.40}$$

$$(\bar{P}_D)_i = (\bar{P}_D)_{i+1} \text{ on } \Gamma_{i,i+1} \qquad \text{for } i = 1, 2, \ldots, n-1 \tag{3.41}$$

and

$$k_{x,i}\bar{P}'_{Di} + k_{x,i+1}\bar{P}'_{Di+1} = 0 \qquad \text{on } \Gamma_{i,i+1} \qquad \text{for } i = 1, 2, \ldots, n-1 \tag{3.42}$$

The Laplace transform parameter for layer i is defined as

$$s(k) = \frac{\ln 2}{t_D} k \qquad \text{for } k = 1, \ldots, N_s \tag{3.43}$$

Apply the boundary element algorithm for homogeneous reservoir developed by Koh (1993), Chapter 2, to Eq. (3.38), we have

$$[H]_i \{\overline{P}_D\}_i = [G]_i \{\overline{P}'_D\}_i \qquad \text{for } i = 1, 2, \ldots, n \tag{3.44}$$

Eq. (3.44) is rewritten as

$$[H]_i \{\overline{P}_D\}_i = [G_k]_i \{\overline{P}'_{Dk}\}_i \qquad \text{for } i = 1, 2, \ldots, n \tag{3.45}$$

where

$$[G_k]_i = \frac{1}{k_{x,i}} [G]_i \qquad \text{for } i = 1, 2, \ldots, n \tag{3.46}$$

$$\{\overline{P}'_{Dk}\}_i = k_{x,i} \{\overline{P}'_D\}_i \qquad \text{for } i = 1, 2, \ldots, n \tag{3.47}$$

With two compatible conditions, Eqs. (3.41) and (3.42), we can assemble together the system of matrices, Eq. (3.45). Once the boundary conditions are prescribed, the above system of equations may be solved. The total number of unknowns equals the number of nodes on the external boundaries plus twice the number of nodes on the interface boundaries.

For improving computational efficiency and avoiding numerical problem, the proposed technique may also be used in homogeneous reservoir. As pointed out by Koh (1993), one of the disadvantages of the BEM is that it produces unsymmetric and densely populated matrix. The subregion technique transforms a fully populated matrices into banded matrices yielding more computational efficiency. The problem with a large number of unknowns can also be solved by using this technique.

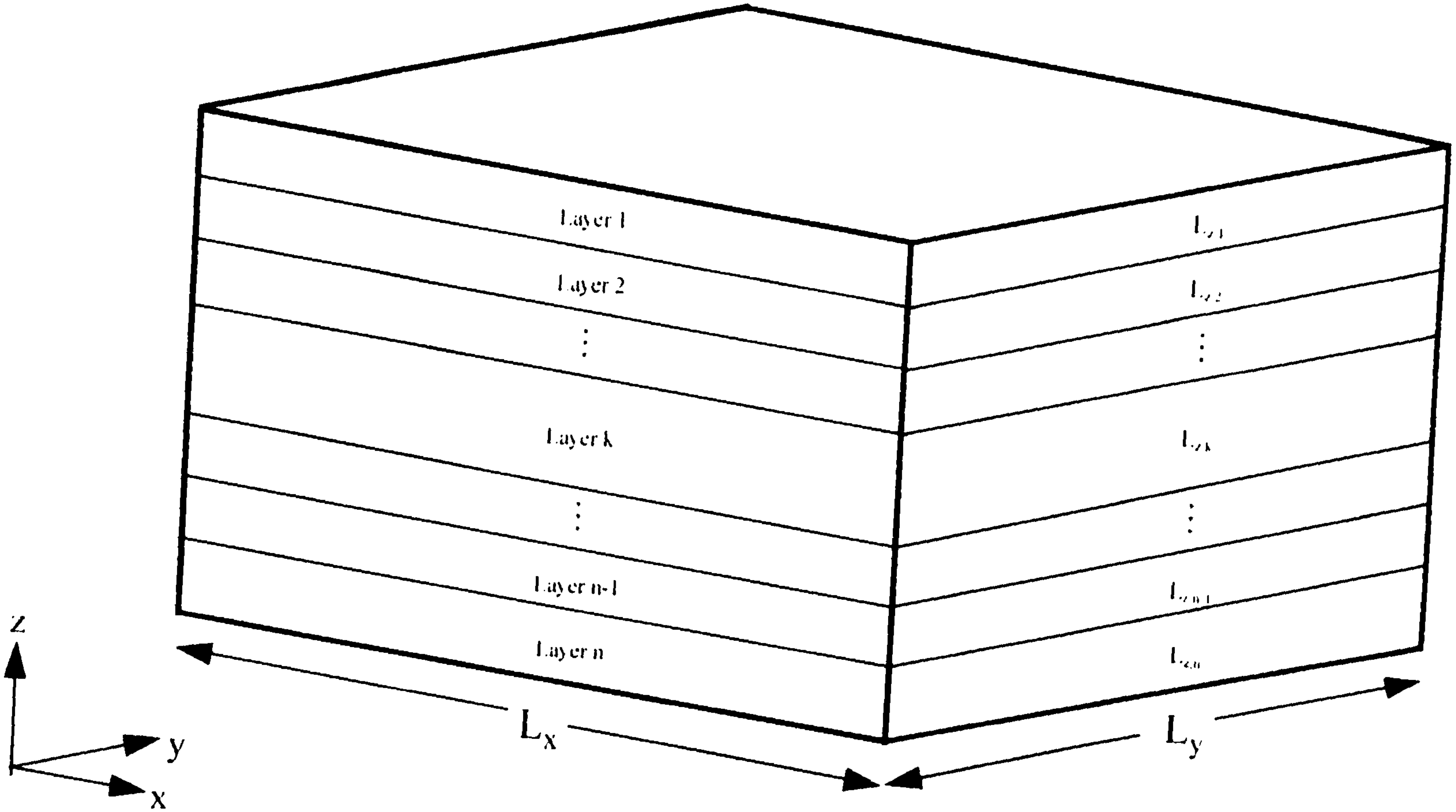

Figure 3.2 A Multi-Layer Reservoir Model

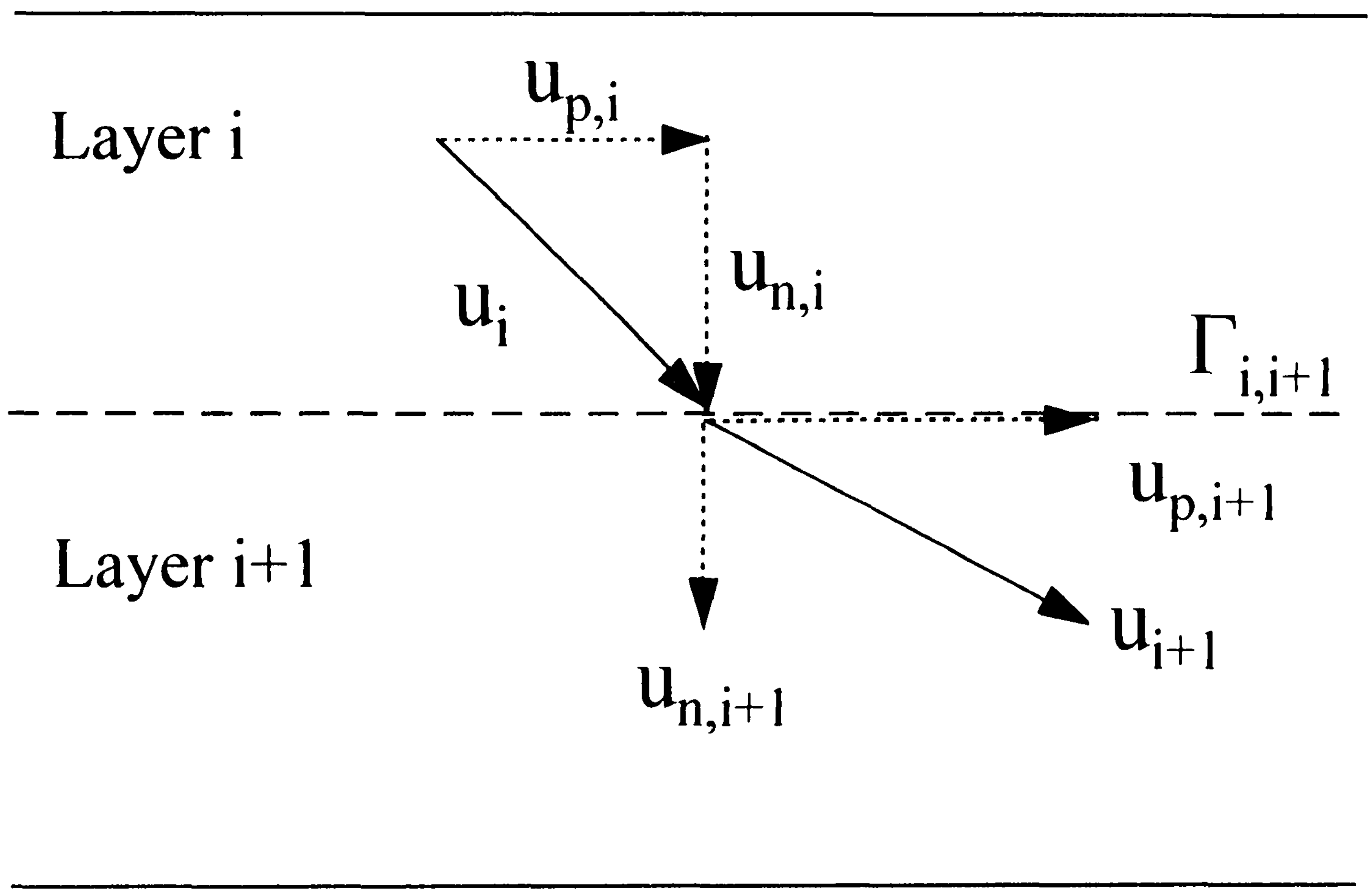

Figure 3.3 Velocity Deflection Across The Interface Boundary

3.2.2) Assembly of Equations

This section illustrates how the proposed algorithm works. Consider the two-dimensional domain, shown in Fig. 3.4. The domain is divided into three subregions illustrated in Fig. 3.5. The order of nodes are renumbered for each subdomain. Each subregion can be treated as a homogeneous domain. Apply boundary element algorithm to each subregion, we have the system of algebraic equations for region 1, 2, and 3, respectively, as

$$\begin{bmatrix} h^1_{11} & h^1_{12} & h^1_{13} & h^1_{14} \\ h^1_{21} & h^1_{22} & h^1_{23} & h^1_{24} \\ h^1_{31} & h^1_{32} & h^1_{33} & h^1_{34} \\ h^1_{41} & h^1_{42} & h^1_{43} & h^1_{44} \end{bmatrix} \begin{Bmatrix} \overline{PP}^1_{D1} \\ \overline{PP}^1_{D2} \\ \overline{PP}^1_{D3} \\ \overline{PP}^1_{D4} \end{Bmatrix} = \begin{bmatrix} g^1_{11} & g^1_{12} & g^1_{13} & g^1_{14} \\ g^1_{21} & g^1_{22} & g^1_{23} & g^1_{24} \\ g^1_{31} & g^1_{32} & g^1_{33} & g^1_{34} \\ g^1_{41} & g^1_{42} & g^1_{43} & g^1_{44} \end{bmatrix} \begin{Bmatrix} \overline{P}'_{D1,1} \\ \overline{P}'_{D2,1} \\ \overline{P}'_{D3,1} \\ \overline{P}'_{D4,1} \end{Bmatrix} \tag{3.48}$$

$$\begin{bmatrix} h^2_{11} & h^2_{12} & h^2_{13} & h^2_{14} & h^2_{15} & h^2_{16} \\ h^2_{21} & h^2_{22} & h^2_{23} & h^2_{24} & h^2_{25} & h^2_{26} \\ h^2_{31} & h^2_{32} & h^2_{33} & h^2_{34} & h^2_{35} & h^2_{36} \\ h^2_{41} & h^2_{42} & h^2_{43} & h^2_{44} & h^2_{45} & h^2_{46} \\ h^2_{51} & h^2_{52} & h^2_{53} & h^2_{54} & h^2_{55} & h^2_{56} \\ h^2_{61} & h^2_{62} & h^2_{63} & h^2_{64} & h^2_{65} & h^2_{66} \end{bmatrix} \begin{Bmatrix} \overline{PP}^2_{D1} \\ \overline{PP}^2_{D2} \\ \overline{PP}^2_{D3} \\ \overline{PP}^2_{D4} \\ \overline{PP}^2_{D5} \\ \overline{PP}^2_{D6} \end{Bmatrix}$$

$$= \begin{bmatrix} g^2_{11} & g^2_{12} & g^2_{13} & g^2_{14} & g^2_{15} & g^2_{16} \\ g^2_{21} & g^2_{22} & g^2_{23} & g^2_{24} & g^2_{25} & g^2_{26} \\ g^2_{31} & g^2_{32} & g^2_{33} & g^2_{34} & g^2_{35} & g^2_{36} \\ g^2_{41} & g^2_{42} & g^2_{43} & g^2_{44} & g^2_{45} & g^2_{46} \\ g^2_{51} & g^2_{52} & g^2_{53} & g^2_{54} & g^2_{55} & g^2_{56} \\ g^2_{61} & g^2_{62} & g^2_{63} & g^2_{64} & g^2_{65} & g^2_{66} \end{bmatrix} \begin{Bmatrix} \overline{P}'_{D1,2} \\ \overline{P}'_{D2,2} \\ \overline{P}'_{D3,2} \\ \overline{P}'_{D4,2} \\ \overline{P}'_{D5,2} \\ \overline{P}'_{D6,2} \end{Bmatrix} \tag{3.49}$$

and

$$\begin{bmatrix} h_{11}^{3} & h_{12}^{3} & h_{13}^{3} \\ h_{21}^{3} & h_{22}^{3} & h_{23}^{3} \\ h_{31}^{3} & h_{32}^{3} & h_{33}^{3} \end{bmatrix} \begin{Bmatrix} \overline{PP}_{D1}^{3} \\ \overline{PP}_{D2}^{3} \\ \overline{PP}_{D3}^{3} \end{Bmatrix} = \begin{bmatrix} g_{11}^{3} & g_{12}^{3} & g_{13}^{3} \\ g_{21}^{3} & g_{22}^{3} & g_{23}^{3} \\ g_{31}^{3} & g_{32}^{3} & g_{33}^{3} \end{bmatrix} \begin{Bmatrix} \overline{P}'_{D1,3} \\ \overline{P}'_{D2,3} \\ \overline{P}'_{D3,3} \end{Bmatrix} \tag{3.50}$$

At interface 1-2, the required compatibility conditions can be expressed as

$$\overline{PP}_{D2}^{1} = \overline{PP}_{D1}^{2} = \overline{PP}_{D2} \tag{3.51}$$

$$\overline{PP}_{D3}^{1} = \overline{PP}_{D2}^{2} = \overline{PP}_{D3} \tag{3.52}$$

$$\overline{PP}_{D4}^{1} = \overline{PP}_{D3}^{2} = \overline{PP}_{D4} \tag{3.53}$$

$$\overline{P}'_{D2} = \overline{P}'_{D2,1} + \overline{P}'_{D1,2} \tag{3.54}$$

$$\overline{P}'_{D3} = \overline{P}'_{D3,1} + \overline{P}'_{D2,2} = 0 \tag{3.55}$$

and

$$\overline{P}'_{D4} = \overline{P}'_{D4,1} + \overline{P}'_{D3,2} \tag{3.56}$$

At interface 2-3, the required compatibility conditions can be expressed as

$$\overline{PP}_{D5}^{2} = \overline{PP}_{D1}^{3} = \overline{PP}_{D6} \tag{3.57}$$

$$\overline{PP}_{D6}^{2} = \overline{PP}_{D2}^{3} = \overline{PP}_{D7} \tag{3.58}$$

$$\overline{P}'_{D6} = \overline{P}'_{D5,2} + \overline{P}'_{D1,3} \tag{3.59}$$

$$\overline{P}'_{D7} = \overline{P}'_{D6,2} + \overline{P}'_{D2,3} \tag{3.60}$$

Combine Eqs. (3.48) - (3.60) and rearrange in the matrix form as follows.

$$
\begin{bmatrix}
h^1_{11} & h^1_{12} & h^1_{13} & h^1_{14} & & & & & -g^1_{12} & -g^1_{13} & -g^1_{14} & & \\
h^1_{21} & h^1_{22} & h^1_{23} & h^1_{24} & & & & & -g^1_{22} & -g^1_{23} & -g^1_{24} & & \\
h^1_{31} & h^1_{32} & h^1_{33} & h^1_{34} & & & & & -g^1_{32} & -g^1_{33} & -g^1_{34} & & \\
h^1_{41} & h^1_{42} & h^1_{43} & h^1_{44} & & & & & -g^1_{42} & -g^1_{43} & -g^1_{44} & & \\
 & h^2_{11} & h^2_{12} & h^2_{13} & h^2_{14} & h^2_{15} & h^2_{16} & & g^2_{11} & g^2_{12} & g^2_{13} & -g^2_{15} & -g^2_{16} \\
 & h^2_{21} & h^2_{22} & h^2_{23} & h^2_{24} & h^2_{25} & h^2_{26} & & g^2_{21} & g^2_{22} & g^2_{23} & -g^2_{25} & -g^2_{26} \\
 & h^2_{31} & h^2_{32} & h^2_{33} & h^2_{34} & h^2_{35} & h^2_{36} & & g^2_{31} & g^2_{32} & g^2_{33} & -g^2_{35} & -g^2_{36} \\
 & h^2_{41} & h^2_{42} & h^2_{43} & h^2_{44} & h^2_{45} & h^2_{46} & & g^2_{41} & g^2_{42} & g^2_{43} & -g^2_{45} & -g^2_{46} \\
 & h^2_{51} & h^2_{52} & h^2_{53} & h^2_{54} & h^2_{55} & h^2_{56} & & g^2_{51} & g^2_{52} & g^2_{53} & -g^2_{55} & -g^2_{56} \\
 & h^2_{61} & h^2_{62} & h^2_{63} & h^2_{64} & h^2_{65} & h^2_{66} & & g^2_{61} & g^2_{62} & g^2_{63} & -g^2_{65} & -g^2_{66} \\
 & & & & & h^3_{11} & h^3_{12} & h^3_{13} & & & & g^3_{11} & g^3_{12} \\
 & & & & & h^3_{21} & h^3_{22} & h^3_{23} & & & & g^3_{21} & g^3_{22} \\
 & & & & & h^3_{31} & h^3_{32} & h^3_{33} & & & & g^3_{31} & g^3_{32}
\end{bmatrix}
\begin{Bmatrix}
\overline{PP}_{D1} \\ \overline{PP}_{D2} \\ \overline{PP}_{D3} \\ \overline{PP}_{D4} \\ \overline{PP}_{D5} \\ \overline{PP}_{D6} \\ \overline{PP}_{D7} \\ \overline{PP}_{D8} \\ \bar{P}'_{D21} \\ \bar{P}'_{D31} \\ \bar{P}'_{D41} \\ \bar{P}'_{D52} \\ \bar{P}'_{D62}
\end{Bmatrix}
$$

$$
= \begin{bmatrix}
g^1_{11} & & & & & & & \\
g^1_{21} & & & & & & & \\
g^1_{31} & & & & & & & \\
g^1_{41} & & & & & & & \\
 & g^2_{11} & g^2_{12} & g^2_{13} & g^2_{14} & & & \\
 & g^2_{21} & g^2_{22} & g^2_{23} & g^2_{24} & & & \\
 & g^2_{31} & g^2_{32} & g^2_{33} & g^2_{34} & & & \\
 & g^2_{41} & g^2_{42} & g^2_{43} & g^2_{44} & & & \\
 & g^2_{51} & g^2_{52} & g^2_{53} & g^2_{54} & & & \\
 & g^2_{61} & g^2_{62} & g^2_{63} & g^2_{64} & & & \\
 & & & & & g^3_{11} & g^3_{12} & g^3_{13} \\
 & & & & & g^3_{21} & g^3_{22} & g^3_{23} \\
 & & & & & g^3_{31} & g^3_{32} & g^3_{33}
\end{bmatrix}
\begin{Bmatrix}
P'_{D1} \\ \bar{P}'_{D2} \\ \bar{P}'_{D3} \\ \bar{P}'_{D4} \\ \bar{P}'_{D5} \\ \bar{P}'_{D6} \\ \bar{P}'_{D7} \\ \bar{P}'_{D8}
\end{Bmatrix}
\tag{3.61}
$$

Once the boundary conditions are prescribed. the above matrix can be rearranged and solved for the unknowns.

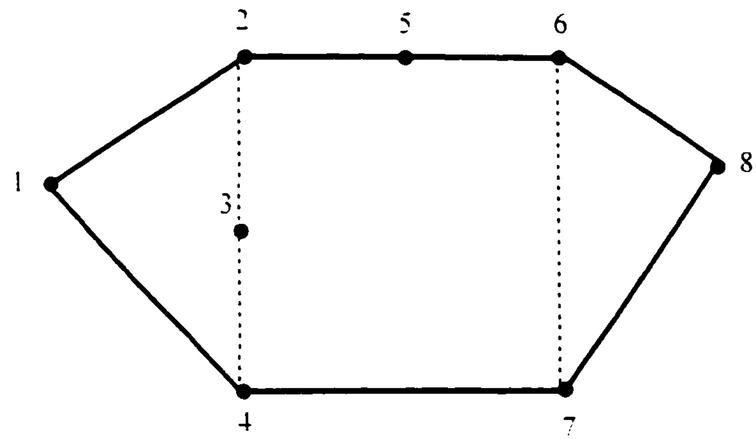

Figure 3.4 A Two-Dimensional Domain Used to Illustrate The Proposed Algorithm

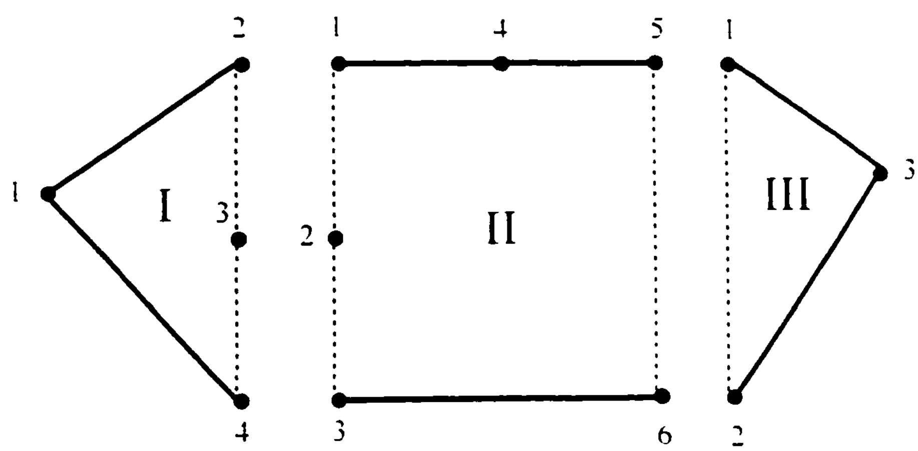

Figure 3.5 Three Subdomains

3.2.3) Solution of Equations

Gaussisan elimination is used by Koh (1993) to the system of equations for single-layer homogeneous reservoir. This method fails to solve Eq. (3.61) correctly. In this study, the Gauss elimination with column pivoting only is used to solve the system of equations.

Chapter 4

VALIDATION

Three different cases with available solutions, listed below, are used to check the developed algorithm.

(1) Finite linear aquifer.

(2) A horizontal well in closed rectangular reservoir, and

(3) A horizontal well in a multi-layer reservoir with cross flow

Case 1: Finite Linear Aquifer

In this case, the dimensionless pressure and time are redefined, respectively, as

$$P_D = \frac{khb}{141.2qB\mu L}(p_i - p) \tag{4.1}$$

and

$$t_D = \frac{0.0002637k}{\phi\mu c L^2}t \tag{4.2}$$

The domain of interested is a rectangular reservoir with impermeable lateral, lower, and upper boundaries. Two different types of boundary, (a) sealed outer boundary and (b) constant pressure at outer boundary, are considered in this study. Nabor and Barham (1964) presented the analytical solutions for both cases. They are

$$P_D = \left(t_D + \frac{1}{3}\right) - \frac{2}{\pi^2}\sum_{n=1}^{\infty}\left\{\frac{\exp\left(-n^2\pi^2 t_D\right)}{n^2}\right\} \tag{4.3}$$

for sealed outer boundary and

$$P_D = 1 - \frac{8}{\pi^2}\sum_{n=odd}^{\infty}\left\{\frac{\exp(-n^2\pi^2 t_D/4)}{n^2}\right\} \tag{4.4}$$

for constant pressure at outer boundary. Figure 4.1(1) shows the discretized boundaries of two-layer model consisting of 106 nodes and 208 elements in each layer. The properties of the aquifers are the followings:

k_{x1} = 1.0 md,	k_{x2} = 1.0 md
k_{y1} = 1.0 md,	k_{y2} = 1.0 md
k_{z1} = 1.0 md,	k_{z2} = 1.0 md
ϕ_1 = 0.1,	ϕ_2 = 0.1

The pressure response of sealed outer boundary aquifer are plotted in Fig. 4.1(2) showing reasonable agreement with the analytical solution and Koh's work.

Figure 4.1(3) presents the dimensionless pressure versus dimensionless time for constant pressure at outer boundary aquifer. It is clearly seen that the presented algorithm fits very well with the analytical solution.

Case 2: A Horizontal Well in Closed Rectangular Reservoir

A horizontal well located in a finite anisotropic sealed rectangular box reservoir produces at a constant rate. Several analytical solutions were documented in the literature. But only two of them will be considered here. Thompson et al. (1991) presented an effective algorithm to evaluate the pressure response with minimal computation efforts. The drawback of their model is the line-source assumption which does not correctly represent the pressure response at very early time. Thus, Kuchuk and

Habashy 's model (1996) is also included here. Their model correctly determines the pressure response at the very early time. But their model is only for a system with infinite horizontal direction. Therefore, this model cannot be used to check the present work at very late time when the horizontal boundary effects are observed.

Figure 4.2(1) shows a discretized reservoir with 300 nodes and 592 elements on layer '1' and with 194 nodes and 384 elements on layer '2'. The discretized wellbore is shown in Fig. 4.2(2). The systems have the following properties.

k_{x1} = 1.0 md.	k_{x2} = 1.0 md
k_{y1} = 1.0 md.	k_{y2} = 1.0 md
k_{z1} = 1.0 md.	k_{z2} = 1.0 md
ϕ_1 = 0.1.	ϕ_2 = 0.1

The pressure responses from this study, shown in Fig. 4.2(3), matches very well with the analytical solutions and Koh's work, one-layer boundary algorithm, for the whole dimensionless time of interested.

8.3 Case 3: A Horizontal Well in A Multi-layer Reservoir with Cross flow

The only analytical solution of this system available in the literature is by Kuchuk and Habashy (1996). As stated in Case 2, this model assumes that the system is infinite in the horizontal direction. Thus, only early portion of pressure response will be used to validate this work. Figure 4.3(1) shows the discretized system consisting of two layers with 492 nodes and 976 elements on layer '1' and with 386 nodes and 768 elements on layer '2'. The wellbore discretization is the same as that of Case 2. The reservoir has the followings properties.

k_{x1} = 1.0 md. k_{x2} = 0.1 md

k_{y1} = 1.0 md. k_{y2} = 0.1 md

k_{z1} = 1.0 md. k_{z2} = 0.1 md

ϕ_1 = 0.2. ϕ_2 = 0.1

Figure 4.3(2) compares the analytical solution and the two-layer boundary element algorithm. Good agreement can be clearly seen for $t_D < 10^5$ beyond when the boundary effects is observed.

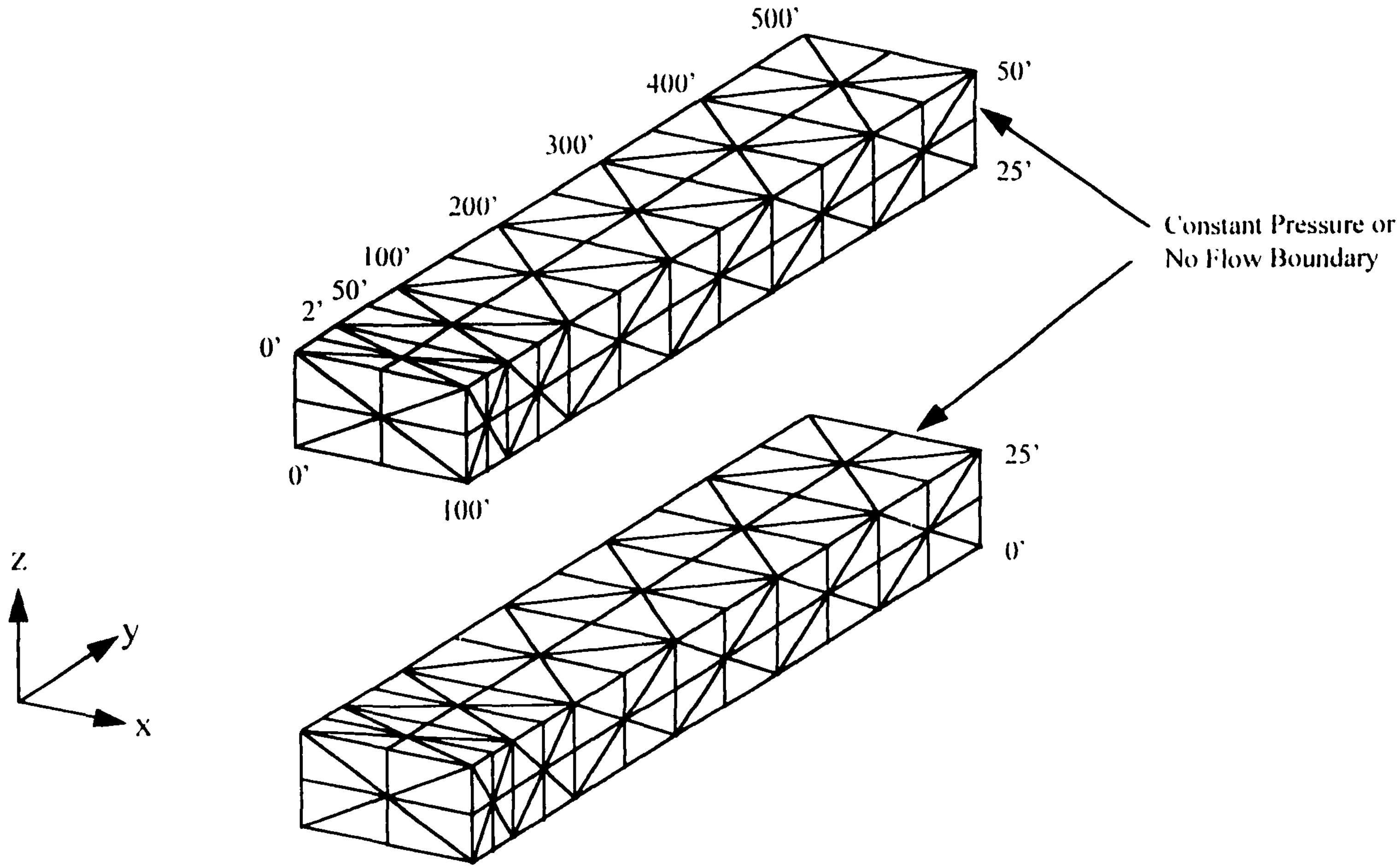

Figure 4.1.1 Boundary Discretization for Case 1

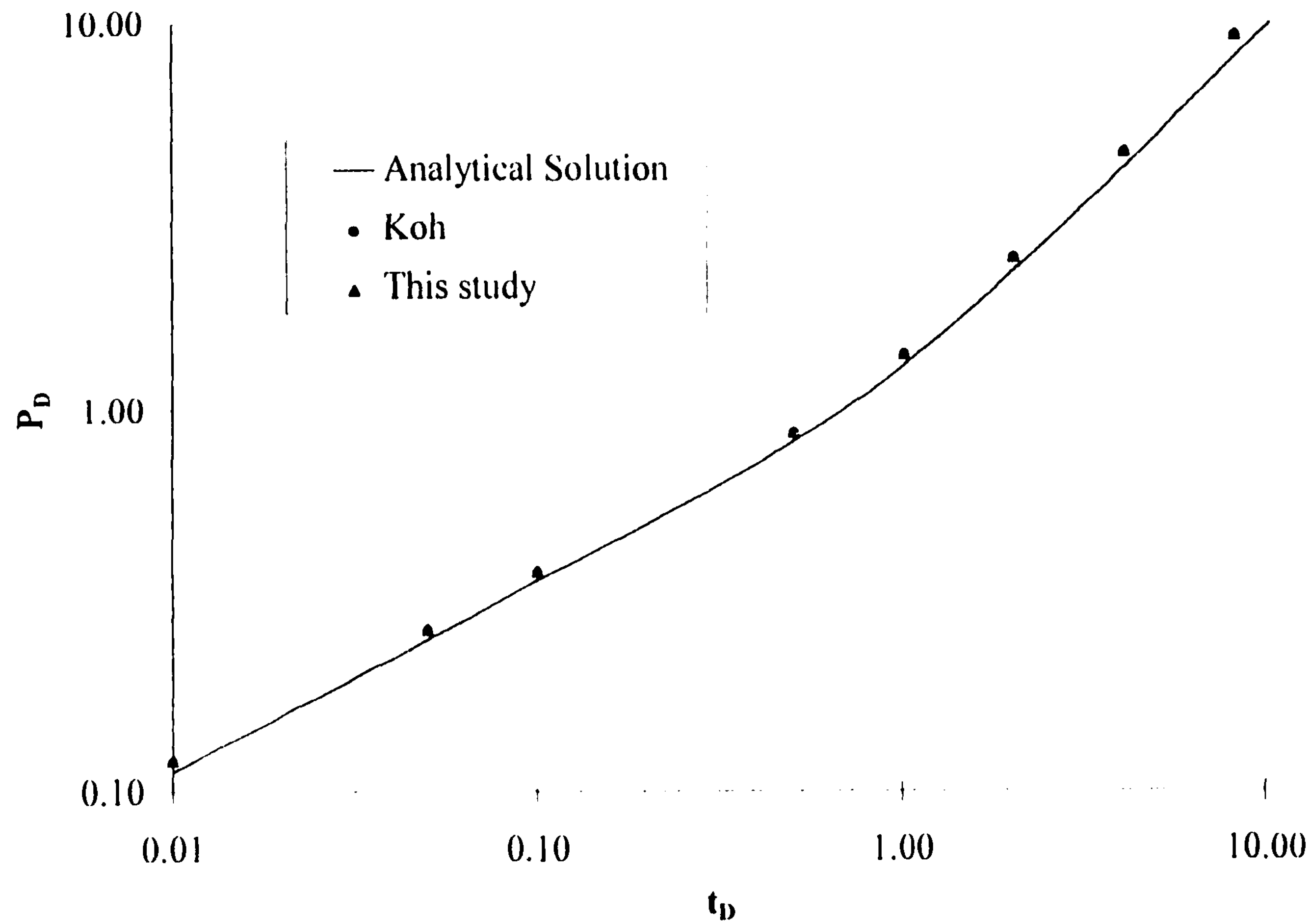

Figure 4.1.2 Finite Linear Aquifer with Sealed Outer Boundary

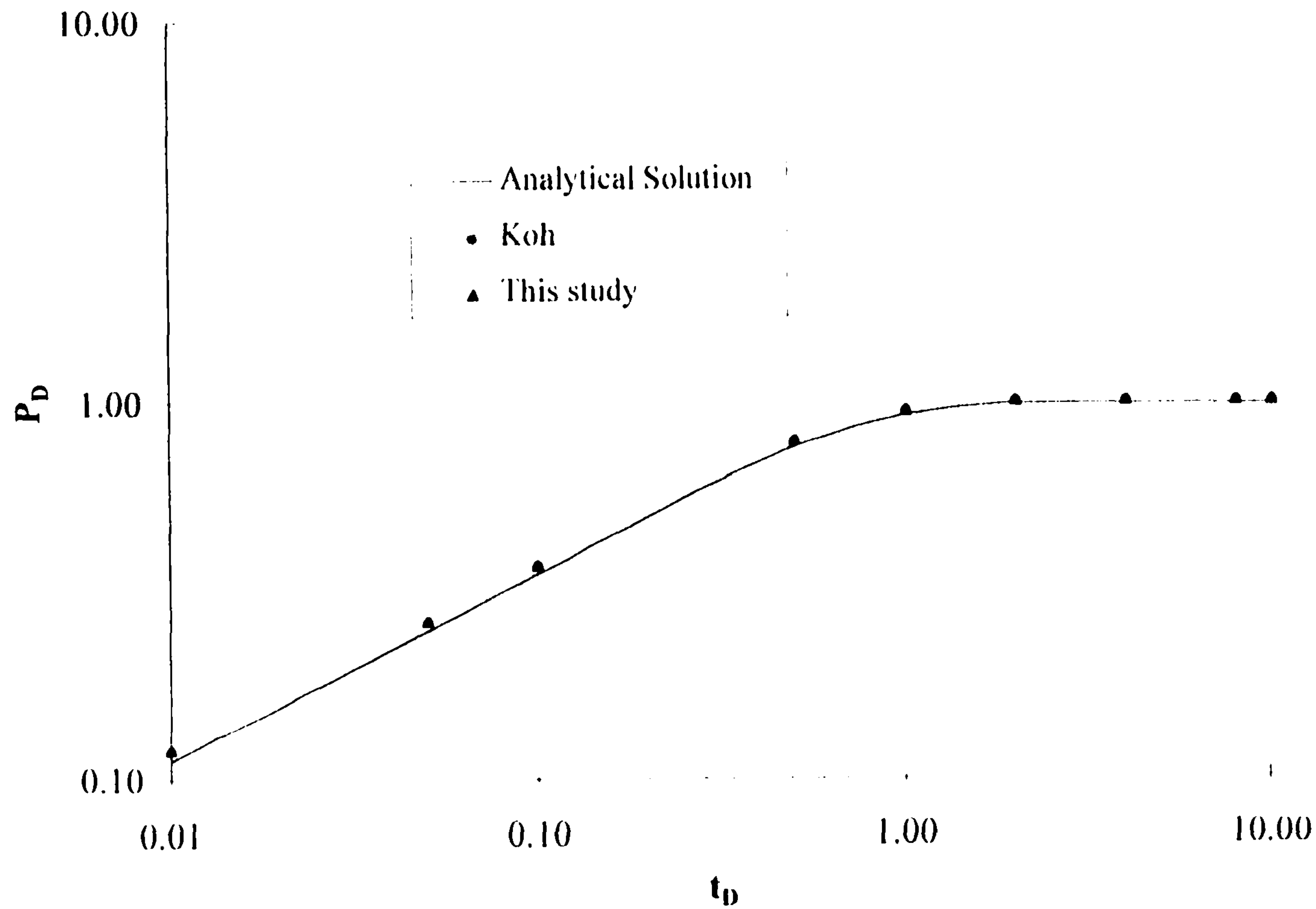

Figure 4.1.3 Finite Linear Aquifer with Constant Pressure at Outer Boundary

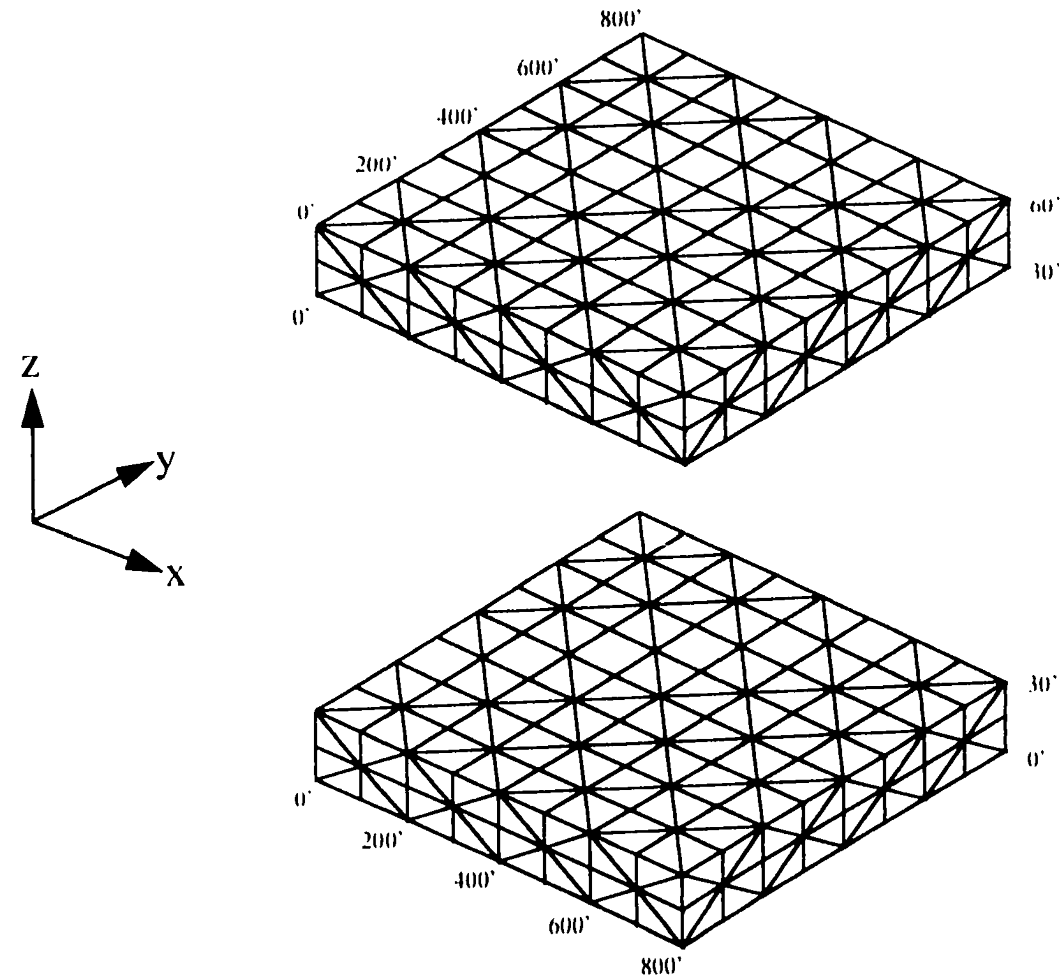

Figure 4.2.1 System Discretization for Case 2

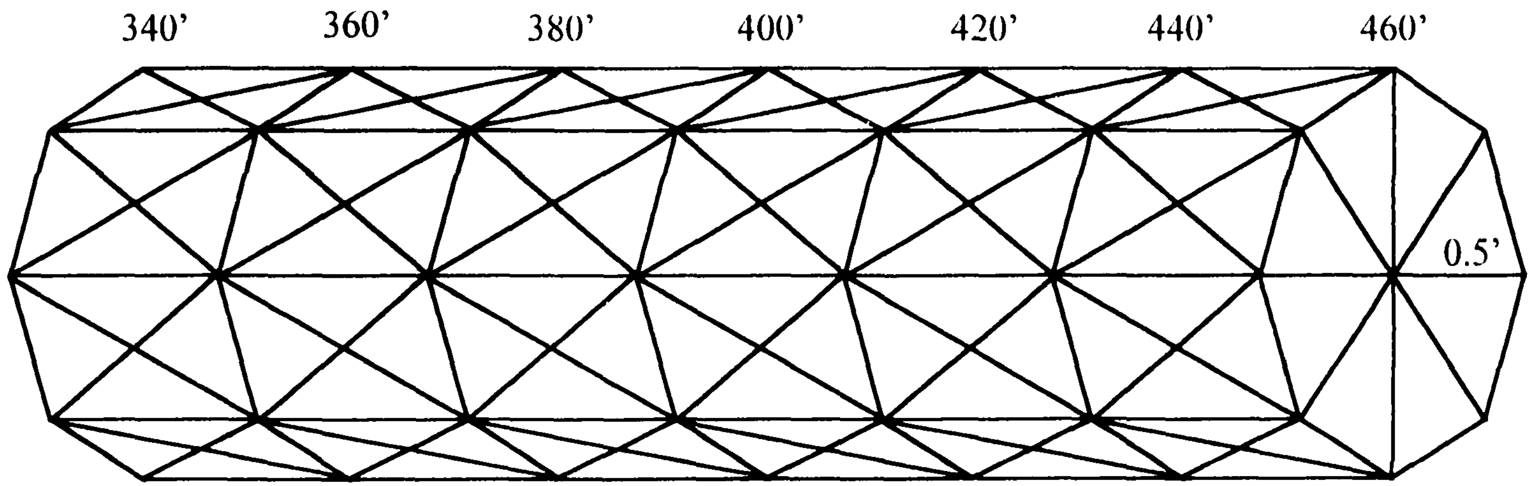

Figure 4.2.2 Wellbore Discretization for Case 2 (After Koh, 1993)

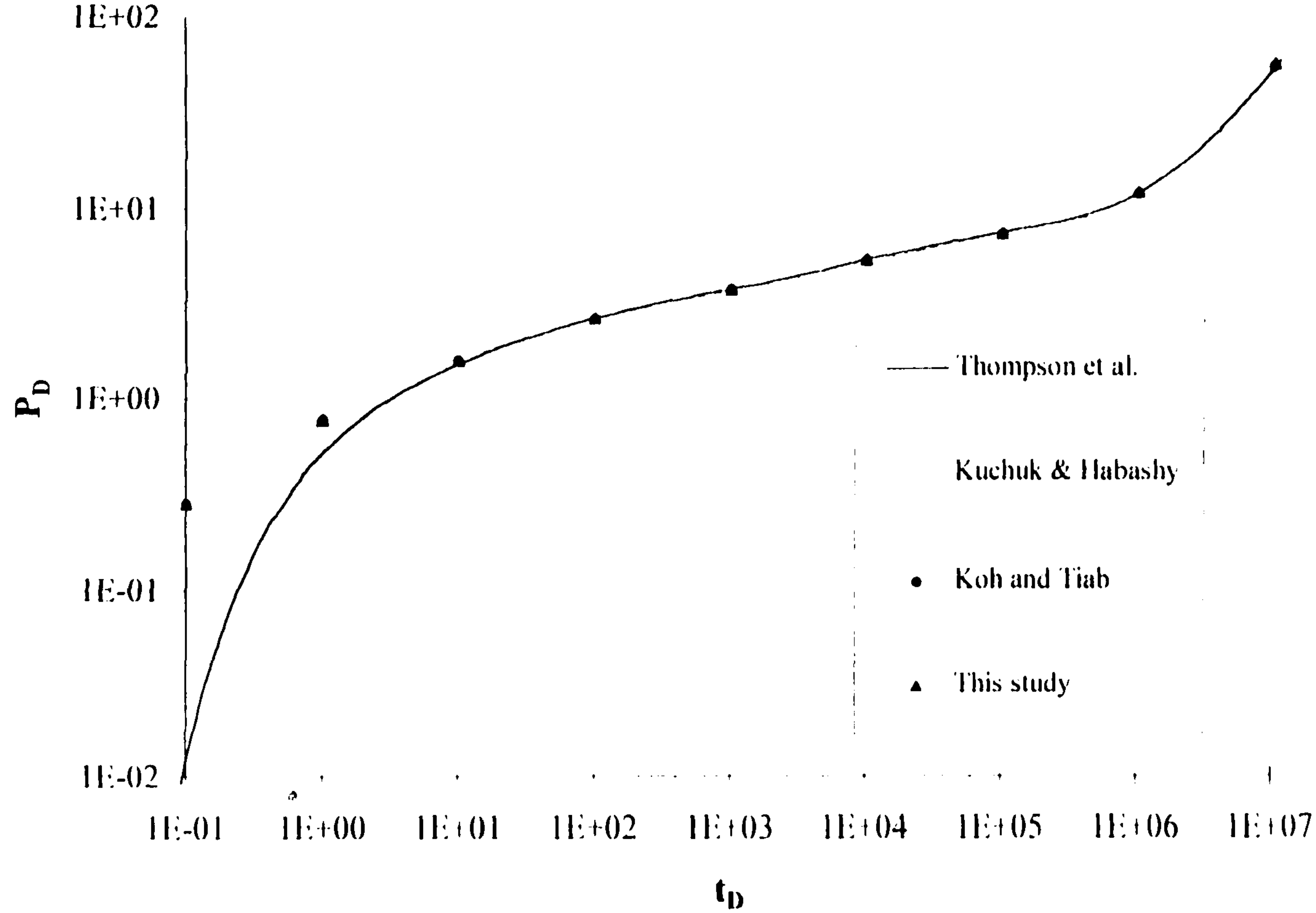

Figure 4.2.3 A Horizontal Well in Closed Rectangular Reservoir

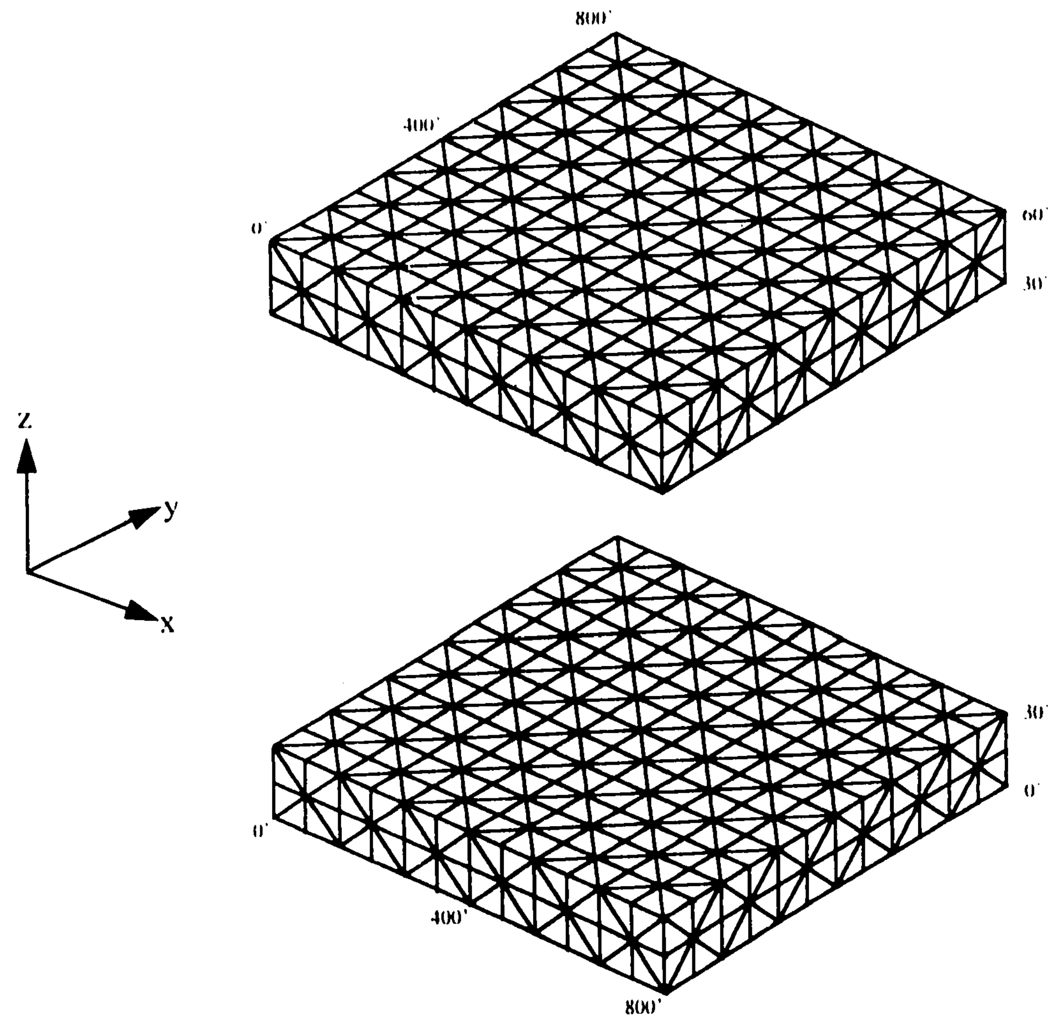

Figure 4.3.1 System Discretization for Case 3

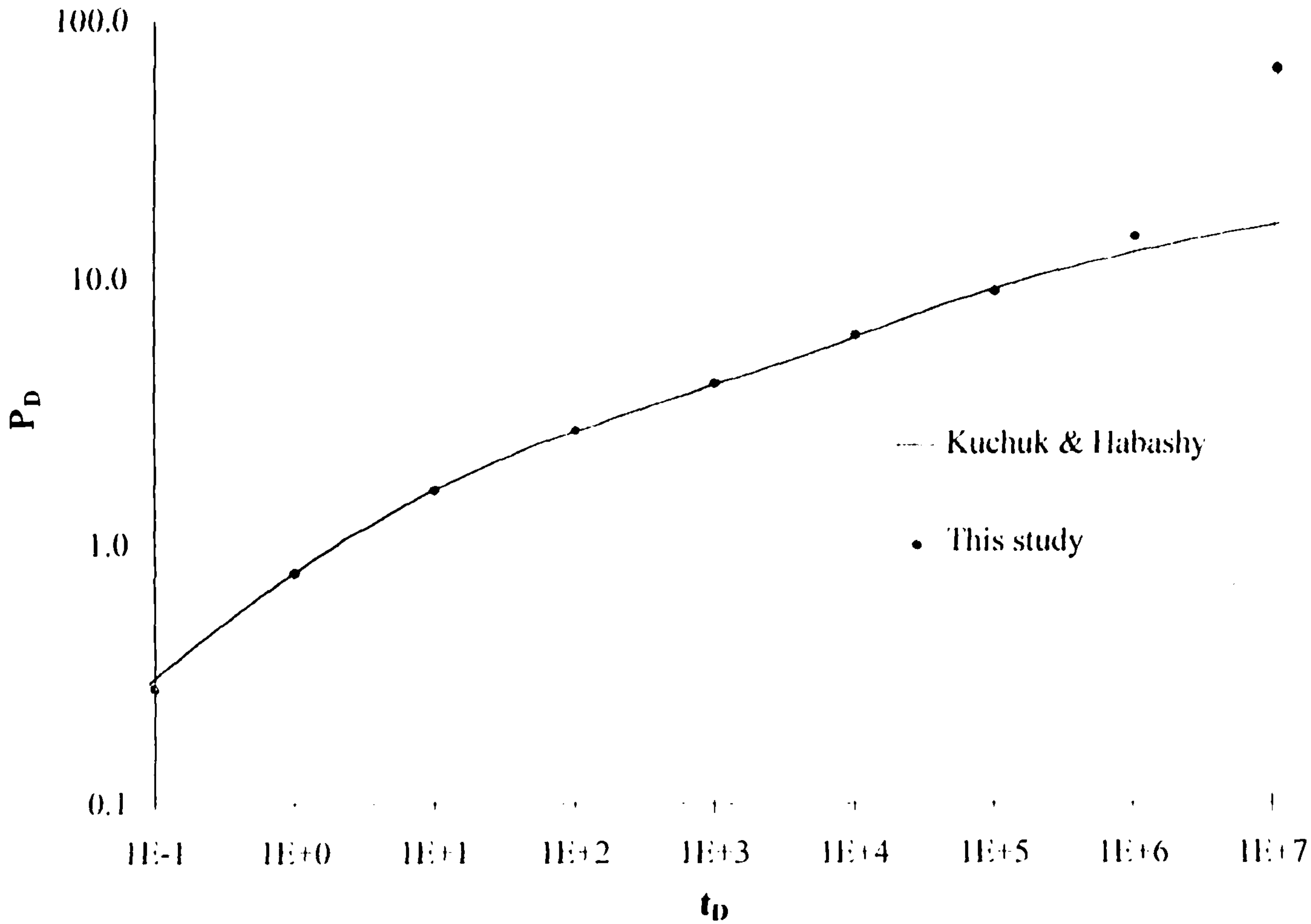

Figure 4.3.2 A Horizontal Well in A Multi-layer Reservoir with Cross flow

Chapter 5

APPLICATIONS OF THE BOUNDARY ELEMENT METHOD TO SIMULATE PRESSURE PERFORMANCE IN COMPLICATED SYSTEMS

The developed boundary element method is applied to solve the three dimensional fluid problems which the analytical solutions do not exist. Eight different cases will be included in this chapter including:

(1) A horizontal well in a two-layer reservoir.

(2) A horizontal well in a two-layer reservoir with gas-cap drive.

(3) A horizontal well in a two-layer reservoir with bottom-water drive.

(4) A horizontal well in a two-layer reservoir with gas-cap and bottom-water drives.

(5) A horizontal well intersecting a two-layer reservoir.

(6) A snake-shape horizontal well intersecting a two-layer reservoir.

(7) A horizontal well intersecting a three-layer reservoir.

(8) A vertical well intersecting a two-layer reservoir without cross flow.

Different types of plots of the dimensionless pressure and the dimensionless pressure derivative versus the dimensionless time including log-log plot, semi-log plot, and Cartesian plots are used to investigate the wellbore performance for each case.

The radius of investigation is the distance from the wellbore in which can be reached by a pressure disturbance after the well is opened for production for time t (hr.) defined by Lee (1982) as:

$$r = \sqrt{\frac{kt}{948\phi\mu c_t}} \tag{5.1}$$

Solve the above equation for time as

$$t = \frac{948\phi\mu c_t r^2}{k} \tag{5.2}$$

Substitute Eq. 5.2 into Eq. 3.25 yields

$$t_D = \frac{0.0002637\, k_{x,1}}{\phi_1 \mu c_t r_w^2} t$$

$$= \frac{k_{x,1}}{4k}\left(\frac{r}{r_w}\right)^2 \tag{5.3}$$

Eq. (5.3) can be used to identify when the boundary and/or the interface effect will be observed at the wellbore. It should be noted that this dimensionless time is just an approximation. Since the boundary effect on the dimensionless pressure derivative is dependent on the scale of a graph.

The performance of a well with partial-penetration is summarized in Appendix B. Understanding its effects may assist us to understand the performance of a horizontal well in a more complicated system.

Table 5.1 summarizes the general dimensionless pressure equation and slopes of the dimensionless pressure derivative for four primary distinct flow regimes. Especially the dimensionless pressure derivative, they can be used to identify each flow regime.

Flow Regime	The General Dimensionless Equation	Slope of P'_D
radial flow	$P_D = m^*\log(t_D)+b$	0.00
linear flow	$P_D = m^*t_D^{1/2} + b$	0.50
bilinear flow	$P_D = m^*t_D^{1/4} + b$	0.25
spherical	$P_D = m^*t_D^{-1/2} + b$	-0.50

where b and m are constants.

Table 5.1 The Relationship Between P_D And t_D For Different Flow Regimes

Dimensionless Pressure Derivative During Infinite-Acting Flow

During the infinite-acting flow period, the dimensionless pressure is expressed as

$$P_D(t_D, r_D) = -\frac{1}{2}\mathrm{Ei}\left(\frac{-r_D^2}{4t_D}\right) \tag{5.4}$$

$$\approx \frac{1}{2}\left[\ln\left(\frac{t_D}{r_D^2}\right) + 0.80907\right] \qquad \text{for } t_D/r^2_D > 100, \tag{5.5}$$

where the exponential integral is defined by

$$\mathrm{Ei}(-x) = -\int_x^\infty \frac{e^{-u}}{u}du \tag{5.6}$$

$$\approx \ln(x) + 0.5772 \quad \text{for } x < 0.0025 \tag{5.7}$$

At the wellbore, $r_D = 1$, the dimensionless pressure derivative with respect to $\ln(t_D)$ during the first radial-flow period is obtained by differentiate Eq. (5.5) as

$$\frac{\partial P_D}{\partial \ln(t_D)} = 0.5 \tag{5.8}$$

Eq.(5.8) is the standard technique used to detect the first radial-flow around the wellbore. The basic assumption behind this solution, Eq. (5.4), is that the reservoir is isotropic. Hence, the wellbore is a cylinder in the dimensionless coordinate illustrated in Fig. 5.1. But this is not the case for a horizontal well since the vertical permeability is always much lower than the horizontal permeability. Thus, the wellbore becomes an ellipse in the dimensionless coordinate as shown in Fig. 5.2. The variable R_k used in Fig. 5.2 is defined as

$$R_k = \frac{k_{max}}{k_{min}} \tag{5.9}$$

where k_{max} and k_{min} are the two principle permeabilities, maximum and minimum, respectively, on the horizontal plane

The value of dimensionless pressure derivative during the infinite-acting flow period as a function of the permeability will be studied here. The physical model considered here is shown in Fig. 5.3. The reservoir is assumed to be infinite in horizontal direction. The top and bottom boundaries are no-flow boundaries.

The results from the numerical study are illustrated in Figs. 5.4 and 5.5 on linear and .semi-log scale, respectively. The dimensionless pressure derivative with respect to $\ln(t_D)$ during this period can be expressed in term of the permeability ratio as:

$$P_D' = \frac{1}{2}\sqrt{\frac{k_{max}}{k_{min}}} \tag{5.10}$$

where k_{max} and k_{min} are the maximum and minimum horizontal permeabilities, respectively. It should be noted that when the permeability ratio (R_k) is equal to one, the dimensionless pressure derivative is 0.5.

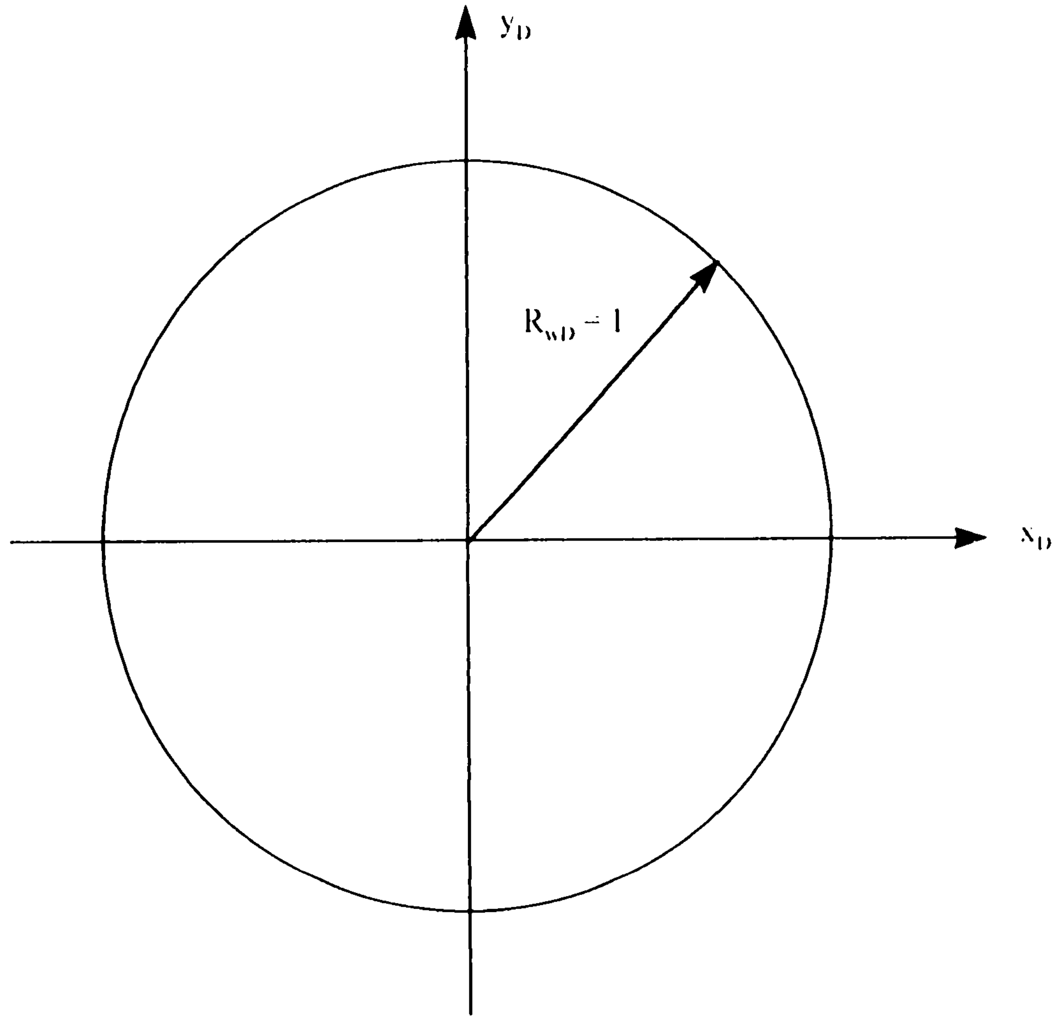

Figure 5.1 A Wellbore in The Cartesian Coordinate

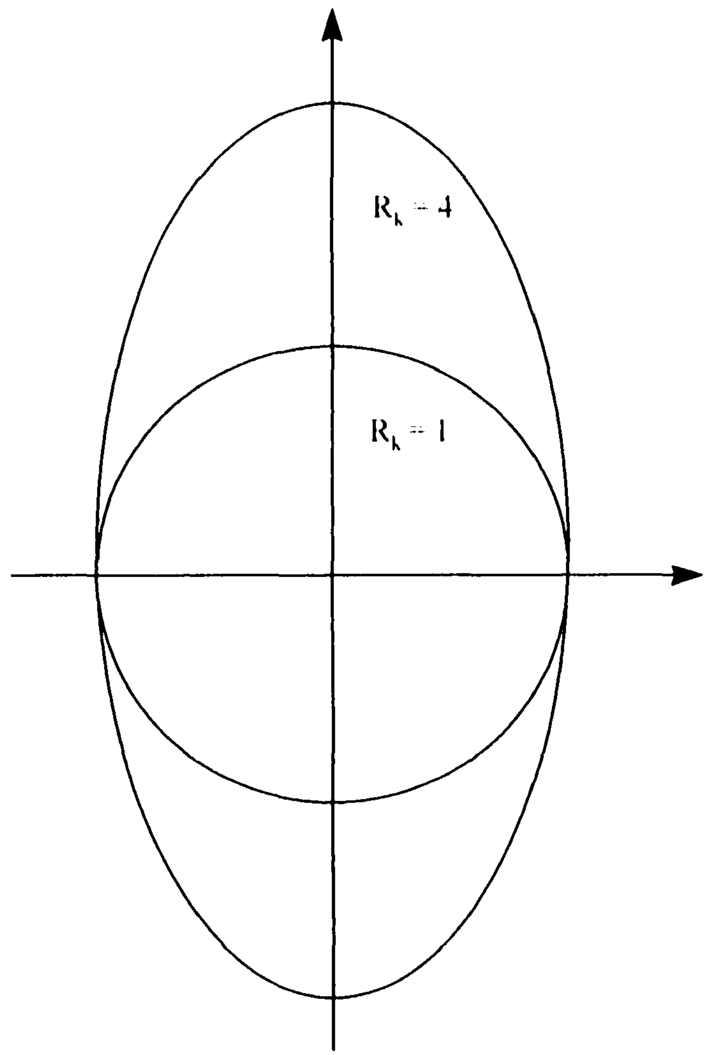

Figure 5.2 A Wellbore in The Dimensionless Coordinate

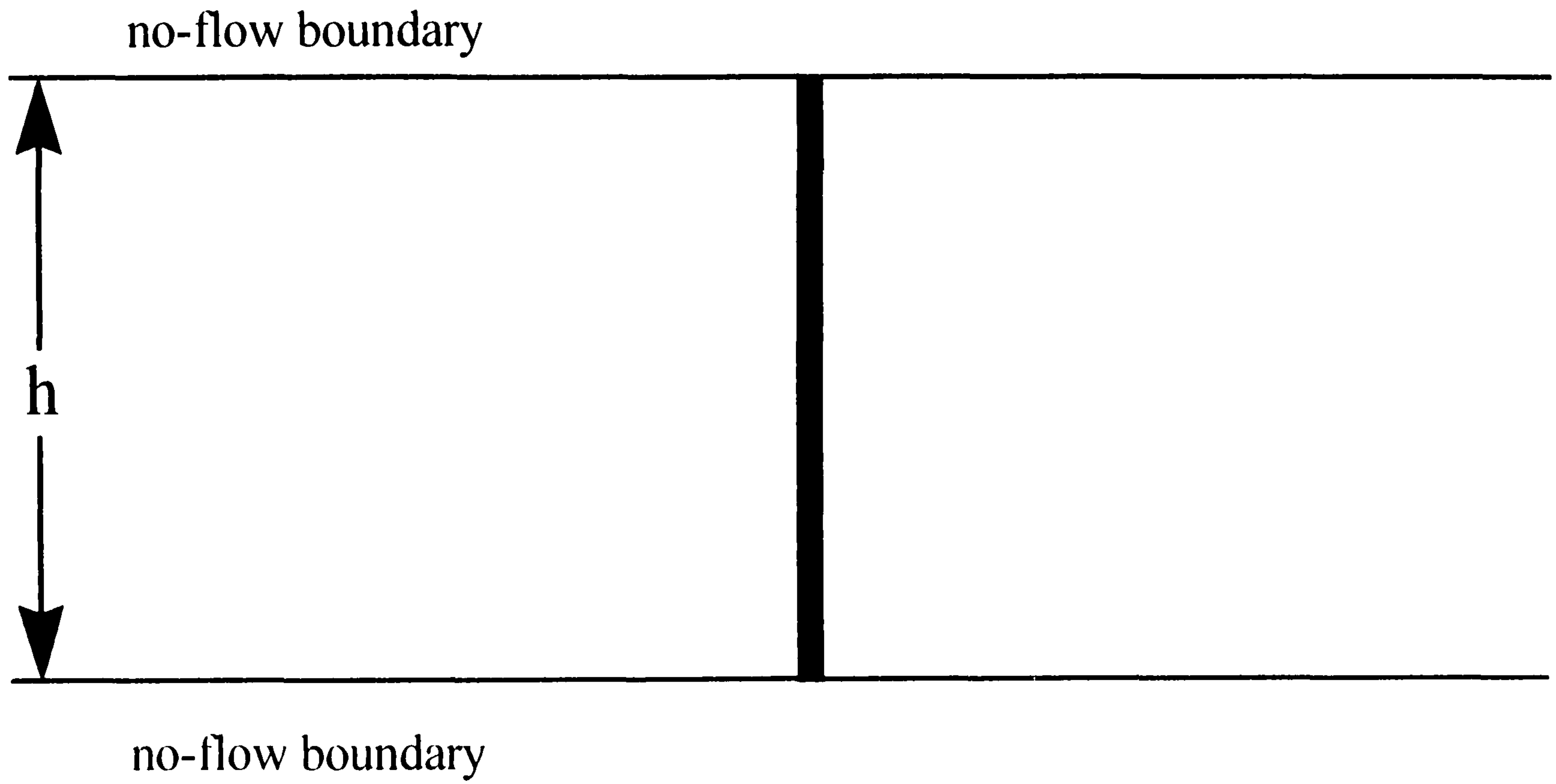

Figure 5.3 The Reservoir Model Considered in This Study

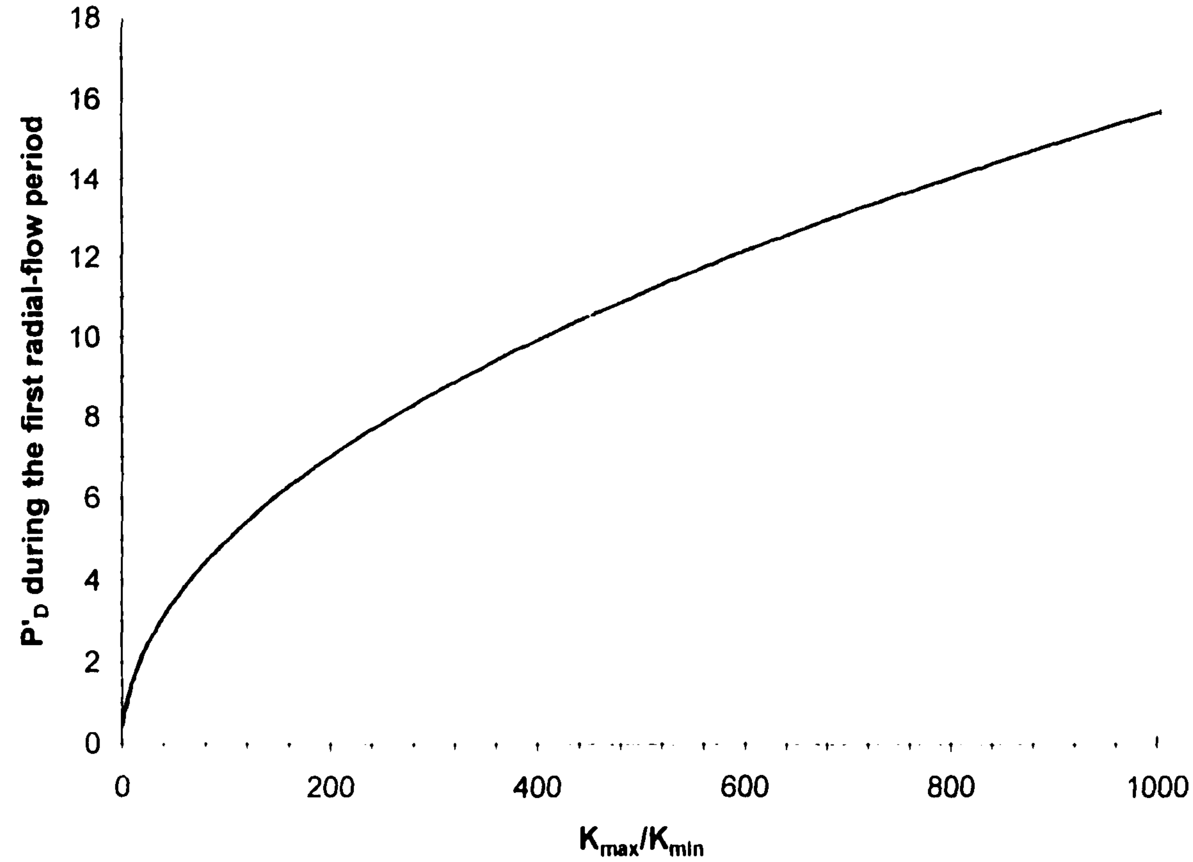

Figure 5.4 The Relationship Between Dimensionless Pressure Derivative and The Permeability Ratio on The Linear Scale

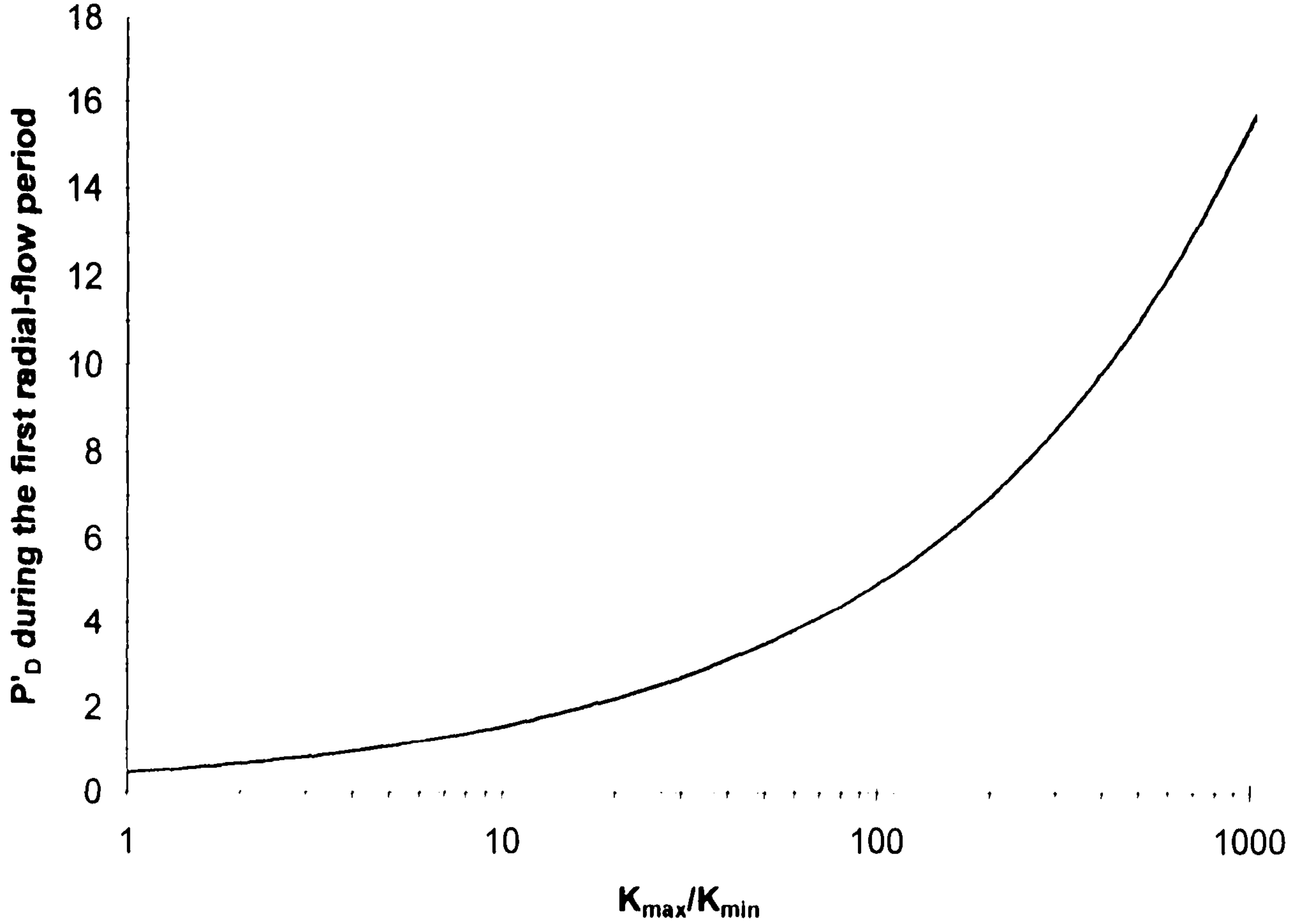

Figure 5.5 The Relationship Between Dimensionless Pressure Derivative and The Permeability Ratio on The Semi-log Scale

Case 1: A Horizontal Well in Two-Layer Reservoir

The reservoir is consisted of two different layers shown in Fig. 5.1.1. The wellbore is centrally located in the first layer paralleling to y direction. The top and bottom boundaries are no-flow boundaries. The effects of wellbore location, distance between a wellbore and the interface, the effects of the permeabilities are investigated in this study. The properties of each layer are the following.

$L_w = 100$ ft

$L_x = 1000$ ft.

$L_y = 1000$ ft.

$L_{z1} = 50$ ft.	$L_{z2} = 50$ ft.
$k_{x,1} = 1.0$ md	$k_{x,2} = 0.1$ md
$k_{y,1} = 1.0$ md	$k_{y,2} = 0.1$ md
$k_{z,1} = 0.1$ md	$k_{z,2} = 0.01$ md
$\phi_1 = 0.1$	$\phi_2 = 0.1$

Two different cases are included in this section. The permeability ratio is defined in this section as:

$$R_k = \frac{k_{x,1}}{k_{x,2}} \tag{5.1.1}$$

The distance between the horizontal well and the interface is denoted by L. Table 5.1.1 shows the shortest distances between the wellbore and the boundaries. This Table couple with Eq. (5.3) can be used to calculate the approximate dimensionless time when the pressure disturbance reaches these boundaries. Table 5.1.2 and 5.1.3 show these dimensionless times for different values of R_k.

	distance to the boundary			
L, ft	top	bottom	x-direction	y-direction
5	45	55	500	450
25	25	75	500	450
40	10	90	500	450

Table 5.1.1 The Shortest Distances from The Wellbore To The Boundaries for Case 1

		Dimensionless time, t_D			
L, ft	interface	top	bottom	x-direction	y-direction
5	250	20250	$2.5*10^5$	$2.5*10^5$	$2.0*10^5$
25	6250	6250	$2.6*10^5$	$2.5*10^5$	$2.0*10^5$
40	16000	1000	$2.7*10^5$	$2.5*10^5$	$2.0*10^5$

Table 5.1.2 The Dimensionless Times for The Pressure Disturbance to Travel from The Wellbore to The Boundaries for Case 1 and $R_k = 10$

Dimensionless time, t_D					
L, ft	interface	top	bottom	x-direction	y-direction
5	250	20250	2750	-	-
25	6250	6250	8750	-	-
40	16000	1000	18500	-	-

Table 5.1.3 The Dimensionless Times for The Pressure Disturbance to Travel from The Wellbore to The Boundaries for Case 1 and $R_k = 0.1$

Note that first the dimensionless times for the pressure transient to travel from the wellbore to the bottom boundary are subjected to error. Because the pressure disturbance must travel through the interface where the defection of velocity occurs. The actual dimensionless time should be greater than those calculated from Eq. 5.3. Hence those calculated dimensionless times are the minimum dimensionless time. Second, the approximate dimensionless times when the pressure disturbance reaches the boundaries in x-direction and y-direction are ambiguous for $R_k = 0.1$. Because the horizontal well is located in the lower-permeability layer. The radius of investigation travels slower in this layer. But it travels faster in the bottom layer. Hence, the boundaries in x-direction and y-direction may be reached from either the top or bottom layer. But these dimensionless times should be no more than those required for $R_k = 10$. Hence, these exact dimensionless times are unknown.

Fig. 5.1.2 illustrates the discretized reservoir model using nonuniform grid. Since the source is located at the center of the reservoir. this area is discretized by using smaller triangular elements. At the boundary far away form the source. the larger uniform triangular elements are used. The 2-D boundary discretization is illustrated in Fig. 5.1.3. The number of nodes and elements in each layer are:

Later #1

- number of nodes = 656
- number of triangular elements = 1424

Later #2

- number of nodes = 598
- number of triangular elements = 1216

The time t_p at the end of partial penetration effect is given in Appendix B as

$$t_p = \frac{3792.2\phi\mu c_t h^2}{k_z} F_p \tag{B.18}$$

which can be expressed in term of the dimensionless time as

$$t_{Dp} = \frac{k_{x,1}}{k_x}\left(\frac{L_y}{r_w}\right)^2 \bullet F_p \tag{5.1.2}$$

The perforation ratio is

$$\frac{L_w}{L_y} = \frac{100}{1000} = 0.1 \tag{5.1.3}$$

Since the horizontal well is centrally located in layer #1. then

$$\bar{b}_p = 0 \tag{5.1.4}$$

From Fig. B.5. and Eqs. (5.1.3) and (5.1.4). we have

$F_p = 0.535$ (5.1.5)

Substitute Eq. (5.1.5) and the known parameters into Eq. (5.1.2) yields

$$t_{Dp} = \frac{1}{1}\left(\frac{1000}{0.5}\right)^2 \bullet 0.535 = 2.14 * 10^6 \qquad (5.1.6)$$

Compare the dimensionless time in Eq. (5.1.6) with ones in Tables 5.1.2 and 5.1.3, it is clearly seen that the partial penetration effect will be masked by the boundary effects.

The log-log plots of P_D and P'_D versus t_D for L = 5 ft are illustrated in Figs. 5.1.4 (a) - (c) . It is clearly seen that the dimensionless pressures for both cases are not much different. Hence, the dimensionless pressure derivative is the primary tool for investigating the pressure-transient performance for a horizontal well. The well is located closer to the interface than to the top or bottom boundary. Therefore, the interface effect will appear before the top no-flow boundary effect. Shortly after the well is opened for production, there exist the first radial flow regime corresponding to the vertical radial flow around the wellbore. This flow regime is identified when the dimensionless pressure derivative has zero-slope straight line as shown in Fig. 5.1.4(c). Due to the permeability anisotropy, the dimensionless pressure derivative is not 0.5. Instead, it is

$$P'_D = \frac{\partial P_D}{\partial \ln(t_D)} = 1.56 \qquad (5.1.7)$$

since $(k_x/k_z) = 10$. In addition, the radial flow regime can also be identified on the semi-log plot of the dimensionless pressure versus the dimensionless time. Fig. 5.1.4(b) illustrates the existence of the first radial flow regime. It should be noted that the dimensionless pressure and the dimensionless time are based on the permeability in the x-direction of the top layer. Hence, we observe the same dimensionless pressure for both cases during infinite-acting flow period. This flow regime is ended when the pressure transient reaches the interface at $t_D \approx 250$.

For $R_k = 10$, when the wellbore feels the interface effect, the dimensionless pressure derivative is increased. The increment in the dimensionless pressure derivative is due to the effect of lower-permeability formation on the wellbore. In contrast, for $R_k = 0.1$, when the wellbore feels the effect of higher-permeability formation, the dimensionless pressure derivative is decreased. When the wellbore feels all of the boundaries, there exists a pseudo-steady state flow. During this flow regime, the dimensionless pressure derivative yield a straight line with slope of 1.0 on the log-log plot.

For $R_k = 0.1$, the pressure transient reaches the bottom no-flow boundary at $t_D \approx 2750$. When the pressure disturbance reaches the top no-flow boundary at $t_D \approx 2*10^4$. The dimensionless pressure derivative starts to deviate from the straight line and increases. The pseudo-steady is observed when the pressure disturbance reached all of the boundaries. For a long period of production, the dimensionless pressure and the dimensionless pressure derivative merge and form a log-log straight line. It should also be noted that during the pseudo-steady state flow, the dimensionless pressure derivative for both cases become identical.

Figs. 5.1.5 (a) - (c) listed in Appendix C, illustrate the dimensionless pressures and the dimensionless pressure derivatives for L = 25 ft. The horizontal wells are in the middle of layer #1. Hence, the boundary effect and the interface effect will be observed at the same time. In addition, the infinite-acting or radial flow will be longer than that of the previous case, L = 5 ft. This can be clearly seen in Fig. 5.1.5(c). The partial-penetration effect can be observed, in Fig. 5.1.5(c), in which the dimensionless pressure derivative deviates from the horizontal straight line. The overall performance is similar to that of the previous case. But the lengths of each flow regime are different. The horizontal well feel the top no-flow boundary and the bottom layer at the same time, $t_D \approx 6250$. For $R_k = 10$, after the transition period, there exists the second radial flow regime. In contrast, for $R_k = 0.1$, the dimensionless pressure derivative is decreased during this period since the interface effect is stronger than the top no-flow boundary effect. The pressure transient reaches the bottom boundary at $t_D \approx 8750$. The lateral boundary effects for cases can be observed at $t_D \approx 2*10^5$ and 10^5 for $R_k = 10$ and $R_k = 0.1$, respectively. For $R_k = 0.1$, the radius of investigation travels vertically to the higher-permeability layer and then travel horizontally along this layer until it reaches the lateral boundaries. Therefore, the pseudo-steady state for $R_k = 0.1$ appears before that for $R_k = 10$.

The dimensionless pressures and the dimensionless pressure derivatives performance for L = 40 ft. are illustrated in Figs. 5.1.6(a) - (c). The length of the first radial flow period is in between those for L = 5 ft. and L = 25 ft. due to the distances from the wellbore to the interface and the top no-flow boundary, shown in Table 5.1.1. During the first radial flow, for both cases, we can observe the partial penetration effect on the dimensionless pressure derivative. The end of the first radial flow, $t_D \approx 10^3$, occurs when the pressure disturbance reaches the top no-flow boundary. The dimensionless pressure derivatives are increased. When the radius of investigation reaches the interface, $t_D \approx 1.6*10^4$, the dimensionless pressure derivatives for $R_k = 10$ and $R_k = 0.1$ are different as shown in Figs. 5.1.6 (a) and (c). The pseudo-steady state flow is observed when all of the no-flow boundaries are felt at the wellbore.

Fig. 5.1.7(a) - (d) illustrate the dimensionless pressures and the dimensionless pressure derivatives for R_k = 10 as a function of the distance from the wellbore to the interface. The dimensionless pressures and the dimensionless pressure derivatives are the same for the first-radial flow and the pseudo-steady state flow periods. The differences are during the middle period. The differences are evident in the dimensionless pressure derivatives. The dimensionless pressure for L = 5 ft. yields the highest value since the wellbore has the closest distance to the lower-permeability layer, layer #2. While the dimensionless pressure for L = 25 ft yields the lowest value because the wellbore is in the middle of layer #1. The Cartesian plot of the dimensionless pressures versus the dimensionless time are shown in Fig. 5.1.7(d). During the pseudo-steady flow, the dimensionless pressure is a linear function of the dimensionless time. All of the three cases have the same slope but different intercepts. The different intercepts lead to different shape factors (C_A).

The dimensionless pressures and the dimensionless pressure derivatives for different values of L's for R_k = 0.1 are shown in Figs. 5.1.8 (a) - (d). The dimensionless pressure derivatives, for all cases, are the same during infinite-acting flow and pseudo-steady state flow. The dimensionless pressure for L = 5 ft. yields the lowest value since it has the least distance to the higher-permeability layer. While, for L = 40 ft, the dimensionless pressure is the highest value because the wellbore is located far away from the interface and is the closest to the top no-flow boundary. There exists only one semi-log straight line, corresponding to the first radial-flow regime, for each case. Fig. 5.1.8(d) illustrates the Cartesian plot of the dimensionless pressures versus the dimensionless time during the pseudo-steady state. The slope of the straight line is not a function of the distance from the wellbore to the interface. The slopes for $R_k = 10$ and $R_k = 0.1$ are the same during this period.

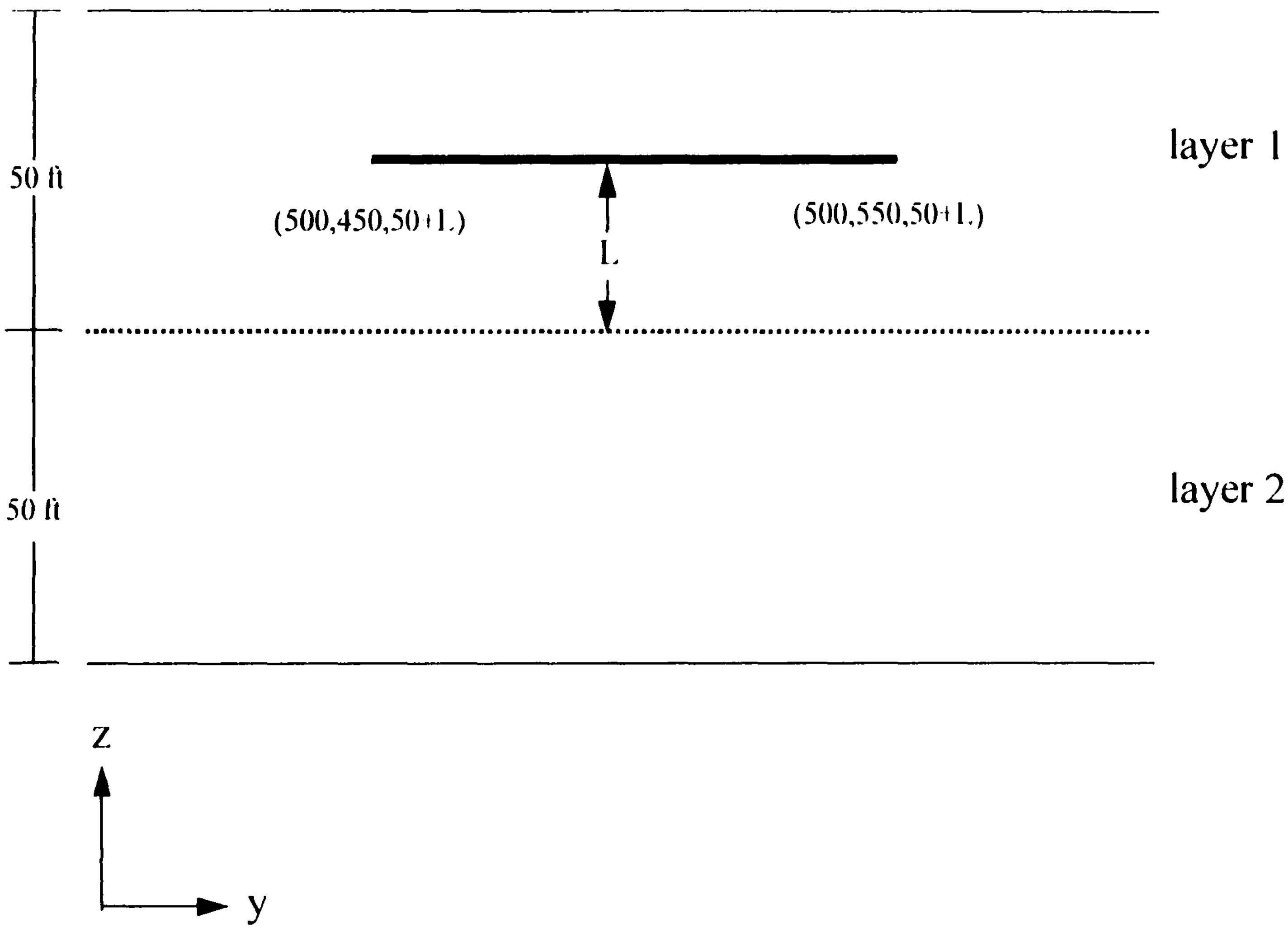

Figure 5.1.1 Reservoir Model for Case 1

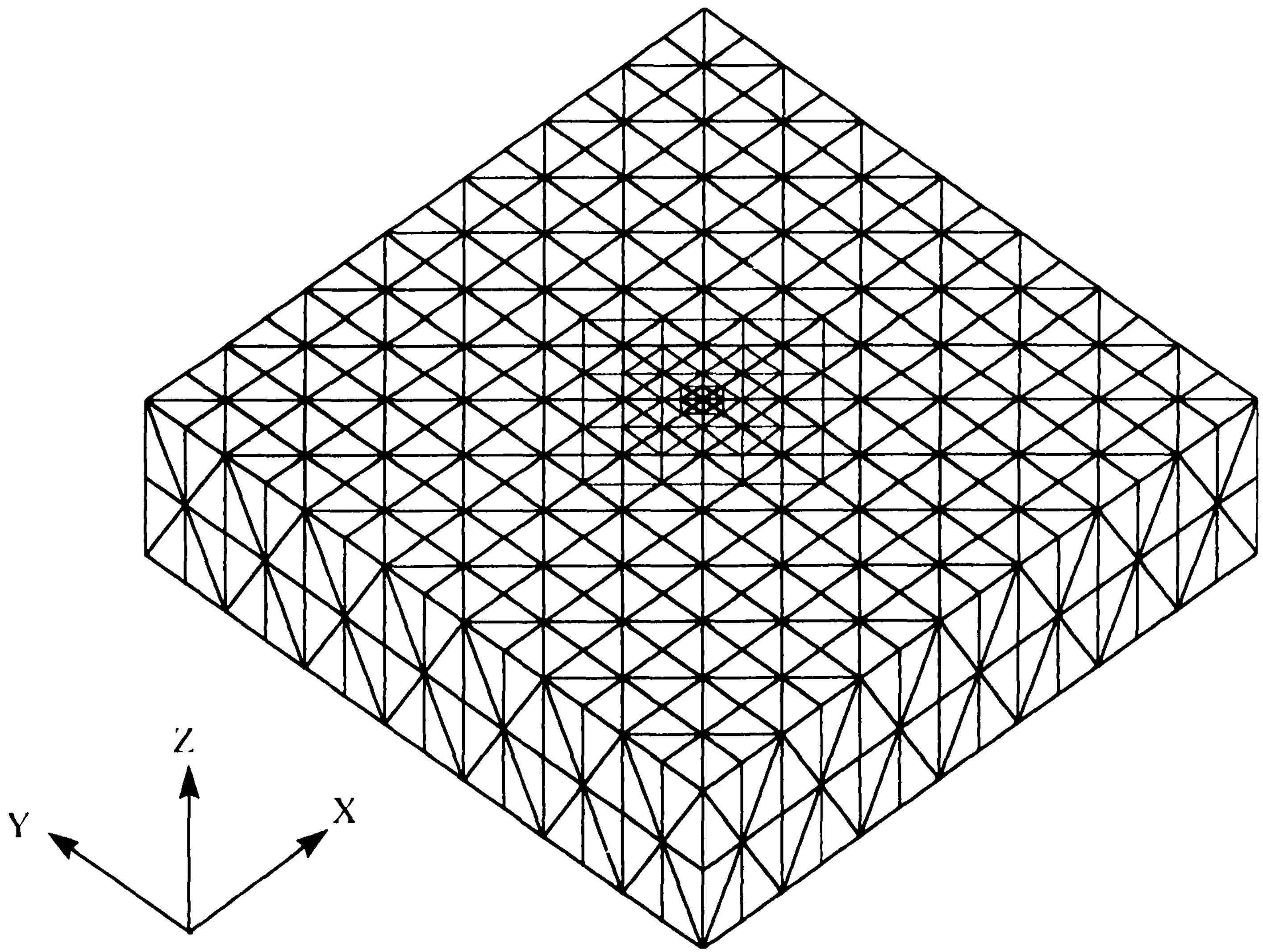

Figure 5.1.2 Reservoir Discretization for Case 1

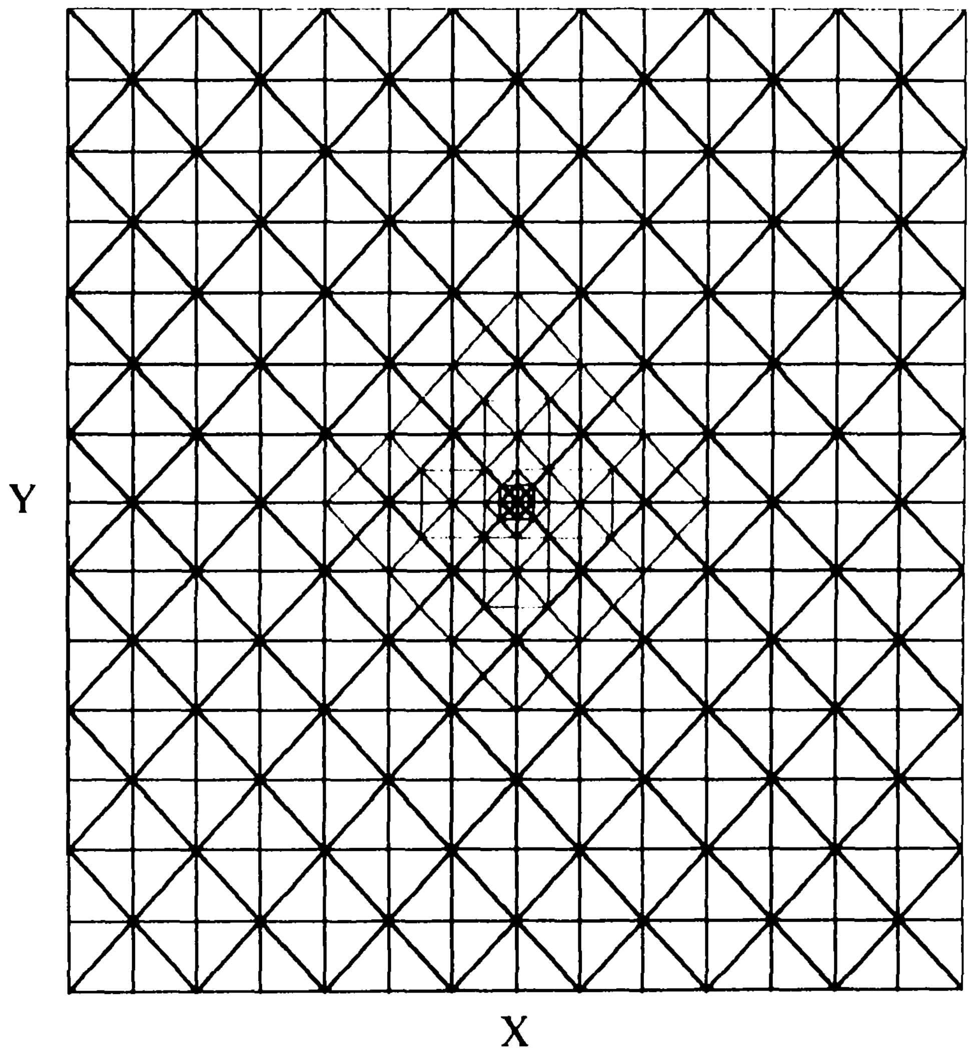

Figure 5.1.3 Reservoir Discretization for Case 1 in 2-D

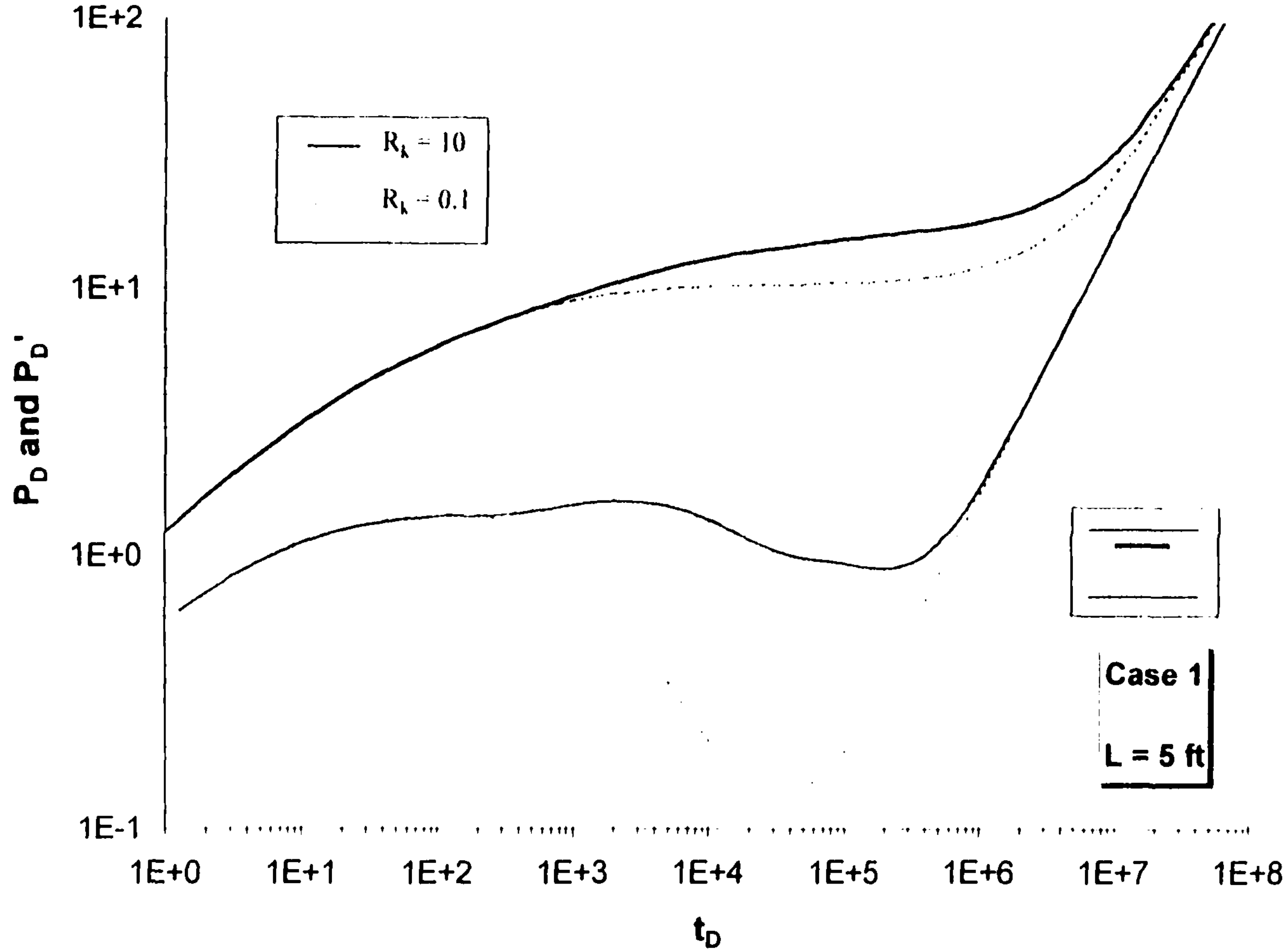

Figure 5.1.4(a) Dimensionless Pressure and Dimensionless Pressure Derivative Behavior for Case 1 and L = 5 ft.

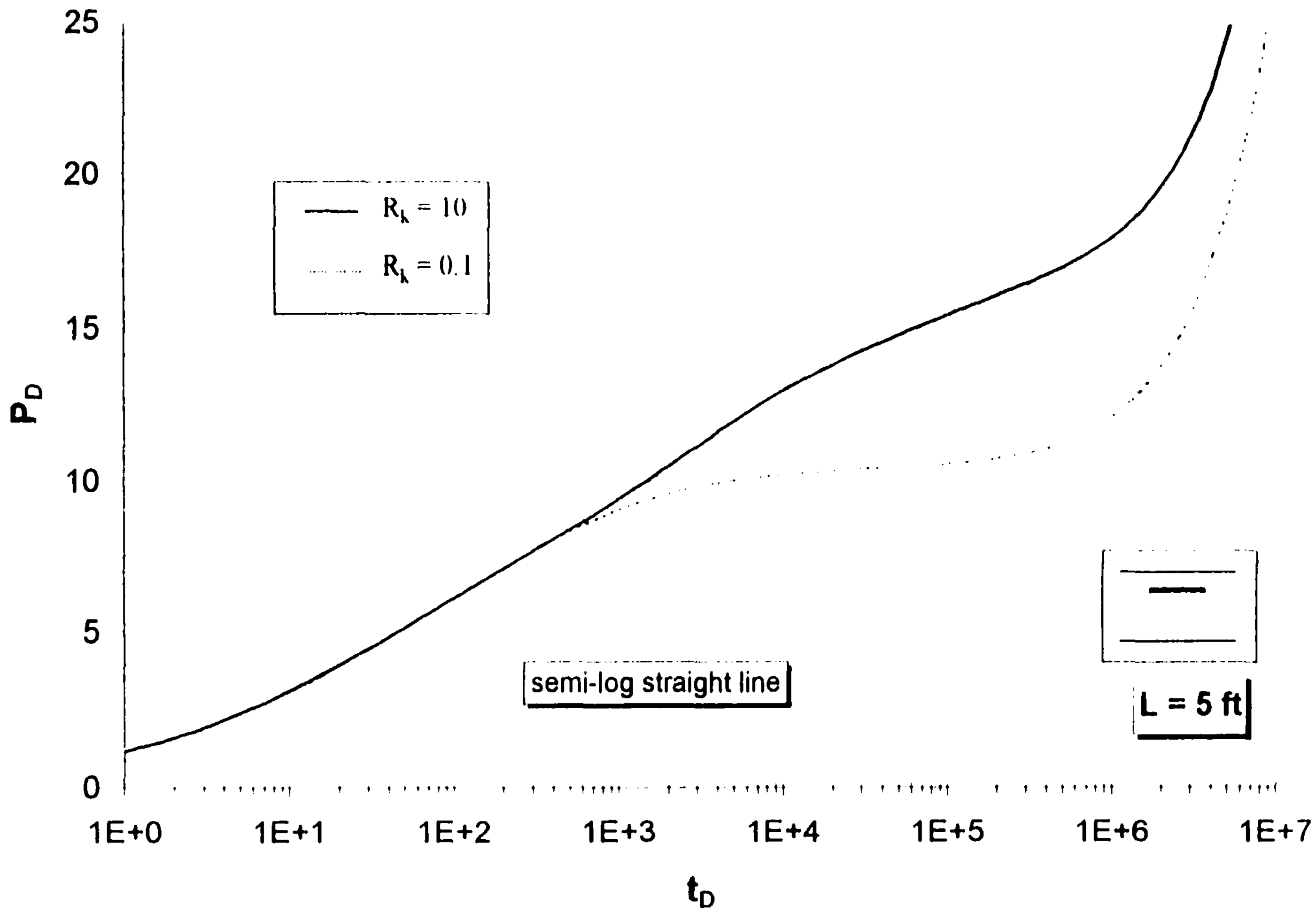

Figure 5.1.5(b) Dimensionless Pressure Behavior for Case 1 and L = 5 ft.

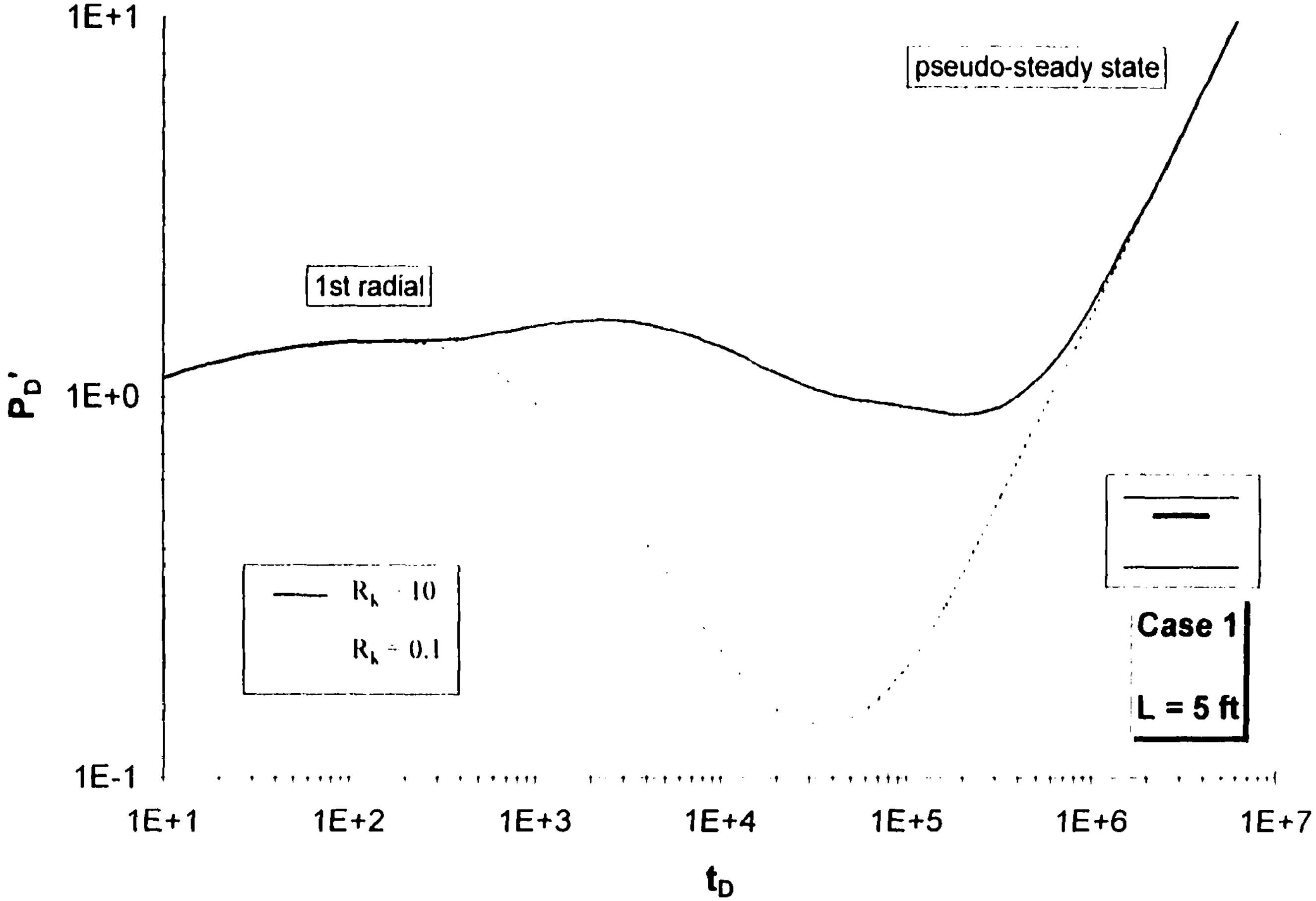

Figure 5.1.5(c) Dimensionless Pressure Derivative Behavior for Case 1 and L = 5 ft.

Case 2: A Horizontal Well in Two-Layer Reservoir with Gas-Cap Drive

The reservoir model is the same as that in Case 1. In this case, the top boundary and the bottom boundary are flowing boundary and no-flow boundary, respectively, shown in Fig. 5.2.1. The dash line represents the flowing boundary and the solid line represents no-flow boundary. At the flowing boundary or gas-oil interface, the dimensionless pressure is set to be zero since the pressure is assumed to be constant. Three different values of L's, 5 ft., 25 ft., and 40 ft. for both $R_k = 10$ and $R_k = 0.1$ are investigated in this section.

Before the pressure transient reaches the top flowing boundary, the wellbore performances should be the same as those in Case 1. The dimensionless pressures and the dimensionless pressure derivatives for L = 5 ft. are shown in Figs. 5.2.2(a) - (c) listed in Appendix D. The pressure transient reaches the gas-oil interface at $t_D \approx 20250$. For $t_D <$ 20250, the dimensionless pressures and the dimensionless pressure derivatives are the same as those shown in Figs. 5.1.4 (a)-(c). Once the pressure transient reaches the top flowing boundary, the dimensionless pressure derivatives are decreased for both cases. The dimensionless pressures become constants indicating that the steady state is reach.

Figs. 5.2.3 (a) - (d) illustrate the dimensionless pressures and the dimensionless pressure derivatives for L = 25 ft. For $t_D < 6250$, before the pressure transient reaches the top flowing boundary, the wellbore performances are the same as those in Figs. 5.1.5(a) - (c). For $R_k = 10$, the dimensionless pressure derivative is decreased when the radius of investigation reaches the top flowing boundary and the interface. The effect of flowing boundary is stronger that that of lower-permeability layer. For $R_k = 0.1$, the dimensionless pressure derivative is decreased more than that of $R_k = 10$ because of the combination of top flowing boundary and the higher-permeability effects. The pressure disturbance travels faster in the bottom layer for $R_k = 0.1$. Hence, the lateral boundary effect can be observed faster for $R_k = 0.1$ than for $R_k = 10$. At $t_D \approx 7*10^4$, for $R_k = 0.1$, the dimensionless pressure derivative starts to deviate from the derivative trend line and to form the small portion of horizontal straight line. This is the indication of the second radial flow regime. Figs. 5.2.3 (b) and (d) illustrate the semi-log plot of the dimensionless pressures versus the dimensionless time. In Fig. 5.2.3(b), there exists the first long radial flow for both cases and the small-slope second semi-log straight line for $R_k = 0.1$. This second semi-log straight line is highlighted in Fig. 5.2.3(d). Once the radius of investigation reaches all of the boundaries, the steady state is reached.

The dimensionless pressure and the dimensionless pressure derivative for L = 40 ft is illustrated in Figs. 5.2.4 (a) - (d). Before the radius of investigation reaches the interface or the boundaries, $t_D < 10^3$, the wellbore performances are the same as those in Figs. 5.1.6 (a) - (c). Once the top flowing boundary effect is observed, $t_D \approx 10^3$, the dimensionless pressure derivatives are decreased for both cases. The dimensionless pressure derivatives for both cases are the same until the radius of investigation reaches the interface, at $t_D \approx 1.6*10^4$. For $R_k = 10$, the slope of the dimensionless pressure derivative is slightly increased since the top flowing boundary effect is greater than the effect of lower-permeability layer. In contrast, the dimensionless pressure derivative for $R_k = 0.1$ forms another straight line with bigger negative slope due to the effect of the higher permeability layer. Following this period, there exists the second radial flow when the pressure disturbance reaches the lateral boundaries, $t_D \approx 6*10^4$. This second radial flow is not observed for R_k = 10. Figs. 5.2.4 (b) and (d) illustrate the semi-log plot of the dimensionless pressure versus the dimensionless time. There exists one and two semi-log straight lines for R_k = 10 and R_k = 0.1, respectively. The second semi-log straight line is illustrated in Fig. 5.2.4(d).

Figs. 5.2.5 (a) - (c) illustrate the dimensionless pressures and the dimensionless pressure derivatives for R_k = 10 for different values of L's. For L = 5 ft, the dimensionless pressure yields the highest value since it has the smallest distance from the wellbore to the lower-permeability formation. The dimensionless pressure for L = 40 ft is the lowest because it is located near the constant pressure boundary. For all cases, there exist only two flow regimes, the first radial flow and the steady state flow. It should be noted that the mathematical model used in this study does not account for:

- moving boundary,
- gas and/or water conning problem(s)

The gas-oil and oil-water contacts are assumed to be constant-pressure boundaries where the dimensionless pressure is set to be zero. Hence, there is no movement of gas or oil entering the domain of interested.

The dimensionless pressures and the dimensionless pressure derivatives for R_k = 0.1 are shown in Figs. 5.2.6 (a) - (c). For L = 5 ft, the dimensionless pressure is the lowest since it has the smallest distance from the wellbore to the higher permeability layer. The dimensionless pressure for L = 25 ft is the highest. All cases have the first radial flow regime. There exists the short second radial flow regime for L = 25 and 40 ft. Hence, the distance (L) controls the types of the second flow regime.

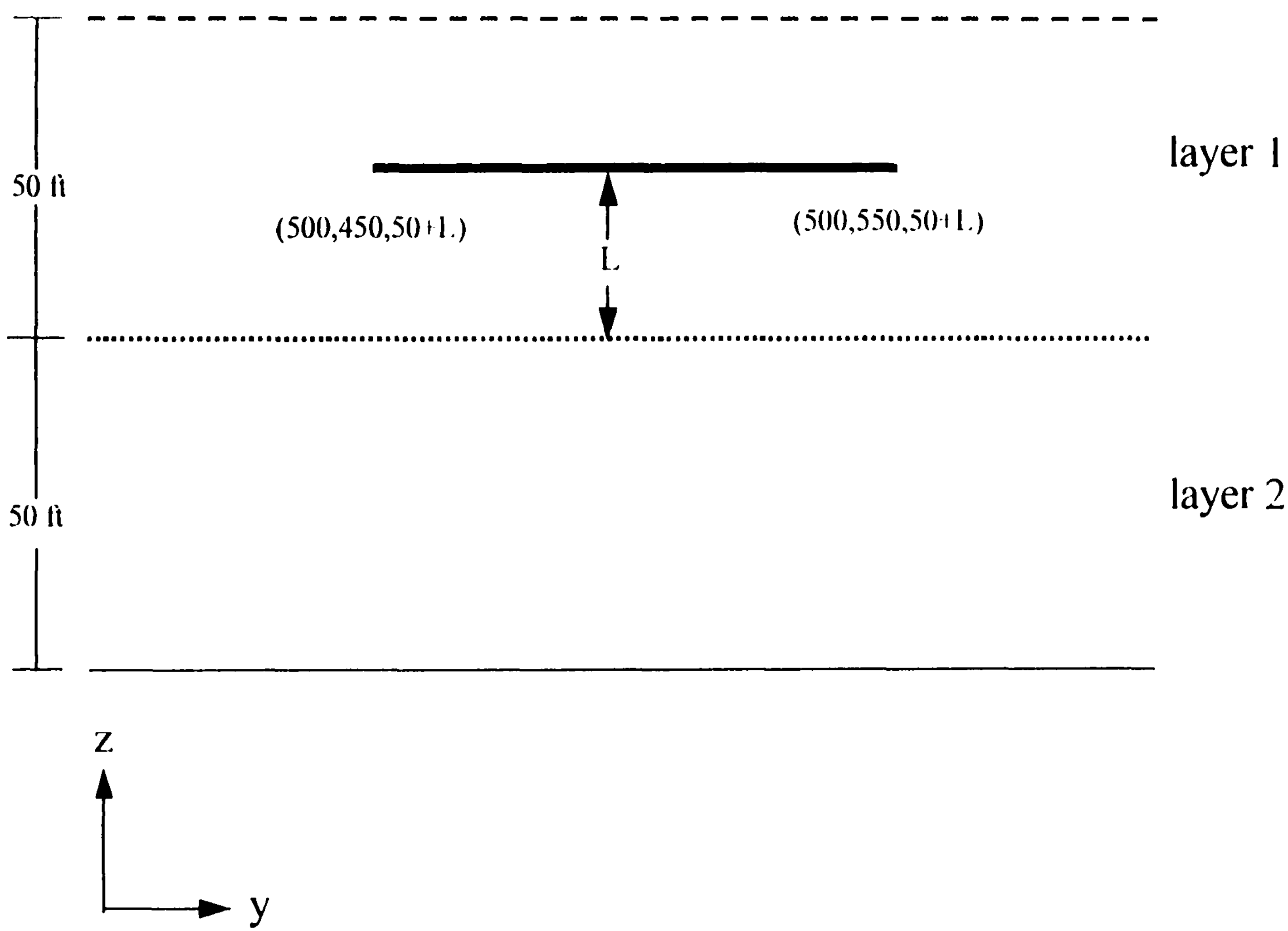

Figure 5.2.1 Reservoir Model for Case 2

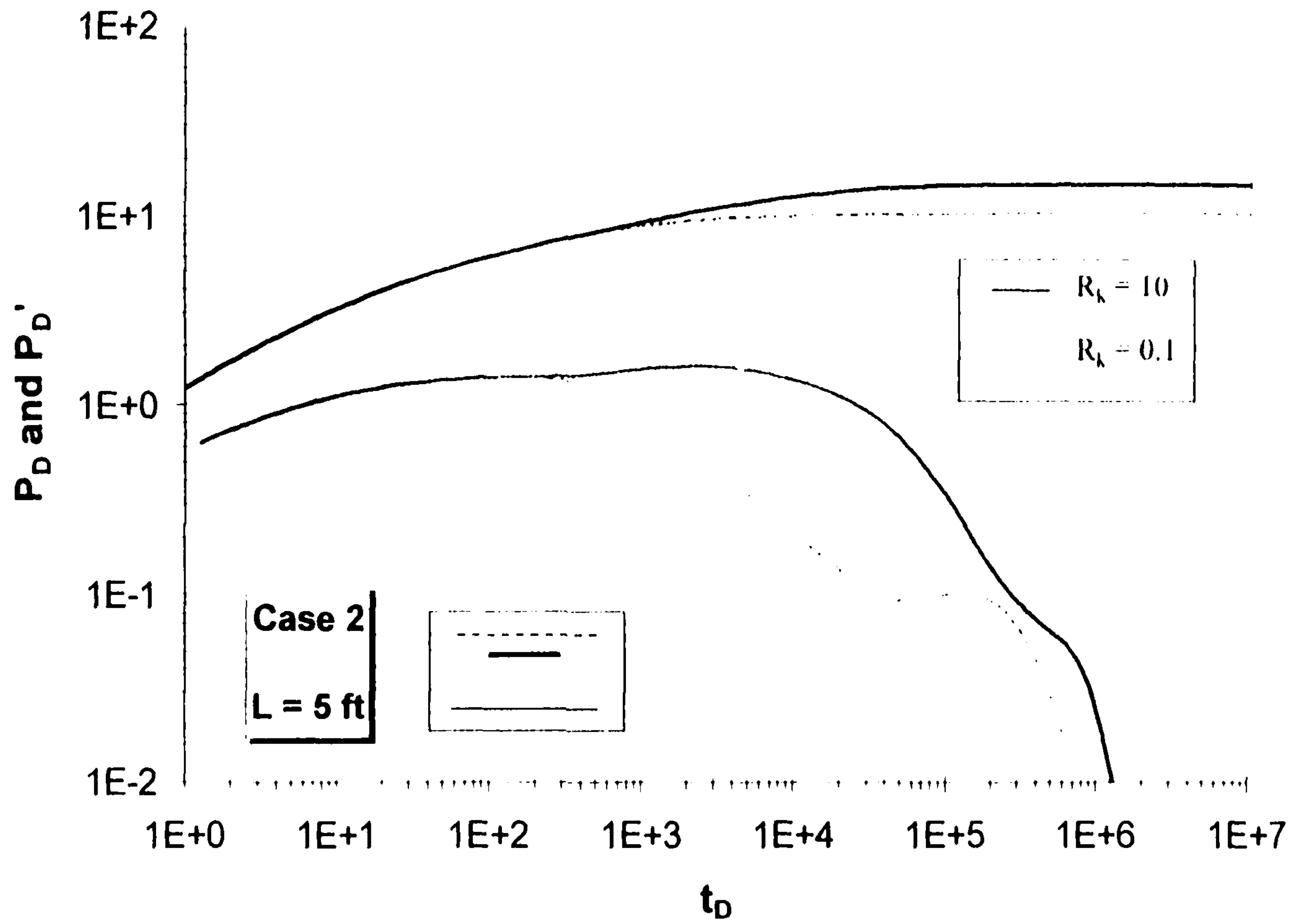

Figure 5.2.2(a) Dimensionless Pressure and Dimensionless Pressure Derivative Behavior for Case 2 and L = 5 ft.

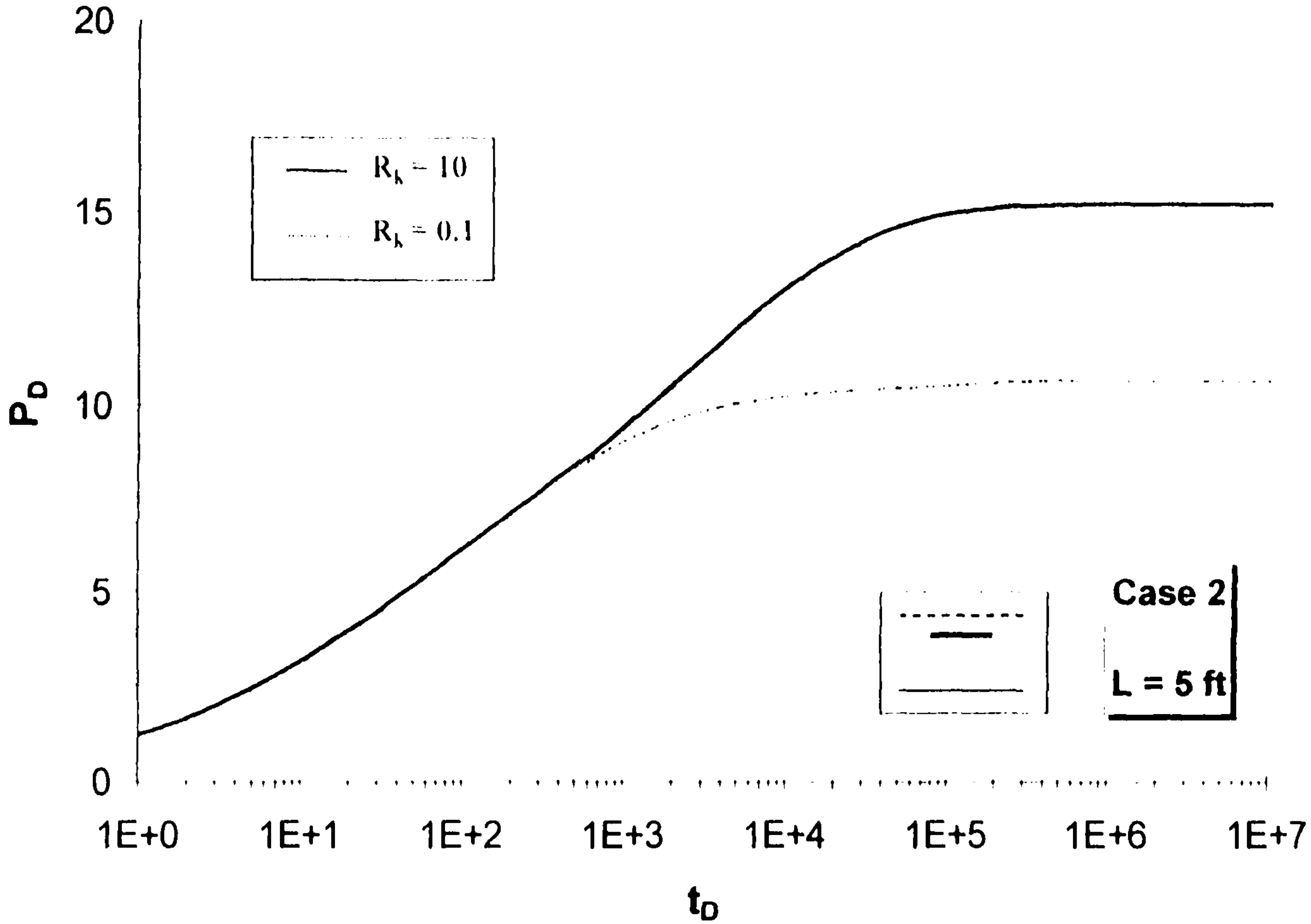

Figure 5.2.2(b) Dimensionless Pressure Behavior for Case 2 and L = 5 ft.

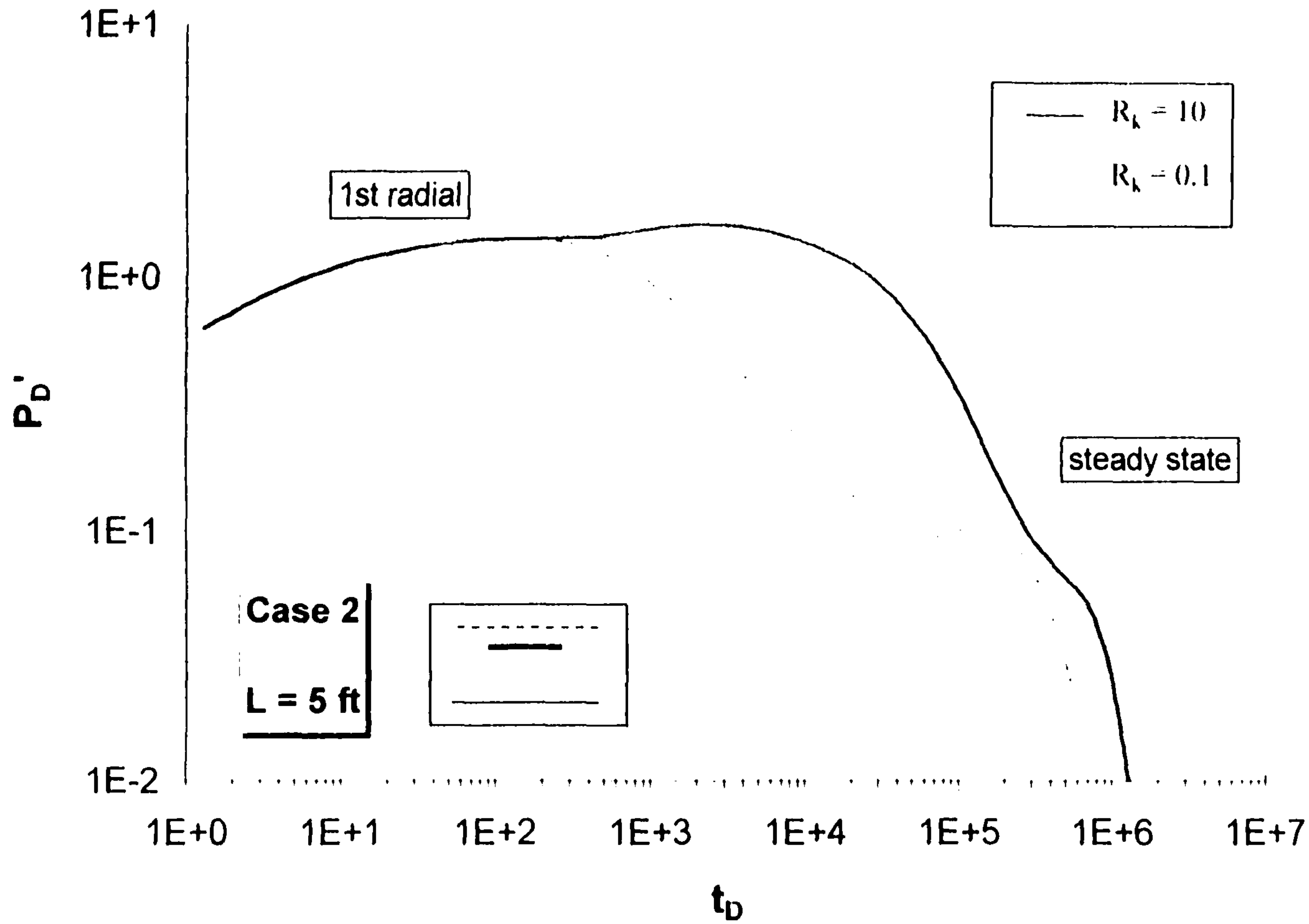

Figure 5.2.2(c) Dimensionless Pressure Derivative Behavior for Case 2 and L = 5 ft.

Case 3: A Horizontal Well in Two-Layer Reservoir with Bottom-Water Drive

The reservoir model is the same as that in Case 1. In this case, the top boundary and the bottom boundary are no-flow boundary and flowing boundary, respectively, shown in Fig. 5.3.1. The solid line represents no-flow boundary and the dash line represents the flowing boundary. At the flowing boundary or oil-water interface, the dimensionless pressure is set to be zero since the pressure is assumed to be constant. Three different values of L's, 5 ft., 25 ft., and 40 ft. for both $R_k = 10$ and $R_k = 0.1$ are investigated in this section.

Before the pressure transient reaches the top flowing boundary, the wellbore performances should be the same as those in Case 1. The dimensionless pressures and the dimensionless pressure derivatives for L = 5 ft. are shown in Figs. 5.3.2(a) - (c). The bottom boundary effect can be observed at the wellbore at $t_D \approx 2.5*10^5$ and $1.5*10^4$ for $R_k = 10$ and $R_k = 0.1$, respectively, shown in Fig. 5.3.2(c). For $R_k = 0.1$, it should be noted that the radius of investigation reaches the bottom boundary before it reaches the top boundary although the well is located closer to the top boundary that to the bottom boundary. Because the vertical permeability in the bottom layer is ten times bigger than that in the top layer. Once the radius of investigation reach the bottom flowing boundary, the steady state is observed.

For L = 25 ft., the well is located in the middle of Layer #1. The dimensionless pressures and the dimensionless pressure derivatives are shown in Figs. 5.3.3 (a)-(c) listed in Appendix E. Before the pressure transient reaches the bottom flowing boundary, the well performances are the same as those shown in Figs. 5.1.5 (a)-(c). The bottom water drive effect can be observed at the wellbore at $t_D \approx 3*10^5$ and $2*10^4$ for $R_k = 10$ and $R_k = 0.1$, respectively. Once the bottom flowing boundary is felt, the steady state is reached.

Figs. 5.3.4 (a) - (c) illustrate the dimensionless pressures and the dimensionless pressure derivatives for L = 40 ft. The wellbore performances are the same as those in Figs. 5.1.6 (a)-(c) before the bottom boundary effect can be observed at the wellbore. The pressure transient reaches the water-oil contact at $t_D \approx 3.5*10^5$ and $4.5*10^4$ for $R_k = 10$ and $R_k = 0.1$, respectively. Shortly after this period, there exists steady-state flow regime.

Figs. 5.3.5 (a) - (c) illustrate the dimensionless pressures and the dimensionless pressure derivatives for different values of L's for $R_k = 10$. Fig. 5.3.5(b) illustrates the semi-log plot of the dimensionless pressure versus the dimensionless time. The dimensionless pressure derivatives are shown in Fig. 5.3.5(c).

The dimensionless pressures and the dimensionless pressure derivatives for $R_k = 0.1$ are shown in Figs. 5.3.6 (a) - (c). The dimensionless pressure and the dimensionless pressure derivative are a function of the distance from the wellbore to the interface. The longer the distance, the higher the pressure and the pressure derivative are. Fig. 5.3.6 (b) illustrates the semi-log plot of the dimensionless pressure versus the dimensionless time. All cases have the radial flow regime. Once the bottom boundary is reach by the radius of investigation, we observe steady-state flow.

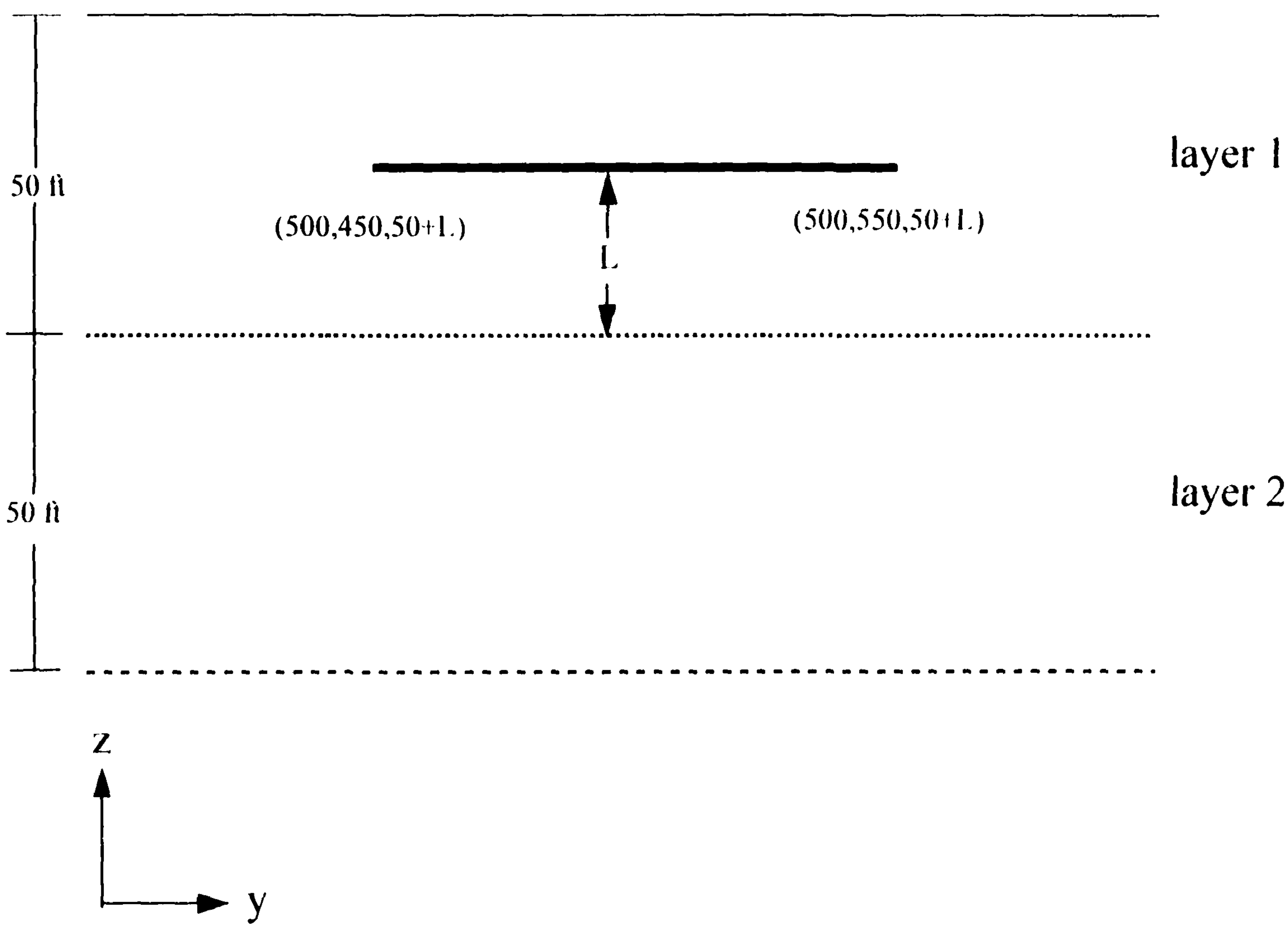

Figure 5.3.1 Reservoir Model for Case 3

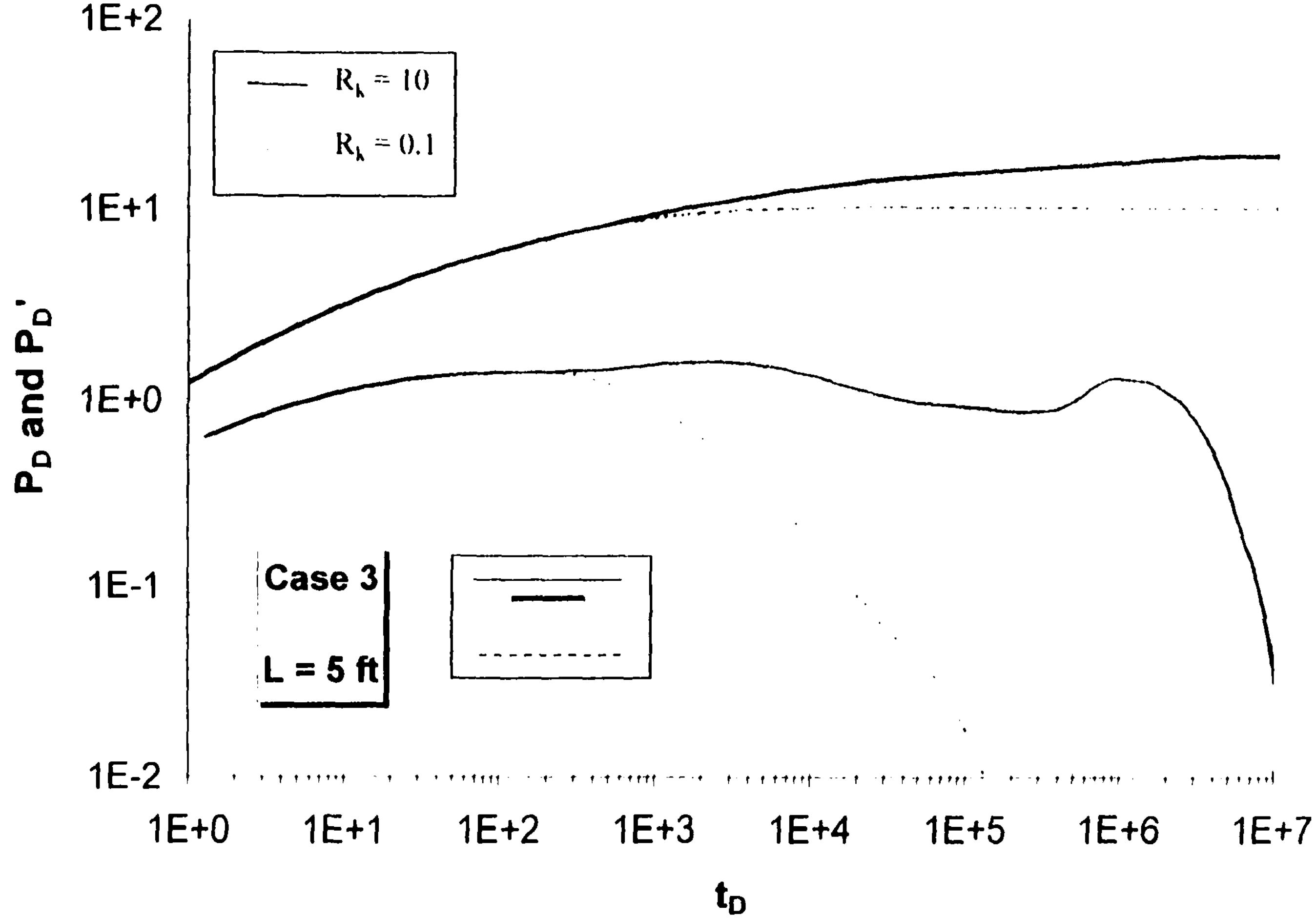

Figure 5.3.2(a) Dimensionless Pressure and Dimensionless Pressure Derivative Behavior for Case 3 and L = 5 ft.

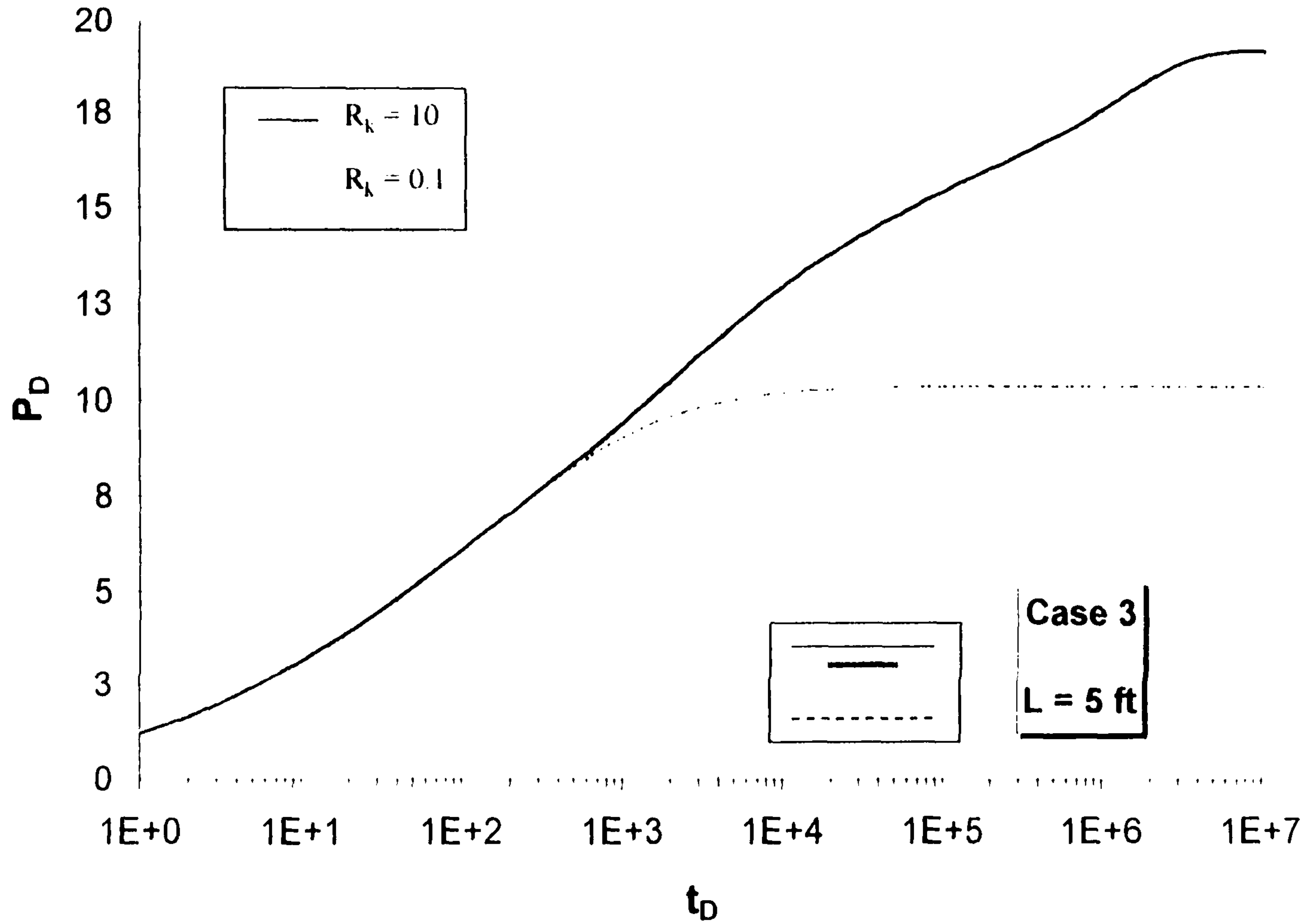

Figure 5.3.2(b) Dimensionless Pressure Behavior for Case 3 and L = 5 ft.

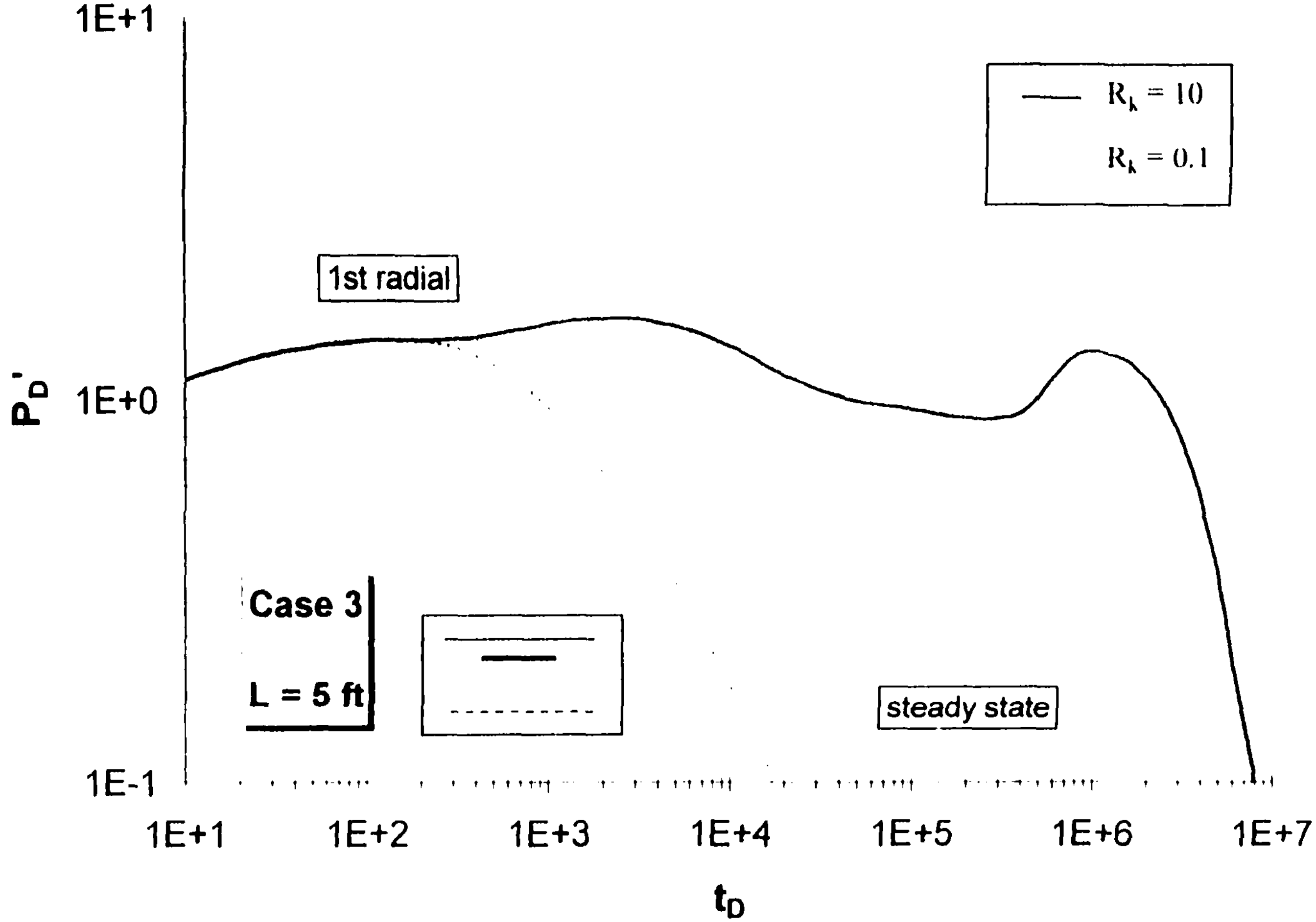

Figure 5.3.2(c) Dimensionless Pressure Derivative Behavior for Case 3 and L = 5

Case 4: A Horizontal Well in Two-Layer Reservoir with Gas-Cap and Bottom-Water Drive

The reservoir model is the same as that in Case 1. In this case, the top and the bottom boundaries are constant-pressure boundaries. Fig. 5.3.1 illustrates the reservoir system considered in this case. The dash line represents flowing boundary. At the flowing boundaries, gas-oil contact and oil-water contact, the dimensionless pressures are set to be zero since the pressure is assumed to be constant. Three different values of L's, 5 ft., 25 ft., and 40 ft. for both $R_k = 10$ and $R_k = 0.1$ are investigated in this section.

Before the pressure transient reaches the top or bottom constant-pressure boundaries, the wellbore performances should be the same as those in Case 1. The dimensionless pressures and the dimensionless pressure derivatives for L = 5 ft. are shown in Figs. 5.4.2(a) - (c). Following the infinite-acting flow regime, the interface effect appears where the dimensionless pressure derivatives for both $R_k = 10$ and $R_k = 0.1$ are different, at $t_D = 250$. The second flow regime for both cases are distorted by the top and bottom flowing boundary effects, respectively. These flow periods are shorter than those in Case 1. Once the constant-pressure boundary is reach by the radius of investigation, the dimensionless pressure is becoming a constant. This effect causes the dimensionless pressure derivative to decrease leading to the steady state.

The dimensionless pressures and the dimensionless pressure derivatives for L = 25 ft. are shown in Figs. 5.4.3 (a) - (c) listed in Appendix F. The radius of investigation reaches the top flowing boundary and the interface at the same time since the wellbore is located at the middle of layer #1. The top flowing boundary effect can be observed at $t_D \approx 6250$ causing the decrement in the dimensionless pressure derivative and the constant dimensionless pressure. There is only one transient flow regime for this case.

Figs. 5.4.4 (a) - (c) illustrate the dimensionless pressures and the dimensionless pressure derivatives for L = 40 ft. Since the wellbore is located closer to the top flowing boundary, the top boundary effect will be observed first. There exists only one flow regime. When the radius of investigation reach the top flowing boundary, $t_D \approx 10^3$, the dimensionless pressure derivatives are decreased. The dimensionless pressure derivatives for $R_k = 10$ and $R_k = 0.1$ are different when the wellbore feels the interface effect. Once all of the boundaries are reach by the radius of investigation, we observe the steady state flow.

The dimensionless pressures and the dimensionless pressure derivatives for Case 4 and $R_k = 10$ for different values of L's are shown in Figs. 5.4.5 (a)-(c). The case of L = 40 ft has the lowest dimensionless pressure and dimensionless pressure derivative since it is located far away from the low-permeability layer and close to the constant-pressure boundary. While the case of L = 5 ft. has the highest dimensionless pressure and the dimensionless pressure derivative. For L = 5 ft., there exist the second radial flow regime.

Figs. 5.4.6 (a)-(c) illustrate the dimensionless pressures and the dimensionless pressure derivatives for Case 4 and $R_k = 0.1$. Although the wellbore is located far away from the constant pressure boundary, the case of L = 5 ft. has the lowest dimensionless pressure and dimensionless pressure derivative. While the case of L = 25 ft. has the highest dimensionless pressure and the dimensionless pressure derivative. Since the wellbore is locate far away from either the interface or the constant pressure boundary compared to the other two cases. There is only one transient flow regime for L = 25 and 40 ft.

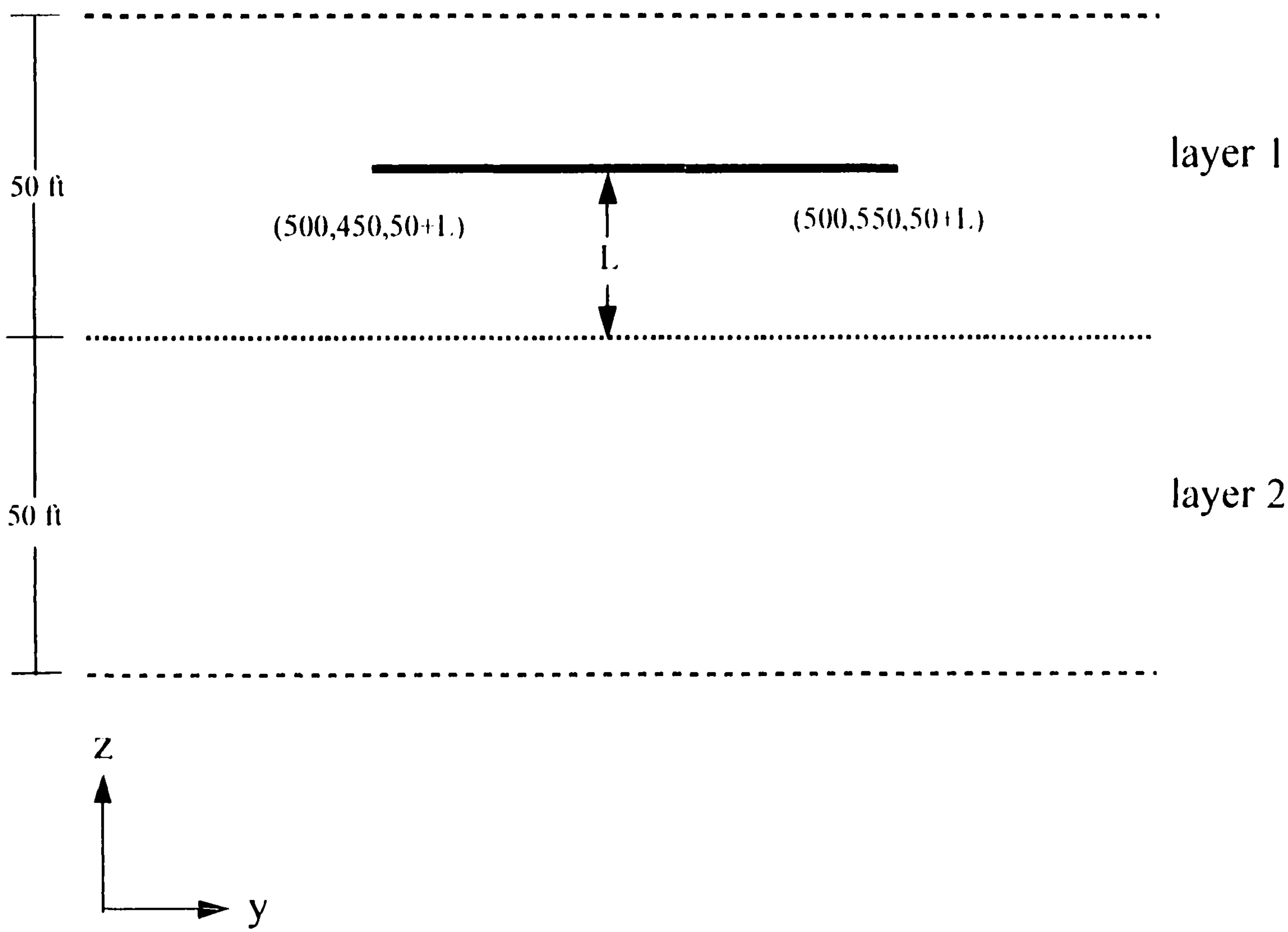

Figure 5.4.1 Reservoir Model for Case 4

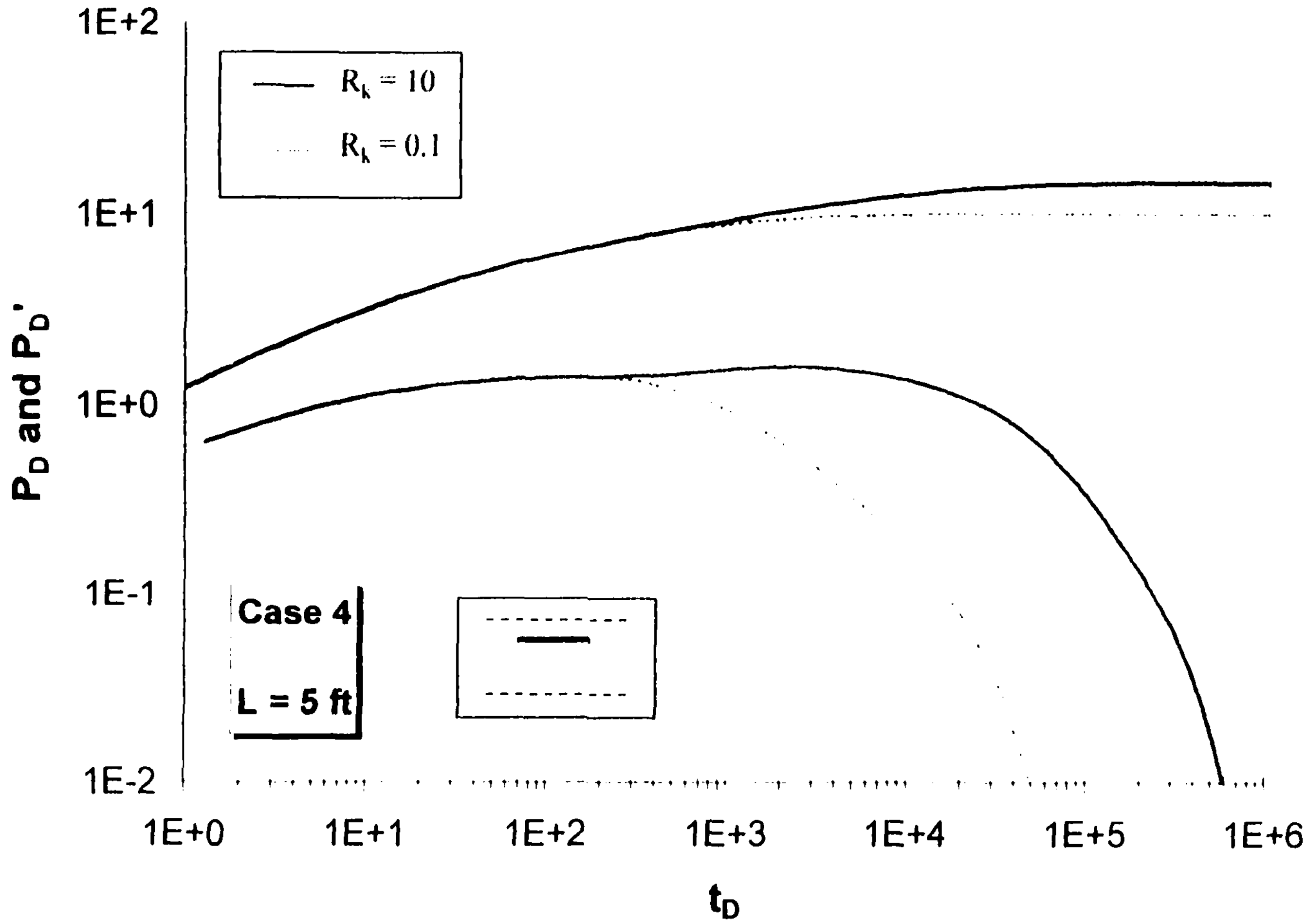

Figure 5.4.2(a) Dimensionless Pressure and Dimensionless Pressure Derivative Behavior

for Case 4 and L = 5 ft.

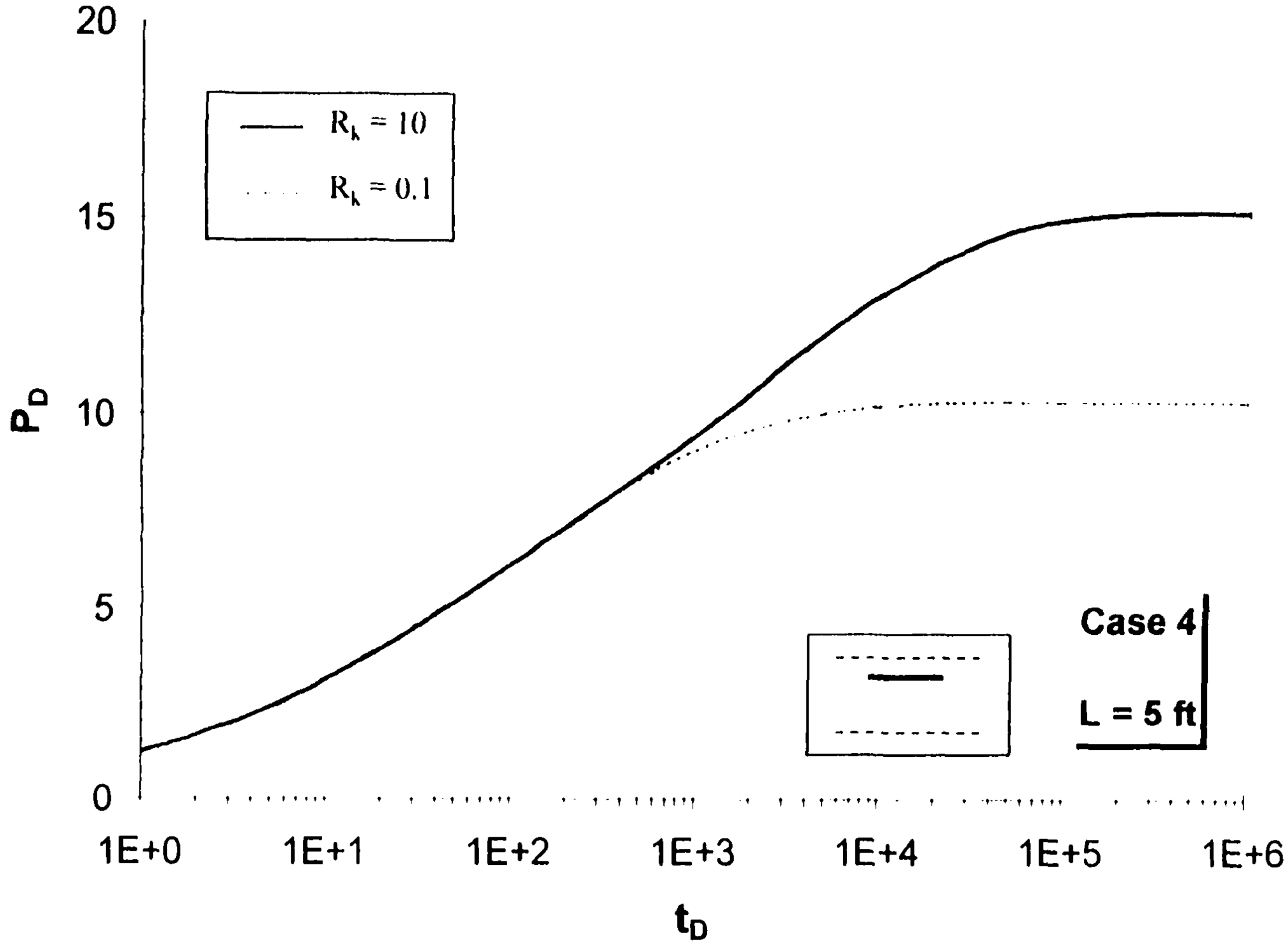

Figure 5.4.2(b) Dimensionless Pressure Behavior for Case 4 and L = 5 ft.

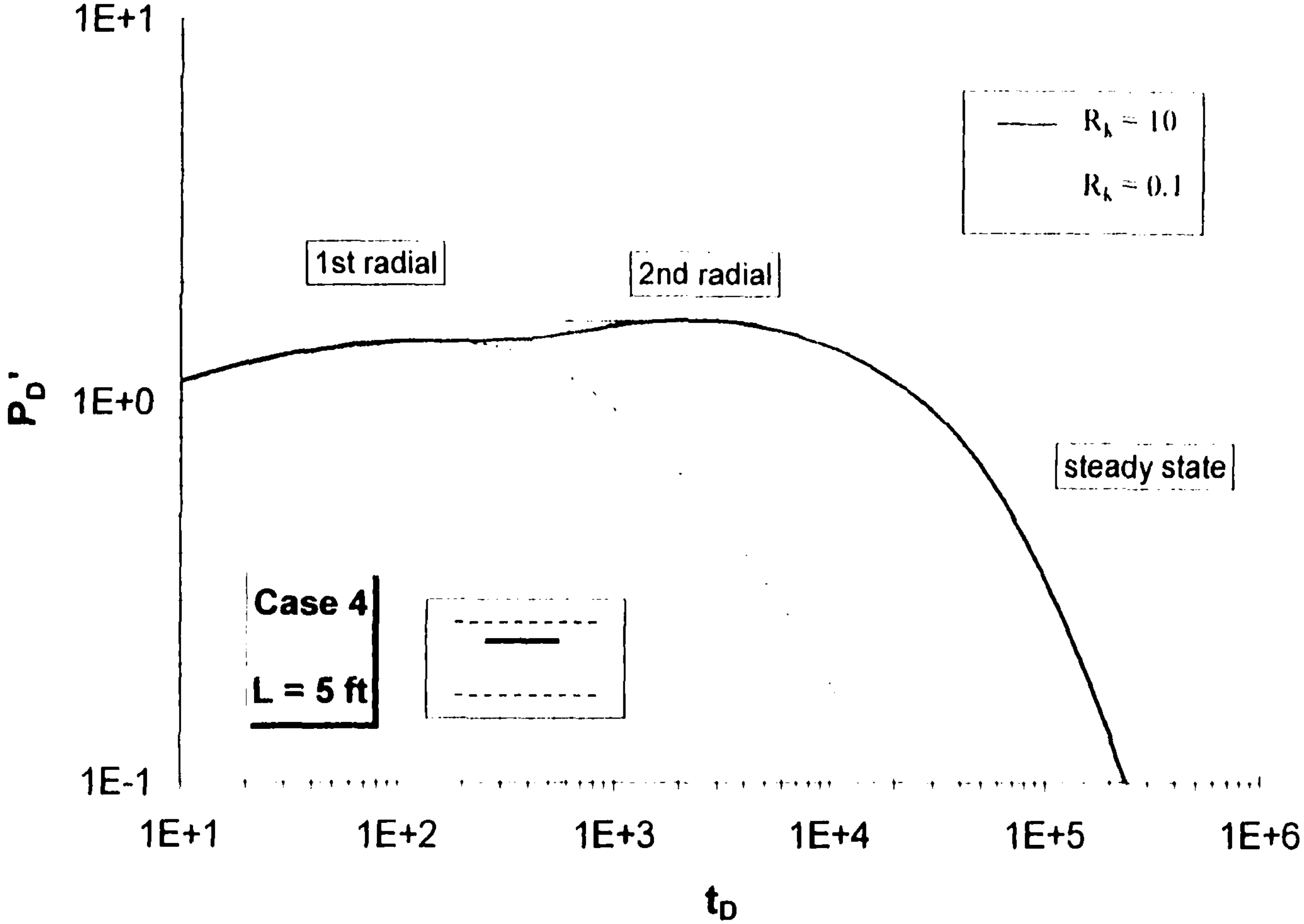

Figure 5.4.2(c) Dimensionless Pressure Derivative Behavior for Case 4 and L = 5 ft

Comparison of The Wellbore Performance of Case 1 - 4

The comparison of the wellbore performance of Case 1-4 can lead to the identification of the boundary effects. The following guide can be used to identify each boundary effect.

- The dimensionless pressure of Case 1 and 2 are the same until the top boundary effect is observed at the wellbore.
- The dimensionless pressure of Case 1 and 3 are the same until the bottom boundary effect is observe at the wellbore.
- The dimensionless pressure of Case 2 and 4 are the same until the bottom boundary effect is observed at the wellbore.

The combination of these comparisons and the previous plots gives information about the behavior of the horizontal well.

Figs. 5.4.7(a) - (c) illustrate the dimensionless pressures and the dimensionless pressure derivatives for R_k = 10 and L = 5 ft. The pressure transient reaches the top boundary before it reaches the bottom boundary. The semi-log plot of the dimensionless pressure versus the dimensionless time is shown in Fig. 5.4.7(b). Case 2 and 4 do not have the second semi-log straight line because of the top flowing boundary effect. These second radial flow regime is also identified in Fig. 5.2.7(c) as the constant dimensionless pressure derivative.

The dimensionless pressures and the dimensionless pressure derivatives for R_k = 0.1 and L = 5 ft are shown in Figs. 5.4.8(a) - (c). The pressure disturbance reaches the bottom boundary before it reaches the top boundary. In contrast to the case of R_k = 10.

the dimensionless pressure and the dimensionless pressure derivative of Case 2 are bigger than those of Case 3. This happens because the bottom boundary effect is observed before the top boundary effect is.

Figs. 5.4.9(a) - (c) illustrate the dimensionless pressures and the dimensionless pressure derivatives for R_k = 10 and L = 25 ft for different types of boundary conditions. The pressure transient reaches the top boundary before it reaches the bottom boundary.

The dimensionless pressures and the dimensionless pressure derivatives for R_k = 0.1 and L = 25 ft. for different types of boundary conditions are illustrated in Figs. 5.4.10 (a) - (c). The top boundary effect is observed before the bottom boundary effect is. There exists the second radial flow regime only for Case 2.

Figs. 5.4.11(a) - (c) illustrate the dimensionless pressures and the dimensionless pressure derivatives for R_k = 10 and L = 40 ft for four different types of boundary conditions. The top boundary is reached early because the wellbore is located very close to the top boundary. Only Case 1 and 3 have the second radial flow regime. The bottom boundary effect is observed at $t_D \approx 2.5*10^5$.

The dimensionless pressures and the dimensionless pressure derivatives for R_k = 0.1 and L = 40 ft. for different types of boundary conditions are illustrated in Figs. 5.4.12(a) - (c). Similar to the case of R_k = 10, the pressure transient reaches the top boundary before it reaches the bottom boundary.

Case 5: A Horizontal Intersecting A Two-Layer Reservoir

The reservoir model is the same as in Case 1. It consists of two different-permeability layers. But the wellbore configuration is different. The wellbore is intersecting both layers as illustrated in Fig. 5.5.1(a). Three different angles between the wellbore and the horizontal plane, $\theta = 10^o$, 45^o, and 90^o, are considered in this section. The wellbore is parallel to y-direction. Both top and bottom boundaries are only considered to be no-flow boundaries for $\theta = 45^o$ and 90^o . But for $\theta = 10^o$, four different boundary conditions are considered as shown in Fig.5.5.1(b). Half of the wellbore length are located in layer #1 and layer #2. The effects of the wellbore angle (θ) the ratio of permeabilities of layer #1 and of layer #2 are investigated in this section.

The discretized reservoir model is shown in Fig. 5.5.2. The uniform triangular elements are used through the boundaries except at the center of the boundary. Since this area is intersected by the wellbore. Hence, the nonuniform smaller triangular elements are used in this area to handle the source points. Fig. 5.5.3 illustrates the discretized reservoir model in 2-D.

The properties of each layer are the following.

$L_w = 100$ ft

$L_x = 1000$ ft.

$L_y = 1000$ ft.

$L_{z1} = 50$ ft. $\qquad L_{z2} = 50$ ft.

$\phi_1 = 0.1 \qquad \phi_2 = 0.1$

$k_{x,1} = 1.0$ md

$k_{y,1} = 1.0$ md

$k_{z,1} = 0.1$ md

$k_{x,2} = k_{y,2} = 10*k_{z,2}$

The ratio of permeabilities of layer #1 and of layer #2 is defined as

$$R_k = \frac{k_{x,1}}{k_{x,2}} \tag{5.5.1}$$

Three different ratios (R), 1.0, 10.0, and 50.0, are considered in this section.

The distances from the wellbore to each boundary are summarized in Table 5.5.1 Equation 5.3 is applied to calculate the dimensionless time required for the pressure transient to travel from the wellbore to the boundaries. These dimensionless times are shown in Table 5.5.2.

	distance to the boundary, ft			
θ, degree	top	bottom	x-direction	y-direction
10	41.32	41.32	500.00	450.76
45	14.64	14.64	500.00	464.64
90	0.00	0.00	500.00	500.00

Table 5.5.1 The Shortest Distance from The Wellbore to The Boundaries for Case 5

		t_D		
θ, degree	top	bottom	x-direction	y-direction
10	17073	17073	$2.5*10^5$	$2.0*10^5$
45	2143	2143	$2.5*10^5$	$2.2*10^5$
90	0.00	0.00	$2.5*10^5$	$2.5*10^5$

Table 5.5.2 The Dimensionless Times for The Pressure Disturbance to Travel from The Wellbore to The Boundaries for Case 5 and $R_k = 1$

		t_D		
θ, degree	top	bottom	x-direction	y-direction
10	17073	$1.7*10^5$	$2.5*10^5$	$2.0*10^5$
45	2143	21432	$2.5*10^5$	$2.2*10^5$
90	0.00	0.00	$2.5*10^5$	$2.5*10^5$

Table 5.5.3 The Dimensionless Time for The Pressure Disturbance to Travel from The Wellbore to The Boundaries for Case 5 and $R_k = 10$

		t_D		
θ, degree	top	bottom	x-direction	y-direction
10	17073	$8.5*10^5$	$2.5*10^5$	$2.0*10^5$
45	2143	$1.1*10^5$	$2.5*10^5$	$2.2*10^5$
90	0.00	0.00	$2.5*10^5$	$2.5*10^5$

Table 5.5.4 The Dimensionless Time for The Pressure Disturbance to Travel from The Wellbore to The Boundaries for Case 5 and $R_k = 50$

Figs. 5.5.4 (a)-(c) illustrate the dimensionless pressures and the dimensionless pressure derivatives for $\theta = 10^o$ for different values of R_k's. For $R_k = 1$, the two-layer system is simply a homogeneous reservoir. It is clearly seen that the dimensionless pressure increases as the permeability ratio (R_k) increases. The additional dimensionless pressure is required to maintain the same production rate (q). On the semi-log plot. Fig. 5.2.4(b), the slope of the straight line during the infinite-acting flow is also a function of the permeability ratio. The higher the permeability, the higher the slope is. For the homogeneous system, $R_k = 1$, the first radial and the partial-penetration effect are observed at the wellbore for the small values of the dimensionless time, $t_D < 5*10^3$ on the semi-log plot. But the end of the first flow regime can be seen earlier on the dimensionless pressure derivative. Once the radius of investigation reaches the top and the bottom no-flow boundaries, for $R_k = 1$,there exists the second radial flow indicated by the semi-log straight line shown in Fig. 5.5.4(b) and the constant dimensionless pressure derivative shown in Fig. 5.5.4(c). This flow regime is the horizontal radial flow around the long horizontal well. But there do not exist the second radial flow regime for R_k =10 and 50. Once the radius of investigation reaches all of the boundaries, we observe the pseudo-steady state flow. On Fig. 5.5.4(c), the beginning dimensionless time of the pseudo-steady state is a function of the permeability ratio. For the high value of permeability ratio, the pseudo-steady state appears very late. This is due to the relatively low permeability in the bottom layer.

The dimensionless pressures and the dimensionless pressure derivatives for θ = 45° are plotted in Figs. 5.5.5 (a) - (c), in Appendix G. The dimensionless pressures and the dimensionless pressure derivatives for this case are similar to those of the previous case, θ = 10°. The difference is that the dimensionless pressure derivatives are more flat during the first and the second radial flow periods as shown in Fig. 5.5.5(c). In Fig. 5.5.5(b), for R_k = 1,the slopes of the first and the second straight lines are less difference.

Figs. 5.5.6 (a)-(c) illustrate the dimensionless pressures and the dimensionless pressure derivatives for θ = 90°, the vertical well. There is no partial-penetration effect since the wellbore completely penetrates the two-layer system. For R_k = 1, the system becomes the vertical well in a closed rectangular homogeneous reservoir. Due to centrally located wellbore, there are only two different flow regimes; the first radial flow and the steady-state flow regimes. The dimensionless pressure derivative during the infinite-acting flow equals 0.5, shown in Fig. 5.5.6(c), since the radial permeability, horizontally isotropic, is constant and equals to $k_{x,1}$. When the radius of investigation reaches all four lateral boundaries at the same time. we observe the steady-state flow. As expected. the dimensionless pressure derivatives for R_k = 10 and 50 during the infinite-acting flow are higher than that for the homogeneous system. They are not perfectly horizontal straight lines. In the semi-log plot. Fig. 5.5.6(b). we can observe only one straight line for each case.

The dimensionless pressures and the dimensionless pressure derivatives for R_k = 1 and for different angles (θ) are shown in Figs. 5.5.7 (a) - (c). It should be noted that the dimensionless pressure is lowest when the wellbore becomes vertical. For $\theta = 90^o$. the wellbore has the highest radial permeability. $k_r = k_x$. since the vertical permeability does not contribute to the radial flow. Actually. in this special case. there is no vertical flow. But for $\theta \neq 90^o$. the radial permeability is. a function of θ. k_x. k_y. and k_z. less than the horizontal permeability. For $\theta \neq 90^o$. there exists two semi-log straight lines. The slopes of these two straight lines are less different when the angel becomes closer to 90^o or the wellbore is become more vertical. Fig.5.5.7 illustrates the Cartesian plot of the dimensionless pressure versus the dimensionless time during pseudo-steady state flow.

Figs. 5.5.8 (a) - (d) illustrate the dimensionless pressures and the dimensionless pressure derivatives for R_k = 10. The dimensionless pressures and the dimensionless pressure derivatives are similar to those of the previous case. R_k = 1. homogeneous system. But this case yields higher dimensionless pressures and the dimensionless pressure derivatives. There exists only one semi-log straight line as shown in Fig. 5.5.8(b). Fig. 5.5.8(d) illustrates the Cartesian plot of the dimensionless pressure versus the dimensionless time during the pseudo-steady state flow.

The dimensionless pressures and the dimensionless pressure derivatives for R_k = 50 are shown in Figs. 5.5.9 (a) - (d). The dimensionless pressures and the dimensionless pressure derivatives for this case are similar to the previous two cases but they yield the highest the dimensionless pressures and the dimensionless pressure derivatives. There exists only semi-log straight line for each case as shown in Fig. 5.5.9(b). Fig.5.5.9(d) illustrates the Cartesian plot of the dimensionless pressure versus the dimensionless pressure derivative during the pseudo-steady state flow.

Figs. 5.5.10 (a) -(c) illustrate the dimensionless pressures and the dimensionless pressure derivatives for R_k = 10 and $\theta = 10^o$ for four different boundary conditions. These four boundary conditions are shown in Fig. 5.5.1(b). Due to the higher permeability in Layer #1, the radius of investigation travels faster in this layer. Hence, the top boundary is reached before the bottom is. The dimensionless pressures and the dimensionless pressure derivatives are the same for all of the boundary conditions before the wellbore feels the top boundary effect. When the radius of investigation reaches the top boundary, $t_D \approx 1.7*10^4$, there are two different groups of dimensionless pressure response. The first group consists of BC I and BC III in which the top boundary is no-flow boundary. The other corresponds to the top flowing boundary consisting of BC II and BC IV. The dimensionless pressures for BC I and BC III are the same until the radius of investigation reaches the bottom boundary, approximately $t_D = 2.5*10^5$. At the same dimensionless time, the dimensionless pressures for BC II and BC IV are different. When the pressure transient reaches all boundaries, we observe the (pseudo) steady state. Fig. 5.5.10 (b) show the semi-log plot of the dimensionless pressure versus dimensionless time. All of the four boundary conditions have the same first semi-log straight line. Excluding the system with BC I, all systems have the third horizontal straight line during the steady-state flow. For BC I, there exists a pseudo-steady state flow.

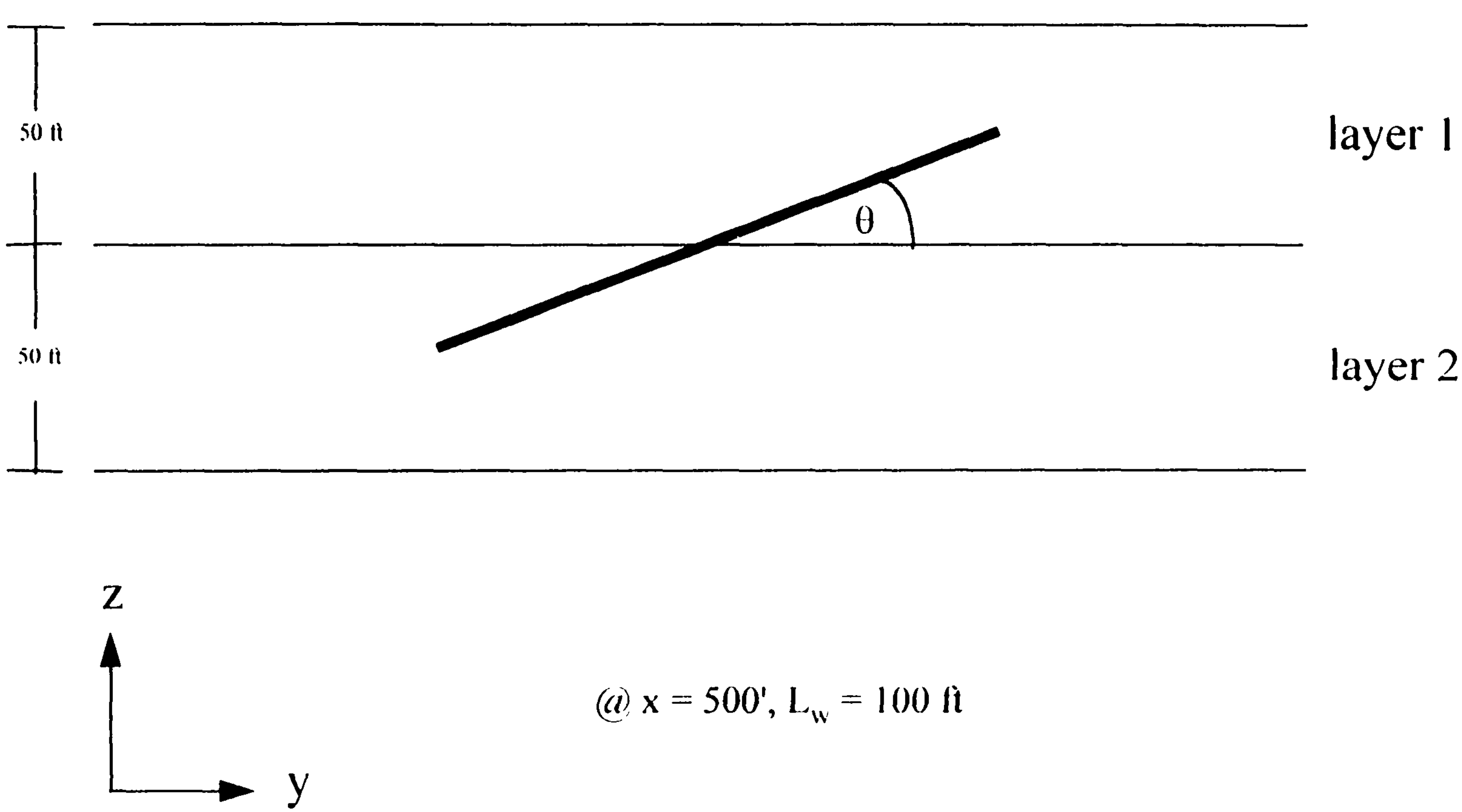

Figure 5.5.1(a) Reservoir Model for Case 5

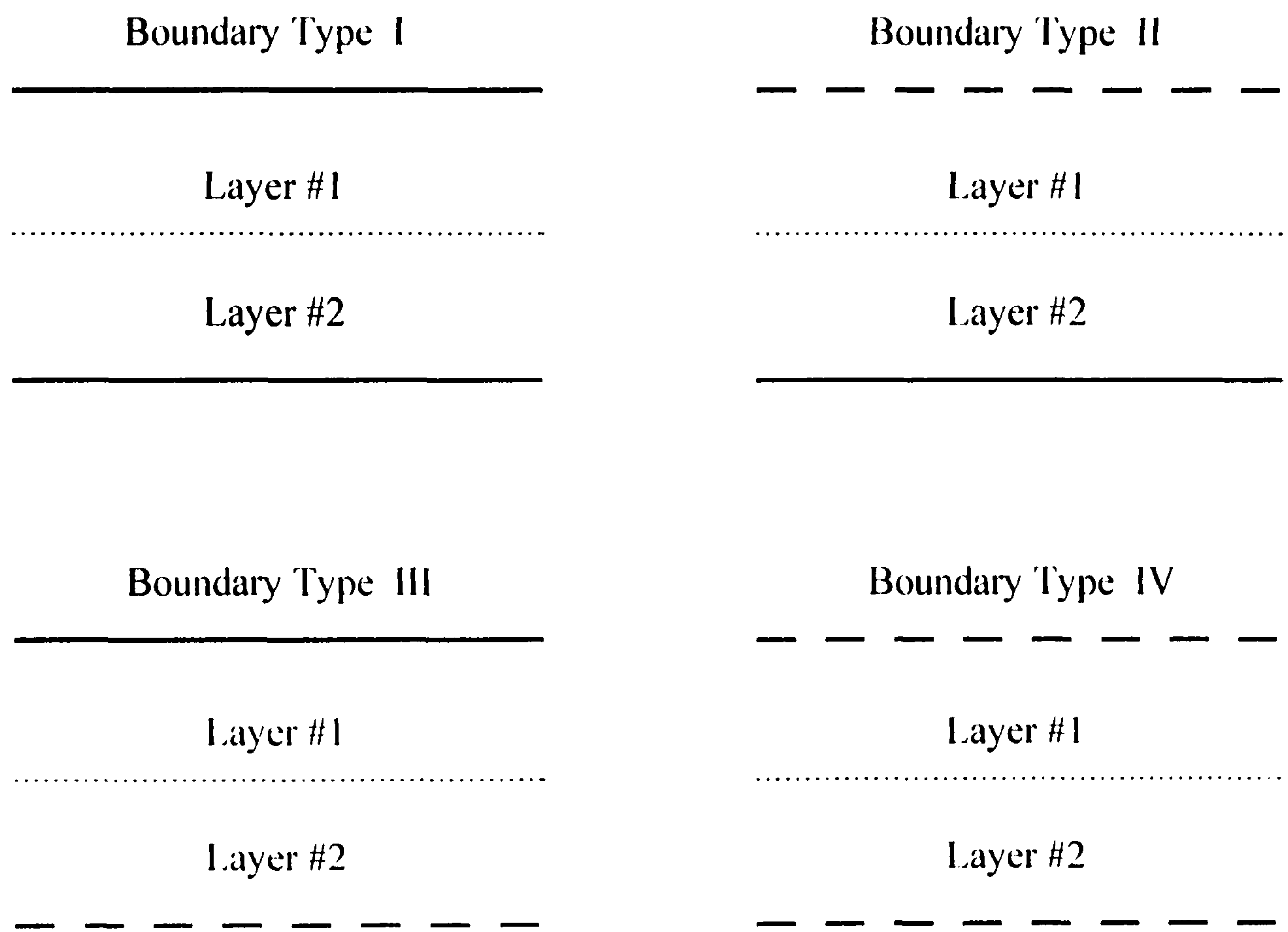

Figure 5.5.1(b) Four Different Types of Boundary Conditions Considered in Case 5

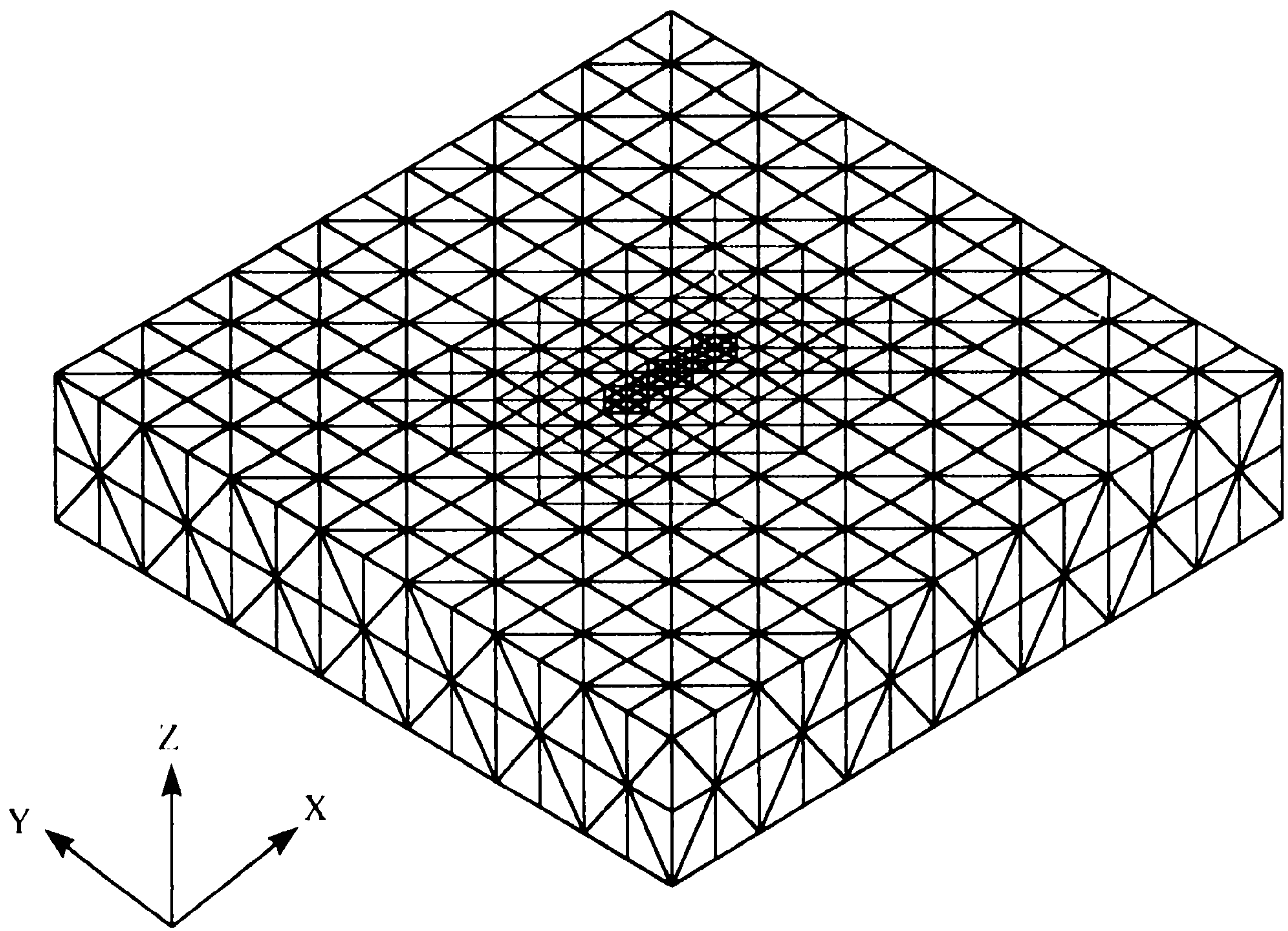

Figure 5.5.2 The Discretized Reservoir Model for Case 5

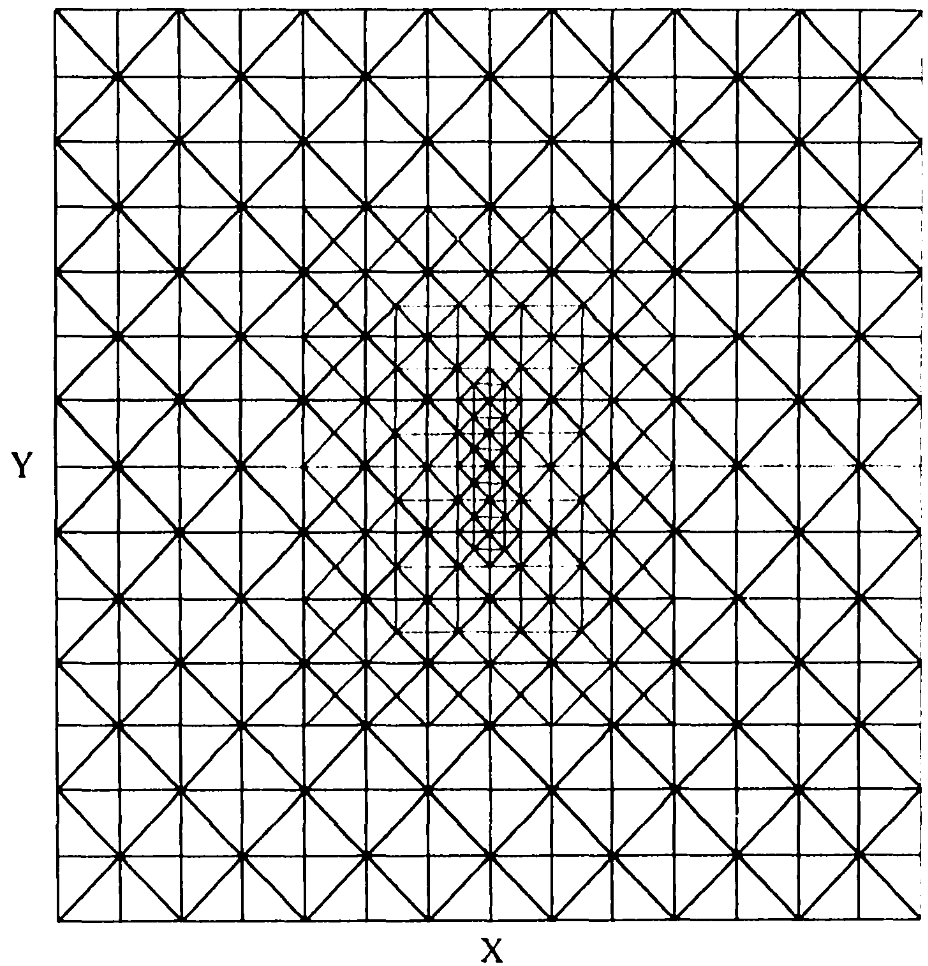

Figure 5.5.3 The Discretized Reservoir Model for Case 5 in 2-D

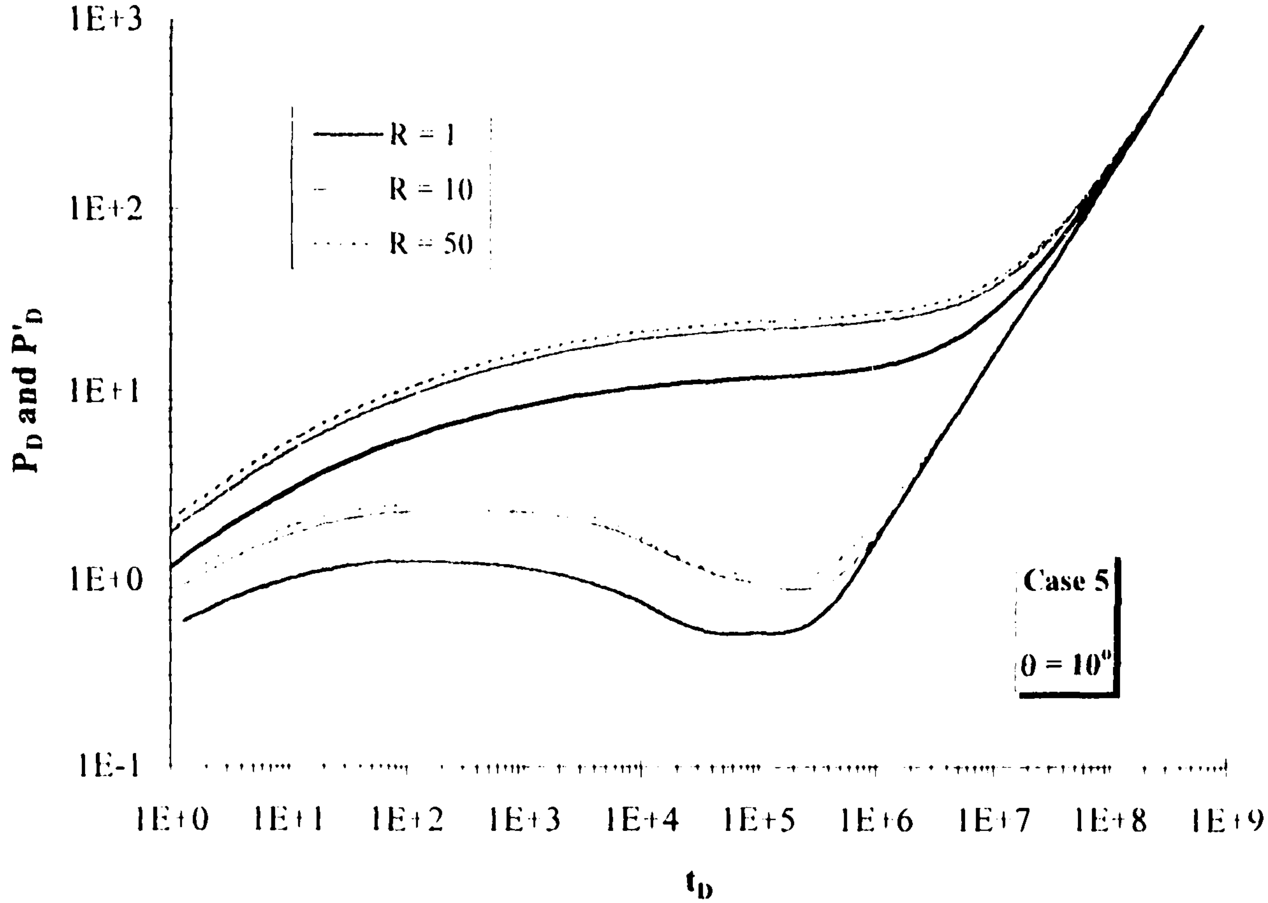

Figure 5.5.4(a) The Dimensionless Pressure and The Dimensionless Pressure Derivative

for Case 5 and $\theta = 10^{\circ}$

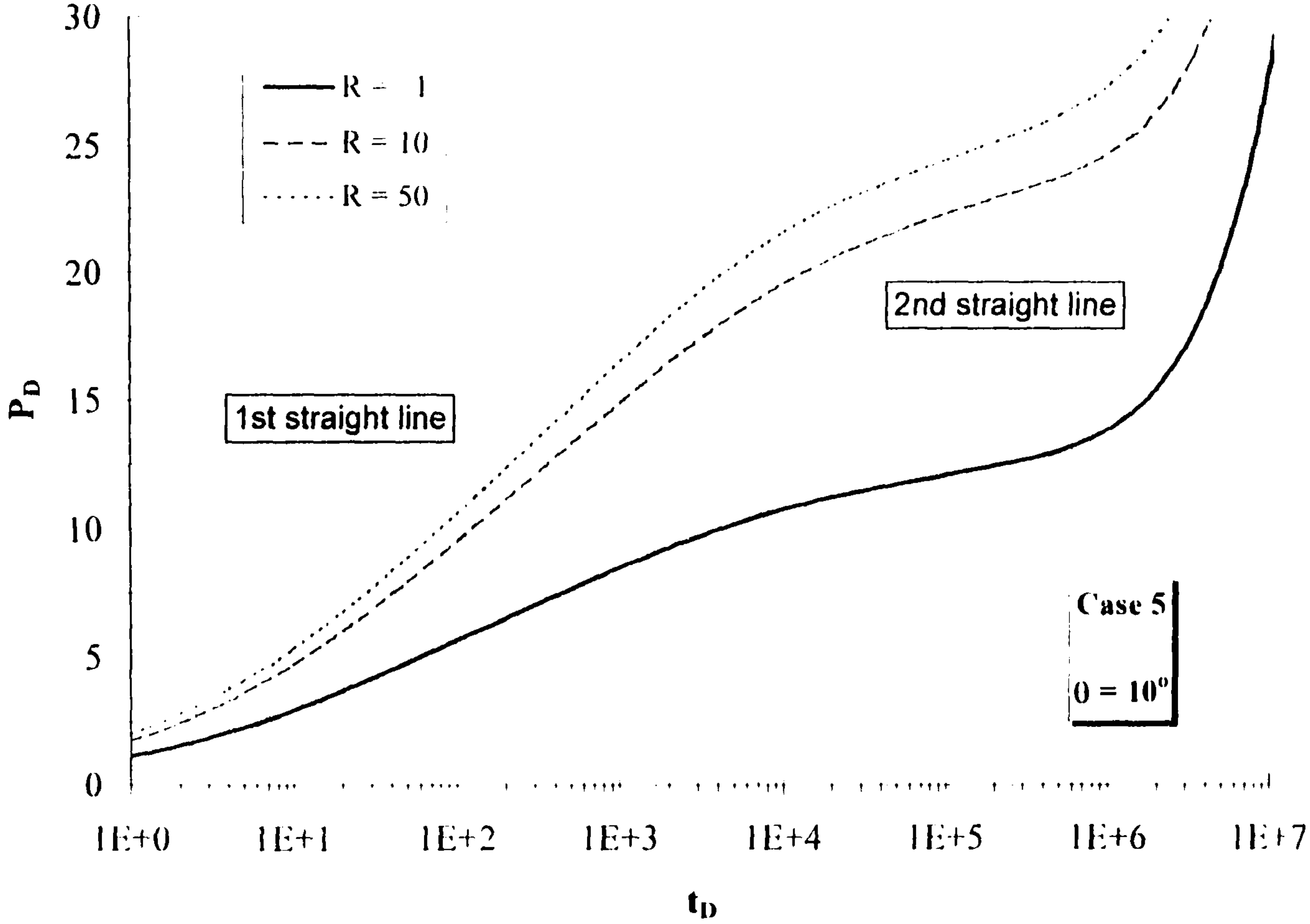

Figure 5.5.4(b) The Dimensionless Pressure for Case 5 and $\theta = 10^\circ$

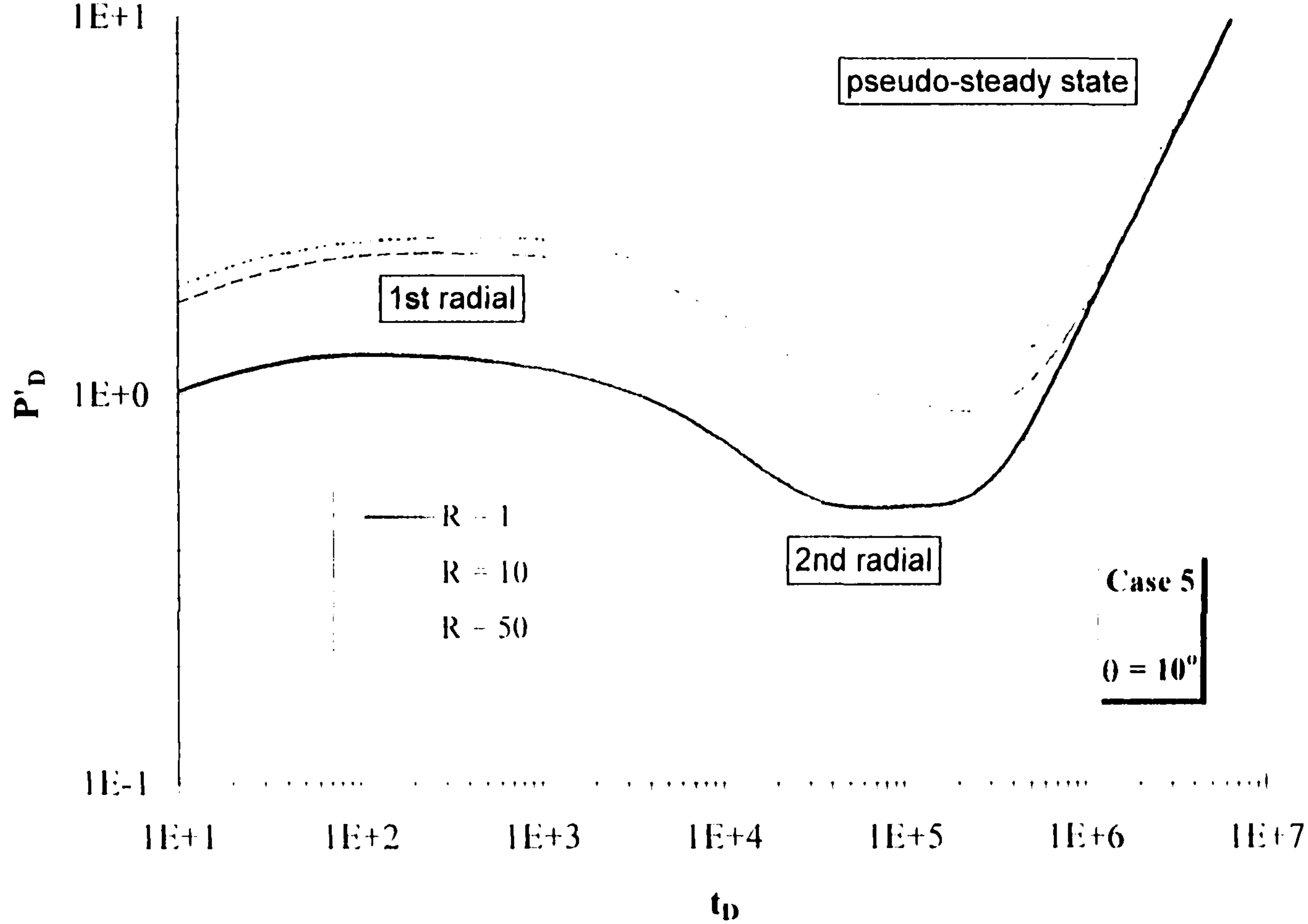

Figure 5.5.4(c) The Dimensionless Pressure Derivative for Case 5 and θ = 10°

Case 6: A Snake-Shape Horizontal Well Intersecting A Two-Layer Reservoir

Fig. 5.6.1 illustrates the horizontal well configuration which intersects both layers. The longer wellbore portion is located in layer #1. The wellbore composes of two portions:

(1) three horizontal-well sections, two sections located in layer #1 and one section located in layer #2, as considered in Case 1.

(2) two inclined well sections considered in Case 5 which intersect both layers. Hence, the wellbore performance must be more complicated that those of the previous cases. The wellbore is symmetry in y-direction and is centrally located in x-direction. The system properties are:

L_w = 272 ft

L_x = 1000 ft.

L_y = 1000 ft.

$L_{z,1}$ = 50 ft. $L_{z,2}$ = 50 ft.

ϕ_1 = 0.1 ϕ_2 = 0.1

$k_{x,1}$ = 1.0 md

$k_{y,1}$ = 1.0 md

$k_{z,1}$ = 0.1 md

$k_{x,2} = k_{y,2} = 10*k_{z,2}$

Two different cases considered in this section are:

- Case A: the top layer has higher permeability.

- Case B: the top layer has lower permeability.

The effects of ratio (R_k) and boundary conditions are considered in this section. Three different values of R_k, 1, 10, and 100 are included. For R_k = 10, four different boundary conditions are studied.

Fig. 5.6.2 illustrates the discretized reservoir model. The system consists of 500 nodes and 1000 triangular elements. Excluding the region around the center of the reservoir, the uniform triangular elements are used. The triangular elements at the center are remodified to handle the source points, the horizontal well. The details of the boundary elements are shown in Fig. 5.6.3. Table 5.6.1 shows the shortest distances from the wellbore to the boundaries. Eq. 5.3 is applied to calculate the approximate dimensionless times required for the pressure transient to travel from the wellbore to the boundaries. These dimensionless times are summarized in Table 5.6.2 and 5.6.3.

boundary	distance, ft
top	25
bottom	25
x-direction	500
y-direction	390

Table 5.6.1 The Shortest Distance from The Wellbore To The Boundaries for Case 6

boundary	t_D		
	$R_k = 1$	$R_k = 10$	$R_k = 100$
top	6250	6250	6250
bottom	6250	62500	625000
x-direction	$2.5*10^5$	$2.5*10^5$	$2.5*10^5$
y-direction	$1.5*10^5$	$1.5*10^5$	$1.5*10^5$

Table 5.6.2 The Dimensionless Time for The Pressure Disturbance to Travel from The Wellbore To The Boundaries for Case 6A

boundary	t_D		
	$R_k = 1$	$R_k = 10$	$R_k = 100$
top	6250	6250	6250
bottom	6250	625	62.5
x-direction	$2.5*10^5$	$2.5*10^4$	$2.5*10^3$
y-direction	$1.5*10^5$	$2.3*10^4$	$2.3*10^3$

Table 5.6.3 The Dimensionless Time for The Pressure Disturbance to Travel from The Wellbore To The Boundaries for Case 6B

For $R_k = 1$, the dimensionless pressure and the dimensionless pressure derivative for Case A and Case B are the same due to the symmetry in the z-direction. The dimensionless pressure and the dimensionless pressure derivative for this case are shown in Figs. 5.6.4 (a) - (c). There exists only one semi-log straight line as shown Fig. 5.6.4(b). The result is confirmed by the straight line of the dimensionless pressure derivative for $t_D \leq 2*10^3$ in Fig. 5.6.4(c). This derivative straight line is horizontal corresponding to the first radial flow regime around the wellbore. Although the reservoir is homogeneous, $R_k = 1$, the dimensionless pressure derivative during the first radial flow is greater than 0.5 because there are two inclined-wellbore sections and three horizontal-wellbore sections. For these two wellbore section, the radial permeability is less than k_x. Hence, the larger pressure drop is required to maintain the same production rate. The first radial flow period is ended before the radius of investigation reaches the top and bottom no-flow boundaries at $t_D \approx 6250$. Once the top and bottom boundaries are reached, there exists the second straight line portion of the dimensionless pressure derivative. But the slope of this line is not zero. This flow regime is due to the horizontal radial flow around the wellbore in x- and y- directions. It is not a perfect radial flow since the dimensionless pressure derivative is not constant. But it is a straight with small value of slope as shown in Fig. 5.6.4(c). Physically, the wellbore length is varied with depth. In the top layer, the wellbore length is greater than that of the bottom layer. This distribution in wellbore length in z-direction distorts the horizontal radial flow. When the pressure transient reaches the lateral boundaries, the dimensionless pressure derivative is increased. Then the pseudo-steady state flow is observed.

Figs. 5.6.5 (a) - (d), in Appendix H, illustrate the dimensionless pressures and the dimensionless pressure derivatives for $R_k = 10$. For Case A, the permeability of the top layer is higher than that of the bottom layer. It should be note that the radius of investigation will reach the top boundary before it will reach the bottom boundary. For Case B, the permeability of the bottom layer is higher. During the transient period, it is clearly seen that the dimensionless pressure for Case A is lower than that for Case B. Since the longer portion of wellbore is located in the higher-permeability layer for Case A. But they are the same during the pseudo-steady state flow. There exists one and two semi-log straight lines for Case A and Case B, respectively, as shown in Fig. 5.6.5(b). For Case A, this semi-log straight line corresponds to the first radial flow around the wellbore. This is due to the dominated effect of the higher permeability since the longer wellbore is located there. But for Case B, there is no perfectly horizontal dimensionless pressure derivative because the bottom boundary effect shows up early at $t_D \approx 625$. When the pressure transient reaches the top boundary, $t_D \approx 6250$, there exist the first radial flow. This flow regime corresponds to the horizontal radial flow around the long horizontal well. The pressure disturbance reaches the boundary in y-direction approximately at $t_D \approx 2.3*10^4$. The value of the dimensionless pressure derivative is increased. There exist another radial flow. Once the pressure transient reaches all boundaries, we observe the pseudo-steady state flow regime. Fig. 5.6.5(d) illustrates the Cartesian plot of the dimensionless pressure versus the dimensionless time during the pseudo-steady state flow. The slopes of the two cases are the same but the intercepts are different.

The dimensionless pressures and the dimensionless pressure derivatives for R_k = 100 are shown in Figs. 5.6.6 (a)-(e). Due to the higher permeability ratio (R_k), the radius of investigation travels much faster in Layer #1 than in Layer #2. During the transient period, the production is supported by the higher-permeability. Fig. 5.4.6 illustrates the semi-log plot of the dimensionless pressure versus the dimensionless time. There exists only one semi-log straight line for each case. For Case A, this semi-log straight line corresponds to the infinite-acting flow around the wellbore. This flow regime is ended when the pressure transient reaches the top boundary. For Case B, there is no the first radial flow because the bottom boundary at $t_D \approx 625$. When the pressure transient reaches the top boundary, there exists the radial flow regime. This flow regime is caused by the horizontal radial flow around the wellbore. The dimensionless pressure derivative for both cases are the same when the pressure transient reaches all boundaries at $t_D \approx 6*10^5$. The steady state usually appears shortly after the dimensionless pressure derivatives are identical. But, in this case, that phenomena does not happen. As shown in Figs. 5.6.6 (a) and (d), shortly after the dimensionless pressure derivatives for both cases become identical, the dimensionless pressure derivatives form the first straight line, for $4*10^5 < t_D < 7*10^6$. For $t_D > 8*10^6$, the dimensionless pressure derivatives form another straight line with higher slope. The second straight line is corresponding to the real pseudo-steady state in which the low-permeability layer also contributes to the production. Fig.5.6.6(e) illustrates the Cartesian plot of the dimensionless pressure versus the dimensionless pressure derivative during the pseudo-steady state flow.

For Case 6A, the comparison of the dimensionless pressures and the dimensionless pressure derivatives for different values of permeability ratio (R_k) is illustrated in Figs. 5.6.7 (a)-(d). The dimensionless pressure is increased when the permeability ratio is increased. The dimensionless pressure and the dimensionless pressure derivative for $R_k = 1$ have the lowest value. There is only one semi-log straight lines for each case as shown in Fig. 5.6.7(b). The slope of each straight increases when the permeability ratio increases. In addition, when the permeability ratio is increased, it will take longer time to see the beginning of the pseudo-steady state. Fig. 5.6.7(d) illustrates the Cartesian plot of the dimensionless pressure versus the dimensionless time during the pseudo-steady state period. The slopes of each line are the same but the intercepts are different.

Figs. 5.6.8 (a) - (d) illustrate the dimensionless pressures and the dimensionless pressure derivatives for Case 6B. The general performance for Case B is similar to that of Case 6A. The dimensionless pressure and the dimensionless pressure derivative for R_k = 1 have the lowest values. There exists only one radial flow regime for each case as shown in Fig. . For $R_k \neq 1$, the radial flow regime shows up late. This flow regime is the horizontal radial flow regime around the long horizontal wellbore. The dimensionless pressure is plotted versus the dimensionless time on Fig. 5.7.8(d). The slopes of each straight line are the same but the intercepts are different.

Four different types of boundary conditions only for R_k 10 will be investigated here. Figs. 5.6.9 (a) - (c) illustrate the dimensionless pressures and the dimensionless pressure derivatives for boundary condition type II. The top and bottom boundaries are flowing and no-flow boundaries, respectively. Before the radius of investigation reaches the top flowing boundary, the dimensionless pressures and the dimensionless pressure derivatives are the same as those for BC I, shown in Figs. 5.6.5 (a) - (c). The semi-log of the dimensionless pressure is show in Fig. 5.6.9(b). There exists only one semi-log straight line for both Case A and Case B. Once the top boundary is reached, the dimensionless pressure derivatives start to decrease for both Case A and Case B illustrated in Fig. 5.6.9(a) and (c). For Case A, when the radius of investigation reaches the bottom no-flow boundary, the slope of the dimensionless pressure derivative increases and forms another straight line. The top boundary effect is stronger than the bottom boundary effect causing the slope of the dimensionless pressure derivative continue dropping. This is when the steady state is reached.

Figs. 5.6.10 (a) - (c) illustrate the dimensionless pressures and the dimensionless pressure derivatives for boundary condition type III. The dimensionless pressures and the dimensionless pressure derivatives for boundary condition type IV are shown in Figs. 5.6.11(a) - (c).

Figs. 5.6.12 (a) - (c) illustrate the dimensionless pressures and the dimensionless pressure derivatives for four different types of boundary conditions for Case A. The dimensionless pressures and the dimensionless pressure derivatives for four different types of boundary conditions for Case B are shown in Figs. 5.6.13 (a) - (c).

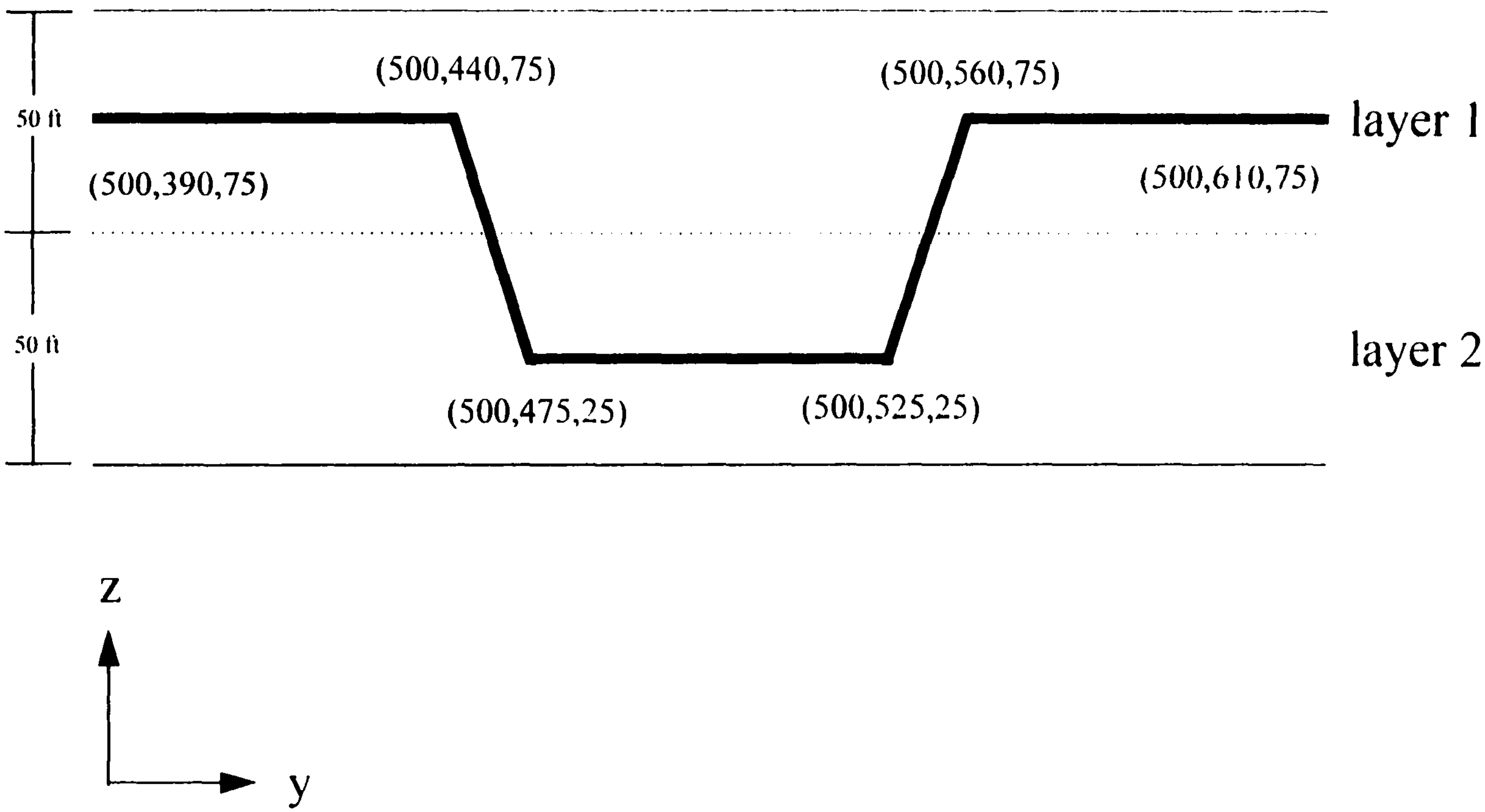

Figure 5.6.1 A Horizontal Well Configuration for Case

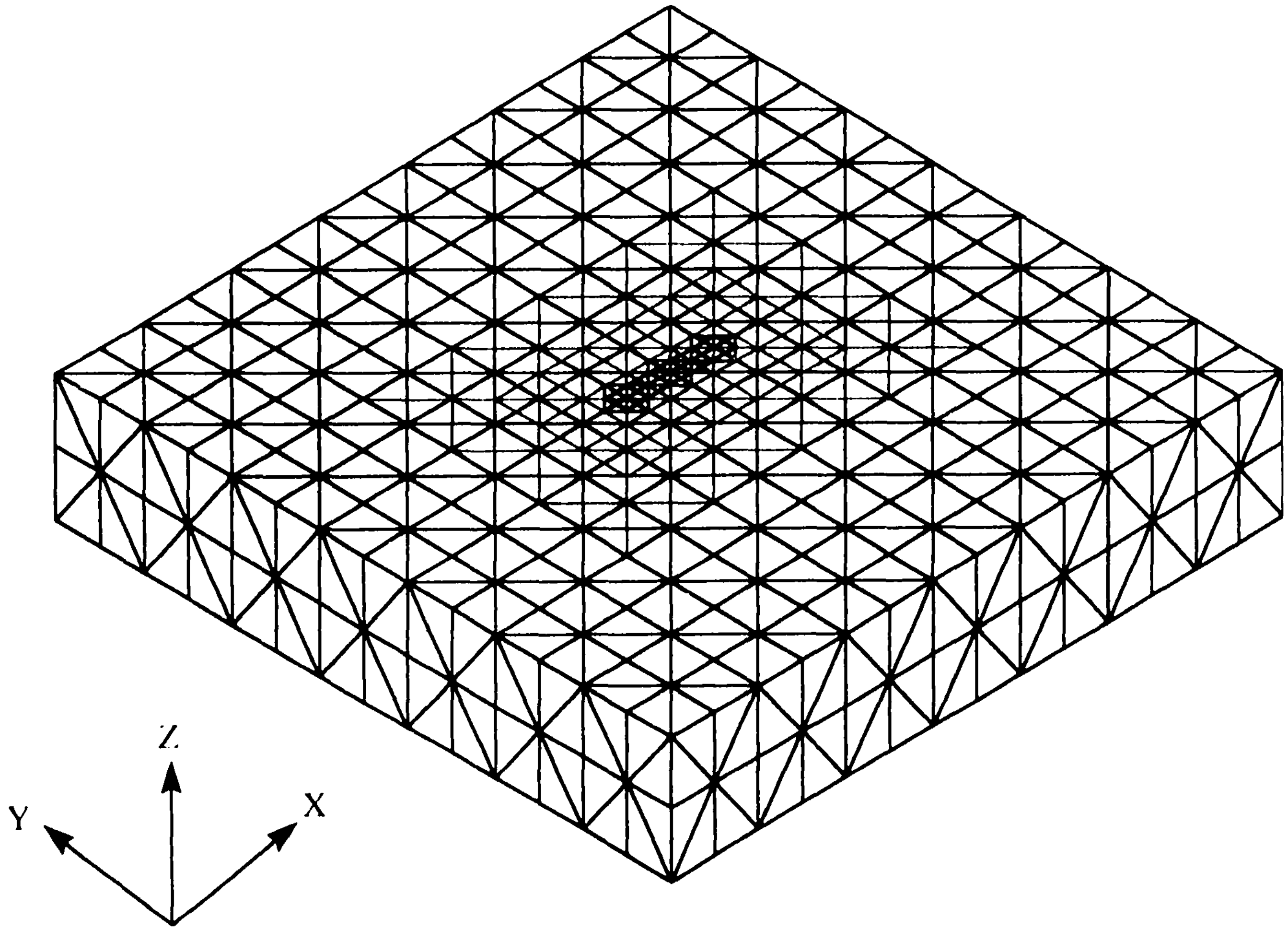

Figure 5.6.2 The Discretized Reservoir Model in 3-D for Case 6

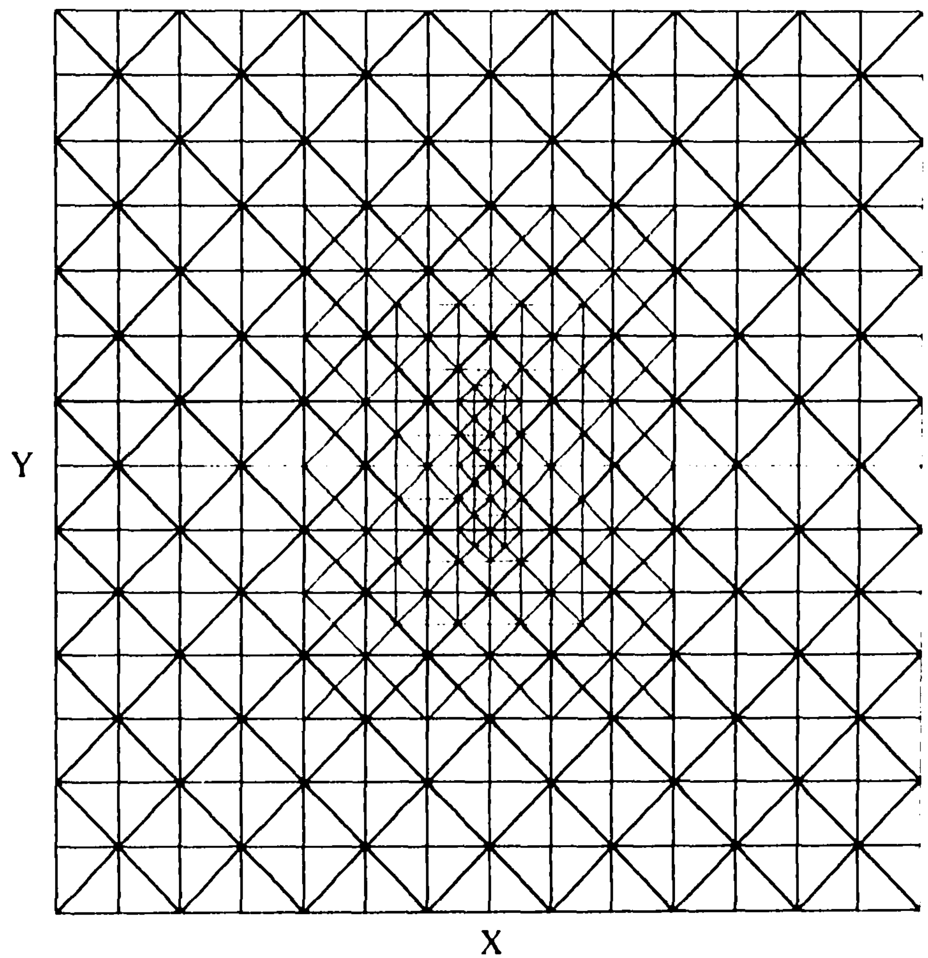

Figure 5.6.3 The Discretized Reservoir Model in 2-D for Case 6

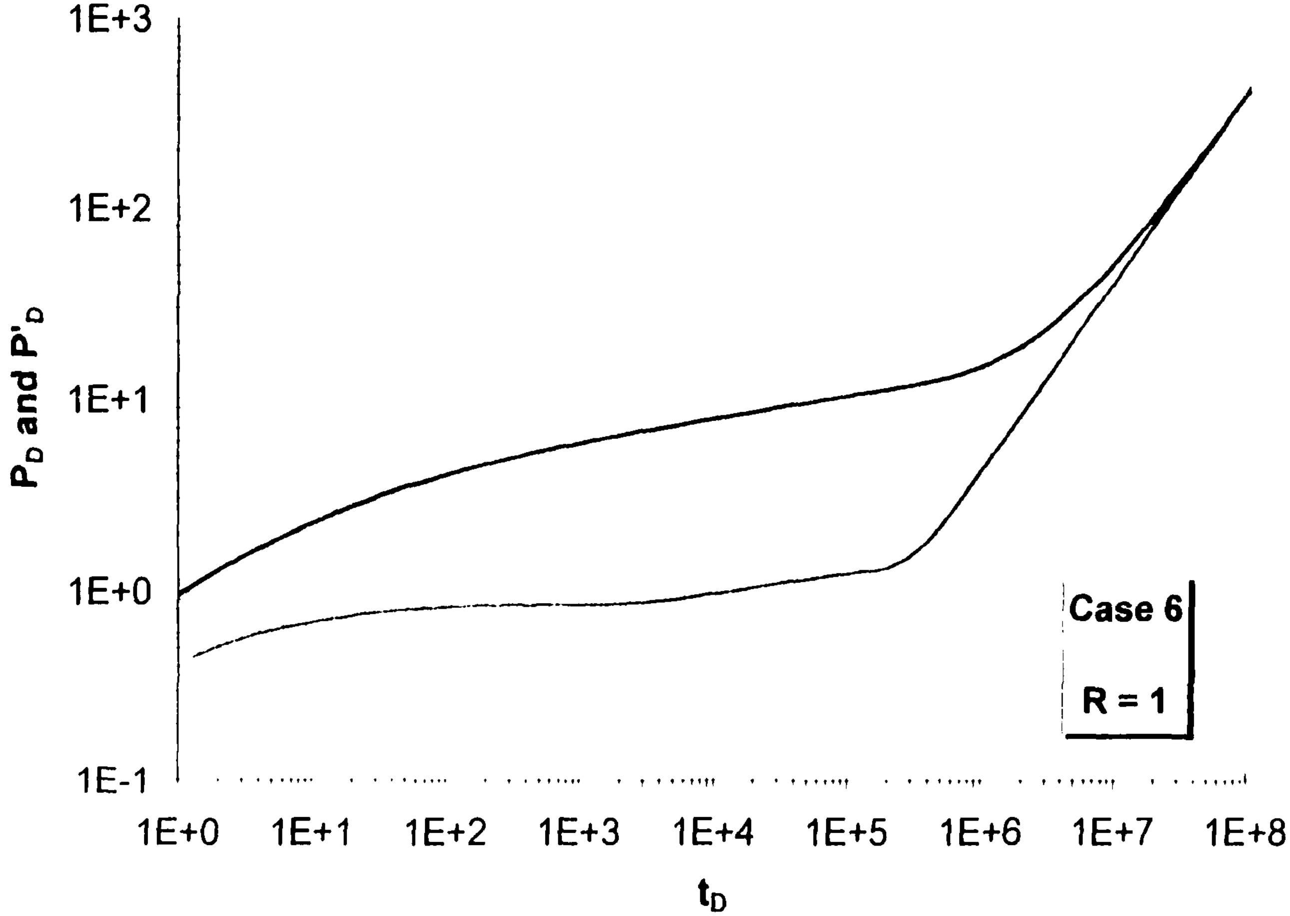

Figure 5.6.4(a) The Dimensionless Pressure and The Dimensionless Pressure Derivative

for Case 6 and $R_k = 1$

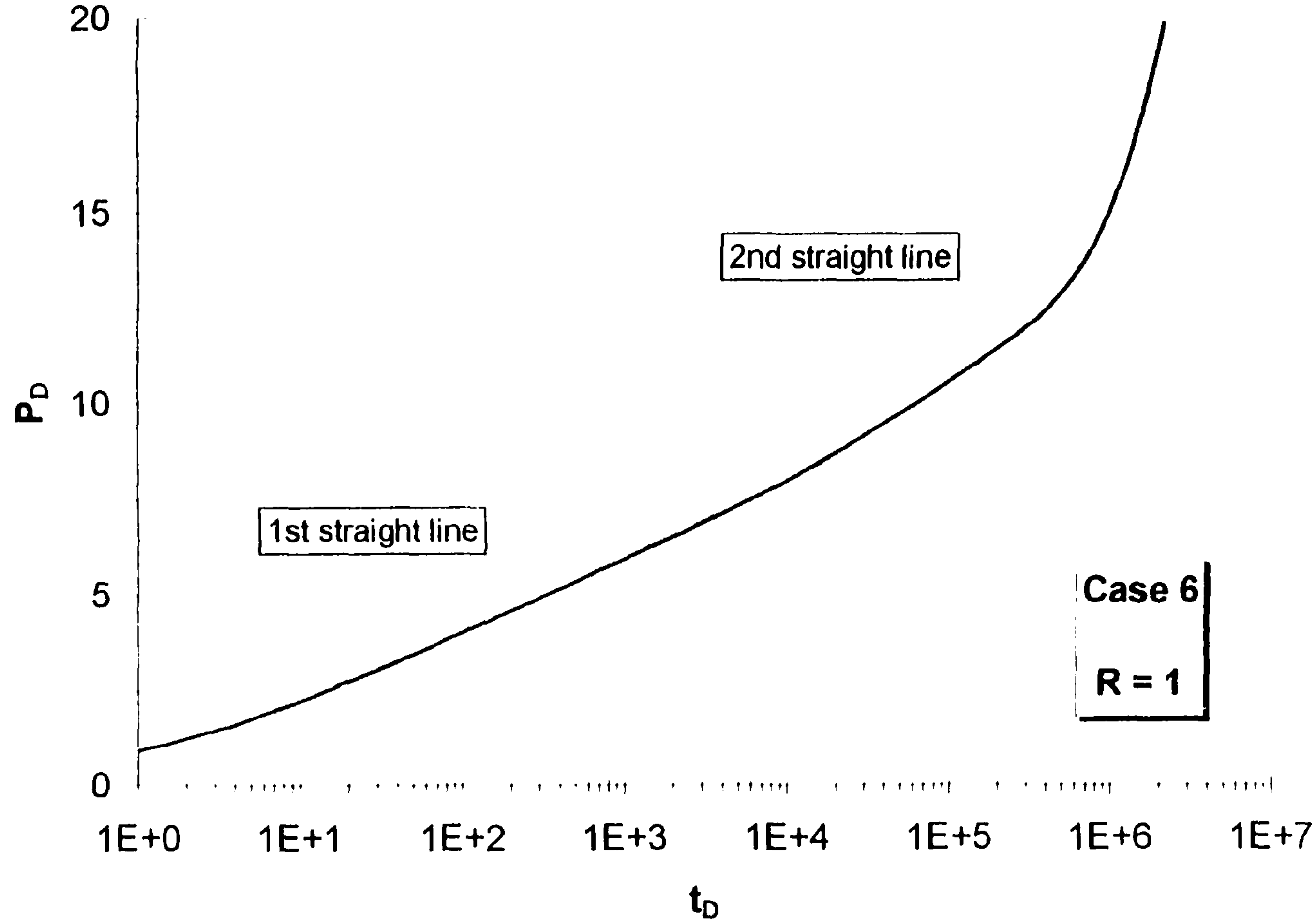

Figure 5.6.4(b) The Dimensionless Pressure for Case 6 and $R_k = 1$

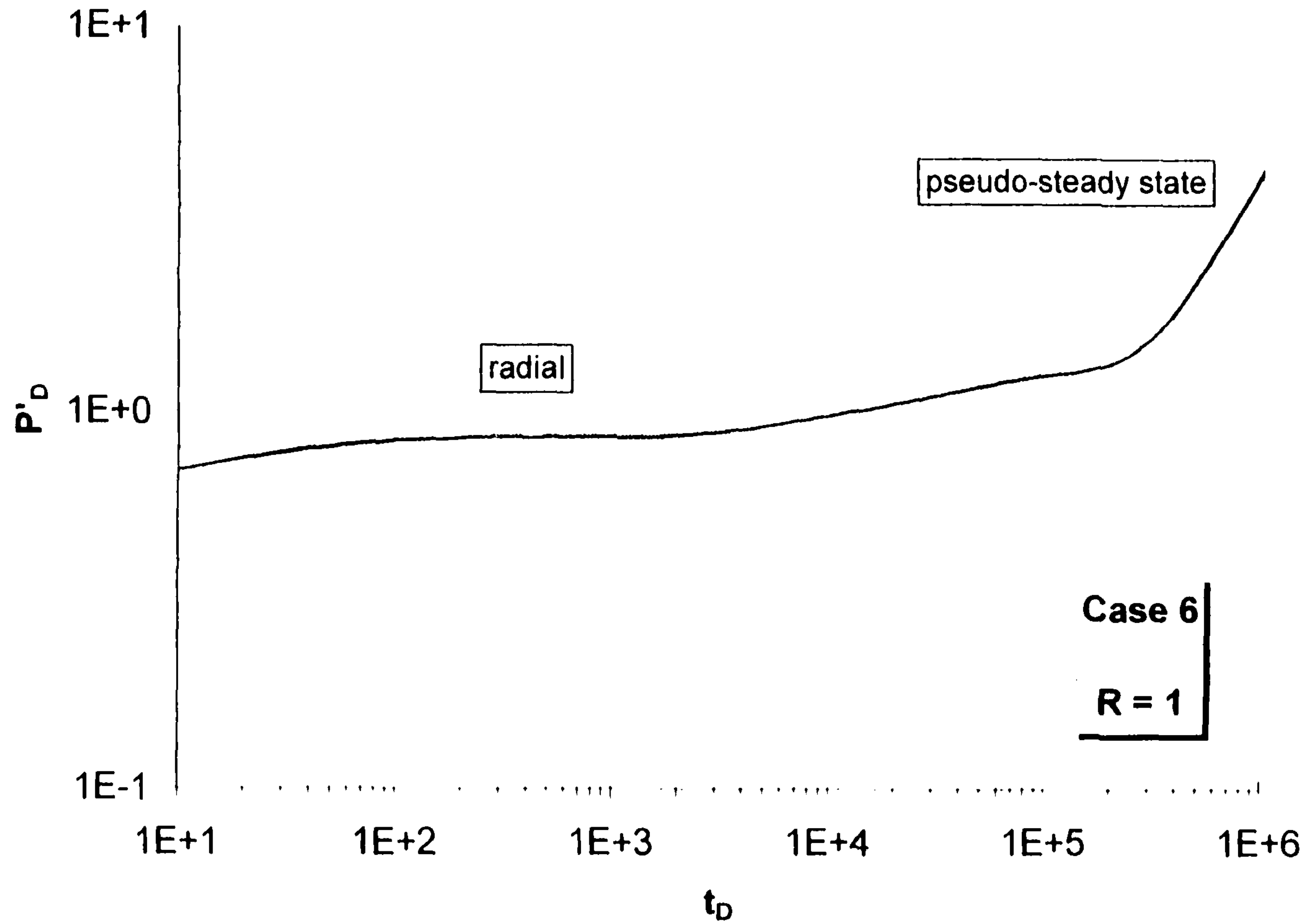

Figure 5.6.4(c) The Dimensionless Pressure Derivative for Case 6 and $R_k = 1$

Case 7: A Horizontal Well in Three-Layer Reservoir With Cross-Flow

The reservoir consists of three distinct layers, shown in Fig. 5.7.1. The wellbore penetrates all three layers. Both top and bottom boundaries are only considered to be no-flow boundaries. Two wellbore angles (θ), 45° and 90°, with respect to the horizontal plane are considered in this section. The permeability decreases with depth. The permeability ratios are defined as:

$$R_{k1} = \frac{k_{x,1}}{k_{x,2}} \tag{5.7.1}$$

$$R_{k2} = \frac{k_{x,2}}{k_{x,3}} \tag{5.7.2}$$

The effect of these permeability ratios will be investigated here. Table 5.7.1 shows twelve different cases covered in this section. The first six cases have the same wellbore angle, θ = 90° while the wellbore angle for the last six cases are 45°. The reservoir discretized model is the same as the one in Case 2 but it consists of three layers. The distances from the wellbore to the boundaries are shown in Table 5.7.2. Table 5.7.3 shows the dimensionless times required for the pressure transient to travel from the wellbore to each boundary.

Figs. 5.2.7 (a)-(e) illustrate the dimensionless pressures and the dimensionless pressure derivatives for Cases 1-6 which have the wellbore angle equal to 90°. For these cases, they are actually the vertical well in multi-layer reservoir. The wellbore penetrates each layer exactly the same length. (≈100/3 ft.). The dimensionless pressure and the dimensionless pressure derivative are increased as the number of Case is increased. Because, for $1 \leq i < 6$, Case i has higher permeability that Case i+1 does. The semi-log plot of the dimensionless pressure versus the dimensionless time is shown in Fig. 5.7.2(b). There exists only semi-log straight line for each case. The result is confirmed by the dimensionless pressure derivatives illustrated in Fig. 5.7.2(c). This first radial flow is indicated by the horizontal dimensionless pressure derivative. The boundary effects can be observed at $t_D \approx 2*10^5$ when the dimensionless pressure derivatives are increased. The beginning dimensionless time of the pseudo-steady state is increased as the permeability is decreased. The pseudo-steady state of Case 1 is observed first and that of Case 6 is observed last as illustrated in Fig. 5.7.2(d). For Case 4 and 5, the permeabilities in layer 1 and 3 are the same. But the permeabilities in the middle layer are different. During the late time, $t_D > 10^6$, the dimensionless pressure derivatives of Case 4 and 5 are merging. Fig. 5.7.2(e) illustrates the Cartesian plot of the dimensionless pressure versus the dimensionless time during pseudo-steady state flow. The slopes of Case 1-5 are about the same but the slope of Case 6 is different. Because we did not observe the pseudo-steady state of Case 6 yet. This is due to the relatively low permeability.

Figs. 5.7.3 (a)-(e), in Appendix I, illustrate the dimensionless pressures and the dimensionless pressure derivatives of Cases 7-12. These cases are a slant well in multi-layer reservoir. The wellbore lengths in layer 1, 2, and 3 are 26.43 ft., 47.14 ft., and 26.43 ft., respectively. The wellbore is parallel to the y-direction. The semi-log plot of the dimensionless pressure versus the dimensionless time is shown in Fig. 5.7.3(b). There exists one semi-log straight line for each case. Fig. 5.7.3(c) illustrates the dimensionless pressure derivative behavior. The general characteristic of these cases are about the same as those of Case 1-6. But there dose not exist a long horizontal dimensionless pressure derivative. The radial flow periods are shorter than those of Case 1-6. The dimensionless pressure derivatives during pseudo-steady state flow are shown in Fig. 5.7.3(d). The beginning dimensionless time of pseudo-steady state is a function of the system permeabilities. For Case 10 and 11, the permeabilities in layer 1 and 3 are the same. But the permeabilities in the middle layer are different. During the late time, $t_D > 10^6$, the dimensionless pressure derivatives of Case 10 and 11 are merging. Fig. 5.7.3(e) illustrate the Cartesian plot of the dimensionless pressure versus the dimensionless time during pseudo-steady state flow. Excluding Case 12, the slopes of all cases are the same. The pseudo-steady state of Case 12 does not appear yet.

Fig. 5.7.4 illustrates the dimensionless pressures and the dimensionless pressure derivatives of Case 1 and 2 which have the same permeabilities in layer 1 and 2. But Case 2 has lower permeability in the bottom layer. The effect of the bottom layer plays an important role since the very small values of the dimensionless time since the dimensionless pressure of Case 2 is higher than that of Case 1. But during pseudo-steady state flow, both cases have the same dimensionless pressure and dimensionless pressure derivatives.

The dimensionless pressures and the dimensionless pressure derivatives for Case 3 and 4. They have different properties in layer 3. The performance of both cases are insignificant difference for $t_D < 2*10^5$. During this period, the production is just coming from layer 1 and 2 only. For $2*10^5 < t_D < 3*10^7$, the wellbore produces partially from the bottom layer since the dimensionless pressure derivatives are different. Case 4 has higher dimensionless pressure since it has lower permeability in the bottom layer. For $t_D >$ $3*10^7$, both cases have the same performance again.

Fig. 5.7.6 illustrated the dimensionless pressures and the dimensionless pressure derivatives for Case 5 and 6. The effect of the bottom layer is observed at $t_D \approx 4*10^6$. This happens after the pressure transient reaches the lateral boundaries at $t_D \approx 2.5*10^5$. During the pseudo-steady flow, there exists the radial flow regime around the wellbore in both layer 1 and 2. This flow regime is ended when the pressure disturbance reaches the boundaries in x and/or y direction.

The dimensionless pressures and the dimensionless pressure derivatives for cases 4 and 5 are shown in Fig. 5.7.7. Case 4 and 5 have the same permeabilities in the layers 1 and 3. They have different permeabilities in layer 2. The layer 2 plays an important role since the beginning because the dimensionless pressures and the dimensionless pressure derivatives for both cases are different from the beginning. They are the same only during the pseudo-steady state flow.

Fig. 5.7.8 illustrates the dimensionless pressures and the dimensionless pressure derivatives for Case 7 and 8. The wellbore angle is 90°. The performance is similar to that of Fig. 5.7.4 which has the vertical well in the same system. The bottom layer plays an important role since the beginning because the dimensionless pressures and the dimensionless pressure derivatives are different. This happens because the bottom-layer permeability and the top-layer permeability are relatively close.

The dimensionless pressures and the dimensionless pressure derivatives for Case 9 and 10 are shown in Fig. 5.7.9. For $t_D < 10^5$, the performance of both cases are insignificant different. During this period, the production is coming from the layer 1 and 2. The effect of the bottom layer can be observed at $t_D \approx 10^5$ when the pressure in layer 1 and 2 start to decline. The dimensionless pressures and the dimensionless pressure derivatives are different during this period. For $t_D > 2*10^7$, the performance of both cases become identical again.

Fig. 5.7.10 illustrates the dimensionless pressures and the dimensionless pressure derivatives for Case 11 and 12 which have the same permeabilities in layer 1 and 2. The effect of the bottom layer can be observed at $t_D \approx 3*10^6$. Due to the relatively low permeability, we can not observe the pseudo-steady state flow in Case 12 yet.

The dimensionless pressures and the dimensionless pressure derivatives of Case 10 and 11 are shown in Fig. 5.7.11. These two cases have the same permeabilities in layer 1 and 3. Case 10 has higher permeability in the middle layer yielding the lower dimensionless pressure and dimensionless pressure derivative. The difference in the magnitudes can be observed since the beginning because the layer 2 plays an important role on the production. The dimensionless pressures become identical during the pseudo-steady state flow.

The effect of the wellbore angle is shown in Figs. 5.7.12 – 17. Fig. 5.7.12 illustrates the dimensionless pressures and the dimensionless pressure derivatives for Case 1 and 7. These two cases have the same permeabilities in all layers. But the wellbore angles are different causing the lower radial permeability for Case 7. In order to maintain the same production rate. Case 7 creates more pressure drop. Once the pressure transient reaches all boundaries, the performance for both cases become identical. The performance for Case 2 and 8, Case 3 and 9, Case 4 and 10, Case 5 and 11, and Case 6 and 12 are illustrated in Figs. 5.7.13 – 17, respectively.

Case #	θ, degree	R_{k1}	R_{k2}
1	90	2	2
2	90	2	10
3	90	10	10
4	90	10	100
5	90	100	10
6	90	100	100
7	45	2	2
8	45	2	10
9	45	10	10
10	45	10	100
11	45	100	10
12	45	100	100

Table 5.7.1 Twelve Cases Consider in Case 7

	Distance, ft			
Case #	top	bottom	x-direction	y-direction
1	0	0	500	500
2	0	0	500	500
3	0	0	500	500
4	0	0	500	500
5	0	0	500	500
6	0	0	500	500
7	14.64	14.64	500	464.6
8	14.64	14.64	500	464.6
9	14.64	14.64	500	464.6
10	14.64	14.64	500	464.6
11	14.64	14.64	500	464.6
12	14.64	14.64	500	464.6

Table 5.7.2 Distances from The Wellbore to The Boundaries for Case 7

	dimensionless time, t_D			
Case #	top	bottom	x-direction	y-direction
1	0	0	$2.5*10^5$	$2.5*10^5$
2	0	0	$2.5*10^5$	$2.5*10^5$
3	0	0	$2.5*10^5$	$2.5*10^5$
4	0	0	$2.5*10^5$	$2.5*10^5$
5	0	0	$2.5*10^5$	$2.5*10^5$
6	0	0	$2.5*10^5$	$2.5*10^5$
7	2143	8753	$2.5*10^5$	$2.2*10^5$
8	2143	$4.3*10^4$	$2.5*10^5$	$2.2*10^5$
9	2143	$2.1*10^5$	$2.5*10^5$	$2.2*10^5$
10	2143	$2.1*10^6$	$2.5*10^5$	$2.2*10^5$
11	2143	$2.1*10^6$	$2.5*10^5$	$2.2*10^5$
12	2143	$2.1*10^7$	$2.5*10^5$	$2.2*10^5$

Table 5.7.3 Time for The Pressure Disturbance to Reach The Boundaries for Case 7

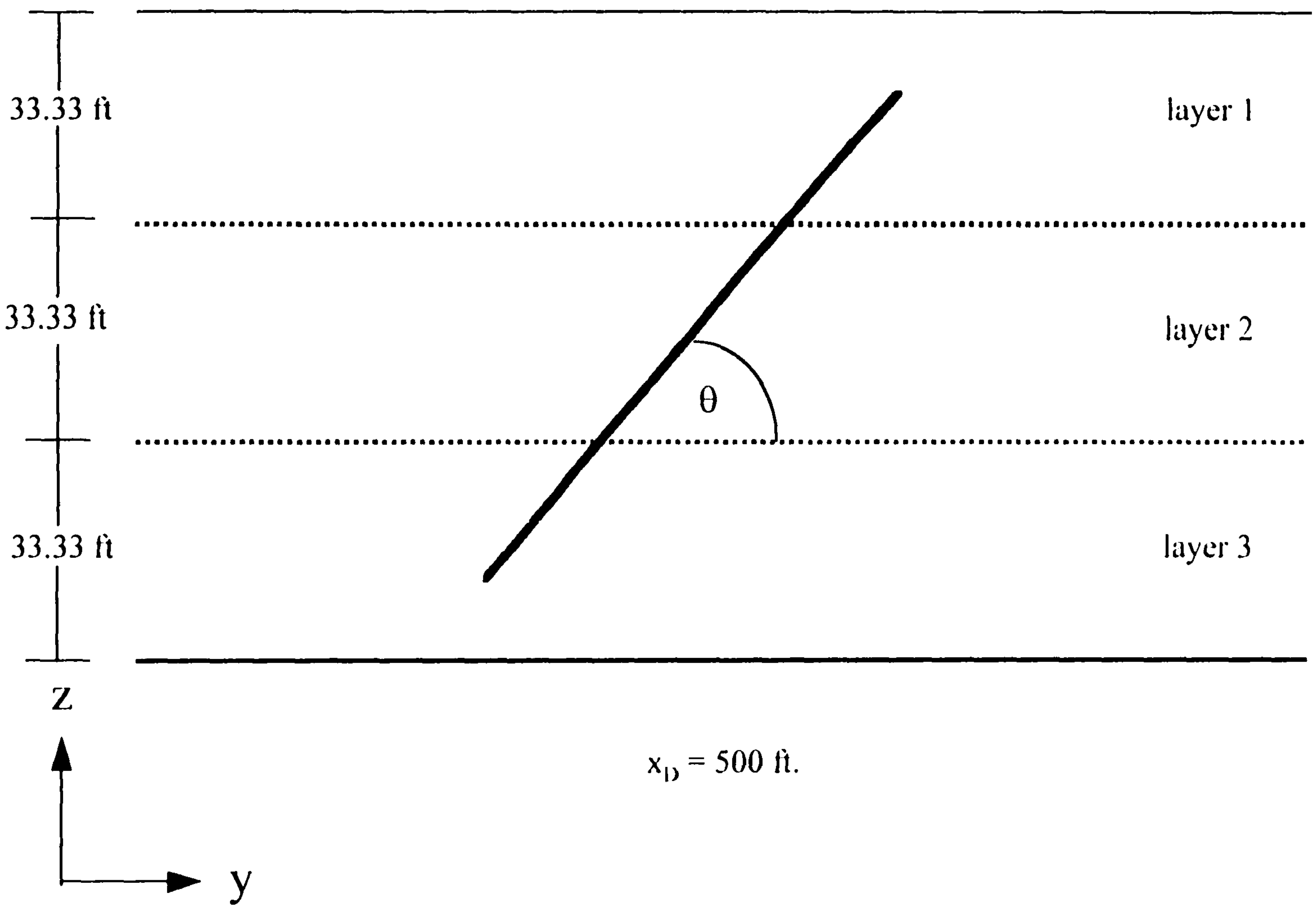

Figure 5.7.1 The Reservoir Model for Case 7.

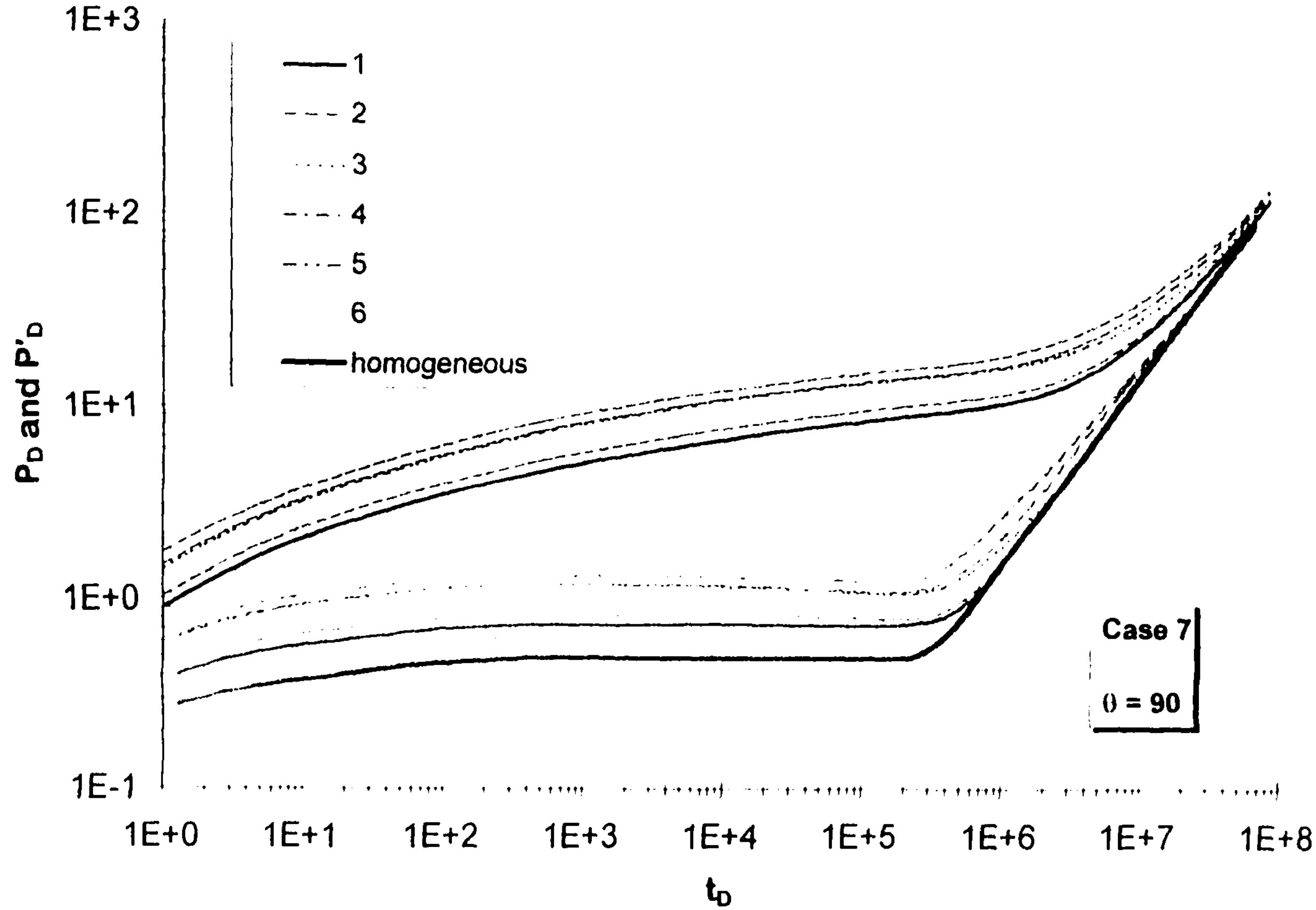

Figure 5.7.2(a) The Dimensionless Pressure and The Dimensionless Pressure Derivative

for Case 7 and $\theta = 90°$

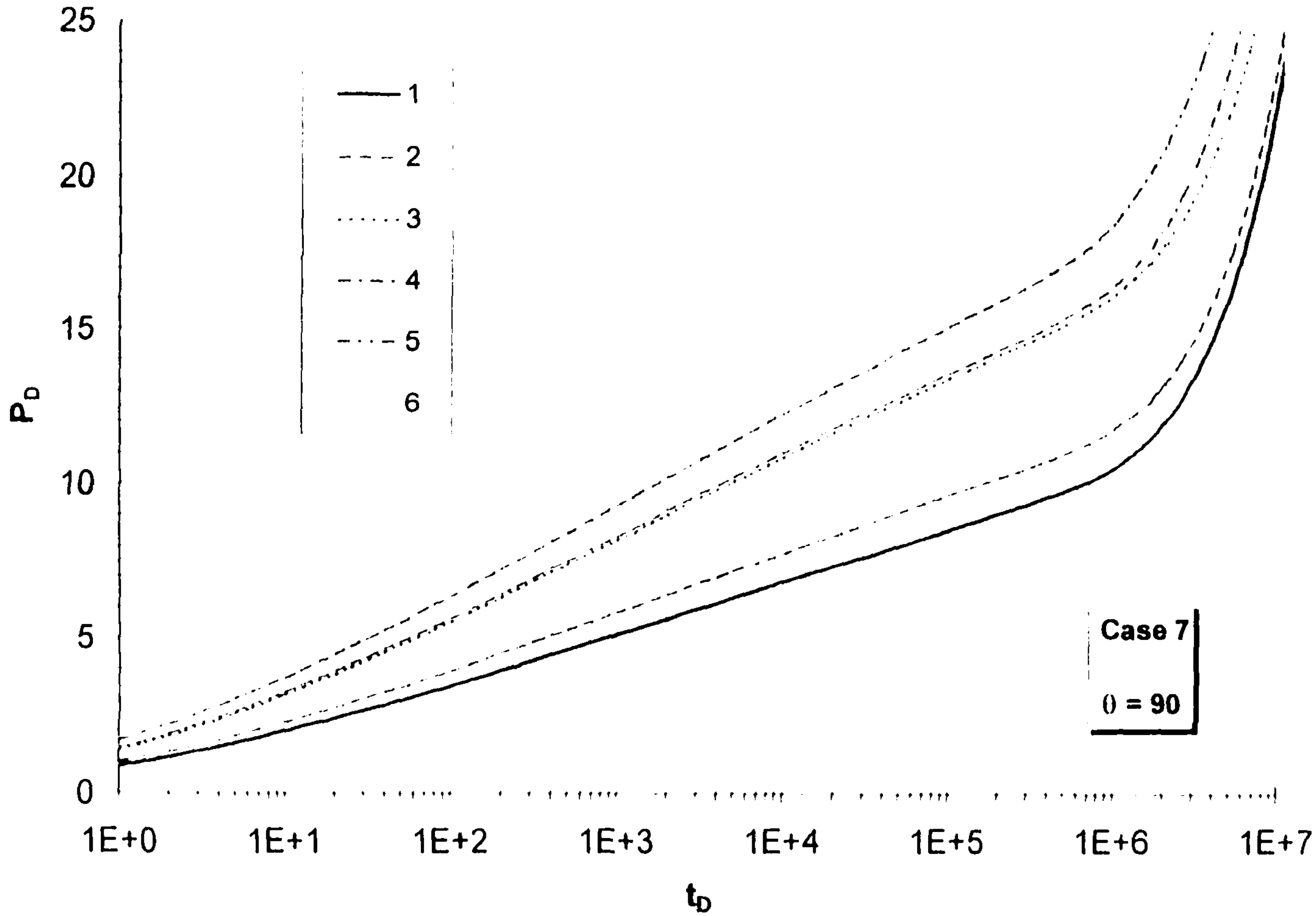

Figure 5.7.2(b) The Dimensionless Pressure for Case 7 and $\theta = 90^{o}$

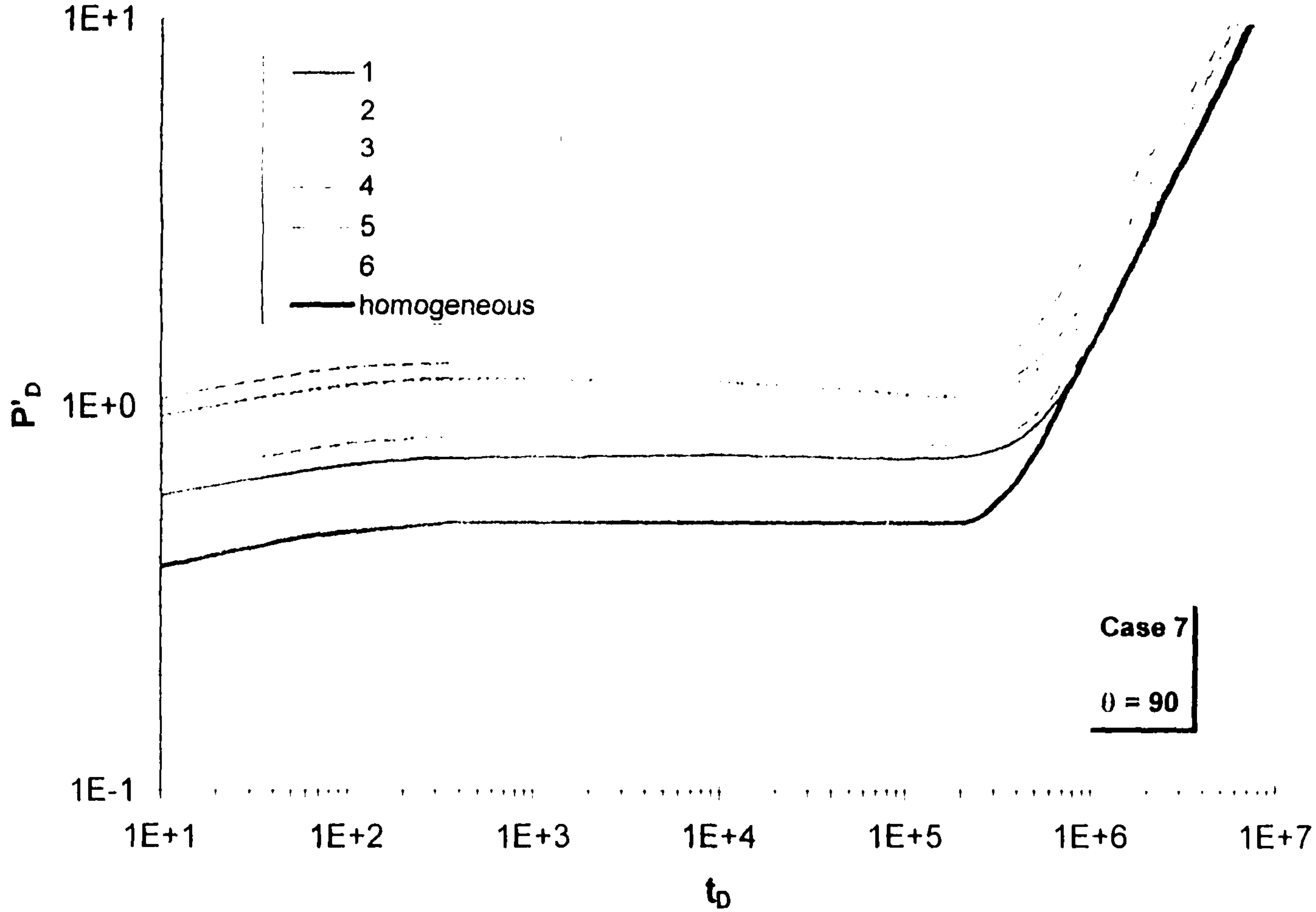

Figure 5.7.2(c) The Dimensionless Pressure Derivative for Case 7 and θ = 90°

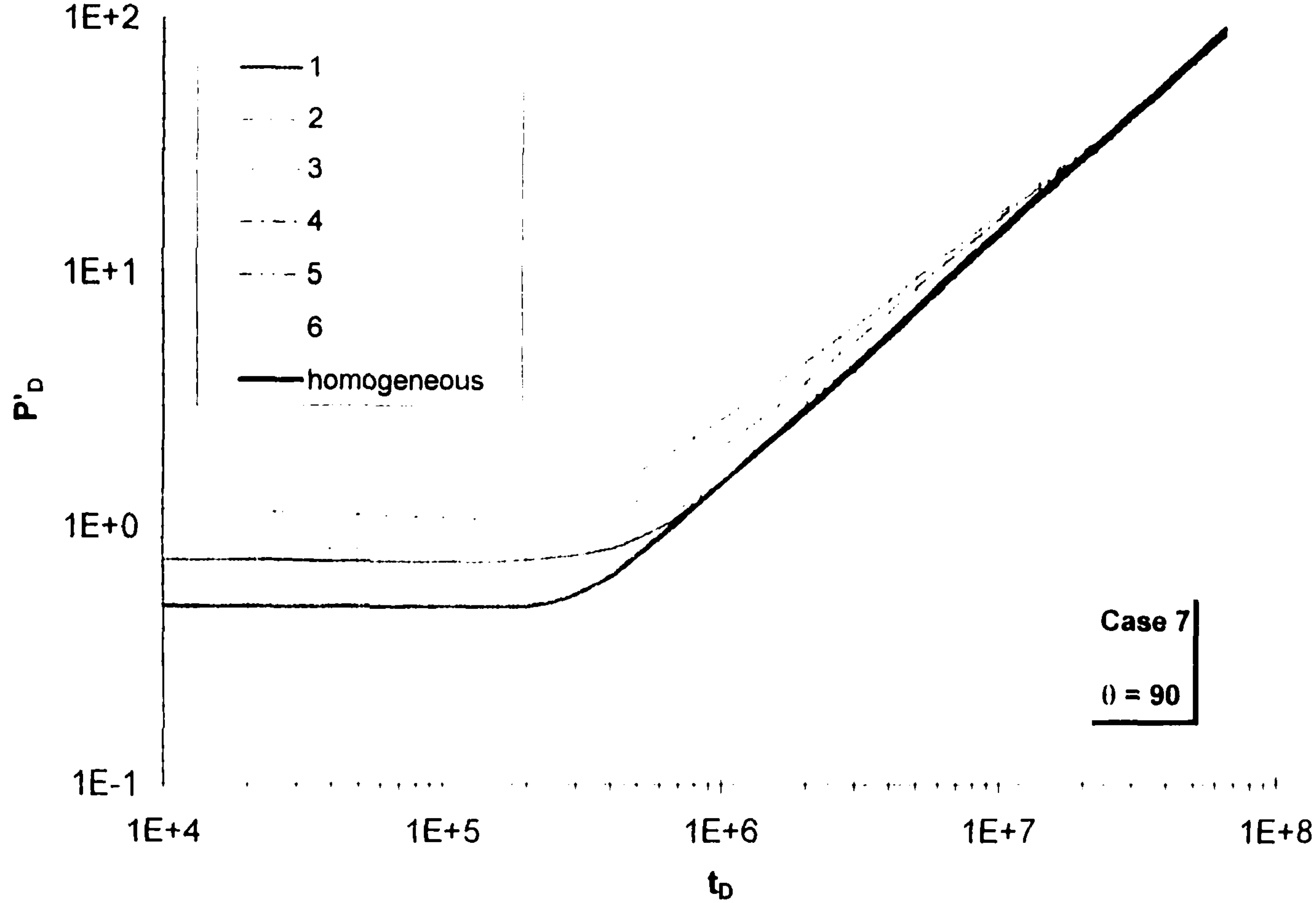

Figure 5.7.2(d) The Dimensionless Pressure Derivative for Case 7 and $\theta = 90°$

during The Pseudo-Steady Flow

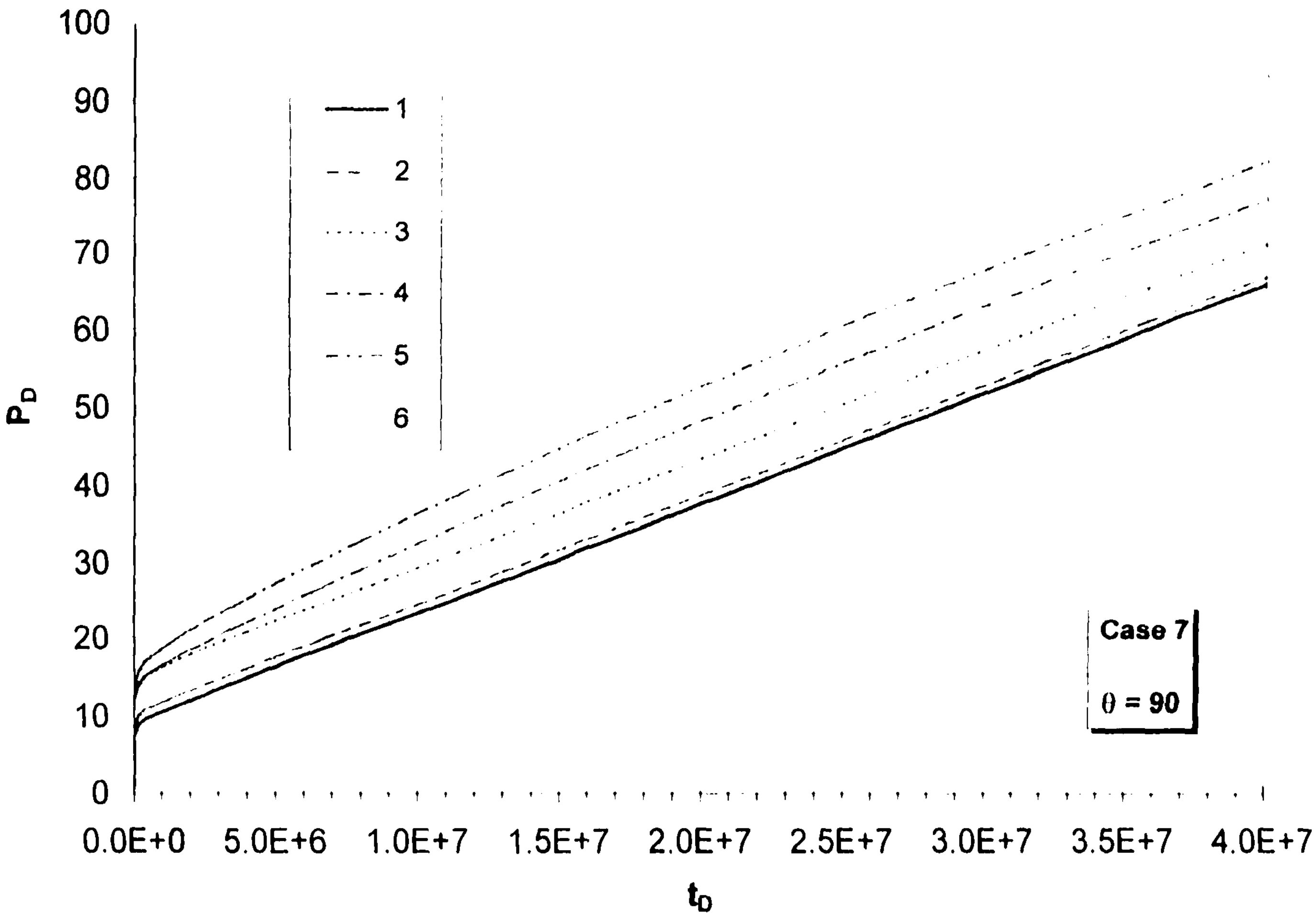

Figure 5.7.2(e) The Dimensionless Pressure for Case 7 and $\theta = 90^0$ on The Cartesian Plot

Case 8: A Vertical Well Intersecting A Two-Layer Reservoir Without Cross Flow

The reservoir model consists of two layers shown in Fig. 5.8.1. But there is a zero-permeability layer between these two layers. Hence, there is no vertical communication between these two layers except flowing through the wellbore. The effect of this permeability ratio on the pressure and pressure derivative will be investigated in this section.

The discretized reservoir model is the same as that in Case 6. The properties of each layer are the following.

$L_w = 100$ ft.

$L_x = 1000$ ft.

$L_y = 1000$ ft.

$L_{z1} = 50$ ft. $\qquad\qquad L_{z2} = 50$ ft.

$\phi_1 = 0.1$ $\qquad\qquad \phi_2 = 0.1$

$k_{x,1} = 1.0$ md.

$k_{y,1} = 1.0$ md.

$k_{z,1} = 0.1$ md.

$k_{x,2} = k_{y,2} = 10*k_{z,2}$

The permeability ratio is defined as

$$R_k = \frac{k_{x,1}}{k_{x,2}} \tag{5.8.1}$$

Except at the wellbore, other boundaries are no flow boundaries including the bottom boundary of layer 1 and the top boundary of layer 2. The pressures at the wellbore are the same for both layer 1 and layer 2.

The wellbore is vertical in this case. Therefore, the flow regime is forced to be radial flow regime for both top and bottom layers before the pressure transient reaches the lateral boundaries. The dimensionless time when the pressure transient reaches these boundaries are shown in Table 5.8.1

R_k	Top layer	Bottom layer
1	$2.5*10^5$	$2.5*10^5$
10	$2.5*10^5$	$2.5*10^6$
100	$2.5*10^5$	$2.5*10^7$
1000	$2.5*10^5$	$2.5*10^8$

Table 5.8.1 The Dimensionless Times for The Pressure Transient to Travel from The Wellbore to The Lateral Boundaries for Case 8

Fig. 5.2.8 illustrates the dimensionless pressure and the dimensionless pressure derivatives for different values of R_k. For $R_k = 1$, the reservoir is homogeneous. Hence, the performance is the same as that for a vertical well in closed-rectangular reservoir. The dimensionless pressure derivative is 0.5 during the infinite-acting flow. This flow regime is horizontal flow around the vertical well. When the pressure transient reaches the lateral boundaries at $t_D \approx 2.5*10^5$. The dimensionless pressure derivative is increased. After the transition period, the pseudo-steady flow is observed. During this flow period, the dimensionless pressure derivative forms a straight line with a slope of 1 on the log-log plot.

For $R_k > 1$, the dimensionless pressure derivative is bigger than 0.5 during the infinite-acting flow. But for $R_k = 100$ and $R_k = 1000$, there is no significant different in the dimensionless pressure derivative. The permeability of the bottom layer is so low that the production during the early time just comes from the top layer. Fig. 5.8.3 illustrates the semi-log plot of the dimensionless pressure versus dimensionless time. There exists a semi-log straight line for each case. For $R_k \geq 100$, the slope of the semi-log straight line is about double that of the homogeneous system.

The dimensionless pressure derivatives during the early time and during the late time are shown in Figs 5.8.4 and 5.8.5, respectively. During the early time, all cases have the radial flow regime because there is no vertical flow in each layer and between the layers. When the pressure transient reaches the lateral boundaries on the top layer, $t_D \approx 2.5*10^5$, the dimensionless pressure derivatives are increased. After the transition period, the dimensionless pressure derivative forms a straight line with a slope of 1. For $R_k > 1$, this is not the real pseudo-steady state. The real pseudo-steady flow comes when the pressure transient on the bottom layer reaches the lateral boundaries. Then dimensionless pressure derivative deviates from the straight. These dimensionless times are given in Table 5.8.1. After the transition period, the dimensionless pressure forms another straight line with a slope of 1. This is the real pseudo-steady state flow regime. During the pseudo-steady state flow, the dimensionless pressure derivative is not a function of the permeability ratio (R_k).

Fig. 5.8.6 illustrates the performance for the system with cross flow and the system without cross flow and R_k = 10. During the infinite-acting flow the dimensionless pressures and the dimensionless pressure derivatives for each case are slightly different. The system with cross flow observes the pseudo-steady flow before the system without cross flow dose. This is due to the communication across the interface between the top higher-permeability layer and the bottom lower-permeability layer. But for the system without cross flow, the lateral boundaries of the bottom layer are observed later due to the lower permeability in the x- and y-directions. When the pressure transient reaches the lateral boundaries of the bottom layer, the dimensionless pressure derivatives of both cases becomes identical.

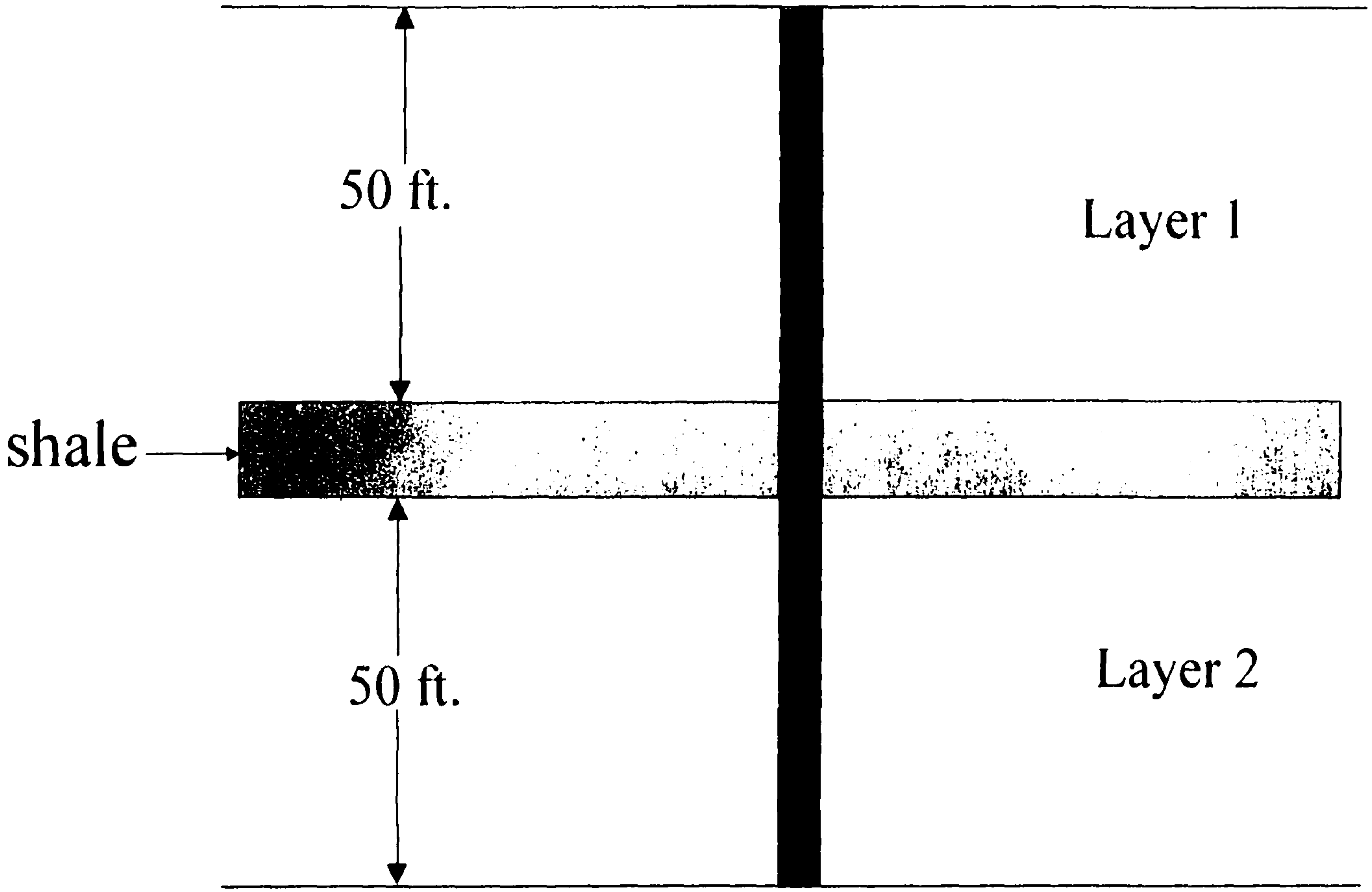

Figure 5.8.1 Reservoir Model for Case 8

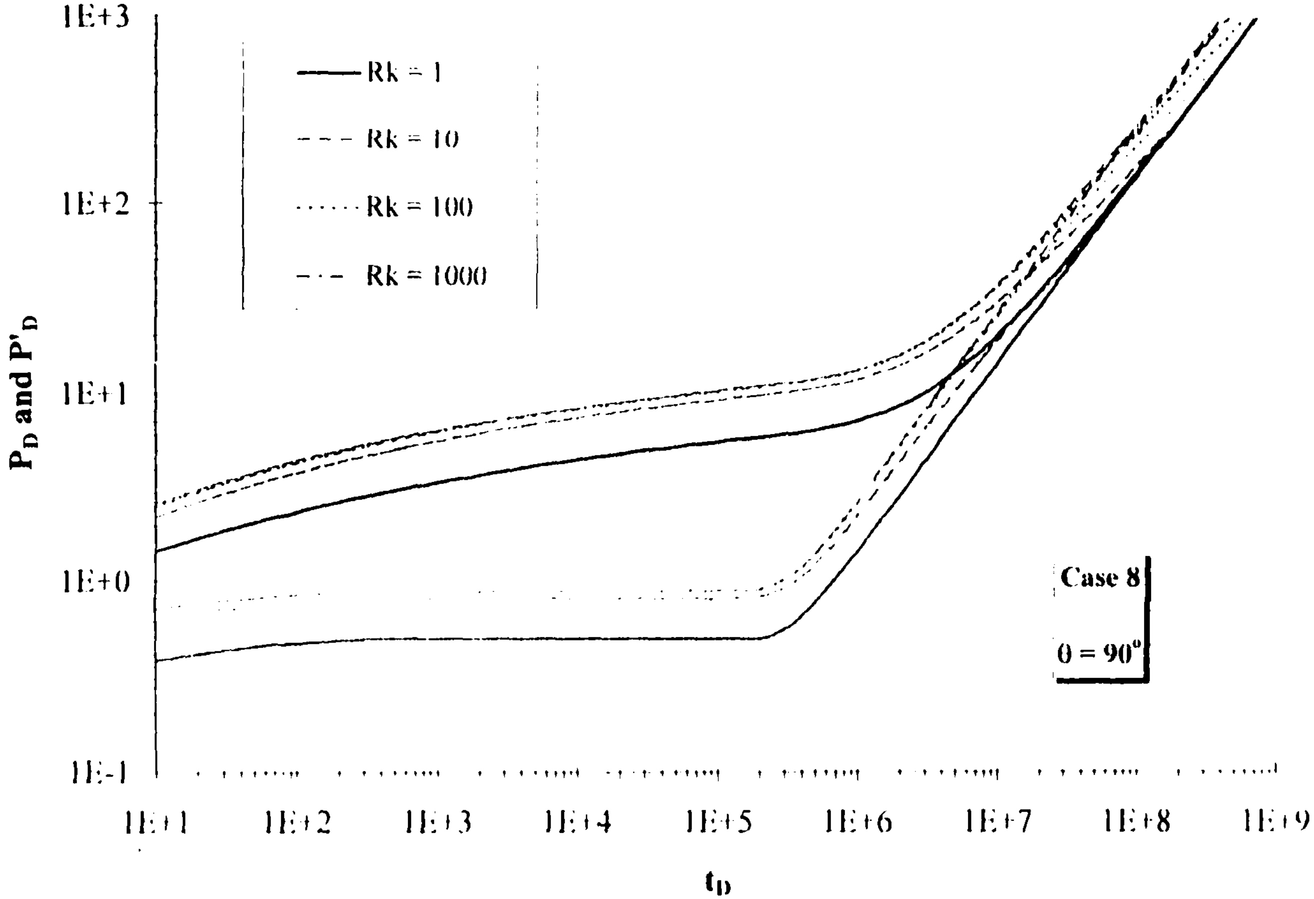

Figure 5.8.2 The Dimensionless Pressure and The Dimensionless Pressure Derivative for Case 8

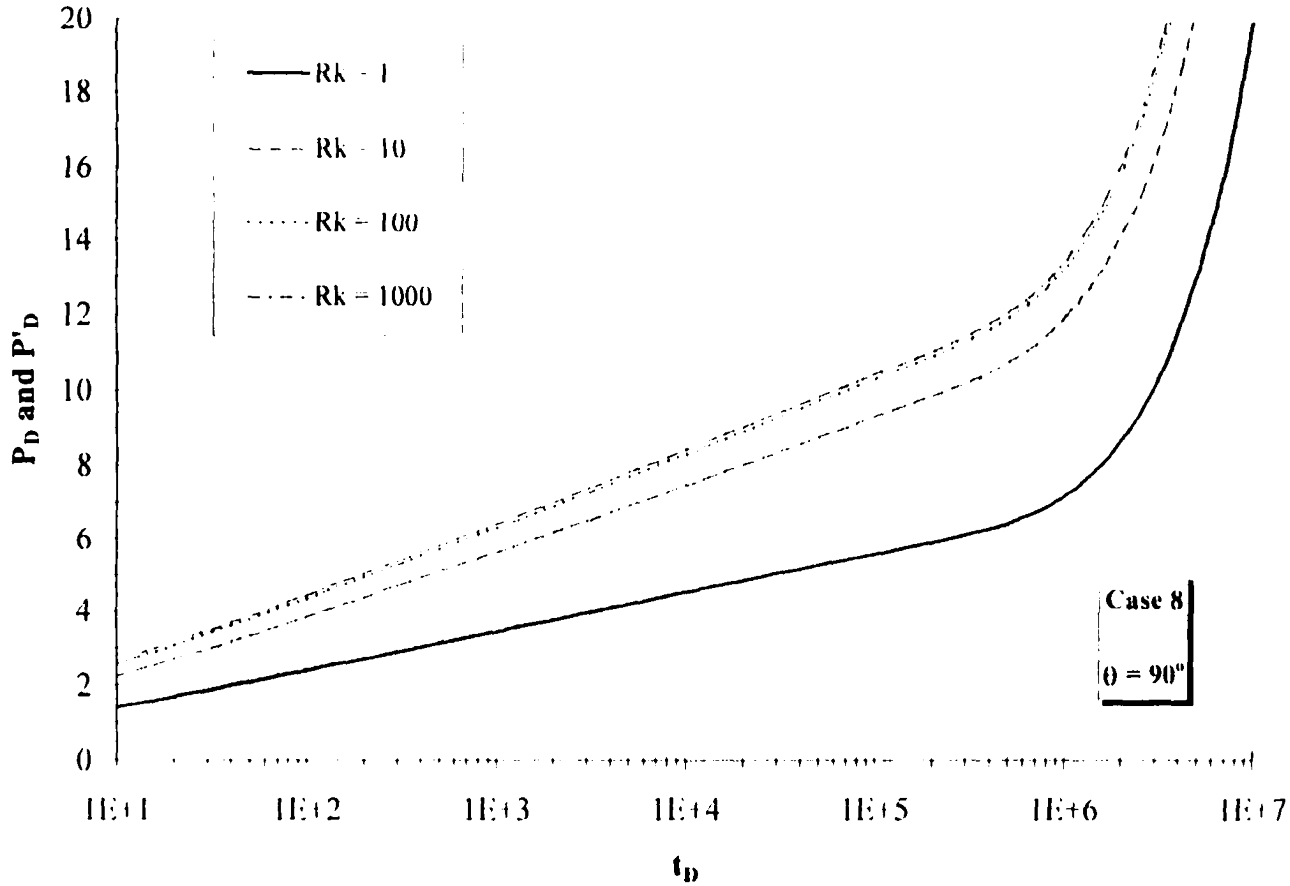

Figure 5.8.3 The Dimensionless Pressure for Case 8

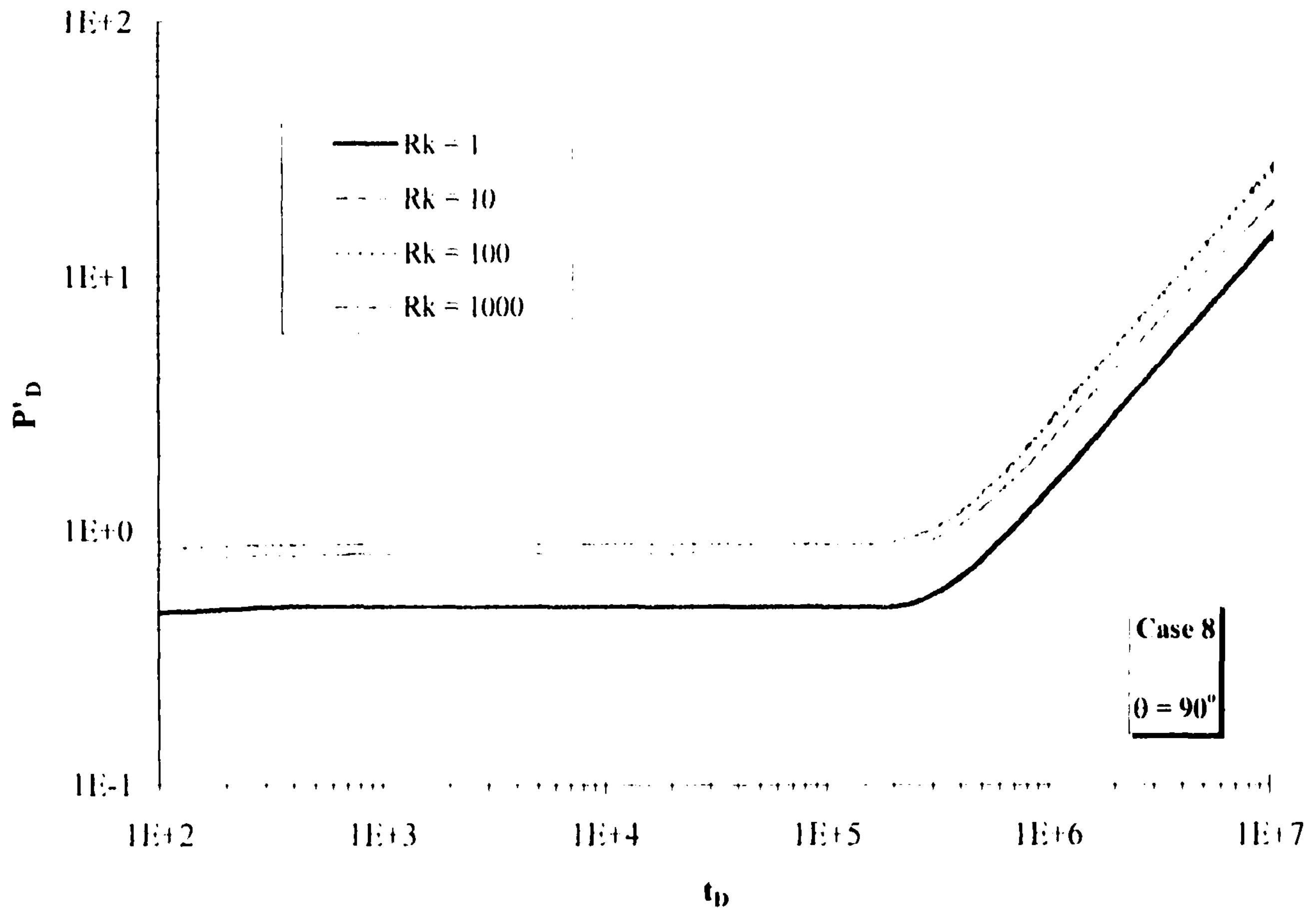

Figure 5.8.4 The Dimensionless Pressure Derivative for Case 8

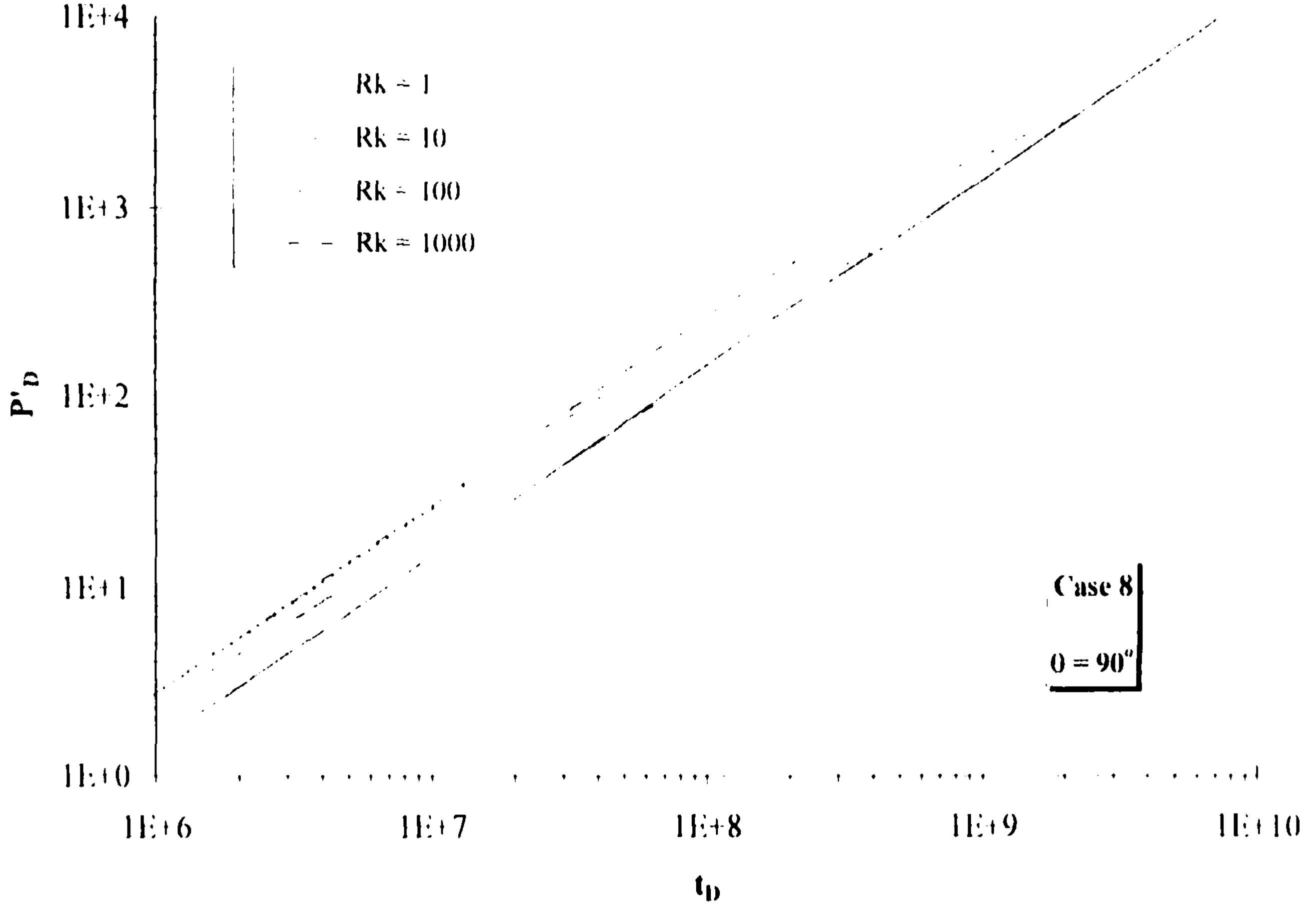

Figure 5.8.5 The Dimensionless Pressure Derivative for Case 8 During The Late-Time Period

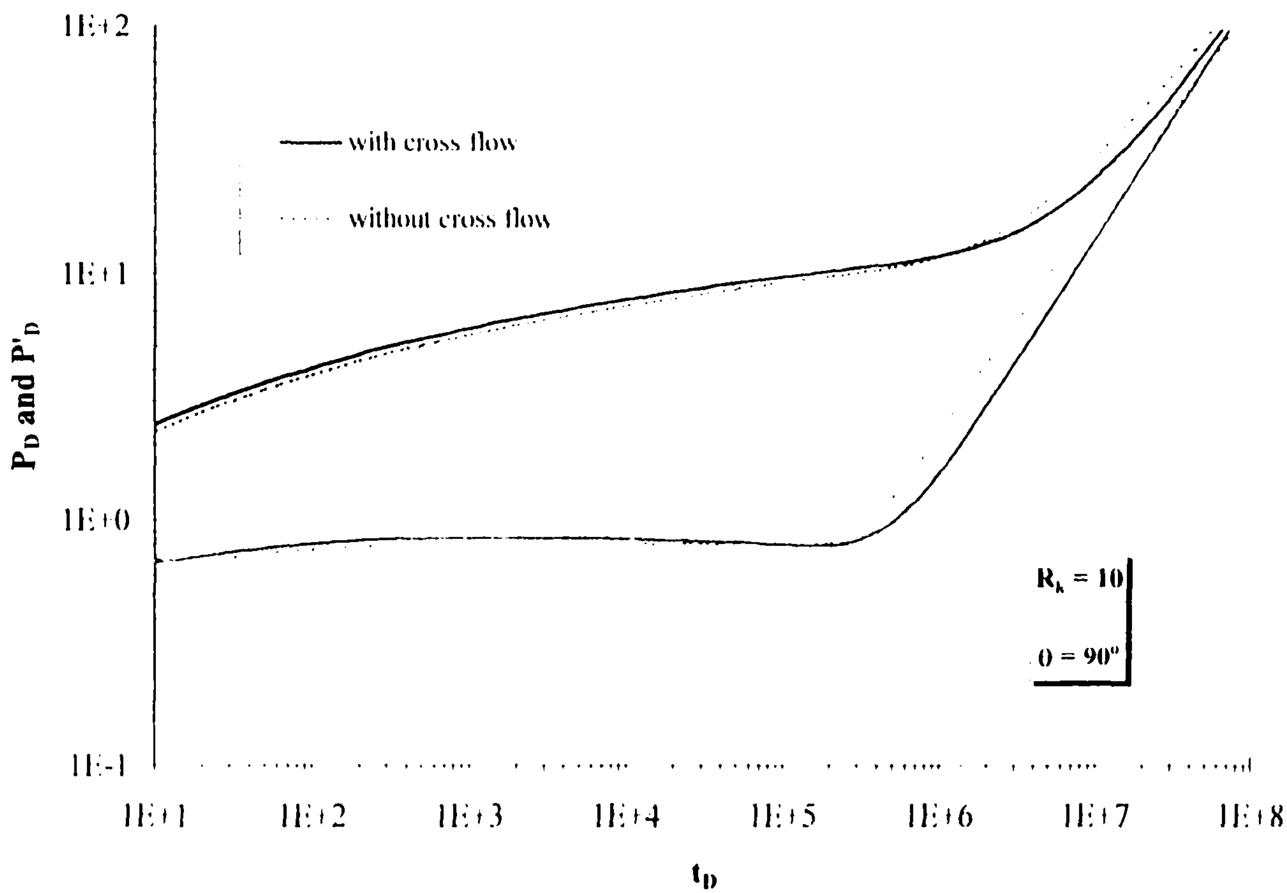

Figure 5.8.6 The Dimensionless Pressure Derivative for $R_k = 10$

Chapter 6

PRESSURE TRANSIENT ANALYSIS IN HORIZONTAL WELL

This chapter developed the so-called the direct synthesis technique for interpretation of pressure transient data without type-curve matching. Three different cases will be included in this chapter.

Case 1: A Horizontal Well in A Two-Layer Reservoir With Cross Flow

The reservoir model considered in this section is the same as one in Section 5.1 shown in Fig. 5.1.1. The following direct synthesis technique is developed to calculate several reservoir parameters including the different permeabilities in the top and bottom layers.

The pressure and pressure derivative for this has several characteristic points and straight line portions including:

- During the first radial flow period, the pressure drop, in psi., is expressed as

$$\Delta P = \frac{162.6 qBu}{\sqrt{k_{x,1} k_{z,1}}\, L_w}\left[\log\left(\frac{\sqrt{k_{x,1} k_{z,1}}\, t}{\phi \mu c_t r_w^2}\right) - 3.23 + 0.868 s\right] \tag{6.1.1}$$

The pressure derivative during this flow period is

$$\frac{\partial \Delta P}{\partial \ln t} = \frac{70.6 qB\mu}{\sqrt{k_{x,1} k_{z,1}}\, L_w} \tag{6.1.2}$$

The value of the derivative $(\partial \Delta P / \partial \ln t)$ can be used to calculate the radial permeability, $\sqrt{k_{x,1} k_{z,1}}$. From Eq. (6.1.1), the semi-log plot of the pressure drop versus time yield a straight line with a slope of

$$m_1 = \frac{162.6 q B \mu}{\sqrt{k_{x,1} k_{z,1}}\, L_w} \tag{6.1.3}$$

This slope can be used to calculate the radial permeability as

$$\sqrt{k_{x,1} k_{z,1}} = \frac{162.6 q B \mu}{m_1 L} \tag{6.1.4}$$

The skin factor can be calculated as

$$s = 1.151 \left[\left(\frac{P_{lm1} - P_{1,hr}}{m_1} \right) - \log \left(\frac{\sqrt{k_{x,1} k_{z,1}}}{\phi \mu c_t r_w^2} \right) + 3.23 \right] \tag{6.1.5}$$

where $(P_{lm1} - P_{1,hr})$ is the pressure drop obtained by extrapolating the semi-log straight line to t = 1 hour.

- During the second radial flow period, the relationship between the pressure derivative and the permeability is expressed as

$$\frac{\partial P_D}{\partial \ln t_D} = -0.0327\ x^5 + 0.204\ x^4 - 0.387\ x^3 + 0.011\ x^2 + 0.711\ x + 0.5$$

$$= \frac{k_{x,1} L_w}{141.2 q B \mu} \frac{\partial \Delta P}{\partial \ln t} \tag{6.1.6}$$

where

$$x = \log \left(\frac{k_{x,1}}{k_{x,2}} \right) \tag{6.1.7}$$

Once we know the permeability in the x-direction of the top layer, Eqs. (6.1.6) and (6.1.7) can be used to calculate the permeability in the bottom layer, $k_{x,2}$.

- During the pseudo-steady flow period, the dimensionless pressure is expressed as

$$p_D \frac{L_y}{L_w}\sqrt{\frac{k_{z,1}}{k_{x,1}}} = 2\pi t_{DA} + \frac{1}{2}\ln\left(\frac{2.246A}{C_A r_{wh}^2}\right) + \frac{L_y}{L_w}s + s_{pt} \tag{6.1.8}$$

The magnitude of the dimensionless pressure derivative is given by

$$\frac{\partial p_D}{\partial \ln t_D} = \frac{2\pi r_w^2}{A}\frac{L_w}{L_y}t_D \tag{6.1.9}$$

where

$$t_{DA} = \frac{0.0002637\sqrt{k_{x,1}k_{z,1}}}{\phi\mu c_t A}t \tag{6.1.10}$$

$$A = L_x L_z \tag{6.1.11}$$

$$r_{wh} = \frac{1}{2}\left[\sqrt[4]{\frac{k_z}{k_x}} + \sqrt[4]{\frac{k_x}{k_z}}\right]r_w \tag{6.1.12}$$

Eqs. (6.1.8) and (6.1.9) are expressed in oil-flied unit as

$$\Delta P = \frac{0.234qB}{\phi c_t L_x L_y L_z}t + \frac{141.2qB\mu}{\sqrt{k_{x,1}k_{z,1}}\,L_y}\left\{\frac{1}{2}\ln\left(\frac{2.246A}{C_A r_{wh}^2}\right) + \frac{L_y}{L_w}s + s_{pt}\right\} \tag{6.1.13}$$

$$\frac{\partial \Delta P}{\partial \ln t} = \frac{0.234qB}{\phi c_t L_x L_y L_z}t \tag{6.1.14}$$

The Cartesian plot of the pressure drop versus time yields a slope of $\frac{0.234qB}{\phi c_t L_x L_y L_z}$ and the interception of $\frac{141.2qB\mu}{\sqrt{k_{x,i}k_{z,i}}\,L_y}\left\{\frac{1}{2}\ln\left(\frac{2.246A}{C_A r_{wh}^2}\right)+\frac{L_y}{L_w}s+s_{pt}\right\}$. From the slope, the reservoir volume $(L_x L_y L_z)$ can be determined.

- The average pressure drop during the pseudo-steady state flow is expressed as

$$\left(\overline{P}-P_{wf}\right)=\frac{141.2qB\mu}{\sqrt{k_{x,i}k_{z,i}}\,L_y}\left\{\frac{1}{2}\ln\left(\frac{2.246A}{C_A r_{wh}^2}\right)+\frac{L_y}{L_w}s+s_{pt}\right\} \tag{6.1.15}$$

Hence, the average reservoir pressure is calculated as

$$\overline{P}=P_{wf}+\frac{141.2qB\mu}{\sqrt{k_{x,i}k_{z,i}}\,L_y}\left\{\frac{1}{2}\ln\left(\frac{2.246A}{C_A r_{wh}^2}\right)+\frac{L_y}{L_w}s+s_{pt}\right\} \tag{6.1.16}$$

- The productivity index is calculated as

$$J=\frac{q}{\left(\overline{P}-P_{wf}\right)}\ \text{stb/d/psi}$$

$$=\frac{0.00708\sqrt{k_{x,i}k_{z,i}}\,L_y}{B\mu\left\{\frac{1}{2}\ln\left(\frac{2.246A}{C_A r_{wh}^2}\right)+\frac{L_y}{L_w}s+s_{pt}\right\}} \tag{6.1.17}$$

- Deviation of the pressure derivative can be used to calculate the directional permeability. The radius of investigation is given as

$$r = \sqrt{\frac{kt}{948\phi\mu c_t}} \qquad (5.1)$$

Given the time and some knowledge of the distance from the wellbore to the boundary, the permeability can be calculated from the above equation.

The procedure for calculating reservoir parameters is the following:

Step 1: Identify the first radial-flow period. Use Eq. (6.1.2) to calculate the product of the permeability, $(k_{x,1}k_{z,1})^{1/2}$. In addition, from the semi-log plot of the pressure versus time, the permeability product can be calculated by using Eq. (6.1.3).

Step 2: Identify the pseudo-steady state flow period. Calculate the slope of the Cartesian plot of the pressure drop versus time during this period. Use Eq. (6.1.14) to calculate the reservoir bulk volume.

Step 3: Calculate the average reservoir pressure during the pseudo-steady flow period by using Eq. (6.1.16) and the intercept of the straight line from Step 2.

Step 4: Calculate the reservoir productivity index using Eq. (6.1.17).

Step 5: From the pressure derivative, identify the time when the pressure derivative deviates from the trend line. Use Eq. (5.1) to calculate the permeability.

Step 6: Calculate the permeability in x-direction of the top layer from the permeability in Step 1 and another permeability in Step 5.

Step 7: Identify the second radial flow period. Solve Eq. (6.1.6) to find the permeability ratio ($k_{x,1}/k_{x,2}$). Calculate the permeability in the x-direction of the bottom layer ($k_{x,2}$) by using the following equation.

$$k_{x,2} = \frac{k_{x,1}}{R_k} \tag{6.1.18}$$

Example

The horizontal well is located 5 ft. from the top boundary The wellbore data and reservoir parameters are

L_w	=	100 ft.
q	=	50 stb/d
B	=	1.2 rb/stb
μ	=	1.0 cp.
ϕ	=	20%
r_w	=	0.5 ft.

The wellbore is located 5 ft. from the interface. The pressure data is given in Table 6.1.

Step 1: During the first radial flow period, the pressure derivative is given as

$$\frac{\partial \Delta P}{\partial \ln t} = \frac{70.6 q B \mu}{\sqrt{k_{x,1} k_{z,1}} L_w} \qquad (6.1.2)$$

$$1.34 = \frac{70.6 * 50 * 1.2 * 1}{\sqrt{k_{x,1} k_{z,1}} * 100}$$

Solve the above equation, we have

$$\sqrt{k_{x,1} k_{z,1}} = 31.61 \text{ md.} \qquad (6.1.25)$$

From the semi-log plot, Fig. 6.1.2, the slope of the straight line is expressed as

$$m_1 = \frac{162.6 q B \mu}{\sqrt{k_{x,1} k_{z,1}} L_w} \qquad (6.1.3)$$

$$3 = \frac{162.6 * 50 * 1.2 * 1}{\sqrt{k_{x,1} k_{z,1}} * 100}$$

Solve the above equation. we have

$$\sqrt{k_{x,1} k_{z,1}} = 32.52 \text{ md.} \tag{6.1.26}$$

Step 2: During the pseudo-steady state flow. the pressure derivative is given as

$$\frac{\partial \Delta P}{\partial \ln t} = \frac{0.234 qB}{\phi c_t L_x L_y L_z} t \tag{6.1.20}$$

From the Cartesian plot of the pressure drop versus time. Fig. 6.1.4. yields the slope and the intercept of 0.05 psi/hr. and 14.1 psi..

$$0.05 = \frac{0.234 * 50 * 1.2}{0.2 * 1.5 * 10^{-5} * L_x L_y L_z}$$

Solve the above equation. we have

$L_x L_y L_z = 0.94 * 10^8$ ft^3

From the intercept. we have

$$\frac{141.2 qB\mu}{\sqrt{k_{x,1} k_{z,1}} L_y} \left\{ \frac{1}{2} \ln\left(\frac{2.246A}{C_A r_{wh}^2} \right) + \frac{L_y}{L_w} s + s_{pt} \right\} = 14.1 \text{ psi}$$

Step 3: The average reservoir pressure is expressed as

$$\overline{P} = P_{wf} + \frac{141.2 qB\mu}{\sqrt{k_{x,1} k_{z,1}} L_y} \left\{ \frac{1}{2} \ln\left(\frac{2.246A}{C_A r_{wh}^2} \right) + \frac{L_y}{L_w} s + s_{pt} \right\} \tag{6.1.22}$$

$$= P_{wf} + 14.1 \text{ psi}$$

Step 4: The productivity index is given as

$$J = \frac{q}{\left(\overline{P} - P_{wf}\right)} \text{ stb/d/psi}$$

$$= \frac{0.00708\sqrt{k_{x,1}k_{z,1}}\,L_x}{B\mu\left\{\frac{1}{2}\ln\left(\frac{2.246A}{C_A r_{wh}^2}\right) + \frac{L_x}{L_w}s + s_{pt}\right\}} \qquad (6.1.23)$$

$$= \frac{q}{14.1}$$

$$= \frac{50}{17.5} = 3.55 \text{ stb/d/psi}$$

Step 5: In Fig. 6.1.3, the pressure derivative deviates at 0.007 hr.

$$r = \sqrt{\frac{kt}{948\phi\mu c_t}} \qquad (5.1)$$

Given $r = 5$ ft. and the deviation time $t = 0.007$ hr.,

$$5 = \sqrt{\frac{k_{z,1} * 0.007}{948 * 0.2 * 1 * 1.5 * 10^{-5}}}$$

Solve the above equation, we have

$k_{z,1}$ = 10.16 md.

Step 6: From Eq. (6.1.25) and the permeability from Step 5, the permeability in the x-direction can be calculated.

$$\sqrt{k_{x,1}k_{z,1}} = 31.61$$

$$\sqrt{k_{x,1} * 10.16} = 31.61$$

Solve the above equation. we have

$k_{x,1} = 98.4$ md.

Step 7: During the second radial flow period. the pressure derivative is expressed as

$$\frac{\partial P_D}{\partial \ln t_D} = -0.0327\ x^5 + 0.204\ x^4 - 0.387\ x^3 + 0.011\ x^2 + 0.711\ x + 0.5 \qquad (6.1.12)$$

$$= 0.01 * k_{x,1}$$

$$= 0.01 * 98.4 = 0.984$$

Solve the above equation for x. we have

$$x = \log\left(\frac{k_{x,1}}{k_{x,2}}\right) = \log\left(\frac{98.4}{k_{x,2}}\right) = 0.99$$

The permeability of the bottom layer is

$k_{x,2} = 10.07$ md.

t(hr.)	P(psi.)	P'	t(hr.)	P(psi.)	P'
1.14E-03	4.15E+00		1.79E+00	1.28E+01	8.32E-01
1.42E-03	4.41E+00	1.165335	2.28E+00	1.30E+01	8.18E-01
1.79E-03	4.67E+00	1.183586	2.84E+00	1.31E+01	8.07E-01
2.28E-03	4.95E+00	1.196909	3.70E+00	1.33E+01	7.90E-01
2.84E-03	5.22E+00	1.207819	4.55E+00	1.35E+01	7.77E-01
3.70E-03	5.53E+00	1.213221	5.69E+00	1.37E+01	7.73E-01
4.55E-03	5.78E+00	1.212233	7.11E+00	1.38E+01	7.81E-01
5.69E-03	6.04E+00	1.215321	9.10E+00	1.40E+01	8.12E-01
7.11E-03	6.31E+00	1.220173	1.14E+01	1.42E+01	8.68E-01
9.10E-03	6.61E+00	1.22772	1.42E+01	1.44E+01	9.60E-01
1.14E-02	6.88E+00	1.23748	1.79E+01	1.47E+01	1.10E+00
1.42E-02	7.15E+00	1.255691	2.28E+01	1.49E+01	1.30E+00
1.79E-02	7.44E+00	1.280158	2.84E+01	1.53E+01	1.56E+00
2.28E-02	7.74E+00	1.306353	3.70E+01	1.57E+01	1.99E+00
2.84E-02	8.03E+00	1.332968	4.55E+01	1.62E+01	2.40E+00
3.70E-02	8.38E+00	1.357353	5.69E+01	1.68E+01	2.94E+00
4.55E-02	8.66E+00	1.368507	7.11E+01	1.75E+01	3.67E+00
5.69E-02	8.96E+00	1.378263	9.10E+01	1.85E+01	4.70E+00
7.11E-02	9.27E+00	1.379847	1.14E+02	1.97E+01	5.87E+00
9.10E-02	9.60E+00	1.368246	1.42E+02	2.12E+01	7.33E+00
1.14E-01	9.90E+00	1.344516	1.79E+02	2.31E+01	9.22E+00
1.42E-01	1.02E+01	1.314476	2.28E+02	2.56E+01	1.17E+01
1.79E-01	1.05E+01	1.275055	2.84E+02	2.85E+01	1.41E+01
2.28E-01	1.08E+01	1.223828	3.70E+02	3.25E+01	1.91E+01
2.84E-01	1.10E+01	1.171875	4.55E+02	3.73E+01	2.47E+01
3.70E-01	1.13E+01	1.100993	5.69E+02	4.31E+01	2.90E+01
4.55E-01	1.15E+01	1.04162	7.11E+02	5.03E+01	3.61E+01
5.69E-01	1.18E+01	0.987911	9.10E+02	6.04E+01	4.60E+01
7.11E-01	1.20E+01	0.941486	1.14E+03	7.19E+01	5.72E+01
9.10E-01	1.22E+01	0.898461	1.42E+03	8.61E+01	7.10E+01
1.14E+00	1.24E+01	0.867297	1.79E+03	1.05E+02	0.00E+00
1.42E+00	1.26E+01	0.847044	2.28E+03	0.00E+00	

Table 6.1 The Pressure Data for Case 6.1

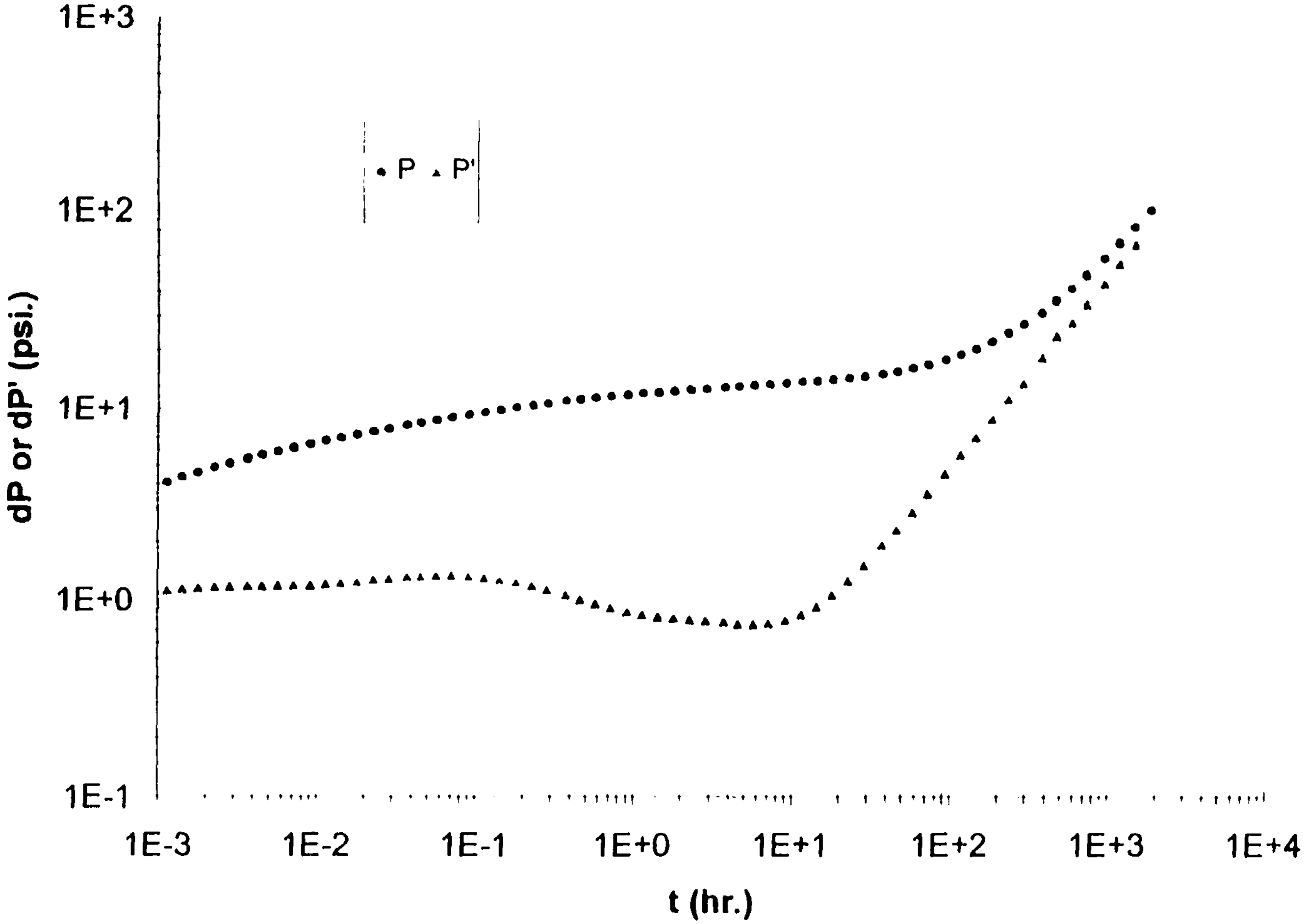

Figure 6.1.1 The Pressure Drop and The Pressure Derivative versus Time for Case 6.1

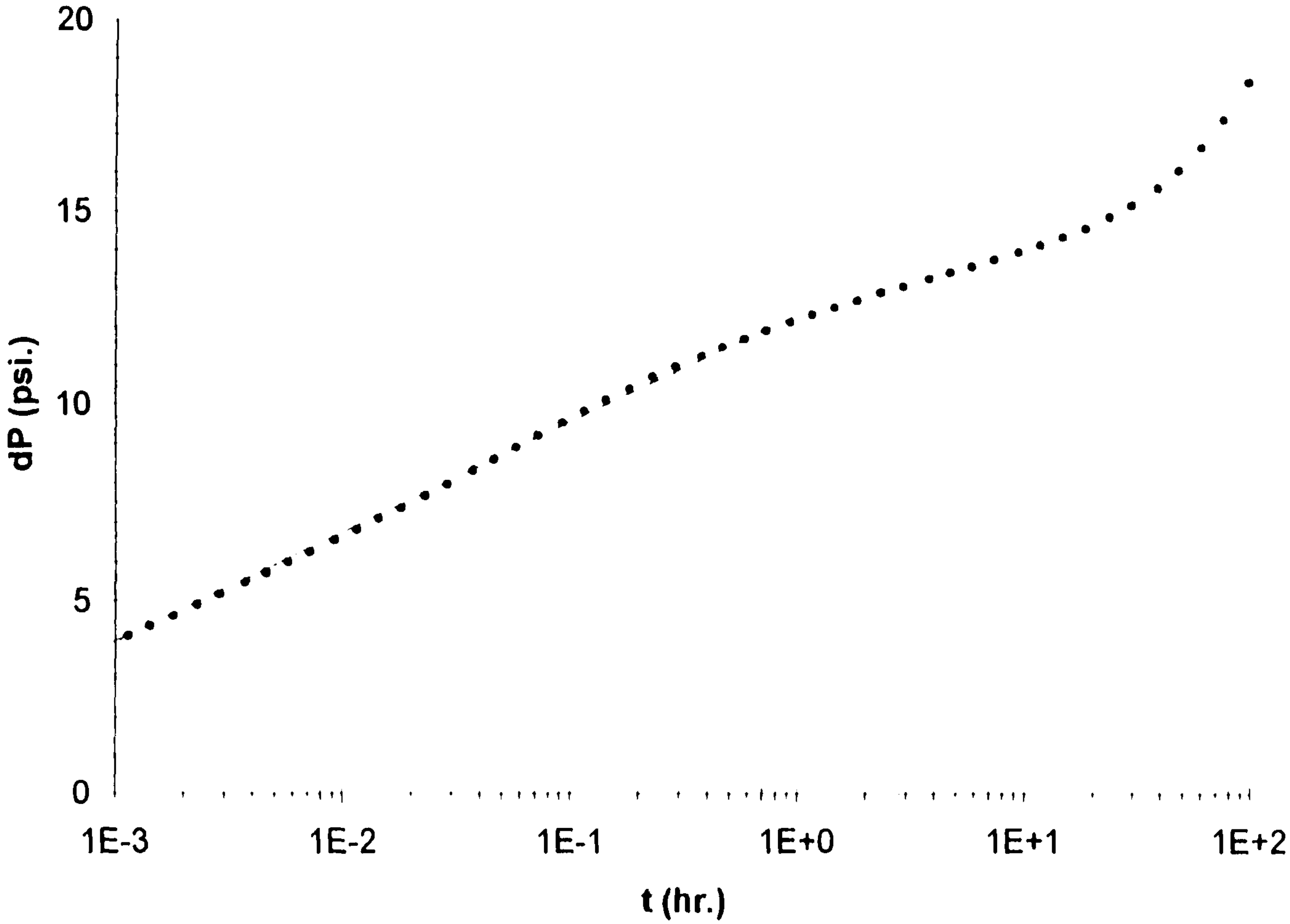

Figure 6.1.2 The Pressure Drop versus Time for Case 6.1

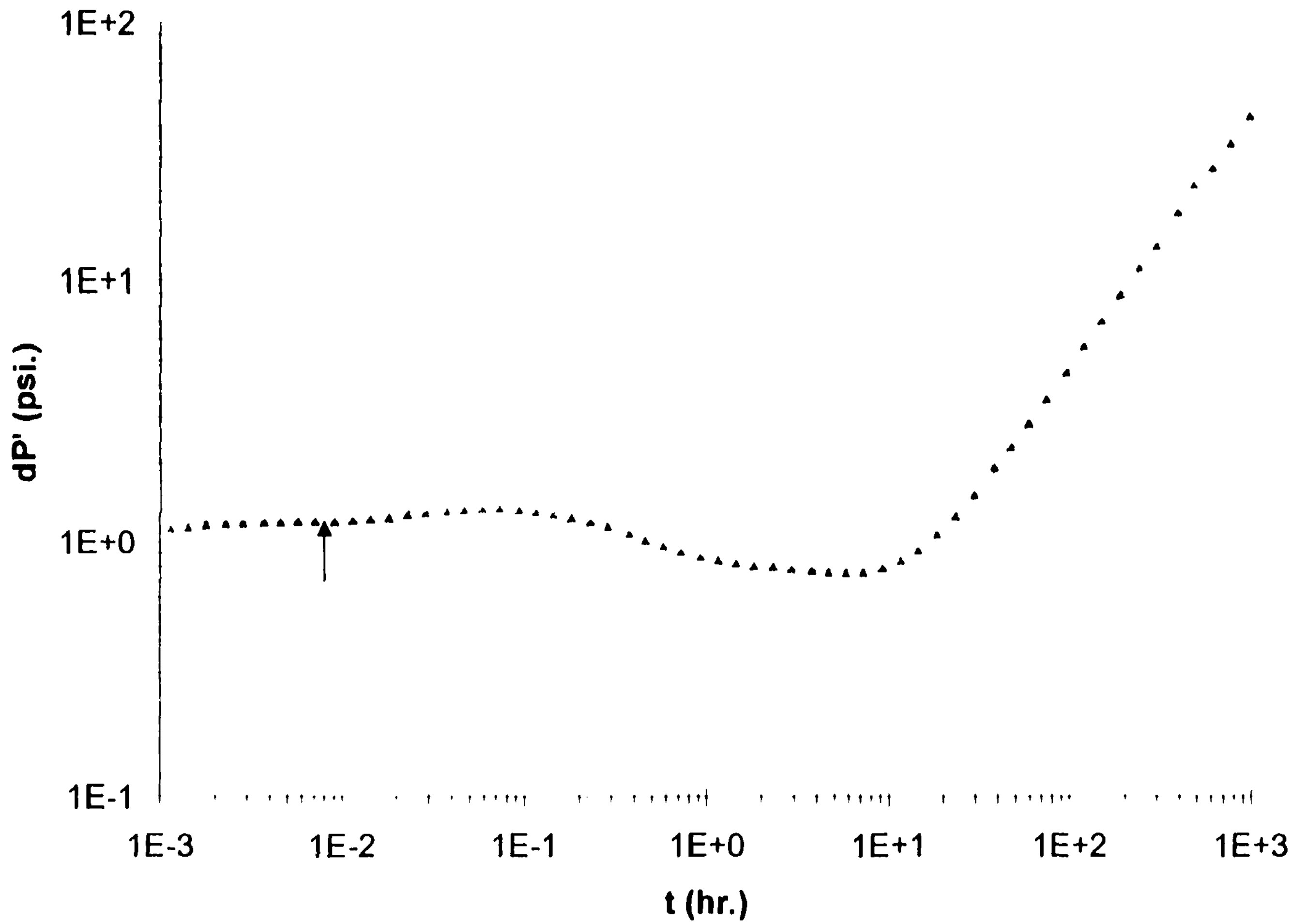

Figure 6.1.3 The Pressure Derivative versus Time for Case 6.1

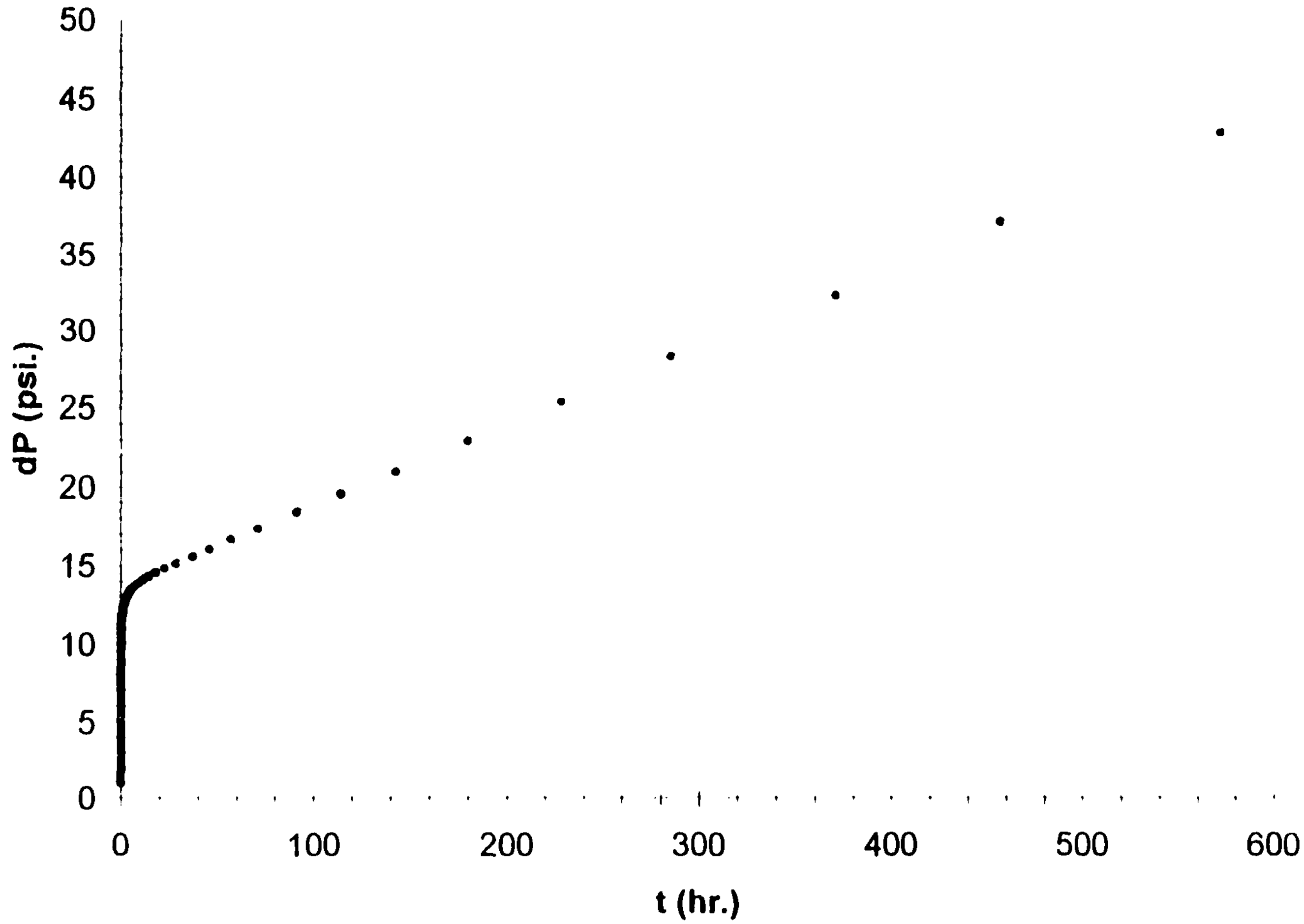

Figure 6.1.4 The Pressure Drop versus Time for Case 6.1

Case 2: A Horizontal Well Intersecting A Two-Layer Reservoir

The reservoir model considered in this section is the same as the one in Section 5.6 shown in Fig. 5.5.1. The following direct synthesis technique is developed to calculate the reservoir parameters including the different permeabilities in the top and bottom layers without type-curve matching.

The pressure and pressure derivative for this has several characteristic points and straight line portions including:

- During the first radial flow, the magnitude of the pressure derivative is expressed as

$$\frac{\partial P_D}{\partial \ln t_D} = c_1 R_k^5 - c_2 R_k^4 + c_3 R_k^3 - c_4 R_k^2 + c_5 R_k + c_6$$

$$= \frac{k_{x,1} L_w}{141.2 qB\mu} \frac{\partial \Delta P}{\partial \ln t} \quad (6.2.1)$$

where, for $0^0 \le \theta \le 90^0$,

$$c_1 = 7.234*10^{-12}\theta^2 - 1.232*10^{-9}\theta + 7.740*10^{-8} \quad (6.2.2a)$$

$$c_2 = 2.140*10^{-9}\theta^2 - 2.496*10^{-7}\theta + 1.237*10^{-6} \quad (6.2.2b)$$

$$c_3 = 8.044*10^{-8}\theta^2 - 1.316*10^{-5}\theta + 7.646*10^{-4} \quad (6.2.2c)$$

$$c_4 = -2.596*10^{-6}\theta^2 + 4.137*10^{-4}\theta - 2.284*10^{-2} \quad (6.2.2d)$$

$$c_5 = 4.091*10^{-5}\theta^2 - 6.339*10^{-3}\theta + 3.312*10^{-1} \quad (6.2.2e)$$

$$c_6 = 1.734*10^{-4}\theta^2 - 2.498*10^{-2}\theta + 1.258*10^{0} \quad (6.2.2f)$$

- During the second radial flow, the magnitude of the pressure derivative is expressed as

$$\frac{\partial P_D}{\partial \ln t_D} = c_1 R_k^5 - c_2 R_k^4 + c_3 R_k^3 - c_4 R_k^2 + c_5 R_k + c_6 \qquad (6.2.3)$$

where, for $0^0 \leq \theta \leq 90^0$,

$$c_1 = 1.829*10^{-12}\theta^2 - 2.692*10^{-10}\theta + 3.191*10^{-8} \qquad (6.2.4a)$$

$$c_2 = -3.008*10^{-10}\theta^2 + 4.303*10^{-8}\theta - 4.981*10^{-6} \qquad (6.2.4b)$$

$$c_3 = 1.944*10^{-8}\theta^2 - 2.689*10^{-6}\theta + 3.001*10^{-4} \qquad (6.2.4c)$$

$$c_4 = -5.910*10^{-7}\theta^2 + 7.956*10^{-5}\theta - 8.695*10^{-3} \qquad (6.2.4d)$$

$$c_5 = 8.385*10^{-6}\theta^2 - 1.113*10^{-3}\theta + 1.224*10^{-1} \qquad (6.2.4e)$$

$$c_6 = 4.262*10^{-6}\theta^2 - 4.687*10^{-4}\theta + 4.236*10^{-1} \qquad (6.2.4f)$$

- During the transition period before pseudo-steady state, there exists a straight line with a slope of 0.8. The length of the straight line (L_{ppss}) is a function of the permeability ratio (R_k). This relationship is expressed as

$$L_{ppss} = 1.451*10^{-9}R_k^5 - 3.992*10^{-7}R_k^4 + 4.054*10^{-5}R_k^3 - 0.00190R_k^2 + 0.0531R_k - 0.0512 \qquad (6.2.5)$$

This equation can be used to calculate the permeability ratio (R_k).

- During pseudo-steady state flow, the dimensionless pressure is expressed as

$$P_D\sqrt{\frac{k_y}{k_x}} = 2\pi t_{DA} + \frac{1}{2}\ln\left(\frac{2.246A}{C_A r_w^2}\right) + s \qquad (6.2.6)$$

where

$$t_{DA} = \frac{0.0002637\sqrt{k_{x,1}k_{y,1}}}{\phi\mu c_t A}t \tag{6.2.7}$$

and

$$A = L_x L_y \tag{6.2.8}$$

Eq. (6.2.6) can be expressed in oil-field unit as

$$\Delta P = \frac{0.234 qB\mu}{\phi\mu c_t L_x L_y L_z}t + \frac{141.2 qB\mu}{\sqrt{k_{x,1}k_{y,1}}\,L_z}\left\{\frac{1}{2}\ln\left(\frac{2.246A}{C_A r_w^2}\right) + s\right\} \tag{6.2.9}$$

The Cartesian plot of ΔP versus time yields a straight line whose slope and interception point are

$$m_{pss} = \frac{0.234 qB\mu}{\phi\mu c_t L_x L_y L_z} \tag{6.2.10}$$

$$I_{pss} = \frac{141.2 qB\mu}{\sqrt{k_{x,1}k_{y,1}}\,L_z}\left\{\frac{1}{2}\ln\left(\frac{2.246A}{C_A r_w^2}\right) + s\right\} \tag{6.2.11}$$

Eq. (6.2.10) can be used to calculate the reservoir volume ($L_x L_y L_z$).

- The average pressure drop during the pseudo-steady flow period is given by

$$\left(\overline{P} - P_{wf}\right) = \frac{141.2 qB\mu}{\sqrt{k_{x,1}k_{y,1}}\,L_z}\left\{\frac{1}{2}\ln\left(\frac{2.246A}{C_A r_w^2}\right) + s\right\} = I_{pss} \tag{6.2.12}$$

Hence, the average reservoir pressure is expressed as

$$\overline{P} = P_{wf} + \frac{141.2 qB\mu}{\sqrt{k_{x,1}k_{y,1}}\,L_z}\left\{\frac{1}{2}\ln\left(\frac{2.246A}{C_A r_w^2}\right) + s\right\} = P_{wf} + I_{pss} \tag{6.2.13}$$

- Productivity index is calculated as

$$J = \frac{q}{\left(\overline{P} - P_{wf}\right)} \text{ stb/d/psi}$$

$$= \frac{0.00708\sqrt{k_{x,1}k_{y,1}}\,L_z}{B\mu\left\{\frac{1}{2}\ln\left(\frac{2.246A}{C_A r_w^2}\right) + s\right\}} \tag{6.2.14}$$

- Deviation of the pressure derivative can be used to calculate the directional permeability or the distance from the wellbore to the interface or boundary. The radius of investigation is expressed as

$$r = \sqrt{\frac{kt}{948\phi\mu c_t}} \tag{5.1}$$

The procedure for calculating reservoir parameters is the following.

Step 1: Identify the transition period before the pseudo-steady state flow. Calculate the length straight line portion (L_{ppss}) during this period. Use Eq. (6.2.5) to solve for the permeability ratio (R_k).

Step 2: Identify the first radial flow regime. Use Eq. (6.2.1) to solve for the permeability in the x-direction of the top layer ($k_{x,1}$).

Step 3: Calculate the permeability in the x-direction of the bottom layer ($k_{x,2}$) by using the following equation.

$$k_{x,2} = \frac{k_{x,1}}{R_k} \tag{6.2.15}$$

Step 4: On the Cartesian plot of the pressure drop versus time, draw the straight line during the pseudo-steady flow period. Determine the slope (m_{pss}) and the interception point (I_{pss}).

Step 5: From the slope, calculate the reservoir volume by using the following equation.

$$L_x L_y L_z = \frac{0.234qB\mu}{\phi\mu c_t m_{pss}} \tag{6.2.16}$$

Step 6: The average reservoir pressure can be calculated by using Eq. (6.2.13).

Step 7: Calculate the productivity index by using Eq. (6.2.14).

Step 8: From the pressure derivative, identify the time when the pressure derivative deviates from the trend line. Use Eq. (5.1) to calculate the distance from the wellbore to the interface or boundary.

Example

The vertical well is located at the center of the reservoir The wellbore data and the reservoir parameters are

L_w	=	100 ft.
q	=	40 stb/d
B	=	1 1 rb/stb
μ	=	1 cp
ϕ	=	0 1
c_t	=	0 00001 psi^{-1}
s	=	0
r_w	=	0 5 ft.

The pressure data is given in Table 6 2

Step 1: During the transition period before pseudo-steady state, there exists a straight line with a slope of s 0.8. The length of the straight line portion is 0.59. The length of this straight line is expressed as

$$L_{ppss} = 1.451*10^{-9}R_k^5 - 3.992*10^{-7}R_k^4 + 4.054*10^{-5}R_k^3 - 0.00190R_k^2 + 0.0531R_k - 0.0512$$

$$= 0.59 \tag{6.2.5}$$

Solving the above equation yield the permeability ratio

$R_k = 40.0$

Step 2: During the first radial flow, for $\theta = 90^o$, the pressure derivative is expressed as

$$\frac{\partial P_D}{\partial \ln t_D} = 2.51*10^{-8}R_k^5 - 3.889*10^{-6}R_k^4 + 0.0002316R_k^3 - 0.00663R_k^2 + 0.0921R_k + 0.4143$$

$$= \frac{k_{x,1}L_w}{141.2qB\mu}\frac{\partial \Delta P}{\partial \ln t}$$

$$= 2.51*10^{-8}*40^5 - 3.889*10^{-6}40^4 + 0.0002316*40^3 - 0.00663*40^2$$

$$+ 0.0921*40 + 0.4143$$

$$= 0.9271$$

$$= \frac{k_{x,1}*100}{141.2*40*1.1*1}5.5$$

Solve the above equation for $k_{x,1}$, we have

$k_{x,1} = 10.47$ md.

Step 3: Calculate the permeability of the bottom layer

$$k_{x,2} = \frac{k_{x,1}}{R_k} \tag{6.2.15}$$

$$= \frac{10.47}{40} = 0.261 \text{ md.}$$

Step 4: During pseudo-steady state flow, on the Cartesian plot illustrated in Fig. 6.2.2, the straight line which is expressed as

$$\Delta P = \frac{0.234qB\mu}{\phi\mu c_t L_x L_y L_z} t + \frac{141.2qB\mu}{\sqrt{k_{x,1}k_{y,1}}L_z}\left\{\frac{1}{2}\ln\left(\frac{2.246A}{C_A r_w^2}\right) + s\right\} \tag{6.2.9}$$

The slope and the intercept are

$$m_{pss} = \frac{0.234qB\mu}{\phi\mu c_t L_x L_y L_z} = 0.097 \tag{6.2.10}$$

$$I_{pss} = \frac{141.2qB\mu}{\sqrt{k_{x,1}k_{y,1}}L_z}\left\{\frac{1}{2}\ln\left(\frac{2.246A}{C_A r_w^2}\right) + s\right\} \tag{6.2.11}$$

$$= 69$$

Step 5: Substitute the known parameters and solve for the reservoir volume as

$$0.097 = \frac{0.234 * 40 * 1.1 * 1}{0.1 * 1 * 0.00001 * L_x L_y L_z}$$

$L_x L_y L_z = 1.06*10^8$ ft^3

Step 6: The average reservoir pressure during the pseudo-steady flow is

$$\overline{P} = P_{wf} + \frac{141.2qB\mu}{\sqrt{k_{x,1}k_{y,1}}L_z}\left\{\frac{1}{2}\ln\left(\frac{2.246A}{C_A r_w^2}\right) + s\right\} \tag{6.2.13}$$

$\overline{P} = P_{wf} + 69$ psi.

Step 7: Productivity index can be calculated as

$$J = \frac{q}{\left(\overline{P} - P_{wf}\right)} \text{ stb/d/psi}$$

$$= \frac{0.00708\sqrt{k_{x,1}k_{y,1}}L_z}{B\mu\left\{\frac{1}{2}\ln\left(\frac{2.246A}{C_A r_w^2}\right) + s\right\}} \tag{6.2.14}$$

$$= \frac{40}{69} = 0.58 \text{ stb/d/psi}$$

Step 8: In Fig. 6.2.3, the pressure derivative deviate from the horizontal line at t = 21 hr.

$$r = \sqrt{\frac{kt}{948\phi\mu c_t}} \tag{5.1}$$

$$= \sqrt{\frac{10.47 * 21}{948 * 0.1 * 1 * 10^{-5}}}$$

$= 481.6$ ft.

This value is the distance from the wellbore to the boundary.

t(hr.)	dp (psi.)	dp' (psi.)	t(hr.)	dp (psi.)	dp' (psi.)
1.2325E-03	1.6763E+01		3.7922E+00	5.8675E+01	5.3395E+00
1.5169E-03	1.7689E+01	4.5576E+00	4.7402E+00	5.9843E+01	5.3152E+00
1.8961E-03	1.8702E+01	4.6512E+00	5.9727E+00	6.1047E+01	5.2916E+00
2.3701E-03	1.9735E+01	4.7426E+00	7.5844E+00	6.2284E+01	5.2542E+00
3.0338E-03	2.0898E+01	4.8340E+00	9.4805E+00	6.3431E+01	5.2278E+00
3.7922E-03	2.1968E+01	4.9067E+00	1.2325E+01	6.4770E+01	5.1865E+00
4.7402E-03	2.3056E+01	4.9887E+00	1.5169E+01	6.5825E+01	5.1566E+00
5.9727E-03	2.4201E+01	5.0757E+00	1.8961E+01	6.6958E+01	5.1899E+00
7.5844E-03	2.5404E+01	5.1550E+00	2.3701E+01	6.8106E+01	5.3067E+00
9.4805E-03	2.6544E+01	5.2334E+00	3.0338E+01	6.9423E+01	5.5779E+00
1.2325E-02	2.7903E+01	5.3045E+00	3.7922E+01	7.0692E+01	5.9990E+00
1.5169E-02	2.8992E+01	5.3415E+00	4.7402E+01	7.2083E+01	6.6562E+00
1.8961E-02	3.0173E+01	5.3930E+00	5.9727E+01	7.3712E+01	7.6231E+00
2.3701E-02	3.1362E+01	5.4372E+00	7.5844E+01	7.5674E+01	8.9881E+00
3.0338E-02	3.2685E+01	5.4676E+00	9.4805E+01	7.7849E+01	1.0680E+01
3.7922E-02	3.3886E+01	5.4766E+00	1.2325E+02	8.0966E+01	1.3293E+01
4.7402E-02	3.5090E+01	5.4923E+00	1.5169E+02	8.3984E+01	1.5948E+01
5.9727E-02	3.6339E+01	5.5081E+00	1.8961E+02	8.7921E+01	1.9534E+01
7.5844E-02	3.7633E+01	5.5118E+00	2.3701E+02	9.2758E+01	2.4046E+01
9.4805E-02	3.8842E+01	5.5236E+00	3.0338E+02	9.9437E+01	3.0400E+01
1.2325E-01	4.0264E+01	5.5213E+00	3.7922E+02	1.0700E+02	3.7709E+01
1.5169E-01	4.1390E+01	5.5057E+00	4.7402E+02	1.1639E+02	4.6905E+01
1.8961E-01	4.2600E+01	5.5116E+00	5.9727E+02	1.2856E+02	5.8925E+01
2.3701E-01	4.3810E+01	5.5189E+00	7.5844E+02	1.4445E+02	7.4697E+01
3.0338E-01	4.5147E+01	5.5169E+00	9.4805E+02	1.6311E+02	9.3290E+01
3.7922E-01	4.6356E+01	5.5024E+00	1.2325E+03	1.9108E+02	1.2120E+02
4.7402E-01	4.7563E+01	5.4993E+00	1.5169E+03	2.1905E+02	1.4911E+02
5.9727E-01	4.8811E+01	5.4975E+00	1.8961E+03	2.5632E+02	1.8633E+02
7.5844E-01	5.0100E+01	5.4837E+00	2.3701E+03	3.0289E+02	2.3284E+02
9.4805E-01	5.1300E+01	5.4796E+00	3.0338E+03	3.6807E+02	2.9794E+02
1.2325E+00	5.2708E+01	5.4576E+00	3.7922E+03	4.4255E+02	3.7233E+02
1.5169E+00	5.3819E+01	5.4256E+00	4.7402E+03	5.3562E+02	4.6532E+02
1.8961E+00	5.5009E+01	5.4133E+00	5.9727E+03	6.5659E+02	5.8617E+02
2.3701E+00	5.6195E+01	5.4007E+00	7.5844E+03	8.1474E+02	
3.0338E+00	5.7500E+01	5.3755E+00			

Table 6.2 The Pressure Data for Case 6.2

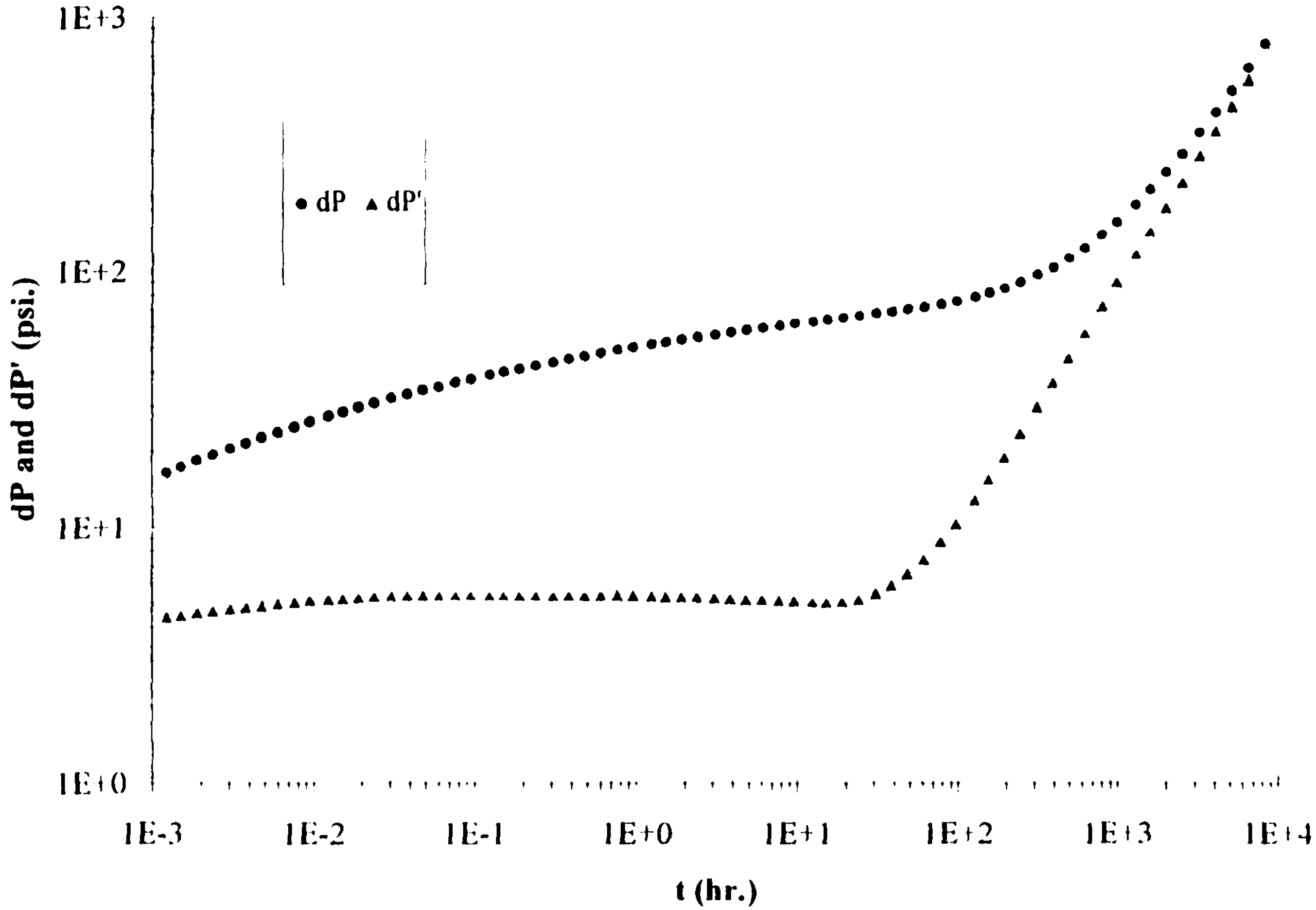

Figure 6.2.1 The Pressure Drop and The Pressure Derivative versus Time for Case 6.2

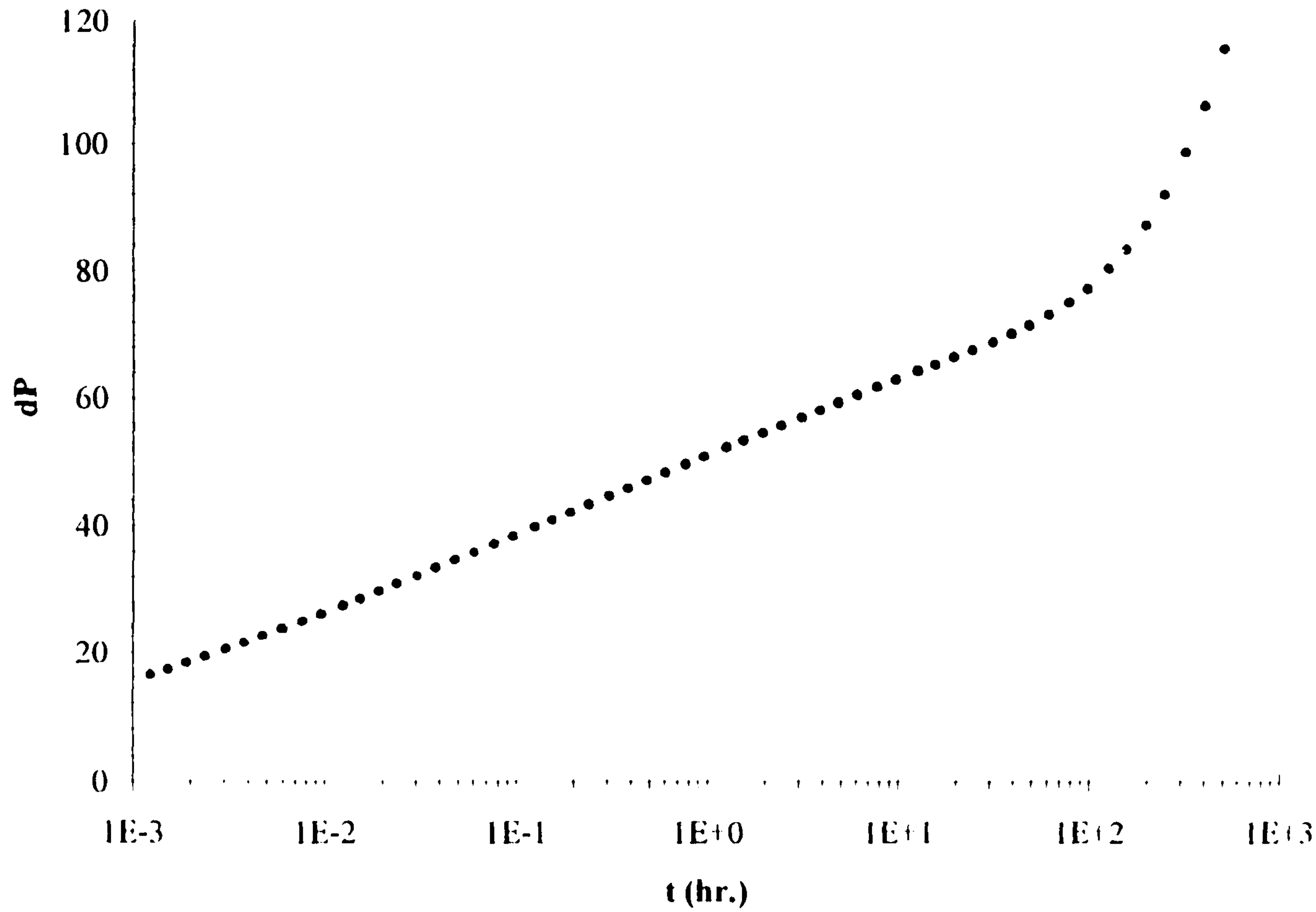

Figure 6.2.2 The Pressure Drop versus Time for Case 6.2

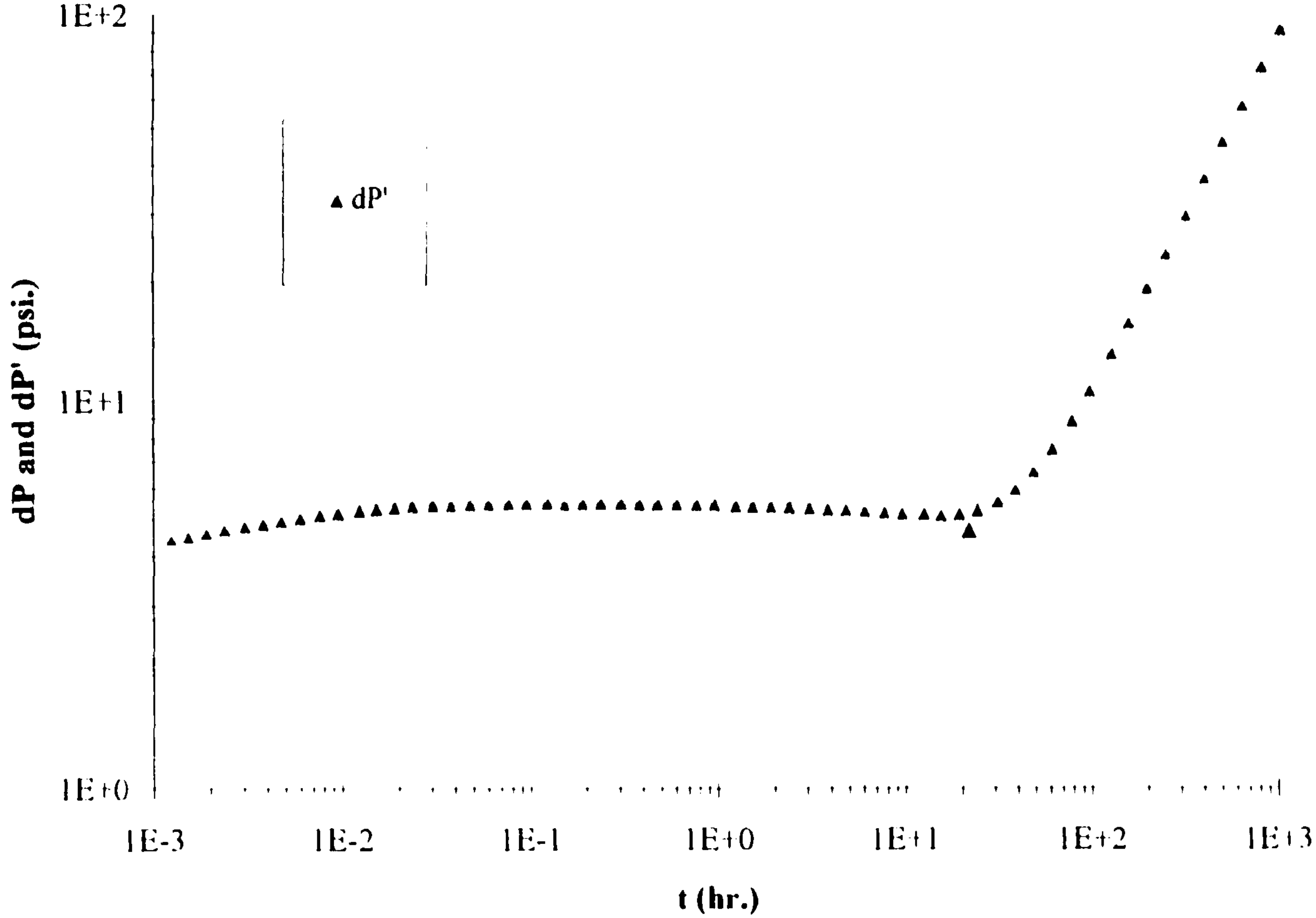

Figure 6.2.3 The Pressure Derivative versus Time for Case 6.2

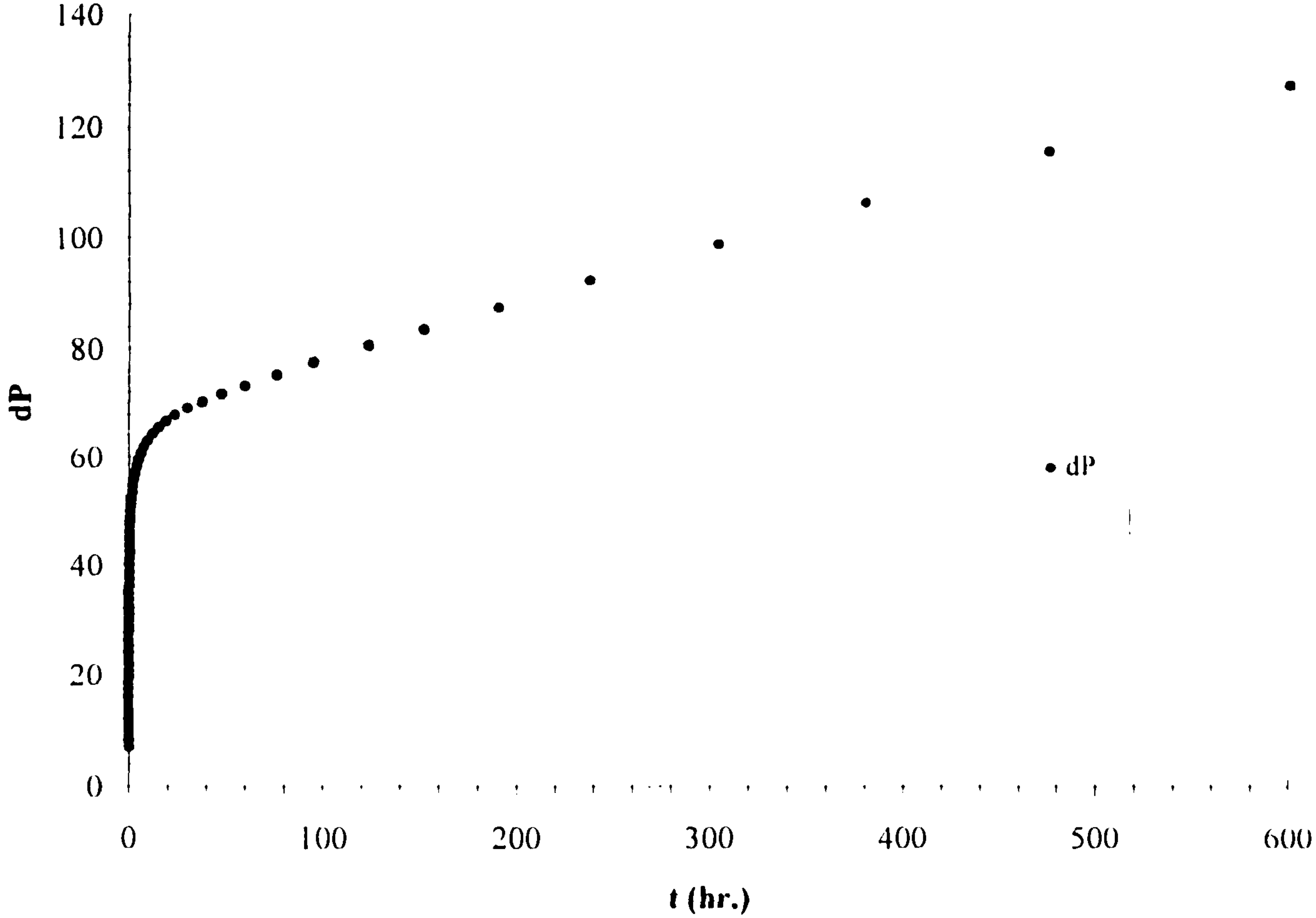

Figure 6.2.4 The Pressure Drop for Case 6.2

Case 3: A Snake-Shape Horizontal Well in A Two-Layer Reservoir

The reservoir model considered in this section is the same as the one in Section 5.6 shown in Fig. 5.6.1. The following direct synthesis technique is developed to calculate the reservoir parameters including the different permeabilities in the top and bottom layers.

The pressure and pressure derivative for this has several characteristic points and straight line portions including:

- During the first radial flow, the magnitude of the dimensionless pressure derivative is expressed a

For Case A,

$$\frac{\partial P_D}{\partial \ln t_D} = -0.1073x^5 + 0.697x^4 - 1.599x^3 + 1.308x^2 + 0.236x + 0.865$$

$$= \frac{k_{x,1} L_w}{141.2qB\mu} \frac{\partial \Delta P}{\partial \ln t} \tag{6.3.1}$$

where

$$x = \log(R_k) \tag{6.3.2}$$

For Case B,

$$\frac{\partial P_D}{\partial \ln t_D} = -0.2184x^5 + 1.3764x^4 - 3.097x^3 + 2.5777x^2 + 0.2973x + 0.8649 \tag{6.3.3}$$

- During the second radial flow, the magnitude of the dimensionless pressure derivative is expressed as

Only for Case B,

$$\frac{\partial P_D}{\partial \ln t_D} = -0.1455x^2 + 0.9126x + 1.2667 \tag{6.3.4}$$

- During the transition period before the pseudo-steady state, there exists a straight line with a slope of 0.8. The length of the transition period can be used to calculate the permeability ratio (R_k). The relationship between the length of this straight line and the permeability ratio is given as

$$L_{ppss} = 1.451*10^{-9}R_k^5 - 3.992*10^{-7}R_k^4 + 4.054*10^{-5}R_k^3 - 0.00190R_k^2 + 0.0531R_k - 0.0512 \tag{6.3.5}$$

- During the pseudo-steady state, the dimensionless pressure is expressed as

$$P_D\frac{L_z}{L_w} = 2\pi t_{DA} + I_{pss} \tag{6.3.6}$$

where I_{pss} is a constant value and is a function of wellbore configuration, wellbore location, and shape of the reservoir. The above equation is expressed in oil-field unit as

$$\Delta P = \frac{0.234qB\mu}{\phi\mu c_t L_x L_y L_z}t + \frac{141.2qB\mu}{k_x L_z}I_{pss} \tag{6.3.7}$$

- The average reservoir pressure during the pseudo-steady state flow period can be expressed as

$$\left(\bar{P} - P_{wf}\right) = \frac{141.2 qB\mu}{k_x L_z} I_{pss} \tag{6.3.8}$$

- Productivity index is given by

$$J = \frac{q}{\left(\bar{P} - P_{wf}\right)} \text{ stb/d/psi}$$

$$= \frac{0.00708 k_x L_z}{qB\mu I_{pss}} \tag{6.3.9}$$

- Deviation time can be used to calculate the direction permeability from the following equation.

$$r = \sqrt{\frac{kt}{948\phi\mu c_t}} \tag{5.1}$$

The procedure for calculating reservoir parameters is the following:

Step 1: Identify the transition period before the pseudo-steady state flow period. Determine the length of the straight whose slope is 0.8. Solve Eq. (6.3.5) for the permeability ratio (R_k).

Step 2: Identify the first radial flow period. Use Eq. (6.3.1) and the permeability ratio from Step 1 to calculate the permeability in the x-direction for the top and the bottom layers.

Step 3: Identify the pseudo-steady flow period. From the Cartesian plot of the pressure drop versus time, draw a straight line. Determine the slope and the intercept of this straight line. Use Eq. (6.3.7) to calculate the reservoir volume

Step 4: Calculate the average reservoir pressure using Eq. (6.3.8).

Step 5: Use Eq. (6.3.9) to calculate the reservoir productivity index.

Step 6: Calculate the distance from the wellbore to the boundary by using Eq. (5.1).

Example

The wellbore data and reservoir parameters are

L_w = 272 ft.

q = 50 stb/d

B = 1.2 rb/stb

μ = 1 cp.

ϕ = 10%

c_t = 0.00002 psi^{-1}

r_w = 0.5 ft.

The production data is given in Table 6.3.

Step 1: During the transition period before the pseudo-steady state, there exists a straight line with a slope of 0.8. and the length is 1.097 log-scale unit. The length of the straight line is expressed as

$$L_{ppss} = 1.451*10^{-9}R_k^5 - 3.992*10^{-7}R_k^4 + 4.054*10^{-5}R_k^3 - 0.00190R_k^2 + 0.0531R_k - 0.0512 \tag{6.3.5}$$

$$= 1.097$$

Solving the above equation, we have

$R_k = 68$

Step 2: During the first radial flow, the pressure derivative is given as

$$\frac{\partial P_D}{\partial \ln t_D} = -0.1073x^5 + 0.697x^4 - 1.599x^3 + 1.308x^2 + 0.236x + 0.865$$

$$= \frac{k_{x,1} L_w}{141.2qB\mu} \frac{\partial \Delta P}{\partial \ln t} \qquad (6.3.1)$$

where

$$x = \log(R_k) \qquad (6.3.2)$$

Substitute R_k from Step 1 into the above equation yields

$x = \log(68) = 1.833$

Substitute x and the known parameters into Eq. (6.3.1) yields

$$1.49 = \frac{k_{x,1} L_w}{141.2qB\mu} \frac{\partial \Delta P}{\partial \ln t}$$

$$= \frac{k_{x,1} * 272}{141.2 * 50 * 1.2 * 1} * 0.446$$

Solving the above equation for $k_{x,1}$, we have

$k_{x,1} = 104.1$ md.

The permeability in the x-direction of the bottom layer is calculated as

$$k_{x,2} = \frac{k_{x,1}}{R_k}$$

$$= \frac{104.1}{68} = 1.53 \text{ md.}$$

Step 3: During the pseudo-steady state, there exists a straight line expressed as

$$\Delta P = \frac{0.234qB\mu}{\phi\mu c_t L_x L_y L_z} t + \frac{141.2qB\mu}{k_x L_z} I_{pss} \qquad (6.3.7)$$

From Fig. 6.3.4, the straight has slope and the intercept of 0.0703 psi/hr and 6.2 psi, respectively.

$$\text{slope} = 0.0703 = \frac{0.234 qB\mu}{\phi\mu c_t L_x L_y L_z}$$

$$= \frac{0.234 * 50 * 1.2 * 1}{0.1 * 1 * 2 * 10^{-5} L_x L_y L_z}$$

$L_x L_y L_z = 99.86 * 10^6 \ ft^2$

$$\text{intercept} = \frac{141.2 qB\mu}{k_x L_z} I_{pss} = 6.2$$

Step 4: The average reservoir pressure can be calculated as

$$\left(\bar{P} - P_{wf}\right) = \frac{141.2 qB\mu}{k_x L_z} I_{pss} \tag{6.3.8}$$

$\bar{P} = P_{wf} + 6.2$

Step 5: Productivity index is calculated as

$$J = \frac{q}{\left(\bar{P} - P_{wf}\right)} \ \text{stb/d/psi}$$

$$= \frac{0.00708 k_x L_z}{qB\mu I_{pss}} \tag{6.3.9}$$

$$= \frac{50}{6.2} = 8.06 \ \text{stb/d/psi}$$

Step 6: From Fig. 6.3.3, the pressure derivative deviate from the trend line at t = 0.12 hr

The distance from the wellbore can be calculated by using Eq. (5.1) as

$$r = \sqrt{\frac{kt}{948\phi\mu c_t}} \tag{5.1}$$

$$r = \sqrt{\frac{10*0.12}{948*0.1*1*2*10^{-5}}}$$

$= 25.16$ ft.

t (hr.)	dP (psi.)	dP'	t (hr.)	dP (psi.)	dP'
1.19E-03	1.82E+00		4.74E+00	5.92E+00	7.08E-01
1.52E-03	1.92E+00	4.36E-01	6.07E+00	6.09E+00	7.57E-01
1.90E-03	2.02E+00	4.40E-01	7.58E+00	6.27E+00	8.28E-01
2.46E-03	2.13E+00	4.42E-01	9.48E+00	6.46E+00	9.34E-01
3.03E-03	2.22E+00	4.43E-01	1.19E+01	6.69E+00	1.09E+00
3.79E-03	2.32E+00	4.44E-01	1.52E+01	6.97E+00	1.30E+00
4.74E-03	2.42E+00	4.46E-01	1.90E+01	7.29E+00	1.56E+00
6.07E-03	2.53E+00	4.46E-01	2.46E+01	7.75E+00	1.96E+00
7.58E-03	2.62E+00	4.45E-01	3.03E+01	8.19E+00	2.36E+00
9.48E-03	2.72E+00	4.44E-01	3.79E+01	8.78E+00	2.89E+00
1.19E-02	2.82E+00	4.44E-01	4.74E+01	9.49E+00	3.56E+00
1.52E-02	2.93E+00	4.43E-01	6.07E+01	1.05E+01	4.47E+00
1.90E-02	3.02E+00	4.42E-01	7.58E+01	1.16E+01	5.51E+00
2.46E-02	3.14E+00	4.39E-01	9.48E+01	1.30E+01	6.81E+00
3.03E-02	3.23E+00	4.36E-01	1.19E+02	1.47E+01	8.50E+00
3.79E-02	3.32E+00	4.34E-01	1.52E+02	1.70E+01	1.07E+01
4.74E-02	3.42E+00	4.33E-01	1.90E+02	1.97E+01	1.34E+01
6.07E-02	3.52E+00	4.32E-01	2.46E+02	2.37E+01	1.73E+01
7.58E-02	3.62E+00	4.32E-01	3.03E+02	2.77E+01	2.13E+01
9.48E-02	3.71E+00	4.36E-01	3.79E+02	3.30E+01	2.67E+01
1.19E-01	3.81E+00	4.43E-01	4.74E+02	3.97E+01	3.34E+01
1.52E-01	3.92E+00	4.54E-01	6.07E+02	4.90E+01	4.29E+01
1.90E-01	4.02E+00	4.68E-01	7.58E+02	5.98E+01	5.38E+01
2.46E-01	4.14E+00	4.87E-01	9.48E+02	7.32E+01	6.75E+01
3.03E-01	4.24E+00	5.04E-01	1.19E+03	9.08E+01	8.54E+01
3.79E-01	4.36E+00	5.25E-01	1.52E+03	1.14E+02	1.09E+02
4.74E-01	4.47E+00	5.49E-01	1.90E+03	1.41E+02	1.38E+02
6.07E-01	4.61E+00	5.74E-01	2.46E+03	1.83E+02	1.81E+02
7.58E-01	4.74E+00	5.95E-01	3.03E+03	2.25E+02	2.25E+02
9.48E-01	4.87E+00	6.15E-01	3.79E+03	2.82E+02	2.86E+02
1.19E+00	5.01E+00	6.33E-01	4.74E+03	3.54E+02	3.65E+02
1.52E+00	5.17E+00	6.47E-01	6.07E+03	4.57E+02	4.79E+02
1.90E+00	5.31E+00	6.57E-01	7.58E+03	5.79E+02	6.17E+02
2.46E+00	5.48E+00	6.65E-01	9.48E+03	7.36E+02	7.95E+02
3.03E+00	5.62E+00	6.70E-01	1.19E+04	9.47E+02	1.03E+03
3.79E+00	5.76E+00	6.83E-01	1.52E+04	1.23E+03	

Table 6.3 The Pressure Data for Case 6.3

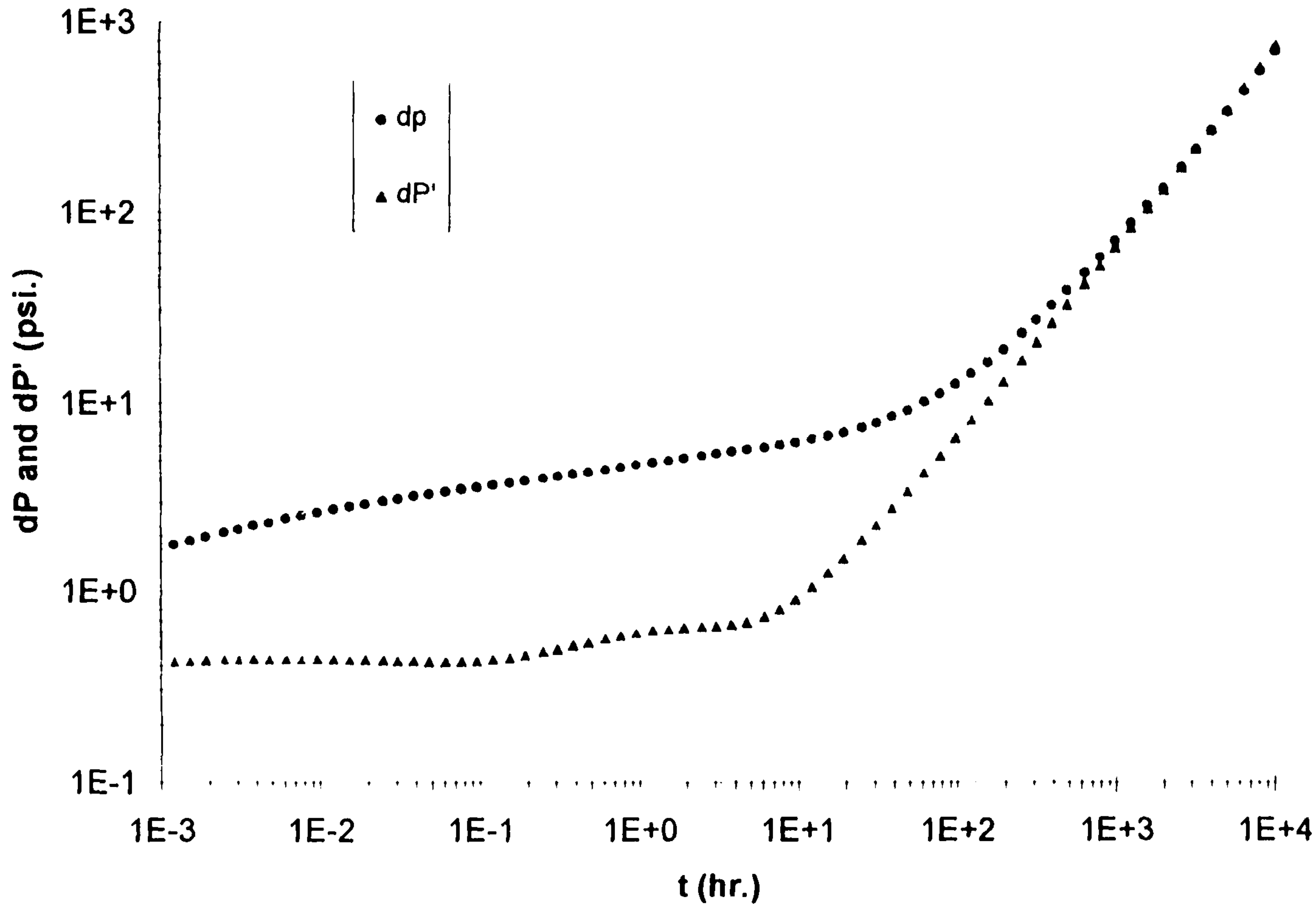

Figure 6.3.1 The Pressure Drop and The Pressure Derivative versus Time for Case 6.3

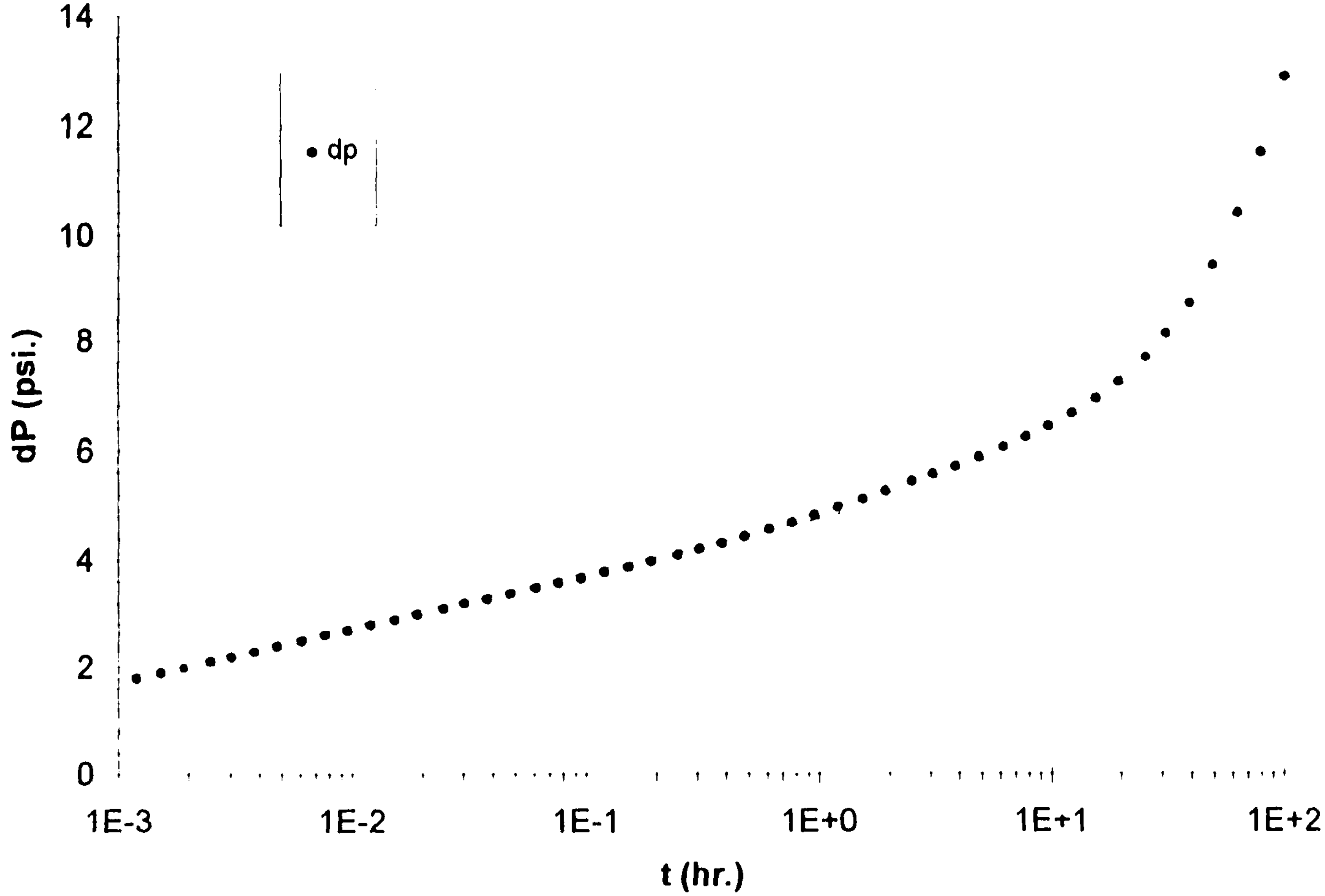

Figure 6.3.2 The Pressure Drop versus Time for Case 6.3

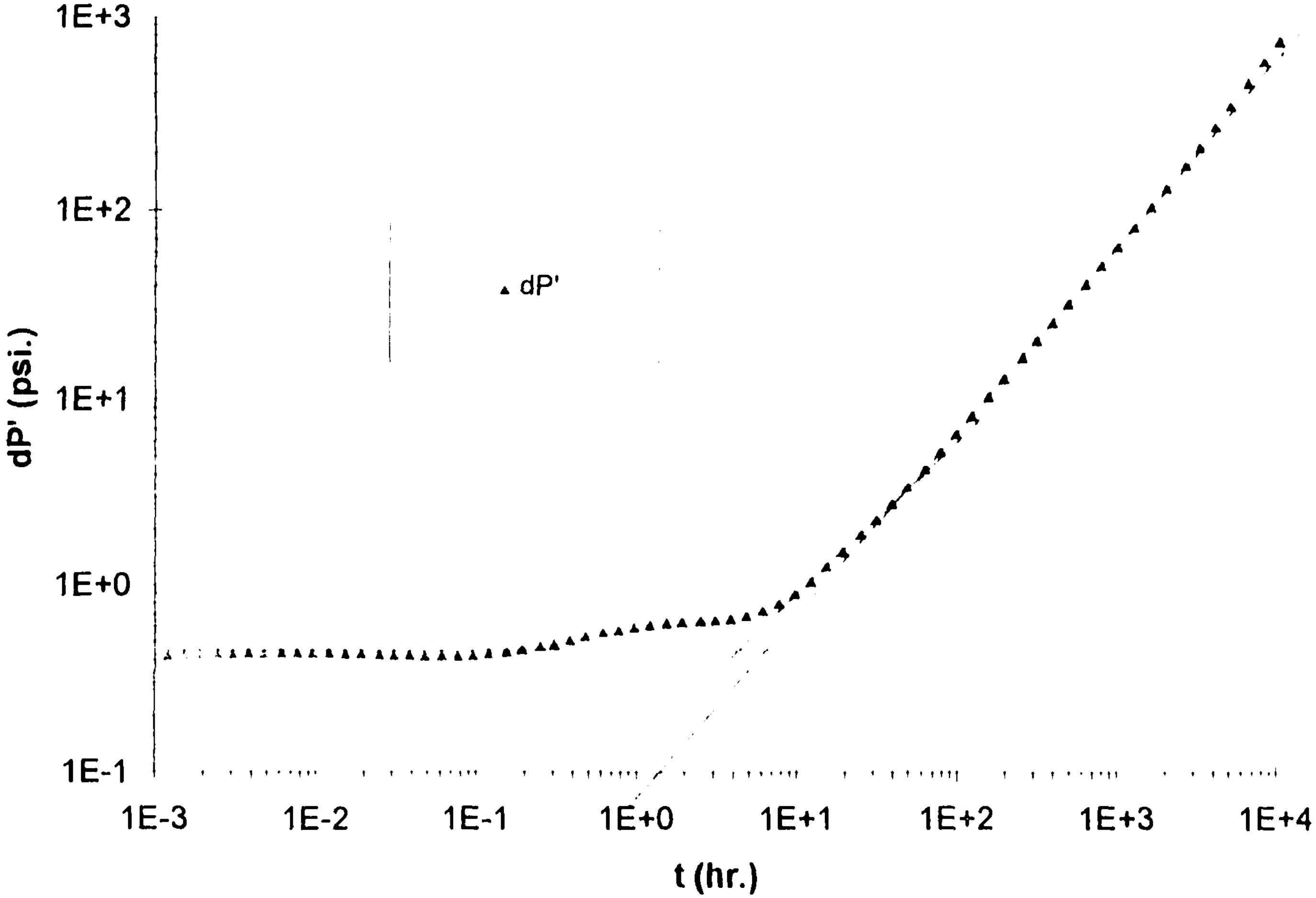

Figure 6.3.3 The Pressure Derivative versus Time for Case 6.3

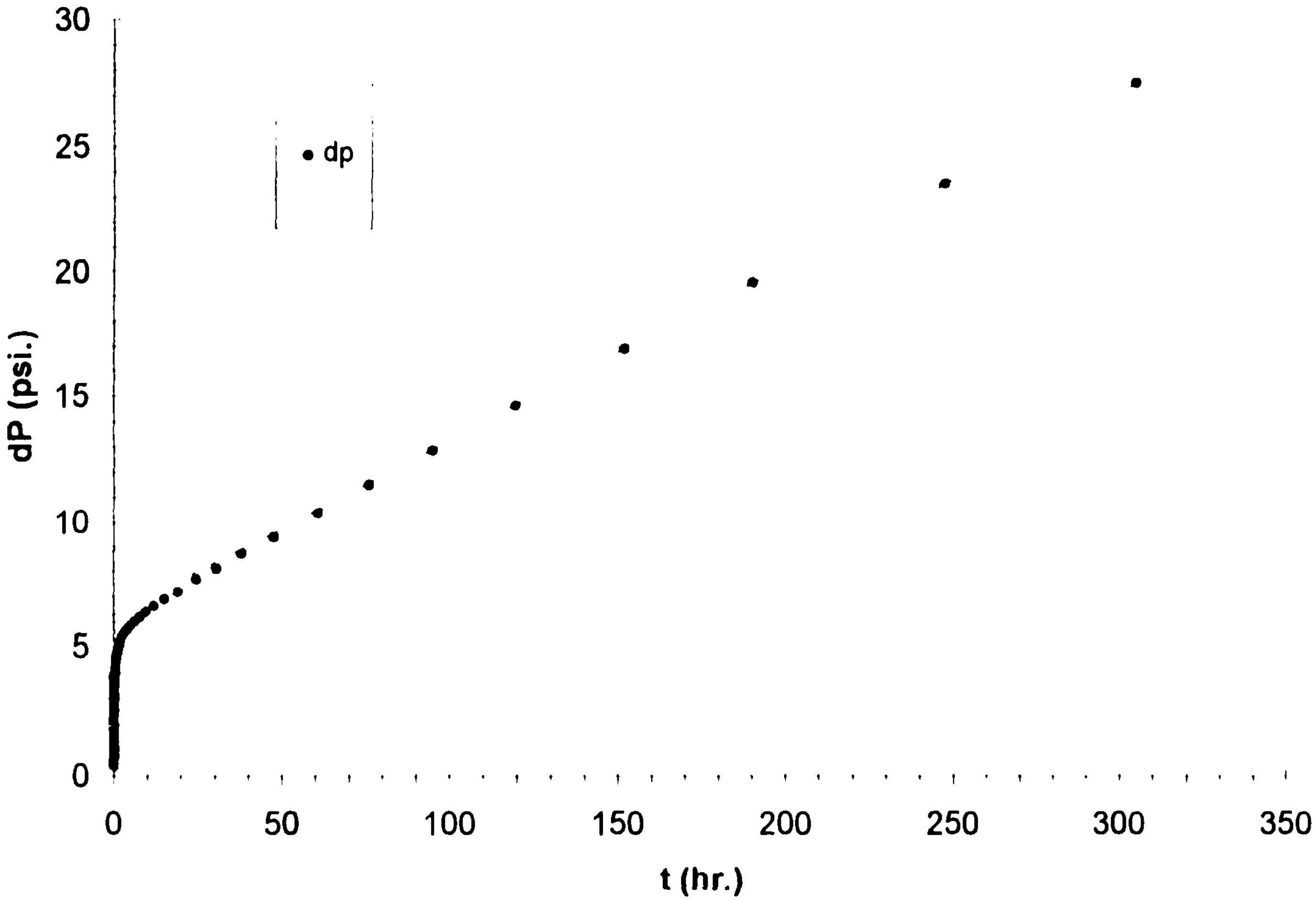

Figure 6.3.4 The Pressure Drop versus Time for Case 6.3

Chapter 7

CONCLUSIONS AND RECOMMENDATIONS

7.1 CONCLUSIONS

This study develops the boundary element algorithm for a vertical, slanted, and horizontal well in multi-layer reservoirs It is based on domain decomposition and a Boundary Element Method for a homogeneous system. On the interface between two different layers, two compatibility conditions used in this study are (i) the potential is continuous across the interface and (ii) the amount of fluid flowing out of one layer must equal the amount of fluid flowing into another layer. The wellbore is considered as an internal boundary Hence, the wellbore radius is finite. The wellbore is assumed to produce at a constant flow rate. The pressure along the wellbore is uniform, independent of location. The algorithm is successfully validated by simulating some simple reservoir systems with available analytical solutions including (i) a finite linear aquifer, (ii) a horizontal well in a closed rectangular homogeneous reservoir, and (iii) a horizontal well in multi-layer reservoir with cross flow.

The developed boundary element method (BEM) is applied to simulate the pressure performance of eight complicated reservoirs whose analytical solutions do not exist. These cases are: (i) a horizontal well in a two-layer reservoir, (ii) a horizontal well in a two-layer reservoir with gas-cap drive, (iii) a horizontal well in a two-layer reservoir with bottom-water drive, (iv) a horizontal well in a two-layer reservoir with gas-cap and bottom-water drives, (v) a horizontal well intersecting a two-layer reservoir, (vi) a snake-shape horizontal well intersecting a two-layer reservoir, (vii) a horizontal well intersecting a three-layer reservoir, and (viii) a vertical well intersecting a two-layer reservoir without cross flow. The effects of permeability, wellbore configuration, wellbore location, distance from the wellbore to the interface, different types of boundary conditions are investigated in this study. Different types of plots of the dimensionless pressure and the dimensionless pressure derivative versus the dimensionless time including log-log plot, semi-log plot, and Cartesian plots are used to investigate the wellbore performance.

Then the new technique, known as direct synthesis, is proposed to enhance the interpretation of the well-test data without type-curve matching. Several unique characteristic points and straight lines of the dimensionless pressure and the dimensionless pressure derivative were identified. The proposed step-by-step procedures are illustrated with several numerical examples.

It is found in this study that

1. The Boundary Element Method only requires discretization of the boundary rather than the whole domain. This advantage is significant for a snake-like horizontal well in a complicated-shape reservoir.
2. For a horizontal well in a two-layer reservoir, the permeability ratio (R_k) only affects the dimensionless pressure derivative during the intermediate time. During the early time and late time, the dimensionless pressure derivative is independent of the permeability ratio. The wellbore performance is similar to that of a horizontal well in homogeneous reservoir during these periods. The difference is the magnitude of the

dimensionless pressure But the magnitude of the dimensionless pressure derivative is a function of the permeability ratio during the second radial flow period

3. For a horizontal well intersecting a two-layer reservoir, the permeability ratio plays an important role from the beginning to the late intermediate time The magnitudes of the dimensionless pressure and the dimensionless pressure derivative are functions of the permeability ratio Before the pseudo-steady state occurs, there exists a log-log straight line of the dimensionless pressure derivative with a slope of 0 8 The length of this straight line (L_{ppss}) is a function of the permeability ratio But during pseudo-steady-state flow period, the wellbore performance is similar to that of a horizontal well in a homogeneous reservoir In order to calculate the properties of the bottom layer, the pressure data must be long enough to have the pseudo-steady state flow period.

4. For a snake-shape horizontal well in a two-layer reservoir, the performance is similar to that of a horizontal well intersecting a two-layer reservoir The differences are the magnitudes of the dimensionless pressure and the dimensionless pressure derivative which are a function of wellbore configuration.

5. For a horizontal well in three-layer reservoir, the permeability ratio has a significant impact on the dimensionless pressure and the dimensionless pressure derivative from the early time to the beginning of the pseudo-steady flow period The larger the value of the permeability ratio, the later the time when we can observe the effect of the lower-permeability layer. But the wellbore performance is independent of the permeability ratio during the pseudo-steady state flow period

7.2 RECOMMENDATIONS

- The wellbore storage and skin effects are beyond the scope of this study Further study may include these two effects to represent the actual performance of the wellbore
- This study is limited only to three-layer reservoirs. Further research works may be done to study the pressure behaviors of reservoirs consisting of more than three layers
- Most of the computational time is spent to calculate the elements in the system of linear equations. Eq (3 44) These elements are calculated by using Gaussian quadrature to approximate the integral equations developed by Koh (1993). The performance of the boundary element method can be improved by finding a faster technique to evaluate these integral equations

NOMENCLATURES

a	=	length of reservoir in x-direction, ft
A	=	area of reservoir, ft^2
[A]	=	coefficient matrix of $\vec{x}$ in standard linear form $[A]\vec{x} = \vec{F}$
b	=	formation thickness, ft
B	=	reservoir width in y-direction, ft
	=	formation volume factor, rb/stb
c_t	=	total compressibility, psi^{-1}
C_A	=	reservoir shape factor
d_{Dn}	=	the normal dimensionless distance from the source point to the field point
d_z	=	distance from the wellbore to the closest boundary, ft
E_1	=	exponential integral
$\vec{F}$	=	right-hand side vector in standard linear form
g_w	=	an impulse response for a horizontal well
$\overline{G}$	=	free space Green's function
[G]	=	coefficient matrix of $\vec{Q}$
h	=	reservoir thickness in z-direction, ft
[H]	=	coefficient matrix of $\vec{P}$
i	=	index
I_{pss}	=	constant used in Eq. (6.3.6)

j	=	index
J	=	productivity index, stb/d/psi
k	=	index
$\bar{K}$	=	permeability tensor
K_o	=	modified Bessel function of the second kind of order 0
K_1	=	modified Bessel function of the second kind of order 1
k_h	=	horizontal permeability, md
k_v	=	vertical permeability, md
k_x	=	permeability in x-direction, md
k_{x1}	=	permeability in x-direction of Layer #1, md
k_y	=	permeability in y-direction, md
k_z	=	permeability in z-direction, md
ln	=	natural logarithm
L	=	wellbore length, ft
L_D	=	dimensionless length defined in Eq. 2.32
L_{ppss}	=	the length of the straight line during transition period before The pseudo-steady state
L_x	=	reservoir length in x-direction, ft
L_y	=	reservoir length in y-direction, ft
L_w	=	wellbore length, ft
L_z	=	reservoir length in z-direction, ft
m_1	=	the slope of the first semi-log straight line
m_2	=	the slope of the straight line on the plot of ΔP versus $t^{0.5}$

m_3	=	the slope of the semi-log straight line for the third flow regime
$\vec{n}$	=	the unit outward normal vector
N_e	=	number of elements
N_n	=	number of nodes
P	=	wellbore pressure, psi
$\tilde{P}$	=	normalizing factor, psi
$P_{1.hr}$	=	the pressure obtained by extrapolating the semi-log straight line to $t = 1$ hr
P_D	=	dimensionless pressure
P_{Di}	=	dimensionless pressure due to an image well
P_i	=	initial reservoir pressure, psi
P_{ini}	=	initial reservoir pressure, psi
P_{wD}	=	dimensionless pressure due to the real well
P_{wf}	=	wellbore pressure, psi
P'_D	=	dimensionless pressure derivative
$\hat{P}_D$	=	specified P_D on the boundary
$\hat{P}'_D$	=	specified P'_D on the boundary
$\overline{P}_D$	=	P_D in Laplace space
ΔP_x	=	pressure drop due to the boundary in x-direction
ΔP_y	=	pressure drop due to the boundary in y-direction
ΔP_z	=	pressure drop due to the boundary in z-direction
q	=	oil production rate, rb/day

r	=	distance from the wellbore, ft
r_D	=	dimensionless distance
r_{DD}	=	dimensionless distance defined in Eq. 2.18
r_w	=	wellbore radius, ft
r_{wh}	=	equivalent horizontal wellbore radius, ft
s	=	mechanical skin
s_p	=	pseudo skin due to partial penetration
t	=	time, hours
t_{e1}	=	the length of the first flow regime, hr
t_{e2}	=	the length of the second flow regime, hr
t_{s3}	=	the beginning of the third flow regime, hr
t_D	=	dimensionless time
t_{DA}	=	area based dimensionless time
u	=	dimensionless variable defined in Eq. 2.17
	=	darcy velocity, ft/hr
u_p	=	darcy velocity parallel to the interface
u_n	=	darcy velocity perpendicular to the interface, ft/hr
V_k	=	the weighting function defined in Eq. 2.92
W	=	a weighting function
w_i	=	a fraction of wellbore area covered by node i
x	=	distance along the reservoir in x-direction, ft
x'	=	x-coordinate of horizontal well axis, ft
x_e	=	the half width of the reservoir, ft

x_0	=	distance from the wellbore to the origin in x-direction
x_D	=	dimensionless distance in x-direction
y	=	distance along the reservoir in y-direction, ft
y^*	=	y-coordinate of horizontal well axis, ft
y_0	=	distance from the wellbore to the origin in y-direction
y_1	=	y-coordinate at the leadng tip of the well, ft
y_D	=	dimensionless distance in y-direction
z	=	distance along the reservoir in z-direction, ft
z^*	=	z-coordinate of horizontal well axis, ft
z_0	=	distance from the wellbore to the origin in z-direction
z_D	=	dimensionless distance in z-direction

Greek

ρ	=	fluid density, lbm/ft^3
ϕ	=	porosity, fraction
ϕ_1	=	porosity of Layer #1, fraction
η_x	=	diffusivity in x-direction
η_y	=	diffusivity in y-direction
η_z	=	diffusivity in z-direction
π	=	a constant, 3.1415926
β	=	dimensionless variable defined in Eq. 2.16
μ	=	viscosity, cp

τ	=	angle of intersection of the two planes containing two adjacent boundary elements
Ψ	=	the flow potential
$\vec{\nabla}$	=	vector differential operator del
∇^2	=	Laplacian operator
ω	=	free-term coefficient
ω_o	=	the solid angle subtended at the boundary source point by its immediate neighborhood within the domain, radian
Γ	=	the boundary
ν_I	=	the variable defined in Eq 3 9
κ_i	=	the dimensionless variable defined in Eq 3 10
θ	=	an angle around the wellbore, degree
$\frac{\partial}{\partial n}$	=	shorthand for $\vec{\nabla} \bullet \vec{n}$
Ω	=	the domain

REFERENCES

Abbaszadeh, M. and Hegeman, P. "Pressure-Transient Analysis for a Slanted Well in a Reservoir With Vertical Pressure Support," SPEFE (Sept. 1990) 277, Trans., AIME, 289

Aguilera, R.A., Cordell, G.M., Nicholl, G.W., Artindale, J.S., Ng, M.C., and Runions, G.A., "Horizontal Wells - Formation Evaluation, Drilling, and Production, including heavy oil recovery," Gulf, 1991.

Anon.. "Elf Tries Horizontal Drilling to Tap Heavy Oil," Oil & Gas J. (Aug. 1, 1983) 81, 48

Anon: "Horizontal Wells Take Steam to Athabasca Tar," Pet. Eng. Intl. (March 1, 1982), -3

Anon: "Technical Advances Broaden the Use of Highly Deviated and Horizontal Drilling Methods," JPT (Feb. 1981) 283-85

Astier, B., Jourdan, A., and Baron, G.: "Efl Well Turns 90 Degrees and Stays There," Pet. Eng. Intl. (Jan. 1981) 53, 40-44.

Babu, D.K. and Odeh, A.S.: "Productivity of a Horizontal Well," SPERE (Nov. 1989) 417

Bendakhlia, H. and Aziz, K.: "Inflow Performance Relationships for Solution-Gas Drive Horizontal Wells," paper SPE 19823 presented at the 1989 Annual Fall Technical Conference and Exhibition, San Antonio, TX, Oct. 8-11.

Bezgire, G E. and Morkiw, L.A. "Esso Resources Horizontal Hole Project at Cold Lake." Pet. Soc. of CIM (May 1979) 79-30-10

Brebbia, C A. and Walker, R.H. Boundary Element Techniques in Engineering, Newnes-Butterworths, London (1980)

Cawvey, J L. "ARCO's Empire Abo Unit Horizontal Drainhole Program Advances, Well Servicing," Well Servicing (July/Aug. 1981)

Clonts, M.D. and Ramey, H J. Jr.: "Pressure Transient Analysis for Wells with Horizontal Drainholes," paper SPE 15116 presented at the 1986 SPE California Regional Meeting, Oakland, April 2-4

Colamasi, C. and Dell Canne, A. "Drainhole Drilling in Sicily," World Oil (March 1963)

Connor, J J. and Brebbia, C A.: "Boundary Element Methods," Boundary Element Methods in Computer Aided Engineering, C.A. Brebbia (ed.), Martinus Nijhoff Publishers, Dodrecht (1984)

Daviau, F. et al.: "Pressure Analysis for Horizontal Wells," SPEFE (Dec. 1988) 716

Eastman, H.J.: "Lateral Drainhole Drilling," Pet. Eng. (Nov. 1954) 36, 57-73

Economides, M.J., Deimbacher, F.X., Brand, C.W., and Heinemann, Z.E.: "Comprehensive Simulation of Horizontal Well Performance," paper SPE 20717 presented at the 1990 Annual Fall Technical Conference and Exhibition, New Orleans, LA Sept. 23-26.

Giannesini, J.F.: "Horizontal Wells," PetroAsia (Jan.-Feb. 1984)

Giger, F.M. and Jourdan, A.P.: "The Four Horizontal Wells Producing Oil in Western

Europe," presented at the Fifth Annual Advances in Petroleum Recovery and Upgrading Technology Conference, Alta., June 14-15

Giger, F M. and Reiss, L H "Reservoir Aspects of Horizontal Drilling," paper SPE 13014 presented at the 1984 SPE Annual Technical Conference and Exhibition, Houston, Sept 16-19

Giger, F M "Horizontal Wells production Techniques in Heterogeneous Reservoirs," paper SPE 13710 presented at the 1985 SPE Middle East Oil Technical Show, Bahrain, March 11-14

Goode, P A. and Thambynayagam, R M "Pressure Drawdown and Buildup Analysis for Horizontal Wells in Anisotropic Media," SPEFE (Dec 1987) 683, Trans., AIME 283.

Goode, P A. and Kuchuk, F J. "Inflow Performance of Horizontal Wells," SPERE (Aug 1991) 319

Goode, P A. and Wilkinson, D J. "Inflow Performance of Partially Open Horizontal Wells," JPT (Aug. 1991) 983

Higgins, R.V. "Factors that Influence Gravity Drainage," Pet. Eng. (May 1953) 35, 83-92.

Holbert, D R.. "Special Practices Allow High Angle Drilling," Oil & Gas J. (Feb 16, 1981) 79, 91-99

Jongkittinarukorn, K. and Tiab, D.: "Analysis of Pressure and Pressure Derivative with and without type-curve matching - A Horizontal Well in Closed-Boundary System," CIM 96-53, 47th Annual Tech. Meeting, Calgary, Canada, June 10-12, 1996.

Joshi, S.D.: "Augmentation of Well Productivity With Slanted and Horizontal Wells," JPT (June 1988) 729; Trans., AIME 285

Joshi, S.D., "Horizontal Well Technology", PennWell, 1991

Jourdan, A. and Baron, G.: "Elf Drills 1,000 ft – Horizontally," Pet. Eng. Intl. (Sept. 1981) 53, 51-58

Jourdan, A.P. and Baron, G.: "Horizontal Well Proves Productivity Advantages," Pet. Eng. Intl. (Oct. 1984) 56, 23-25

Karcher, B.J., Giger, F.M., and Combe, J.: "Some Practical Formula to Predict Horizontal Well Behavior," paper SPE 15430 presented at the 1986 SPE Annual Technical Conference and Exhibition, New Orleans, Oct. 5-8.

Kellog, D.O.: Foundations of Petential Theory, Dover Publications Inc., New York City (1953)

Kikani, J. and Horne, R.N.: "A Convolution Boundary Element Method for Unsteady State Groundwater Flow in Homogeneous Aquifers," Proc., XIII Geothermal Research Engineering Workshop, Stanford U., Stanford, CA (Jan. 19-21, 1988)

Kikani, J. and Horne, R.N.: "Application of Boundary Element Method to Reservoir Engineering Problems," J. of Pet. Science and Engineering, Elsevier Science, New York City (1989) 229-41

Kikani, J. and Horne, R.N.: "Pressure-Transient Analysis of Arbitrary Shaped Reservoirs With The Boundary-Element Method," SPEFE (March 1992) 53-60

Kikani, J. and Horne, R.N.: "Modeling Pressure-Transient Behavior of Sectional

Homogeneous Reservoirs by The Boundary-Element Method." SPEFE (June 1993) 145-152.

Killough, J.E. and Foster, A.P. Jr. "Reservoir Simulation of the Empire Abo Field: The Use of Pseudo in a Multilayer System," SPEJ (Oct. 1979) 279-88.

King, G.R. and Ertekin, T.: "Comparative Evaluation of Vertical and Horizontal Drainage Wells for the Degasification of Coal Seams," SPERE (May 1988) 720.

Koh, L.S. and Tiab, D.: "A Boundary-Element Algorithm for Modeling 3D Horizontal Well Problems Using 2D Grids," SPE 26228 presented at the SPE Petroleum Computer Conference held in New Orleans, Louisiana, (1993).

Koh, L.S., A Boundary-Element Algorithm for Modeling 3-D Fluid Flow Through Porous Media Involving Arbitrarily-Oriented Wells in Arbitrarily-Shaped Reservoirs, Ph.D Dissertation, The University of Oklahoma, 1993.

Kuchuk, F.J. et al.: "Pressure-Transient Behavior of Horizontal Wells With and Without Gas Cap or Aquifer," SPEFE (March 1991) 86; Trans., AIME, 291.

Kuchuk, F.J. and Saaedi, J.: "Inflow Performance of Horizontal Wells in Multilayer Reservoirs," paper SPE 24945 presented at the 1992 SPE Annual Technical Conference and Exhibition, Washington, D.C., Oct. 4-7.

Kuchuk, F.J.: "Pressure Behavior of Horizontal Wells in Multilayer Reservoirs With Crossflow," SPEFE (March 1996), 55-64.

Kuchuk, F.J. and Kader, S.A., "Pressure Behavior of Horizontal Wells in Heterogeneous reservoirs," The Canadian SPE/CIM/CANMET International Conference on Recent advances in Horizontal Well Application, March 20-23, 1994.

Lafe, O.E., Liggett, J.A., and Liu, P.L.F.: "BIEM Solutions to Combinations of Leaky, Layered Confined, Unconfined, Nonisotropic Aquifers," Water Resources Res. (Oct. 1981) 17, No. 5, 1431-44.

Landrum, B.L. and Crawford, P.B.: "Effect of Drainhole Drilling on Productivity Capacity," JPT (Feb. 1955) 55-57.

Lennon, G.P., Liu, P.L.F., and Liggett, J.A.: "Boundary Integral Solutions to Three-Dimensional Unconfined Darcy's Flow," Water Resources Res. (Aug. 1980) 16, No 4, 651-58.

Lichtenberger, G.J.: "Pressure Buildup Test Results From Horizontal Wells in the Pearsall Field of the Austin Chalk," paper SPE 20609 presented at the 1990 SPE Annual Technical Conference and Exhibition, New Orleans, Sept. 23-26.

Liggett, J.A. and Liu, P.L.F.: The Boundary Integral Equation Method for Porous Media Flow, George Allen & Unwin, London (1983).

Liu, P.L.F. and Liggett, J.A.: "Boundary Integral Solutions to Ground-Water Problems," Proc., First Intl. Conf. on App. Num. Modeling, U. of Southampton, U.K. (July 11-15, 1977) 559-69.

Loxam, D.C.: "Texaco Canada Completes Unique Horizontal Drilling Program," Pet. Eng. Intl. (Sept. 1982) 54, 40-52.

Masukawa, J.: "The Application of the Boundary Integral Method to Immiscible Displacement Problems," MS thesis, Stanford U., Stanford, CA (1985).

Masukawa, J. and Horne, R.N.: "The Application of Boundary Integral Method to Immiscible Displacement Problems," SPERE (Aug. 1988) 1069-77.

Moore, W D "ARCO Drills Horizontal Drain Hole for Better Reservoir Placement," Oil & Gas J (Sept 15, 1980) 78

Nabor, G W and Barham, R.H "Linear Aquifer Behavior," J Pet Tech , May 1964, 561-563

Numbere, D T "A General Streamline Modeling Technique for Homogeneous and Heterogeneous Porous Media With Applications to Steamflood Prediction," Ph D dissertation, U of Oklahoma, Norman, (1982).

Numbere, D T and Tiab, D "An Improved Streamline-Generating Technique that Uses The Boundary (Integral) Element Method," SPERE (Aug 1988) 1061-68

Odeh, A.S and Babu, D K "Transient Flow Behavior of Horizontal Wells: Pressure Drawdown and Buildup Analysis," SPEFE (March 1990) 7; Trans., AIME, 289

Ozkan, E and Raghavan, R "Performance of Horizontal Wells Subject to Bottom-water Drive," SPERE (Aug 1990) 375, Trans., AIME, 289

Ozkan, E., Raghavan, R., and Joshi, S D "Horizontal Well Pressure Analysis," SPEFE (Dec 1989) 567; Trans., AIME, 287

Papatzakos, P., Herring, T.R., Martinsen, R., and Skjaeveland, S M "Cone Breakthrough Time for Horizontal Wells," paper SPE 19822 presented at the 1989 Annual Fall Technical Conference and Exhibition, San Antonio, TX, Oct 8-11

Perrine, R.L.: "Well Productivity Increases from Drainholes as Measured by Model Studied," Trans., AIME (1955) 204, 30-34

Pitts, J.P : "ARCO's Lea County Drainhole Proves a Success," Drill Bit (Aug 1980)

Pugh, G.E. "Drilling of Three Horizontal Wells Pattern, Fort Murray, Alberta," paper 82-

83-68 presented at the 1982 Annual Technical Meeting of the Petroleum Soc. of CIM., Calgary, Alta., June 6-9

Reiss, L.H., Jordan, A.P. and Giger, F.M.: "Offshore European Horizontal Wells," paper OTC 4791 presented at the 1984 Offshore Technology Conference, Houston

Reiss, L.H.: "Production From Horizontal Well After 5 Years," JPT (Nov. 1987) 1411, Trans., AIME 283

Roemershauser, A.E. and Hawkins, M.F. Jr.: "The Effect of Slant Hole, Drainhole and Lateral Hole Drilling on Well Productivity," JPT (Feb. 1955) 7, 11-14

Rosa, A.J. and Carvalho, R.S.: "A Mathematical Model for Pressure Evaluation in an Infinite-Conductivity Horizontal Well," SPEFE (Dec. 1989) 559

Rosenzweig, J.J., Korpics, D.C., Crawford, G.E.: "Pressure Transient Analysis of the JX-2 Horizontal Well, Prudhoe Bay, Alaska," paper SPE 20610 presented at the 1990 Annual Fall Technical Meeting and Exhibition.

Sato, K. and Horne, R.: "Perturbation Boundary Element Method for Heterogeneous Reservoirs: Part 1 - Steady-State Flow Problems," SPEFE (Dec. 1993) 306-314

Sato, K. and Horne, R.: "Perturbation Boundary Element Method for Heterogeneous Reservoirs: Part 2 - Transient-Flow Problems," SPEFE (Dec. 1993) 315-322

Shah, P.C., Gupta, D.K., and Deruyck, B.G.: "Field Application of the Method for Interpretation of Horizontal-Well Transient Tests," SPEFE (March 1994) 23

Sherrard, D.W., Brice, B.W., and MacDonald, D.G.: "Application of Horizontal Wells at Prudhoe Bay," JPT (Nov. 1987) 1417

Stone, T.W., Edmunds, N.R., and Kristoff, B.J.: "A Comprehensive Wellbore/Reservoir

Simulator," paper SPE 18419 presented at the tenth SPE Symposium on Reservoir Simulation, Houston, TX Feb 6-8, 1989

Stormont, D H "Increasing Drainage of Oil into the Well by Drainhole Drilling," Oil & Gas J (Aug 17, 1983) 81, 105-08

Stramp, R.L "The Use of Horizontal Drainholes in the Empire Abo Unit," paper SPE 9221 presented at the 1980 SPE Annual Technical Conference and Exhibition, Dallas, Sept 21-24

Striegler, J "ARCO Finishes Fourth Horizontal Drainhole," Oil & Gas J (May 24, 1982) 80, 55-61

Suzuki, K and Nanba, T "Horizontal Well Test Analysis System," paper SPE 20613 presented at the 1990 SPE Annual Technical Conference and Exhibition, New Orleans, Sept 23-26

Thompson, L G, Manrique, J L, and Jelmert, T A "Efficient Algorithms for Computing the Bounded Reservoir Horizontal Well Pressure Response," paper SPE 21827 presented at the Rocky Mountain Regional Meeting and Low-Permeability reservoirs Symposium held in Denver, CO, April 1991

Wash, R. "ARCO's Fourth Successful Drainhole Drilled in Cased Hole," Drill Bit (Sept 1981).

Wittrisch, C. and Jourdan, A. "Horizontal Well Logging by Simphor," Trans Eighth European Formation Evaluation Symposium, London (March 14-15, 1983)

APPENDIX

APPENDIX A

Derivation of Pressure Gradient Along The Wellbore

Assumptions

1. In Figure A.1, x, y, and z are the principal axes of the porous medium.
2. The principal permeabilities in x, y, and z directions are k_x, k_y, and k_z.
3. The gravity effect is neglected.

For $0^0 \le \theta \le 90^0$ and $0^0 \le \phi \le 90^0$, from Figure A.1, the radial flow rate can be calculated as

$$u_r(\gamma) = (u_x, u_y, u_z) \bullet (l, m, n) \tag{A.1}$$

where

$$l = \sin(\phi)\cos(\gamma) - \cos(\phi)\cos(\theta)\sin(\gamma) \tag{A.2}$$

$$m = -\cos(\phi)\cos(\gamma) - \sin(\phi)\cos(\theta)\sin(\gamma) \tag{A.3}$$

$$n = \sin(\theta)\sin(\gamma) \tag{A.4}$$

The flow rates in x, y, and z direction are described by Darcy's law, in field units, as

$$u_x = -0.001127 \frac{k_x}{\mu} \frac{\partial P}{\partial X} \tag{A.5a}$$

$$u_y = -0.001127 \frac{k_y}{\mu} \frac{\partial P}{\partial Y} \tag{A.5b}$$

$$u_z = -0.001127 \frac{k_z}{\mu} \frac{\partial P}{\partial Z} \tag{A.5c}$$

Substitute Eqs. (A.5a)-(A.5c) into (A.1) as

$$u_r = \frac{-0.001127}{\mu} \left(k_x \frac{\partial P}{\partial x}, k_y \frac{\partial P}{\partial y}, k_z \frac{\partial P}{\partial z} \right) \bullet (l, m, n) \tag{A.6}$$

Recall dimensionless variables

$$x_D = \frac{X}{r_w} \tag{A 7a}$$

$$y_D = \frac{Y}{r_w}\sqrt{\frac{k_x}{k_y}} \tag{A 7b}$$

and

$$z_D = \frac{z}{r_w}\sqrt{\frac{k_x}{k_z}} \tag{A 7c}$$

$$P_D = \frac{k_x L_w}{141.2 qB\mu}\left(P_{ini} - P\right) \tag{A 8}$$

Substitute Eqs. (A 7a)-(A 7c) and (A 8) into (A 6) as

$$u_r = \frac{qB}{2\pi r_w L}\left(\frac{\partial P_D}{\partial x_D}, \frac{\partial P_D}{\partial y_D}\sqrt{\frac{k_y}{k_x}}, \frac{\partial P_D}{\partial z_D}\sqrt{\frac{k_z}{k_x}}\right) \bullet (l, m, n) \tag{A 9}$$

$$\phi_2 = \tan^{-1}\left[\tan(\phi)\sqrt{\frac{k_x}{k_y}}\right] \tag{A 10}$$

$$\theta_2 = \tan^{-1}\left[\tan(\theta)\sqrt{\frac{\cos^2\phi - \sin^2\phi(k_x / k_y)}{(k_x / k_z)}}\right] \tag{A 11}$$

Choose x',y',z' such that

x' is perpendicular H too.

y' is parallel to the wellbore axis

Direction of x' is $(\sin\phi_2, -\cos\phi_2, 0)$

Direction of y' is $(\sin\theta_2\cos\phi_2, \sin\theta_2\sin\phi_2, \cos\theta_2)$

Direction of z' is $(-\cos\theta_2\cos\phi_2, -\cos\theta_2\sin\phi_2, \sin\theta_2)$

The partial derivative

$$\frac{\partial P_D}{\partial x_D} = \frac{\partial P_D}{\partial x'}\frac{\partial x'}{\partial x_D} + \frac{\partial P_D}{\partial y'}\frac{\partial y'}{\partial x_D} + \frac{\partial P_D}{\partial z'}\frac{\partial z'}{\partial x_D}$$

$$= \frac{\partial P_D}{\partial x'}\sin\phi_2 + \frac{\partial P_D}{\partial y'}\sin\theta_2\cos\phi_2 - \frac{\partial P_D}{\partial z'}\cos\theta_2\cos\phi_2 \qquad \text{(A.12a)}$$

Similarly,

$$\frac{\partial P_D}{\partial y_D} = -\cos\phi_2\frac{\partial P}{\partial x'} - \sin\theta_2\sin\phi_2\frac{\partial P}{\partial y'} - \cos\theta_2\sin\phi_2\frac{\partial P}{\partial z'} \qquad \text{(A.12b)}$$

$$\frac{\partial P}{\partial z_D} = \cos\theta_2\frac{\partial P}{\partial y'} - \sin\theta_2\frac{\partial P}{\partial z'} \qquad \text{(A.12c)}$$

Substitute (A.12a) - (A.12c) into (A.9) as

$$u_r = \frac{qB}{2\pi r_w L}\left(\frac{\partial P_D}{\partial x'}, \frac{\partial P_D}{\partial y'}, \frac{\partial P_D}{\partial z'}\right)(l', m', n') \qquad \text{(A.13)}$$

$$l' = \sin\phi_2(\sin\phi\cos\gamma - \cos\phi\cos\theta\sin\gamma) - \cos\phi_2\sqrt{\frac{k_y}{k_x}}(\cos\phi\cos\gamma - \sin\phi\cos\theta\sin\gamma) \qquad \text{(A.14a)}$$

$$m' = \sin\theta_2\cos\phi_2(\sin\phi\cos\gamma - \cos\phi\cos\theta\sin\gamma)$$

$$- \sin\theta_2\sin\phi_2\sqrt{\frac{k_y}{k_x}}(\cos\phi\cos\gamma + \sin\phi\cos\theta\sin\gamma)$$

$$+ \cos\theta_2\sin\theta\sin\gamma\sqrt{\frac{k_z}{k_x}} \qquad \text{(A.14b)}$$

$$n' = \cos\theta_2\cos\phi_2(-\sin\phi\cos\gamma + \cos\phi\cos\theta\sin\gamma)$$

$$+ \cos\theta_2\sin\phi_2(\cos\phi\cos\gamma + \sin\phi\cos\theta\sin\gamma)\sqrt{\frac{k_y}{k_x}}$$

$$- \sin\theta_2\sin\theta\sin\gamma\sqrt{\frac{k_z}{k_x}} \qquad \text{(A.14c)}$$

But $\frac{\partial P}{\partial y'} = 0$

$$r_{wx} = r_w / \cos\phi \tag{A 15a}$$

$$\left(r_{wy}\right)_D = \frac{1}{\cos\phi}\sqrt{\frac{k_x}{k_y}} \tag{A 15b}$$

$$r'_{wx} = \frac{\cos\phi_2}{\cos\phi}\sqrt{\frac{k_x}{k_y}} = c \tag{A 15c}$$

$$r_{wz} = r_w / \sin\theta \tag{A 16a}$$

$$\left(r_{wz}\right)_D = \frac{1}{\sin\theta}\sqrt{\frac{k_x}{k_z}} \tag{A 16b}$$

$$r_{wz'} = \frac{\sin\theta_2}{\sin\theta}\sqrt{\frac{k_x}{k_z}} = b \tag{A 16c}$$

The wellbore is an ellipse in x'-z' plane described by

$$\frac{x'^2}{c^2} - \frac{z'^2}{b^2} = 1 \tag{A 17}$$

where

$$x' = c * \cos\gamma = a * \sinh u * \cos\gamma \tag{A 18}$$

$$z' = b * \sin\gamma = * \cosh u * \sin\gamma \tag{A 19}$$

$$\frac{c}{b} = \frac{\sinh u}{\cosh u}$$

$$= \frac{e^{2u} - 1}{e^{2u} + 1} \tag{A 20}$$

$$u = \frac{1}{2}\ln\left(\frac{b + c}{b - c}\right) \tag{A 21}$$

$$\frac{\partial P_D}{\partial u} = \frac{\partial P_D}{\partial x'}\frac{\partial x'}{\partial u} + \frac{\partial P_D}{\partial z'}\frac{\partial z'}{\partial u}$$

$$= a\cosh(u)\cos(\gamma)\frac{\partial P_D}{\partial x'} - a\sinh(u)\sin(\gamma)\frac{\partial P_D}{\partial z'} \tag{A.22}$$

$$\frac{\partial P_D}{\partial \gamma} = -a\sinh(u)\sin(\gamma)\frac{\partial P_D}{\partial x'} - a\cosh(u)\cos(\gamma)\frac{\partial P_D}{\partial z'} \tag{A.23}$$

Solving (A.22) and (A.23) yields

$$\frac{\partial P_D}{\partial x'} = \frac{\cosh(u)\cos(\gamma)\dfrac{\partial P_D}{\partial u} - \sinh(u)\sin(\gamma)\dfrac{\partial P_D}{\partial \gamma}}{a\left[\sinh^2(u)\sin^2(\gamma) + \cosh^2(u)\cos^2(\gamma)\right]} \tag{A.24}$$

$$\frac{\partial P_D}{\partial z'} = \frac{\sinh(u)\sin(\gamma)\dfrac{\partial P_D}{\partial u} - \cosh(u)\cos(\gamma)\dfrac{\partial P_D}{\partial \gamma}}{a\left[\sinh^2(u)\sin^2(\gamma) + \cosh^2(u)\cos^2(\gamma)\right]} \tag{A.25}$$

But $\frac{\partial P_D}{\partial \gamma} = 0$ since the pressure is constant along the wellbore. Direction n is perpendicular to the wellbore and points into the center of the wellbore. The normal derivative can be calculated as

$$\frac{\partial P_D}{\partial n} = \frac{\partial P_D}{\partial u}\frac{\partial u}{\partial n} + \frac{\partial P_D}{\partial \gamma}\frac{\partial \gamma}{\partial n}$$

$$= \frac{\partial P_D}{\partial u}\frac{\partial u}{\partial n} \tag{A.26}$$

since $\frac{\partial \gamma}{\partial n} = 0$. Then

$$\frac{\partial P_D}{\partial u} = \frac{1}{(\partial u/\partial n)}\frac{\partial P_D}{\partial n} \tag{A.27}$$

where

$$\frac{\partial u}{\partial n} = \bar{\nabla} u \bullet \bar{n}$$

$$= \left(\frac{\partial u}{\partial x'}, 0, \frac{\partial u}{\partial z'}\right) \bullet \bar{n} \tag{A.28}$$

From (A.24) and (A.25), we have

$$\frac{\partial u}{\partial x'} = \frac{\cosh(u)\cos(\gamma)}{a\left[\sinh^2(u)\sin^2(\gamma) - \cosh^2(u)\cos^2(\gamma)\right]} \tag{A.29}$$

$$\frac{\partial u}{\partial z'} = \frac{\sinh(u)\sin(\gamma)}{a\left[\sinh^2(u)\sin^2(\gamma) - \cosh^2(u)\cos^2(\gamma)\right]} \tag{A.30}$$

Recall the elliptical equation,

$$\frac{x'^2}{c^2} - \frac{z'^2}{b^2} = 1 \tag{A.17}$$

Differentiate (A.17) with respect to z' yields

$$\frac{2x'}{c^2} - \frac{2z'}{b^2}\frac{dz'}{dx'} = 0 \tag{A.31}$$

Solving for dz'/dx' as

$$\frac{dz'}{dx'} = -\frac{b^2 x'}{c^2 z'} \tag{A.32}$$

which is the slope at point (x',z') on the wellbore surface. Hence, the slope of $\bar{n}$ is

$\left[(c^2 z')/(b^2 x')\right]$. Then

$$\bar{n} = \frac{(b^2 x', 0, c^2 z')}{\sqrt{(b^2 x')^2 + (c^2 z')^2}} \tag{A.33}$$

From (A.28) and (A.33),

$$\frac{\partial u}{\partial n} = \frac{b^2 x' \dfrac{\partial u}{\partial x'} + c^2 z' \dfrac{\partial u}{\partial z'}}{\sqrt{(b^2 x')^2 + (c^2 z')^2}} \tag{A.34}$$

From (A.27), (A.29), (A.30), and (A.34), we have

$$\frac{\partial P_D}{\partial u} = \frac{\sqrt{(b^2 x')^2 - (c^2 z')^2}}{b^2 x' \cosh(u)\cos(\gamma) + c^2 z' \sinh(u)\sin(\gamma)}$$

$$* a\left(\sinh^2(u)\sin^2(\gamma) - \cosh^2(u)\cos^2(\gamma)\right)\frac{\partial P}{\partial n} \tag{A.35}$$

Substitute (A.35) into (A.24) and (A.25) as

$$\frac{\partial P_D}{\partial x'} = \frac{\cosh(u)\cos(\gamma)\sqrt{\left(b^2 x'\right)^2 - \left(c^2 z'\right)^2}}{b^2 x'\cosh(u)\cos(\gamma) - c^2 z'\sinh(u)\sin(\gamma)}\frac{\partial P_D}{\partial n} \tag{A.36}$$

$$\frac{\partial P_D}{\partial z'} = \frac{\sinh(u)\sin(\gamma)\sqrt{\left(b^2 x'\right)^2 - \left(c^2 z'\right)^2}}{b^2 x'\cosh(u)\cos(\gamma) - c^2 z'\sinh(u)\sin(\gamma)}\frac{\partial P_D}{\partial n} \tag{A.37}$$

Substitute (A.18) and (A.19) into (A.36) and (A.37) as

$$\frac{\partial P_D}{\partial x'} = \frac{a * \cosh(u)\cos(\gamma)}{\sqrt{b^2\cos^2(\gamma) - c^2\sin^2(\gamma)}}\frac{\partial P_D}{\partial n} \tag{A.38}$$

$$\frac{\partial P_D}{\partial z'} = \frac{a * \sinh(u)\sin(\gamma)}{\sqrt{b^2\cos^2(\gamma) - c^2\sin^2(\gamma)}}\frac{\partial P_D}{\partial n} \tag{A.39}$$

Then the radial flow can be calculated as

$$u_r = \frac{qB}{2\pi r_w L}\left(\frac{\partial P_D}{\partial x'}, \frac{\partial P_D}{\partial z'}\right)(l', n') \tag{A.40}$$

where

$$l' = \sin\phi_2(\sin\phi\cos\gamma - \cos\phi\cos\theta\sin\gamma) + \cos\phi_2\sqrt{\frac{k_y}{k_x}}(\cos\phi\cos\gamma - \sin\phi\cos\theta\sin\gamma)$$

(A.14a)

and

$$n' = \cos\theta_2\cos\phi_2(-\sin\phi\cos\gamma - \cos\phi\cos\theta\sin\gamma)$$

$$+ \cos\theta_2\sin\phi_2(\cos\phi\cos\gamma - \sin\phi\cos\theta\sin\gamma)\sqrt{\frac{k_y}{k_x}} - \sin\theta_2\sin\theta\sin\gamma\sqrt{\frac{k_z}{k_x}}$$

(A.14c)

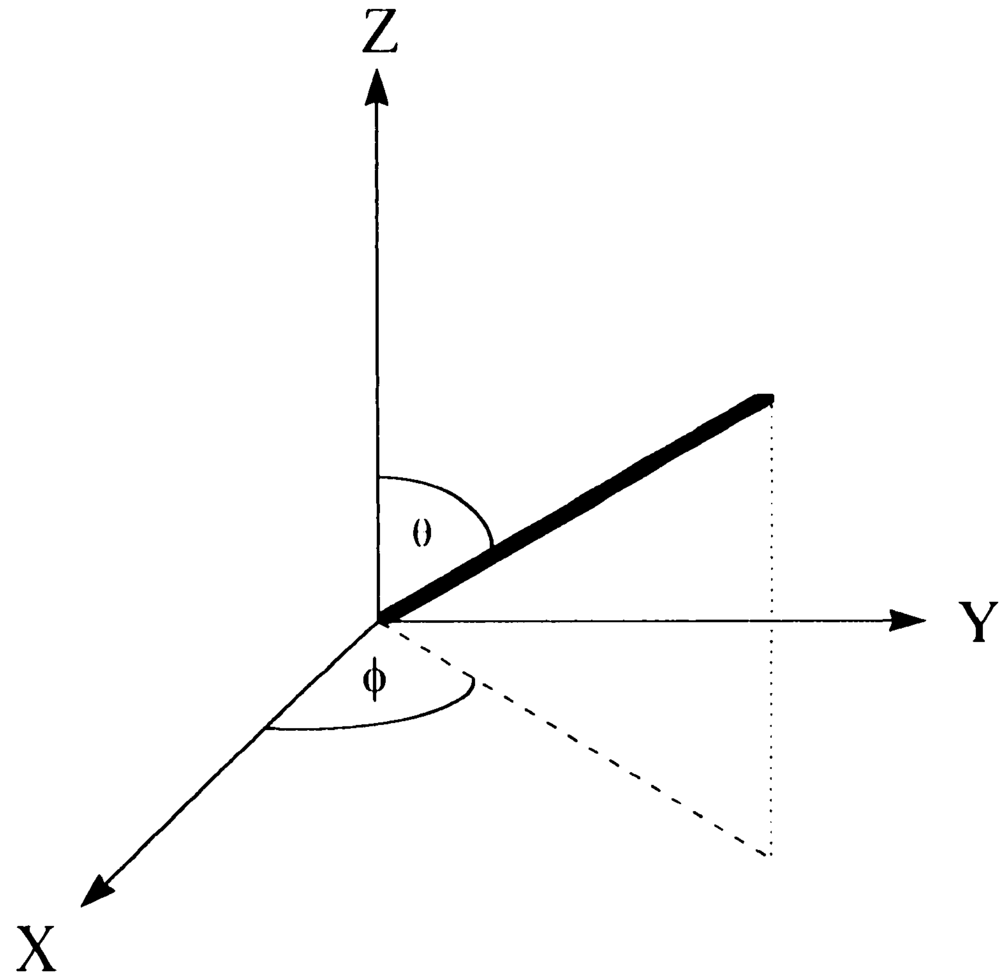

Figure A.1 Wellbore Configuration

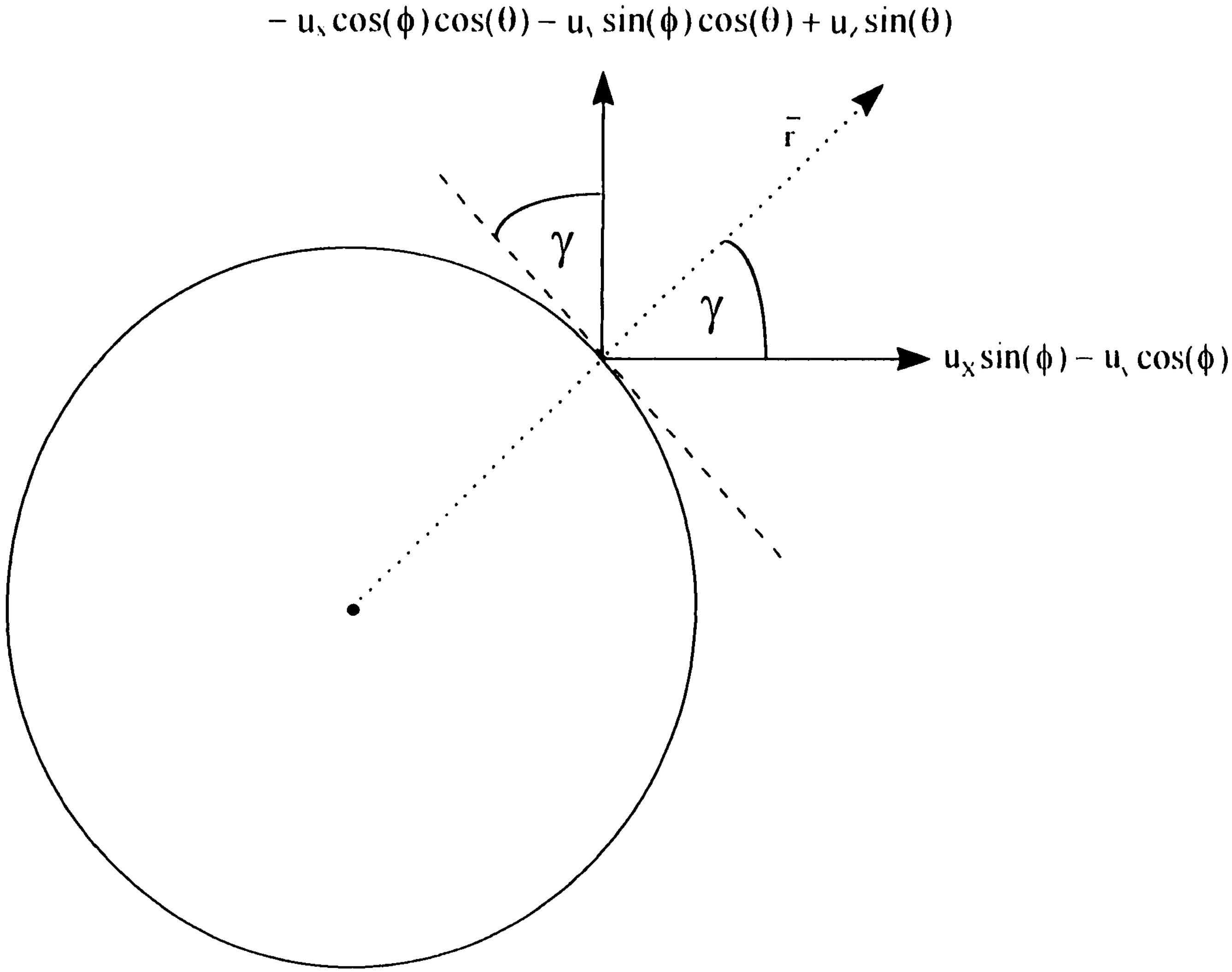

Figure A.2 Velocity Components Around The Wellbore

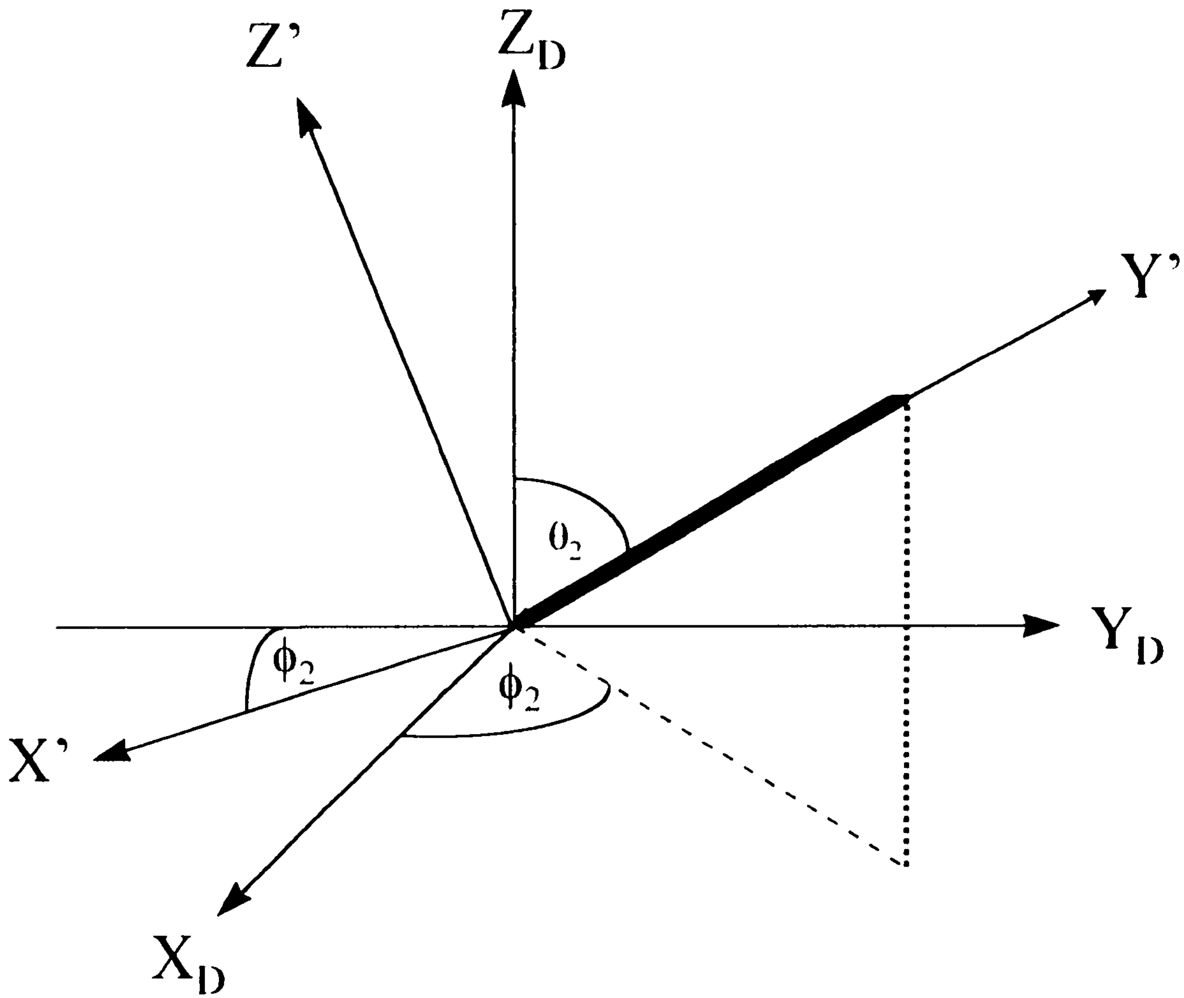

Figure A.3 Wellbore Configuration in Dimensionless Coordinate

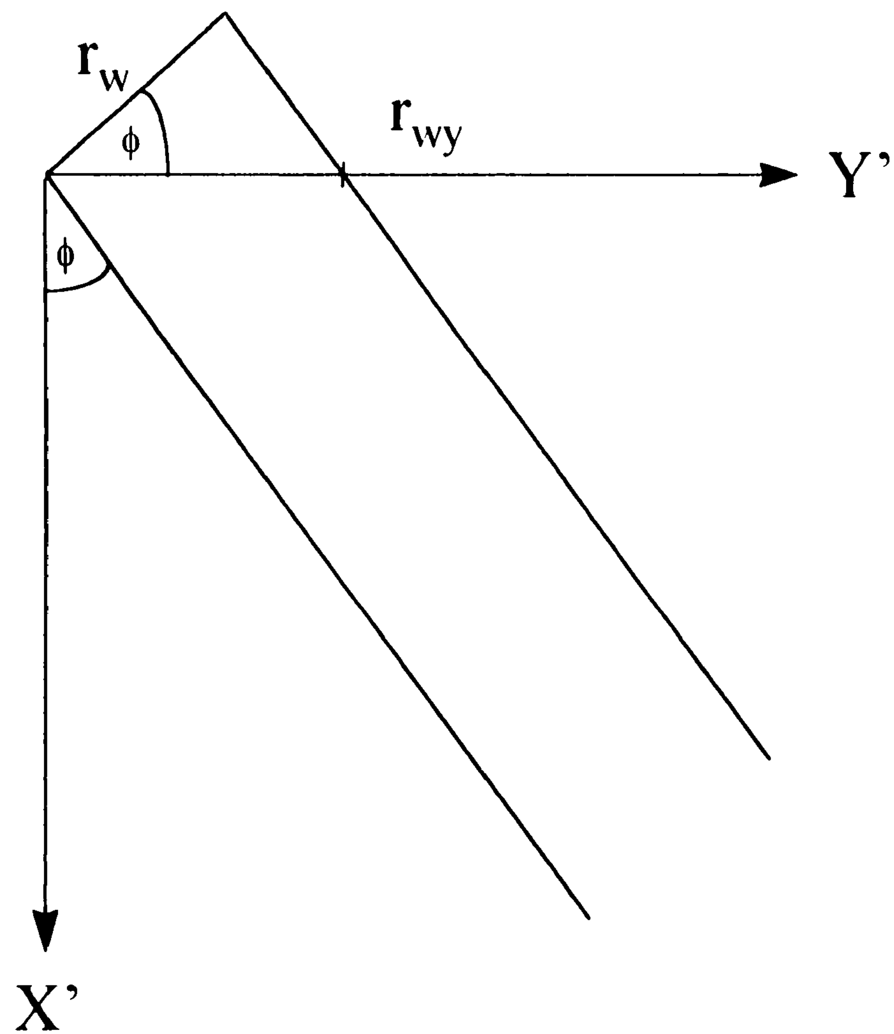

Figure A.4 Wellbore Configuration on The Horizontal Plane

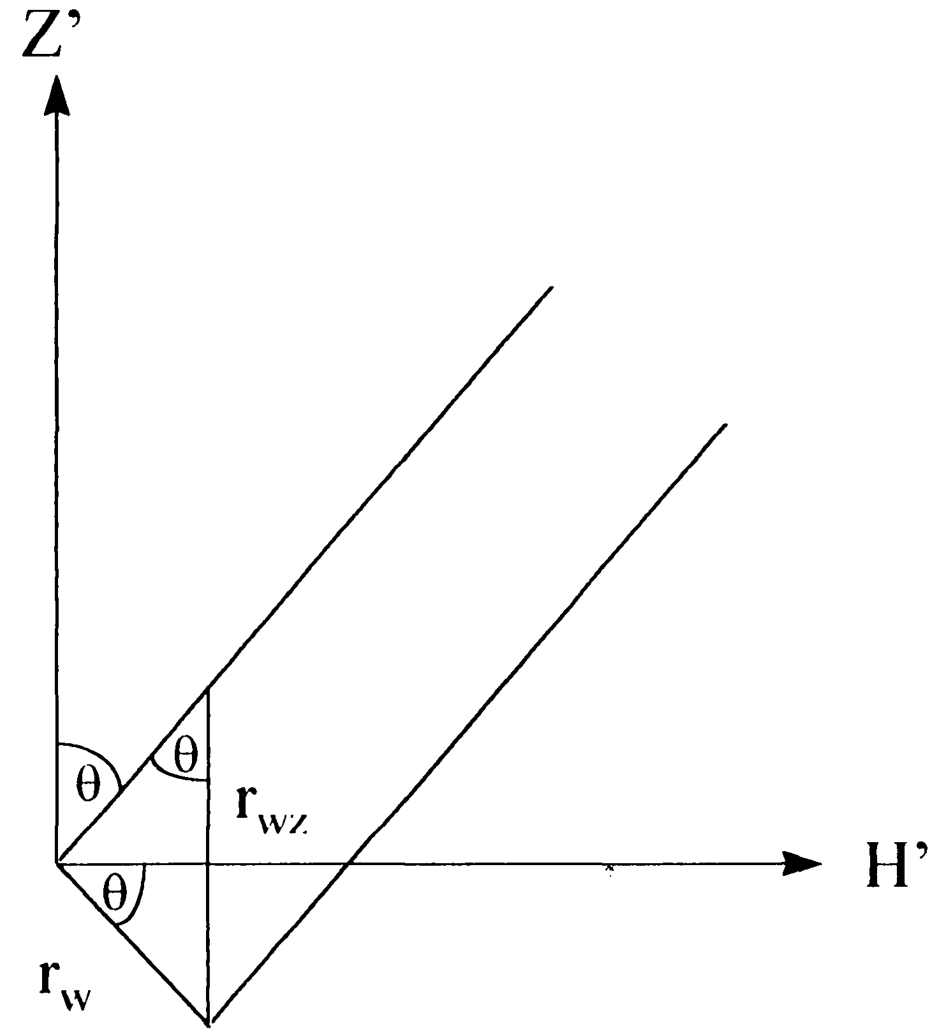

Figure A.5 Wellbore Configuration in The Vertical Plane

APPENDIX B

Partial-Penetration Effect

Pressure response in and around a partially penetrating well was well documented by Streltsova (1988). The reservoir model consider in her study is illustrated in Fig. B.1. The top and bottom boundaries are no-flow boundaries. The formation thickness is h ft and the perforated interval of the well open to flow is h_p. The distances between the top boundary and the top and bottom of the perforated interval are defined as h_1 and h_2, respectively.

The governing differential equation for the pressure distribution in the system is given as:

$$\frac{k}{r}\frac{\partial}{\partial r}\left(r\frac{\partial P}{\partial r}\right) + k_z\frac{\partial^2 P}{\partial z^2} = \phi c_t \mu \frac{\partial P}{\partial t} \tag{B.1}$$

The boundary and the initial conditions are

$$\lim_{r_w \to 0}\left(r_w\frac{\partial P}{\partial r}\right) = -\frac{q}{2\pi T h'_p}, \qquad h'_1 \le z' \le h'_2 \tag{B.2}$$

$$\lim_{r_w \to 0}\left(r_w\frac{\partial P}{\partial r}\right) = 0, \qquad 0 < z' < h'_1,\ h'_2 < z' < 1 \tag{B.3}$$

$$P(r \to \infty, t) = P_i \tag{B.4}$$

$$P(r) = P_i \qquad \text{for } t = 0 \tag{B.5}$$

The space dimensionless variables are defined as:

$$h'_p = \frac{h_p}{h} \tag{B.6}$$

$$h'_1 = \frac{h_1}{h} \tag{B 7}$$

$$h'_2 = \frac{h_2}{h} \tag{B 8}$$

$$z' = \frac{z}{h} \tag{B 9}$$

The pressure response in the reservoir domain of the above mathematical model is given as:

$$P(r,z,t) = P_i - \frac{q\mu}{2\pi kh} \Delta P_D(h'_1, h'_2, r_D, u) \tag{B 10}$$

where

$$\Delta P_D = \frac{1}{2}\left[-Ei(-u) + \frac{2}{\pi h'_p} \sum_{n=1}^{\infty} \frac{1}{n} \left\{ \sin(n\pi h'_2) - \sin(n\pi h'_1) \right\} \cos(n\pi z') W(u,\beta) \right] \tag{B 11}$$

$$W(u,\beta) = \int_u^{\infty} \left(\frac{1}{x} \exp\left\{ -x - \frac{\beta^2}{4x} \right\} \right) dx \tag{B 12}$$

$$u = \frac{\phi \mu c_t r^2}{4kt} \tag{B 13}$$

$$\beta = n\pi r_D \tag{B 14}$$

and

$$r_D = \frac{r}{h}\sqrt{\frac{k_z}{k}} \tag{B 15}$$

To approximate the realistic pressure response at the wellbore, the Eq (B 10) is integrated with respect to z' between h'_1 and h'_2 and divided by $(h'_2 - h'_1)$ Then the pressure response including the skin effect can be expressed as

$$P(r,t) = P_i - \frac{141.2qB\mu}{kh}\left[-\frac{1}{2}Ei\left(\frac{-948\phi\mu c_t r^2}{kt}\right) + \frac{h}{h_p}s + s_p\right] \tag{B.16}$$

where the pseudo-skin factor due to the well's partial penetration is

$$s_p = \frac{W(u,\beta)}{\pi^2 h'^2_p}\sum_{n=1}^{\infty}\left(\frac{1}{n^2}\left[\sin(n\pi h'_2)-\sin(n\pi h'_1)\right]^2\right) \tag{B.17}$$

Fig. B.2 illustrates the transient pressure response at a well of partial completion with h'_p = 0.1, h'_p = 0.2, s = 0, and with the open interval is centrally located in the reservoir. There exists two semi-log straight lines. The first straight line of slope m_1 corresponds to the radial flow around the open interval of the wellbore (h_p). As time progresses, the radius of investigation increases until it reaches the top and bottom boundary. Then the flow to the wellbore is become radial over the entire formation thickness (h). This is when we observe the second straight of slope m. The semi-log straight line of slope m corresponds to a well with complete penetration, h_p = h. Figs. B.3 and C.4 illustrate the pseudo-skin factors for a well with centrally located producing interval and a well with the producing interval adjacent to the top or bottom boundary, respectively.

During the partial-penetration effect period, the flow develops vertical until it is confined by the top and the bottom boundaries. The time t_p at the end of the partial penetration effect given by Jongkittinarukorn and Tiab (1996) as:

$$t_p = \frac{3792.2\phi\mu c_t h^2}{k_z}F_p \tag{B.18}$$

where the value of F_p is shown in Fig. B.5 as a function of perforation ratio (h_p/h) and the dimensionless wellbore location ($\bar{b}_p$). The dimensionless wellbore location is defined as

$$\bar{b}_p = \frac{h - (h_1 - h_2)}{h - h_p} \tag{B.19}$$

The longest distance from the wellbore in which the flow is no longer affected by the partial completion is called the radius of partial-penetration influence ($R_{i,p}$) defined as

$$R_{i,p} = \alpha h \sqrt{\frac{k}{k_z}} \tag{B.20}$$

where

$\alpha = 0.5$ for the open interval is at the center of the formation

$= 1$ for the open interval adjacent either to the top or the bottom of the formation (B.21)

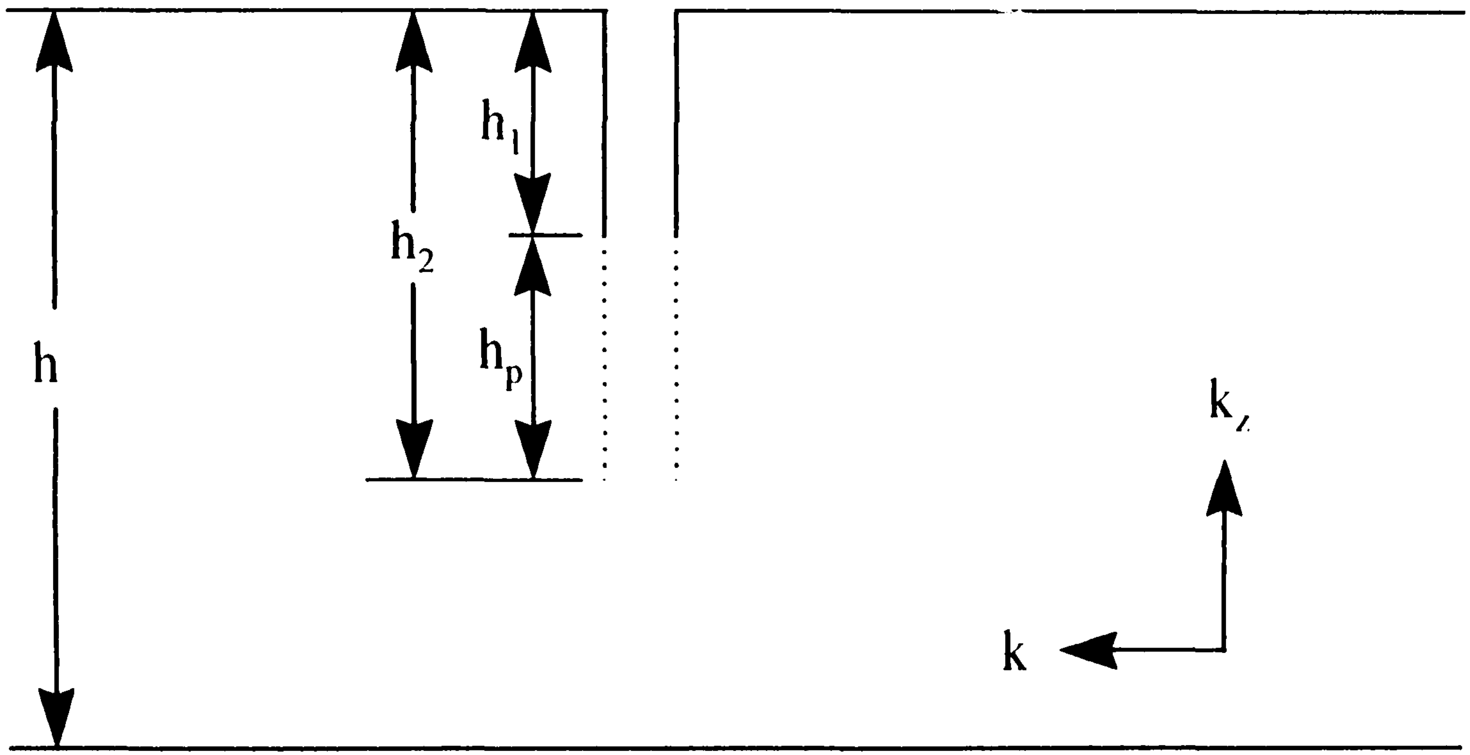

Figure B.1 A Well of Restricted Entry in A Formation With No-Flow Top and Bottom Boundaries

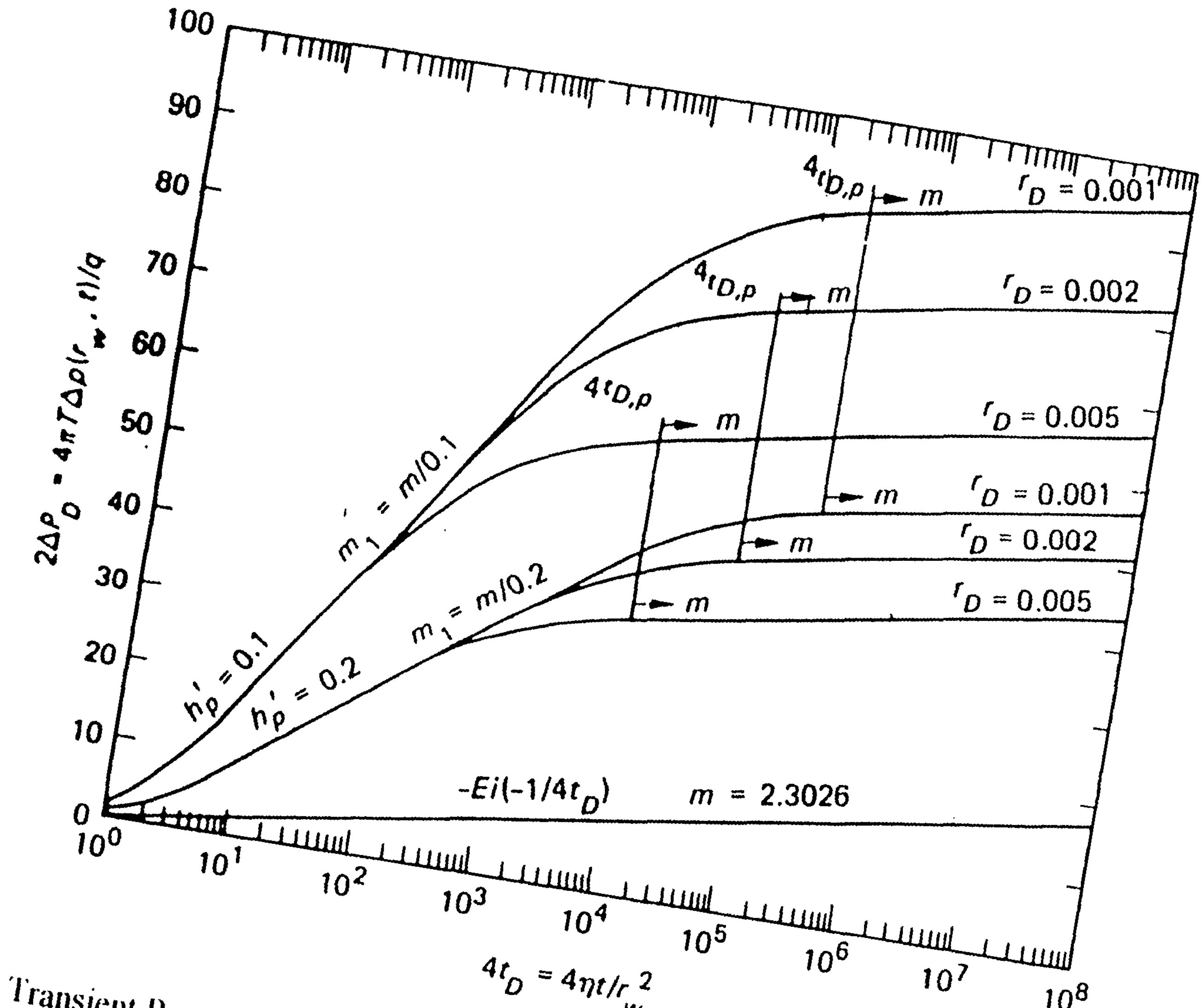

Figure B.2 Transient Pressure Response at a Well of Partial Completion (after Streltsova, 1988)

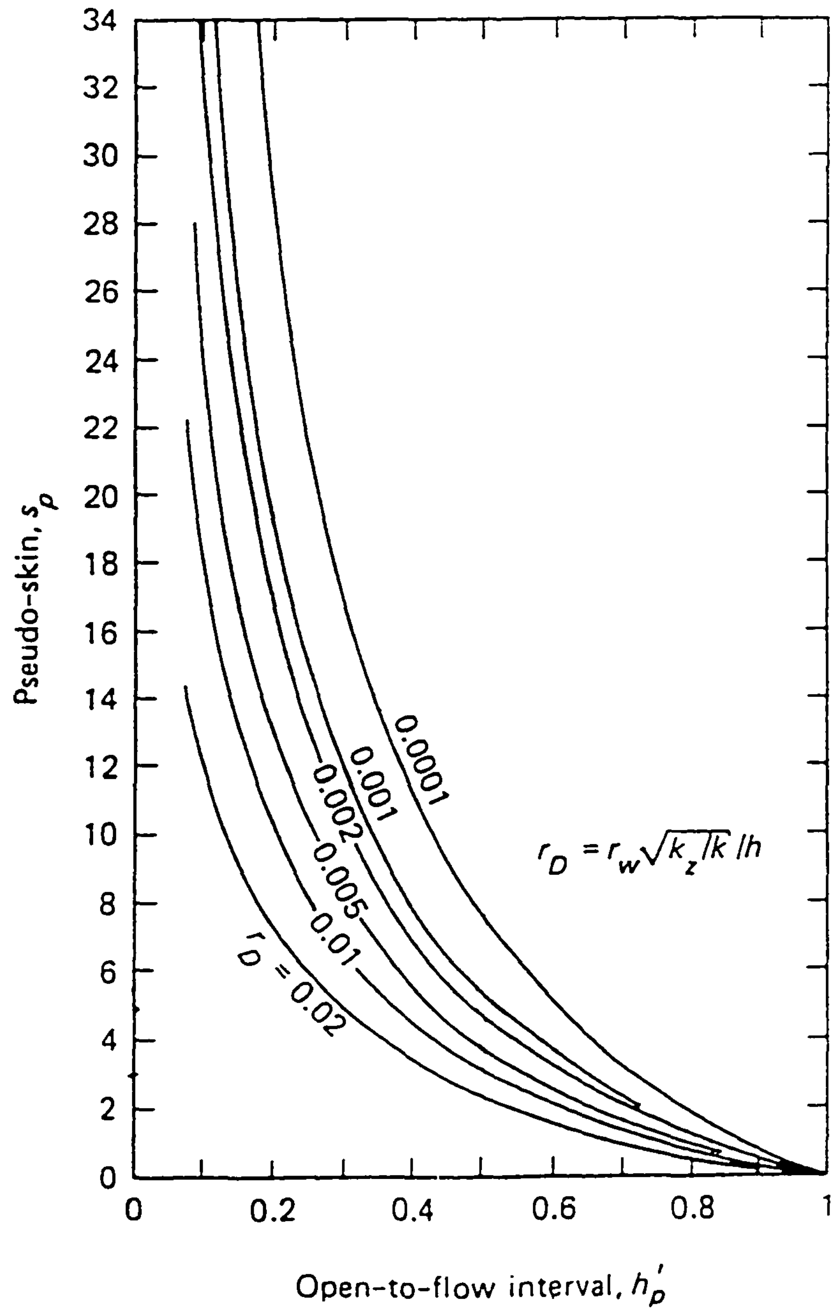

Figure B.3 Pseudo Skin Factor for A Well With A Centrally Located Producing Interval (after Streltsova, 1988)

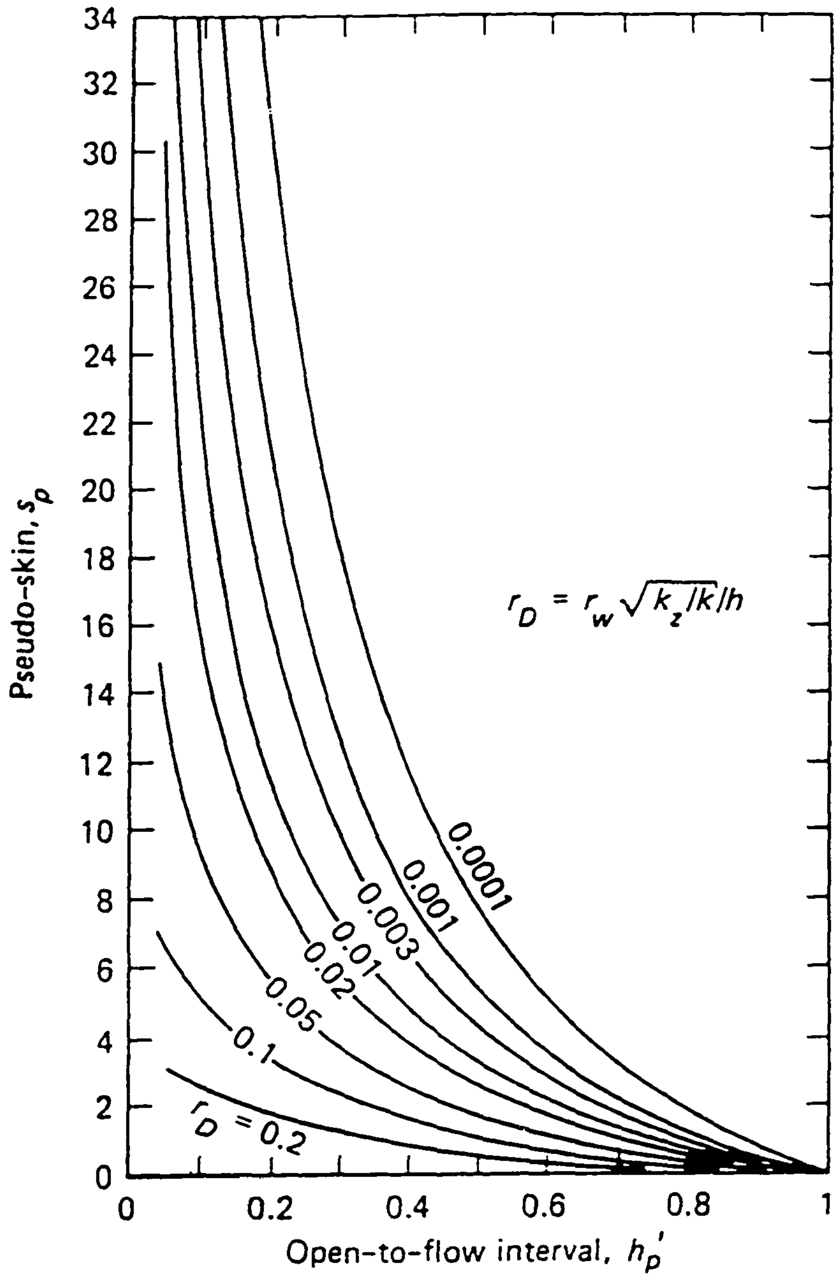

Figure B.4 Pseudo Skin Factor for A Well With The Producing Interval adjacent to either The Top or The Bottom of The Formation (after Streltsova, 1988)

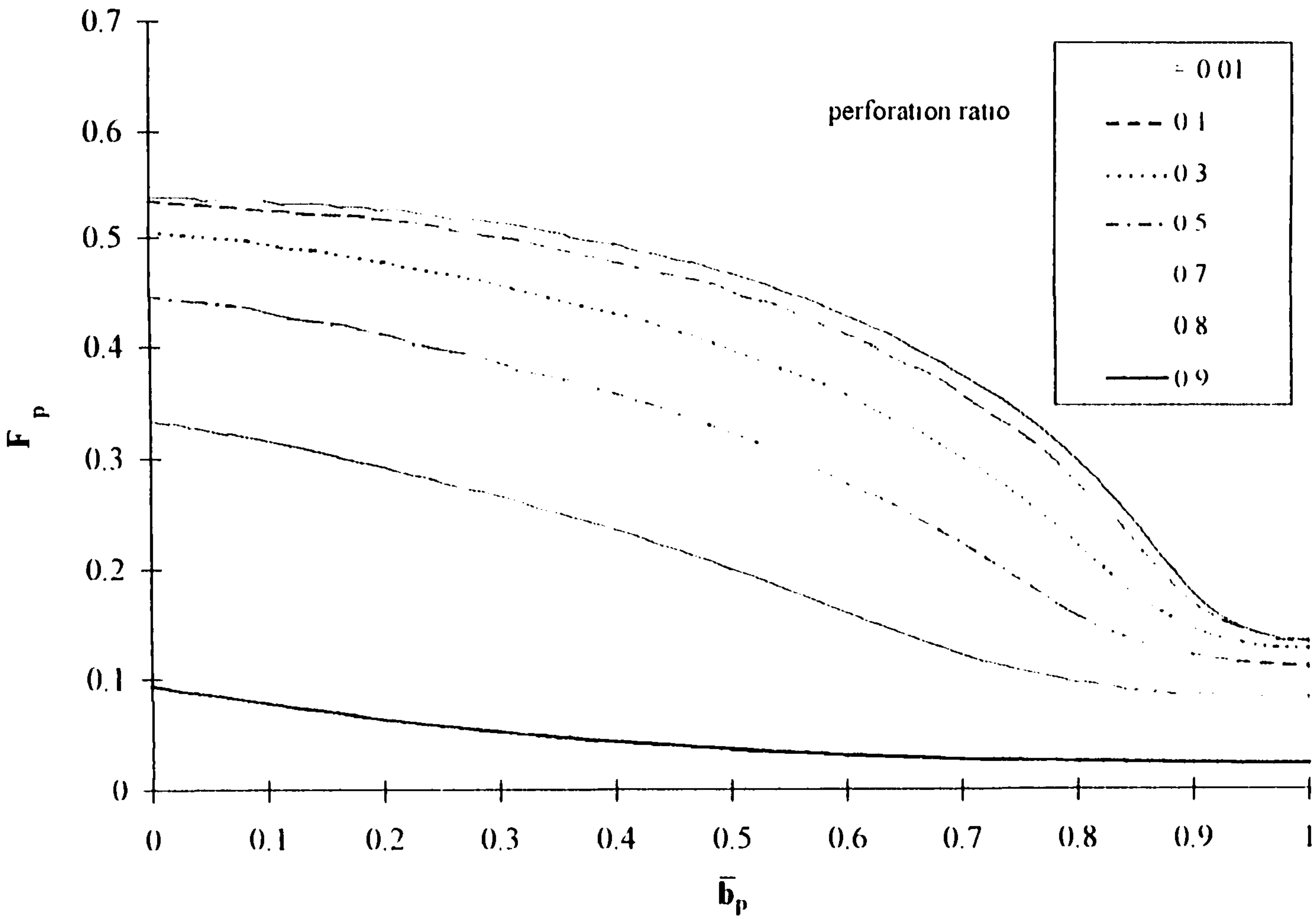

Figure B.5 The End-Time of Partial-Penetration Effect (after Jongkittinarukorn and Tiab, 1996)

APPENDIX C

LIST OF FIGURES IN CASE 5.1

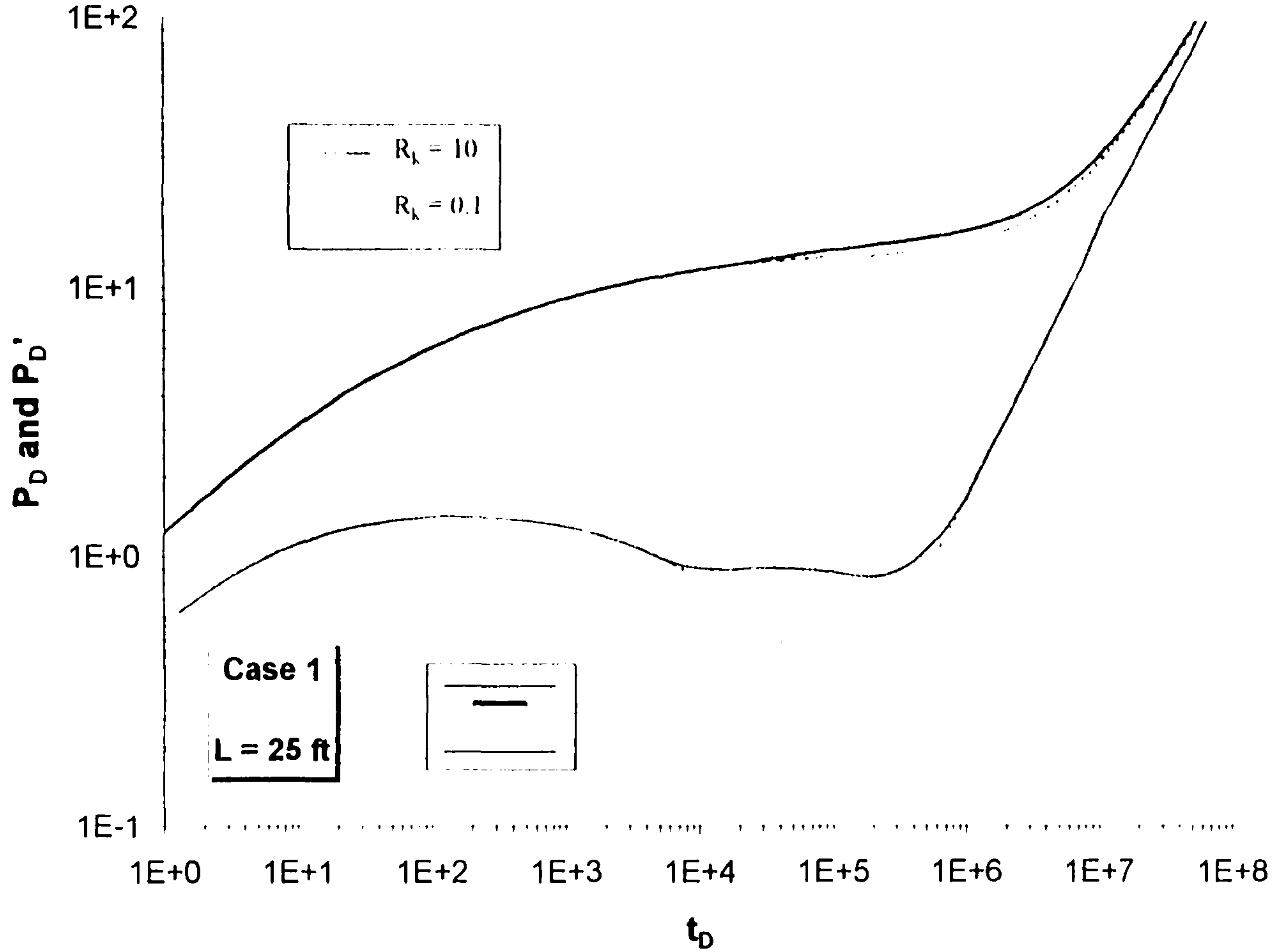

Figure 5.1.6(a) Dimensionless Pressure and Dimensionless Pressure Derivative Behavior for Case 1 and L = 25 ft.

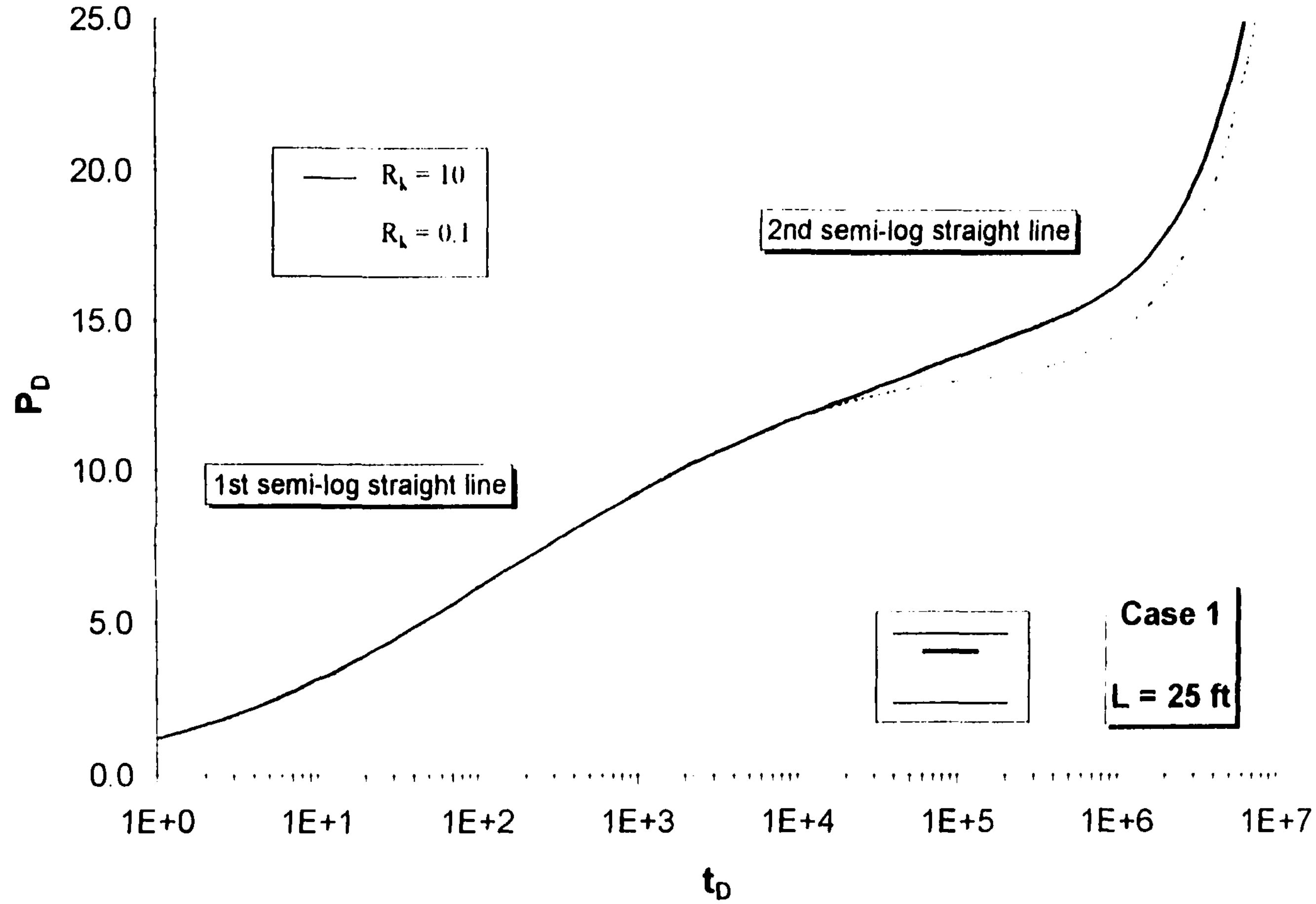

Figure 5.1.6(b) Dimensionless Pressure Behavior for Case 1 and L = 25 ft.

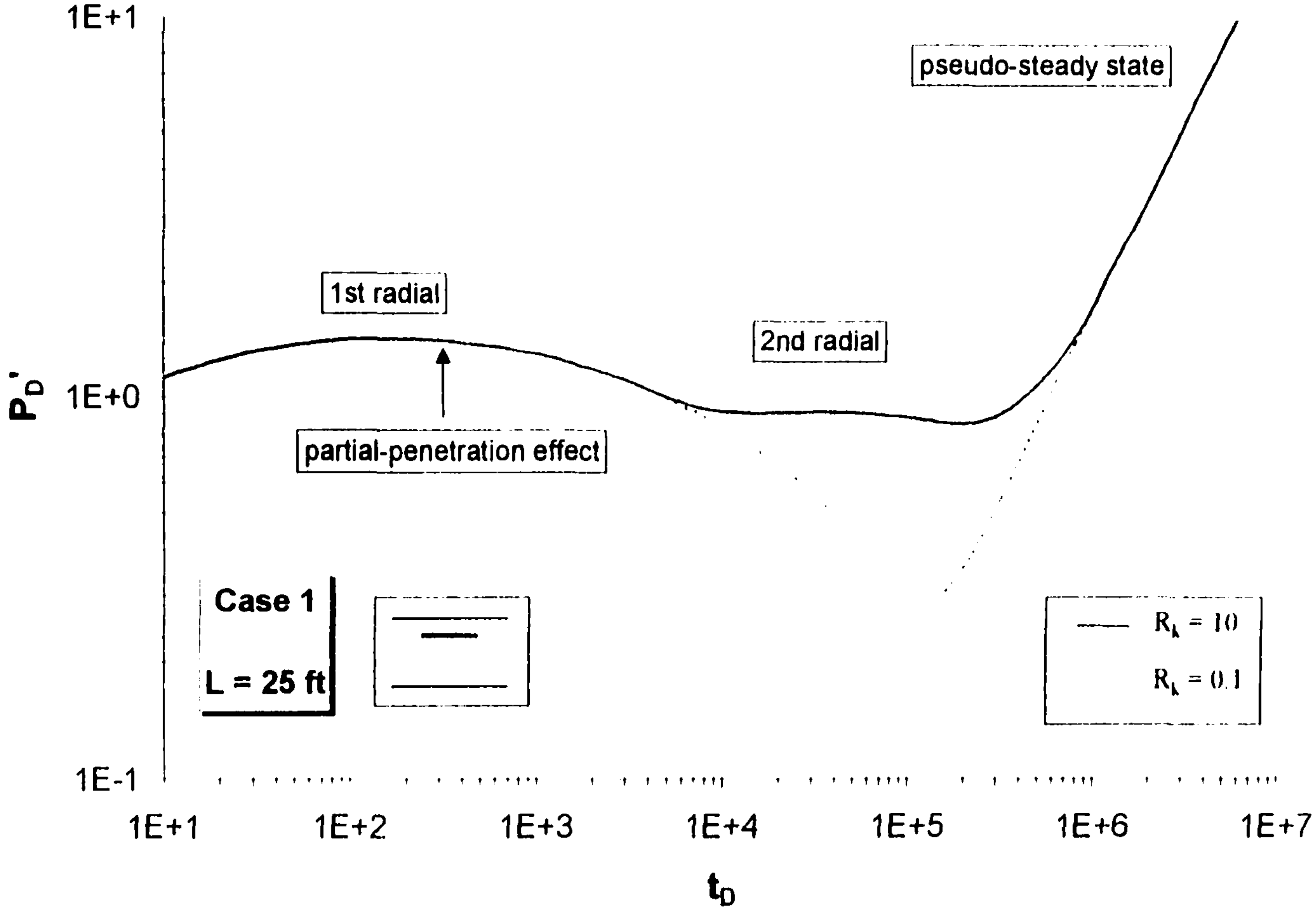

Figure 5.1.6(c) Dimensionless Pressure Derivative Behavior for Case 1 and L = 25 ft.

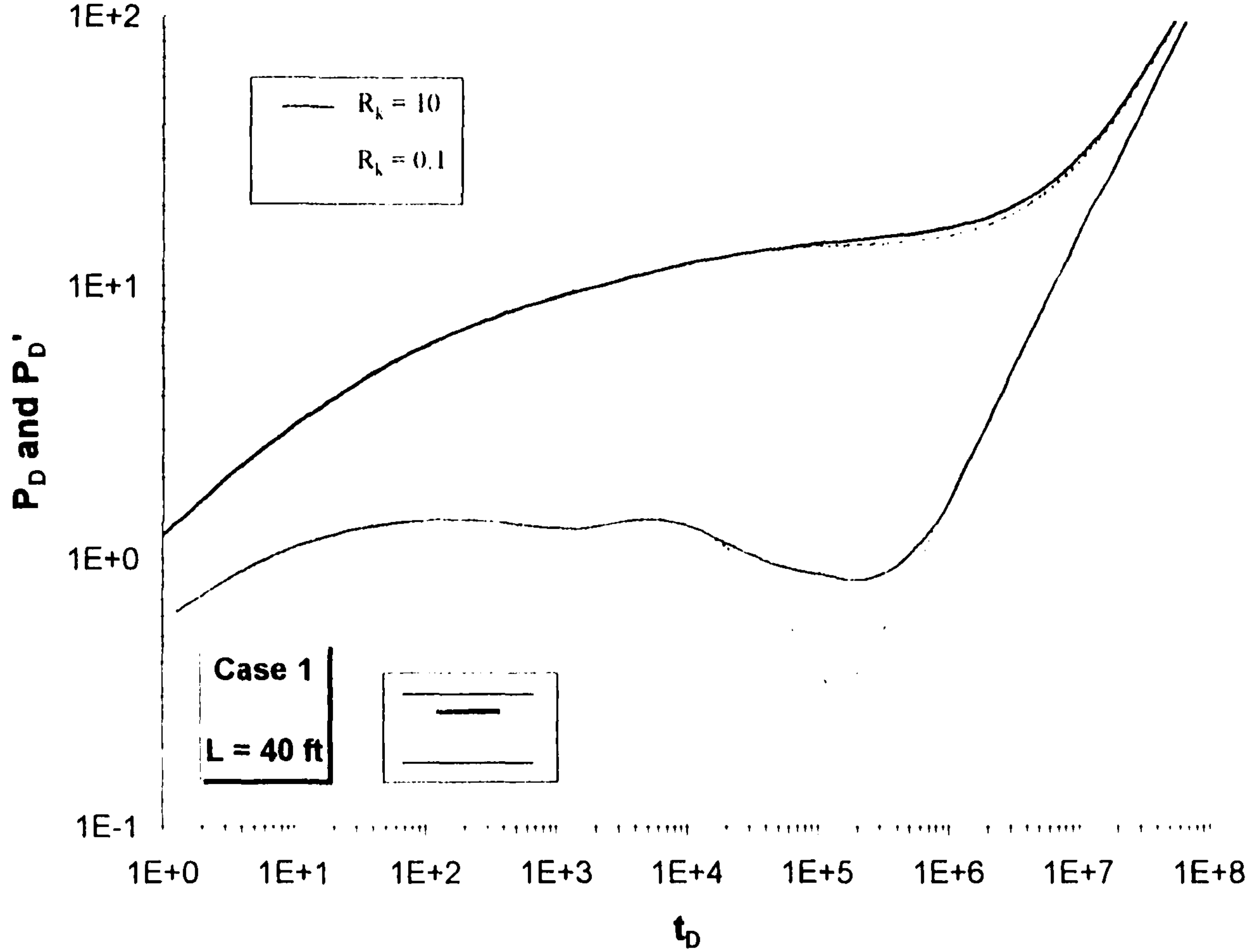

Figure 5.1.7(a) Dimensionless Pressure and Dimensionless Pressure Derivative Behavior for Case 1 and L = 40 ft.

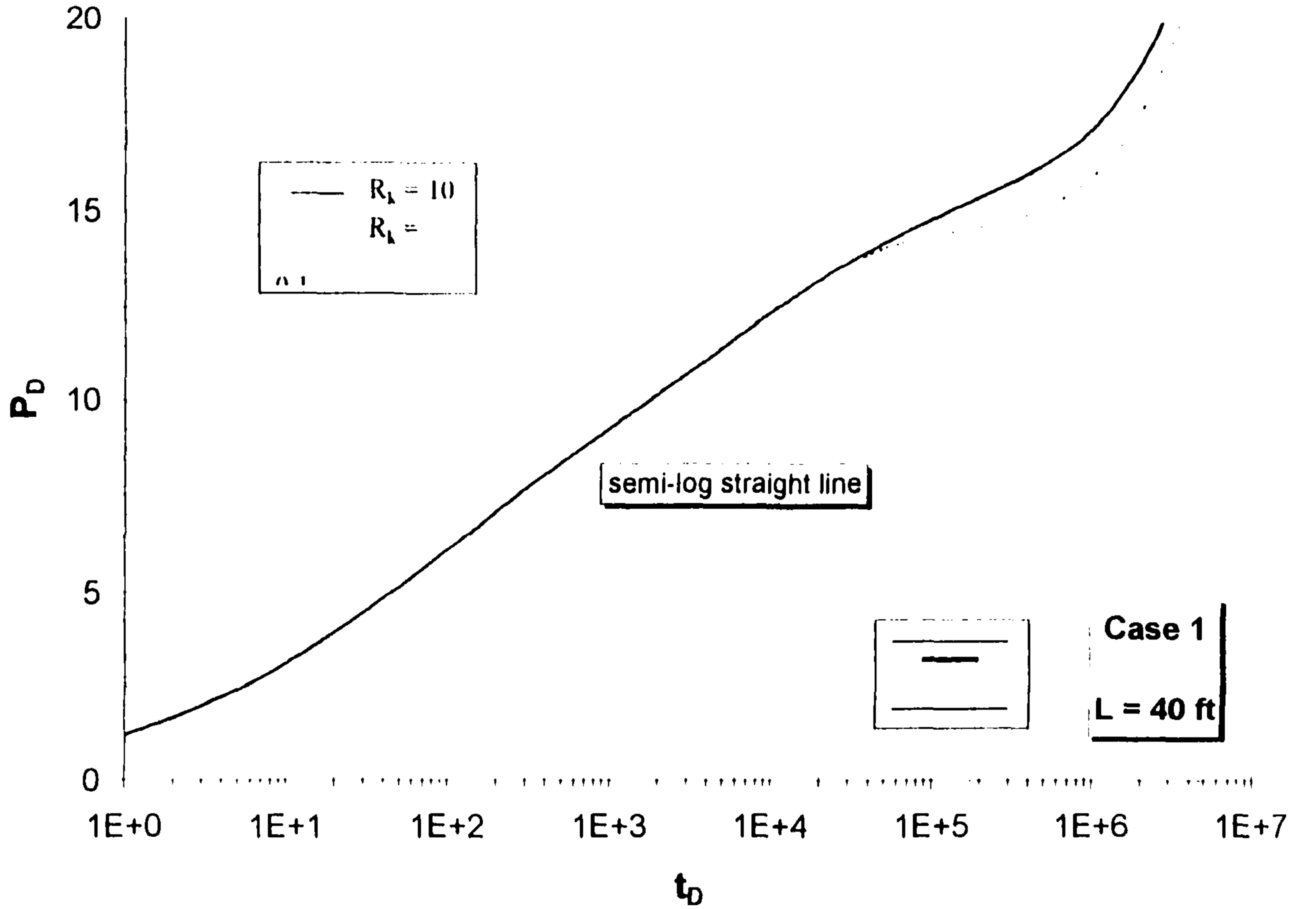

Figure 5.1.7(b) Dimensionless Pressure Behavior for Case 1 and L = 40 ft.

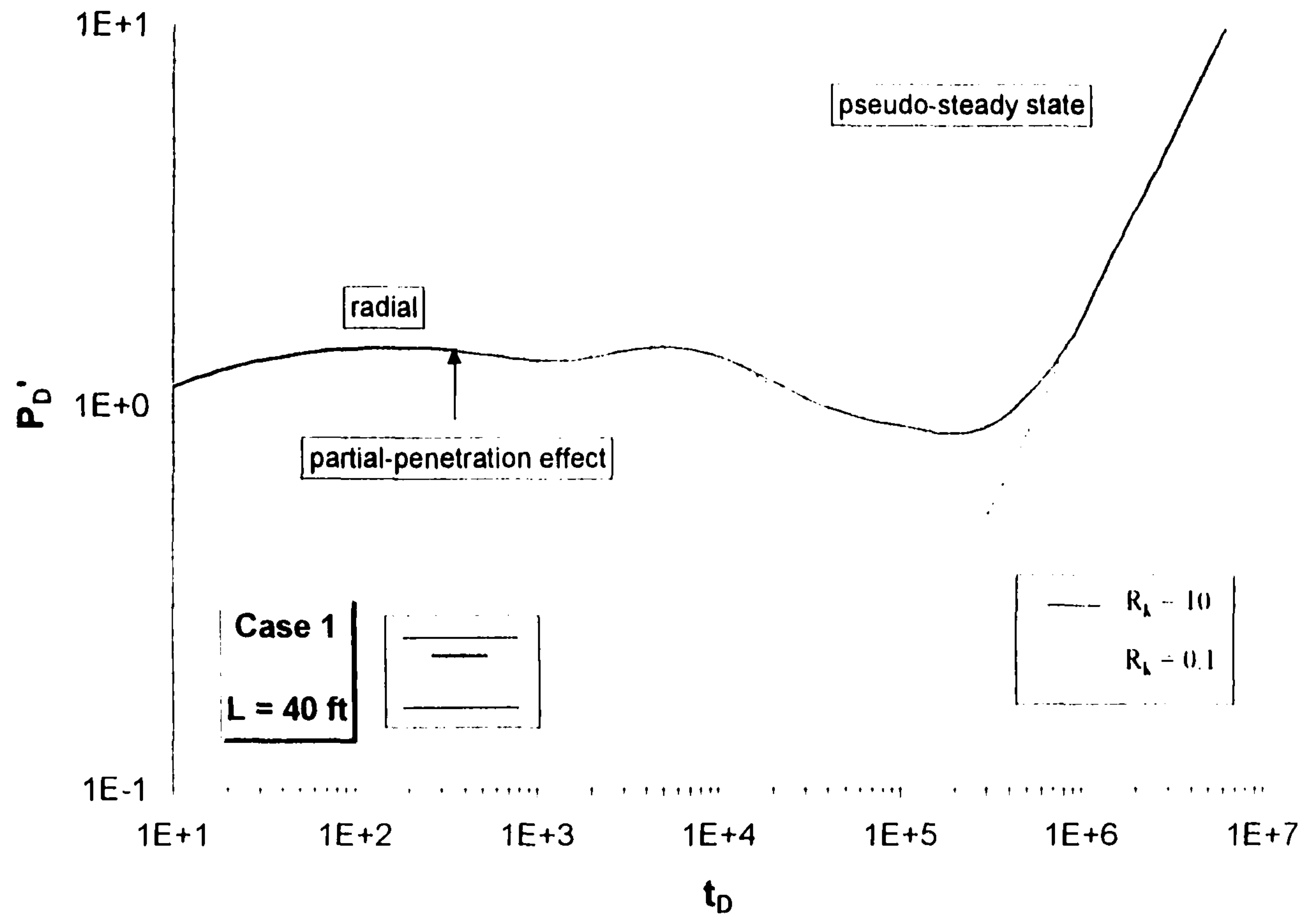

Figure 5.1.7(c) Dimensionless Pressure Derivative Behavior for Case 1 and L = 40 ft.

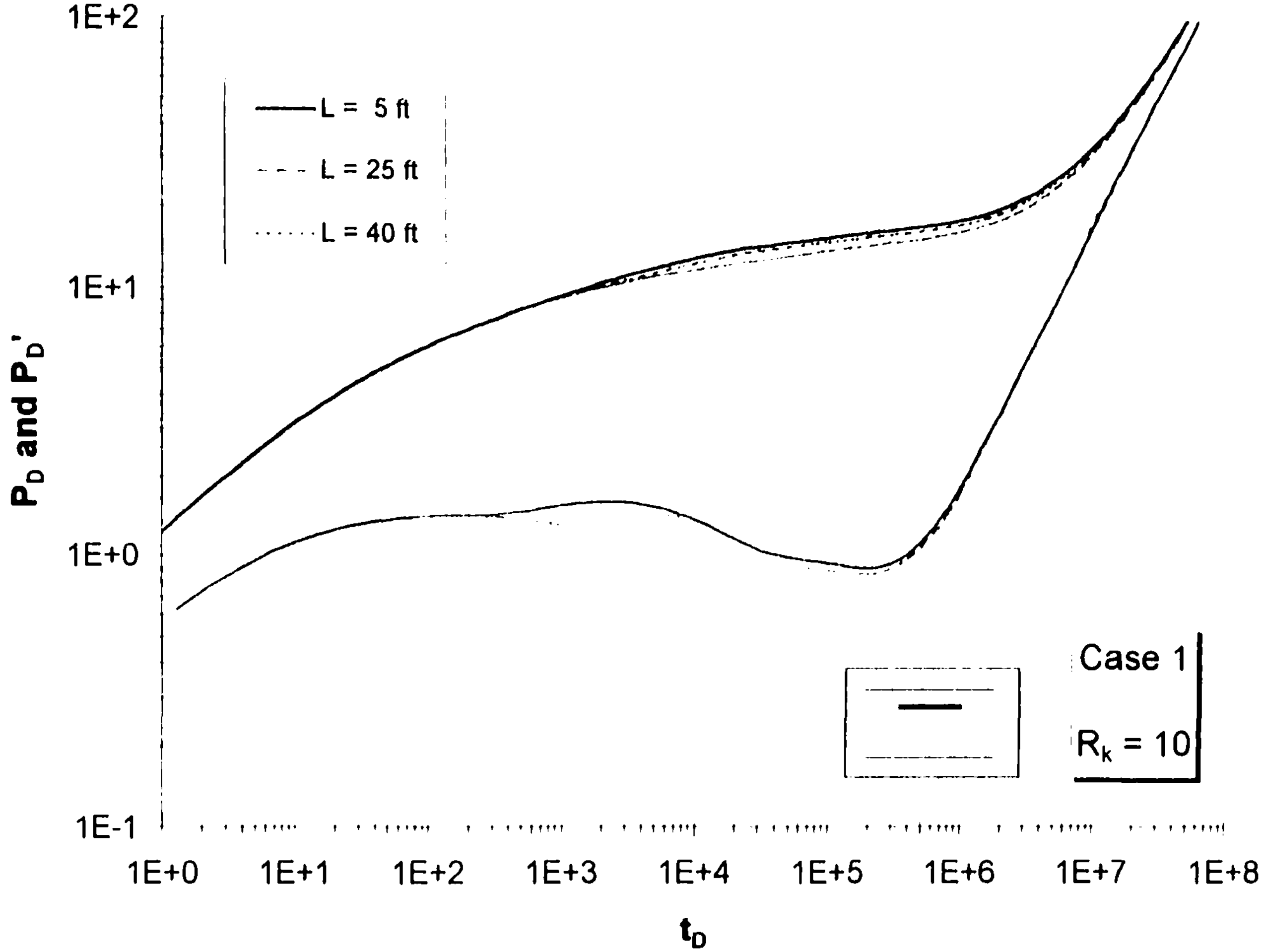

Figure 5.1.8(a) Dimensionless Pressure and Dimensionless Pressure Derivative Behavior

for Case 1 and R_k = 10

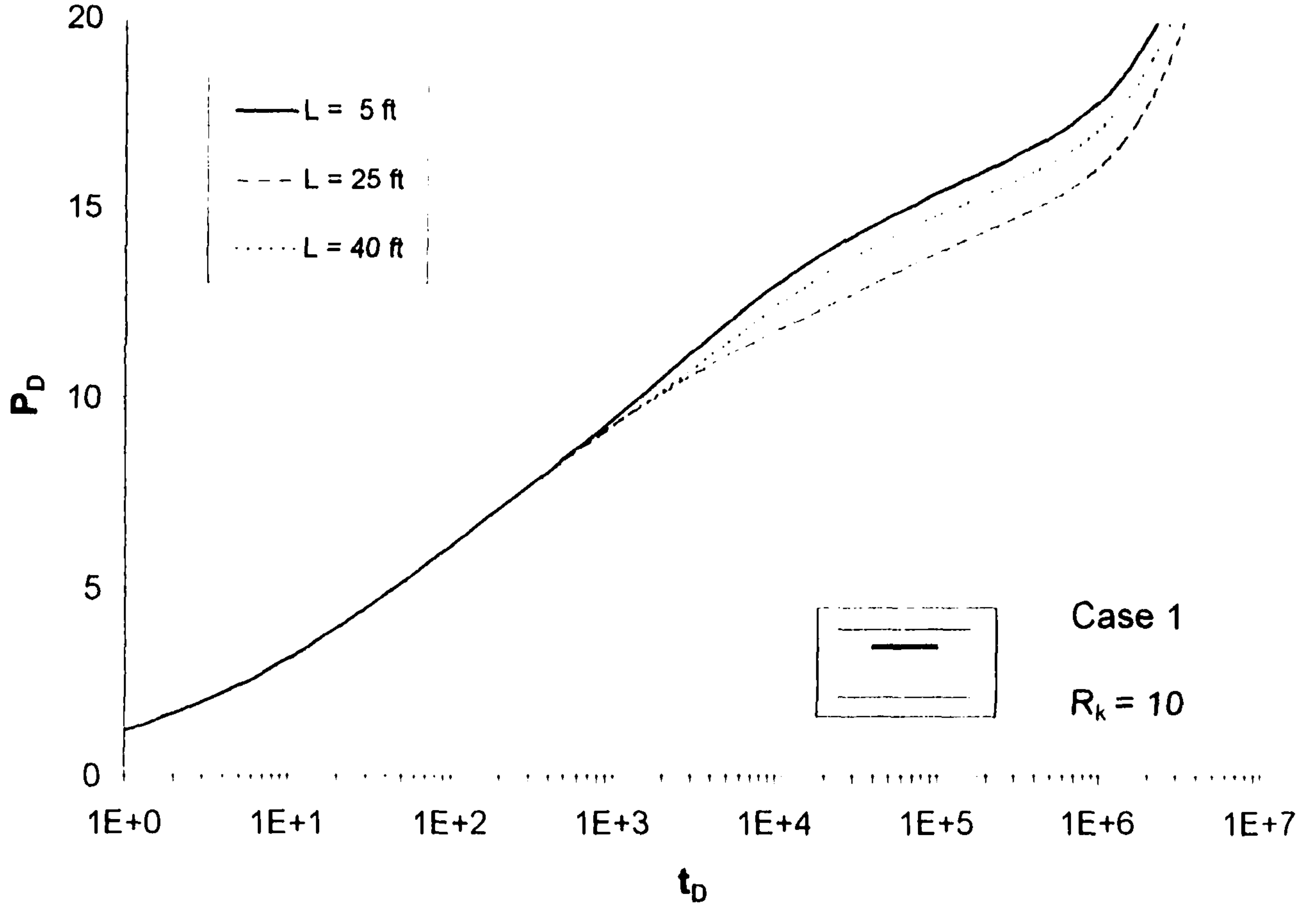

Figure 5.1.8(b) Dimensionless Pressure Behavior for Case 1 and $R_k = 10$

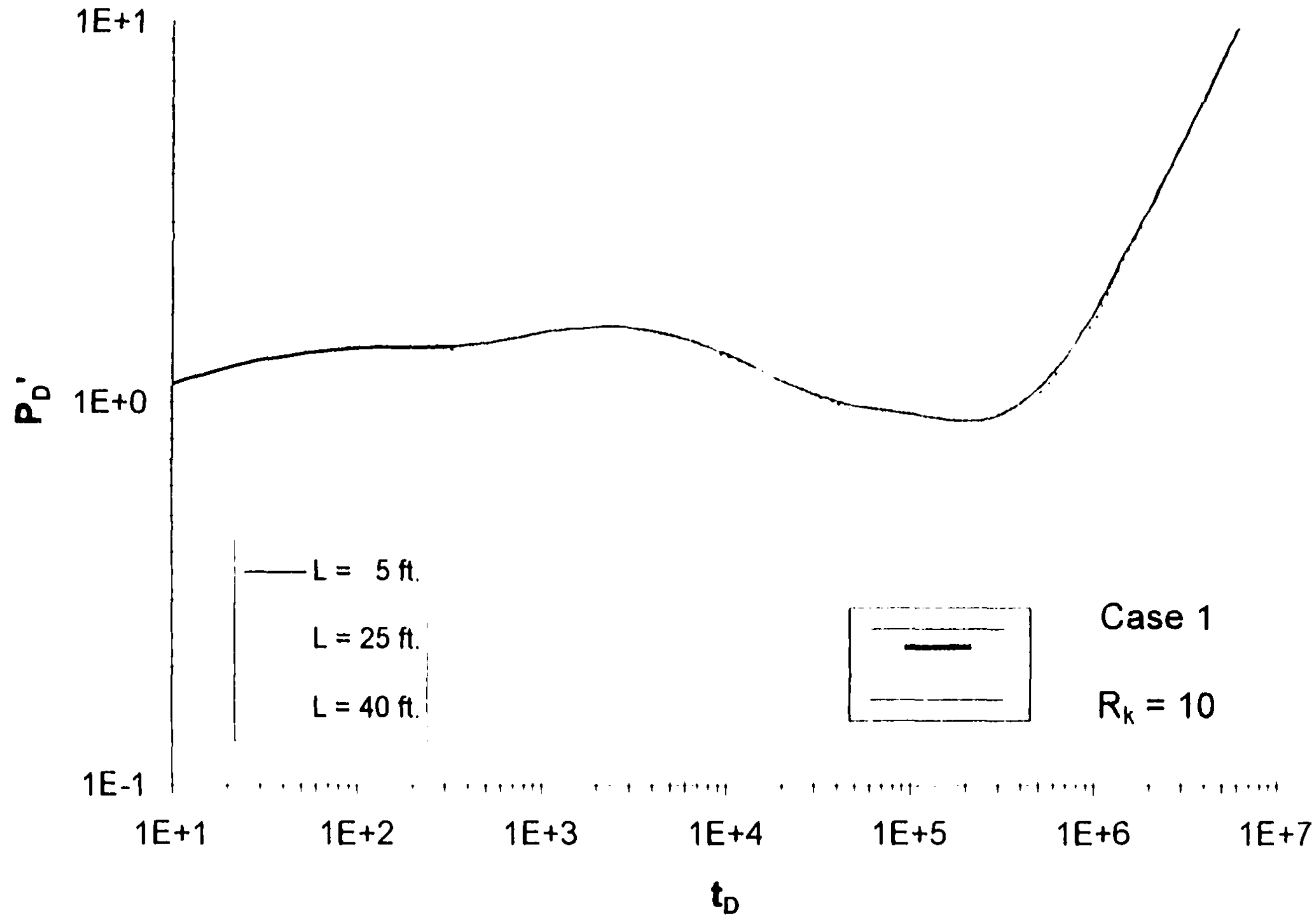

Figure 5.1.8(c) Dimensionless Pressure Derivative Behavior for Case 1 and $R_k = 10$

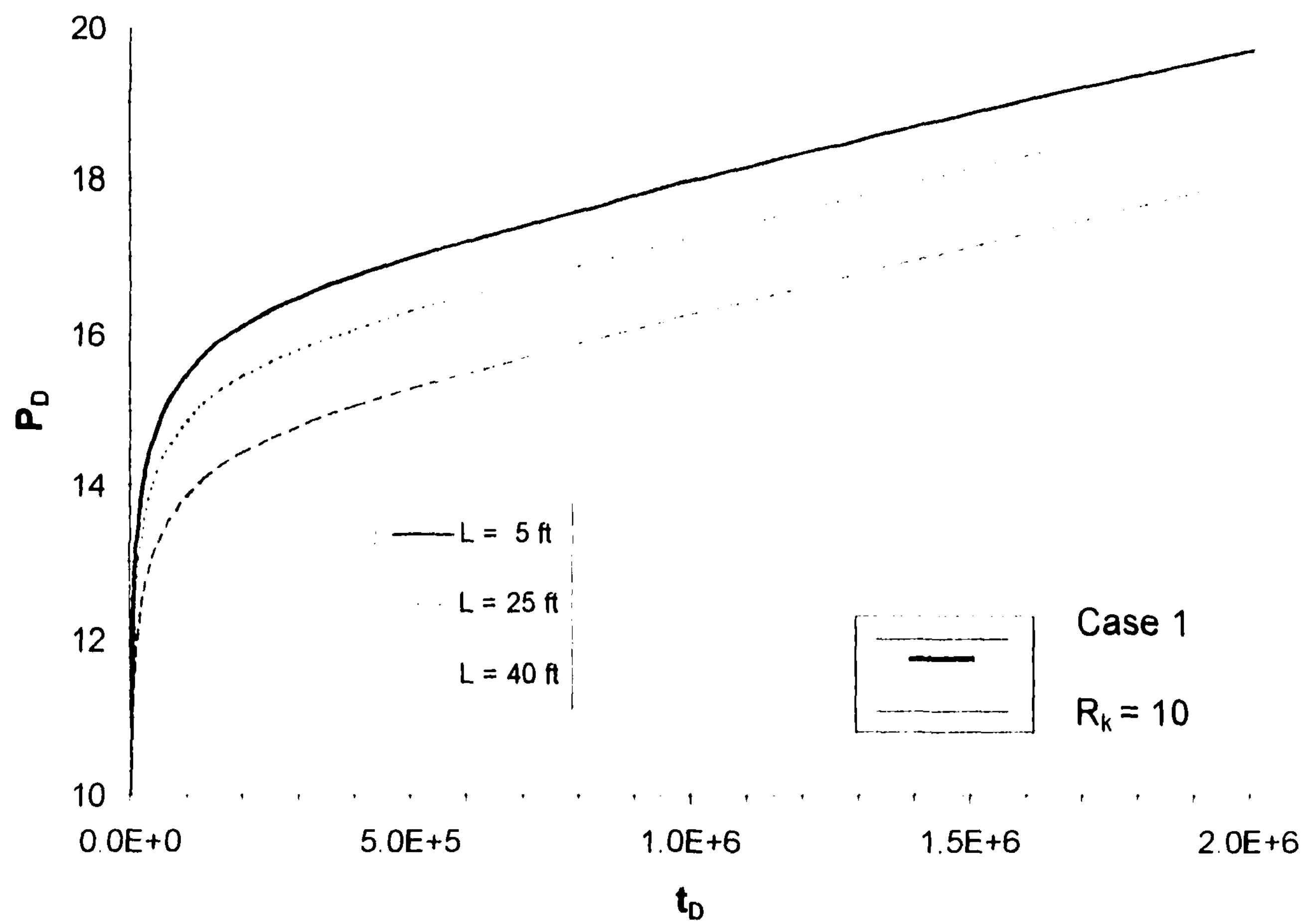

Figure 5.1.8(d) Dimensionless Pressure Behavior during pseudo-steady state for Case 1 and $R_k = 10$

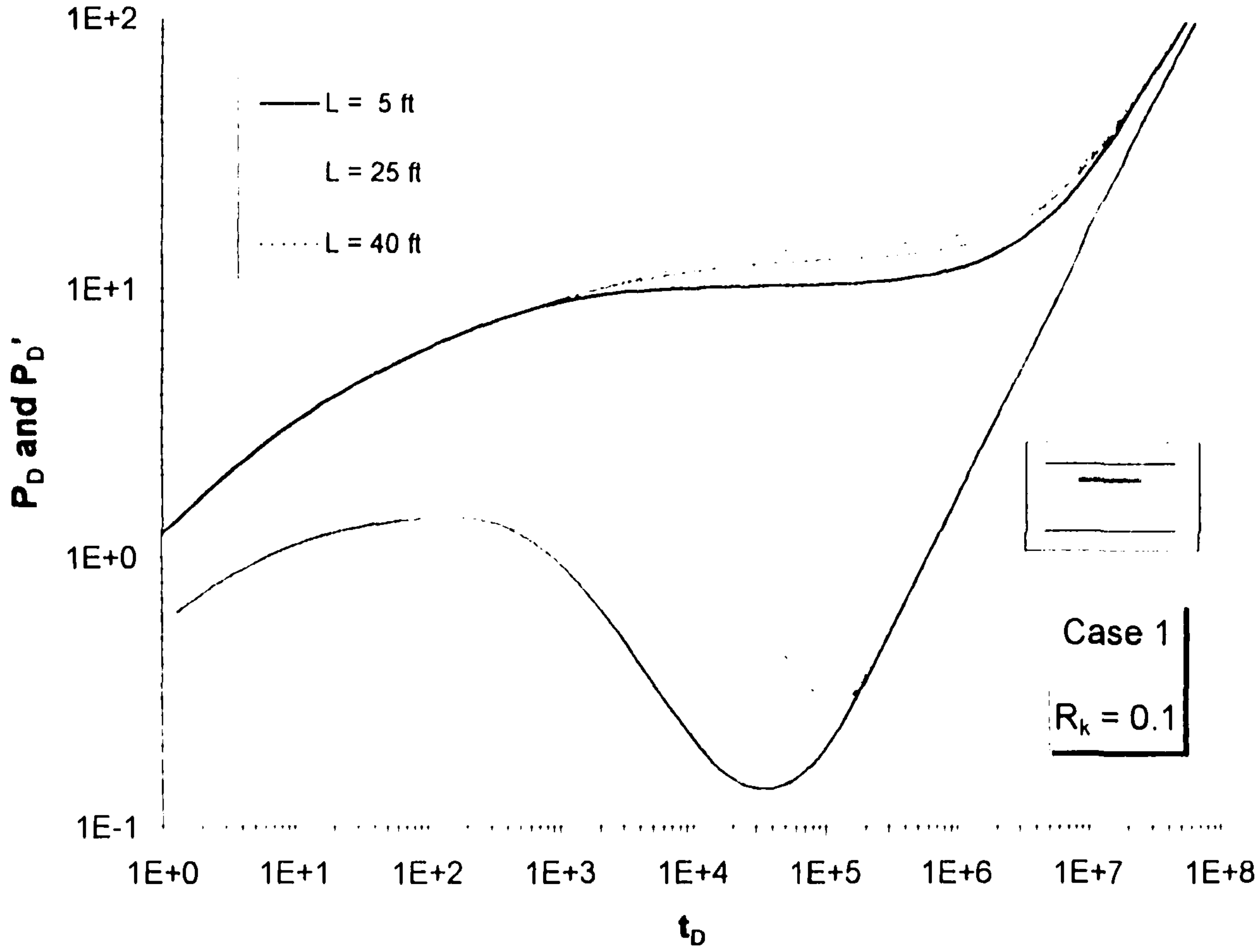

Figure 5.1.9(a) Dimensionless Pressure and Dimensionless Pressure Derivative Behavior for Case 1 and $R_k = 0.1$

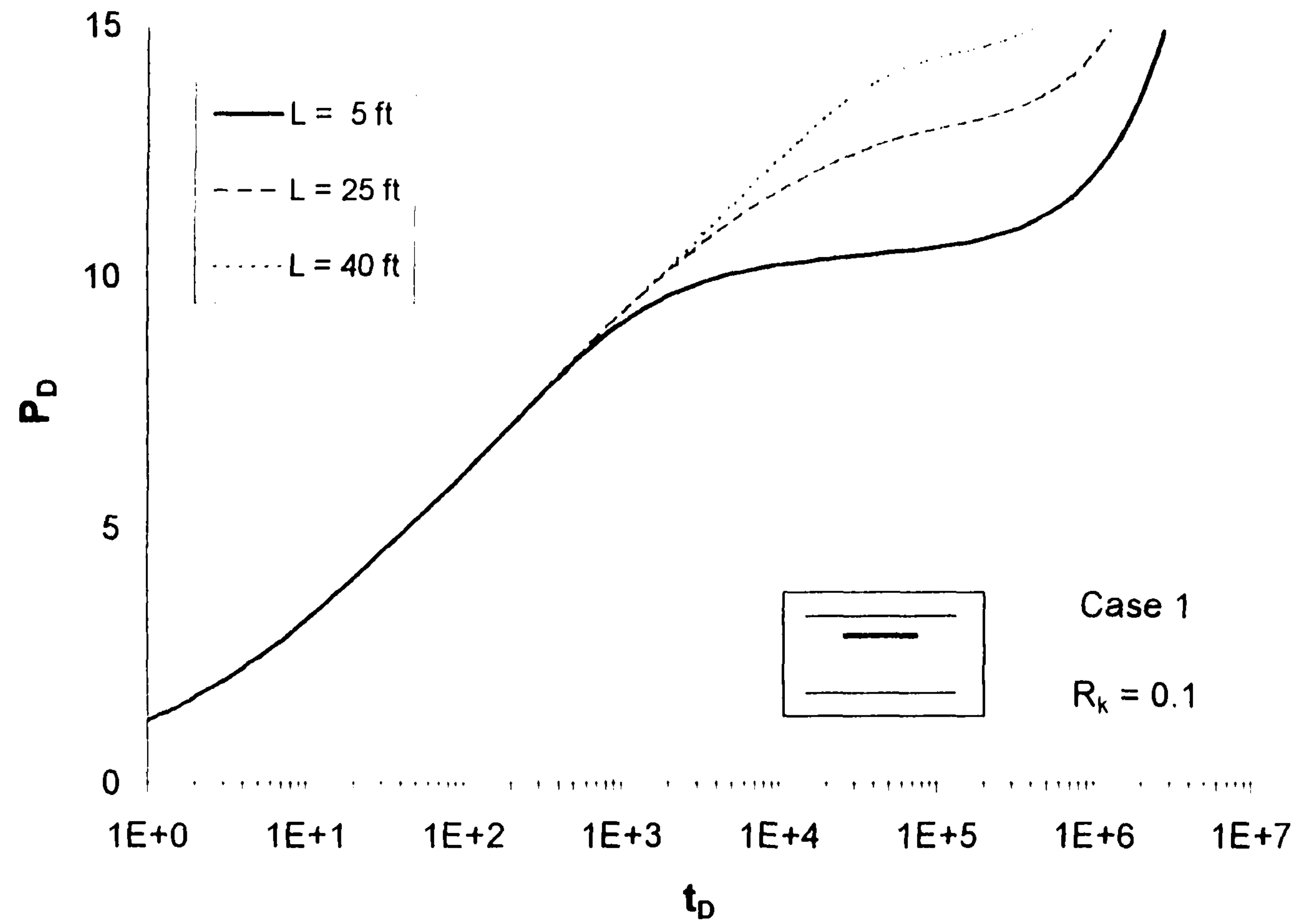

Figure 5.1.9(b) Dimensionless Behavior for Case 1 and R_k = 0.1

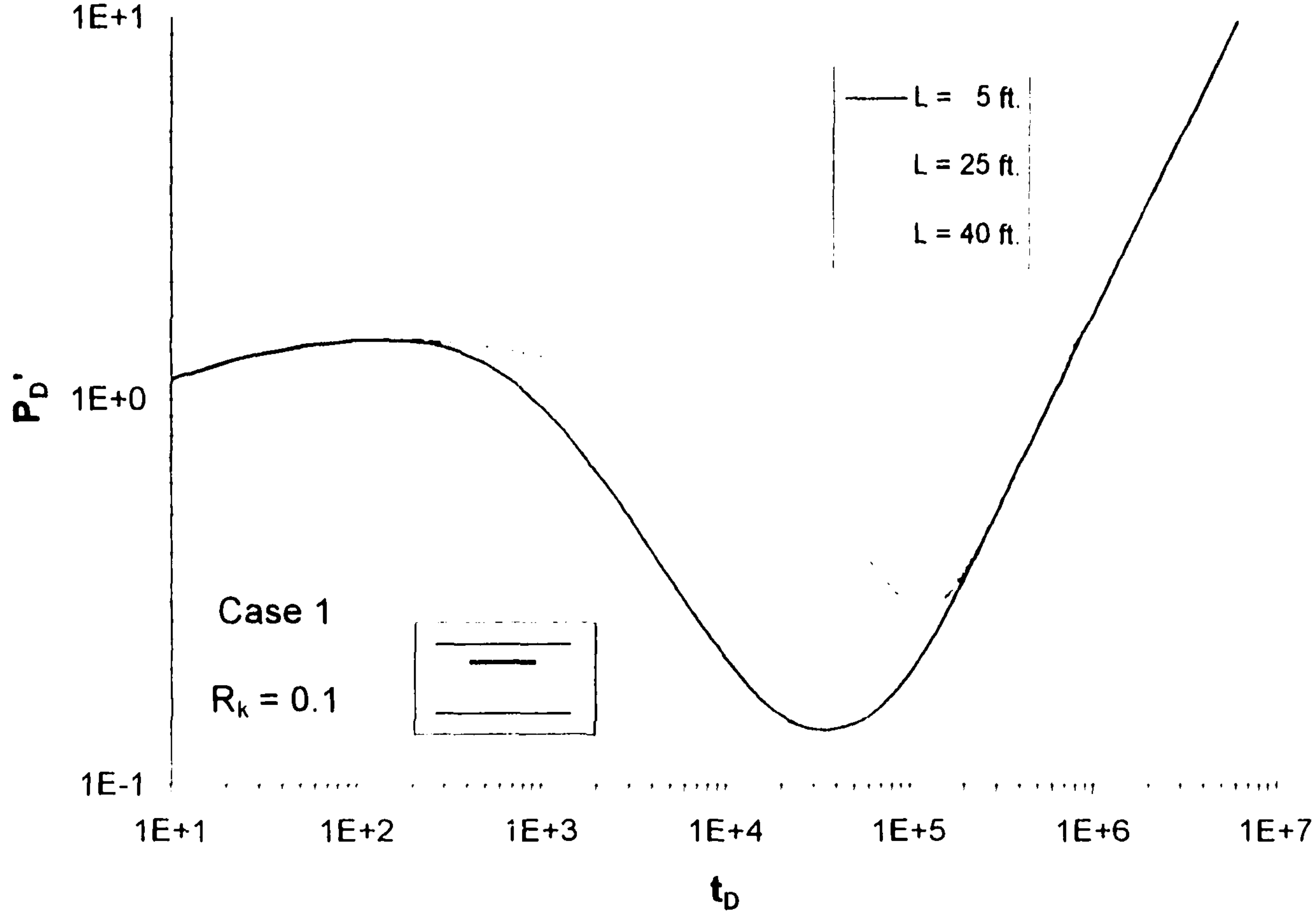

Figure 5.1.9(c) Dimensionless Derivative Behavior for Case 1 and $R_k = 0.1$

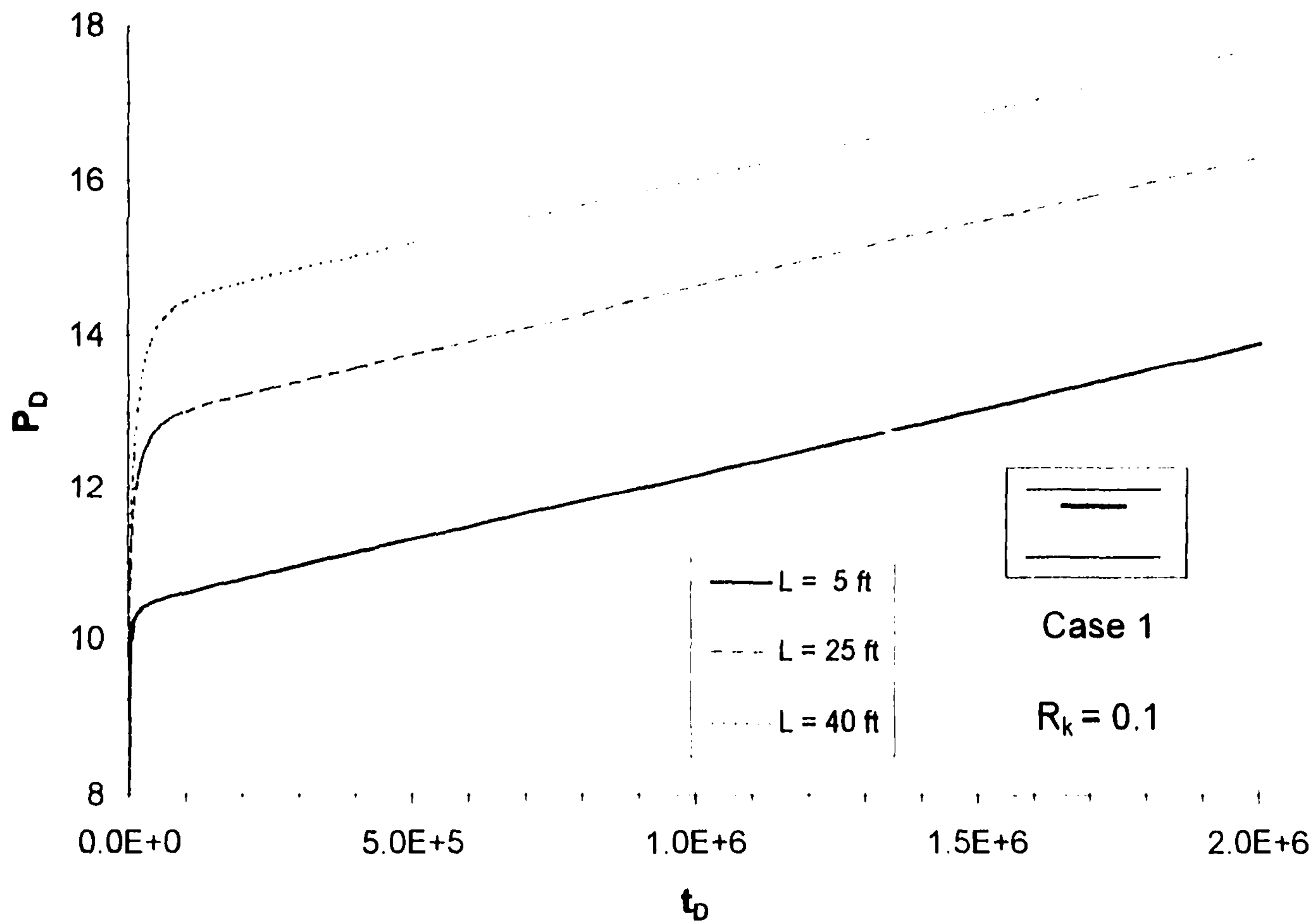

Figure 5.1.9(d) Dimensionless Behavior During Pseudo-Steady State for Case 1 and $R_k = 0.1$

APPENDIX D

LIST OF FIGURES IN CASE 5.2

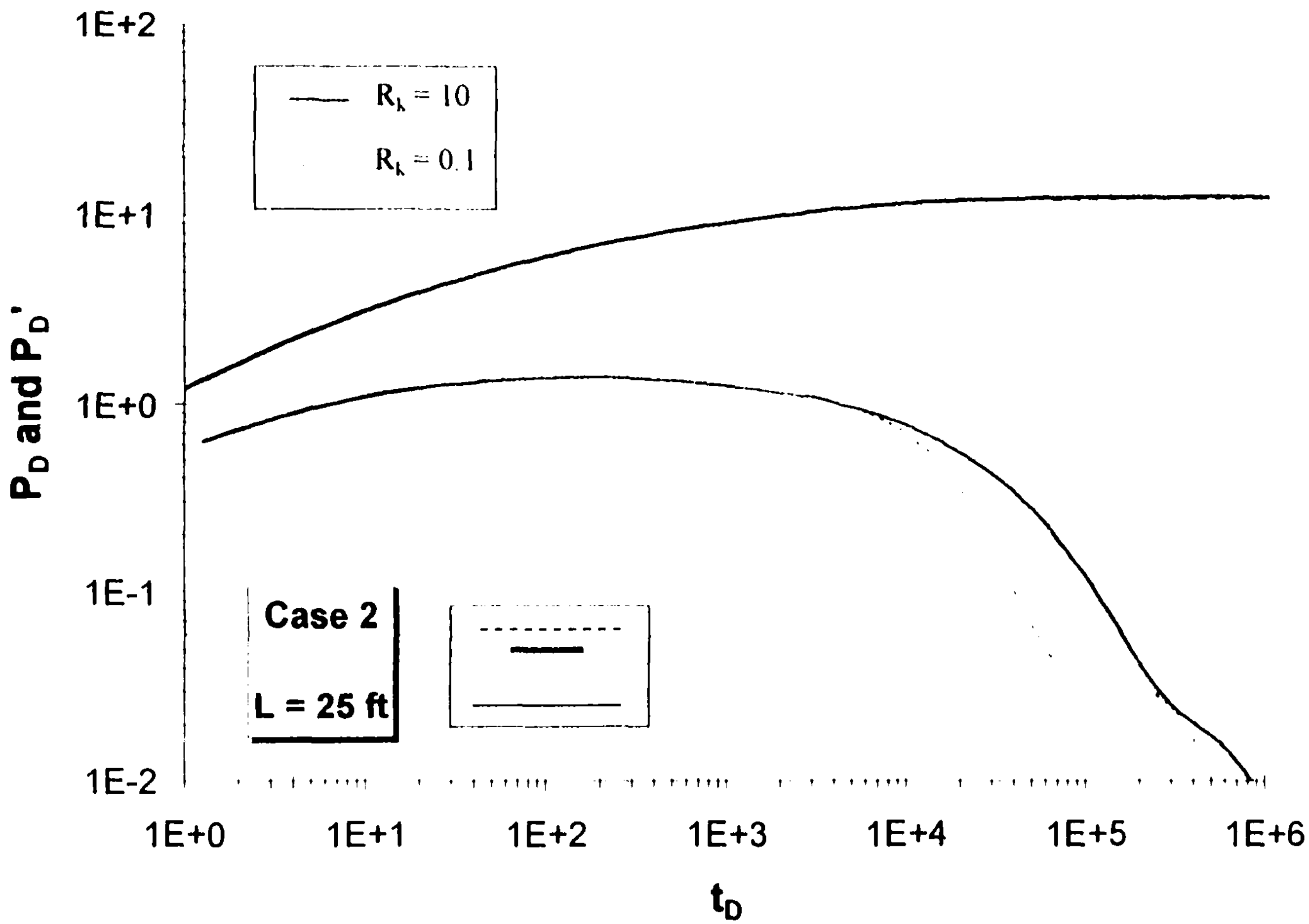

Figure 5.2.3(a) Dimensionless Pressure and Dimensionless Pressure Derivative Behavior

for Case 2 and L = 25 ft.

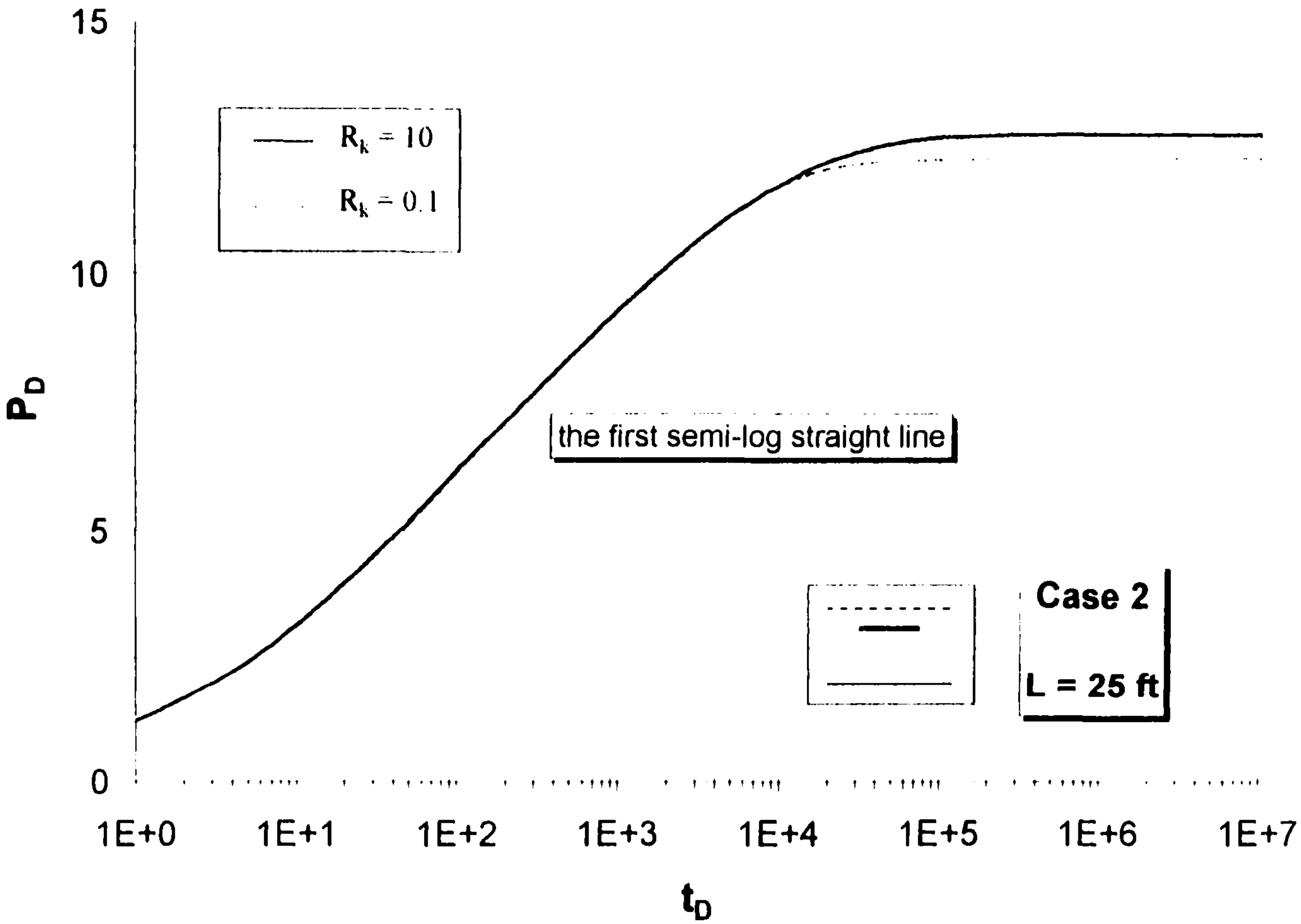

Figure 5.2.3(b) Dimensionless Pressure Behavior for Case 2 and L = 25 ft.

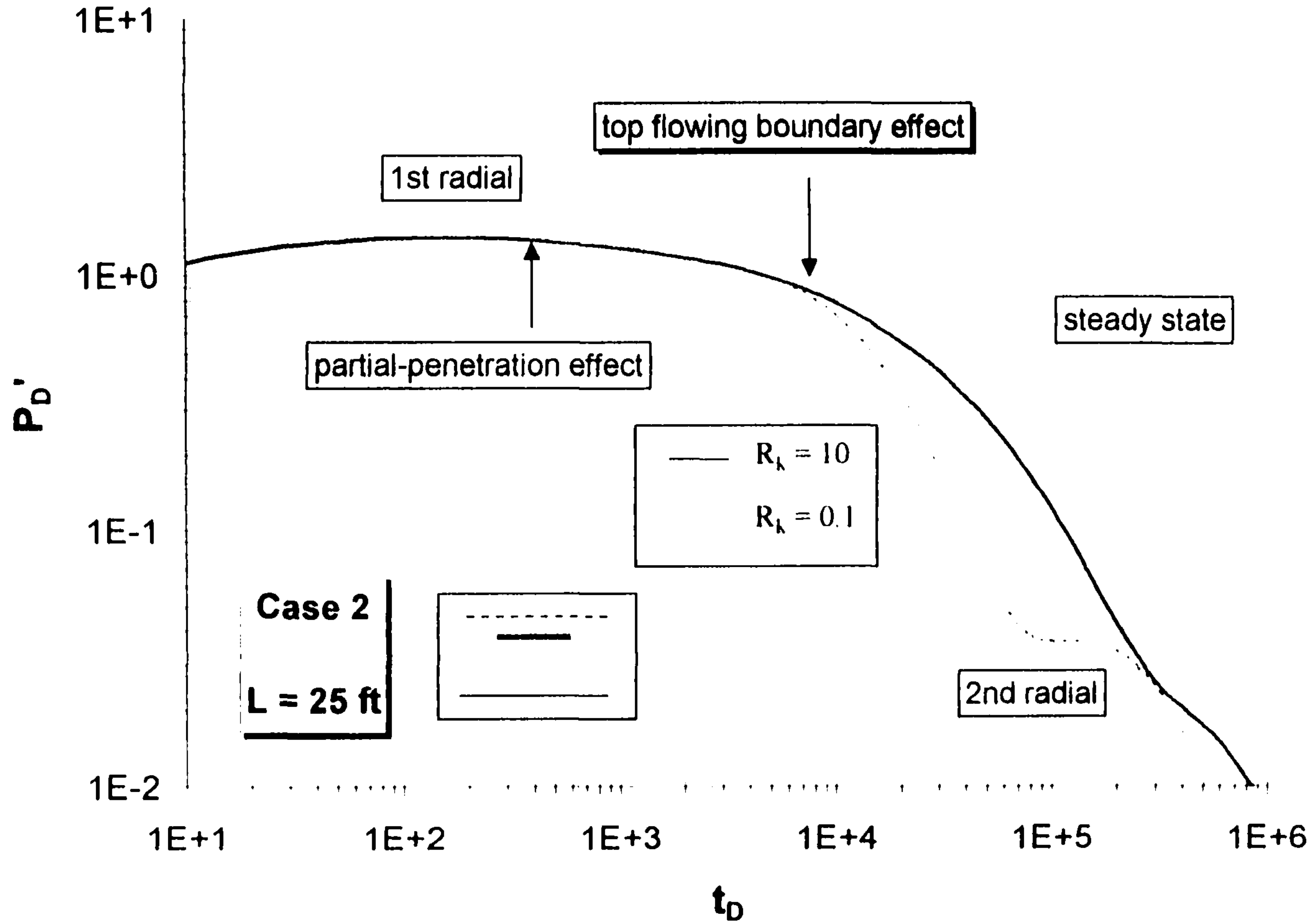

Figure 5.2.3(c) Dimensionless Pressure Derivative Behavior for Case 2 and L = 25 ft.

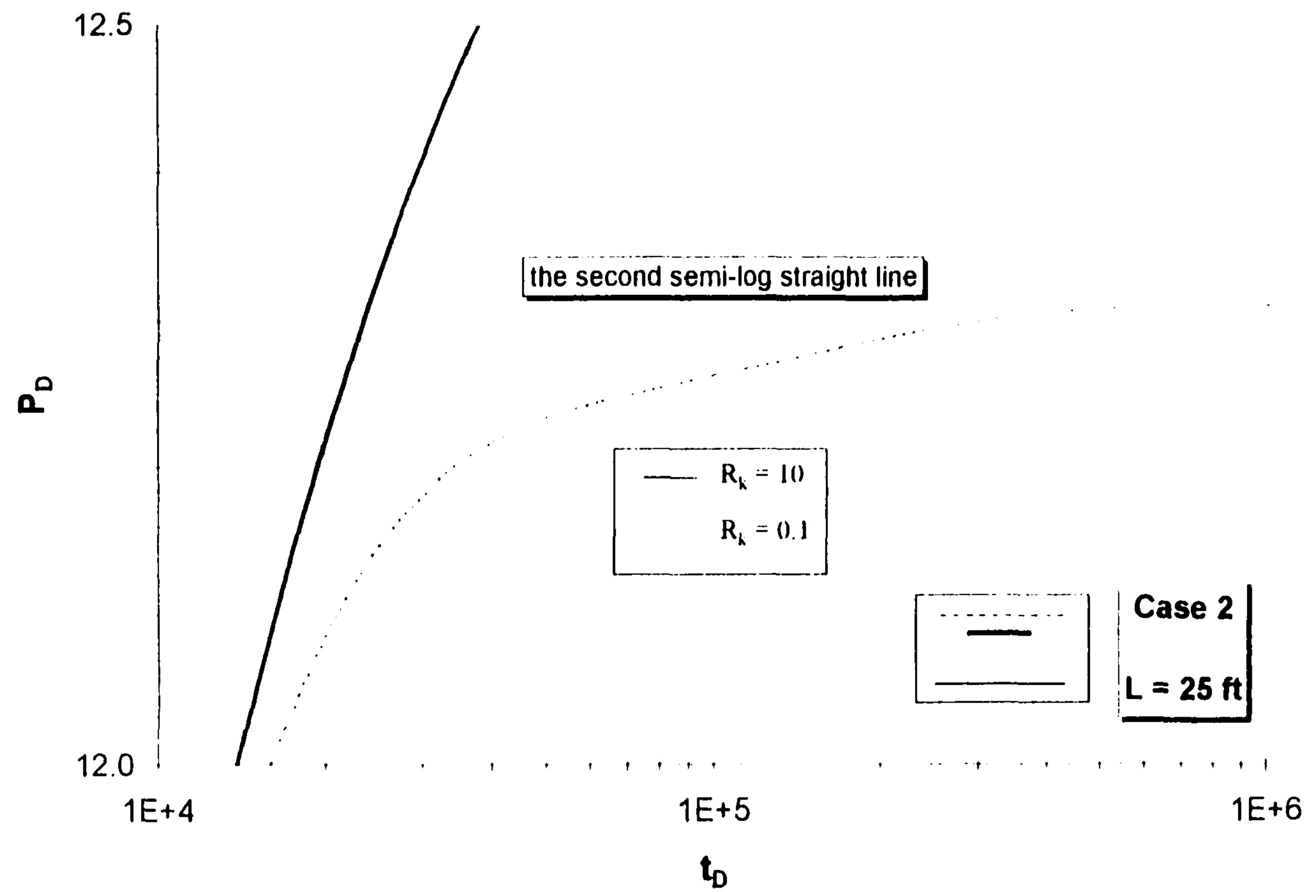

Figure 5.2.3(d) Dimensionless Pressure Behavior for Case 2 and L = 25 ft.

Showing The Second Radial Flow

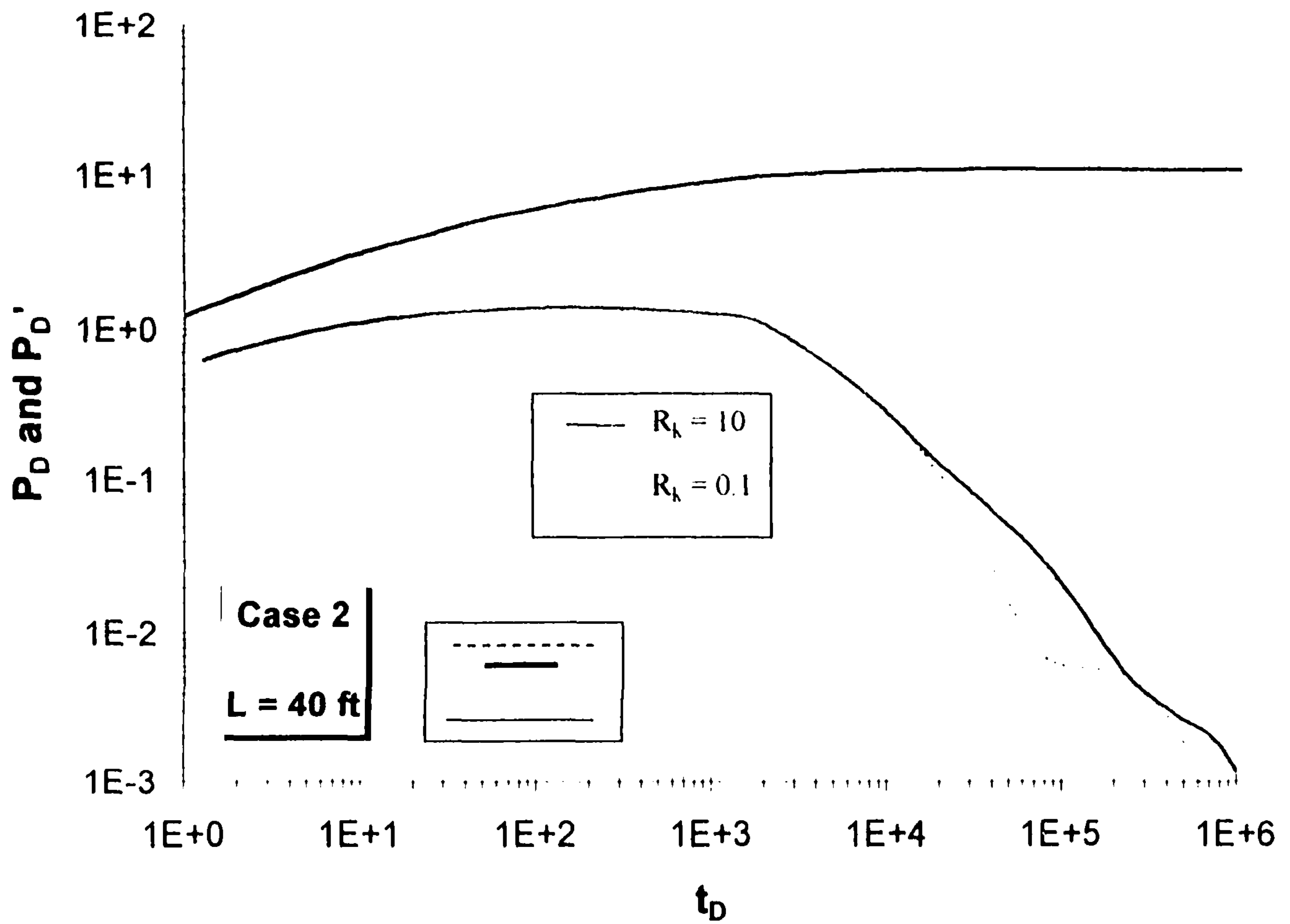

Figure 5.2.4(a) Dimensionless Pressure and Dimensionless Pressure Derivative Behavior for Case 2 and L = 40 ft.

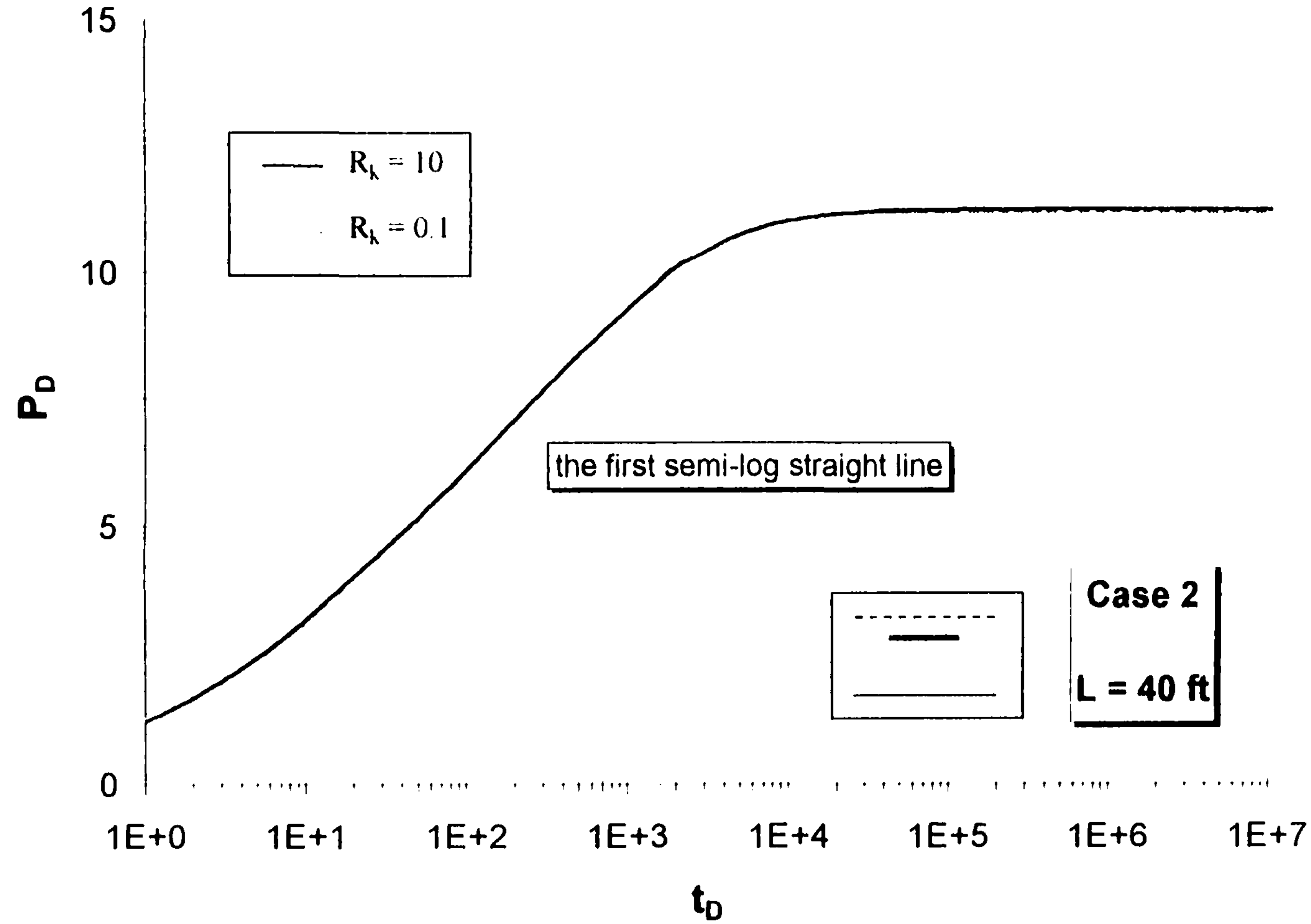

Figure 5.2.4(b) Dimensionless Pressure Behavior for Case 2 and L = 40 ft.

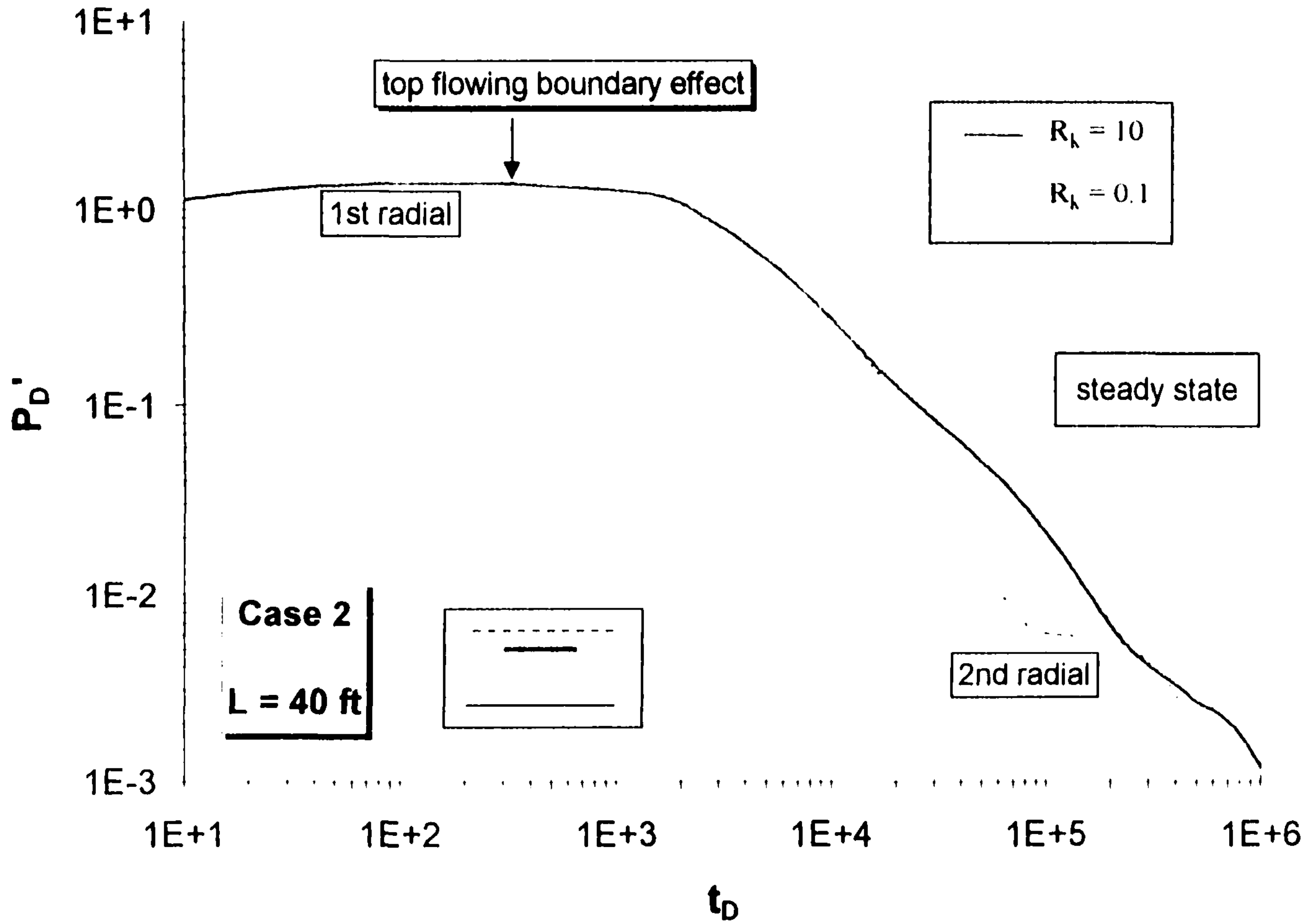

Figure 5.2.4(c) Dimensionless Pressure Derivative Behavior for Case 2 and L = 40 ft.

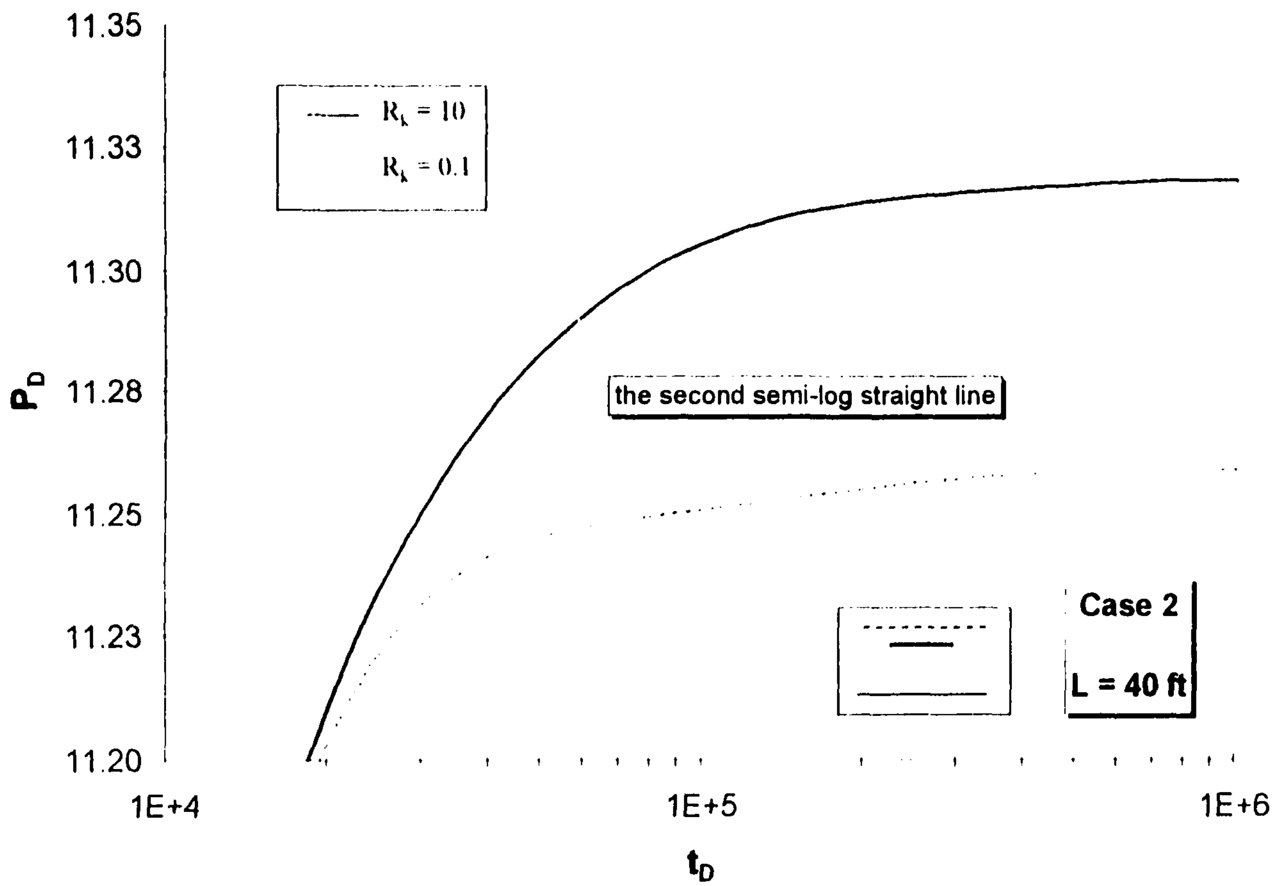

Figure 5.2.4(d) Dimensionless Pressure Behavior for Case 2 and L = 40 ft.

Showing The Second Radial Flow

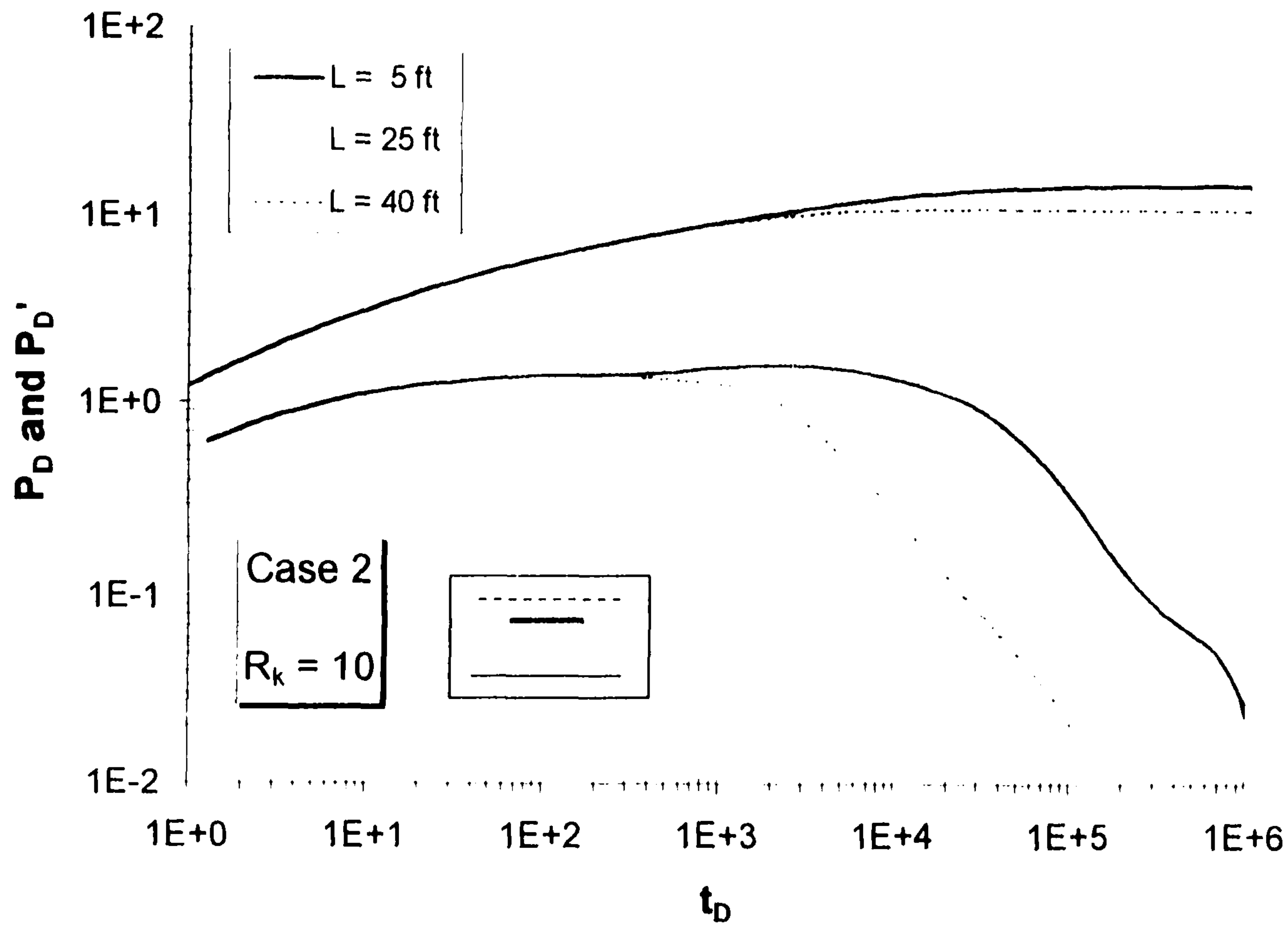

Figure 5.2.5(a) Dimensionless Pressure and Dimensionless Pressure Derivative Behavior for Case 2 and $R_k = 10$

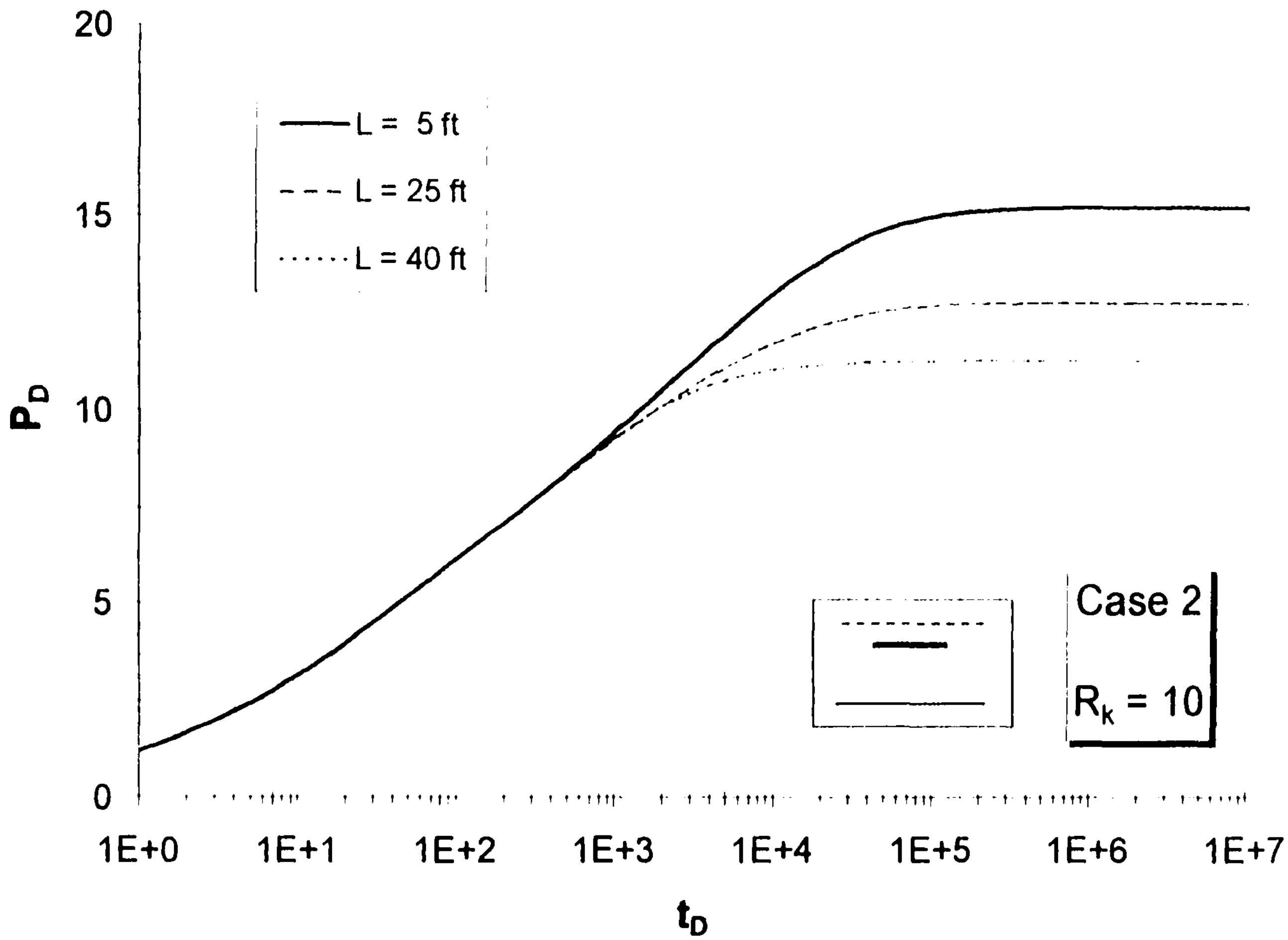

Figure 5.2.5(b) Dimensionless Pressure Behavior for Case 2 and $R_k = 10$

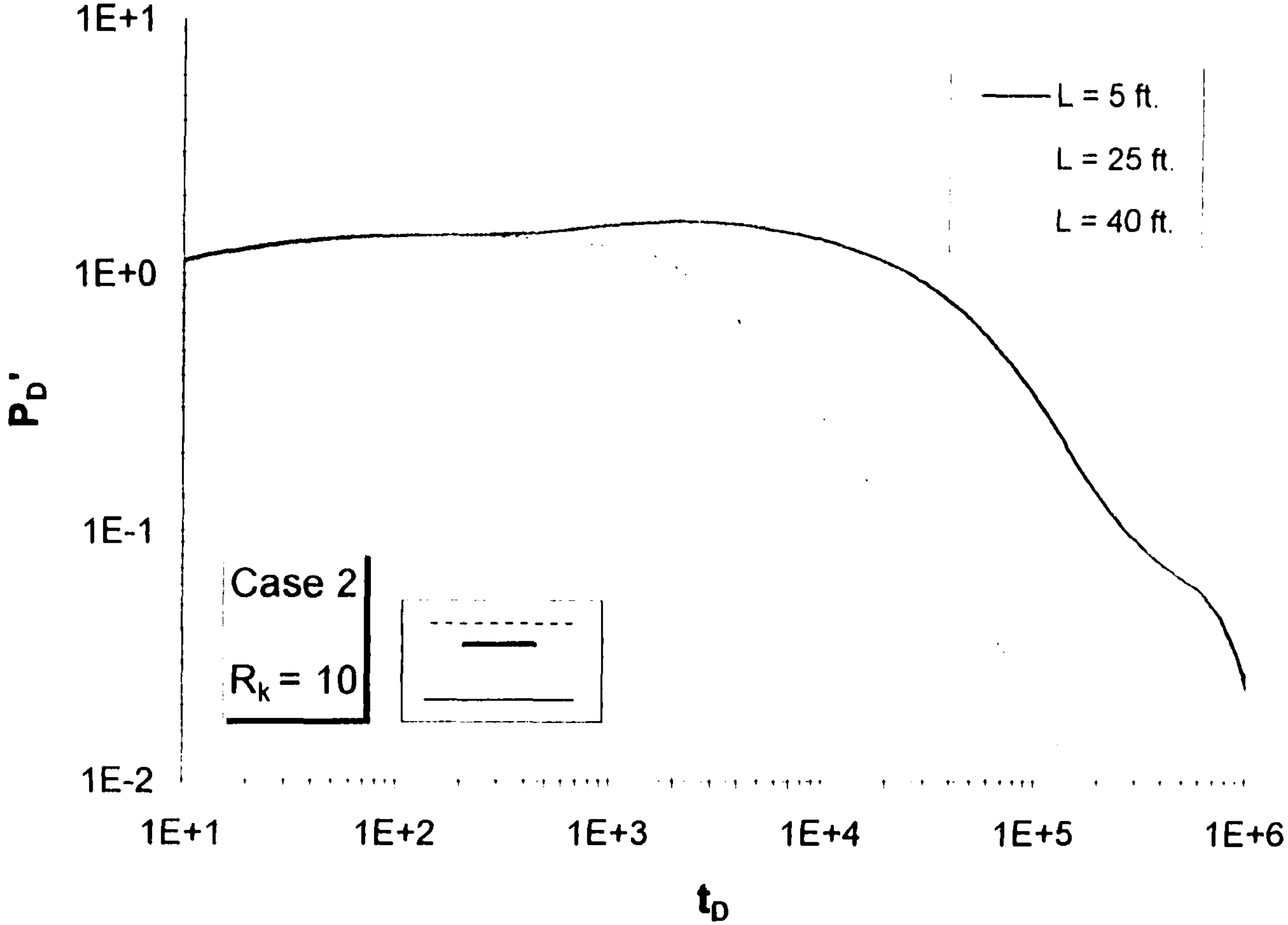

Figure 5.2.5(c) Dimensionless Pressure Derivative Behavior for Case 2 and $R_k = 10$

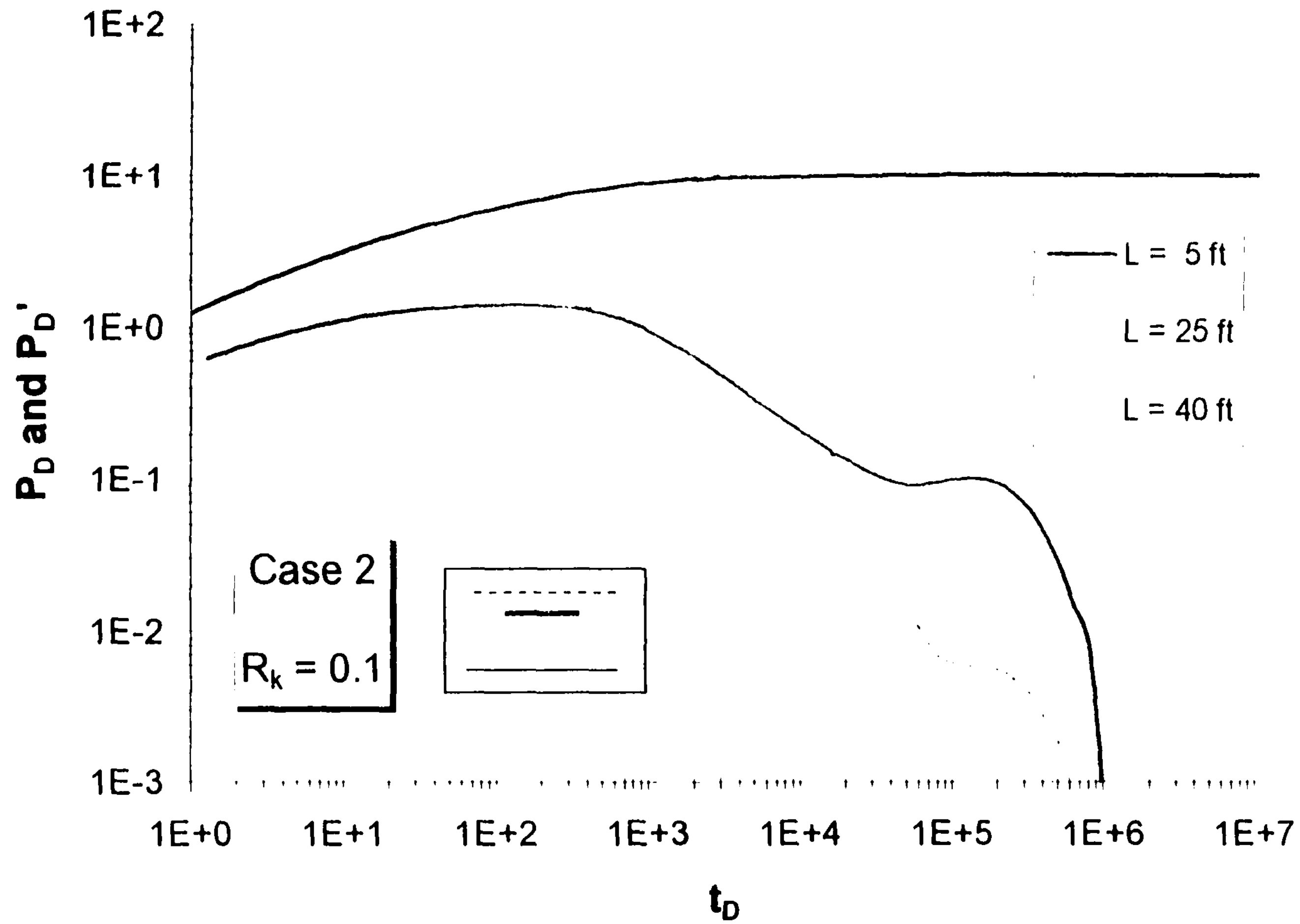

Figure 5.2.6(a) Dimensionless Pressure and Dimensionless Pressure Derivative Behavior

for Case 2 and $R_k = 0.1$

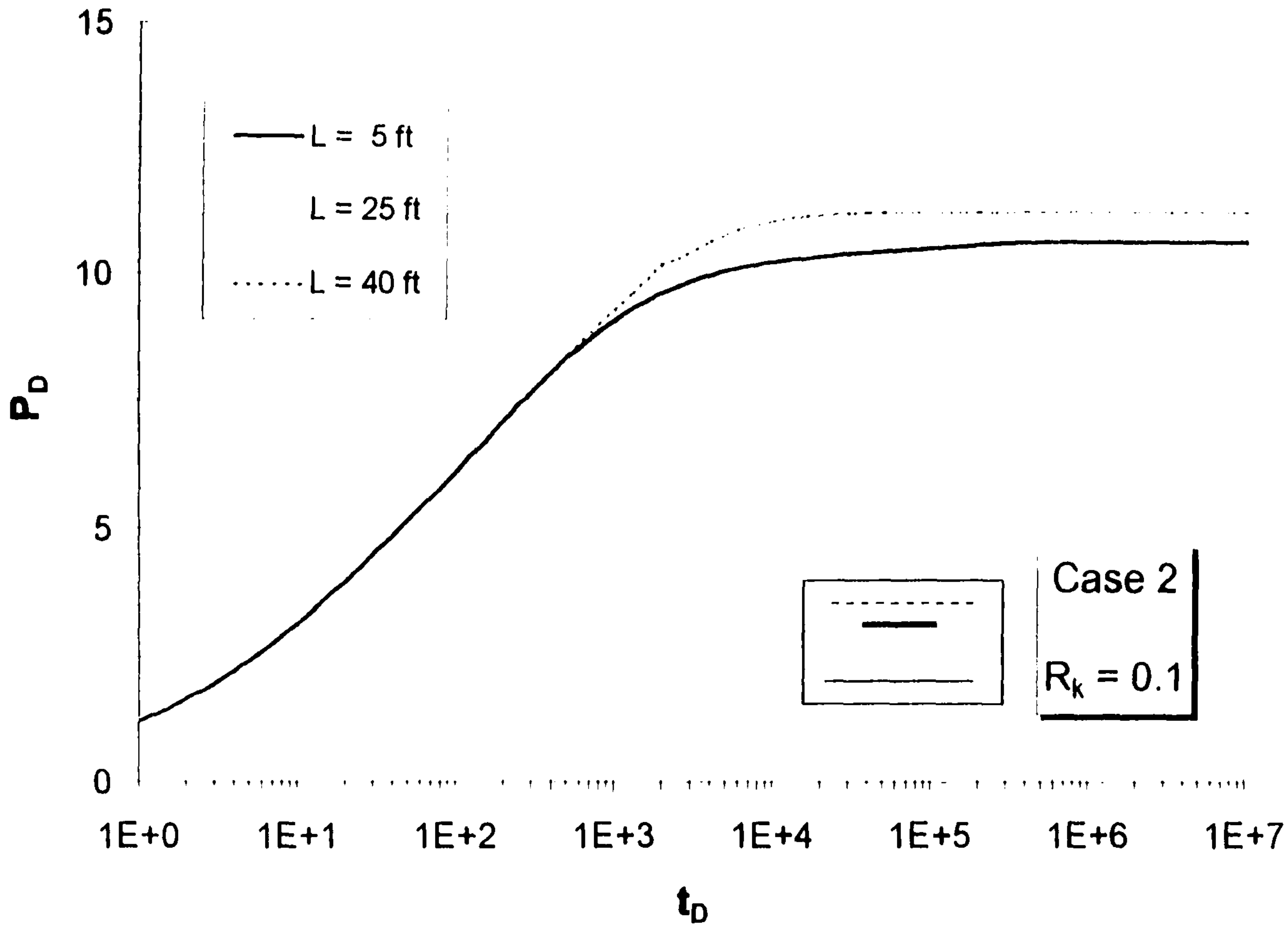

Figure 5.2.6(b) Dimensionless Pressure Behavior for Case 2 and $R_k = 0.1$

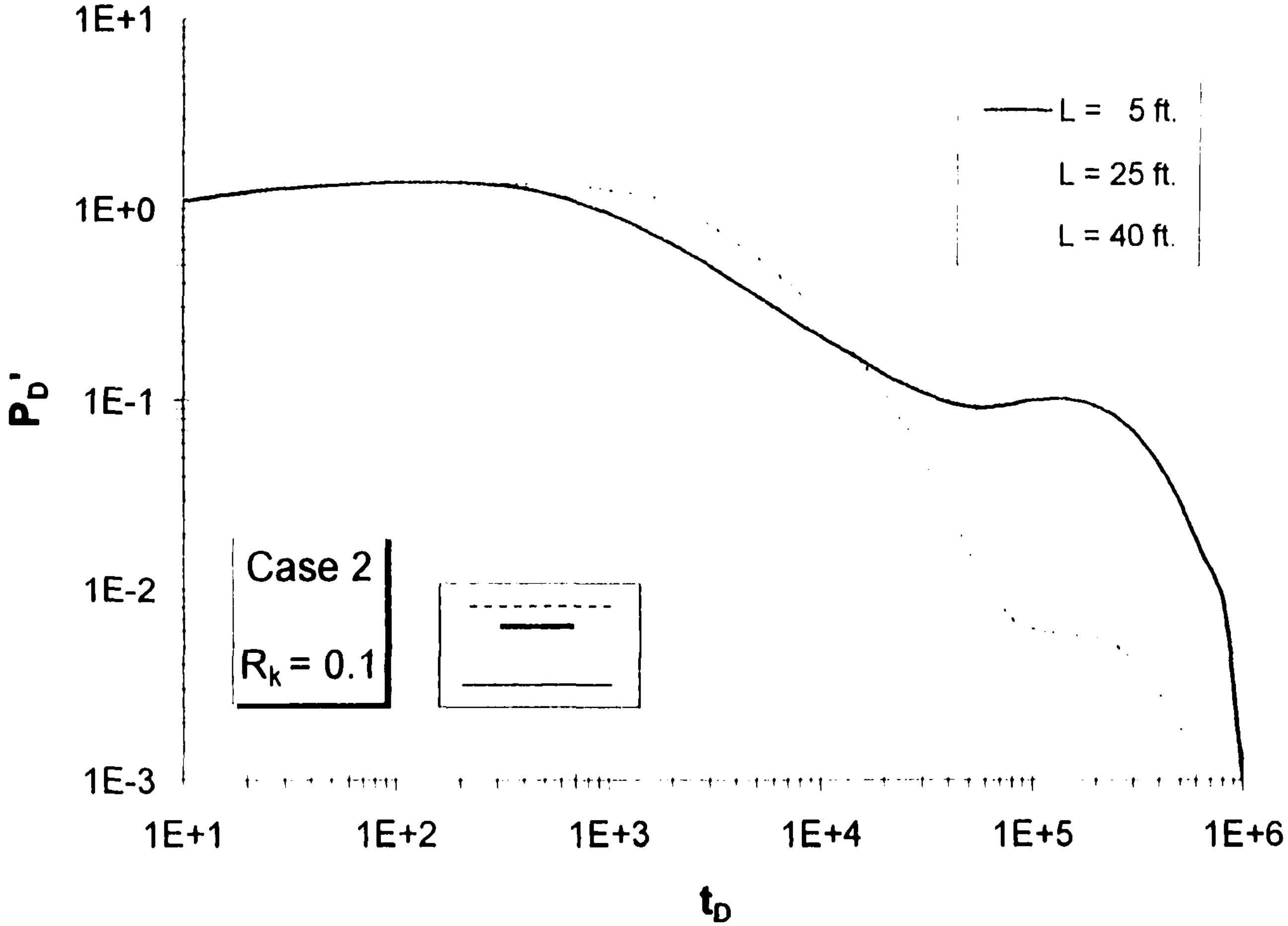

Figure 5.2.6(c) Dimensionless Pressure Derivative Behavior for Case 2 and $R_k = 0.1$

APPENDIX E

LIST OF FIGURES IN CASE 5.3

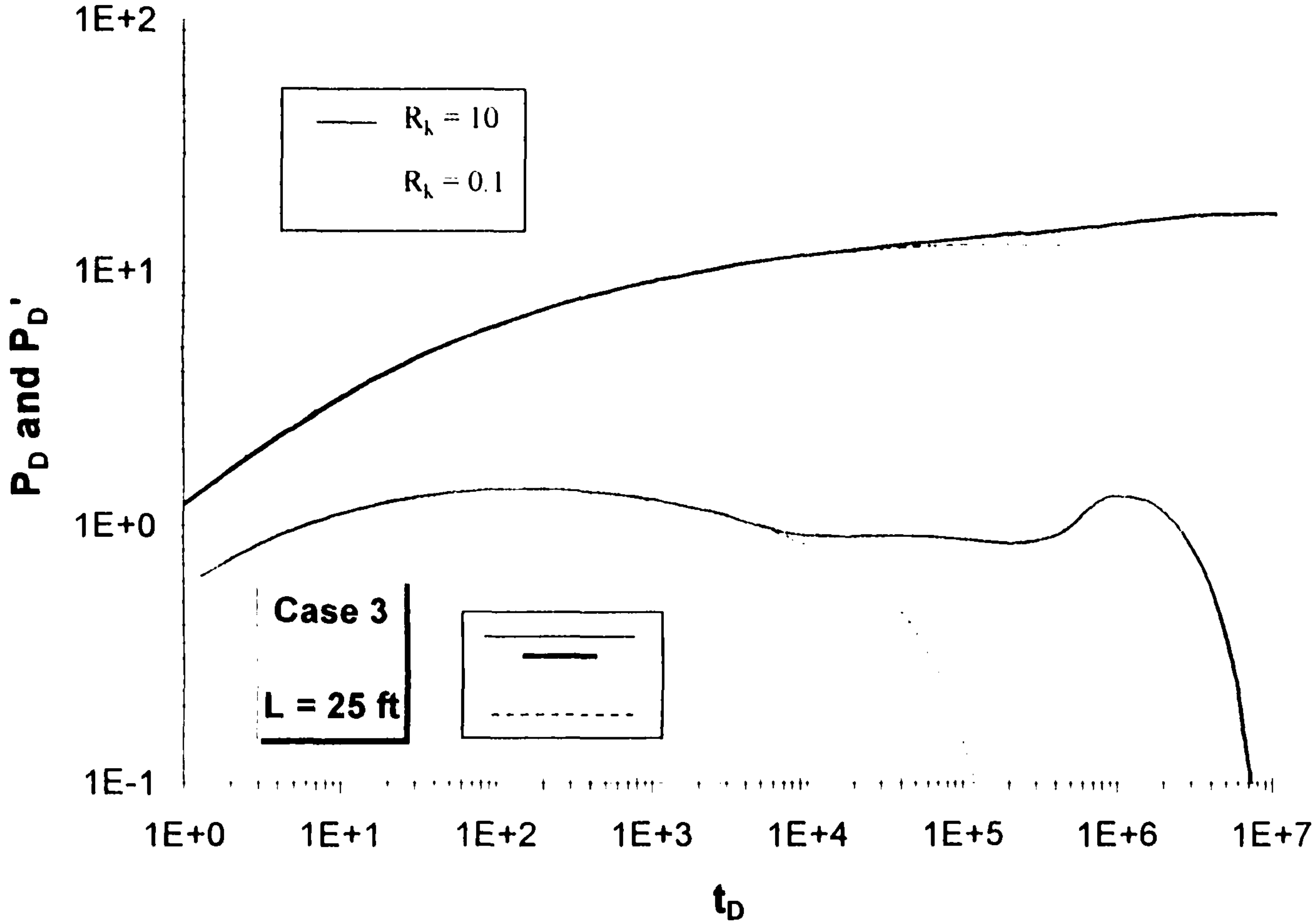

Figure 5.3.3(a) Dimensionless Pressure and Dimensionless Pressure Derivative Behavior

for Case 3 and L – 25 ft.

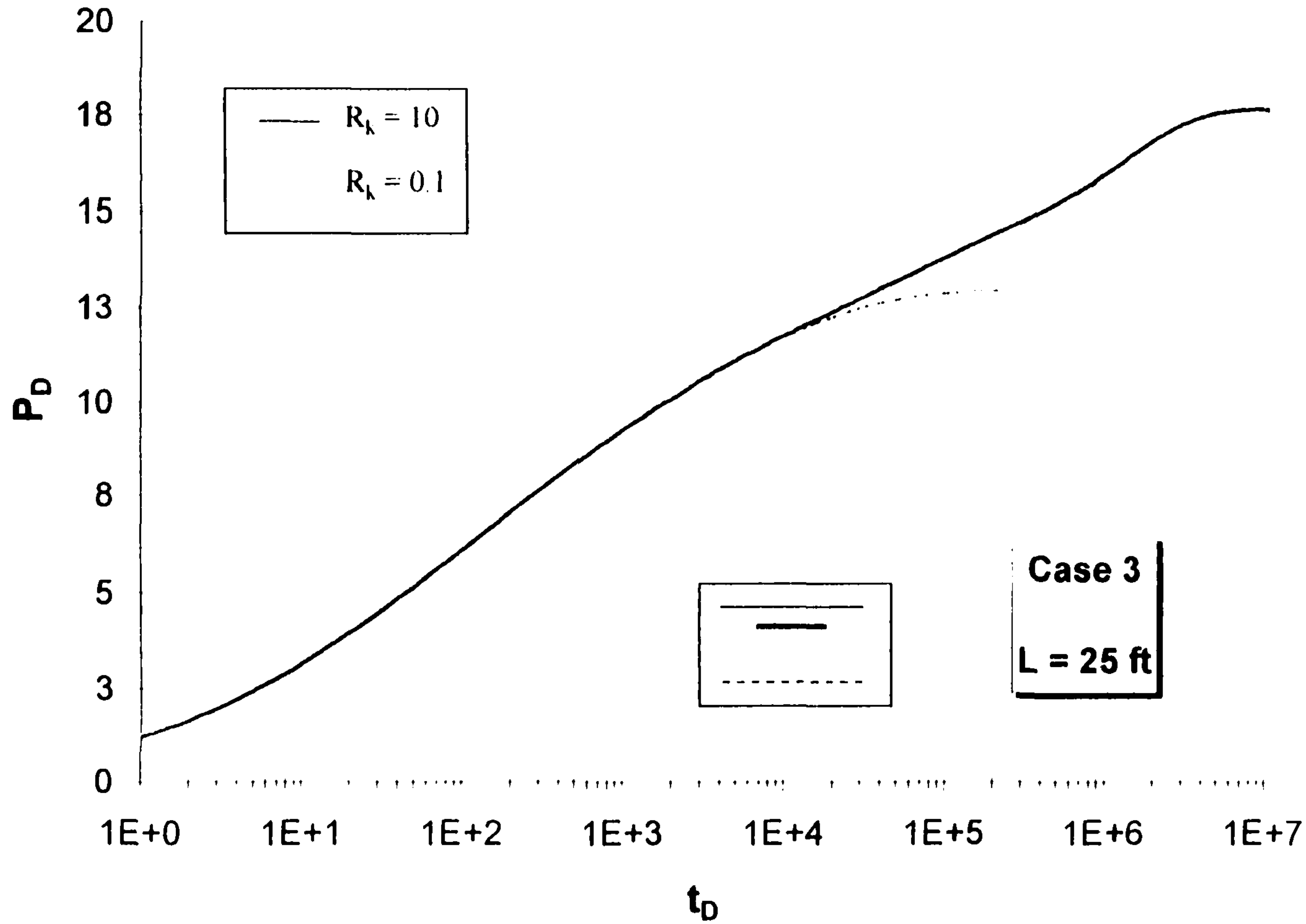

Figure 5.3.3(b) Dimensionless Pressure Behavior for Case 3 and L = 25 ft.

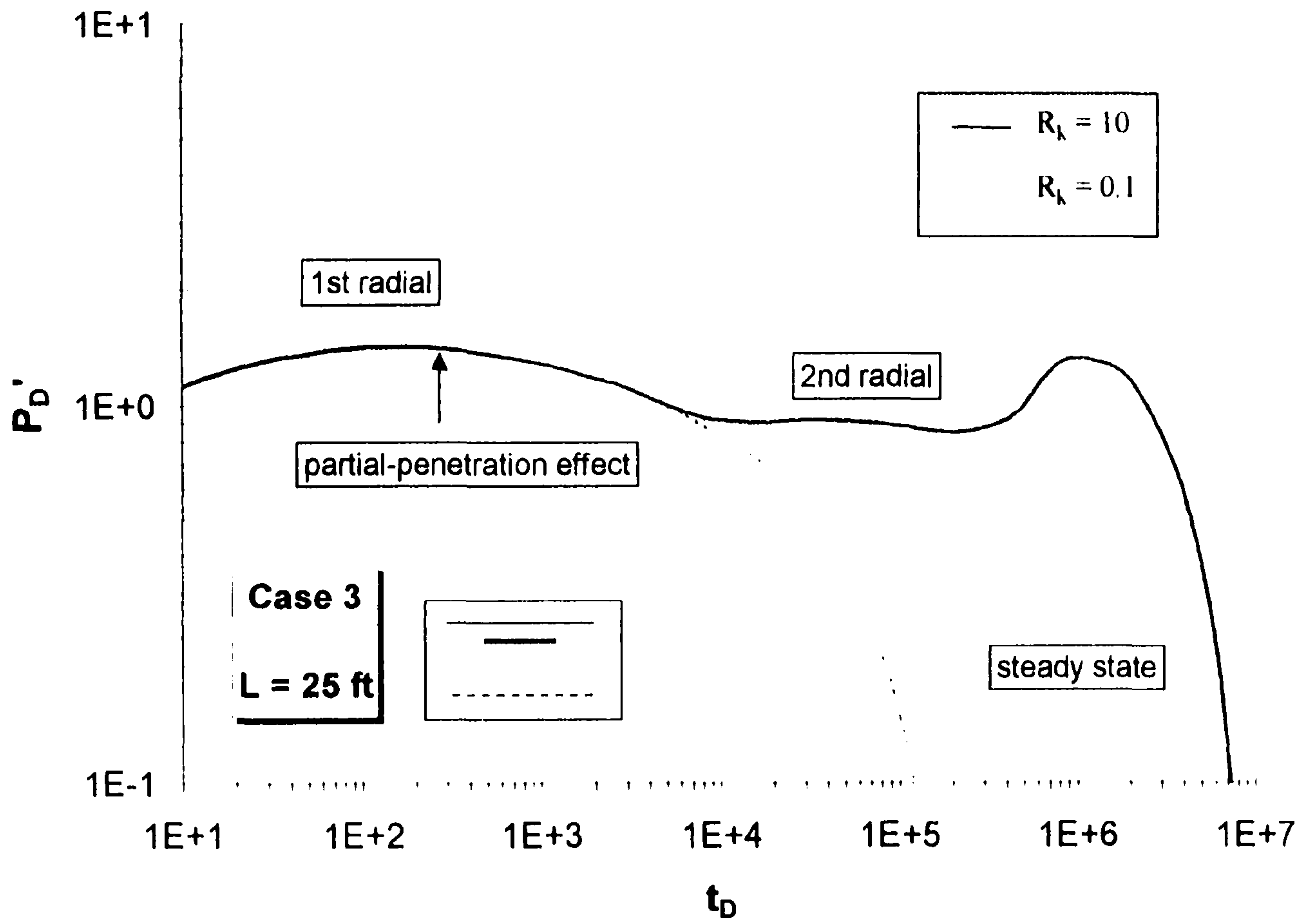

Figure 5.3.3(c) Dimensionless Pressure Derivative Behavior for Case 3 and L = 25 ft.

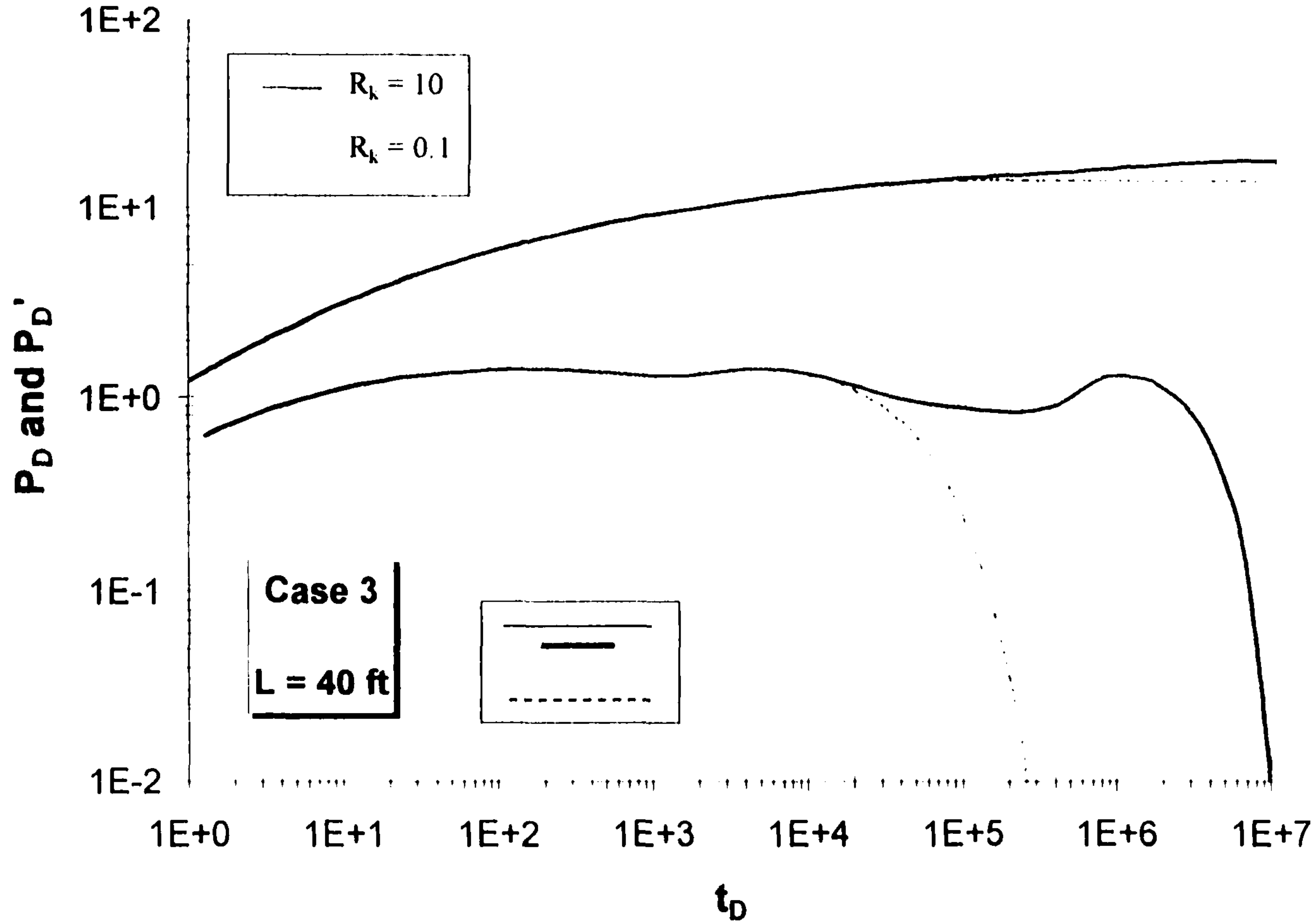

Figure 5.3.4(a) Dimensionless Pressure and Dimensionless Pressure Derivative Behavior for Case 3 and L = 40 ft.

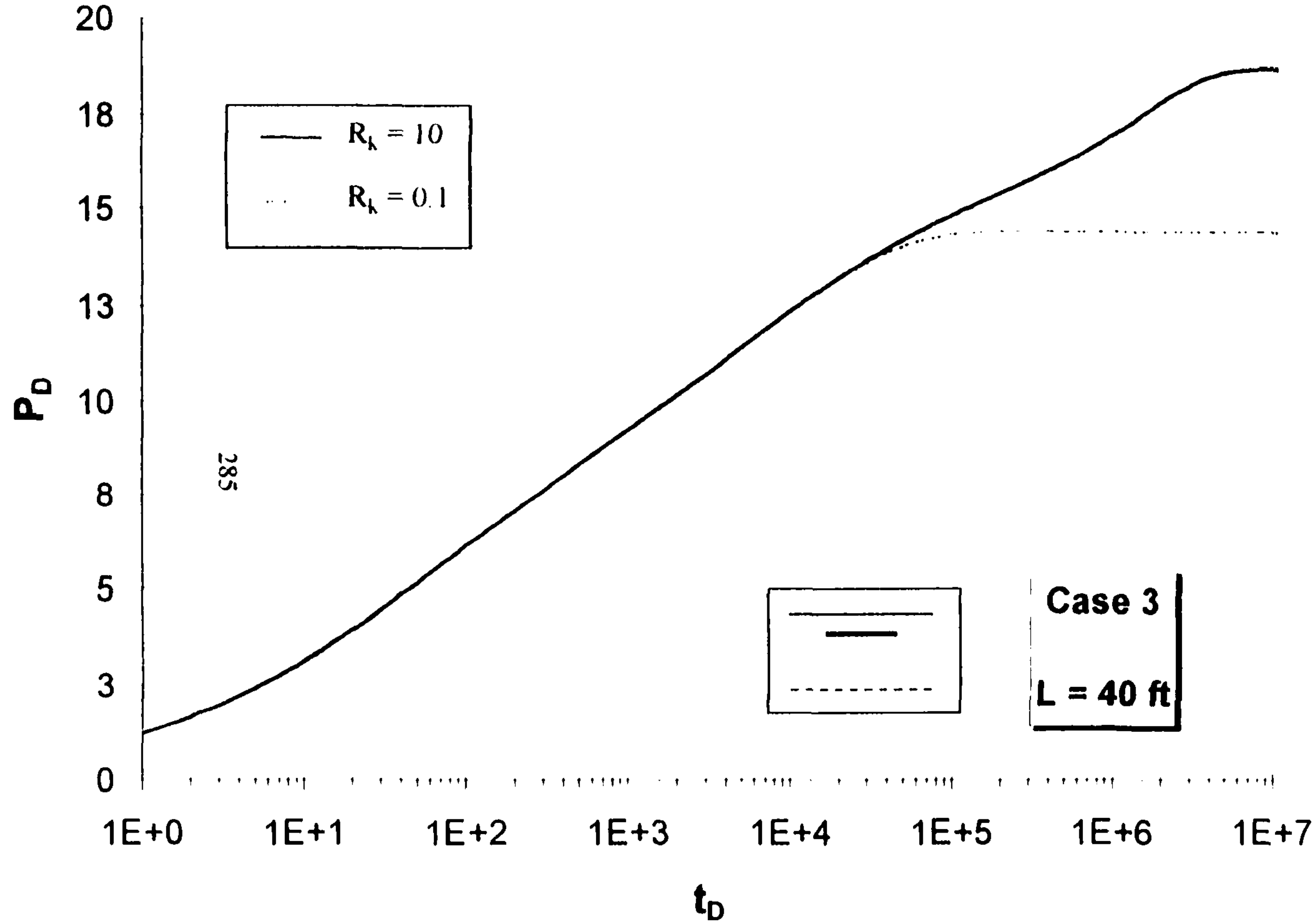

Figure 5.3.4(b) Dimensionless Pressure Behavior for Case 3 and L = 40 ft.

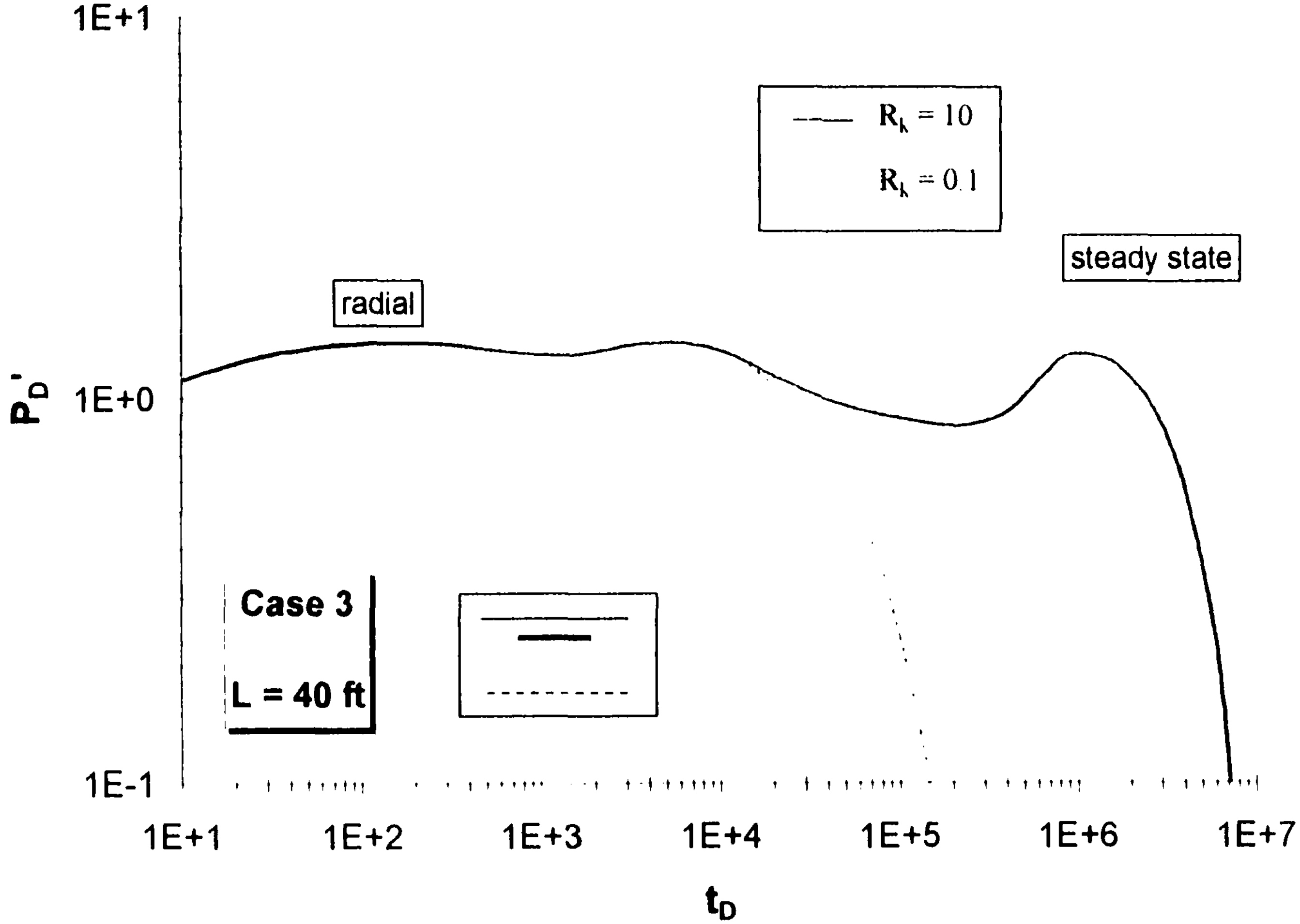

Figure 5.3.4(c) Dimensionless Pressure Derivative Behavior for Case 3 and L = 40 ft.

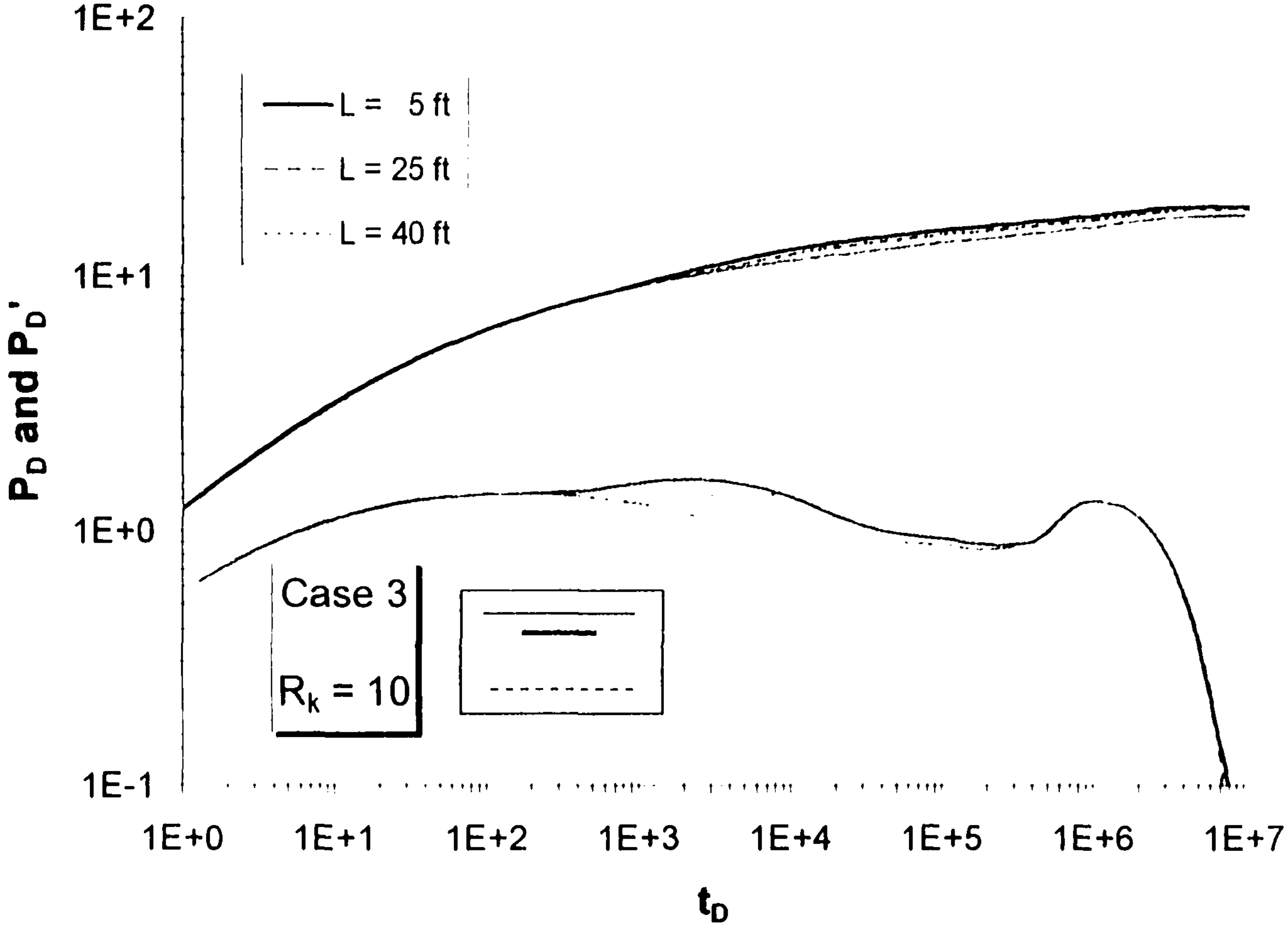

Figure 5.3.5(a) Dimensionless Pressure and Dimensionless Pressure Derivative Behavior

for Case 3 and $R_k = 10$

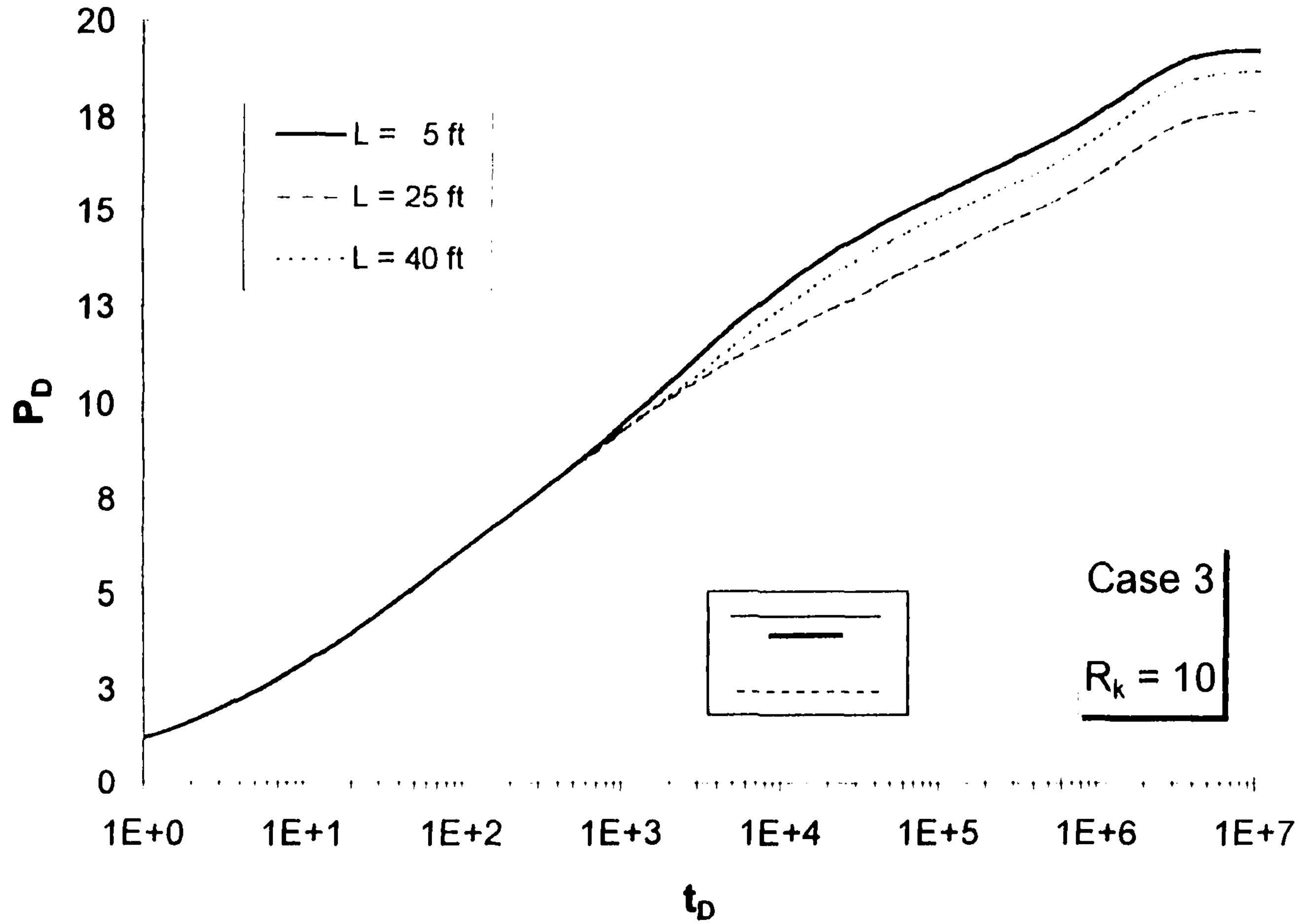

Figure 5.3.5(b) Dimensionless Pressure Behavior for Case 3 and $R_k = 10$

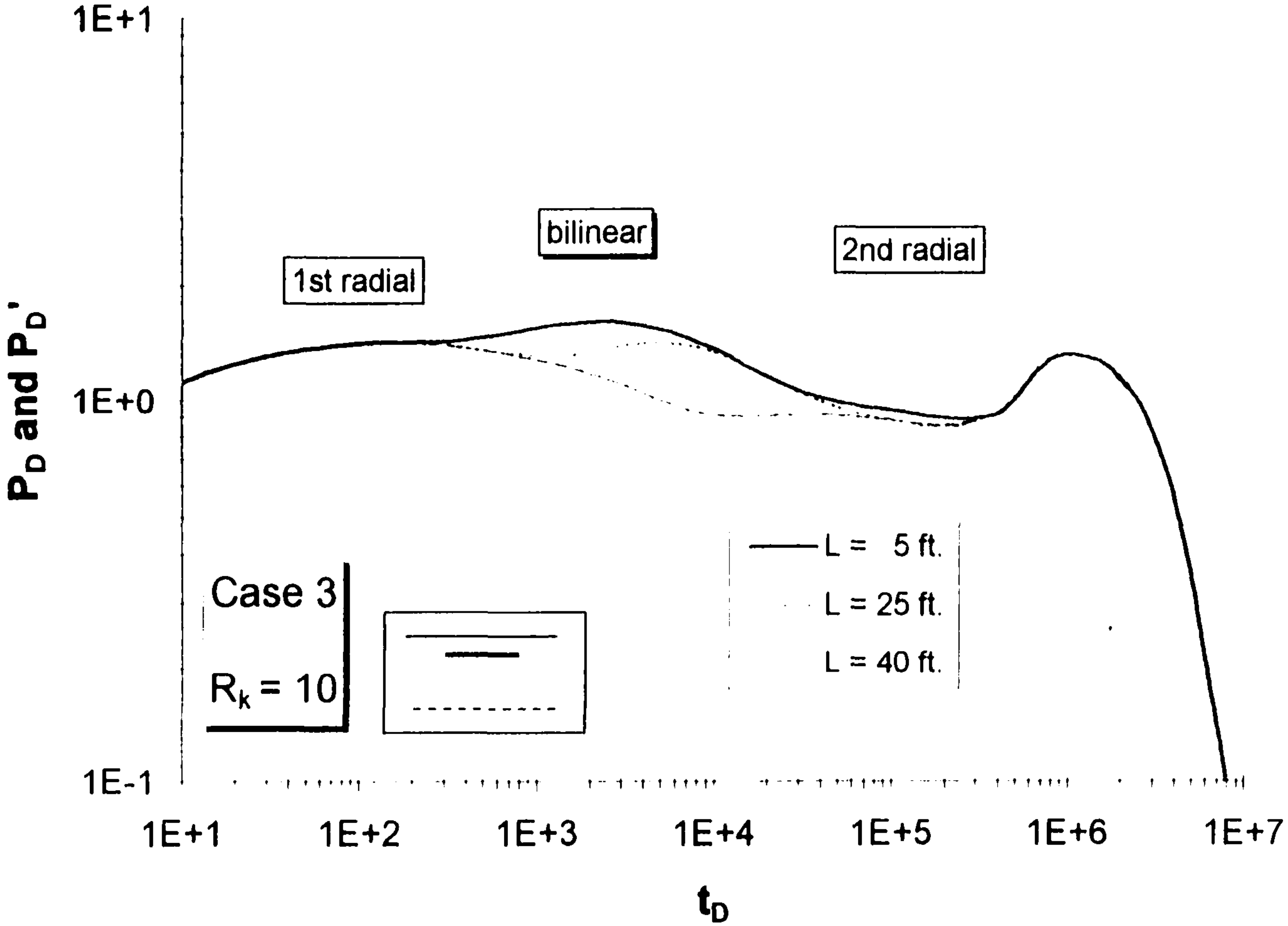

Figure 5.3.5(c) Dimensionless Pressure Derivative Behavior for Case 3 and R_k = 10

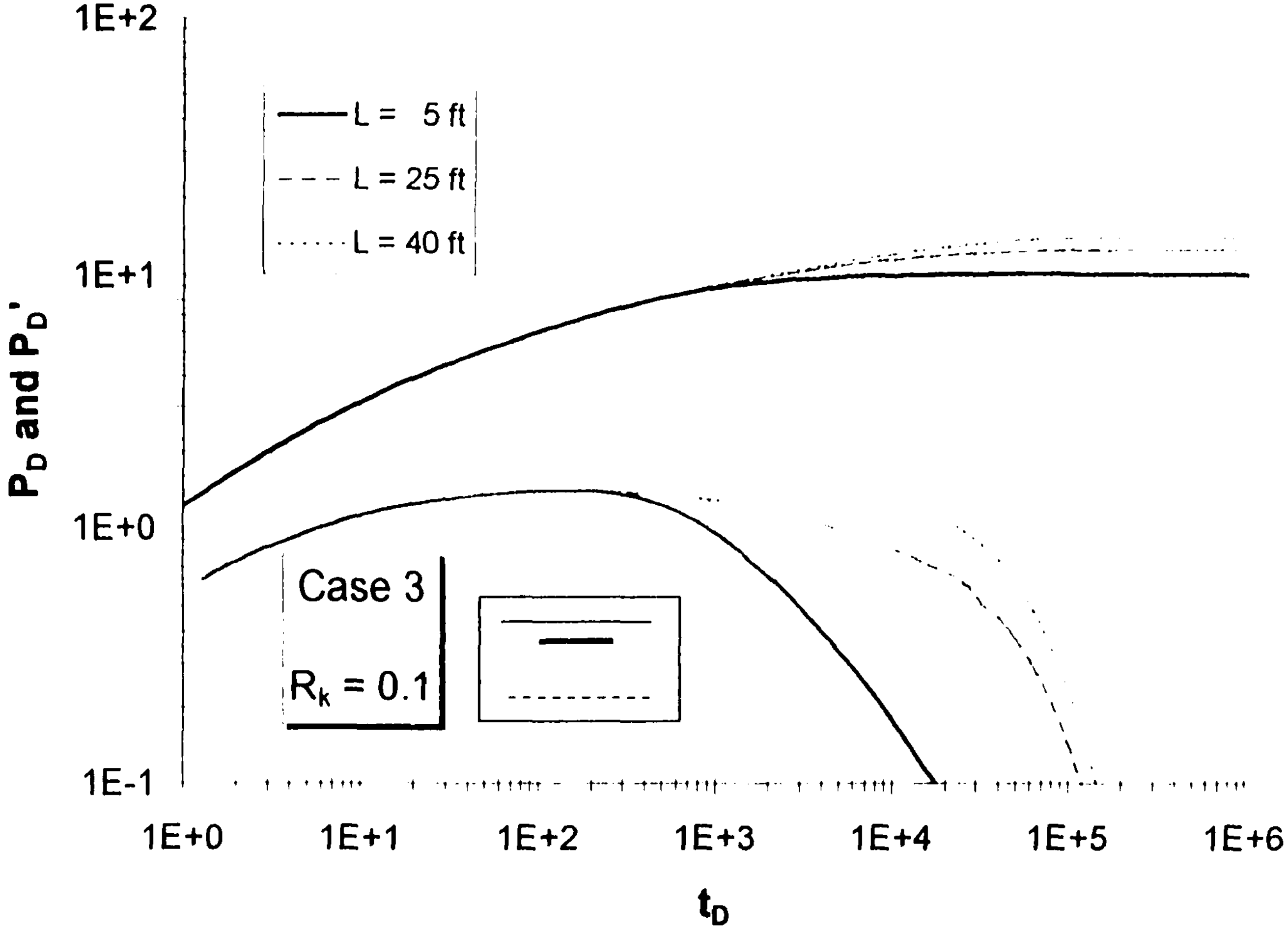

Figure 5.3.6(a) Dimensionless Pressure and Dimensionless Pressure Derivative Behavior for Case 3 and $R_k = 0.1$

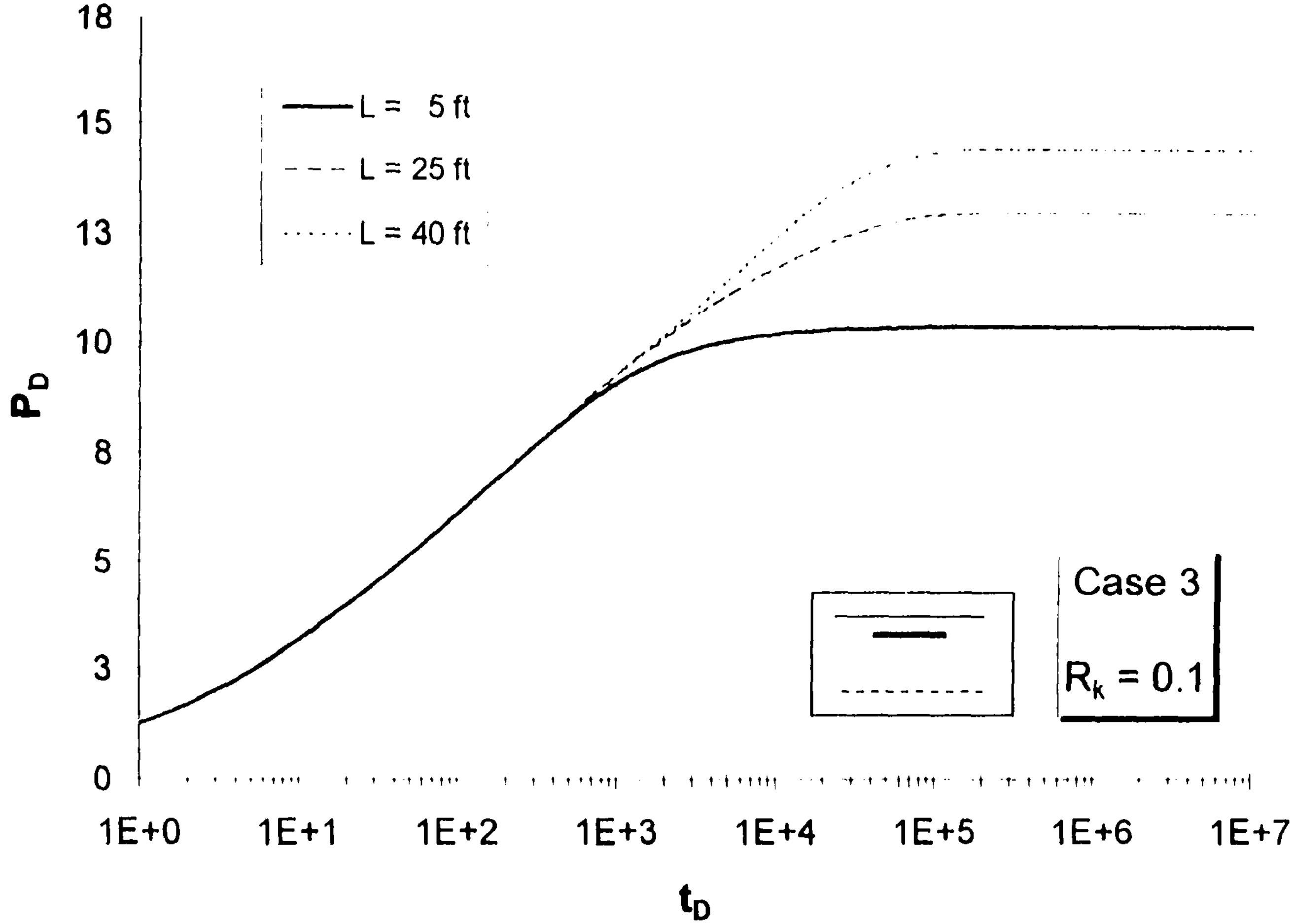

Figure 5.3.6(b) Dimensionless Pressure Behavior for Case 3 and $R_k = 0.1$

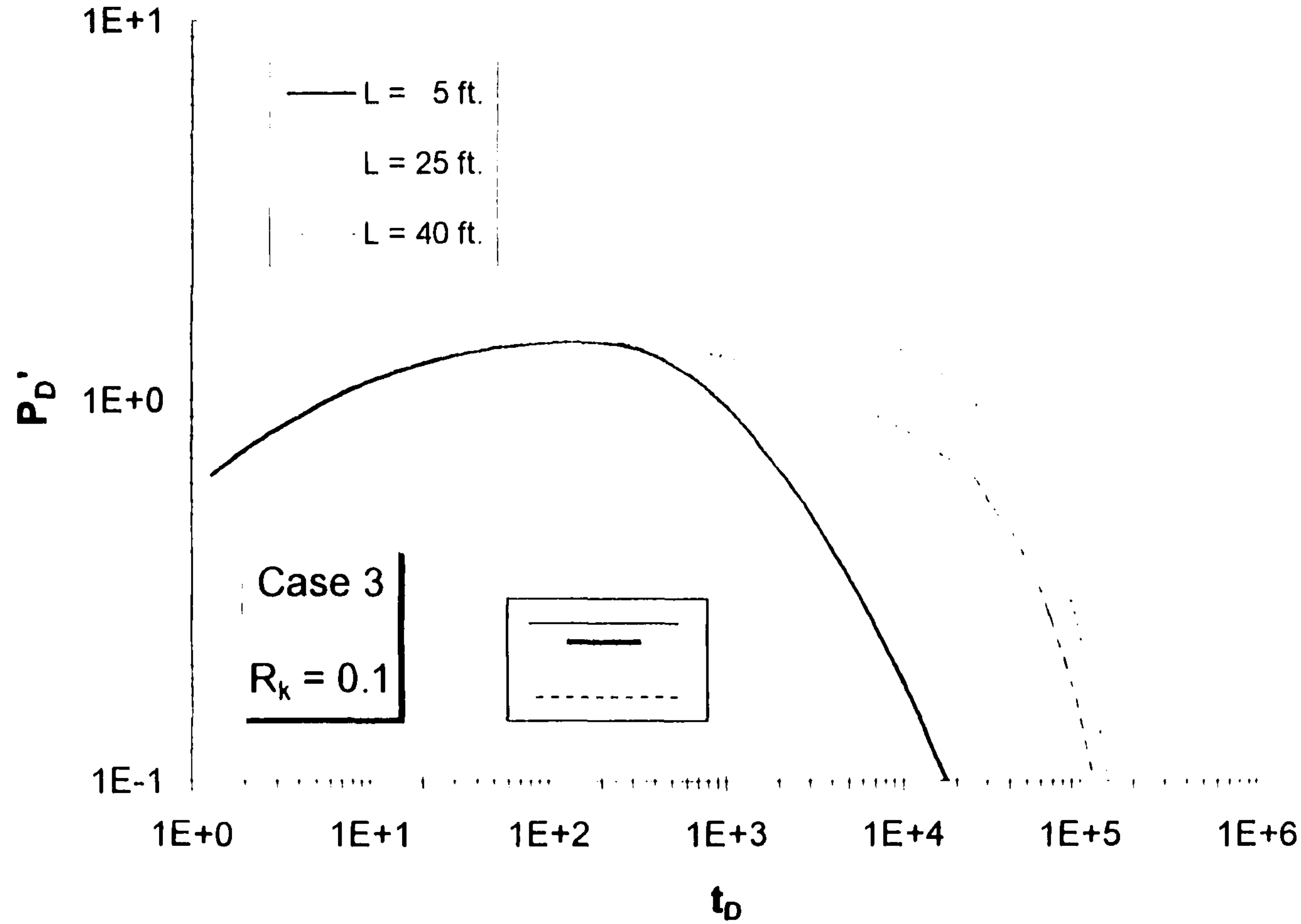

Figure 5.3.6(c) Dimensionless Pressure Derivative Behavior for Case 3 and $R_k = 0.1$

APPENDIX F

LIST OF FIGURES IN CASE 5.4

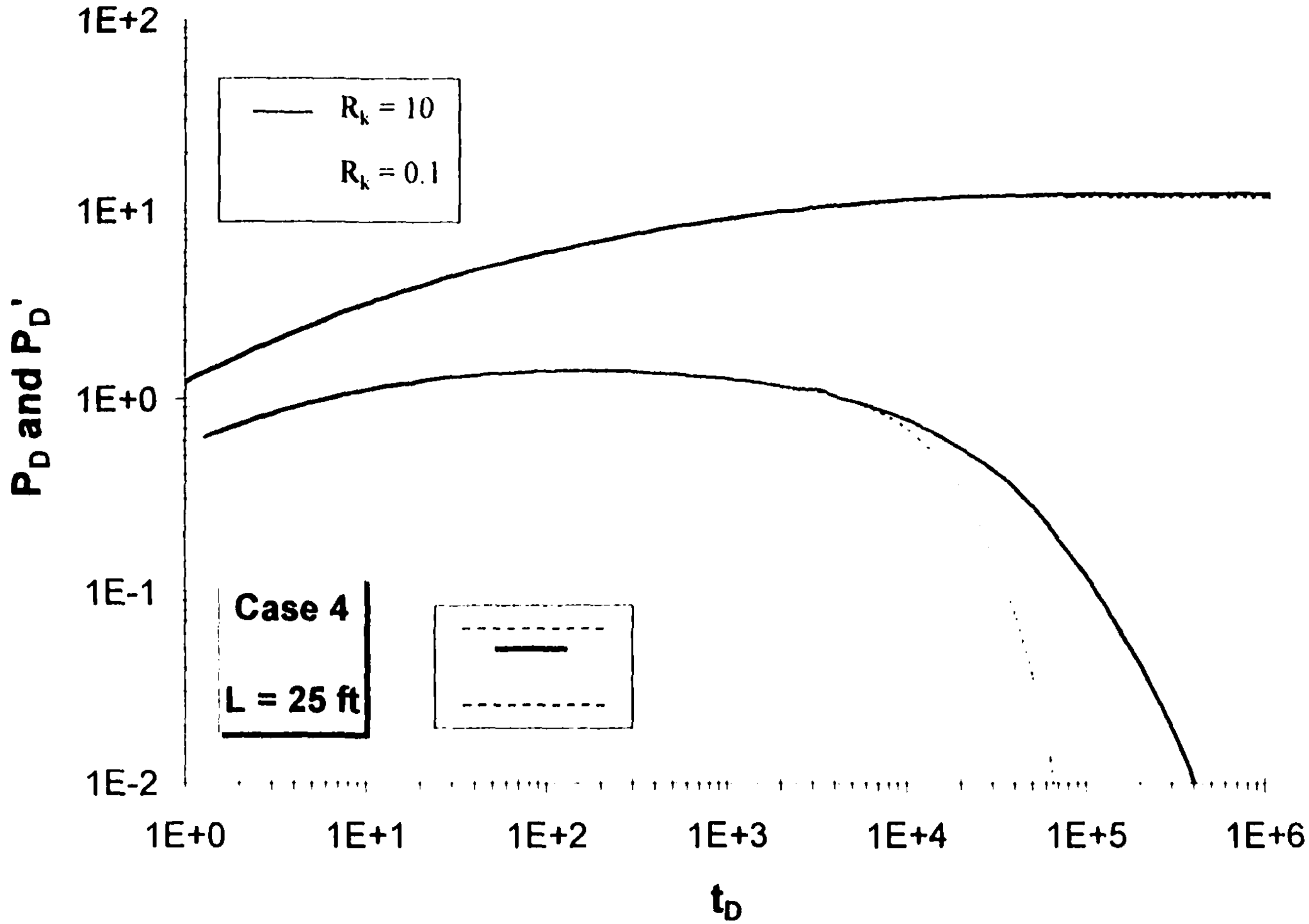

Figure 5.4.3(a) Dimensionless Pressure and Dimensionless Pressure Derivative Behavior

for Case 4 and L = 25 ft.

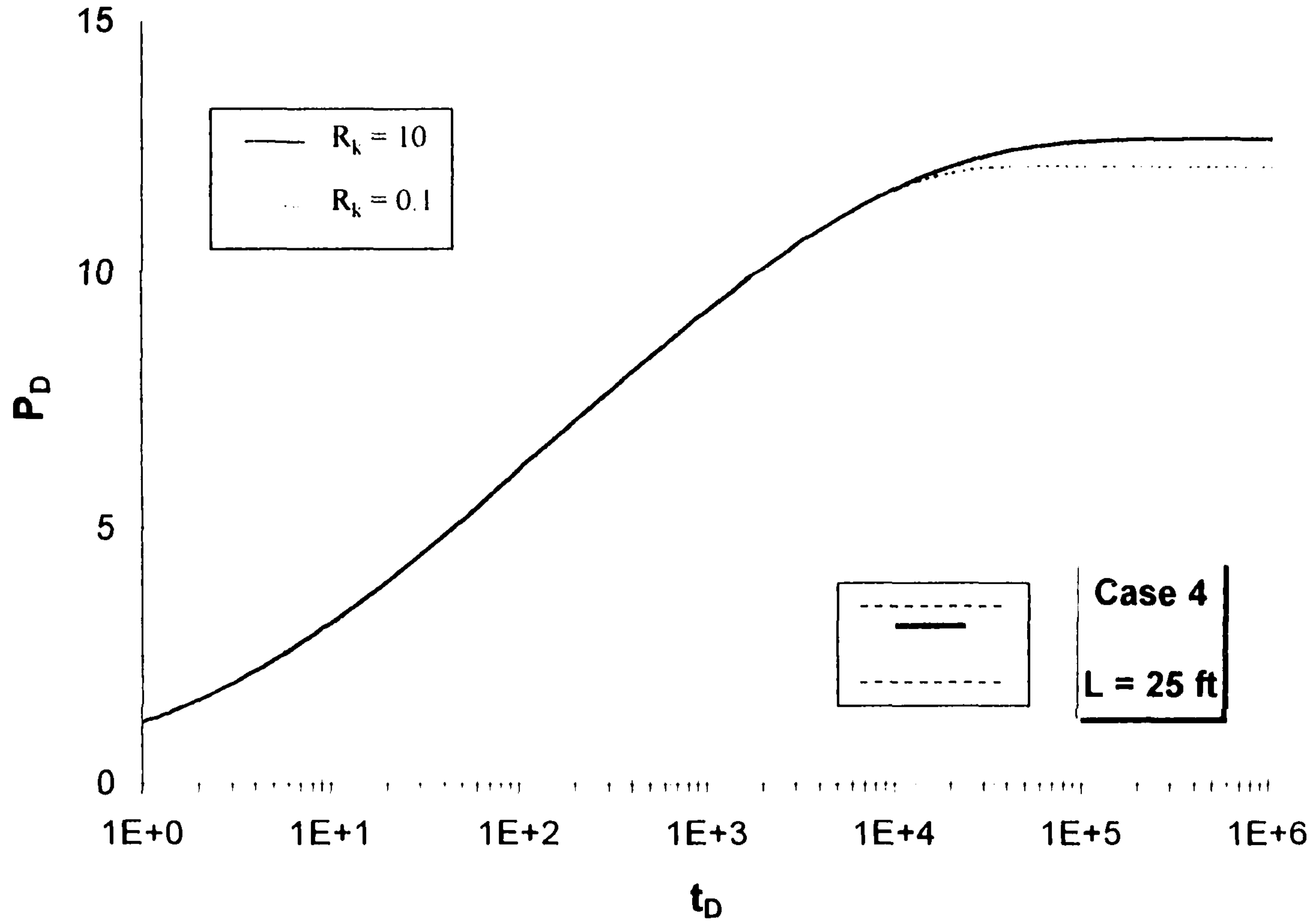

Figure 5.4.3(b) Dimensionless Pressure Behavior for Case 4 and L = 25 ft.

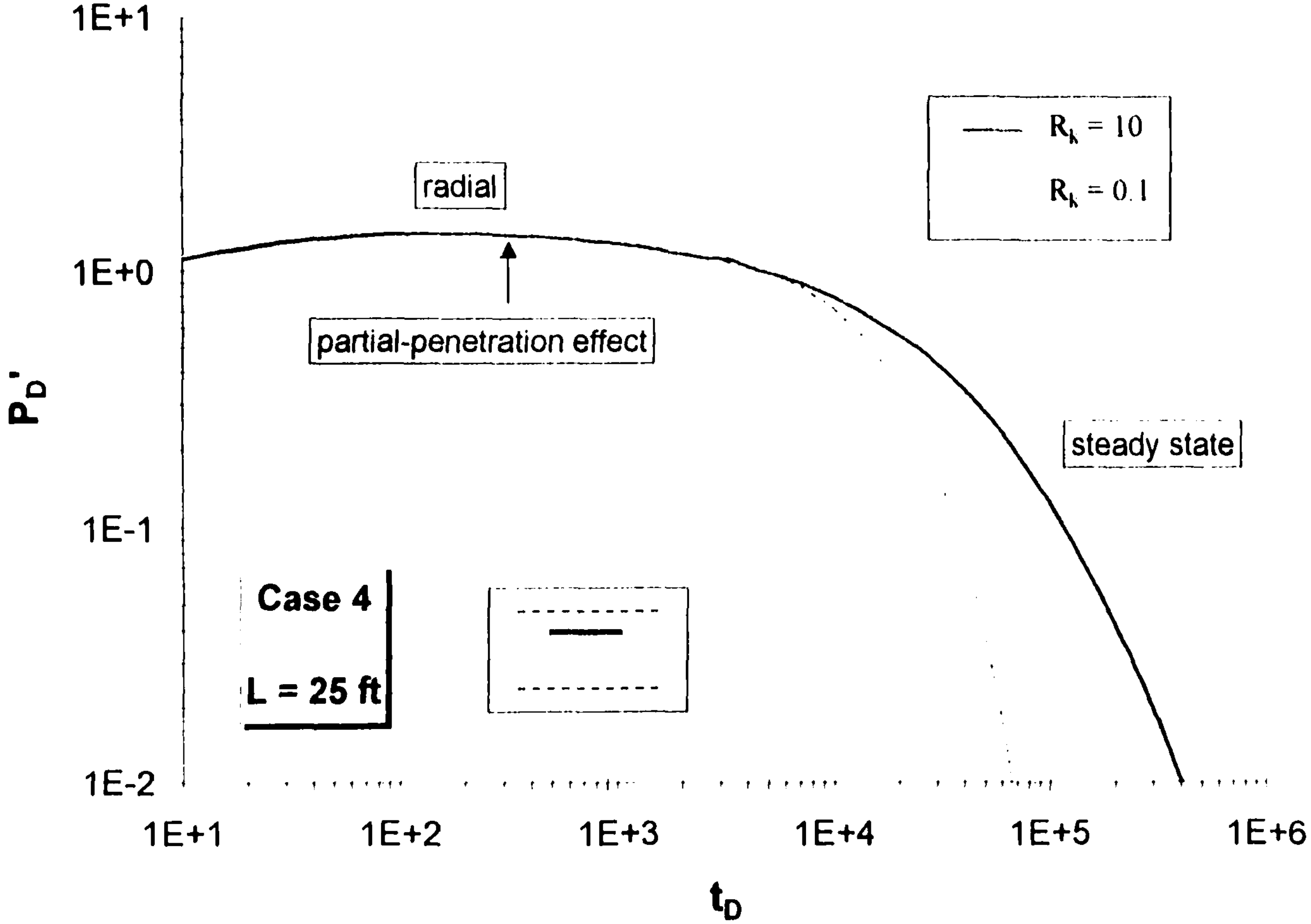

Figure 5.4.3(c) Dimensionless Pressure Derivative Behavior for Case 4 and L = 25 ft.

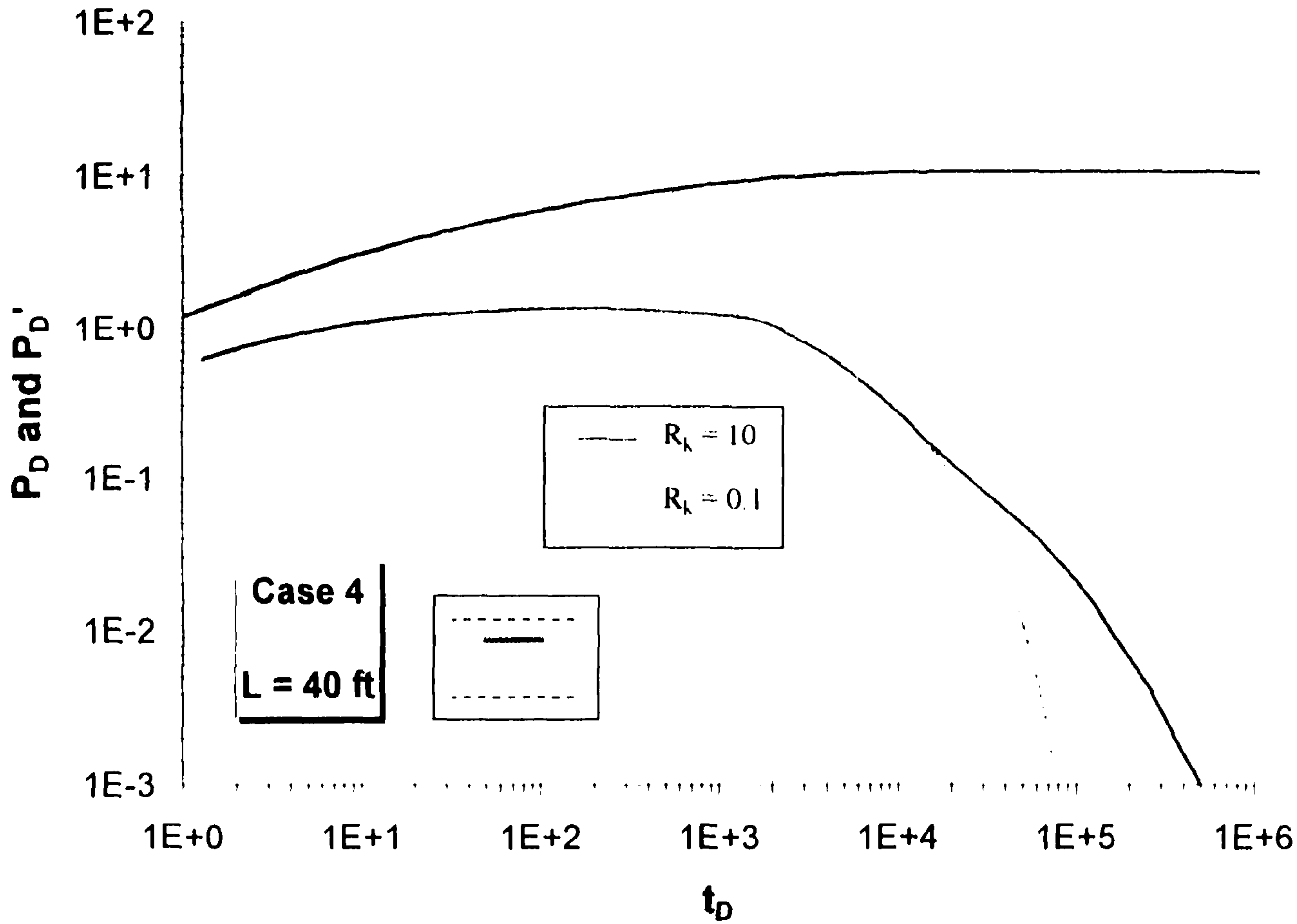

Figure 5.4.4(a) Dimensionless Pressure and Dimensionless Pressure Derivative Behavior for Case 4 and L = 40 ft.

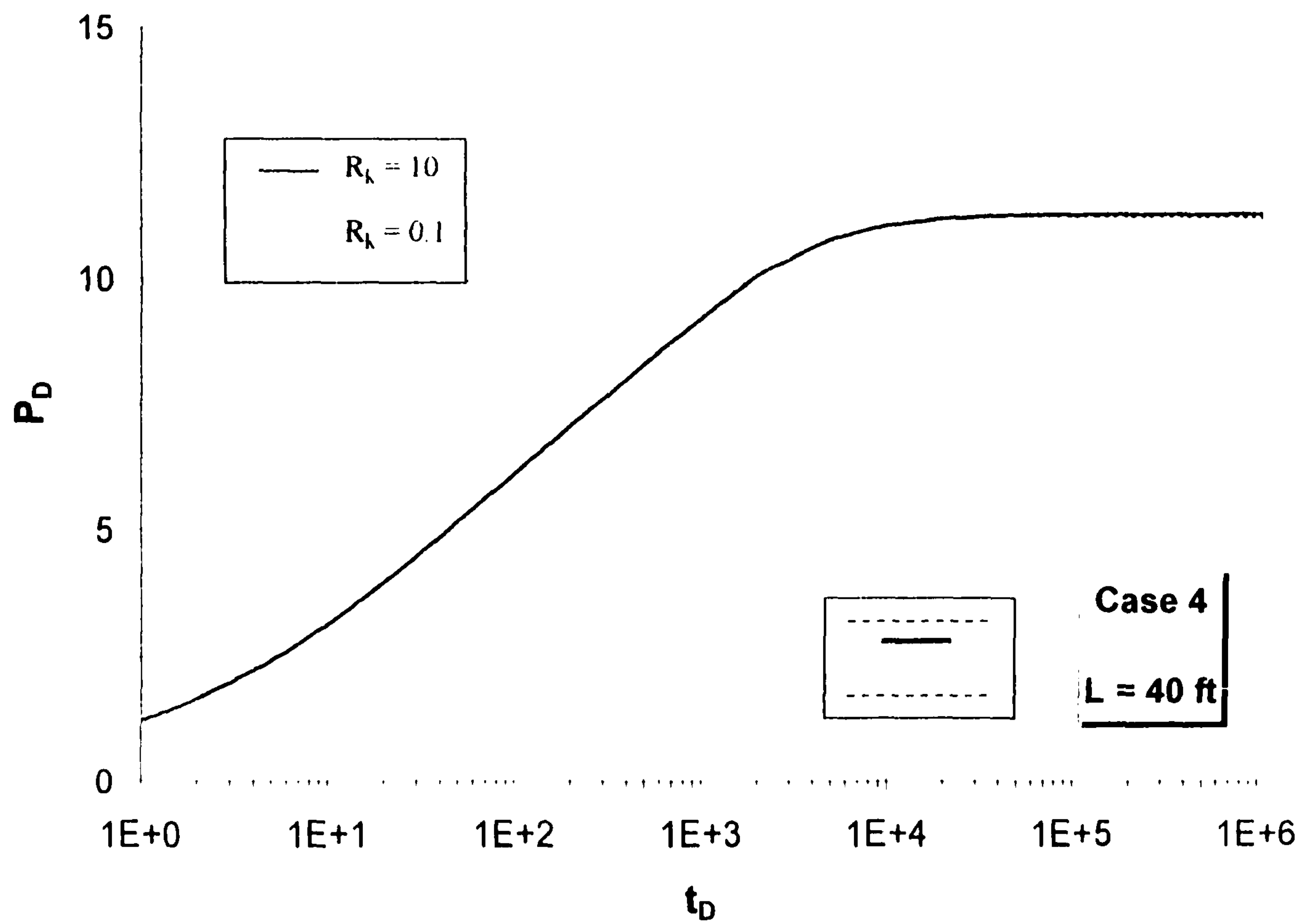

Figure 5.4.4(b) Dimensionless Pressure Behavior for Case 4 and L = 40 ft.

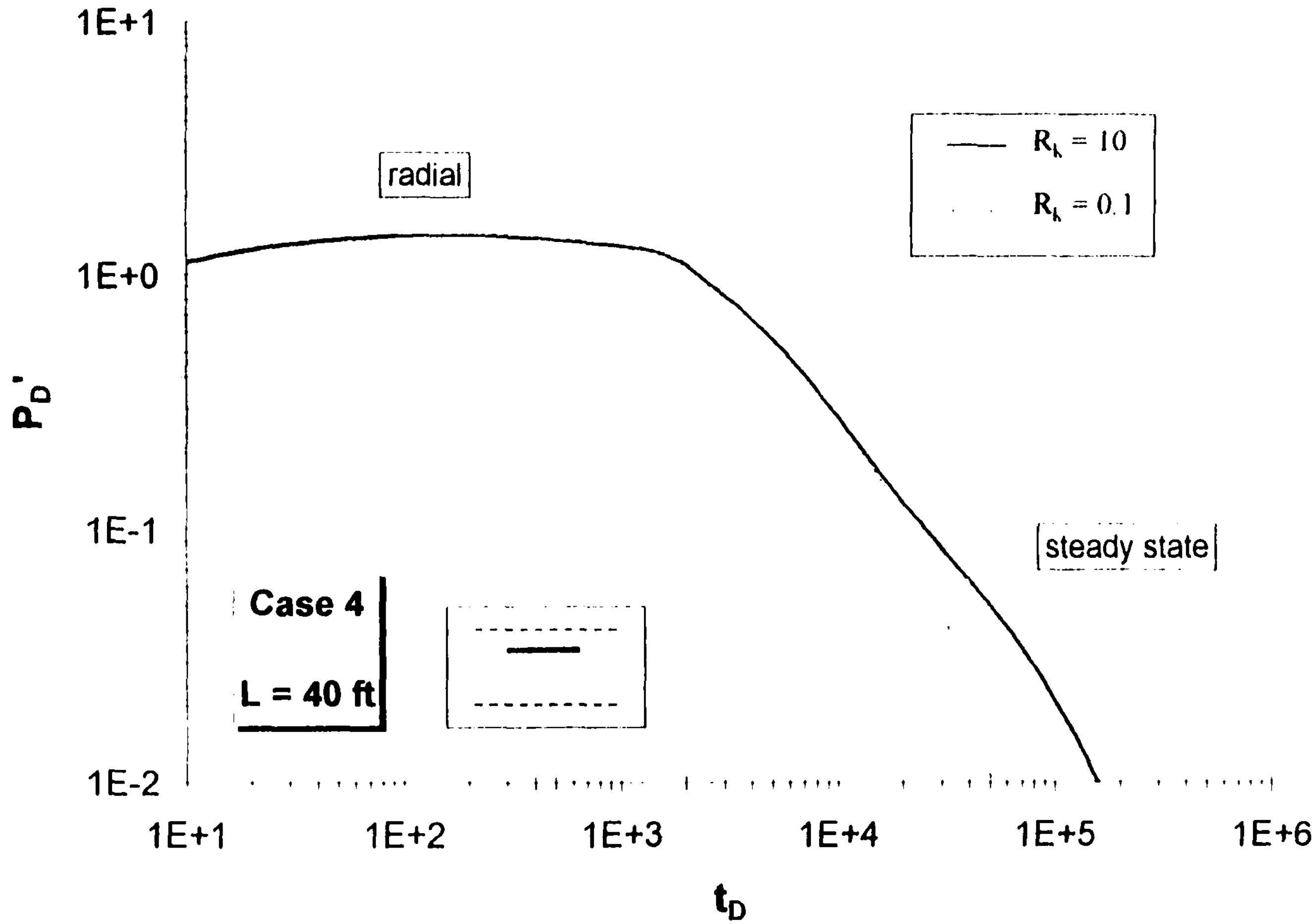

Figure 5.4.4(c) Dimensionless Pressure Derivative Behavior for Case 4 and L = 40 ft.

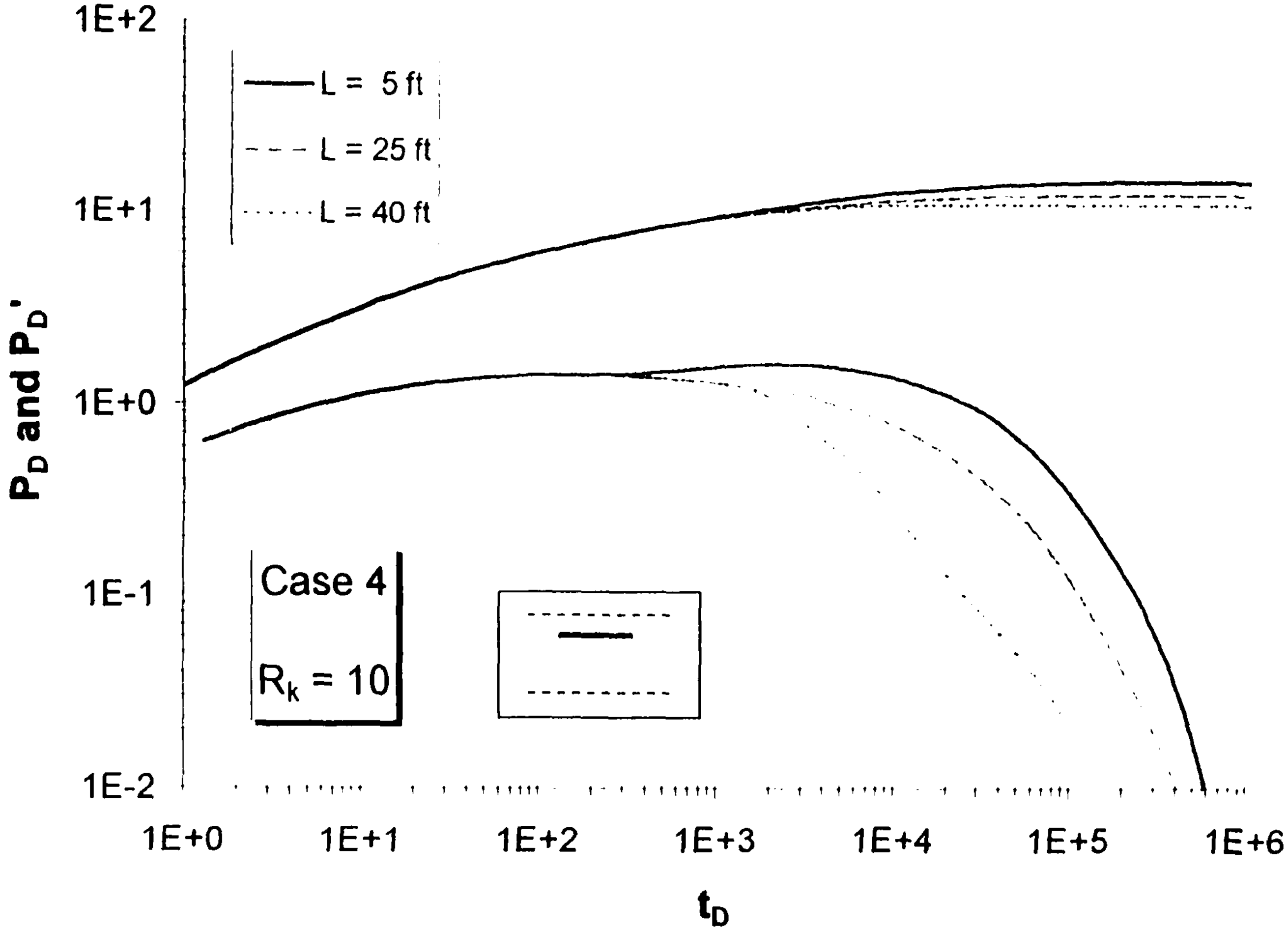

Figure 5.4.5(a) Dimensionless Pressure and Dimensionless Pressure Derivative Behavior for Case 4 and $R_k = 10$

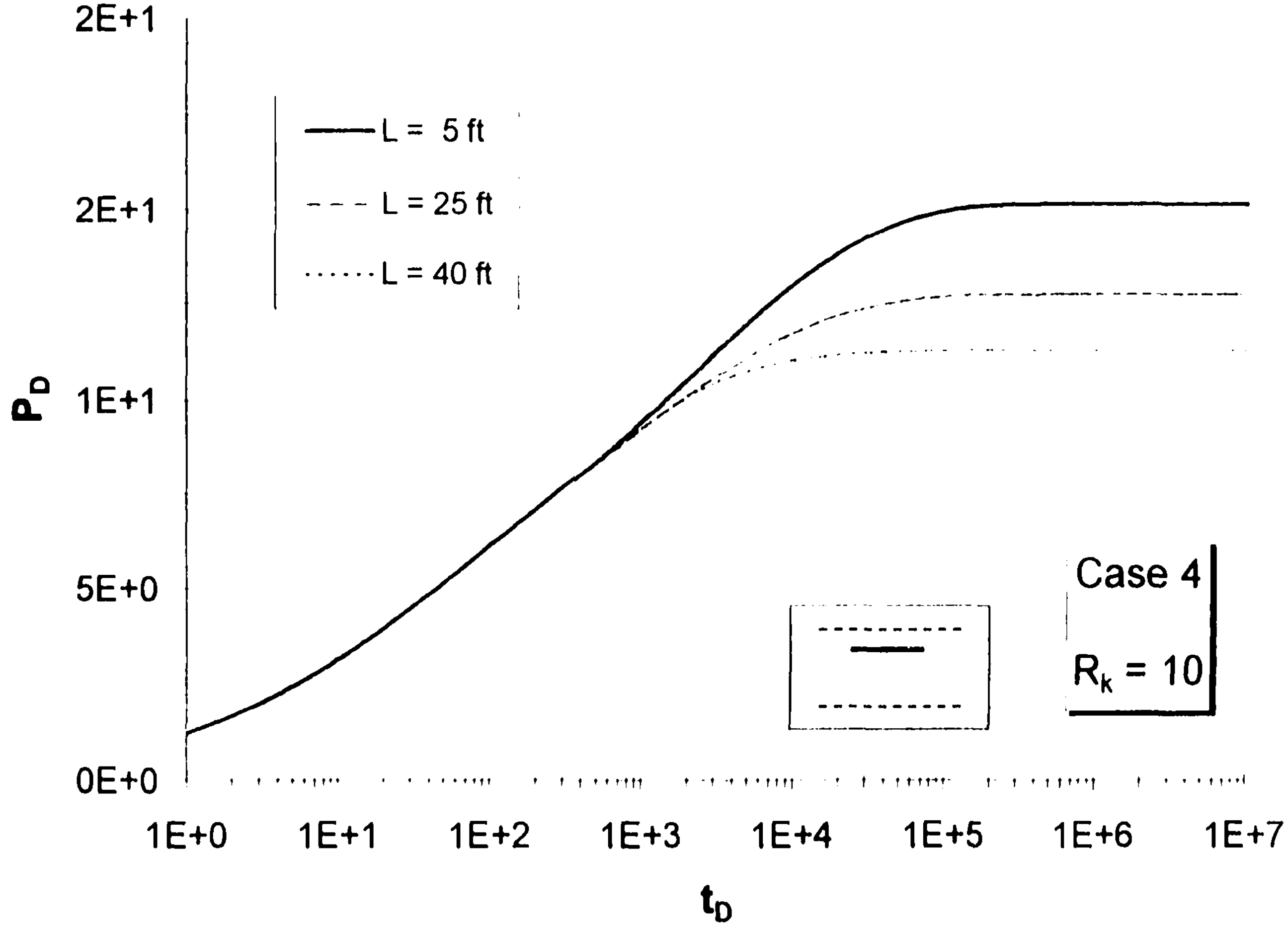

Figure 5.4.5(b) Dimensionless Pressure Behavior for Case 4 and R_k – 10

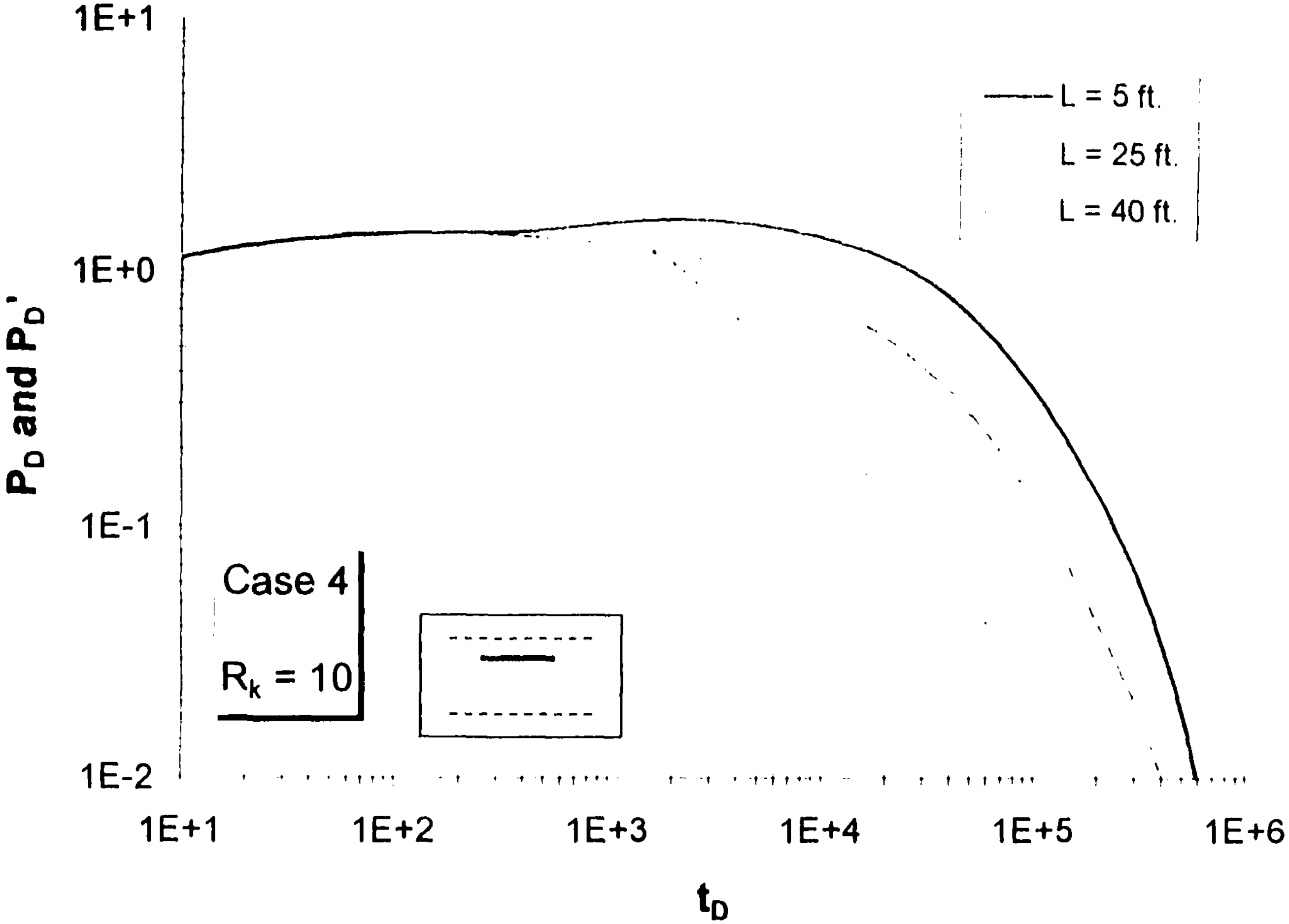

Figure 5.4.5(c) Dimensionless Pressure Derivative Behavior for Case 4 and R_k = 10

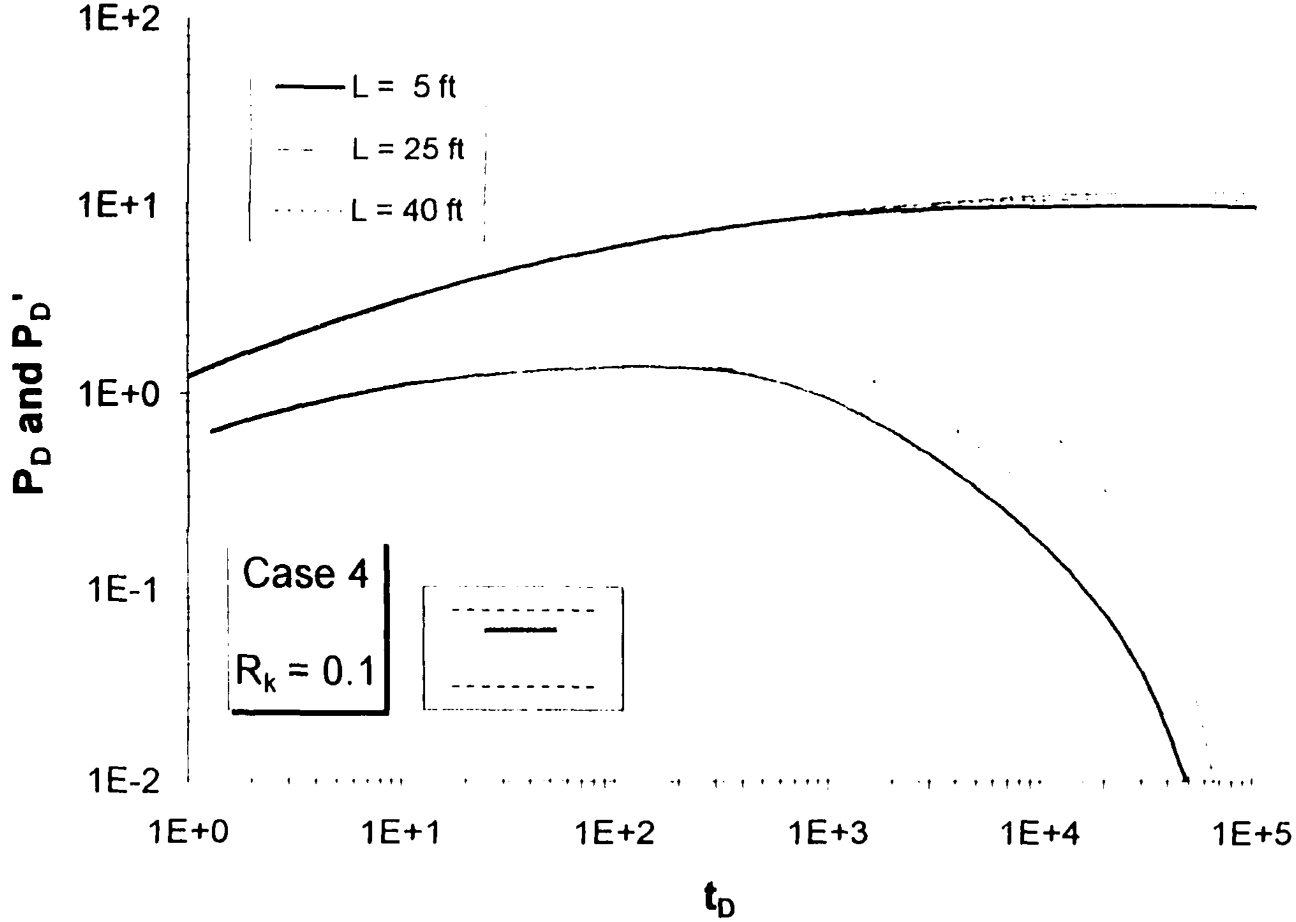

Figure 5.4.6(a) Dimensionless Pressure and Dimensionless Pressure Derivative Behavior for Case 4 and $R_k = 0.1$

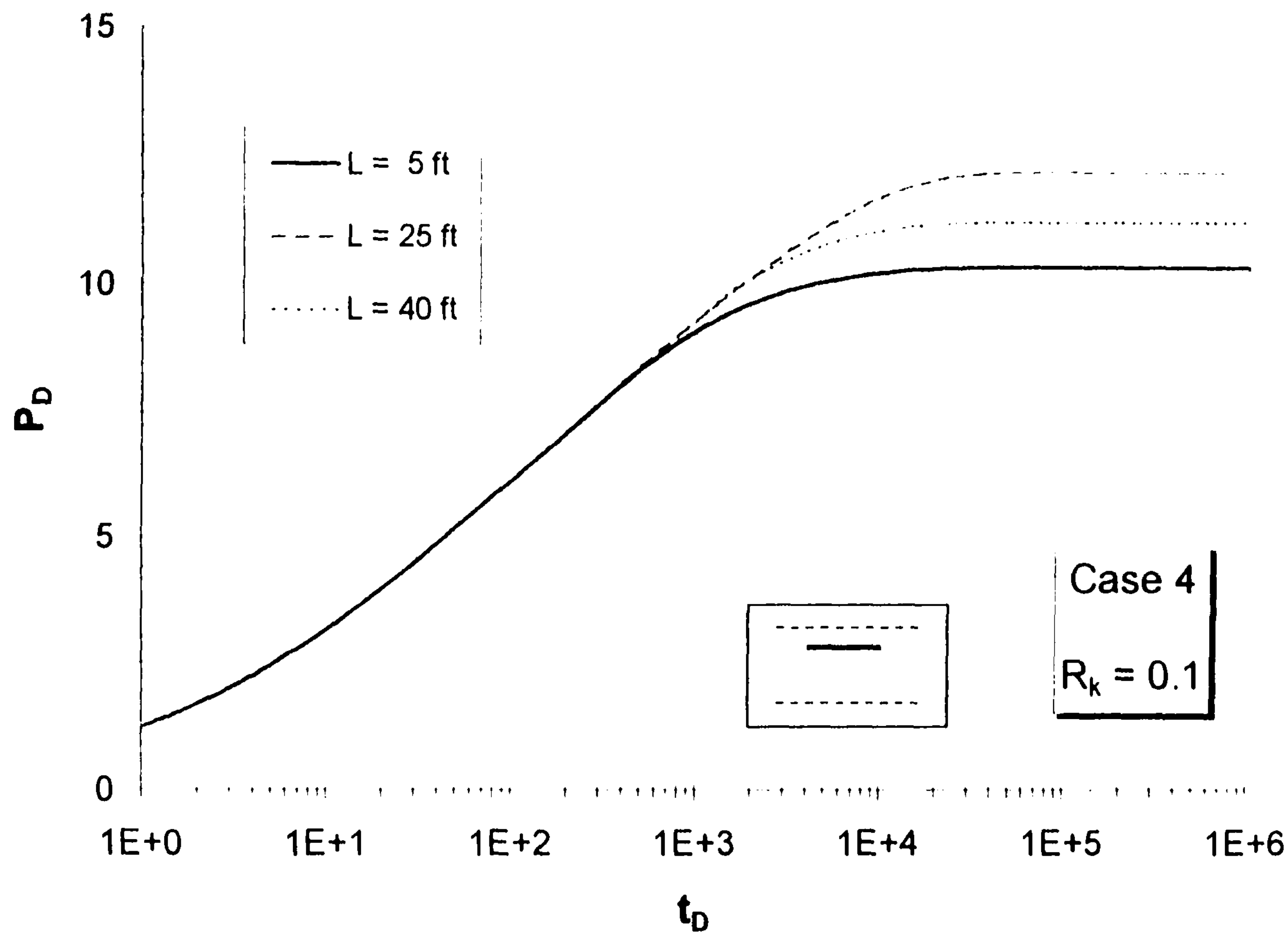

Figure 5.4.6(b) Dimensionless Pressure Derivative Behavior for Case 4 and $R_k = 0.1$

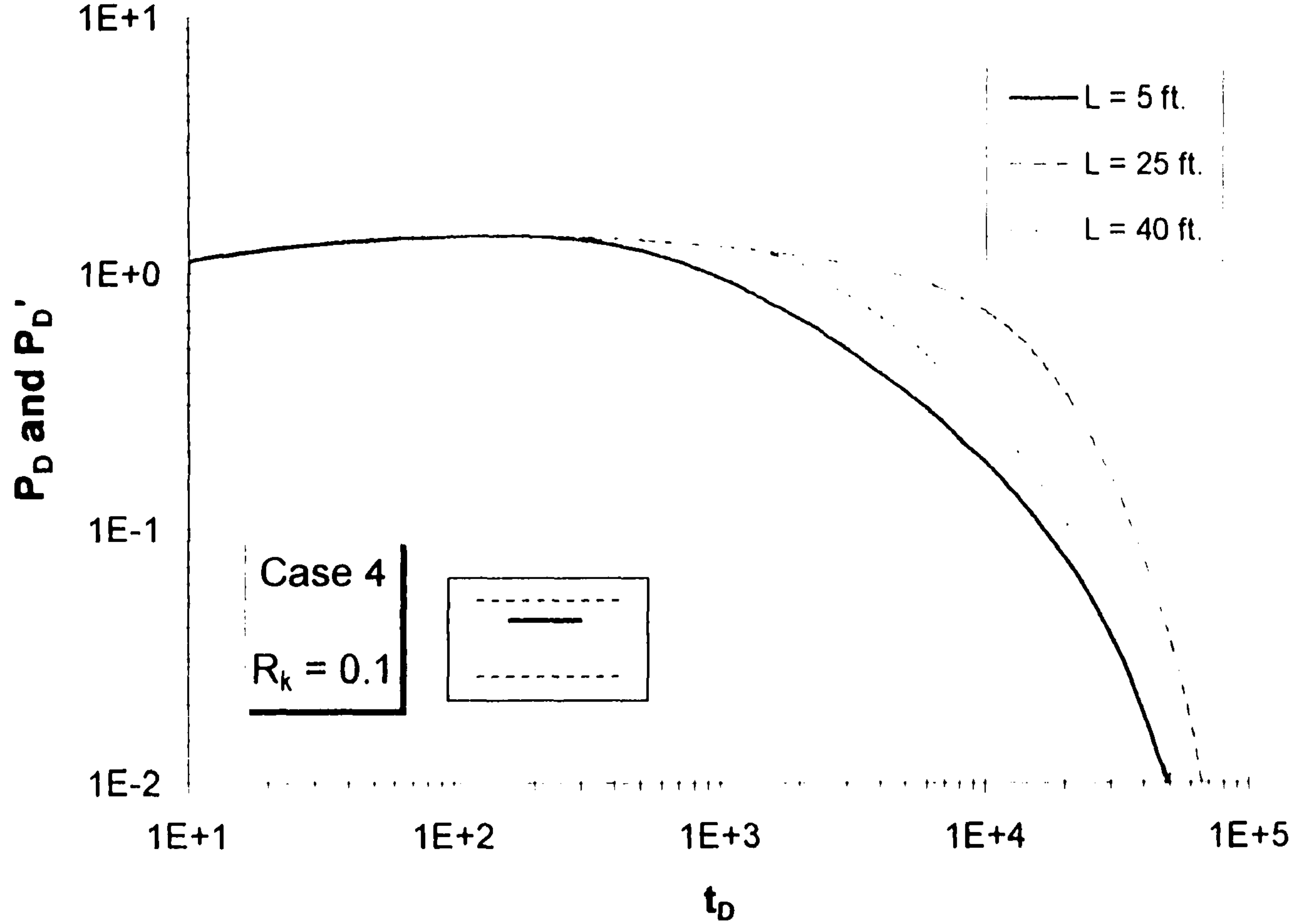

Figure 5.4.6(c) Dimensionless Pressure Derivative Behavior for Case 4 and R_k = 0.1

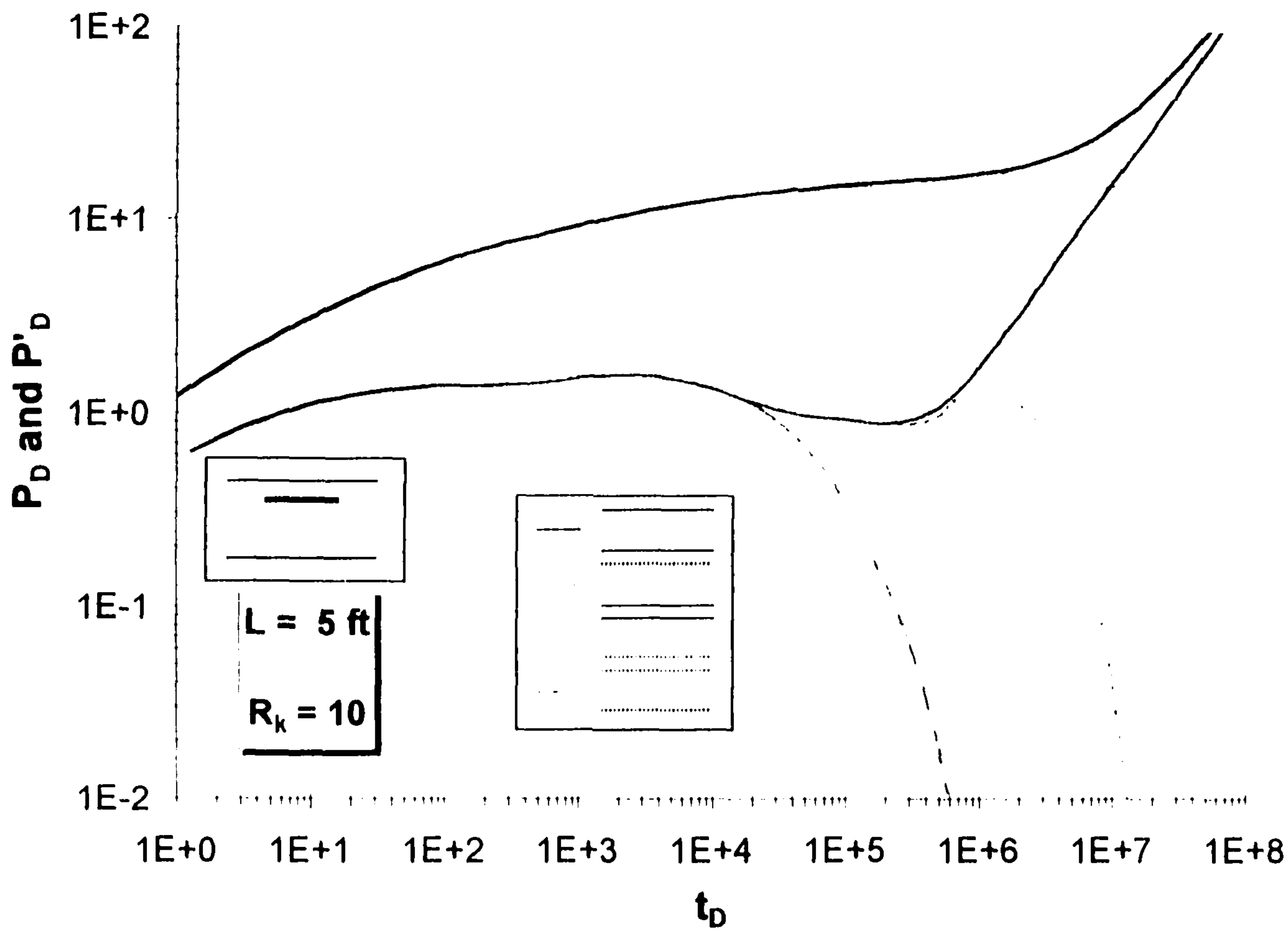

Figure 5.4.7(a) Dimensionless Pressure and Dimensionless Pressure Derivative Performance

for L = 5 ft. and R_k = 10

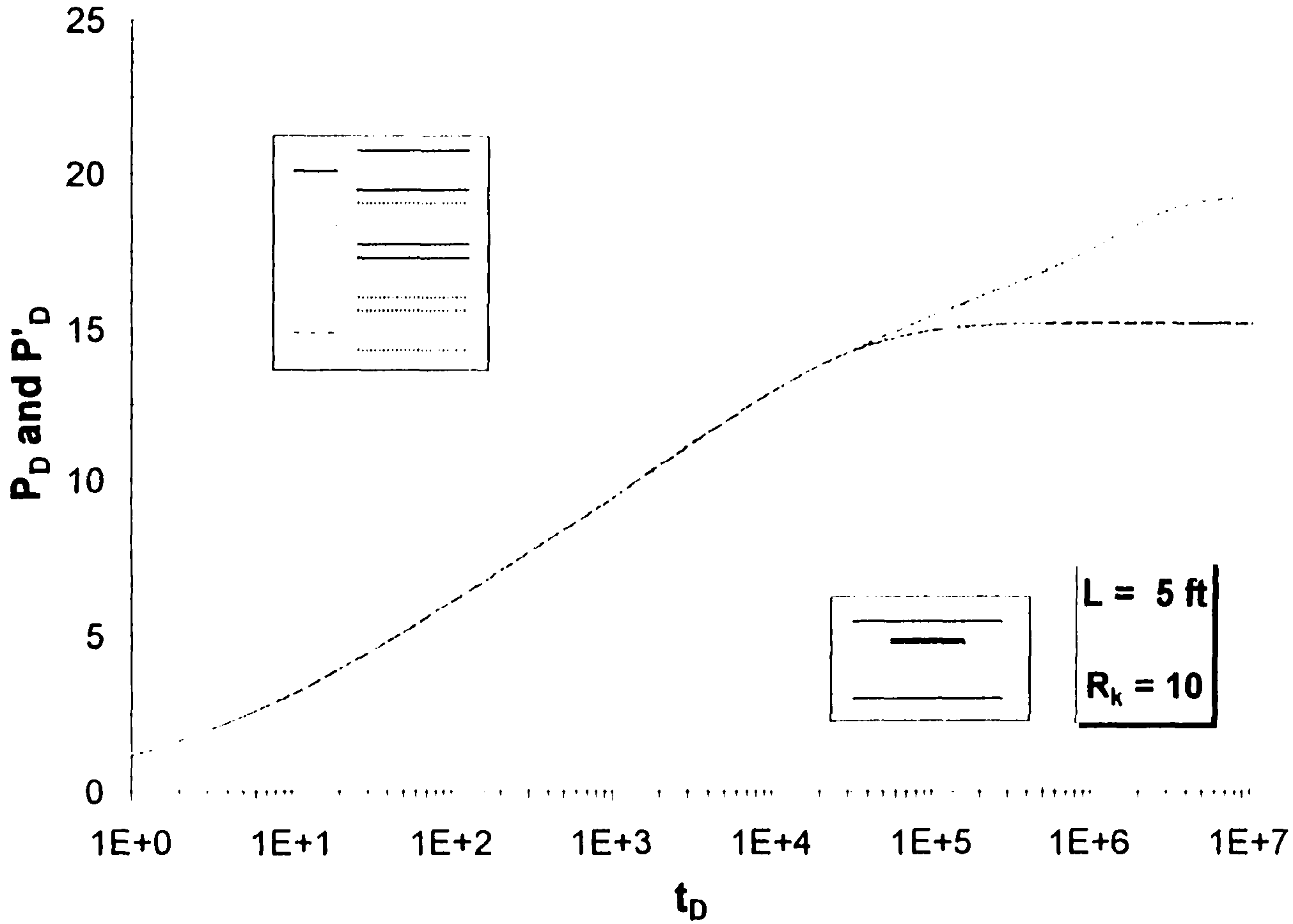

Figure 5.4.7(b) Dimensionless Pressure Derivative Performance for L = 5 ft. and R_k = 10

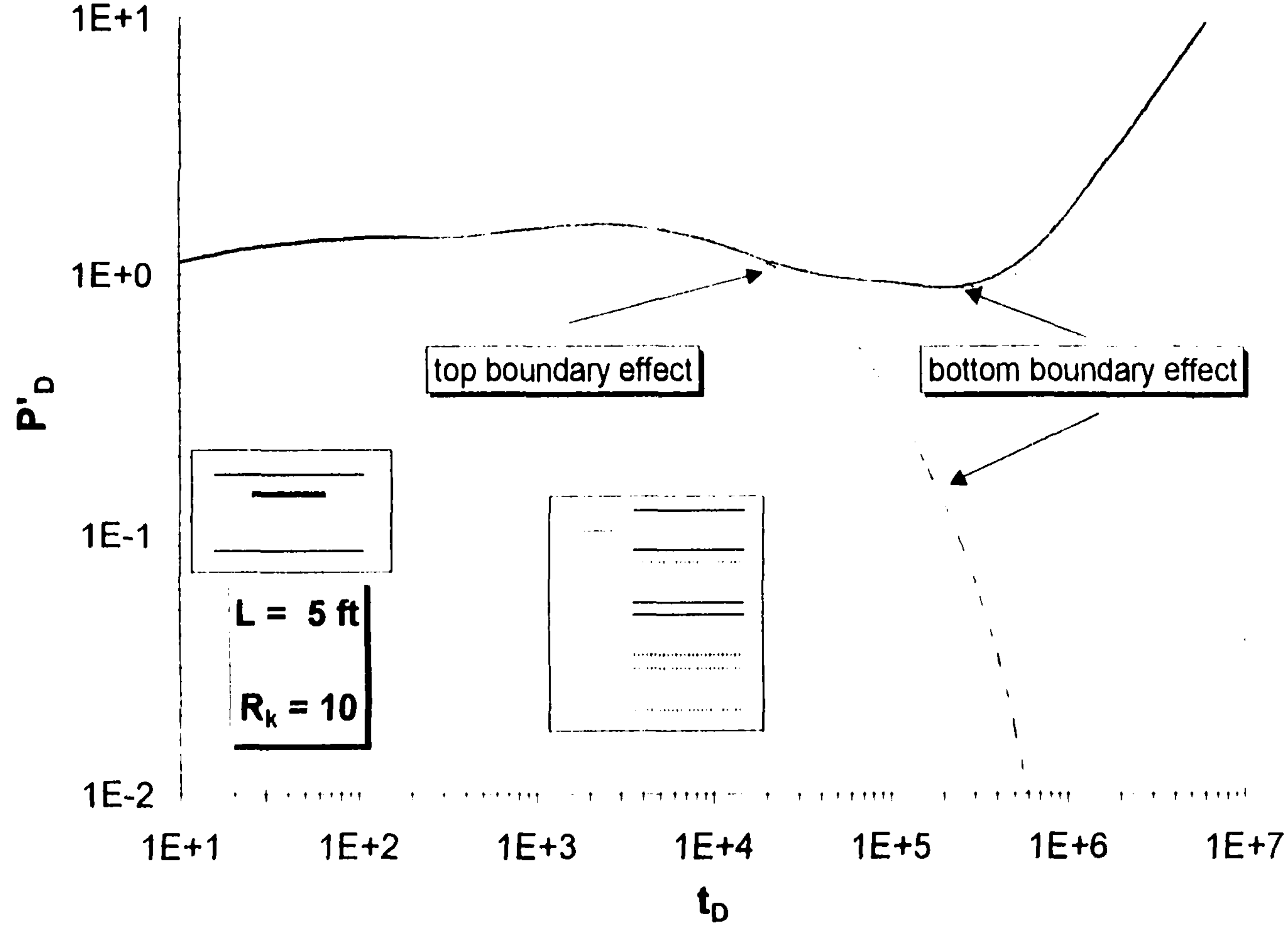

Figure 5.4.7(c) Dimensionless Pressure Derivative Performance for L = 5 ft. and R_k = 10

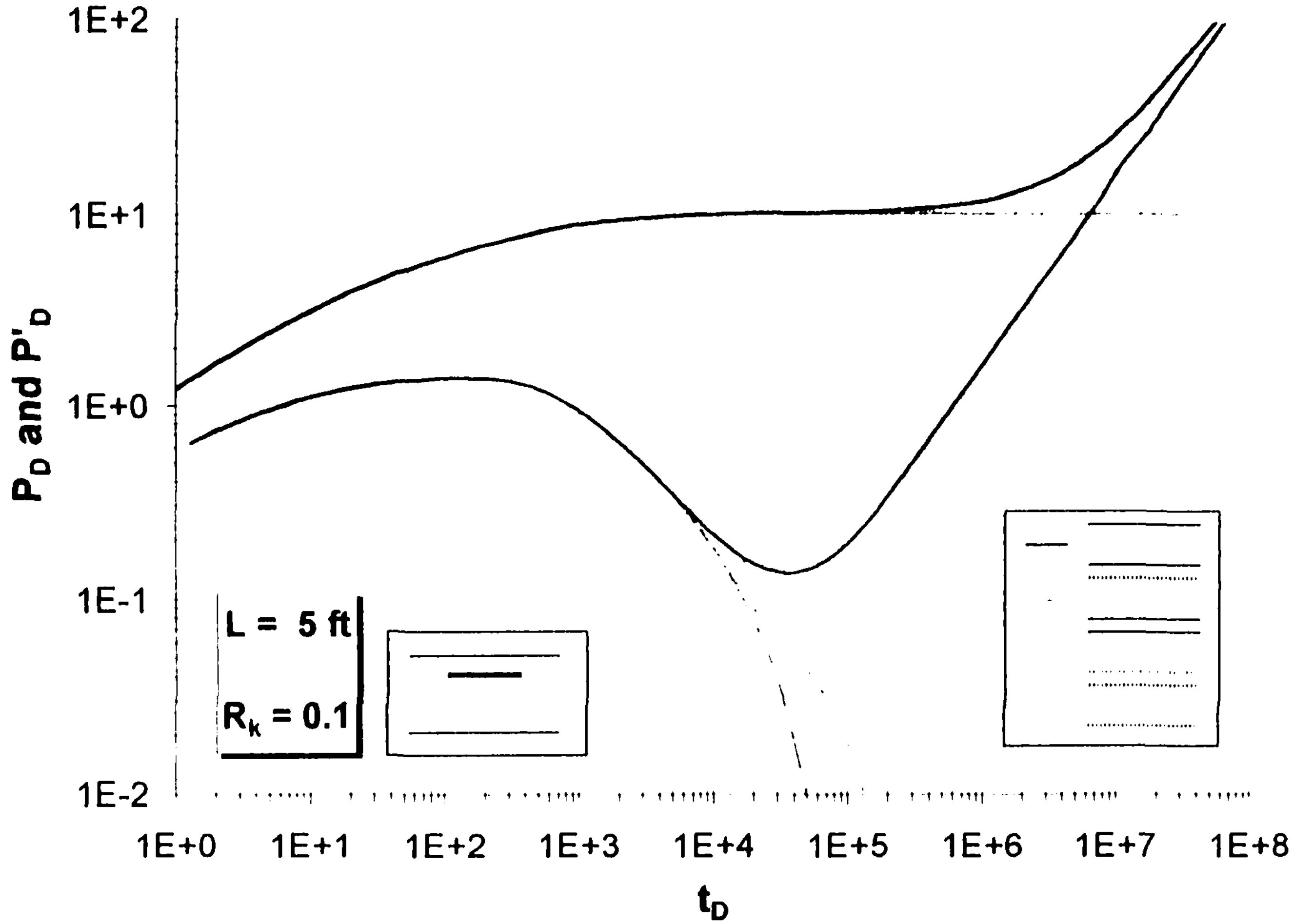

Figure 5.4.8(a) Dimensionless Pressure and Dimensionless Pressure Derivative Performance

for L = 5 ft. and $R_k = 0.1$

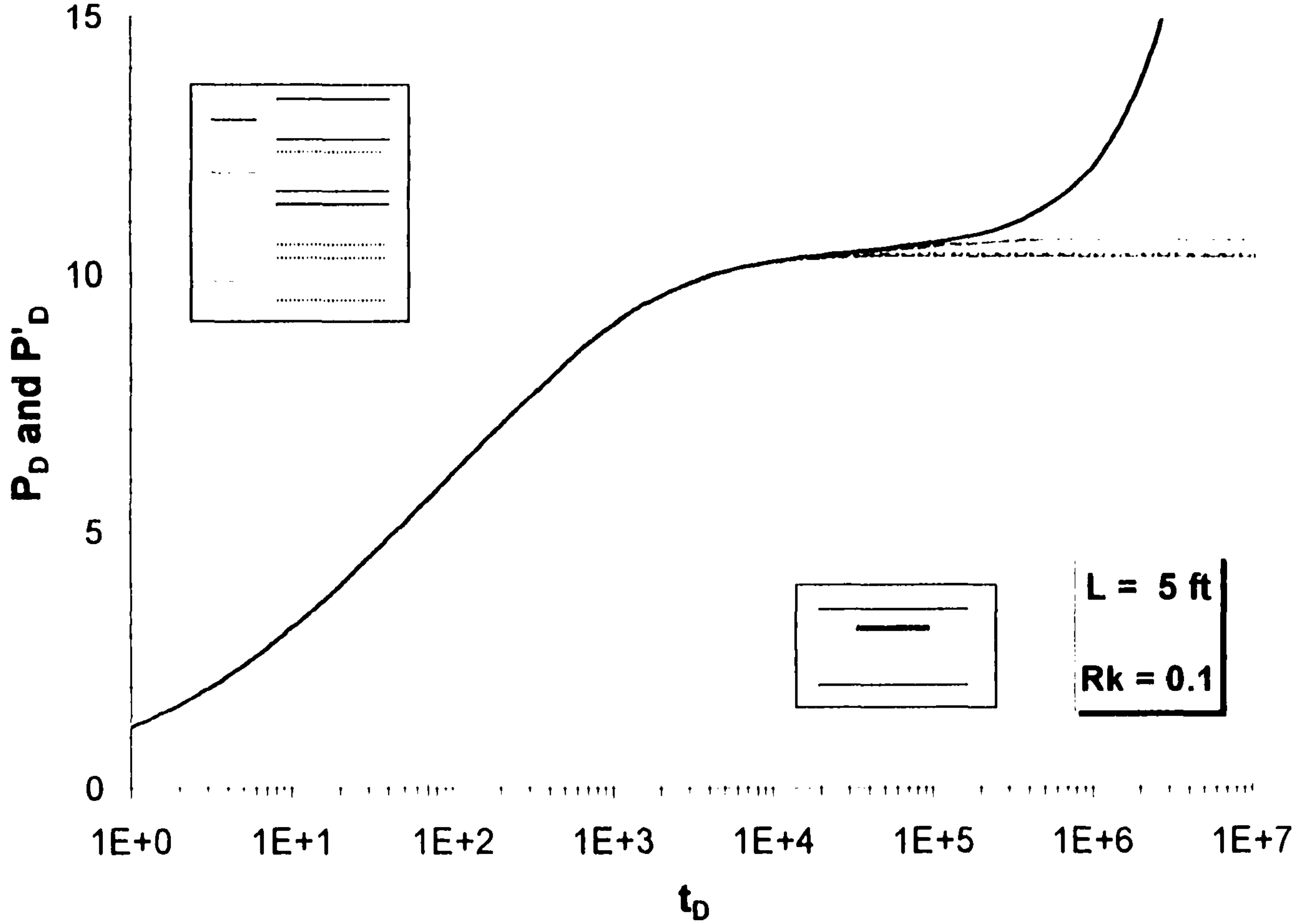

Figure 5.4.8(b) Dimensionless Pressure Performance for L = 5 ft. and R_k = 0.1

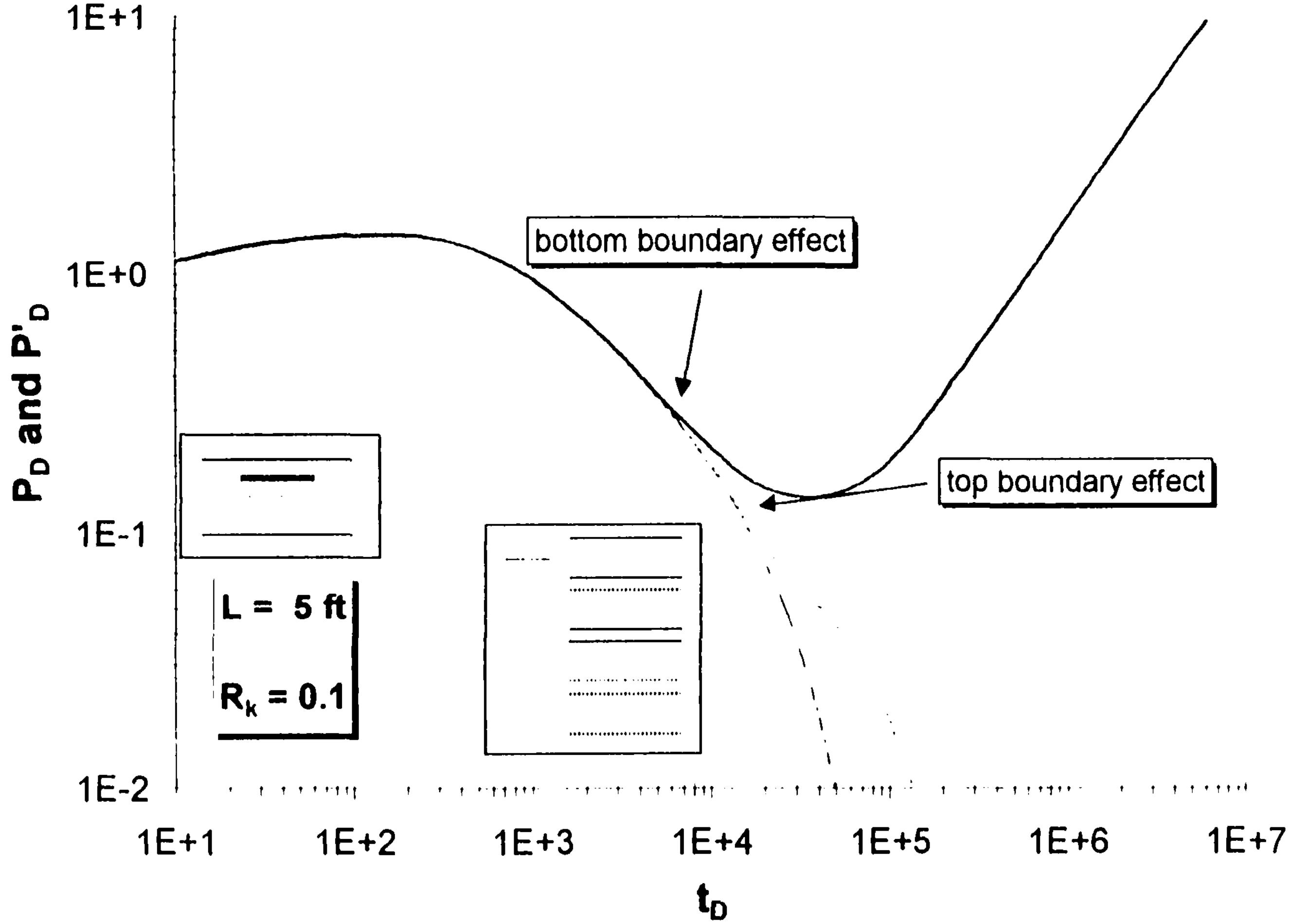

Figure 5.4.8(c) Dimensionless Pressure Derivative Performance for L = 5 ft. and R_k = 0.1

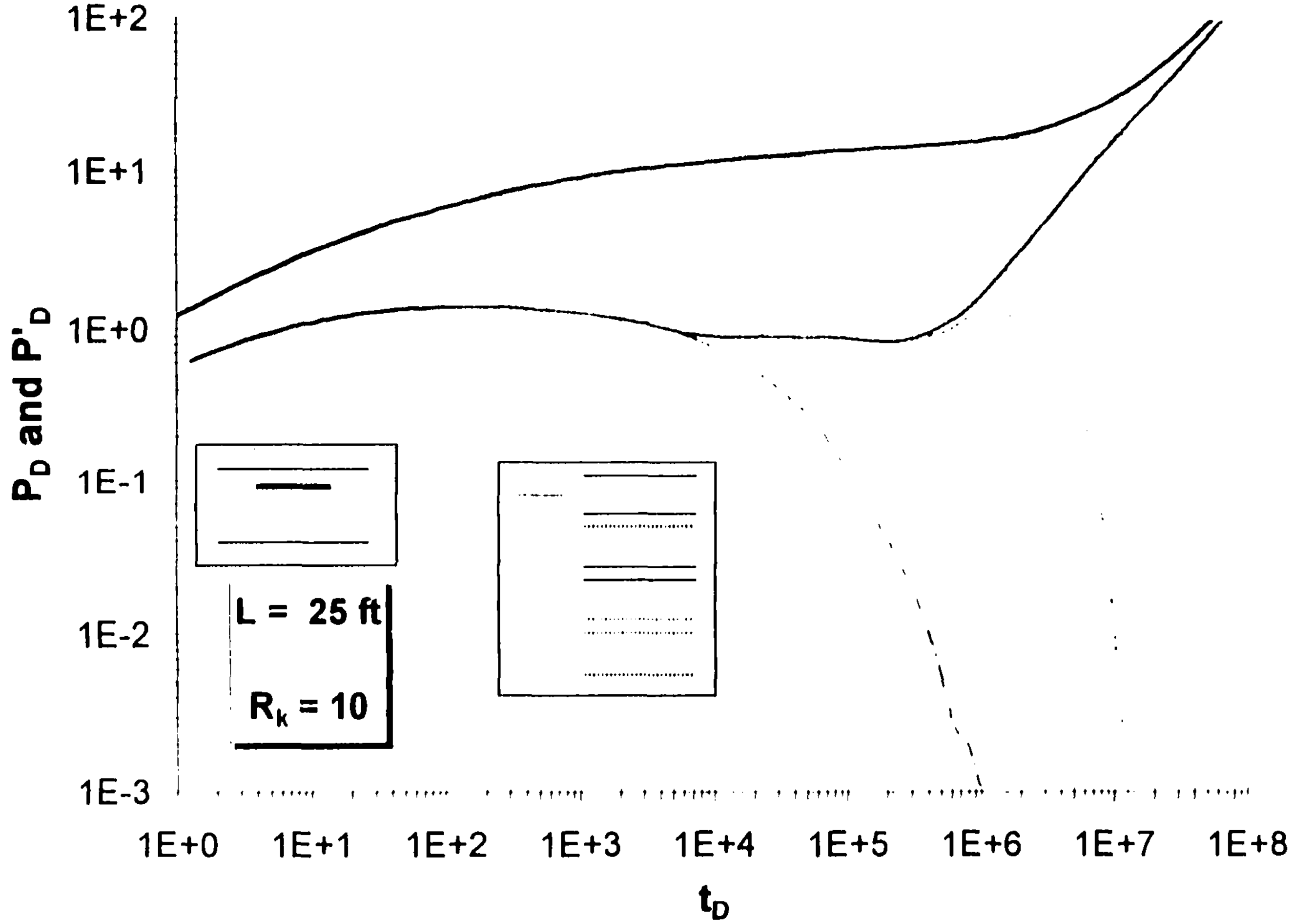

Figure 5.4.9(a) Dimensionless Pressure and Dimensionless Pressure Derivative Performance

for $L = 25$ ft. and $R_k = 10$

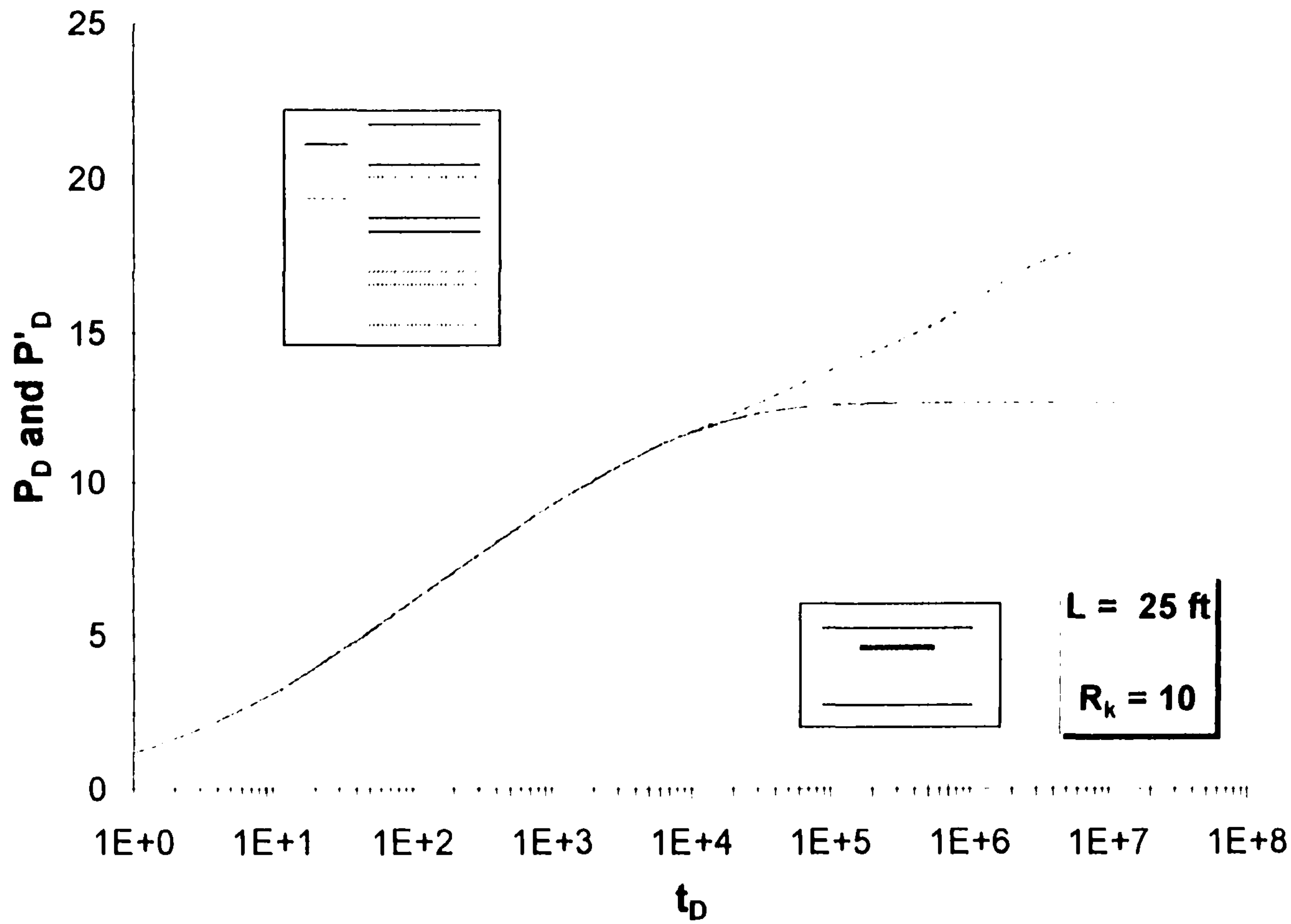

Figure 5.4.9(b) Dimensionless Pressure Performance for L = 25 ft. and R_k = 10

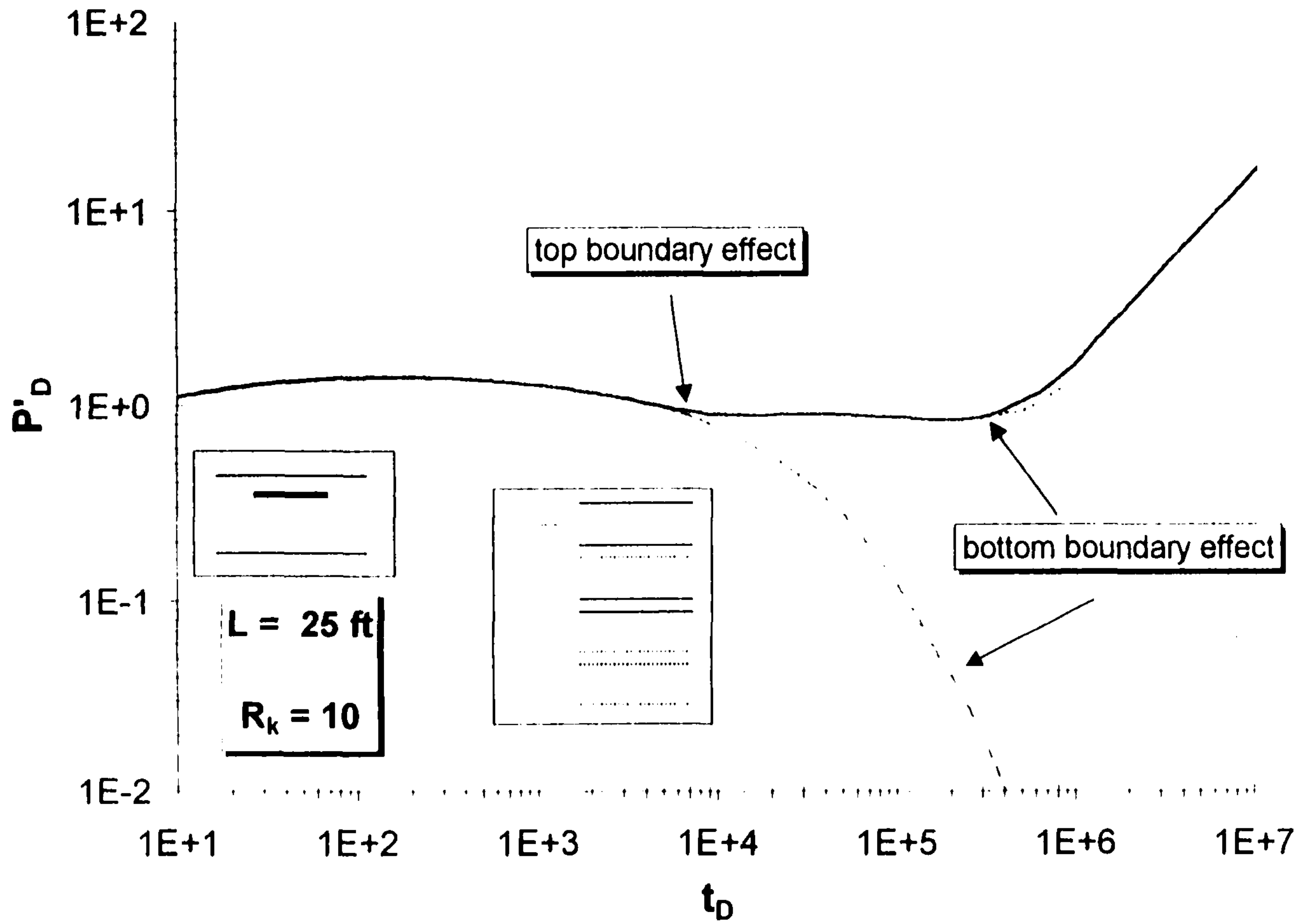

Figure 5.4.9(c) Dimensionless Pressure Derivative Performance for L = 25 ft. and R_k = 10

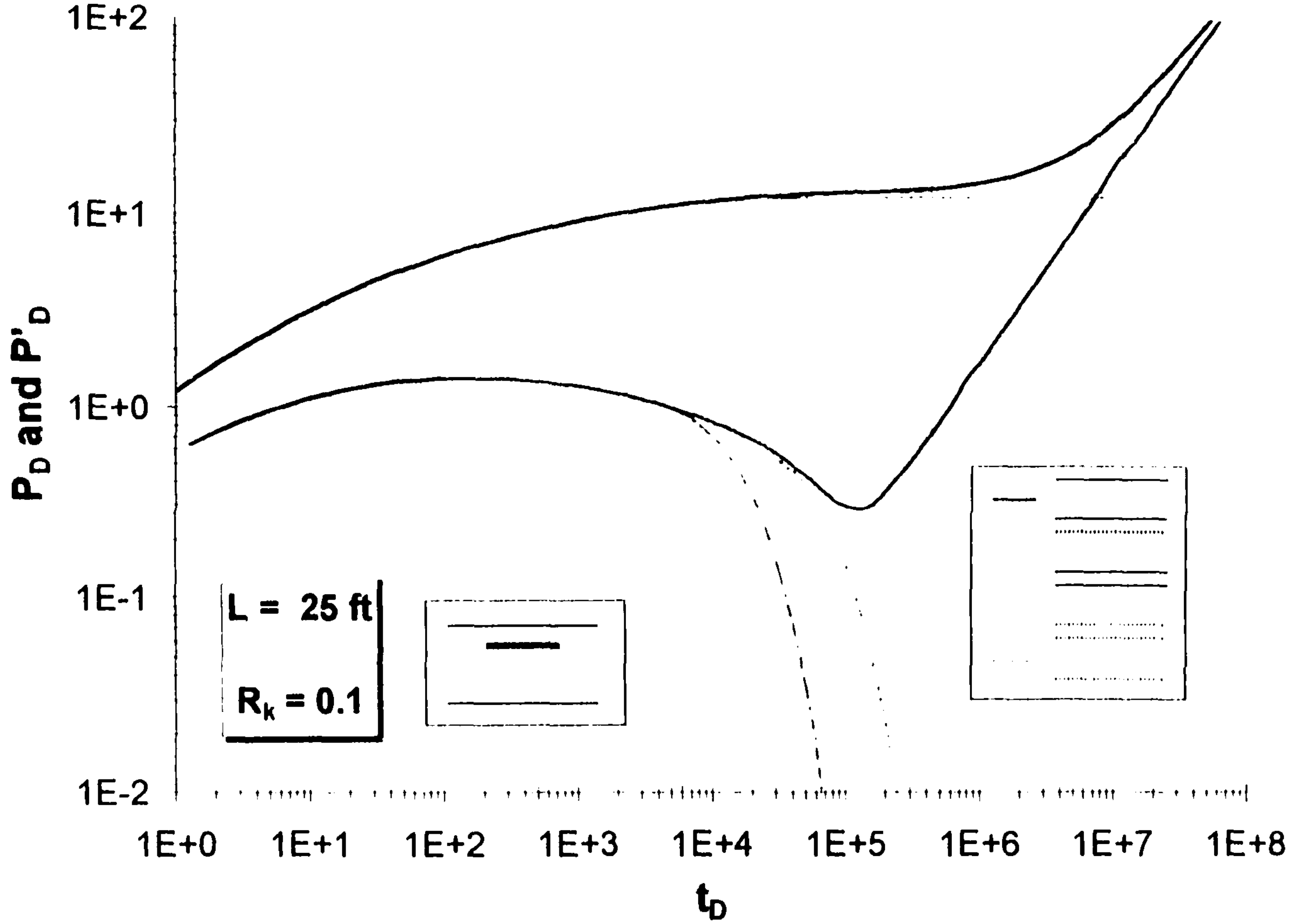

Figure 5.4.10(a) Dimensionless Pressure and Dimensionless Pressure Derivative Performance

for L = 25 ft. and R_k = 0.1

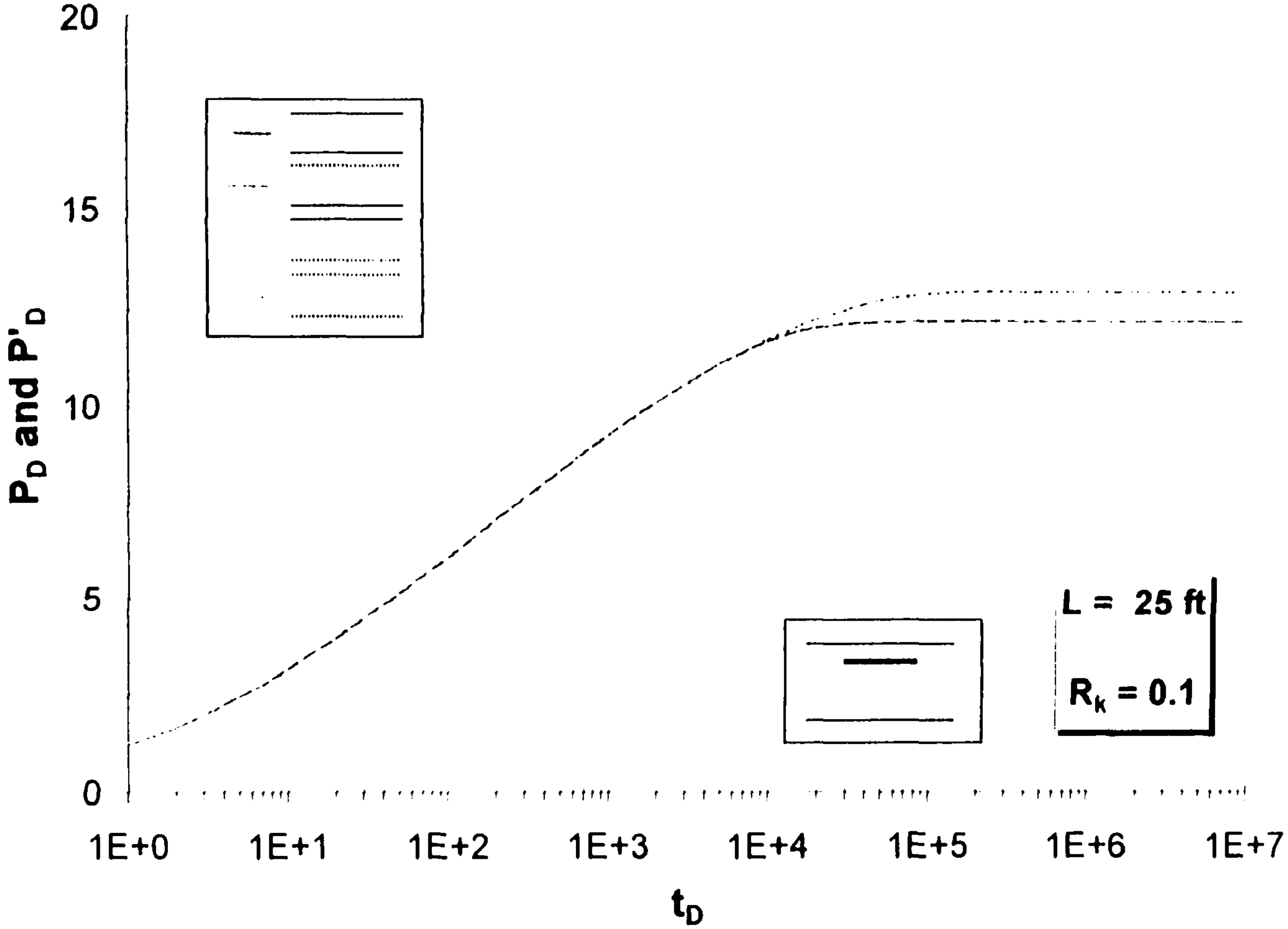

Figure 5.4.10(b) Dimensionless Pressure Performance for L = 25 ft. and R_k = 0.1

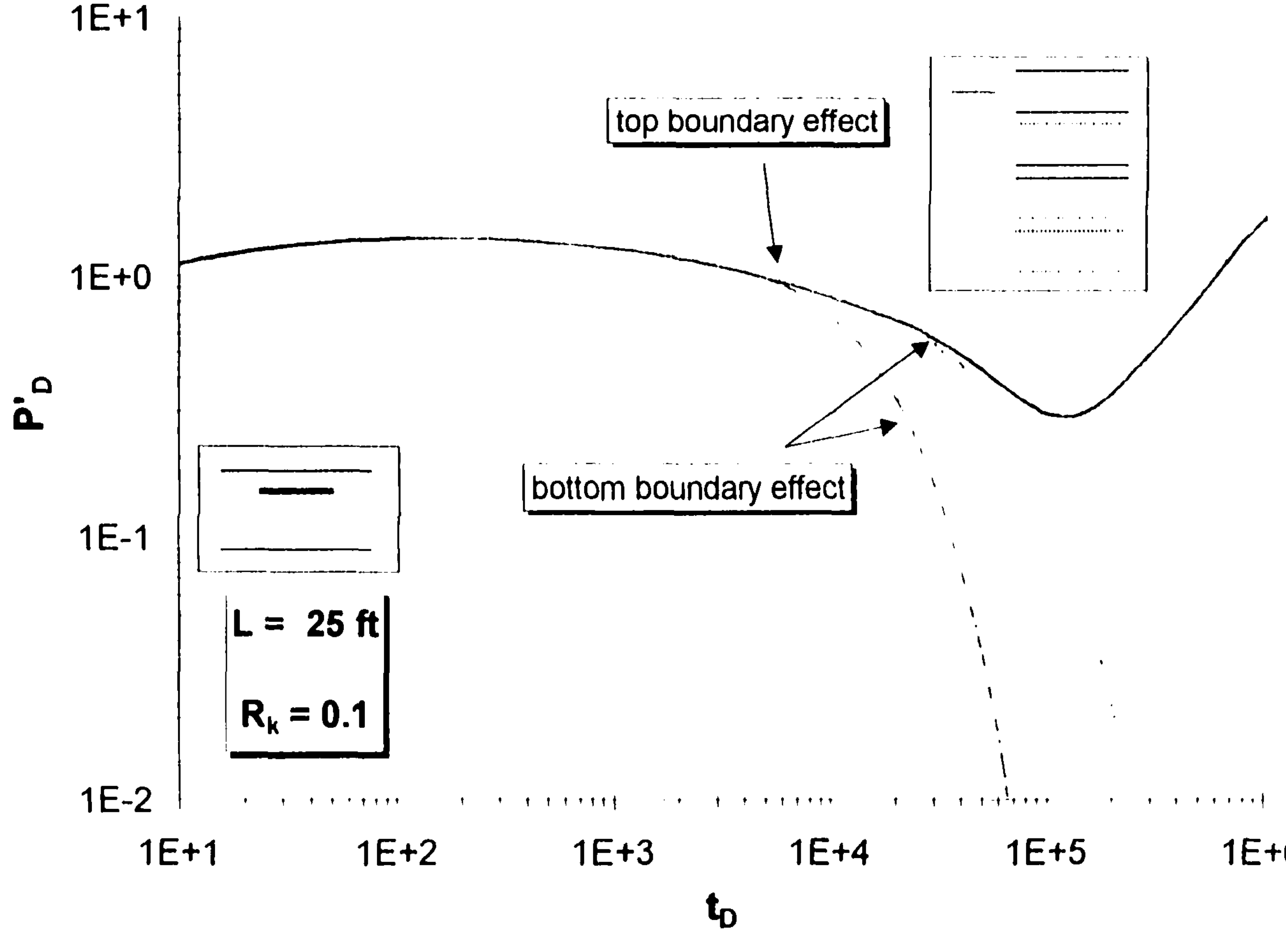

Figure 5.4.10(c) Dimensionless Pressure Derivative Performance for L = 25 ft. and R_k = 0.1

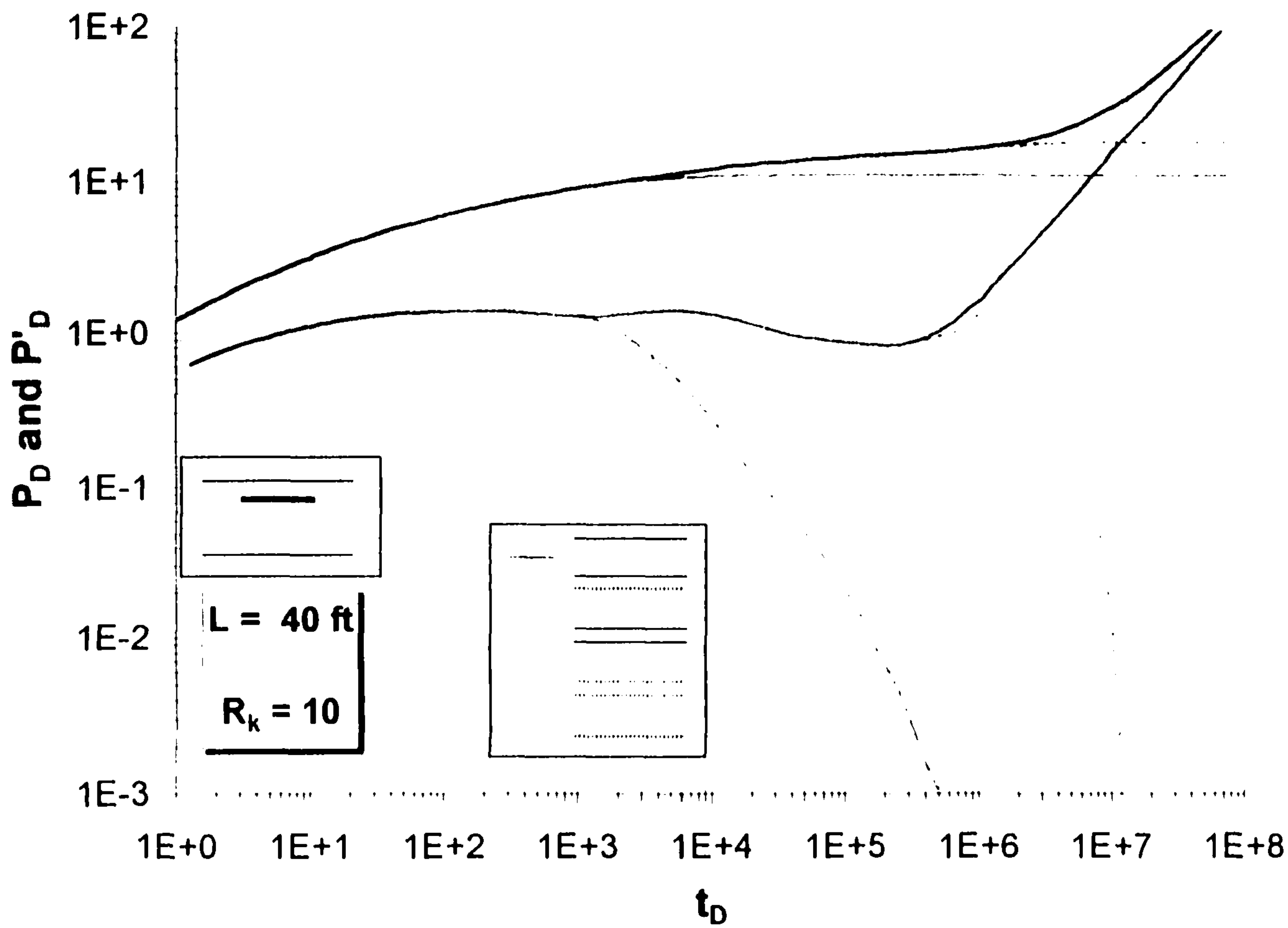

Figure 5.4.11(a) Dimensionless Pressure and Dimensionless Pressure Derivative Performance

for L = 40 ft. and R_k = 10

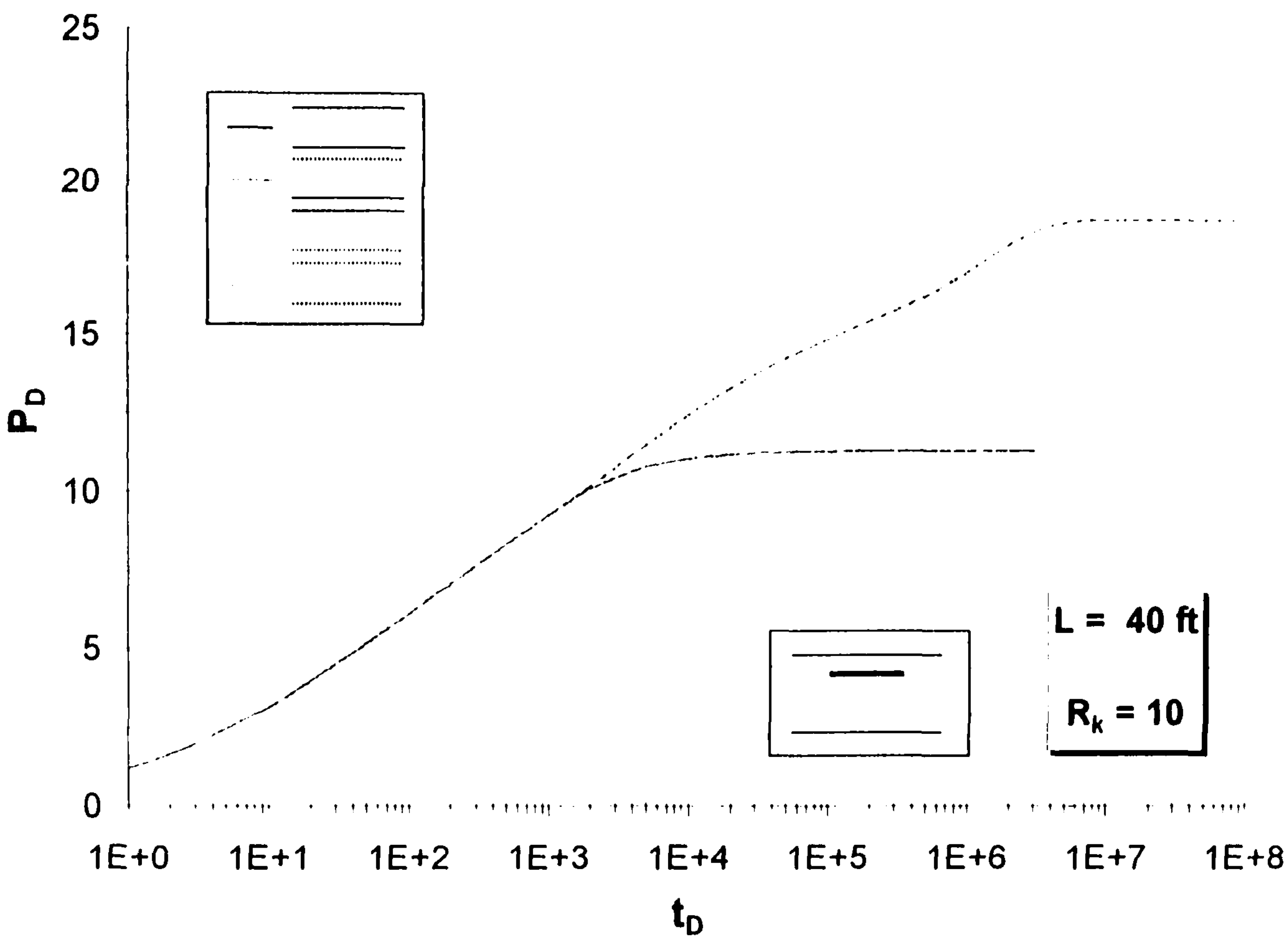

Figure 5.4.11(b) Dimensionless Pressure Performance for L = 40 ft. and R_k = 10

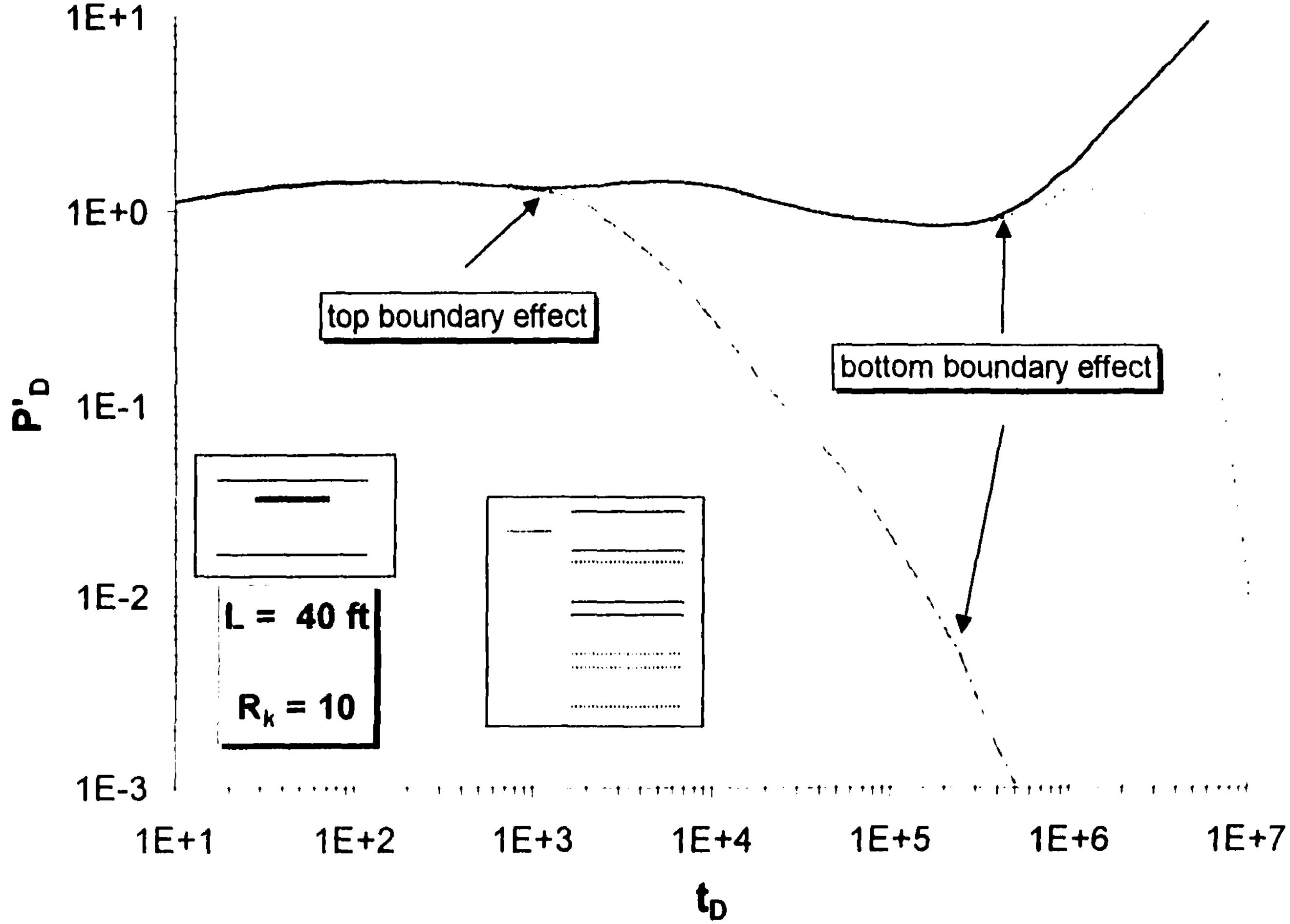

Figure 5.4.11(c) Dimensionless Pressure Derivative Performance for L = 40 ft. and R_k = 10

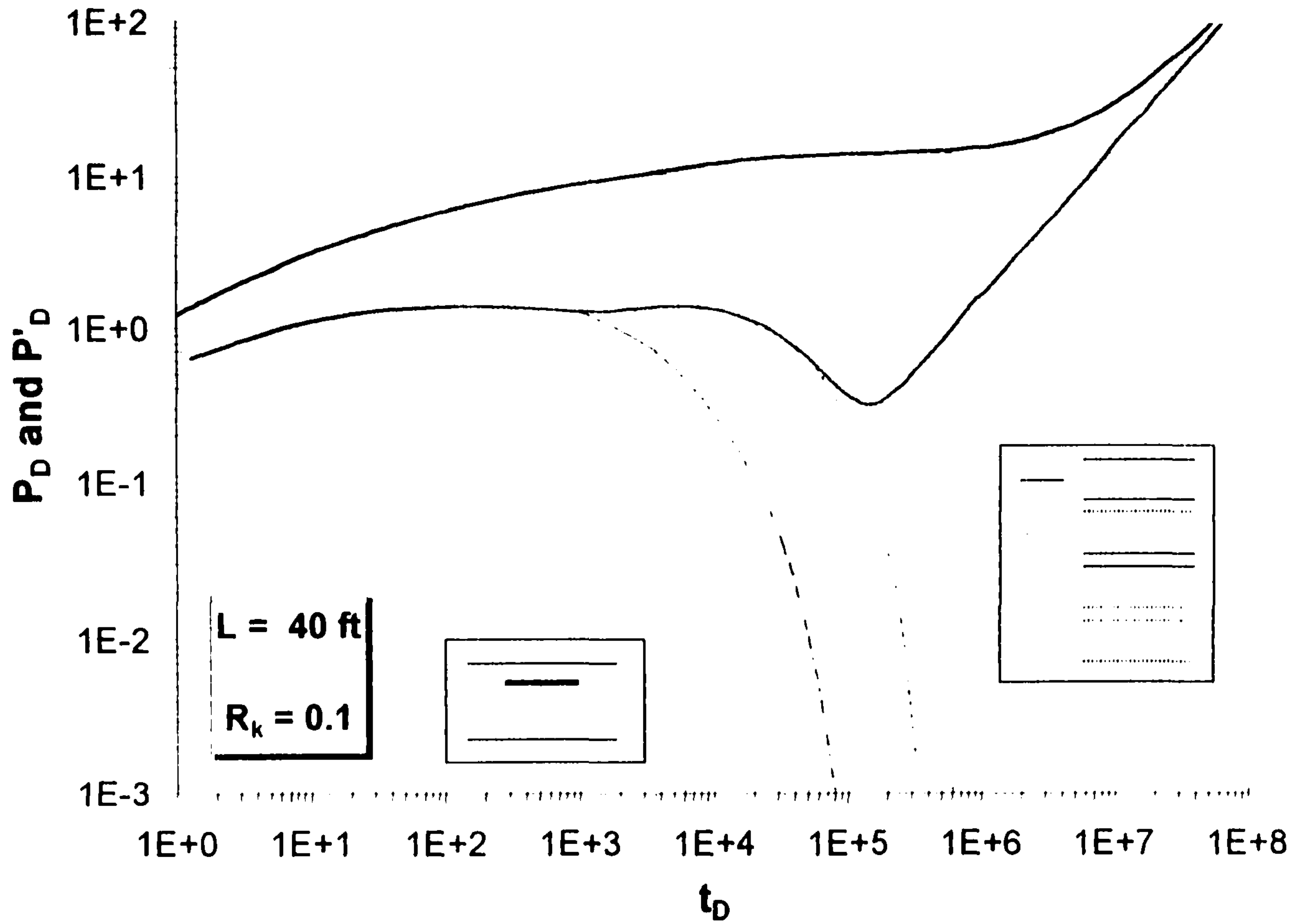

Figure 5.4.12(a) Dimensionless Pressure and Dimensionless Pressure Derivative Performance

for L = 40 ft. and R_k = 0.1

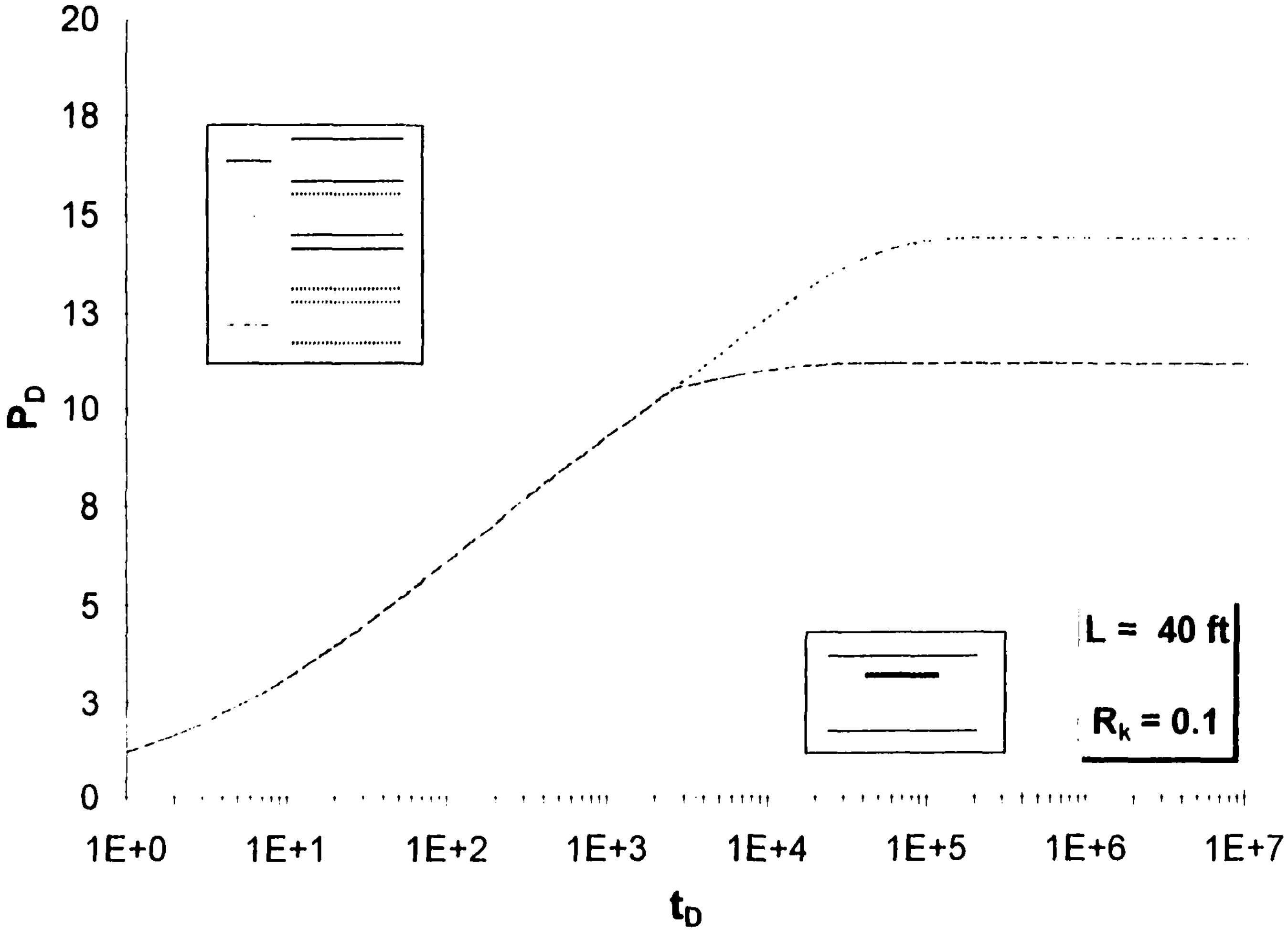

Figure 5.4.12(b) Dimensionless Pressure Performance for L = 40 ft. and R_k = 0.1

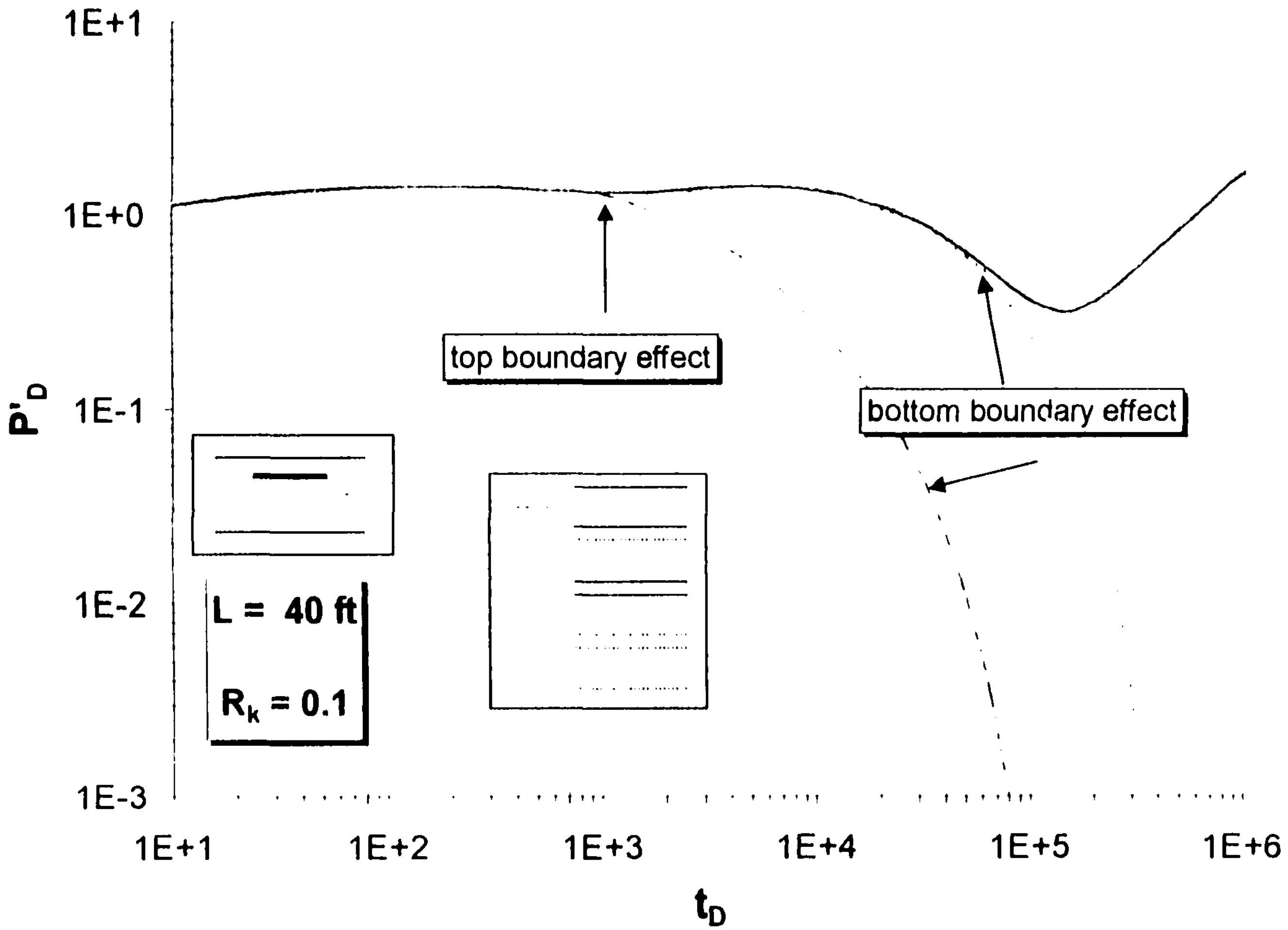

Figure 5.4.12(c) Dimensionless Pressure Derivative Performance for $L = 40$ ft and $R_k = 0.1$

APPENDIX G

LIST OF FIGURES IN CASE 5.5

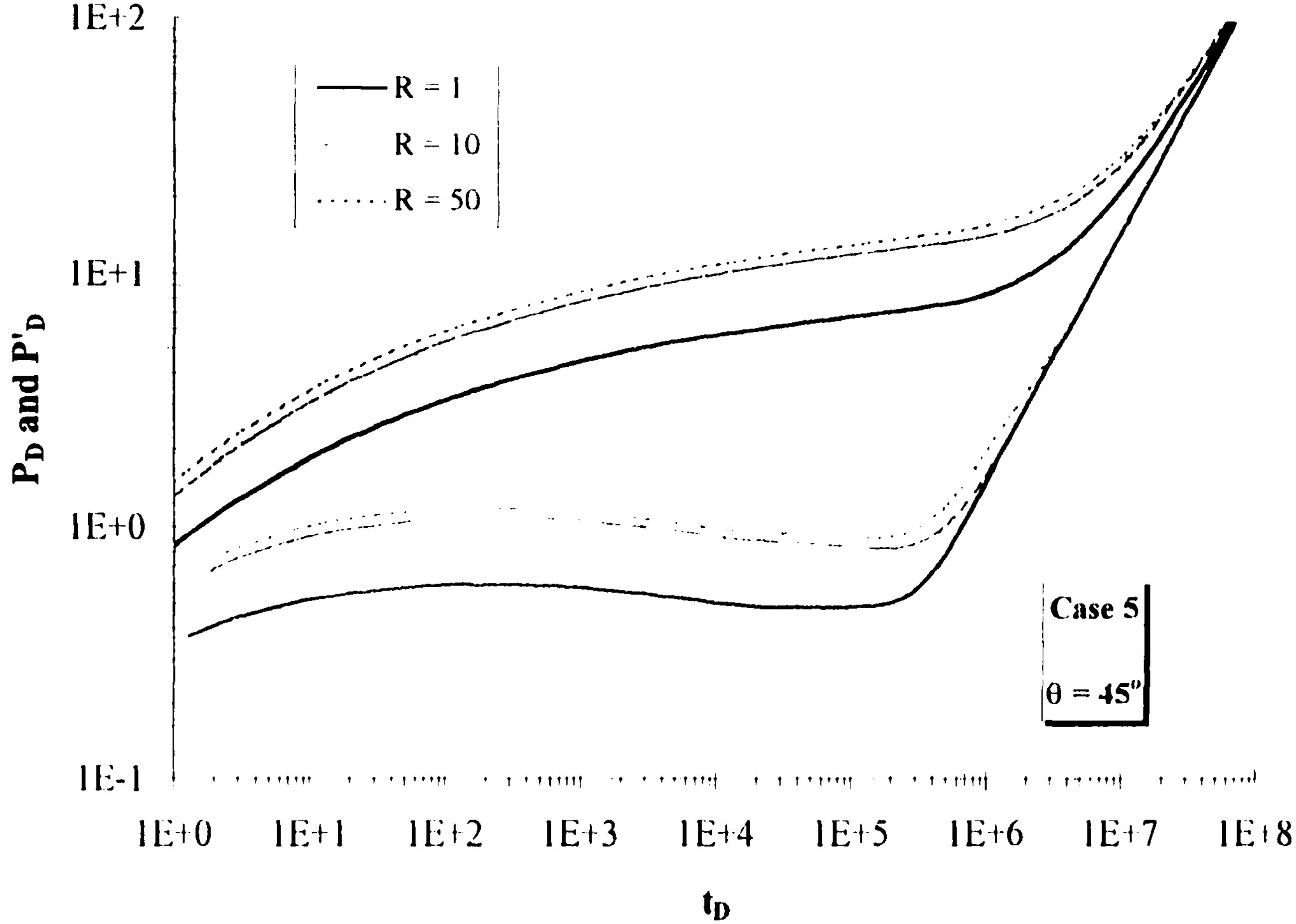

Figure 5.5.5(a) The Dimensionless Pressure and The Dimensionless Pressure Derivative

for Case 5 and $\theta = 45^{0}$

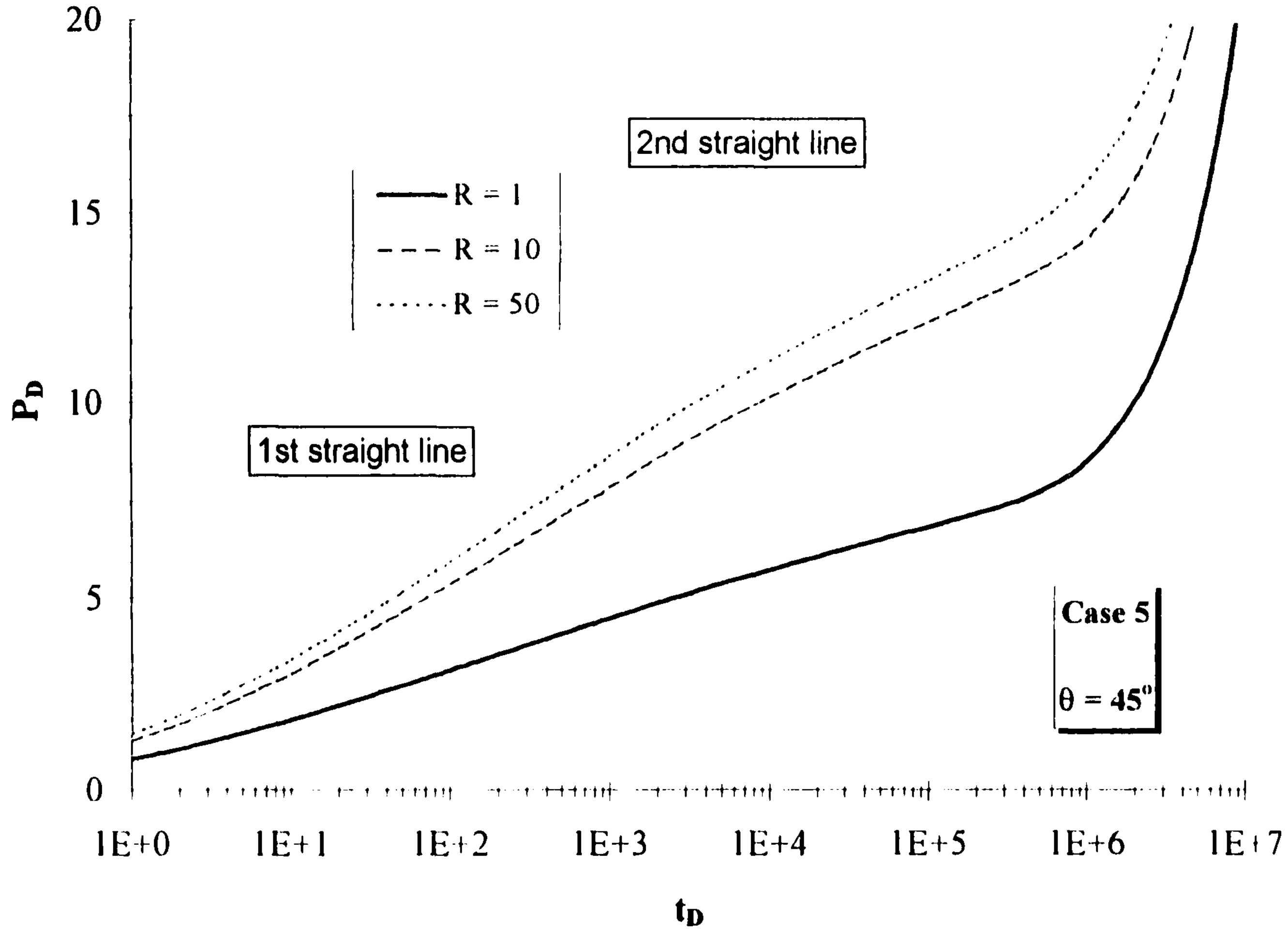

Figure 5.5.5(b) The Dimensionless Pressure for Case 5 and $\theta = 45^{\circ}$

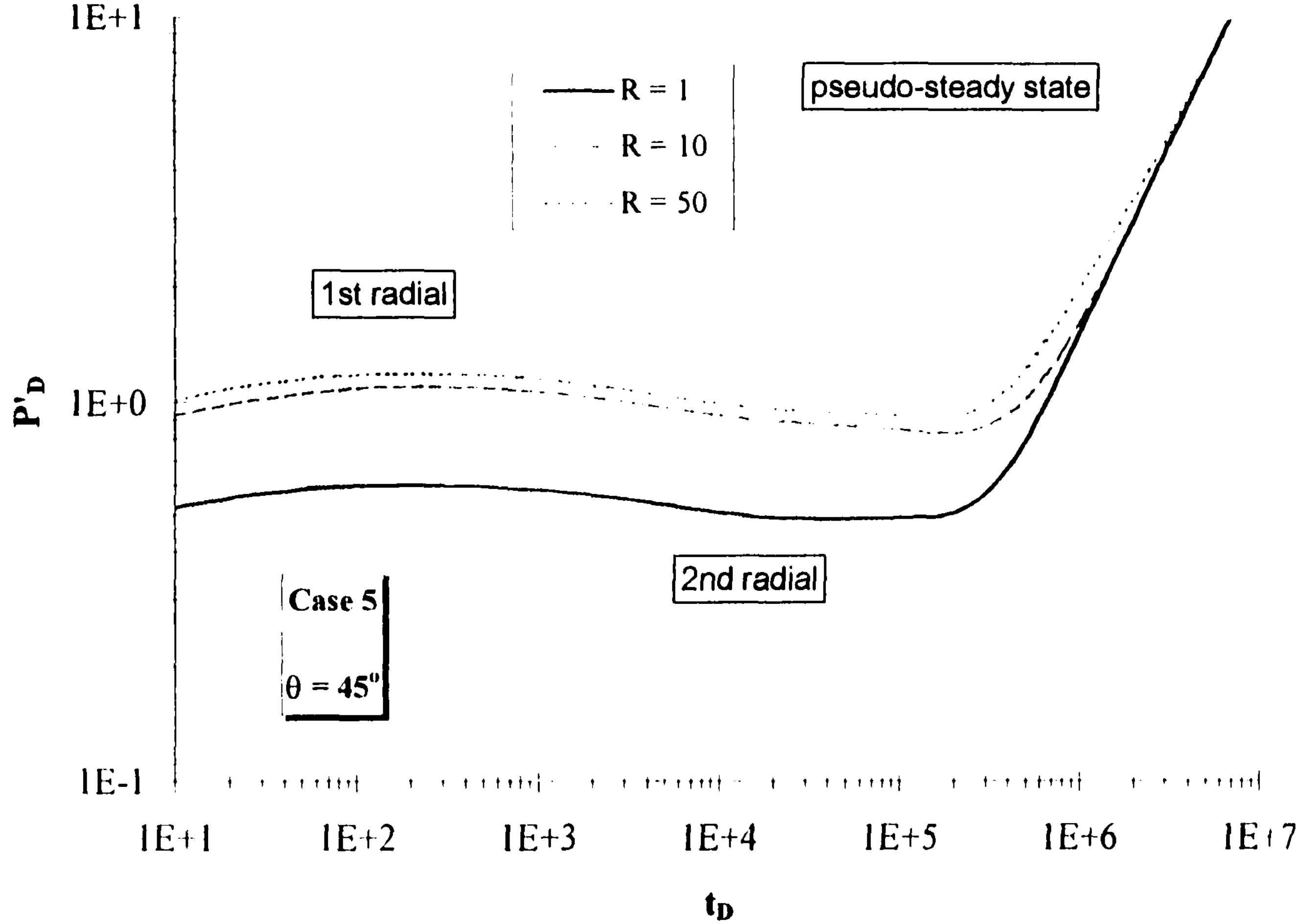

Figure 5.5.5(c) The Dimensionless Pressure Derivative for Case 5 and $\theta = 45^{\circ}$

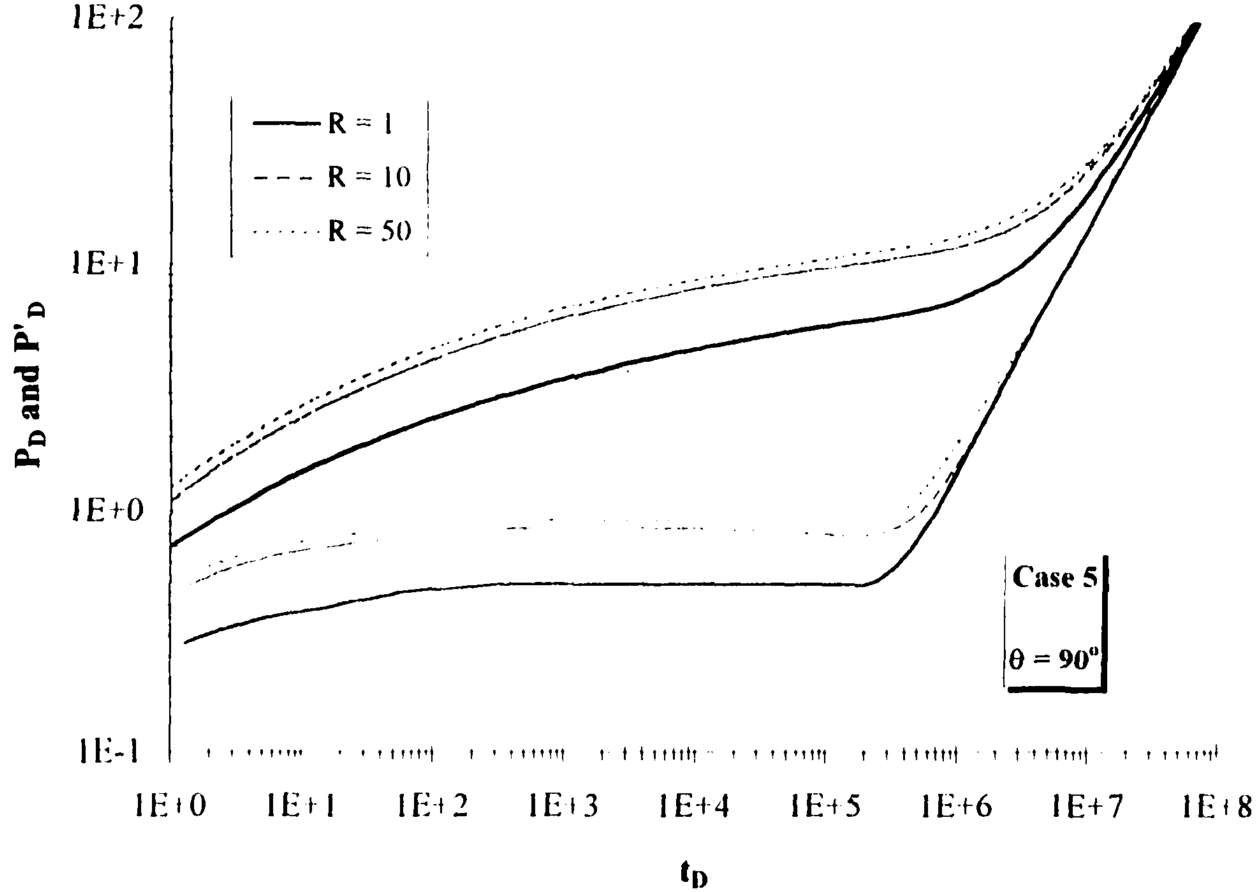

Figure 5.5.6(a) The Dimensionless Pressure and The Dimensionless Pressure Derivative

for Case 5 and θ = 90°

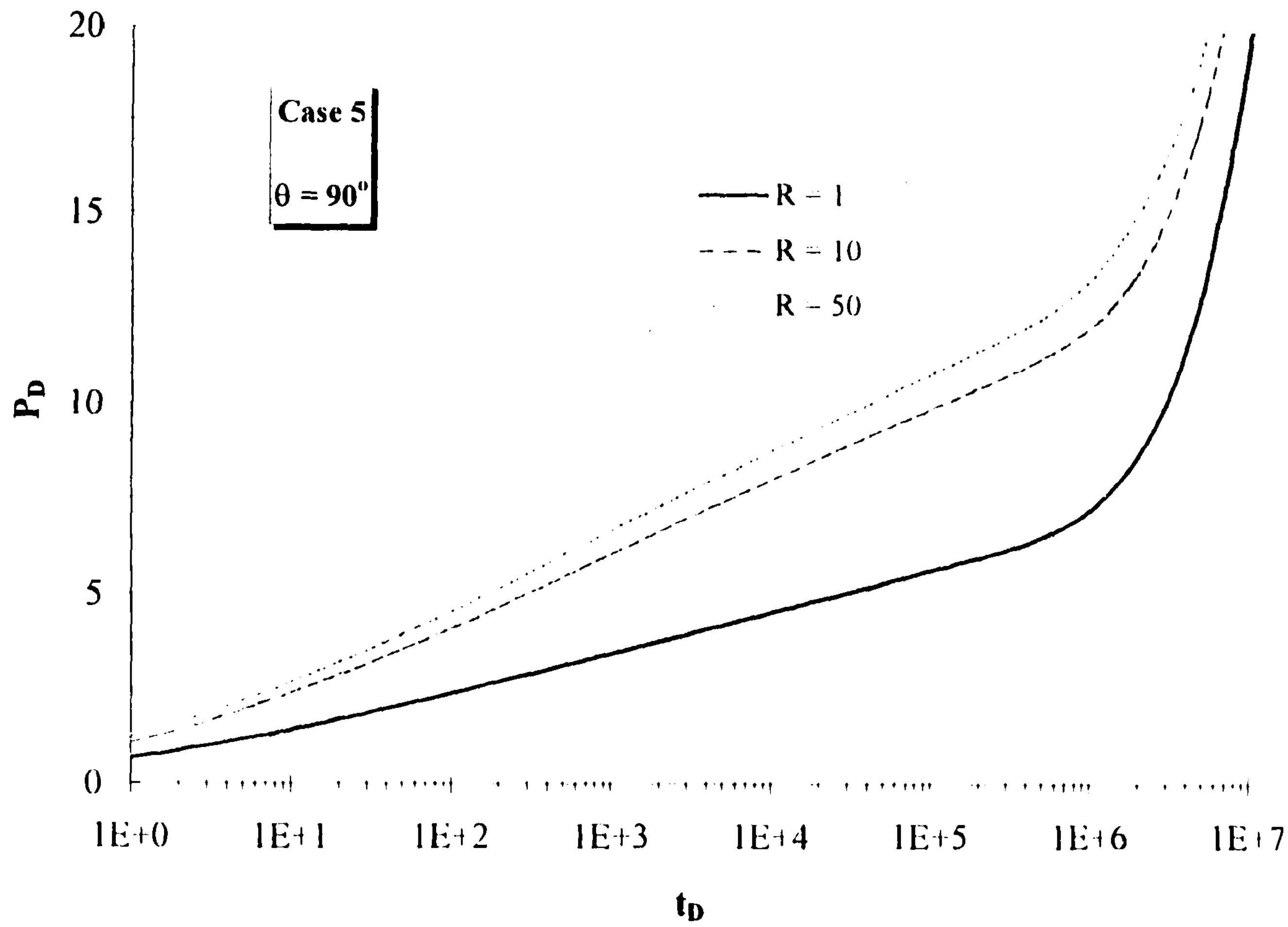

Figure 5.5.6(b) The Dimensionless Pressure for Case 5 and θ = 90°

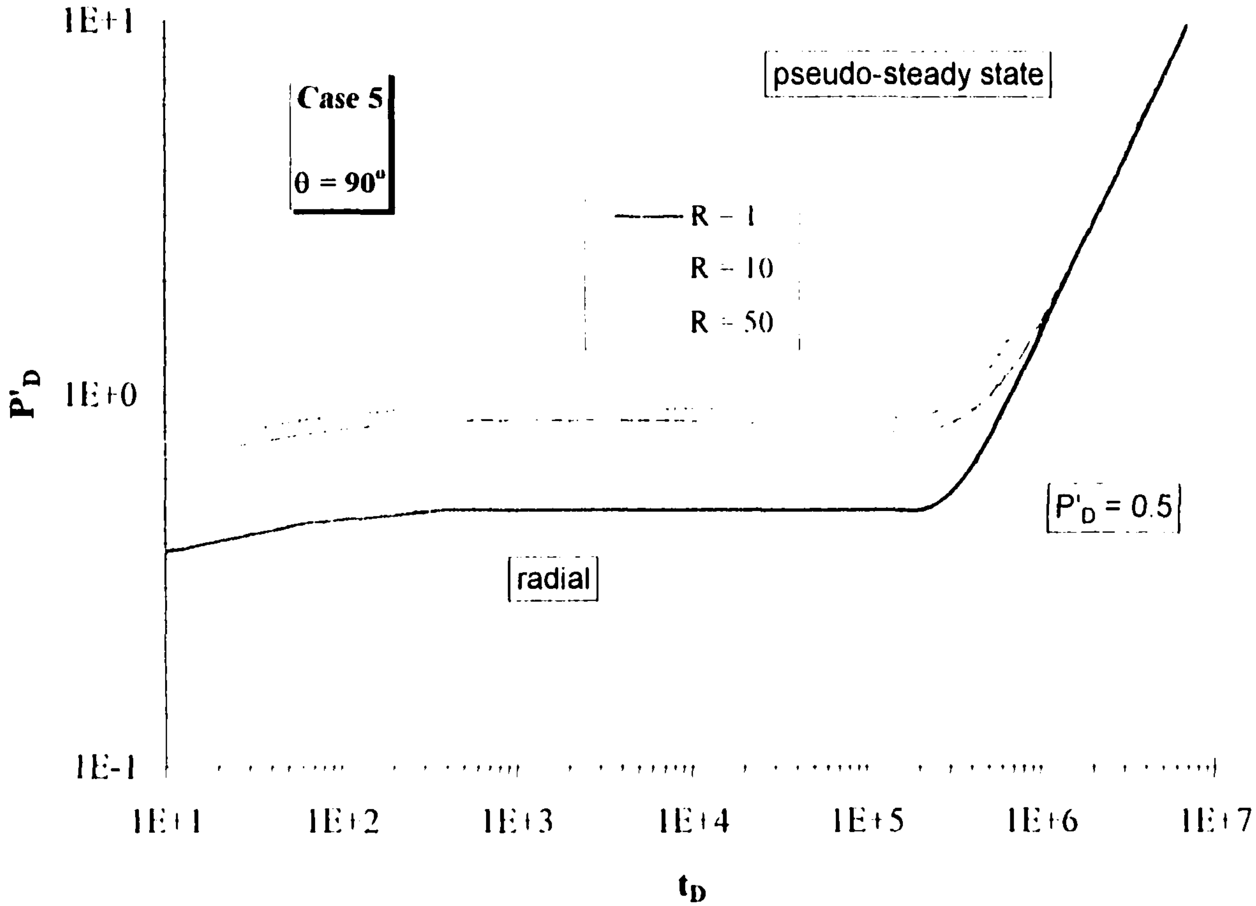

Figure 5.5.6(c) The Dimensionless Pressure Derivative for Case 5 and $\theta = 90°$

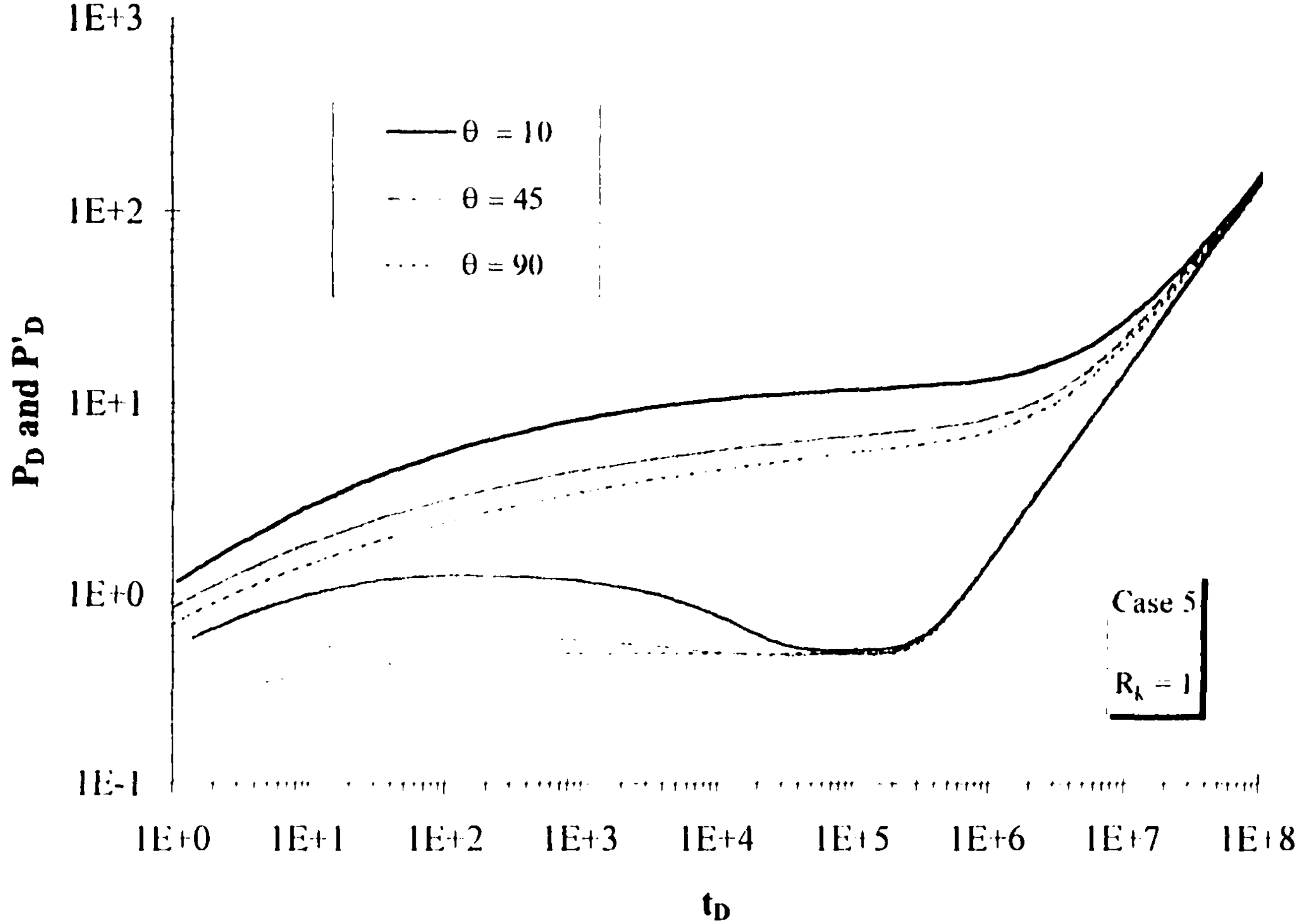

Figure 5.5.7(a) The Dimensionless Pressure and The Dimensionless Pressure Derivative

for Case 5 and $R_k = 1$

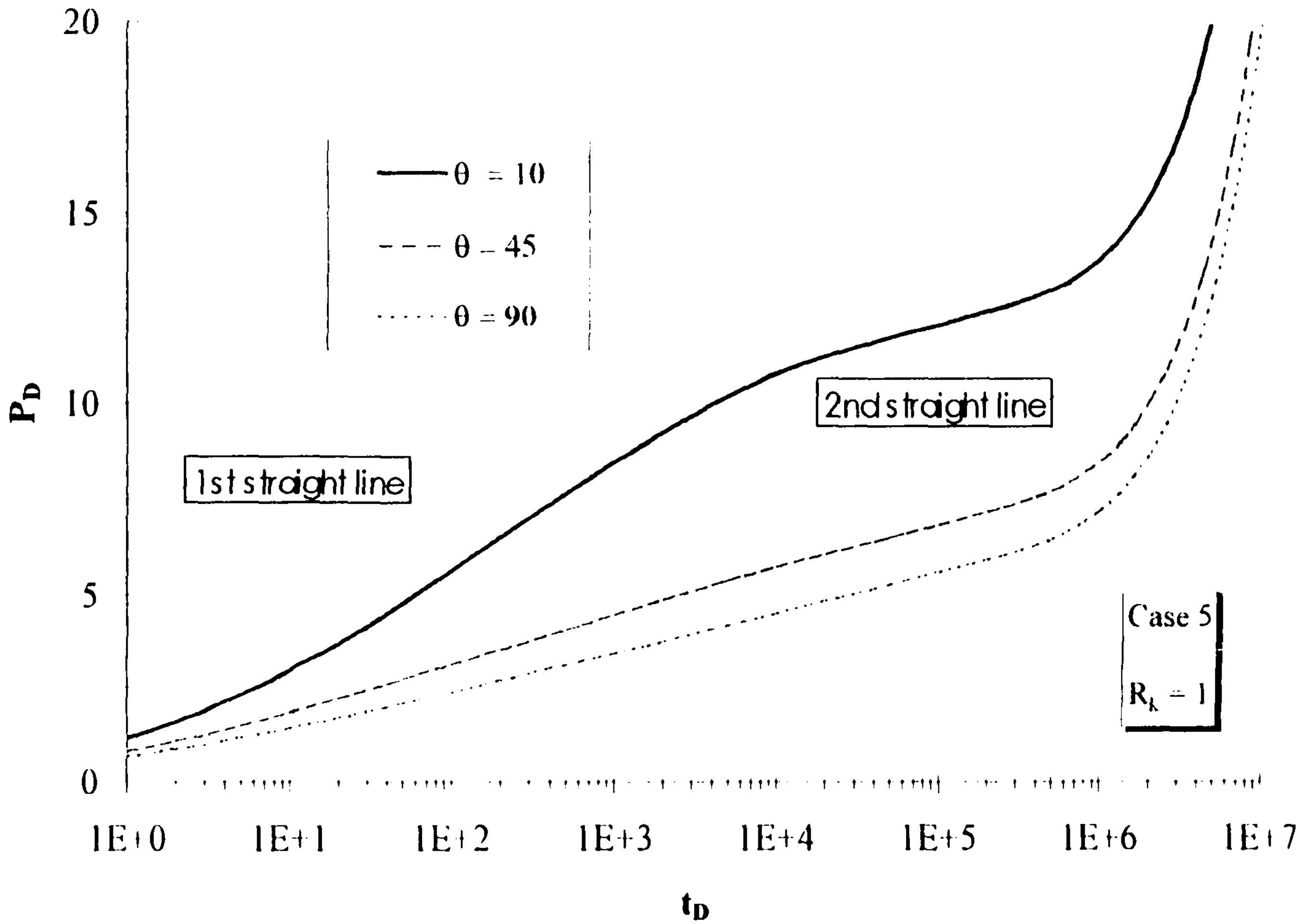

Figure 5.5.7(b) The Dimensionless Pressure for Case 5 and $R_k = 1$

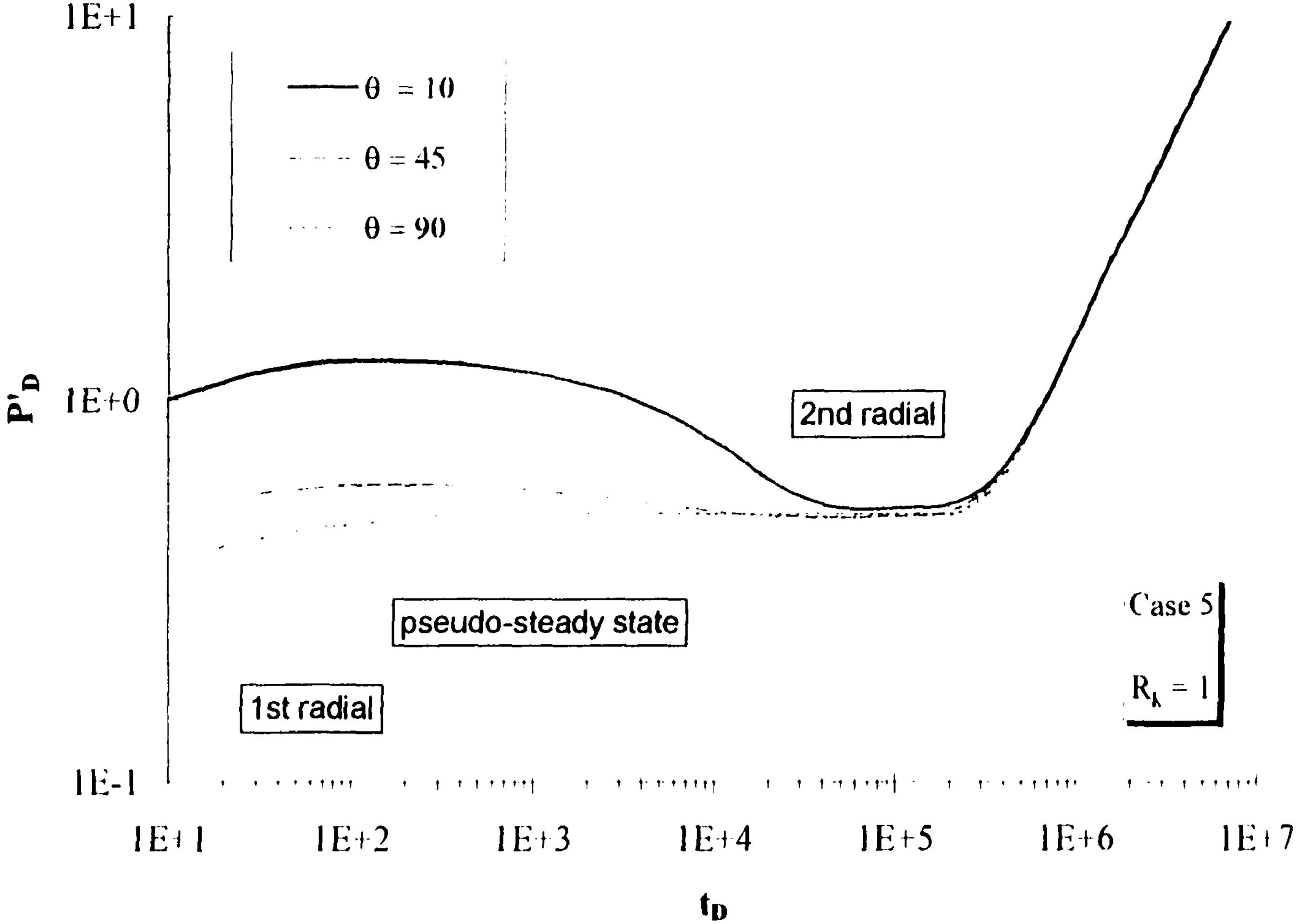

Figure 5.5.7(c) The Dimensionless Pressure Derivative for Case 5 and $R_k = 1$

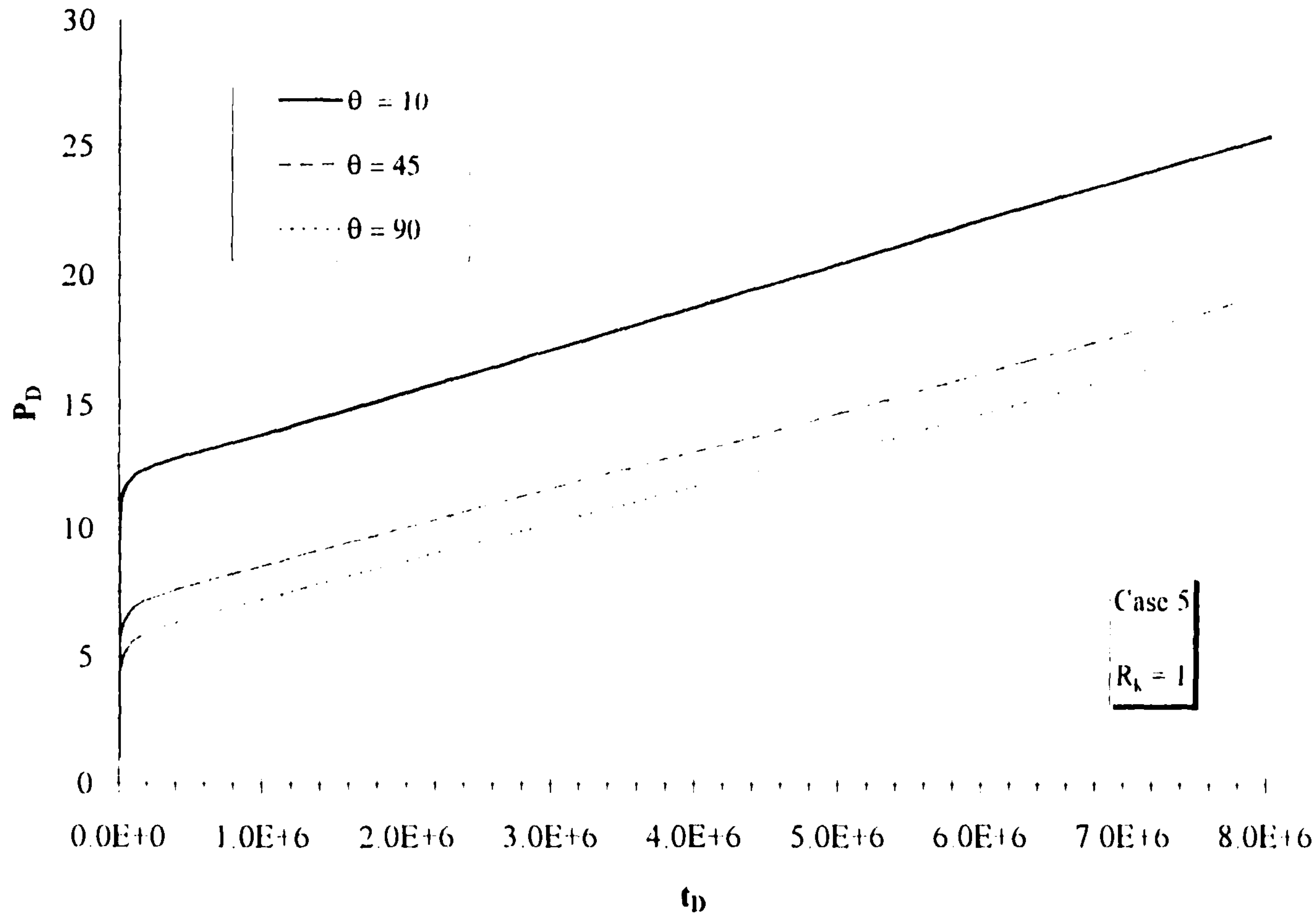

Figure 5.5.7(d) The Dimensionless Pressure for Case 5 and $R_k = 1$ during The Pseudo-Steady State

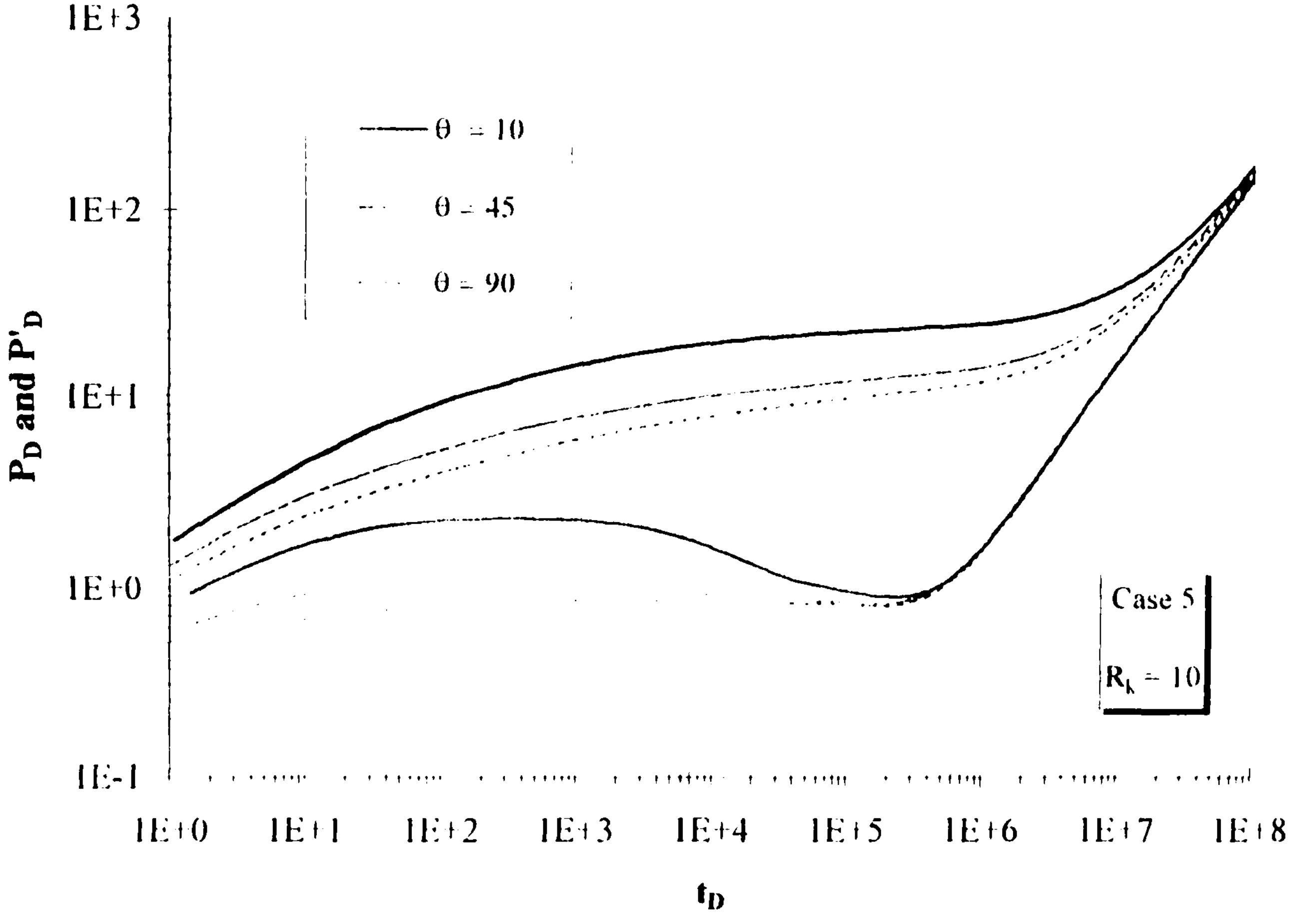

Figure 5.5.8(a) The Dimensionless Pressure and The Dimensionless Pressure Derivative

for Case 5 and $R_k = 10$

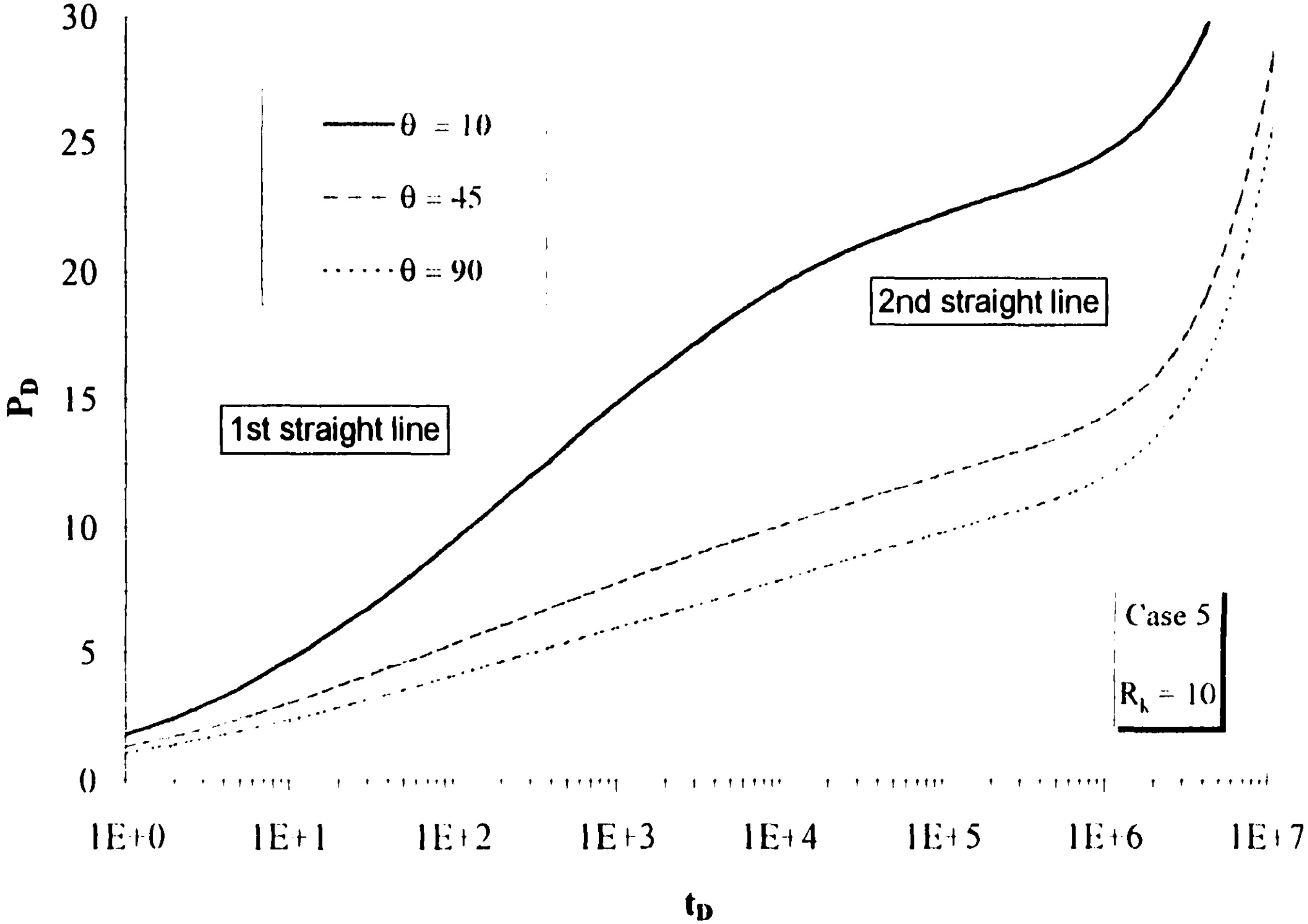

Figure 5.5.8(b) The Dimensionless Pressure for Case 5 and R_k = 10

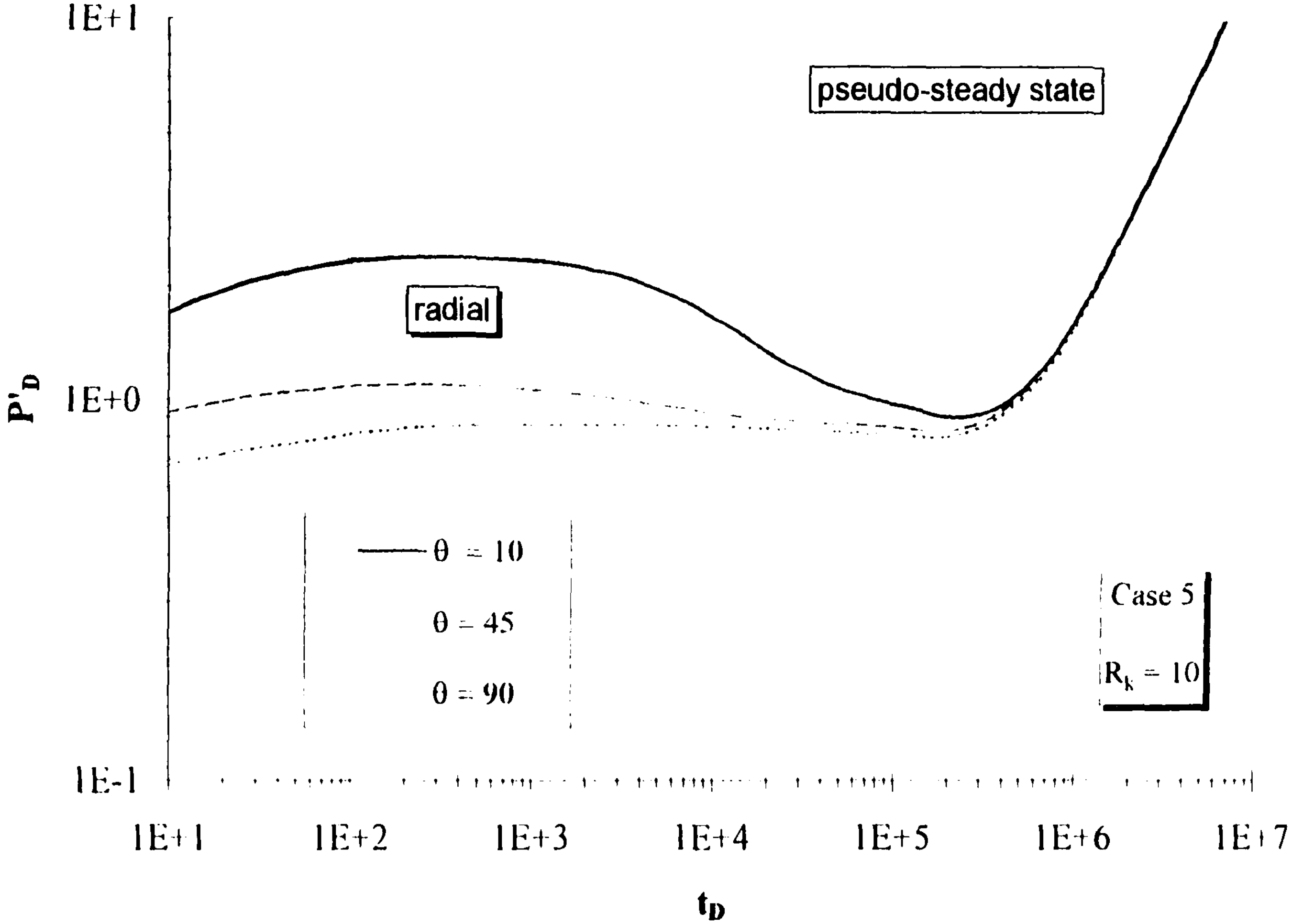

Figure 5.5.8(c) The Dimensionless Pressure Derivative for Case 5 and R_k = 10

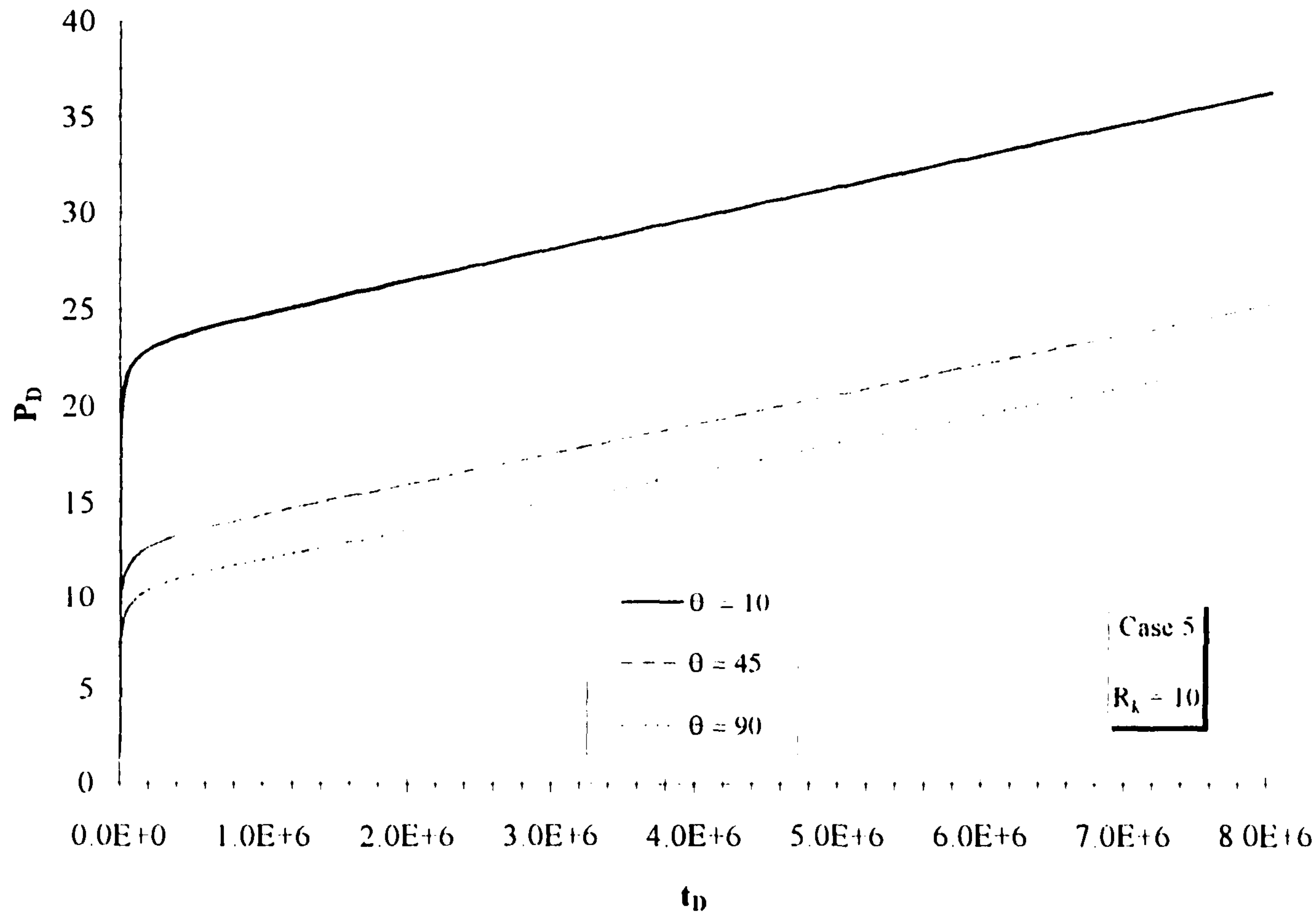

Figure 5.5.8(d) The Dimensionless Pressure for Case 5 and R_k = 10 during pseudo-steady state

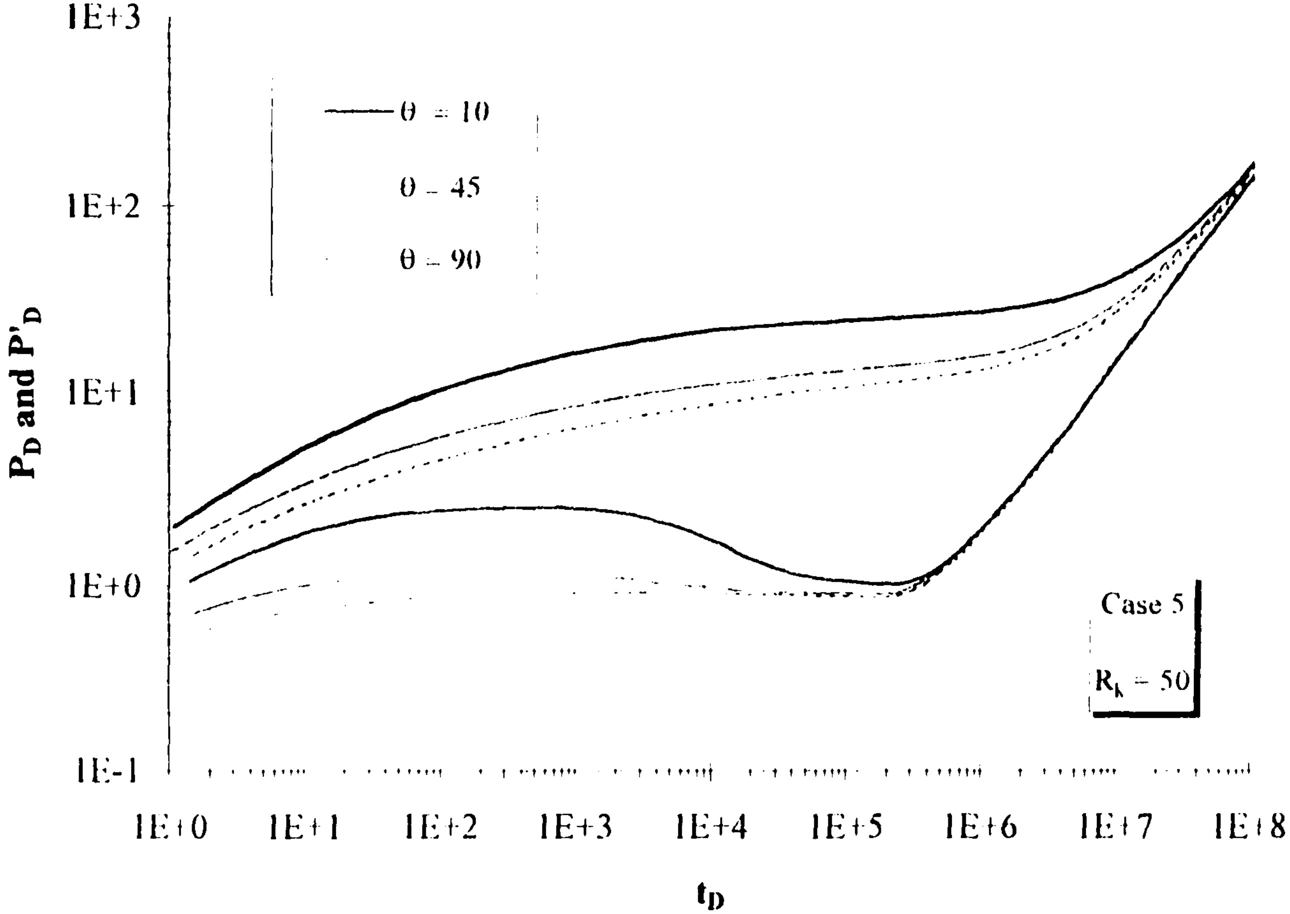

Figure 5.5.9(a) The Dimensionless Pressure and The Dimensionless Pressure Derivative

for Case 5 and $R_k = 50$

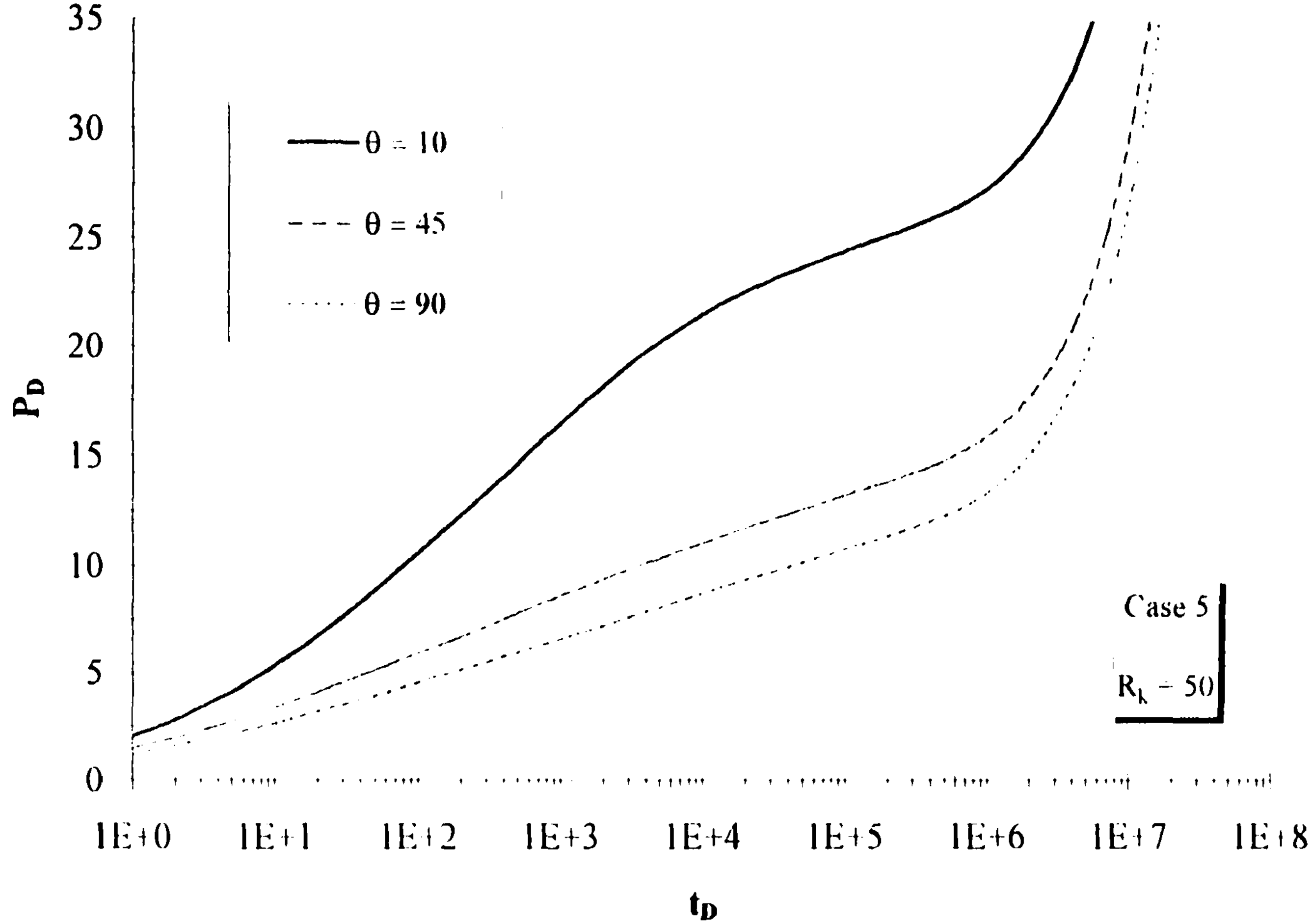

Figure 5.5.9(b) The Dimensionless Pressure for Case 5 and $R_k = 50$

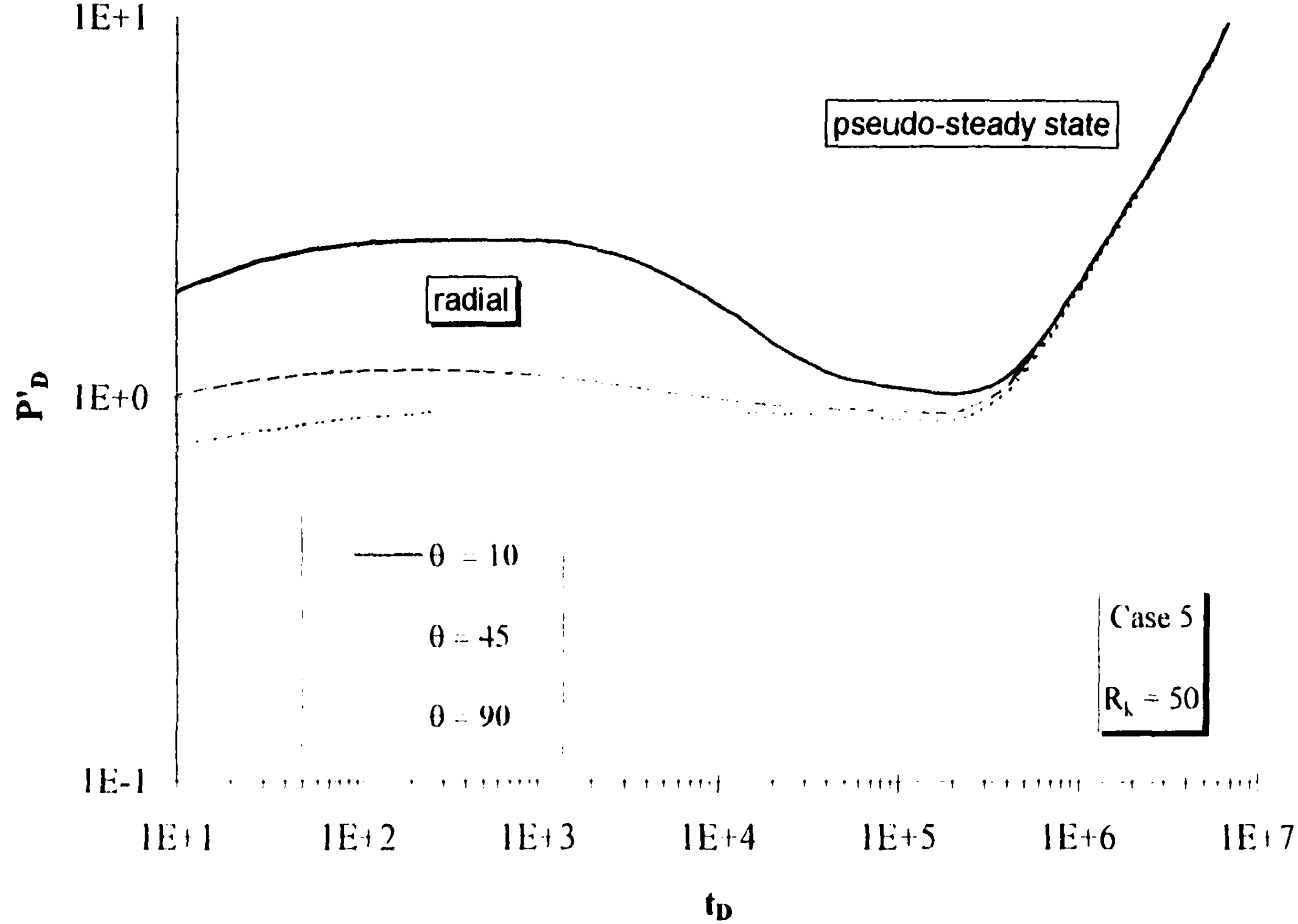

Figure 5.5.9(c) The Dimensionless Pressure Derivative for Case 5 and $R_k = 50$

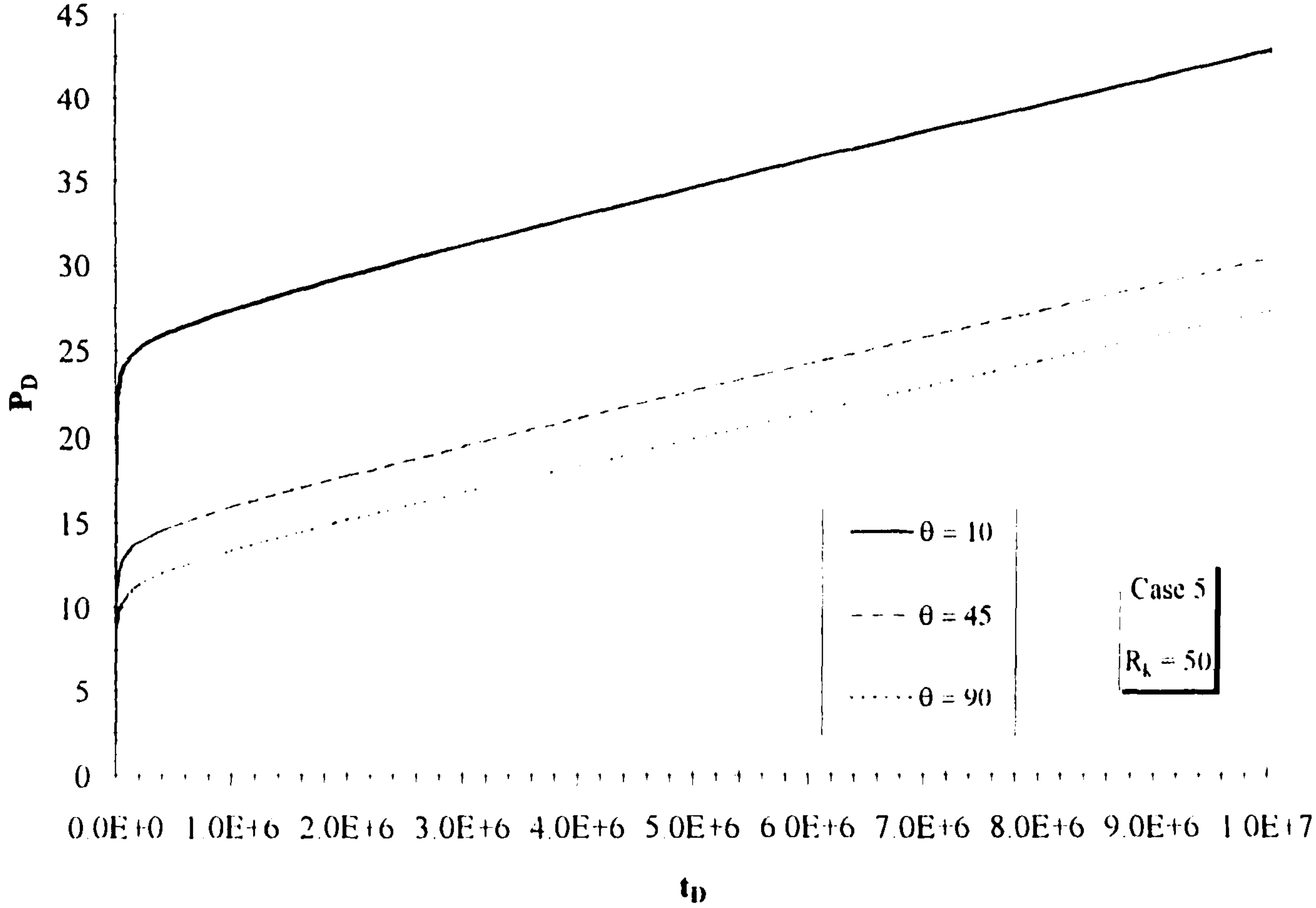

Figure 5.5.9(d) The Dimensionless Pressure for Case 5 and R_k = 50 During Pseudo-Steady State

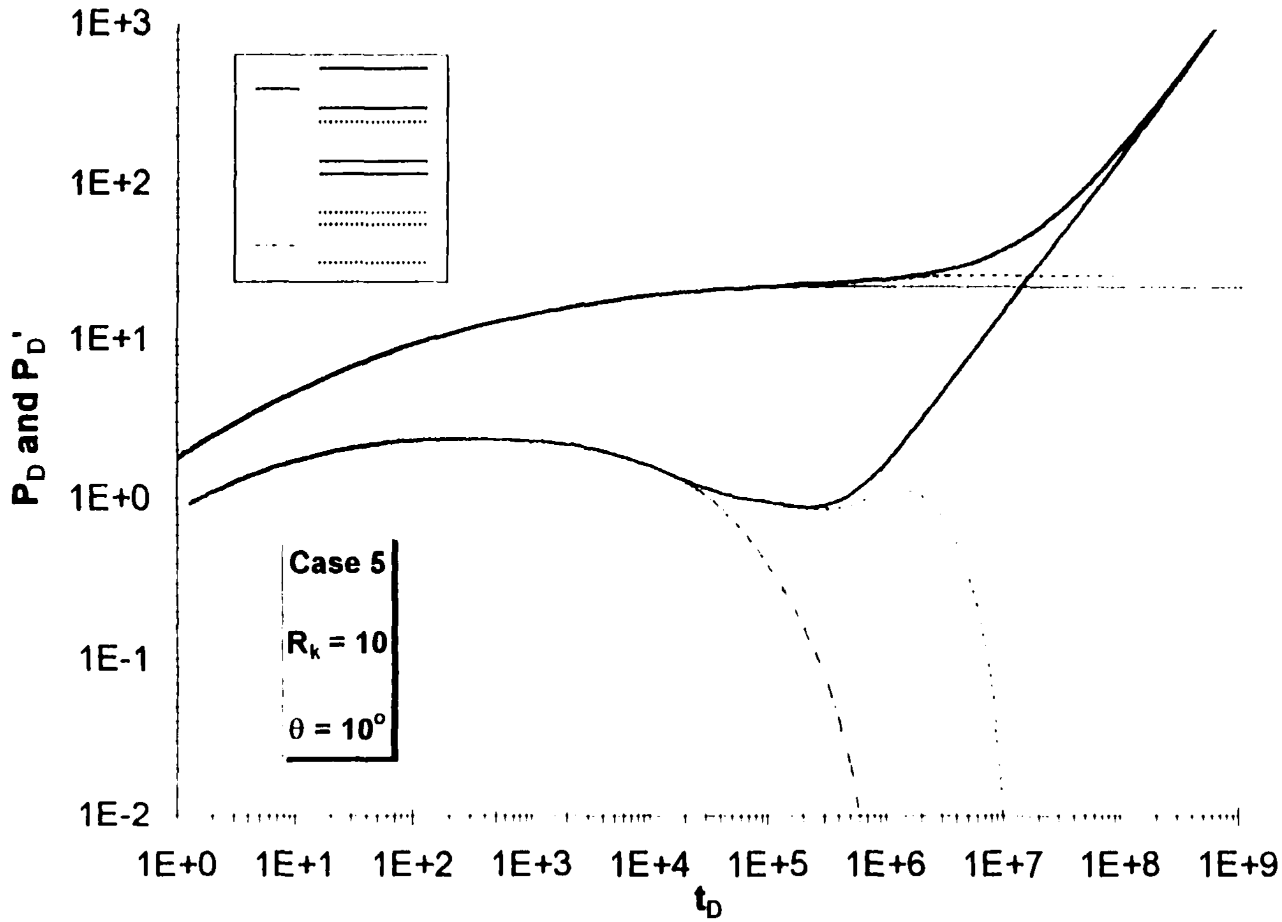

Figure 5.5.10(a) The Dimensionless Pressure and The Dimensionless Pressure Derivative

for Case 5 and $R_k = 10$ For Different Boundary Conditions

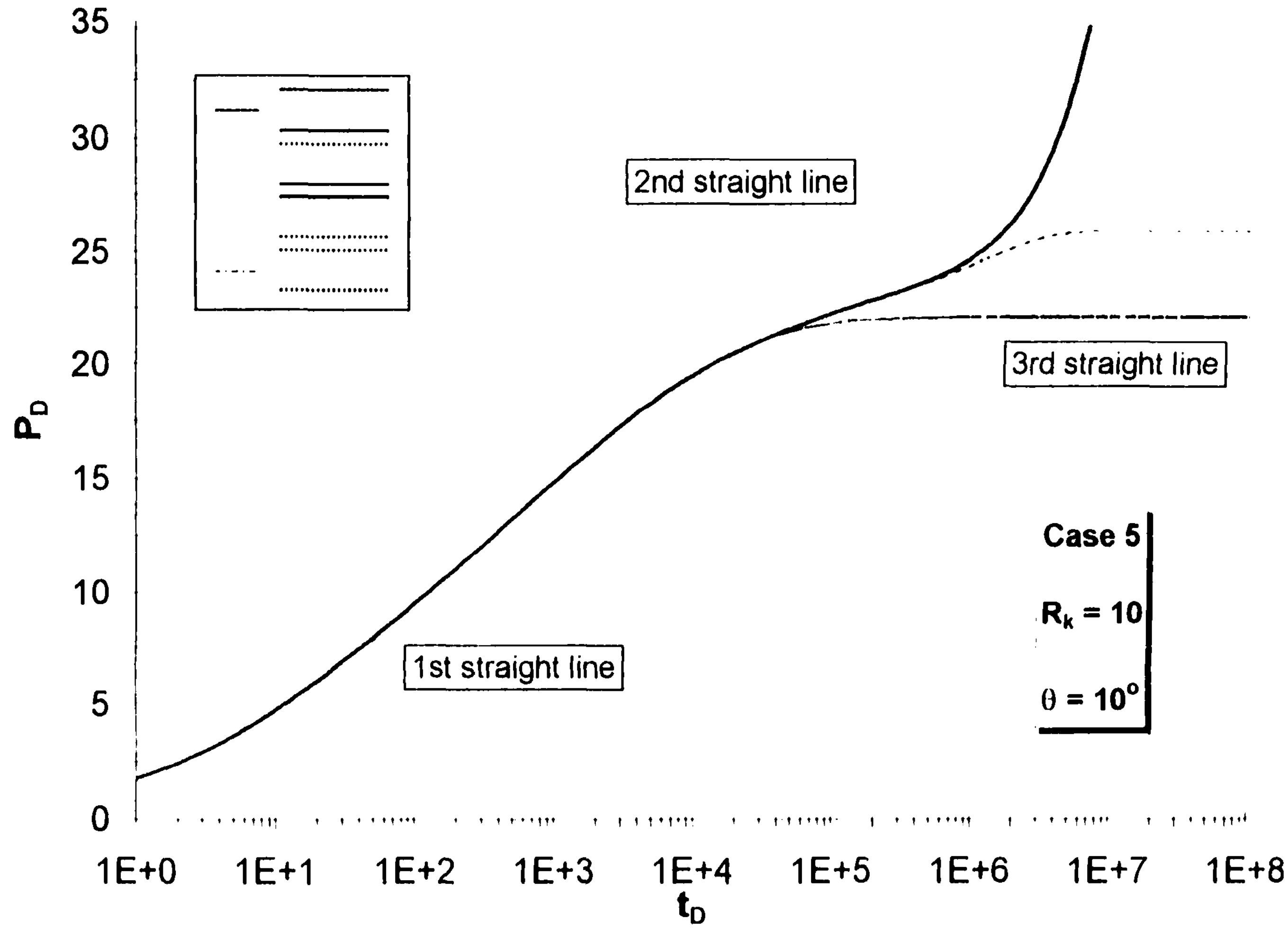

Figure 5.5.10(b) The Dimensionless Pressure for Case 5 and R_k = 10 For Different Boundary Conditions

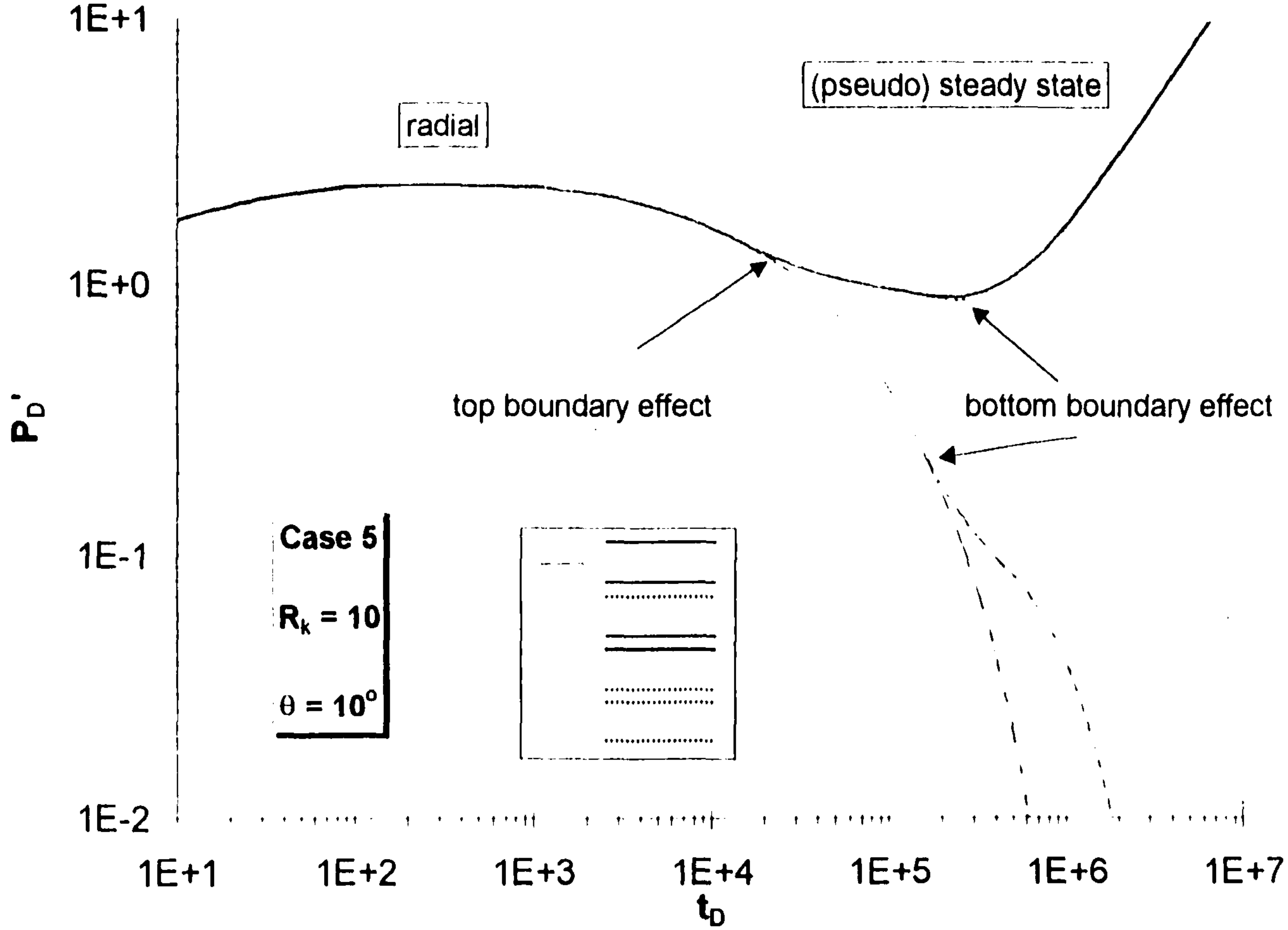

Figure 5.5.10(c) The Dimensionless Pressure Derivative for Case 5 and $R_k = 10$

For Different Boundary Conditions

APPENDIX H

LIST OF FIGURES IN CASE 5.6

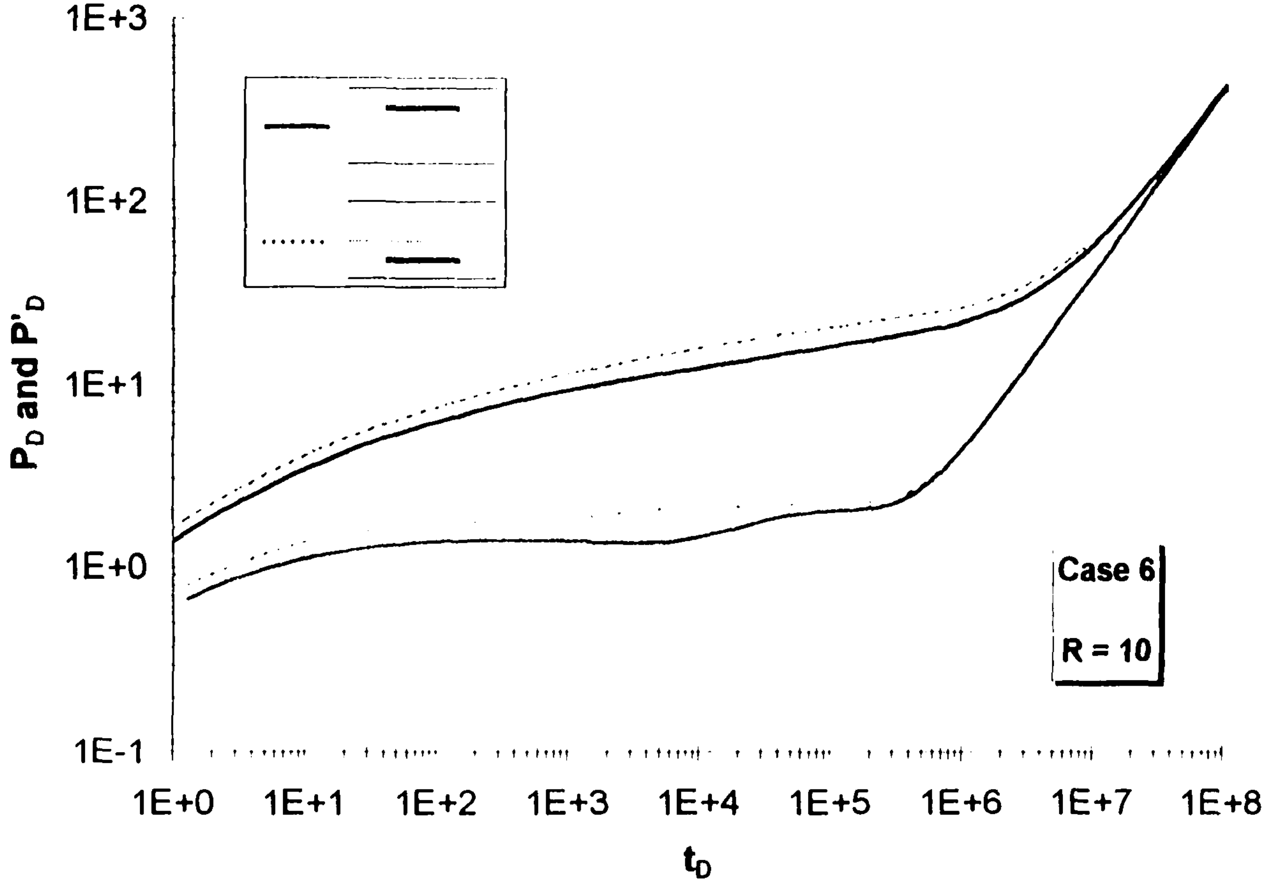

Figure 5.6.5(a) The Dimensionless Pressure and The Dimensionless Pressure Derivative

for Case 6 and $R_k = 10$

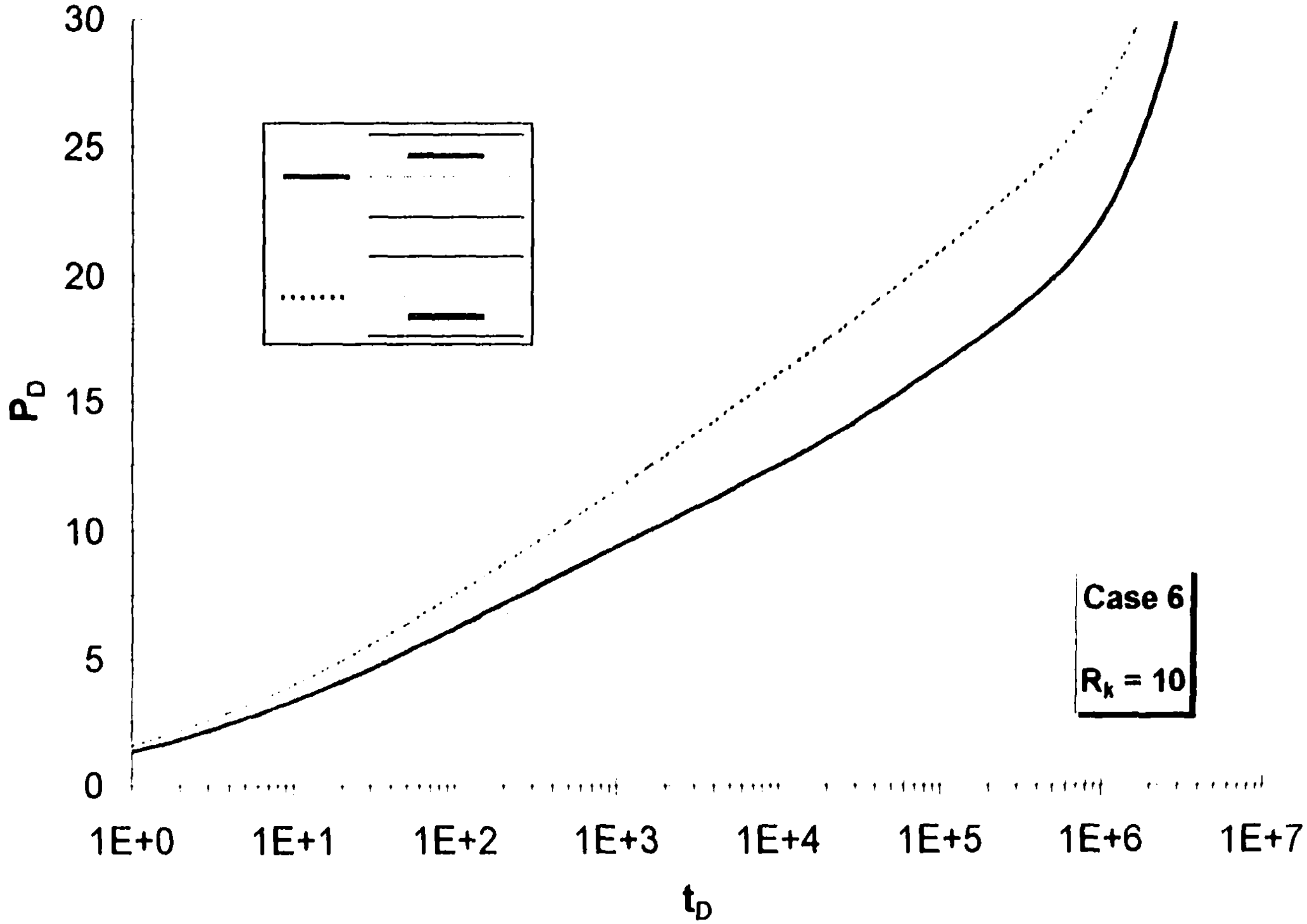

Figure 5.6.5(b) The Dimensionless Pressure for Case 6 and $R_k = 10$

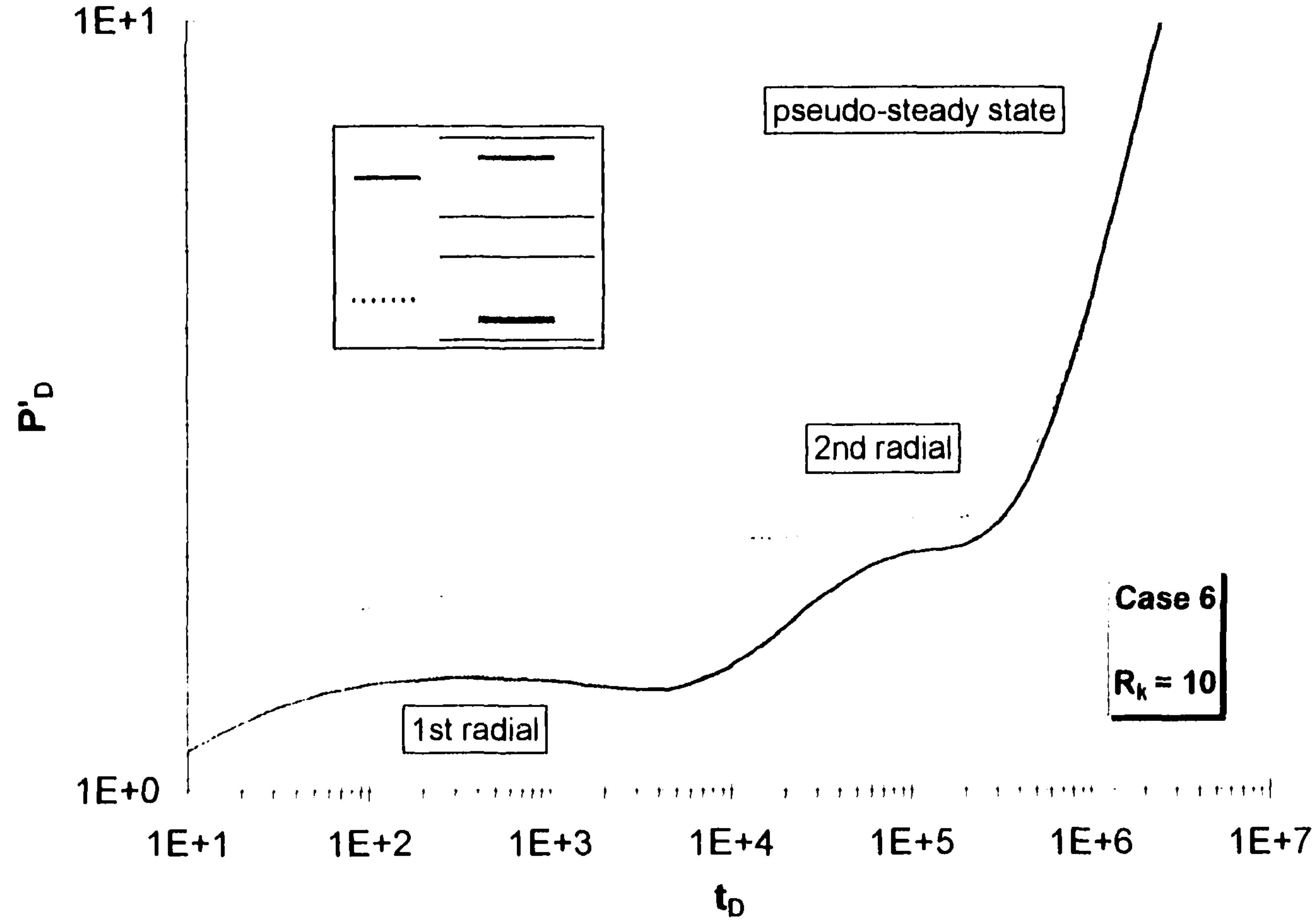

Figure 5.6.5(c) The Dimensionless Pressure Derivative for Case 6 and $R_k = 10$

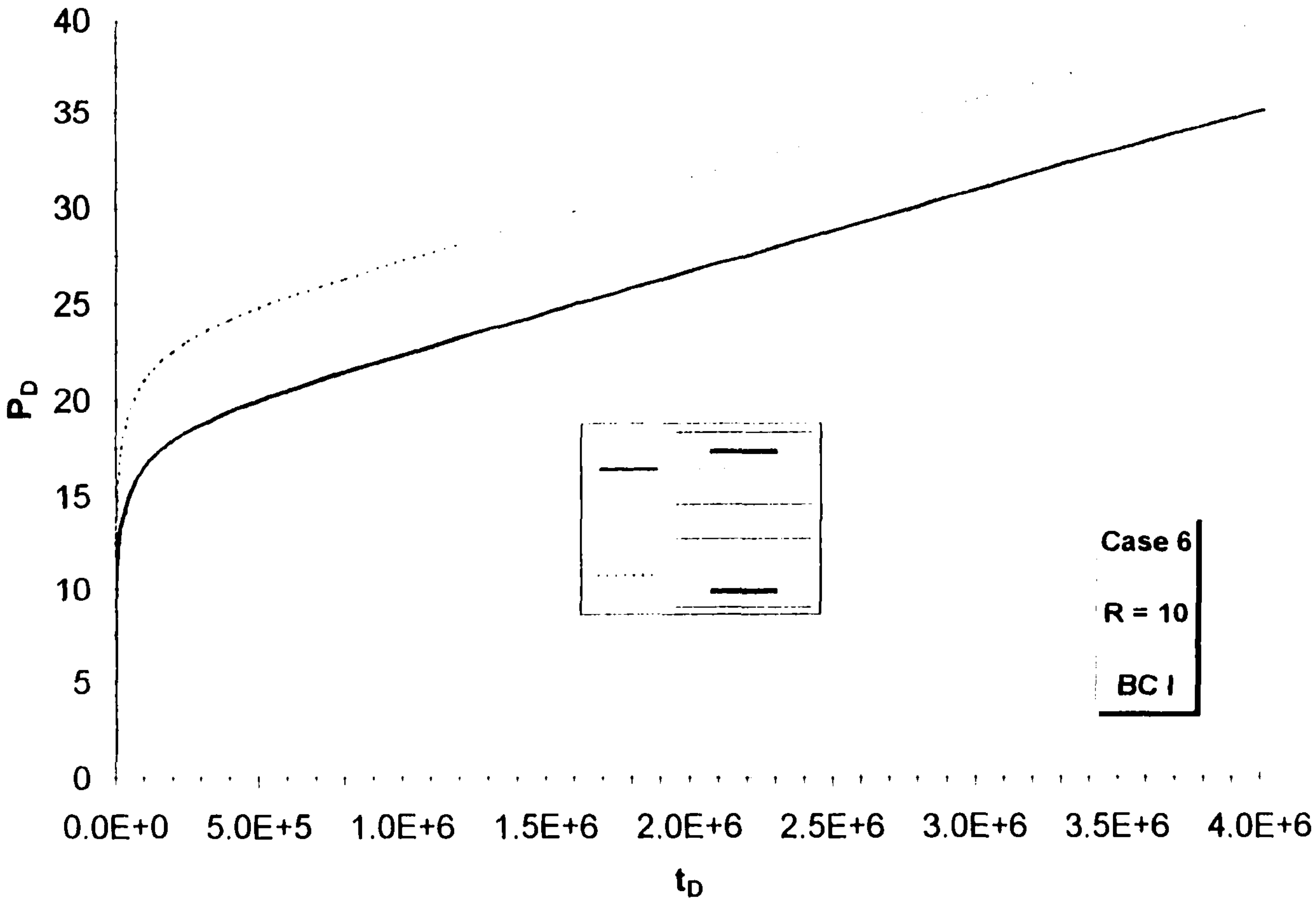

Figure 5.6.5(d) The Dimensionless Pressure for Case 6 and R_k = 10 During Pseudo-Steady State

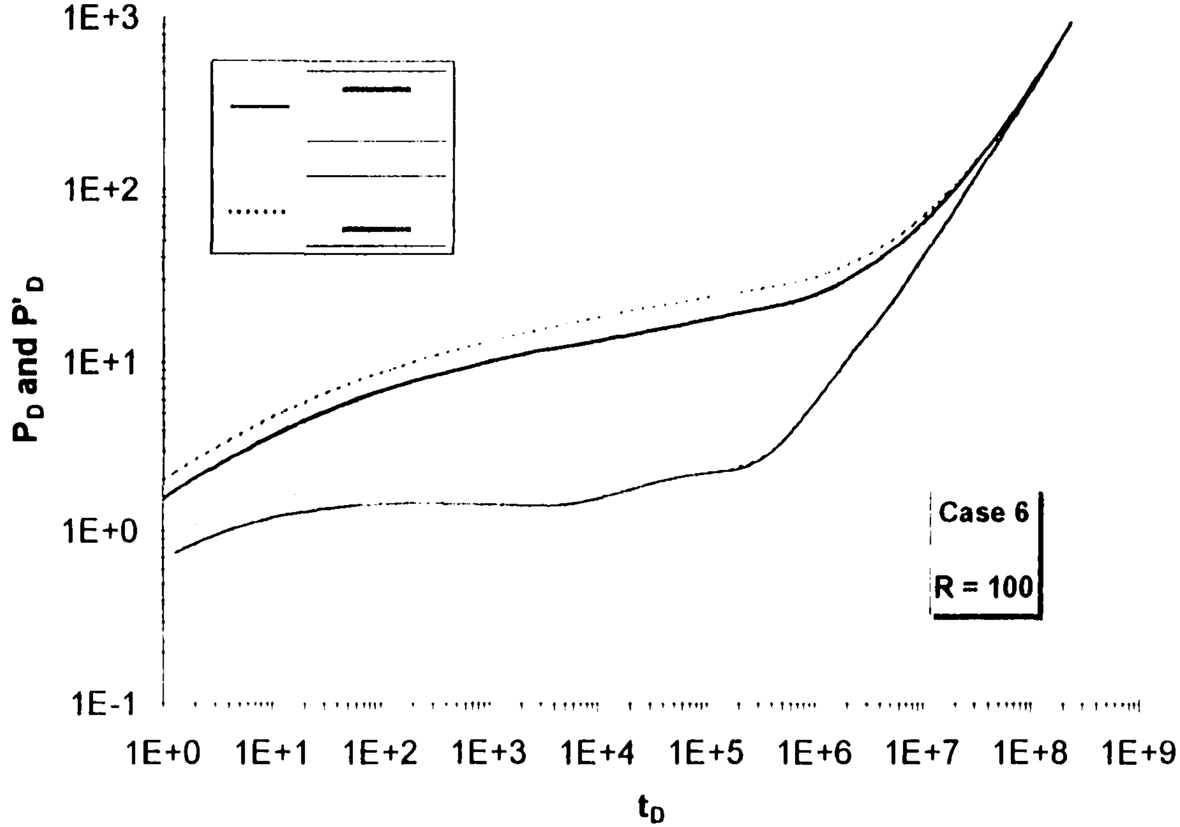

Figure 5.6.6(a) The Dimensionless Pressure and The Dimensionless Pressure Derivative for Case 6 and $R_k = 100$

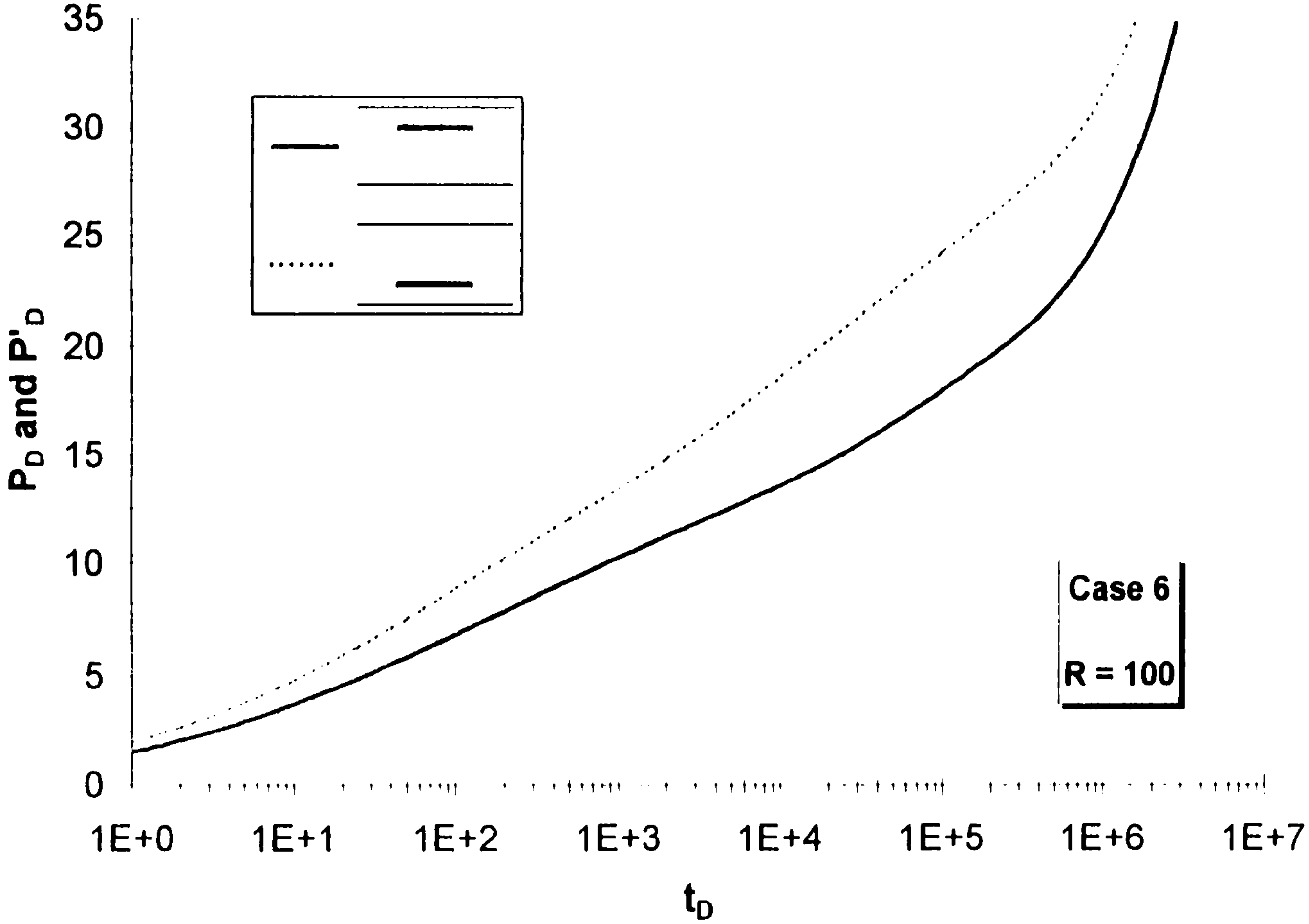

Figure 5.6.6(b) The Dimensionless Pressure for Case 6 and $R_k = 100$

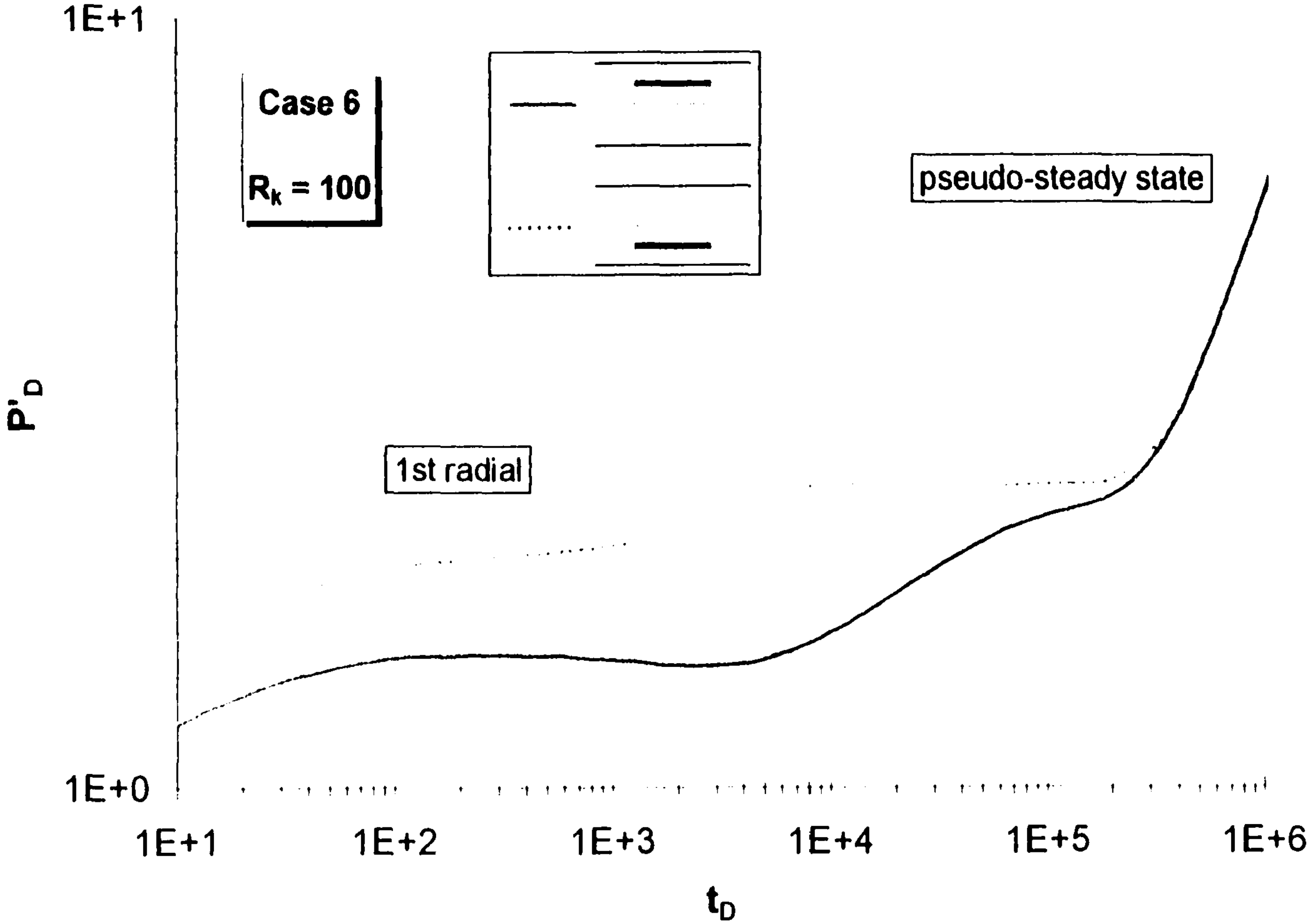

Figure 5.6.6(c) The Dimensionless Pressure Derivative for Case 6 and R_k = 100

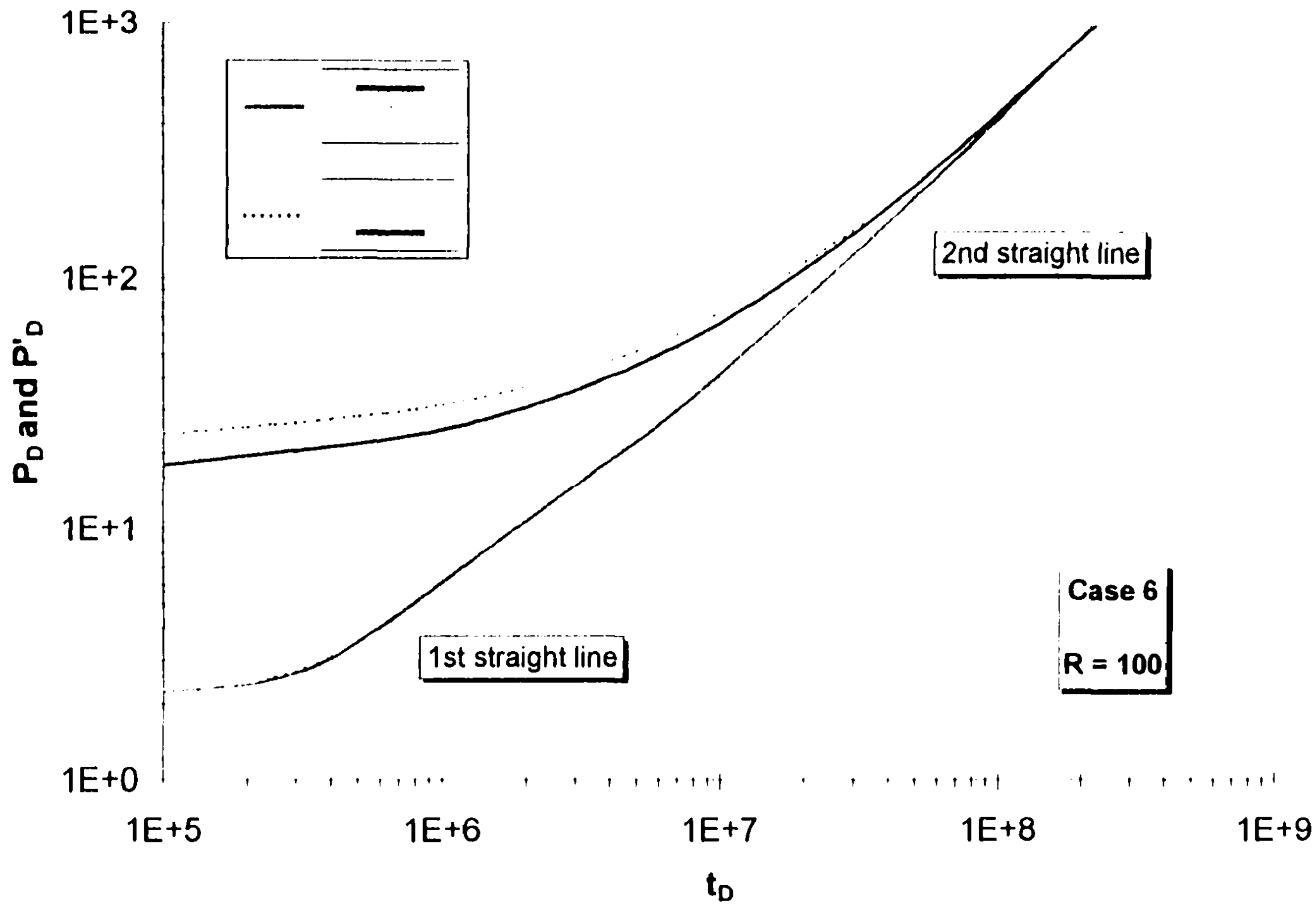

Figure 5.6.6(d) The Dimensionless Pressure and The Dimensionless Pressure Derivative

For Case 6 and R_k = 100 During The Late-Time Period

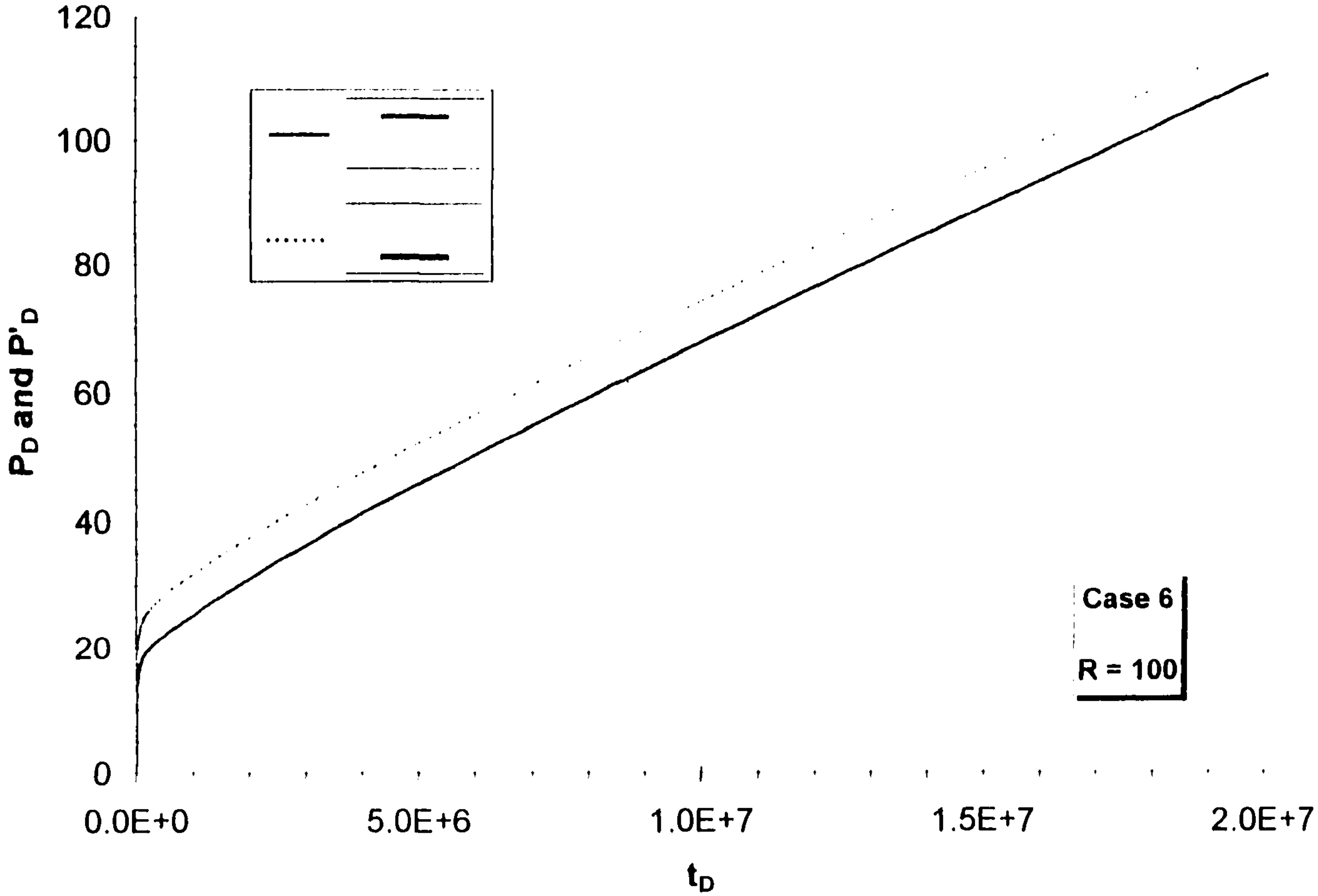

Figure 5.6.6(e) The Dimensionless Pressure for Case 6 and R_k = 100 During Pseudo-Steady Flow

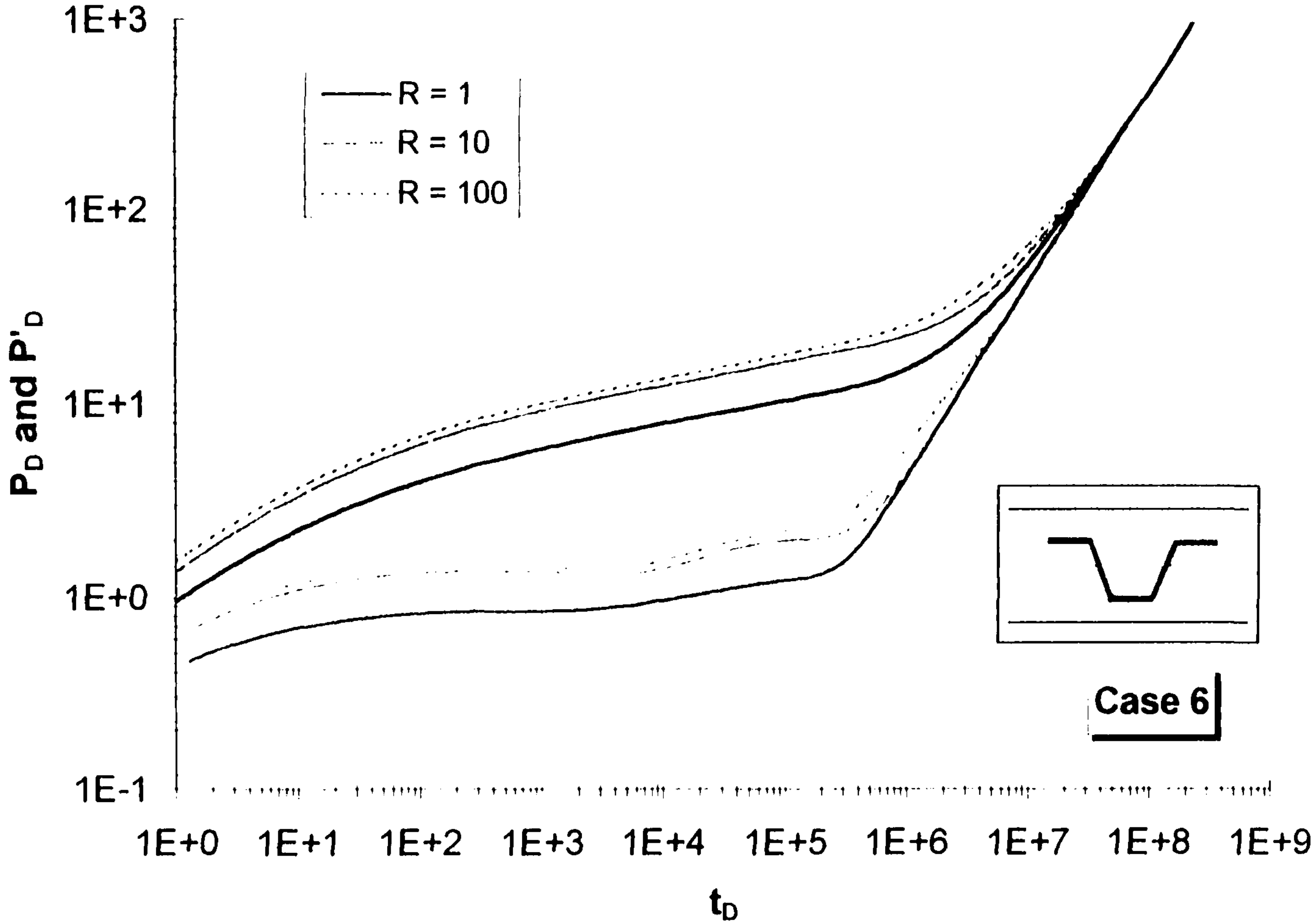

Figure 5.6.7(a) The Dimensionless Pressure and The Dimensionless Pressure Derivative for Case 6

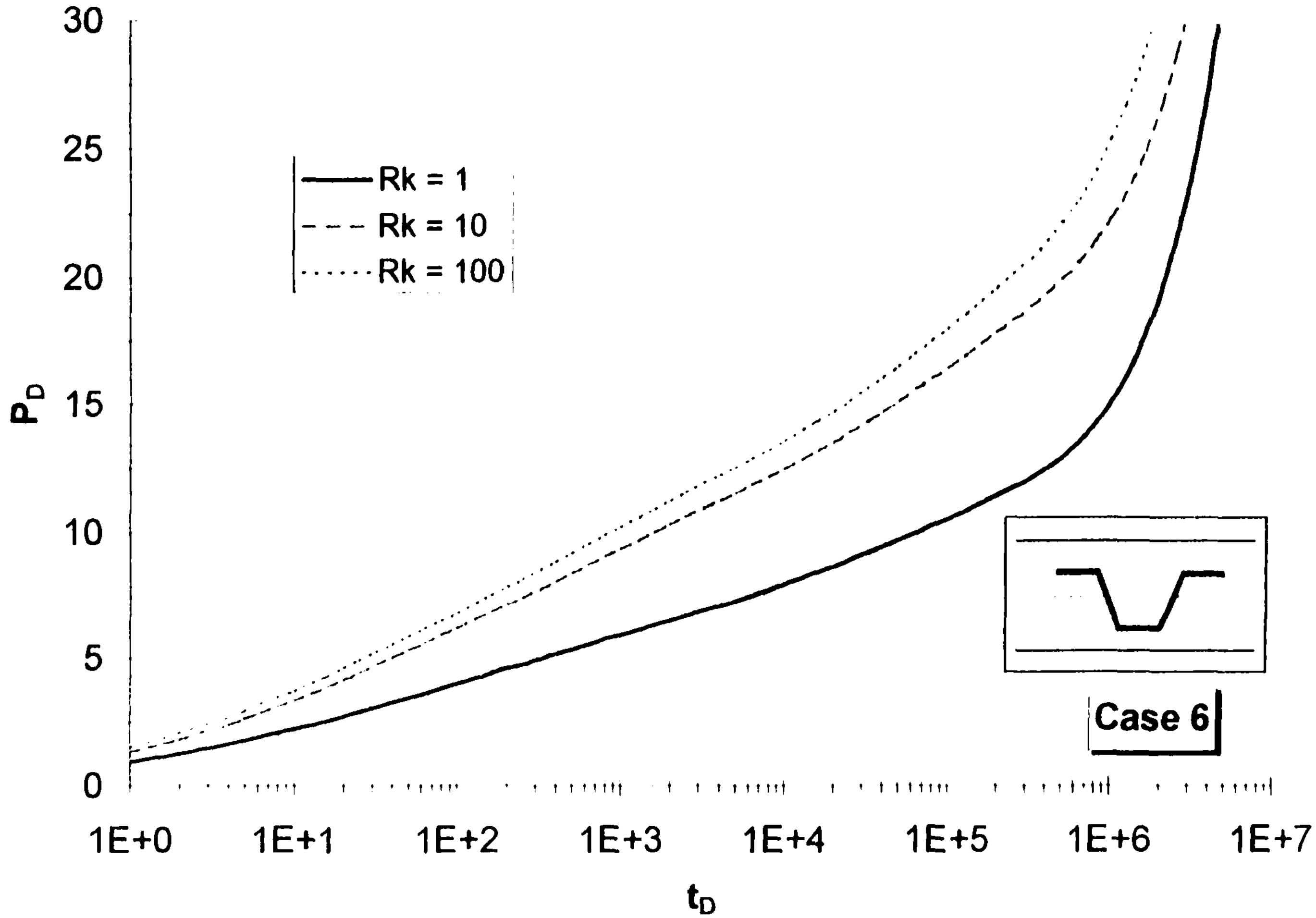

Figure 5.6.7(b) The Dimensionless Pressure for Case 6

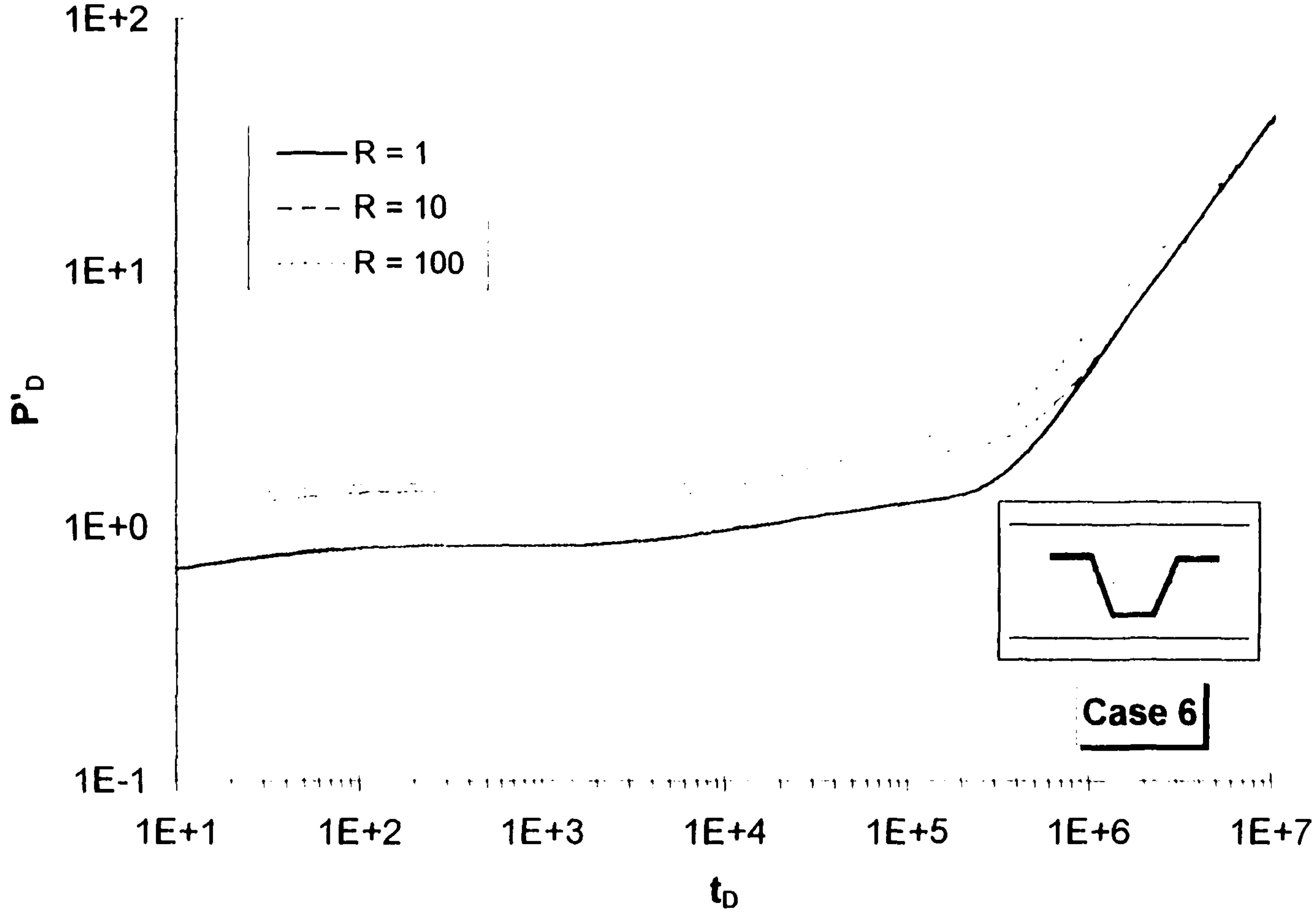

Figure 5.6.7(c) The Dimensionless Pressure Derivative for Case 6

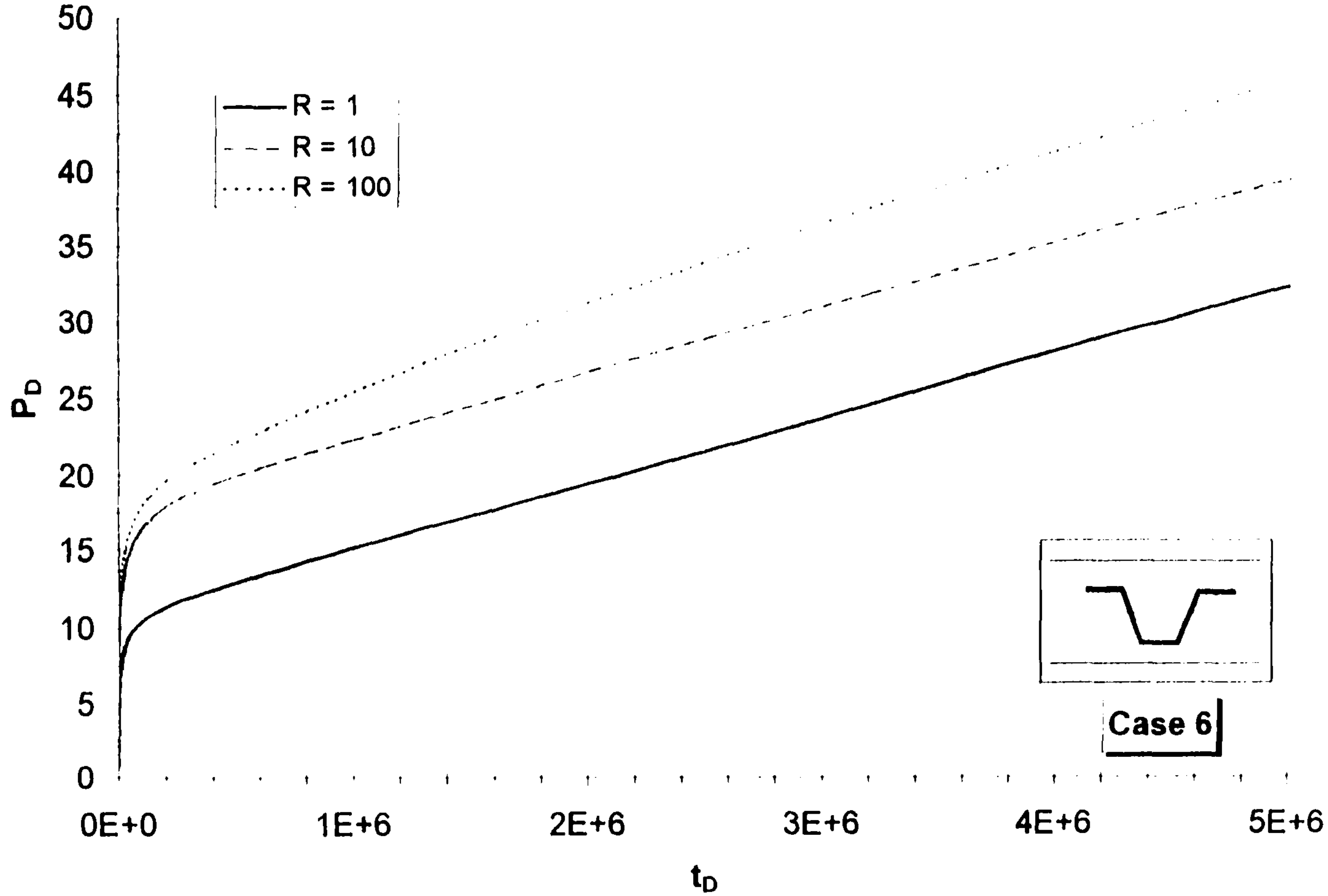

Figure 5.6.7(d) The Dimensionless Pressure for Case 6 During Pseudo-Steady State

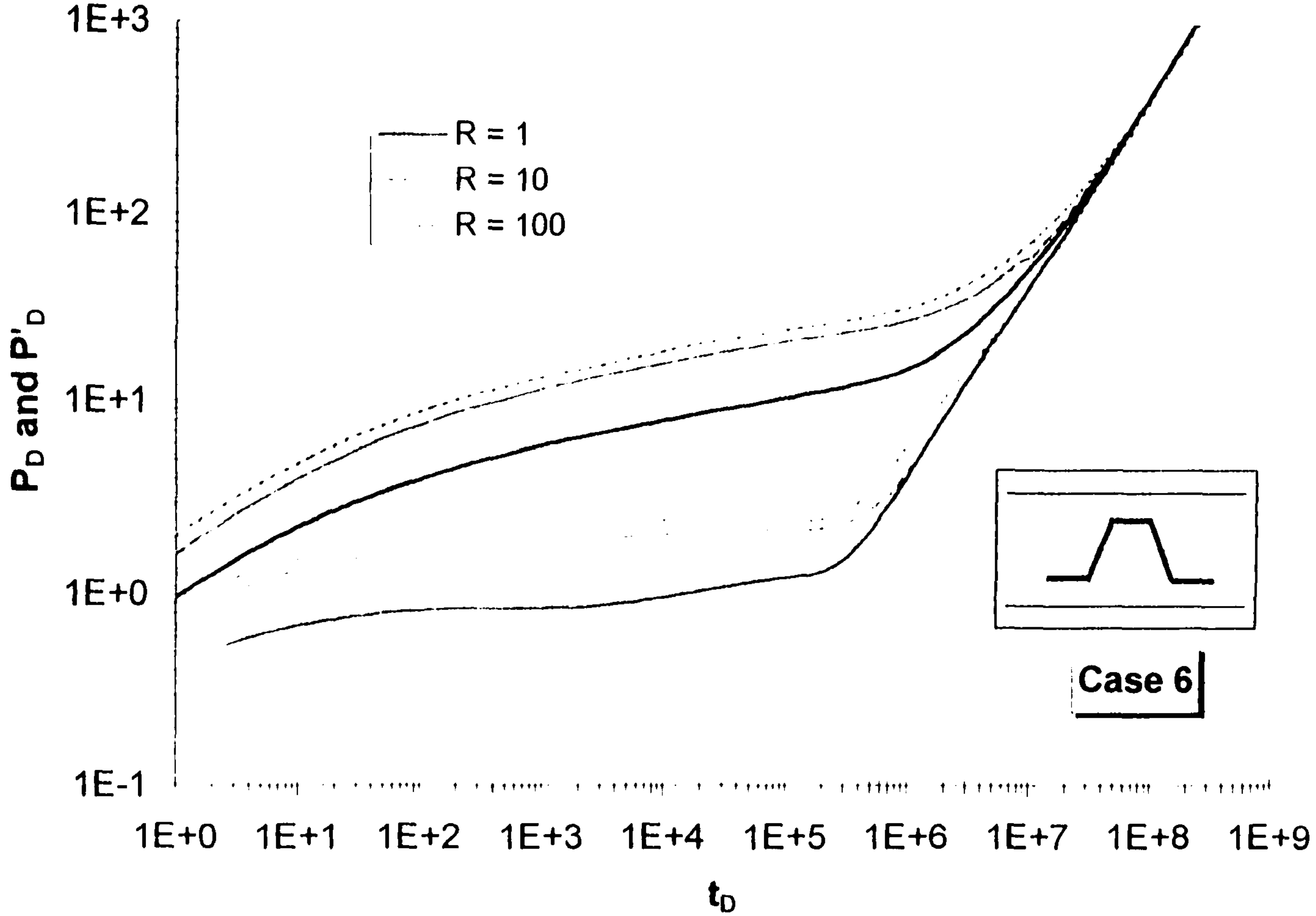

Figure 5.6.8(a) The Dimensionless Pressure and The Dimensionless Pressure Derivative for Case 6

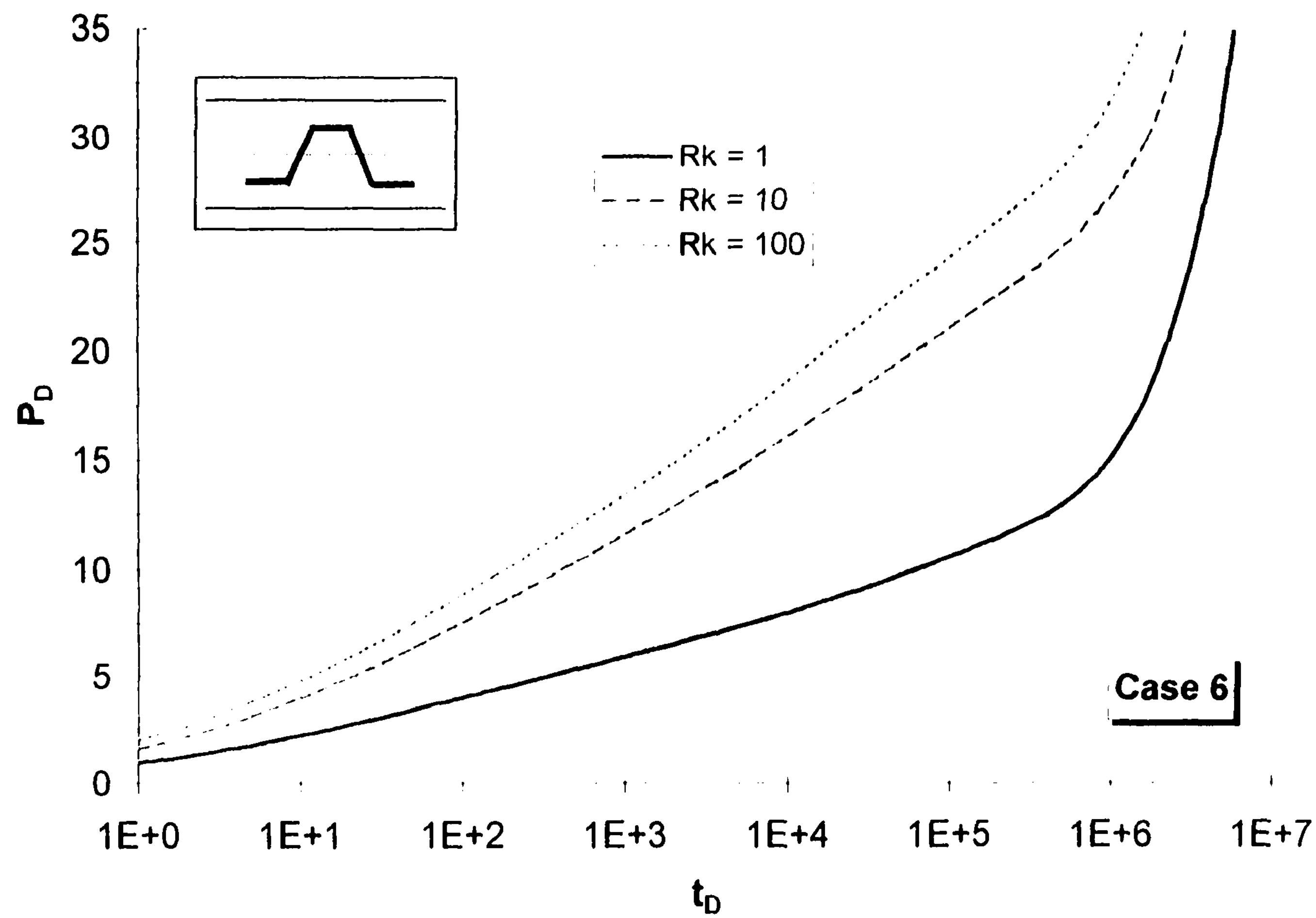

Figure 5.6.8(b) The Dimensionless Pressure and The Dimensionless Pressure Derivative for Case 6

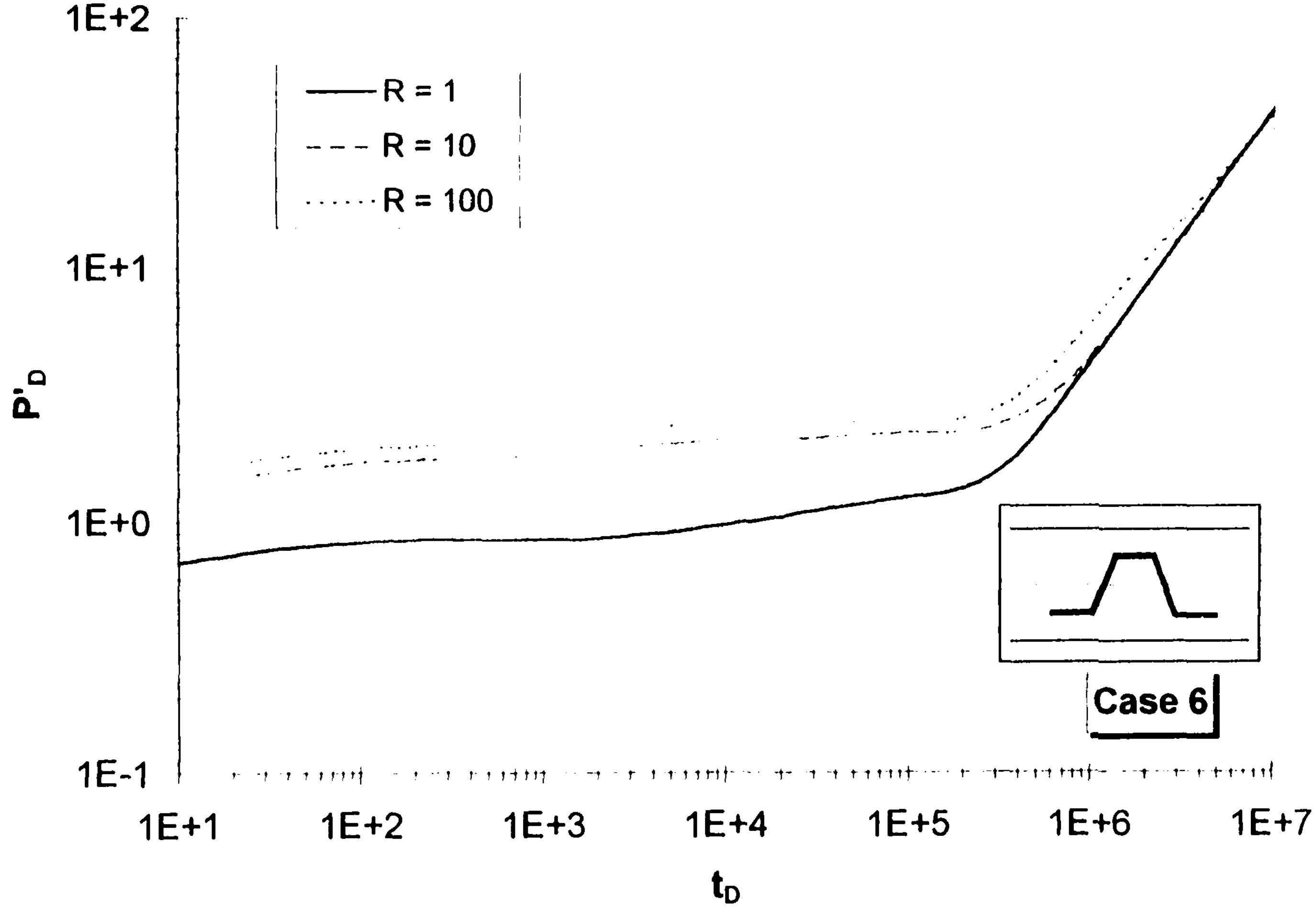

Figure 5.6.8(c) The Dimensionless Pressure Derivative for Case 6

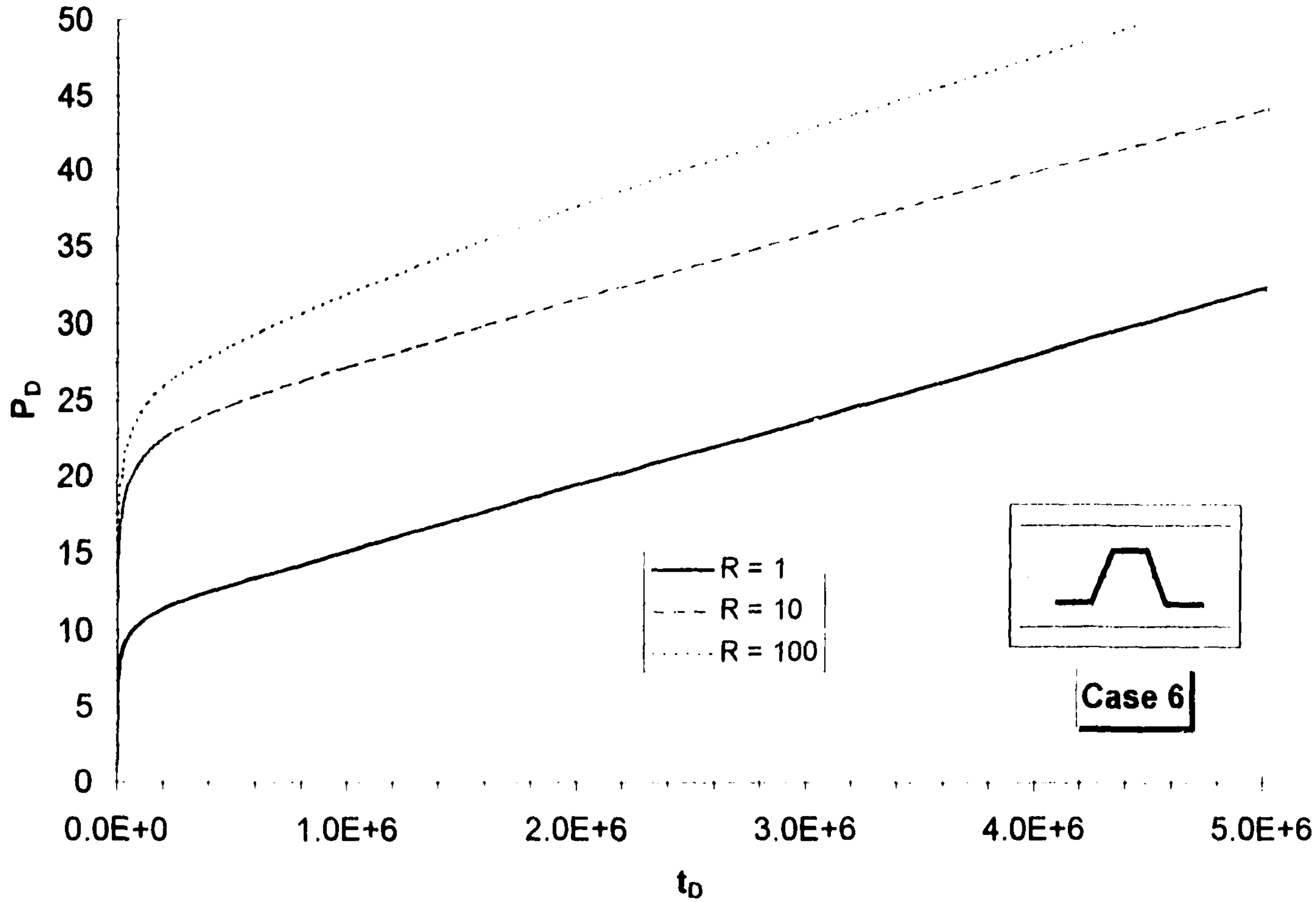

Figure 5.6.8(d) The Dimensionless Pressure and The Dimensionless Pressure Derivative

for Case 6 During Pseudo-Steady State

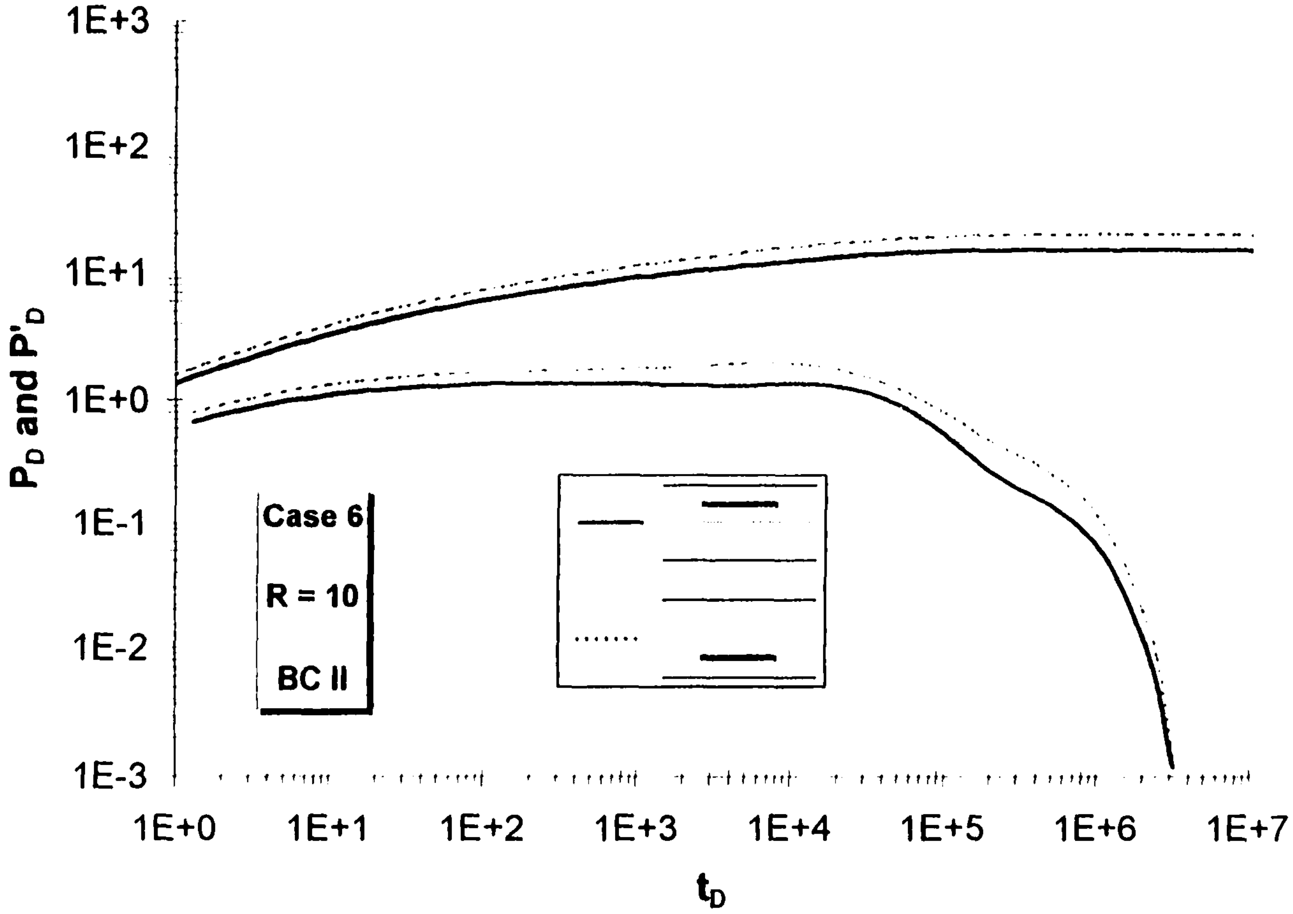

Figure 5.6.9(a) The Dimensionless Pressure and The Dimensionless Pressure Derivative

for Case 6, $R_k = 10$, and BC II

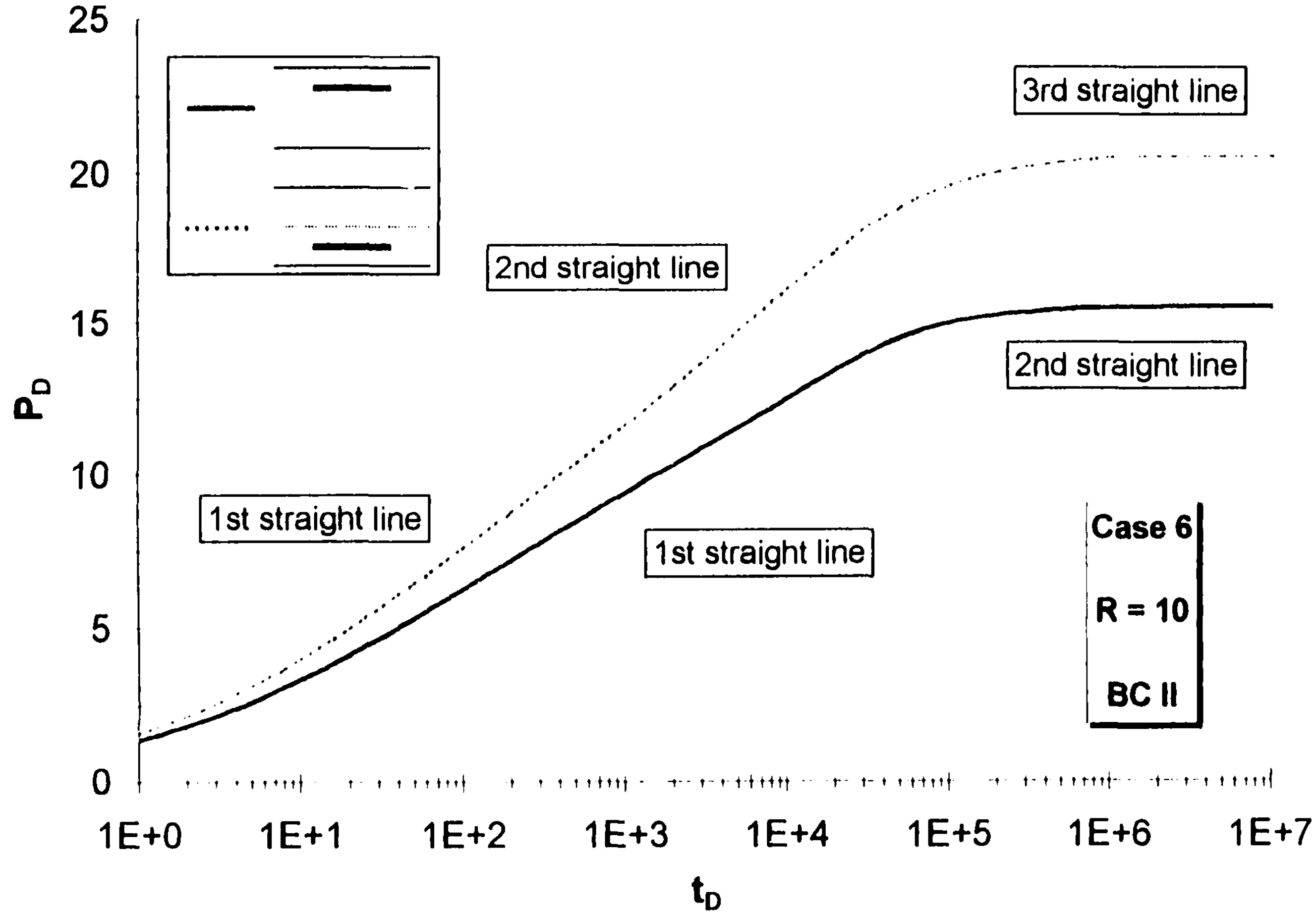

Figure 5.6.9(b) The Dimensionless Pressure for Case 6, R_k = 10, and BC II

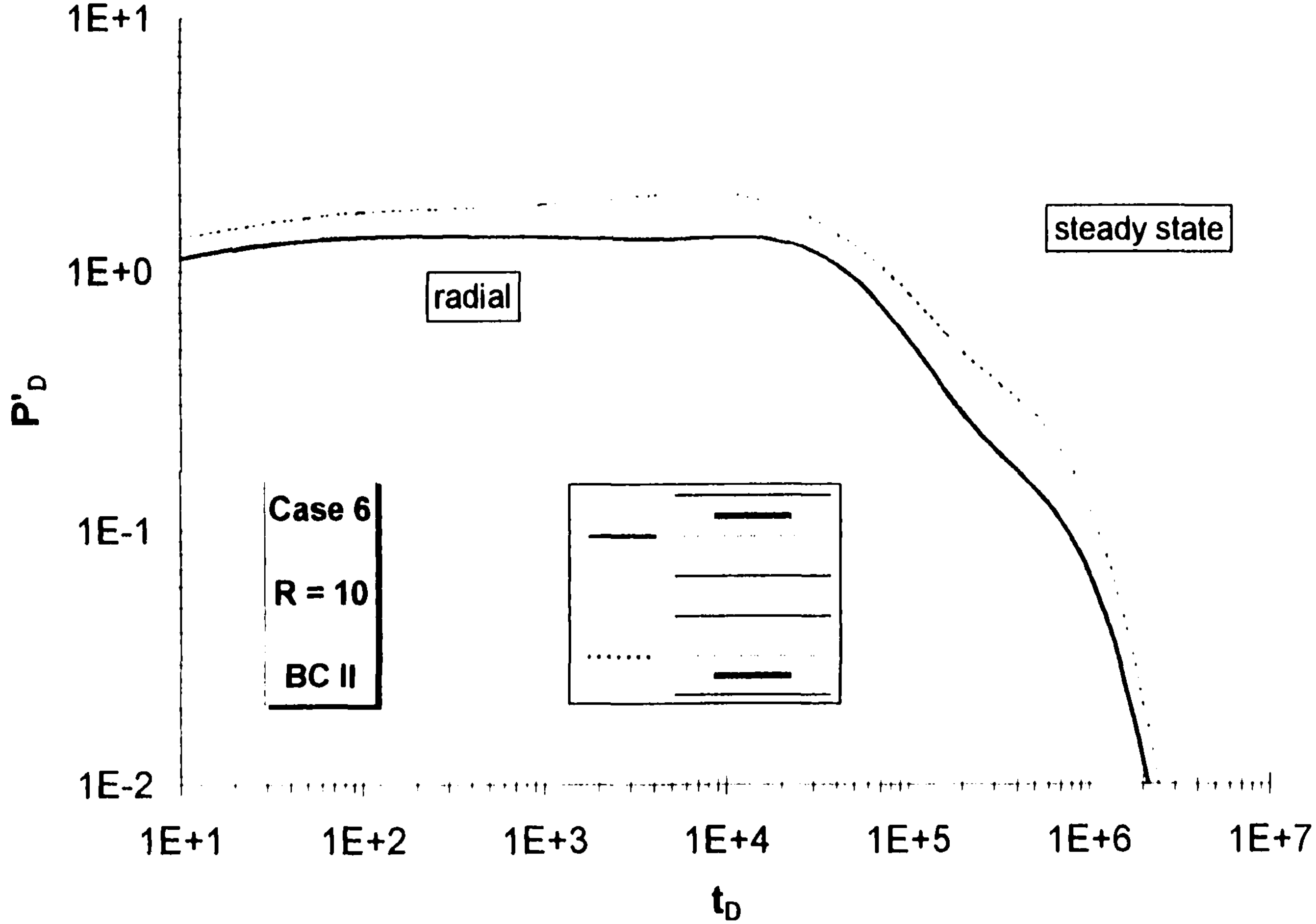

Figure 5.6.9(c) The Dimensionless Pressure Derivative for Case 6, R_k = 10, and BC II

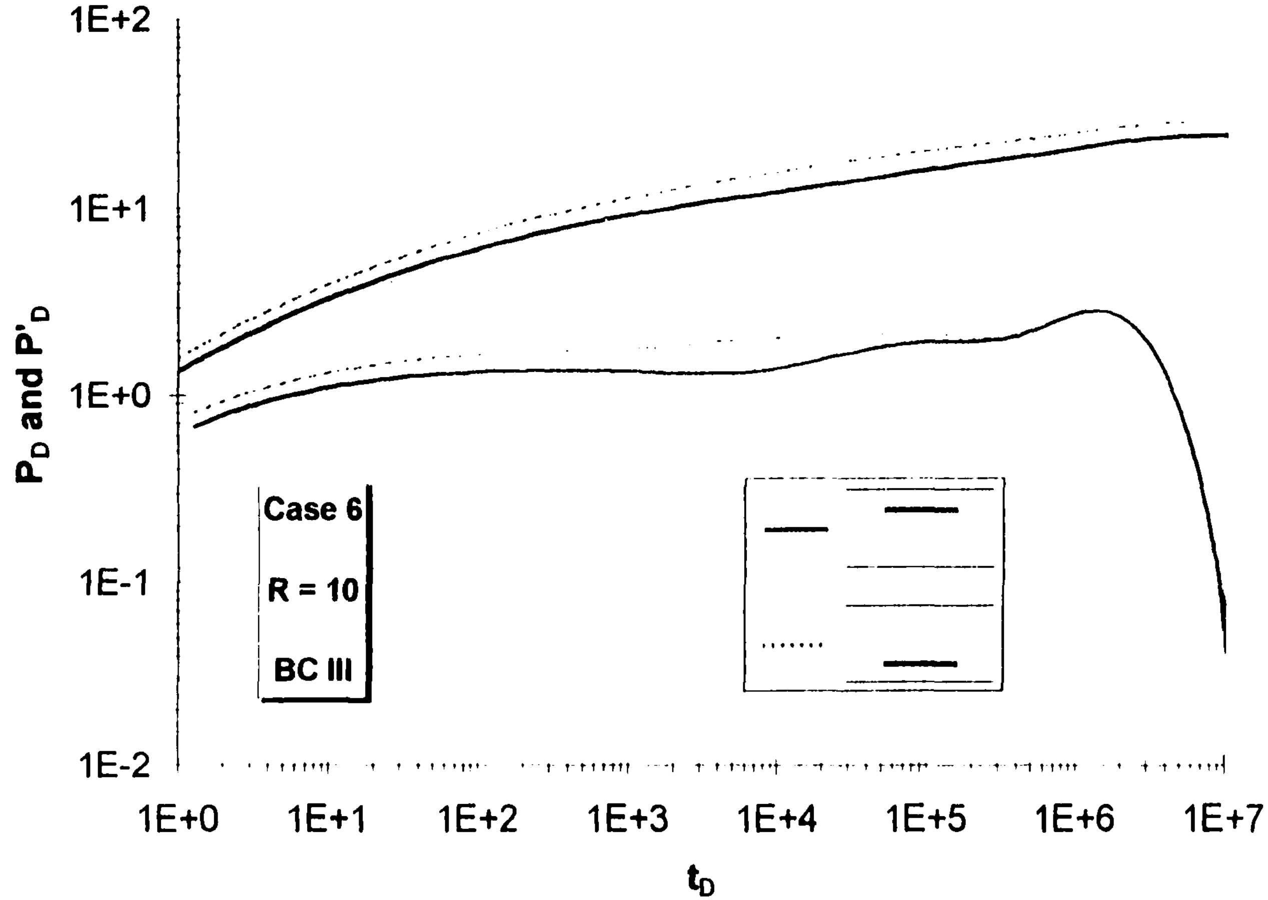

Figure 5.6.10(a) The Dimensionless Pressure and The Dimensionless Pressure Derivative

for Case 6, R_k = 10, and BC III

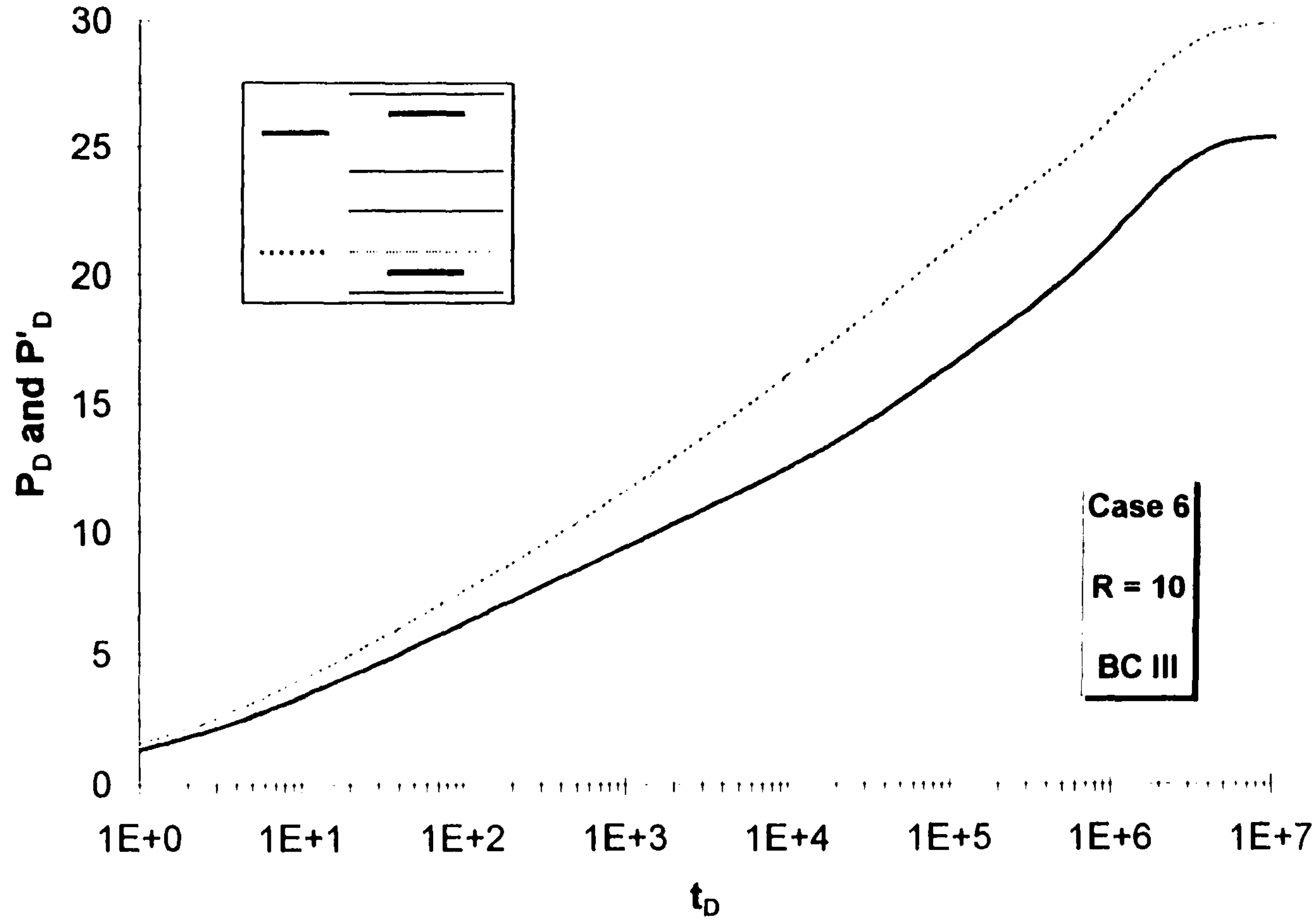

Figure 5.6.10(b) The Dimensionless Pressure for Case 6, $R_k = 10$, and BC III

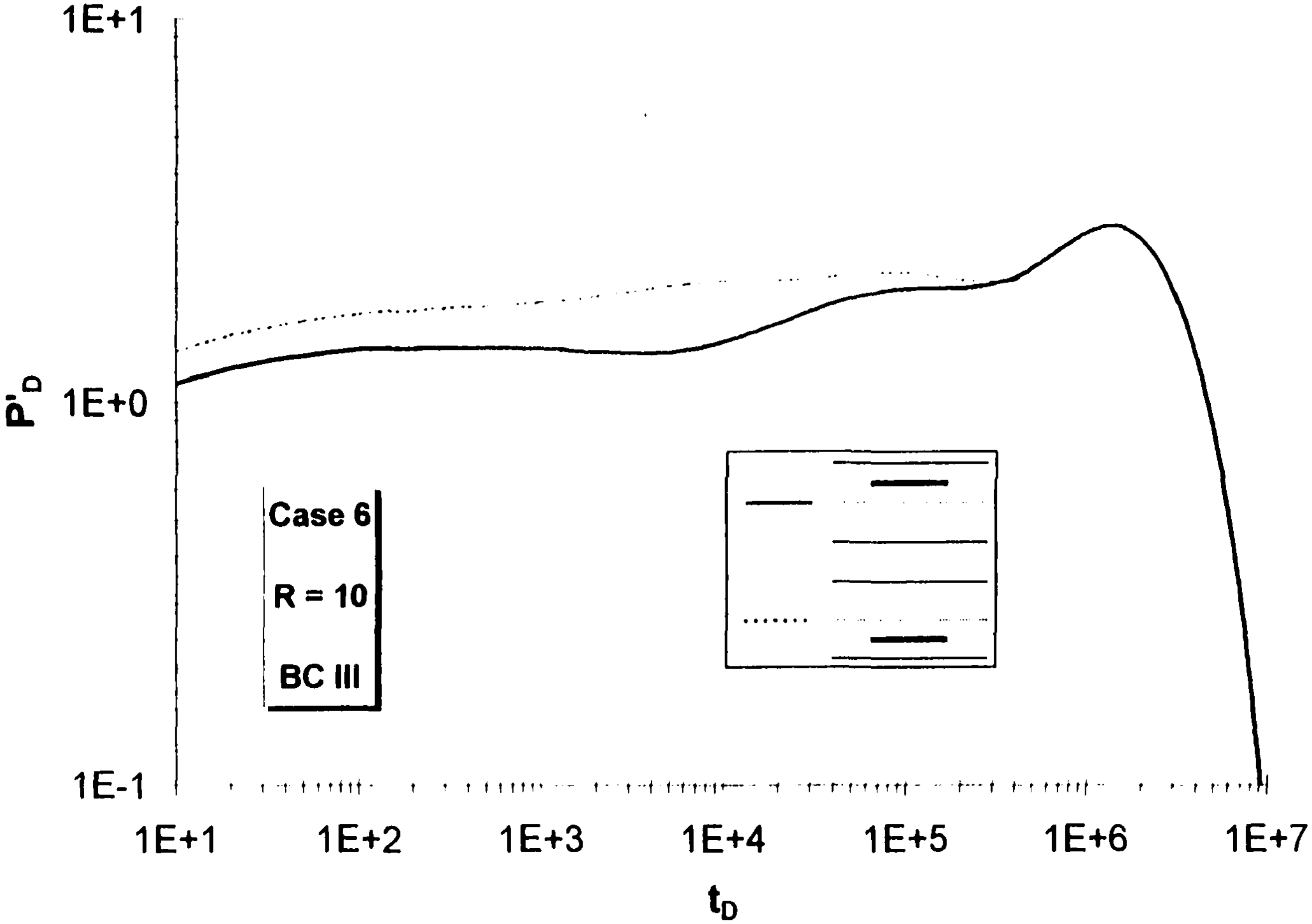

Figure 5.6.10(c) The Dimensionless Pressure Derivative for Case 6, R_k = 10, and BC III

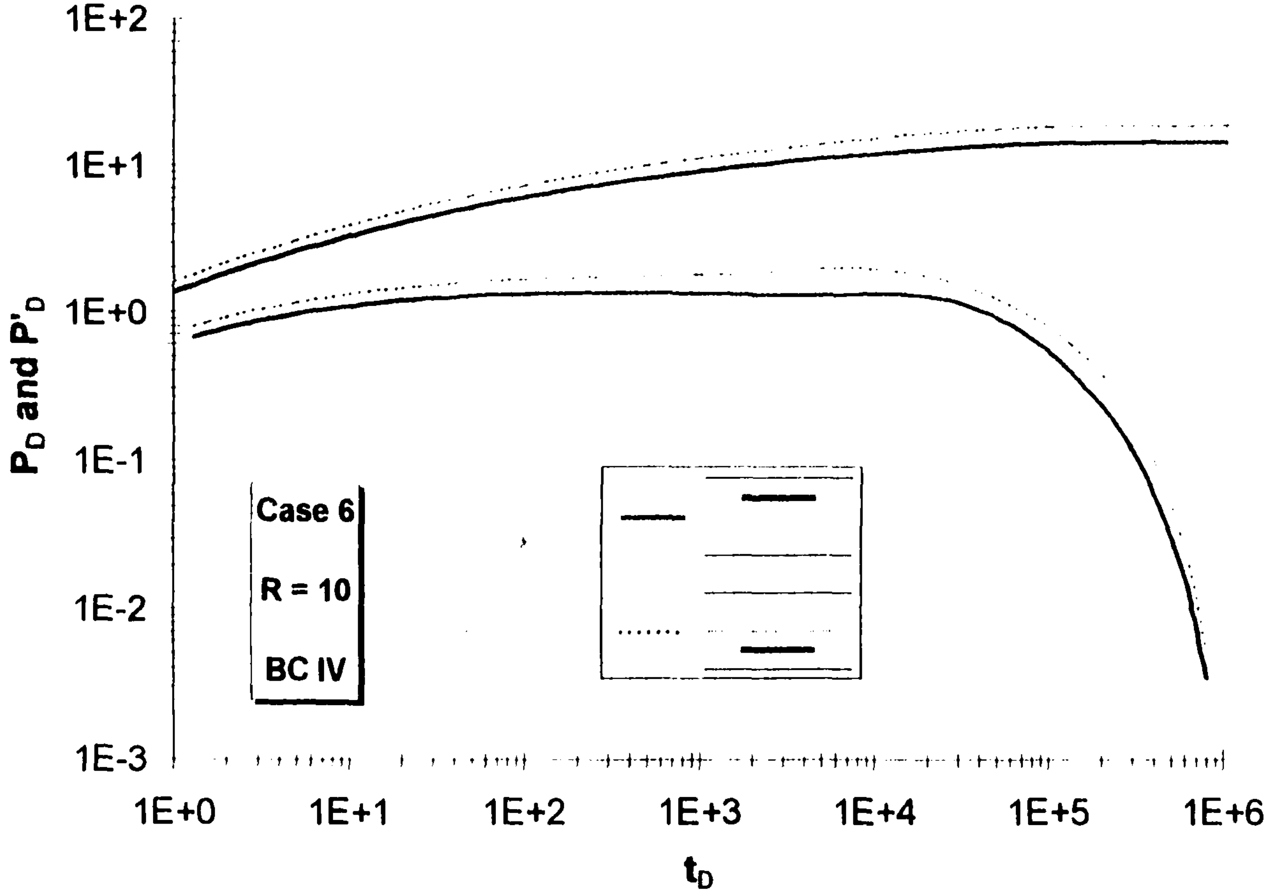

Figure 5.6.11(a) The Dimensionless Pressure and The Dimensionless Pressure Derivative for Case 6, R_k = 10, and BC IV

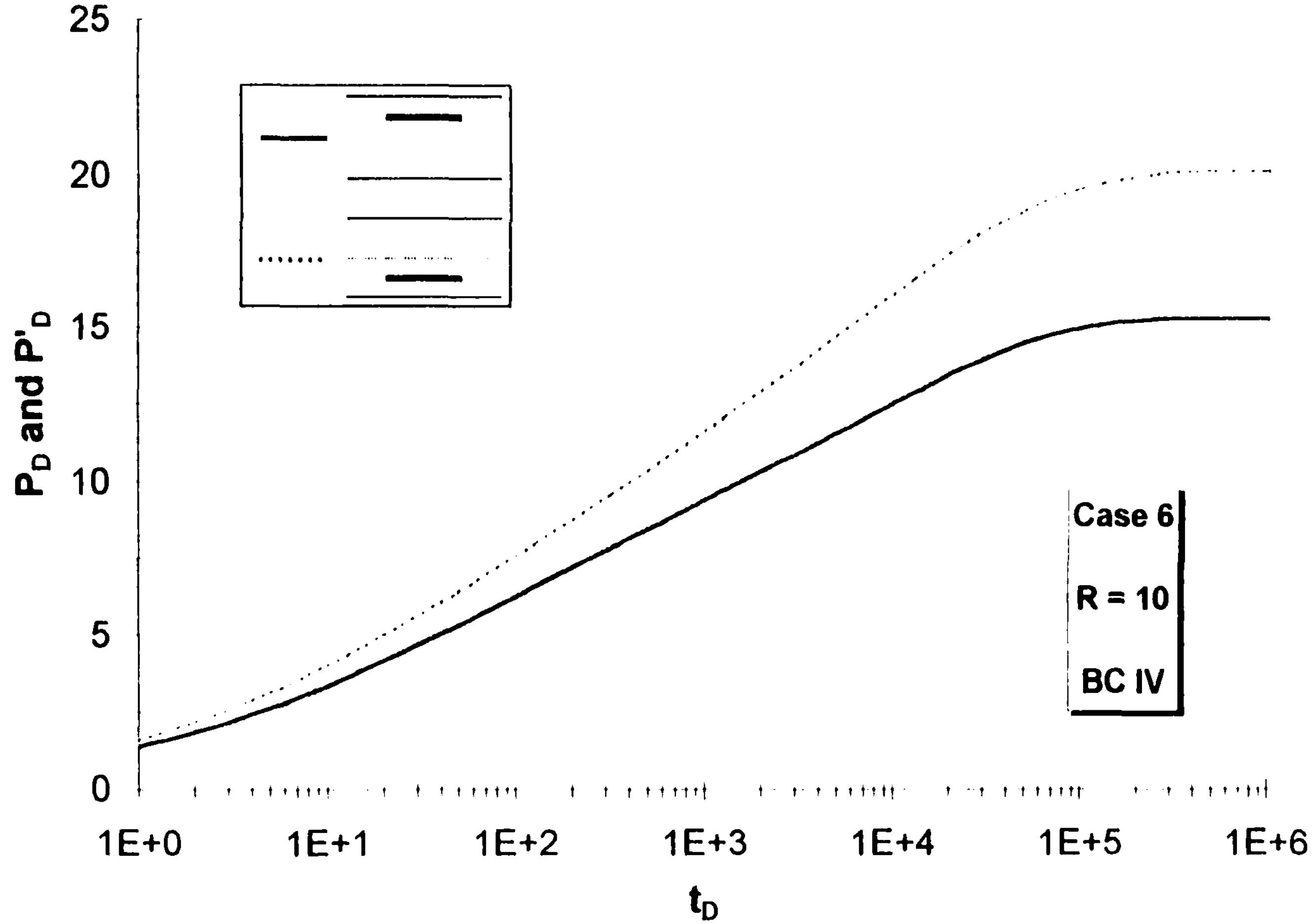

Figure 5.6.11(b) The Dimensionless Pressure for Case 6, $R_k = 10$, and BC IV

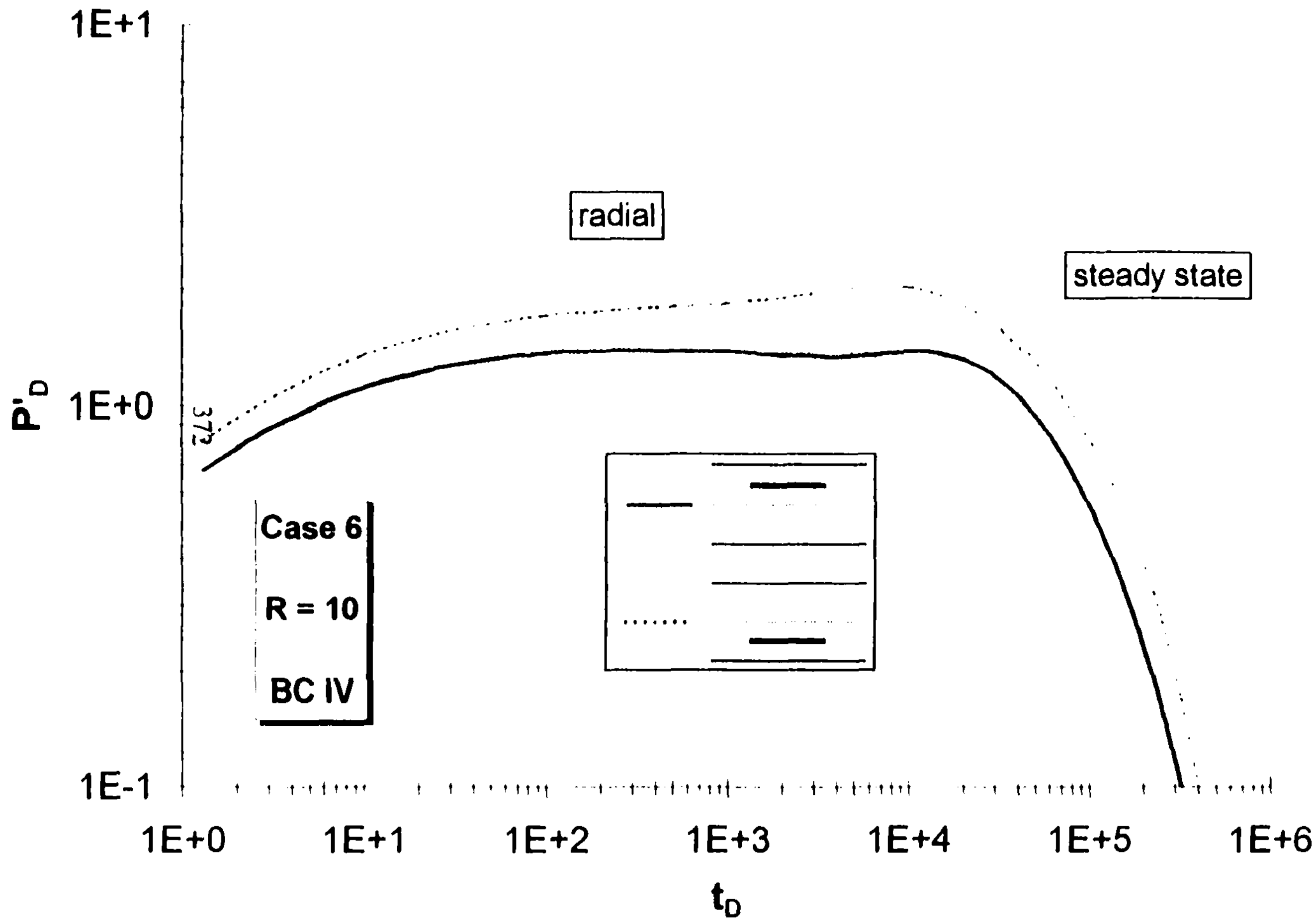

Figure 5.6.11(c) The Dimensionless Pressure Derivative for Case 6, $R_k = 10$, and BC IV

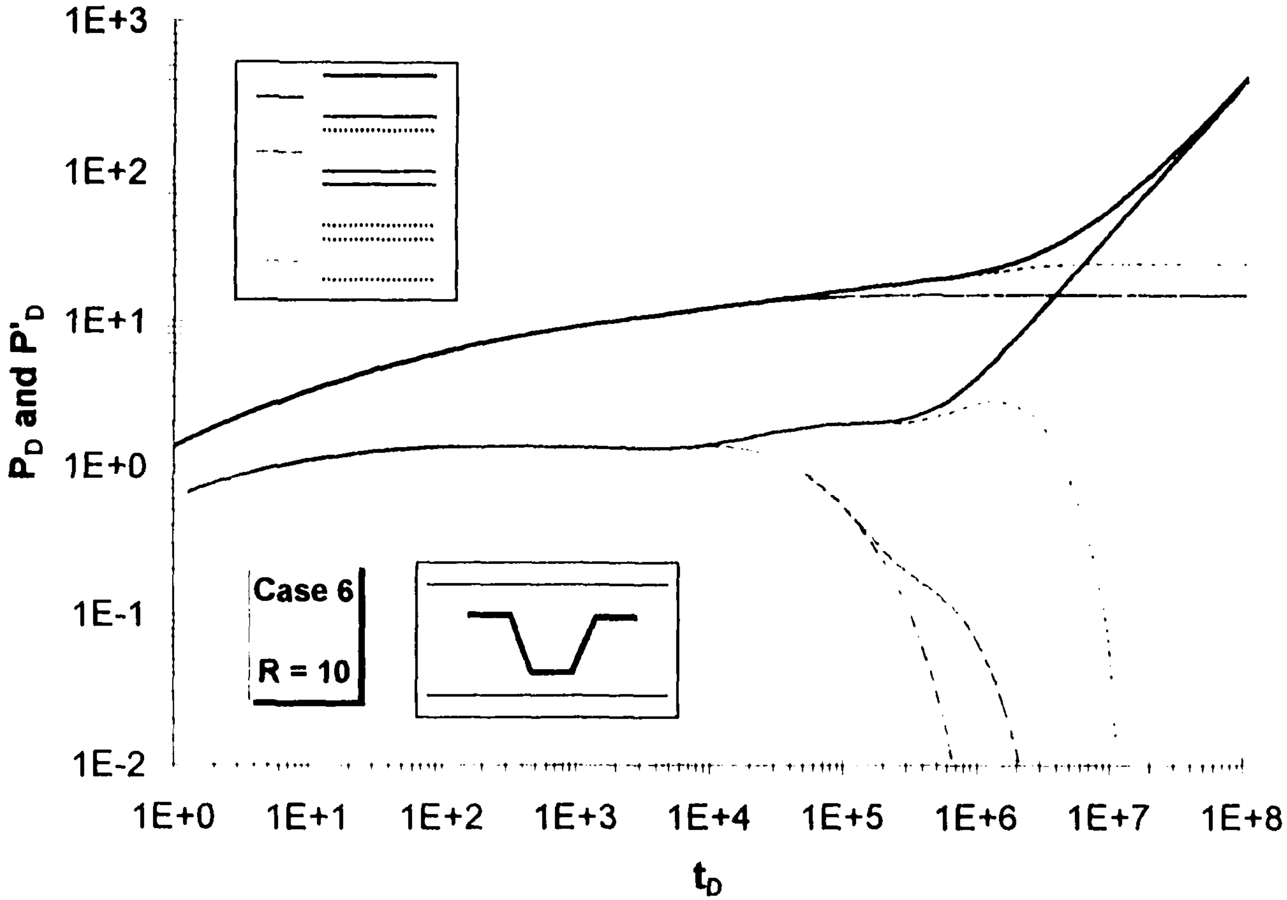

Figure 5.6.12(a) The Dimensionless Pressure and The Dimensionless Pressure Derivative

for Case 6 and R_k = 10

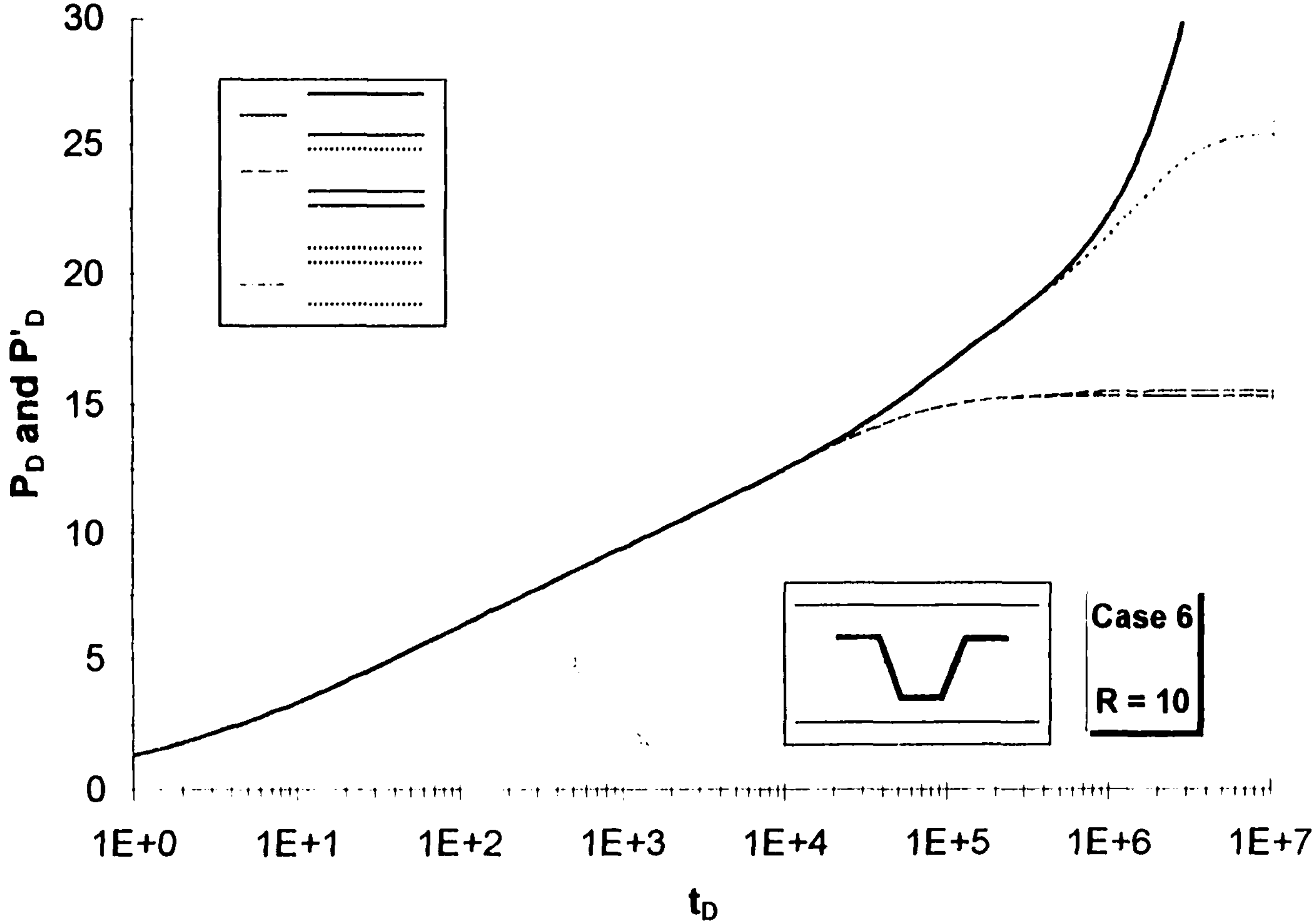

Figure 5.6.12(b) The Dimensionless Pressure for Case 6 and $R_k = 10$

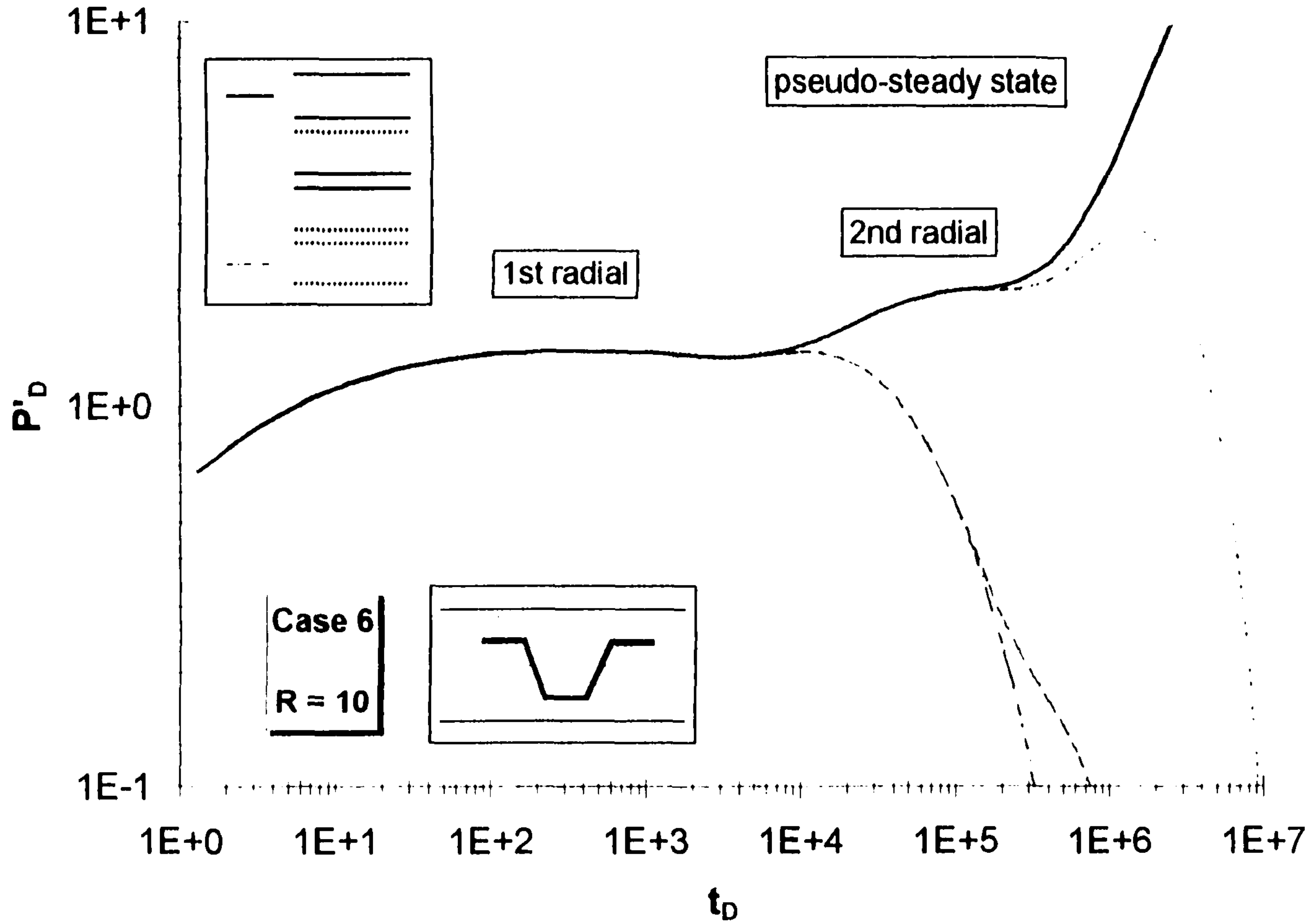

Figure 5.6.12(c) The Dimensionless Pressure Derivative for Case 6 and $R_k = 10$

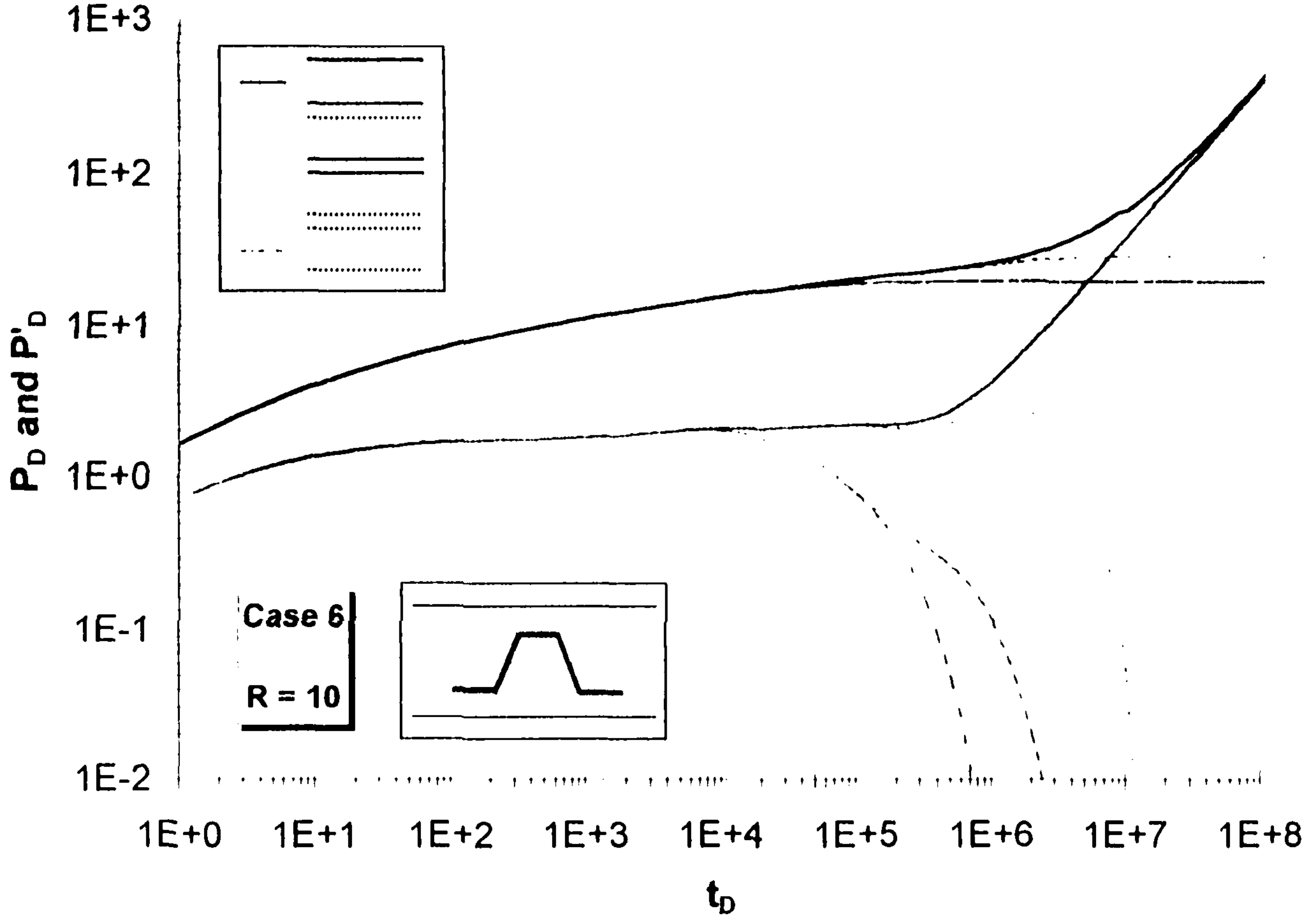

Figure 5.6.13(a) The Dimensionless Pressure and The Dimensionless Pressure Derivative

for Case 6 and $R_k = 10$

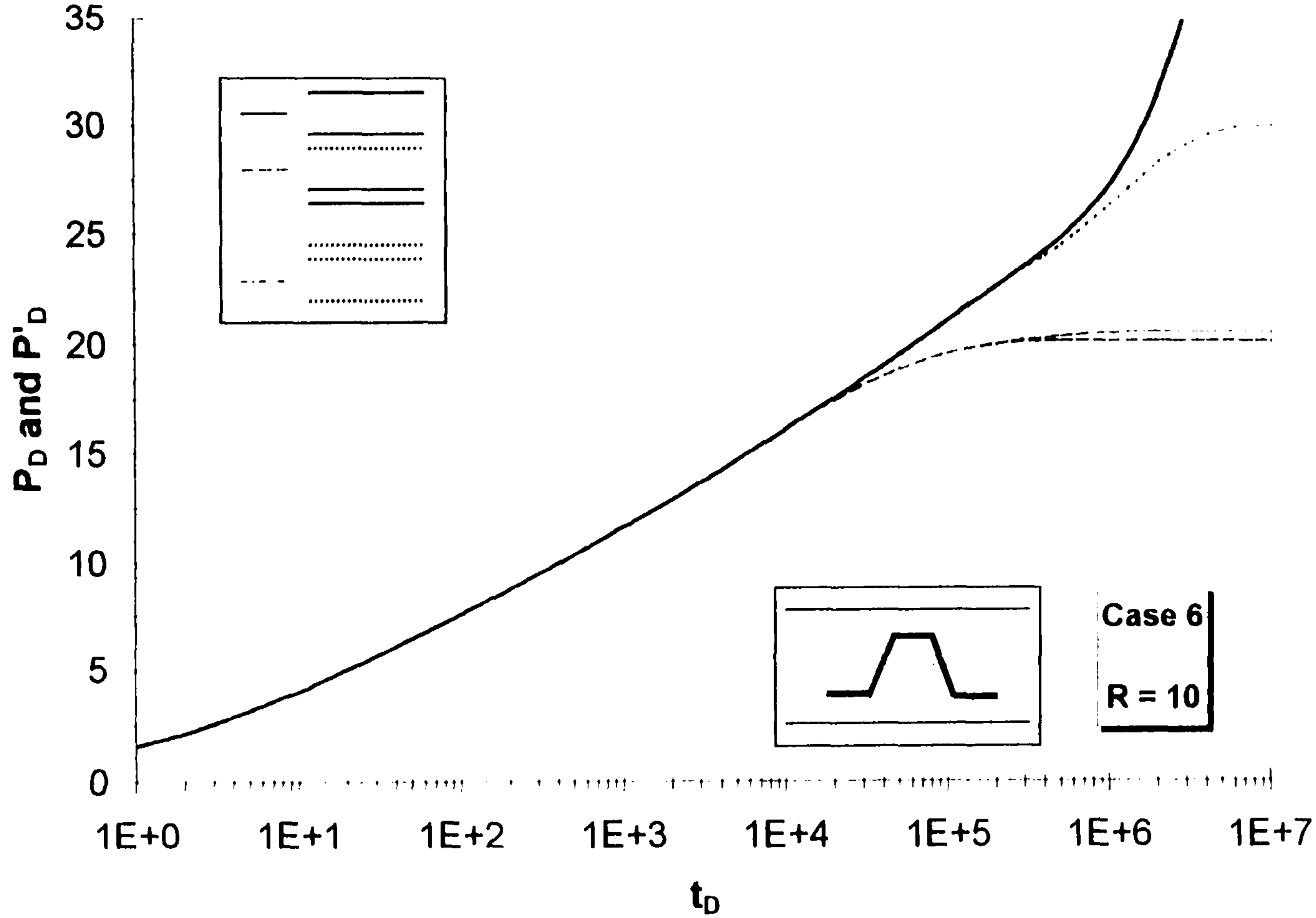

Figure 5.6.13(b) The Dimensionless Pressure for Case 6 and $R_k = 10$

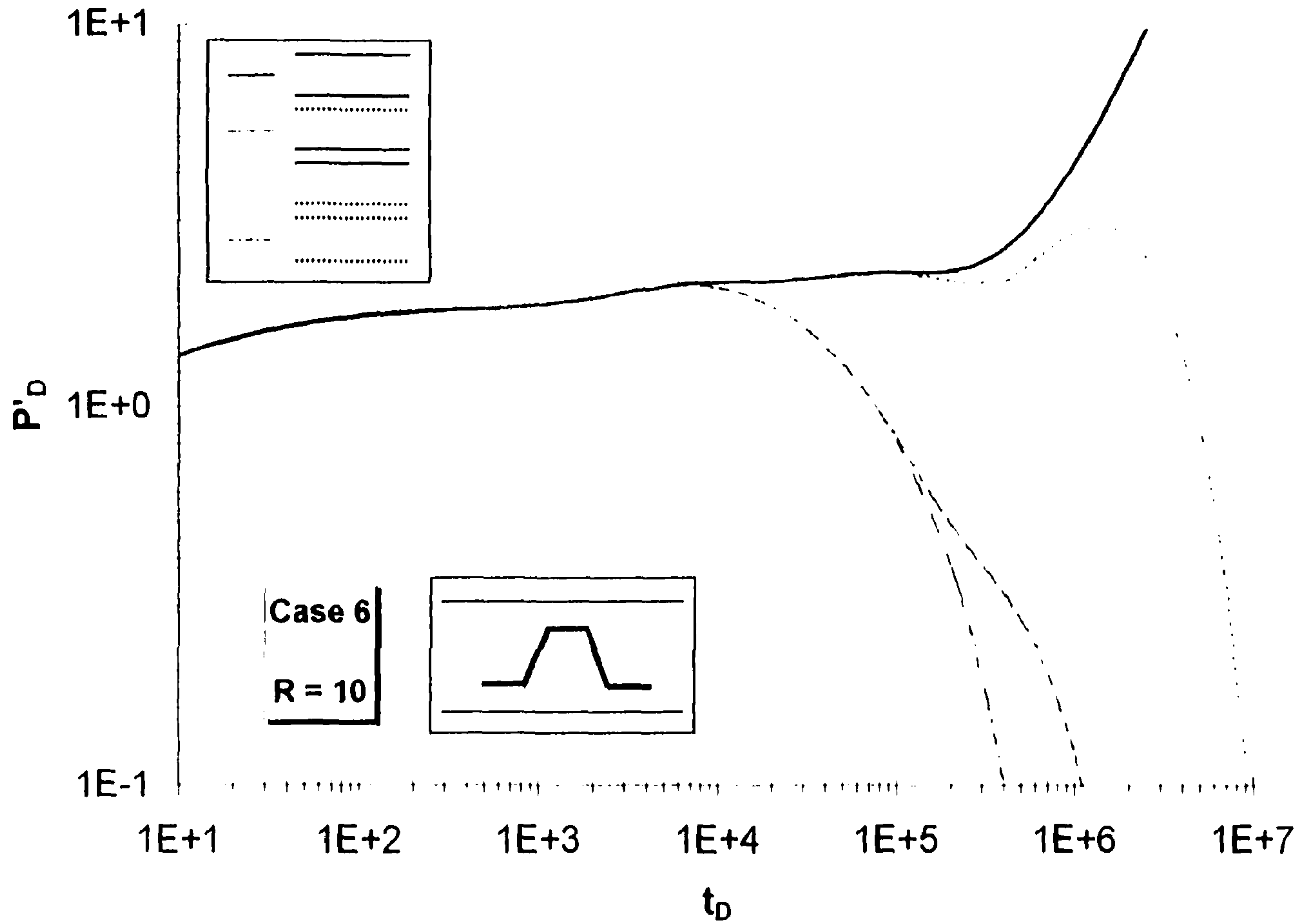

Figure 5.6.13(c) The Dimensionless Pressure Derivative for Case 6 and $R_k = 10$

APPENDIX I

LIST OF FIGURES IN CASE 5.7

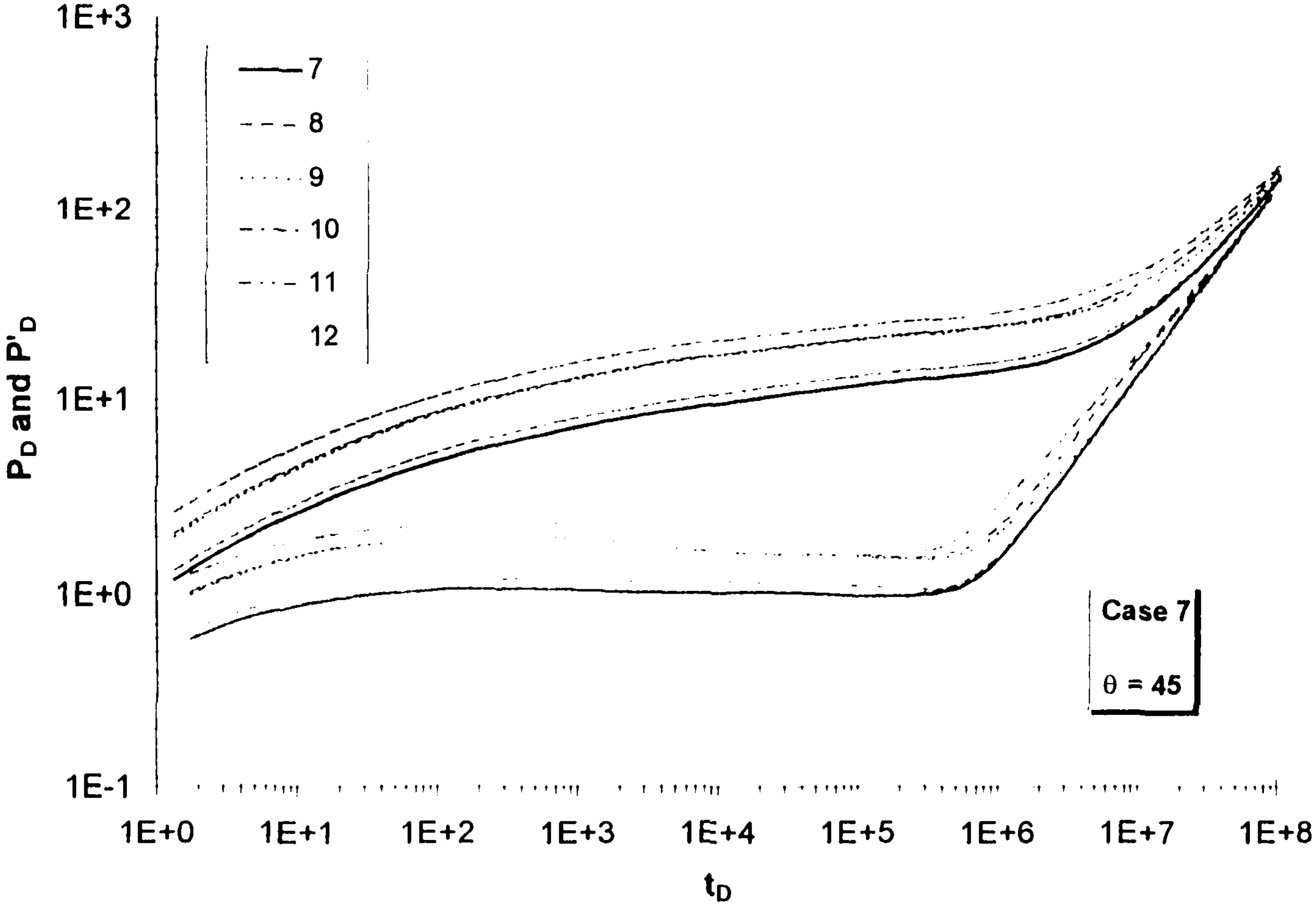

Figure 5.7.3(a) The Dimensionless Pressure and The Dimensionless Pressure Derivative for Case 7 and $\theta = 45^{\circ}$

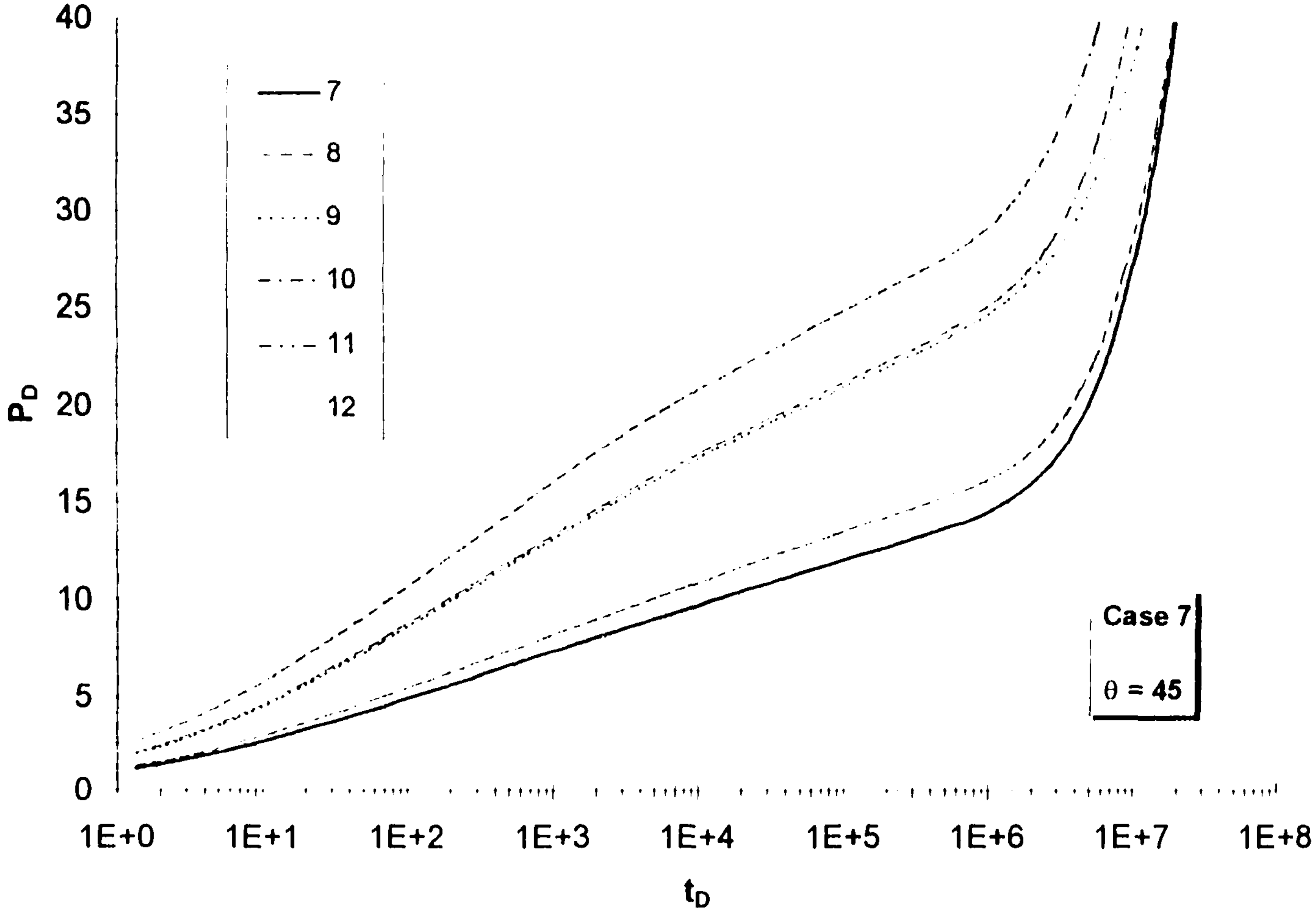

Figure 5.7.3(b) The Dimensionless Pressure for Case 7 and θ = 45°

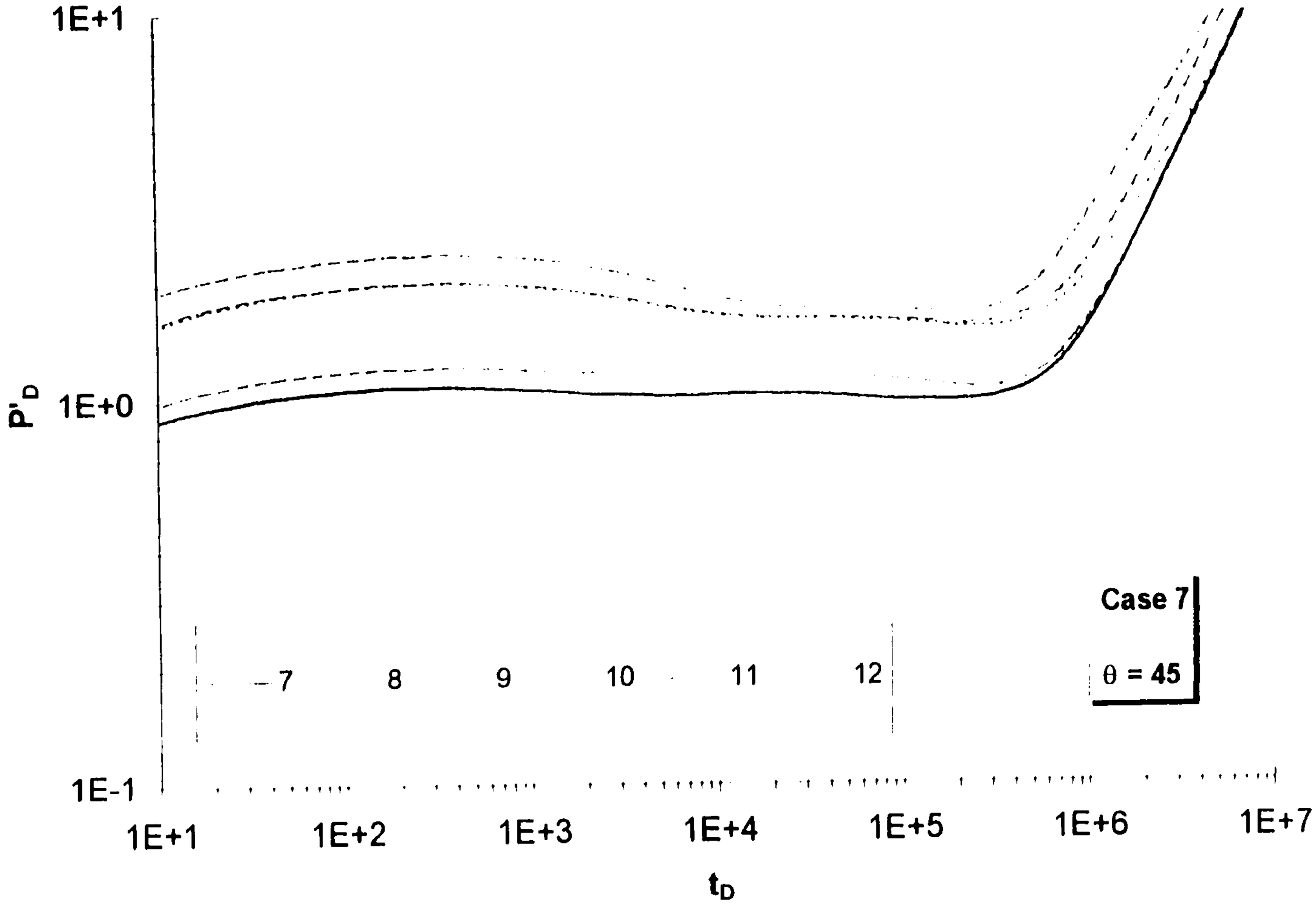

Figure 5.7.3(c) The Dimensionless Pressure Derivative for Case 7 and θ = 45°

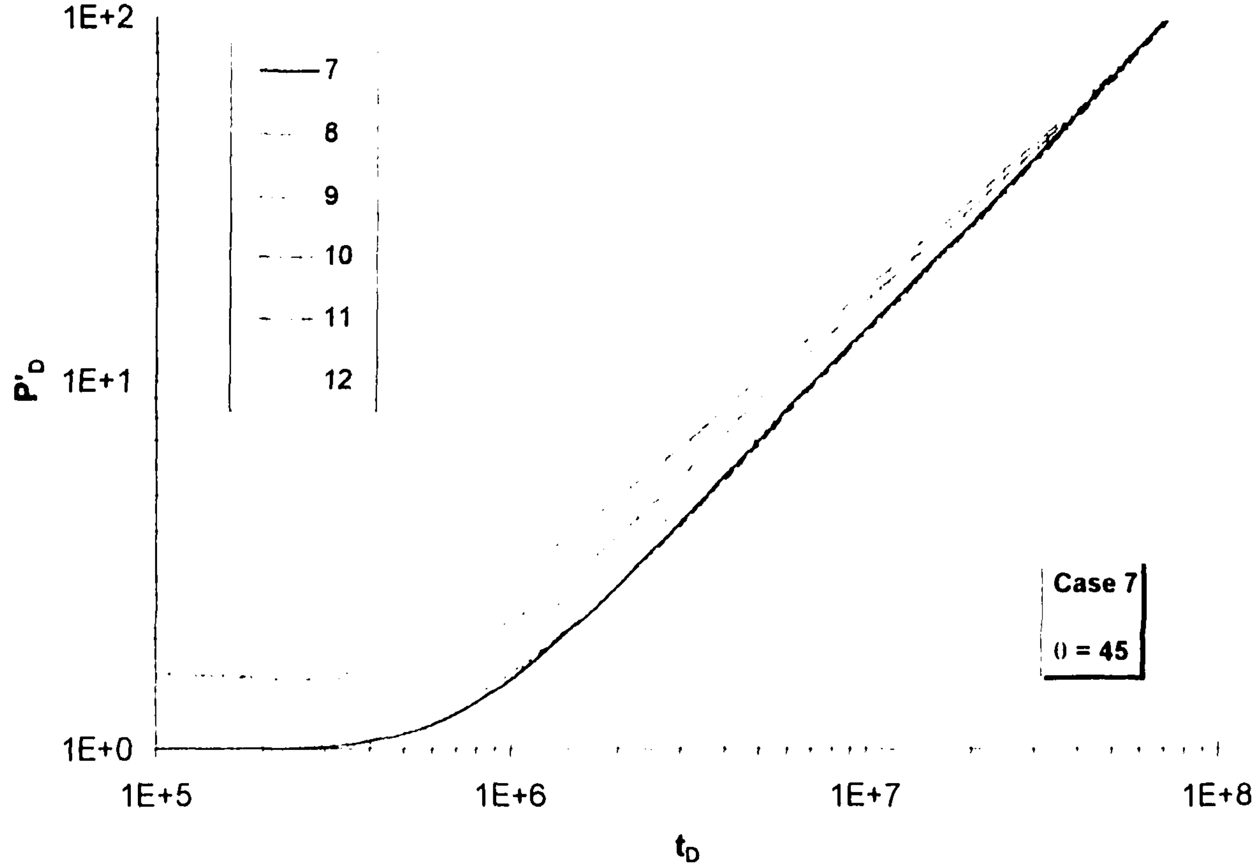

Figure 5.7.3(d) The Dimensionless Pressure Derivative for Case 7 and $\theta = 45^{o}$

During Pseudo-Steady Flow

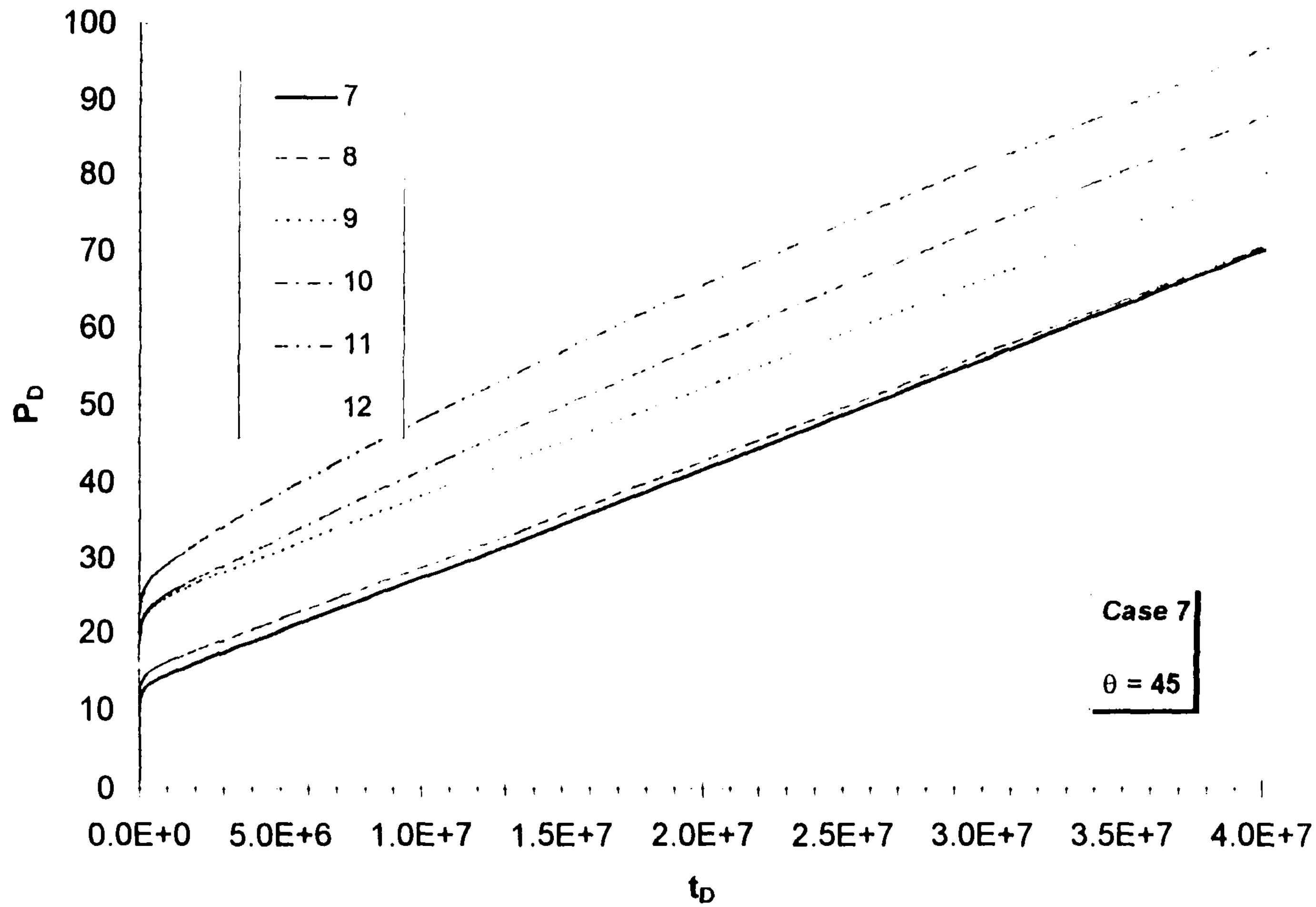

Figure 5.7.3(e) The Dimensionless Pressure for Case 7 and $\theta = 45^{0}$ on The Cartesian Plot

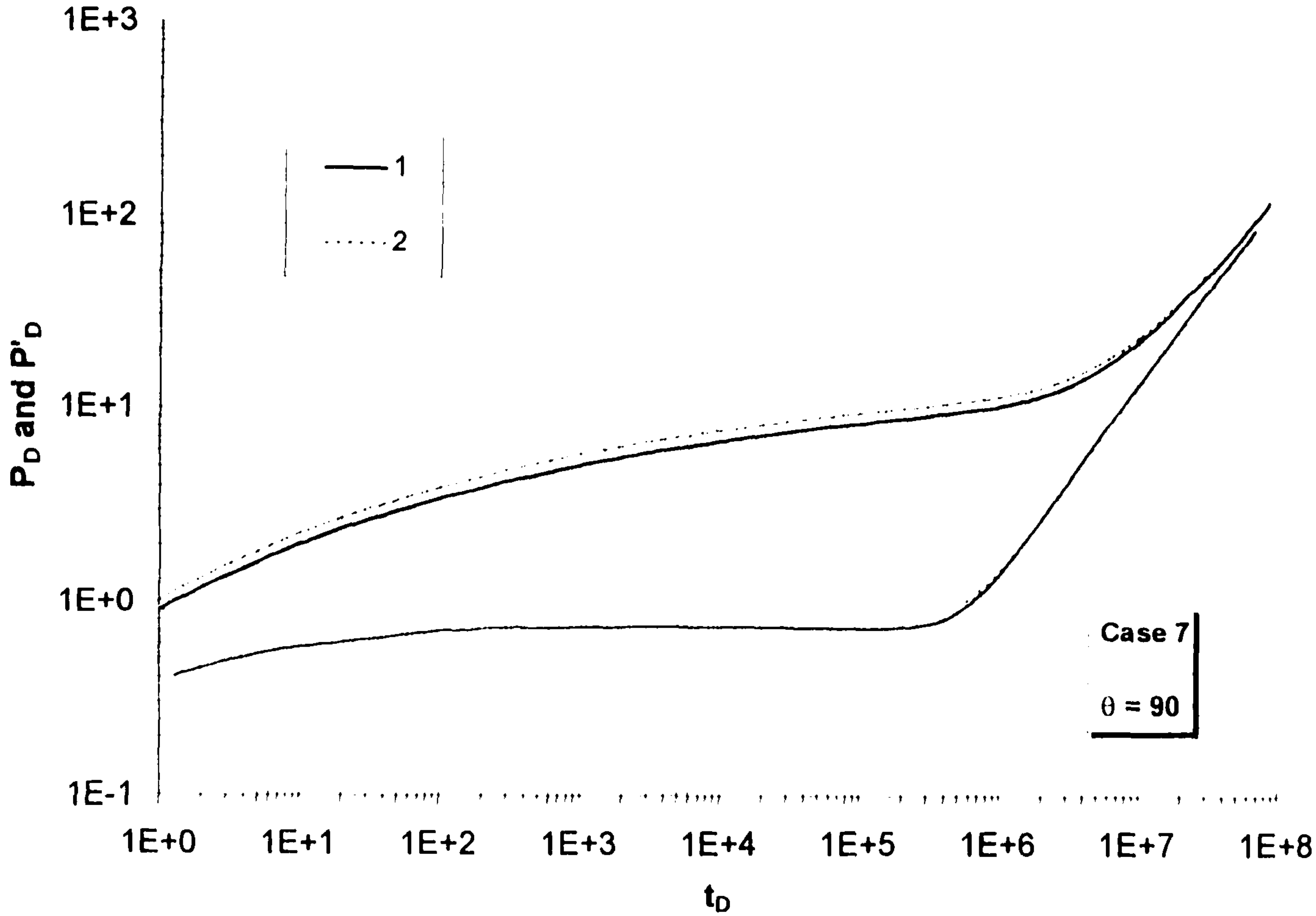

Figure 5.7.4 The Dimensionless Pressure and The Dimensionless Pressure Derivative for Case 7.1 and 7.2

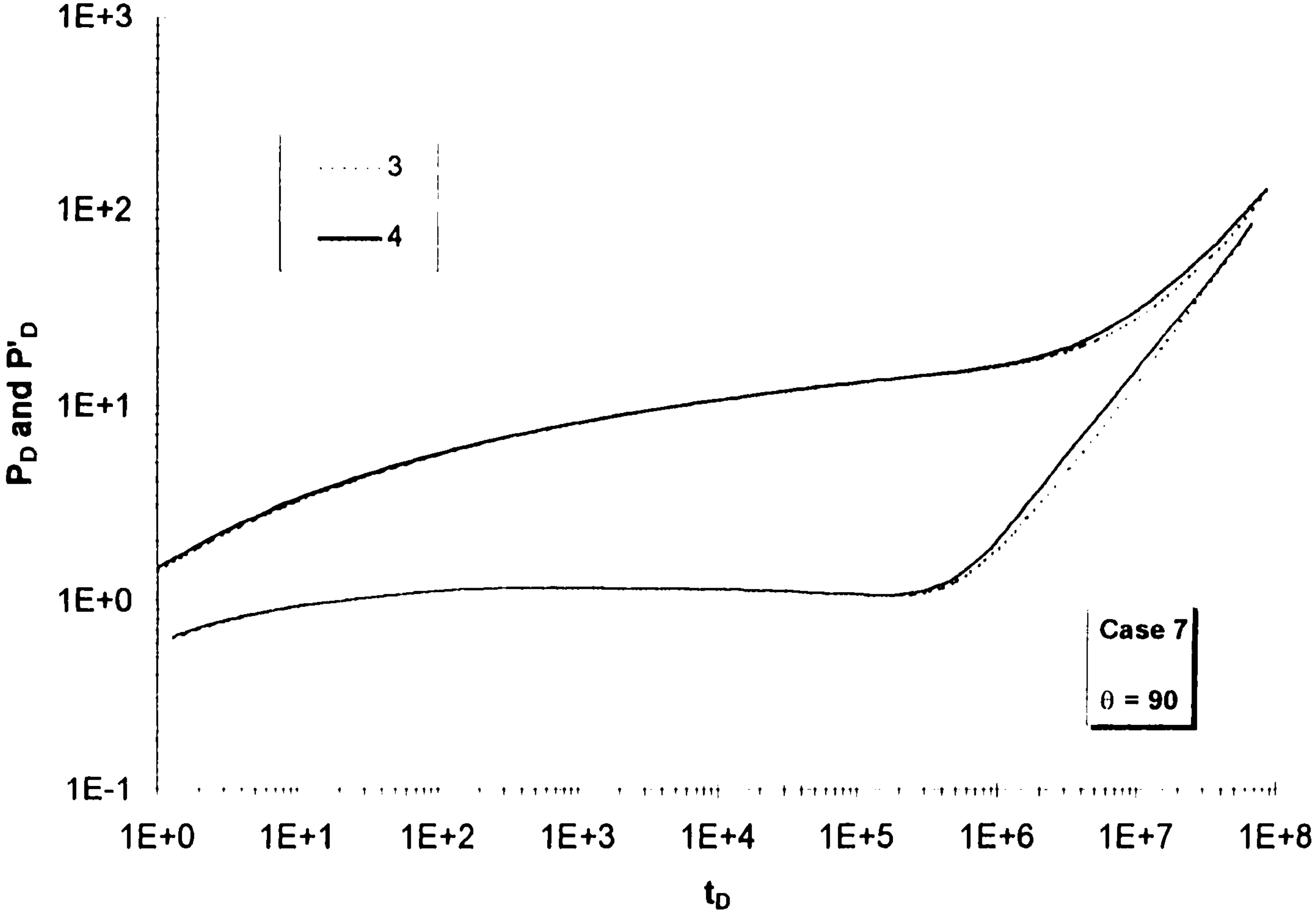

Figure 5.7.5 The Dimensionless Pressure and The Dimensionless Pressure Derivative for Case 7.3 and 7.4

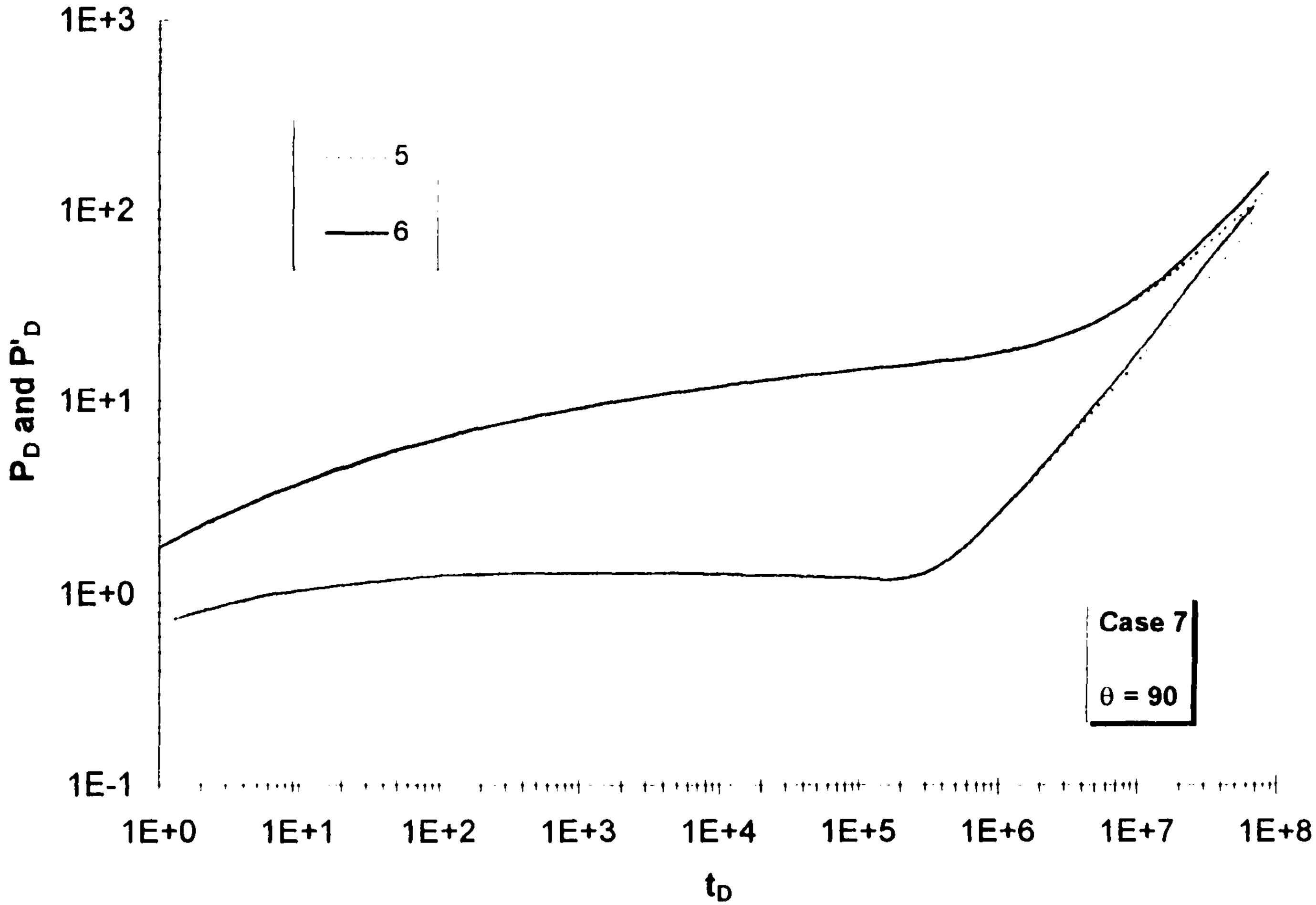

Figure 5.7.6 The Dimensionless Pressure and The Dimensionless Pressure Derivative for Case 7.5 and 7.6

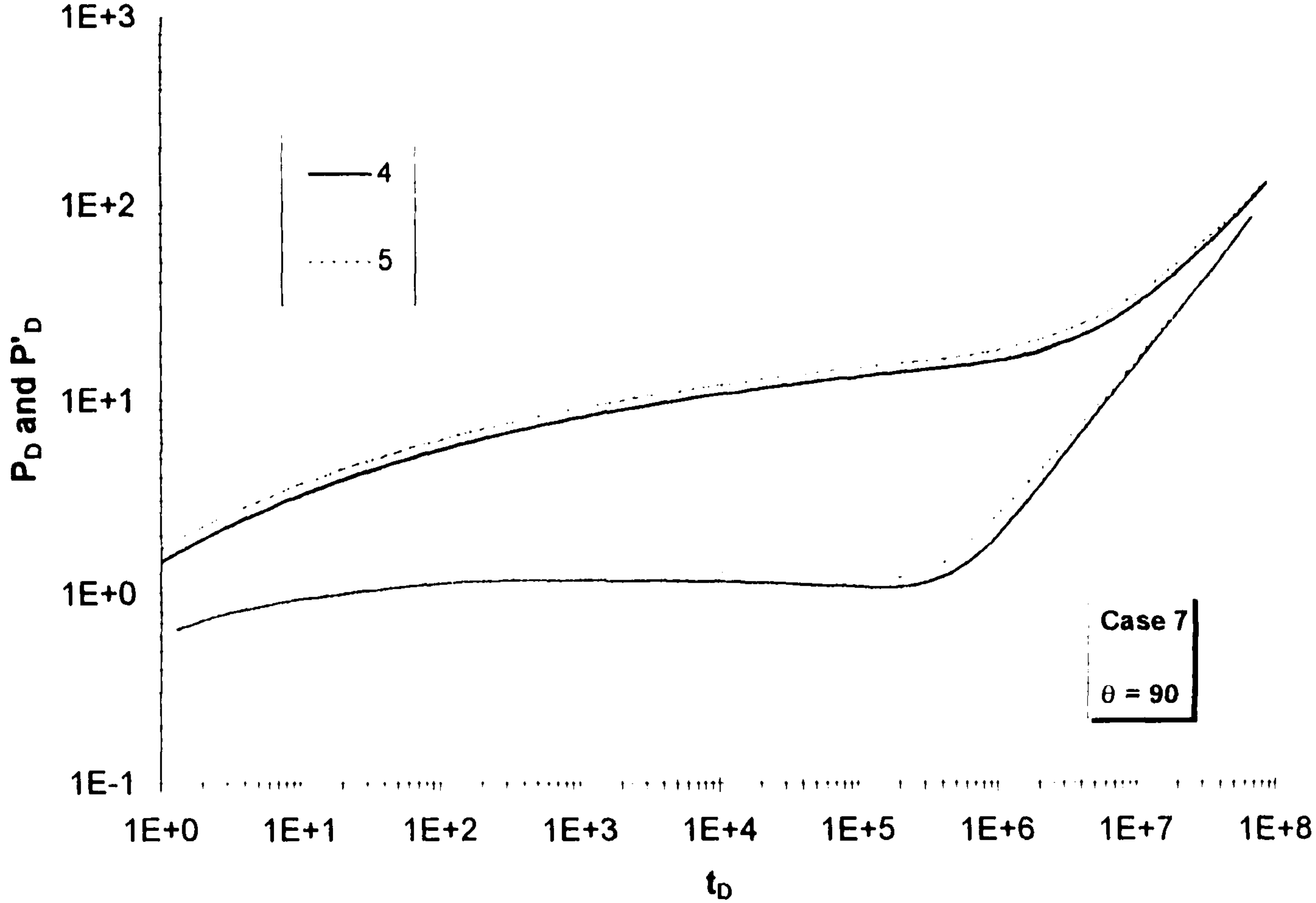

Figure 5.7.7 The Dimensionless Pressure and The Dimensionless Pressure Derivative

for Case 7.4 and 7.5

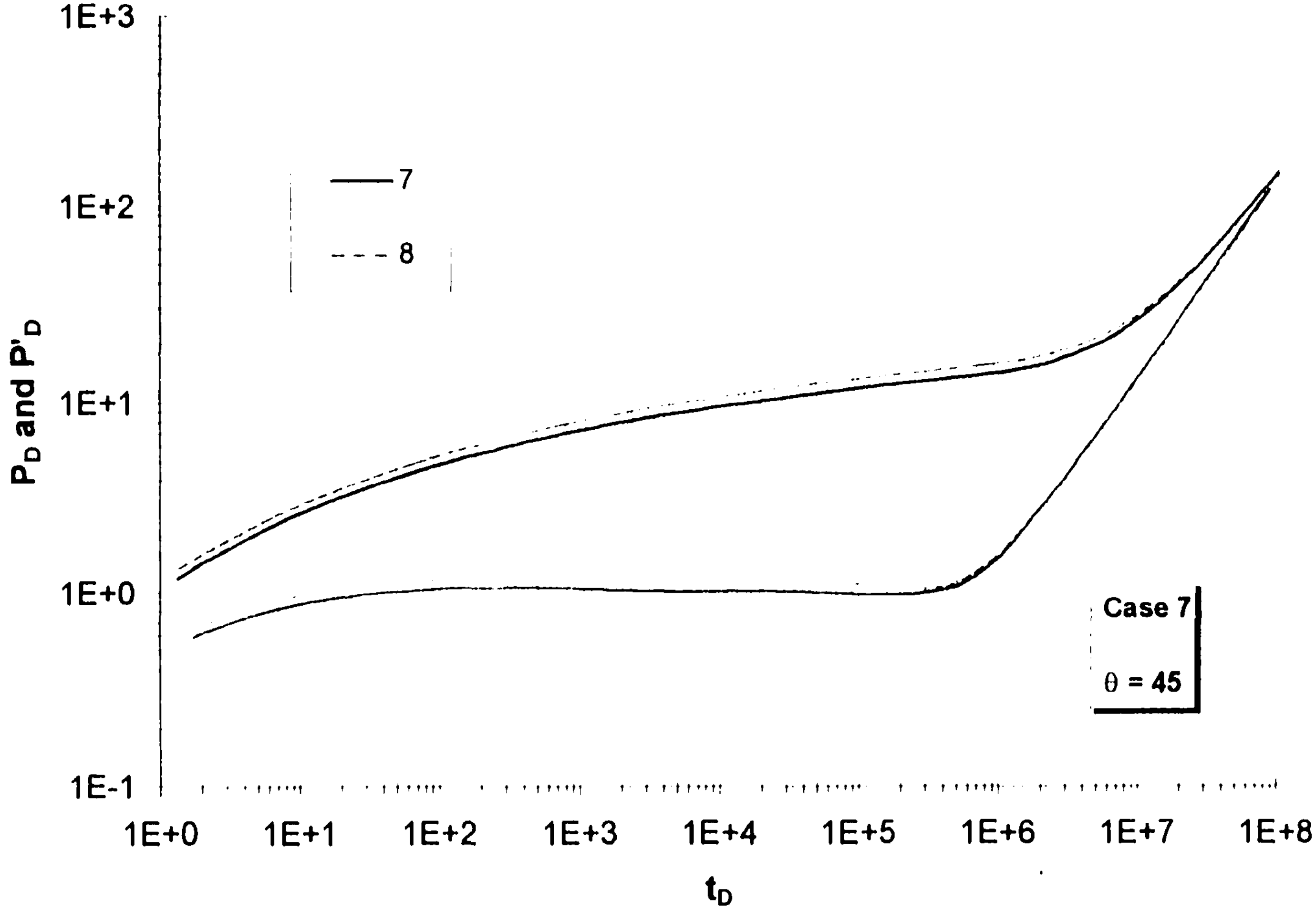

Figure 5.7.8 The Dimensionless Pressure and The Dimensionless Pressure Derivative for Case 7.7 and 7.8

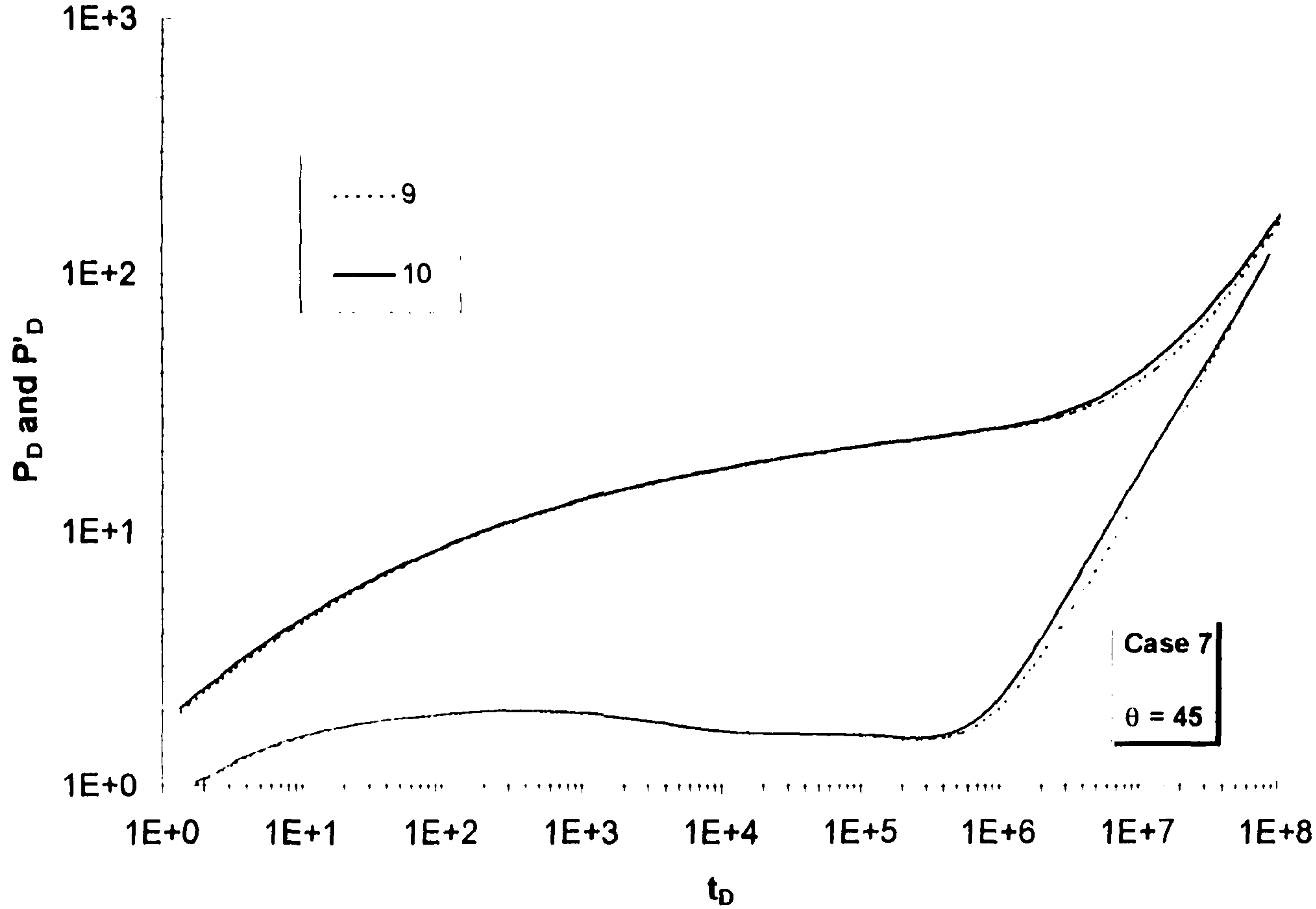

Figure 5.7.9 The Dimensionless Pressure and The Dimensionless Pressure Derivative for Case 7.9 and 7.10

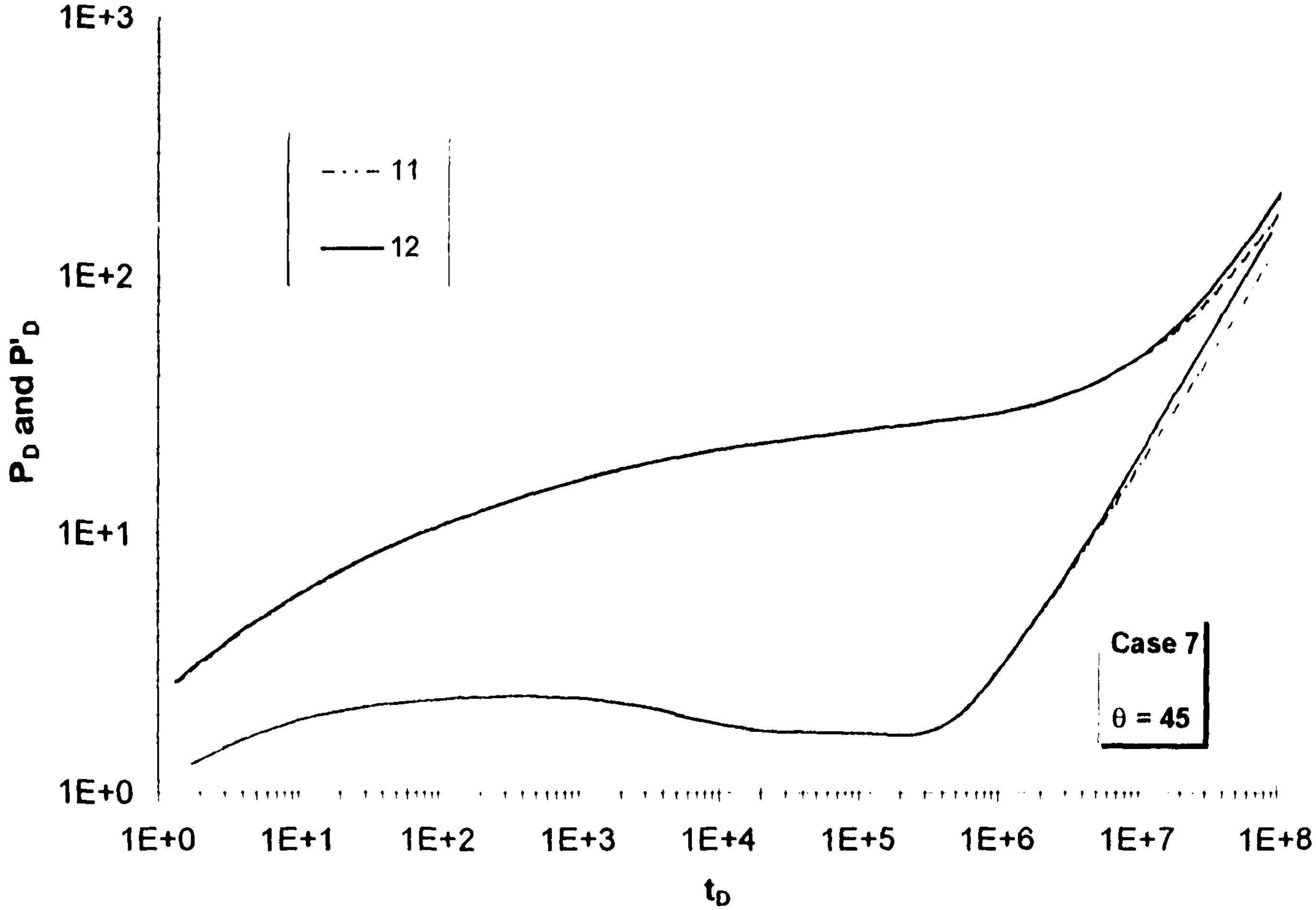

Figure 5.7.10 The Dimensionless Pressure and The Dimensionless Pressure Derivative

for Case 7.11 and 7.12

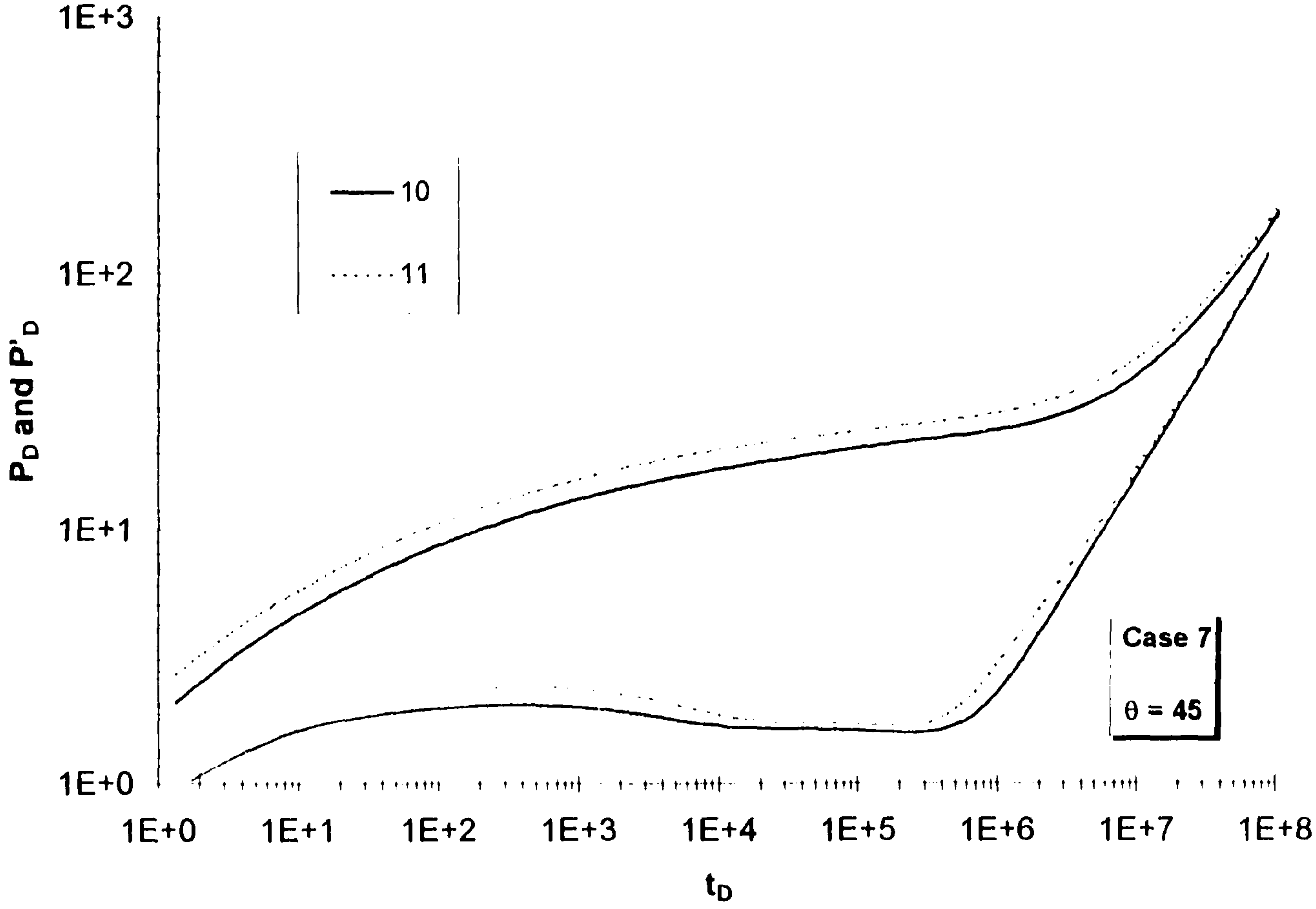

Figure 5.7.11 The Dimensionless Pressure and The Dimensionless Pressure Derivative

for Case 7.10 and 7.11

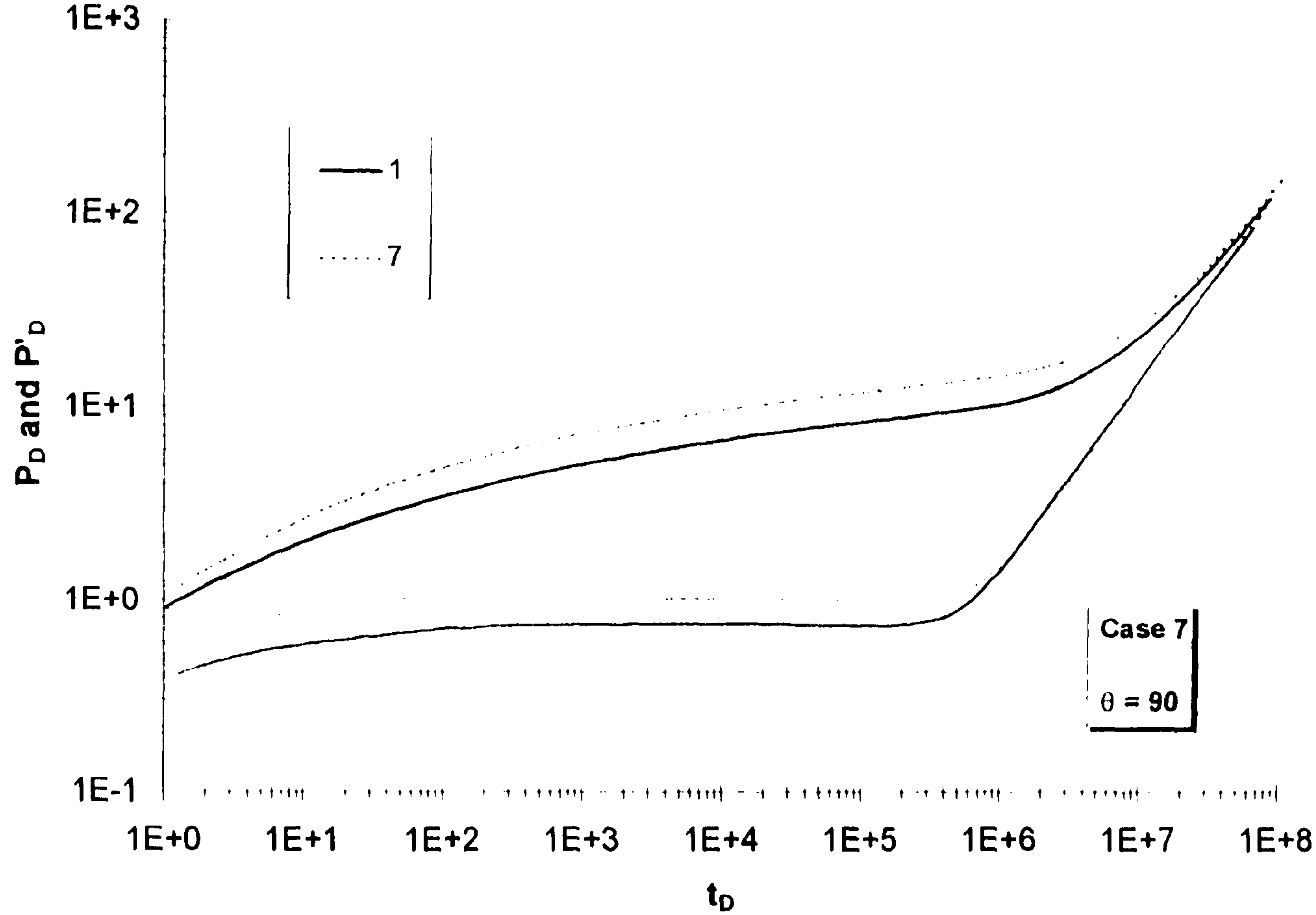

Figure 5.7.12 The Dimensionless Pressure and The Dimensionless Pressure Derivative

for Case 7.1 and 7.7

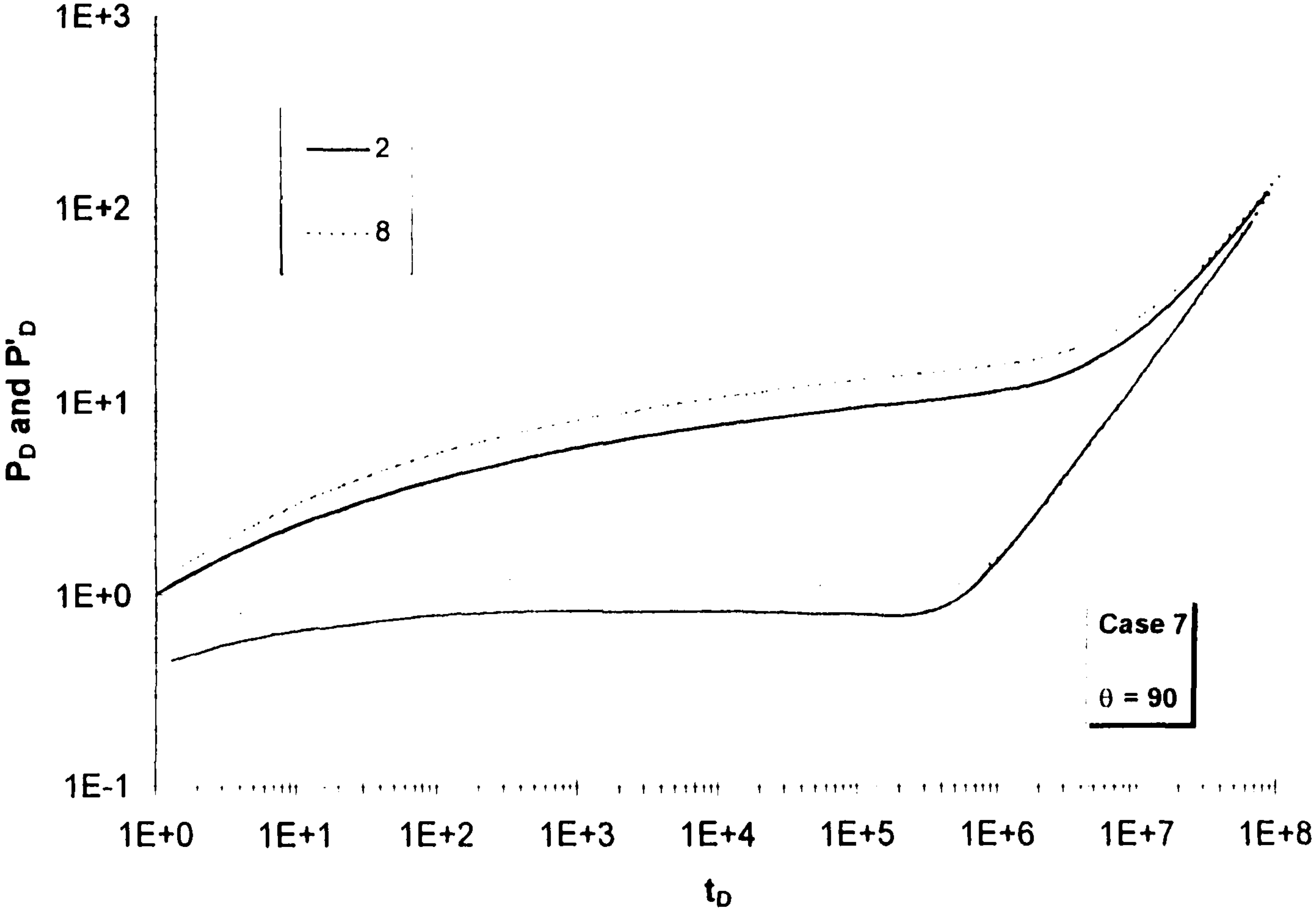

Figure 5.7.13 The Dimensionless Pressure and The Dimensionless Pressure Derivative

for Case 7.2 and 7.8

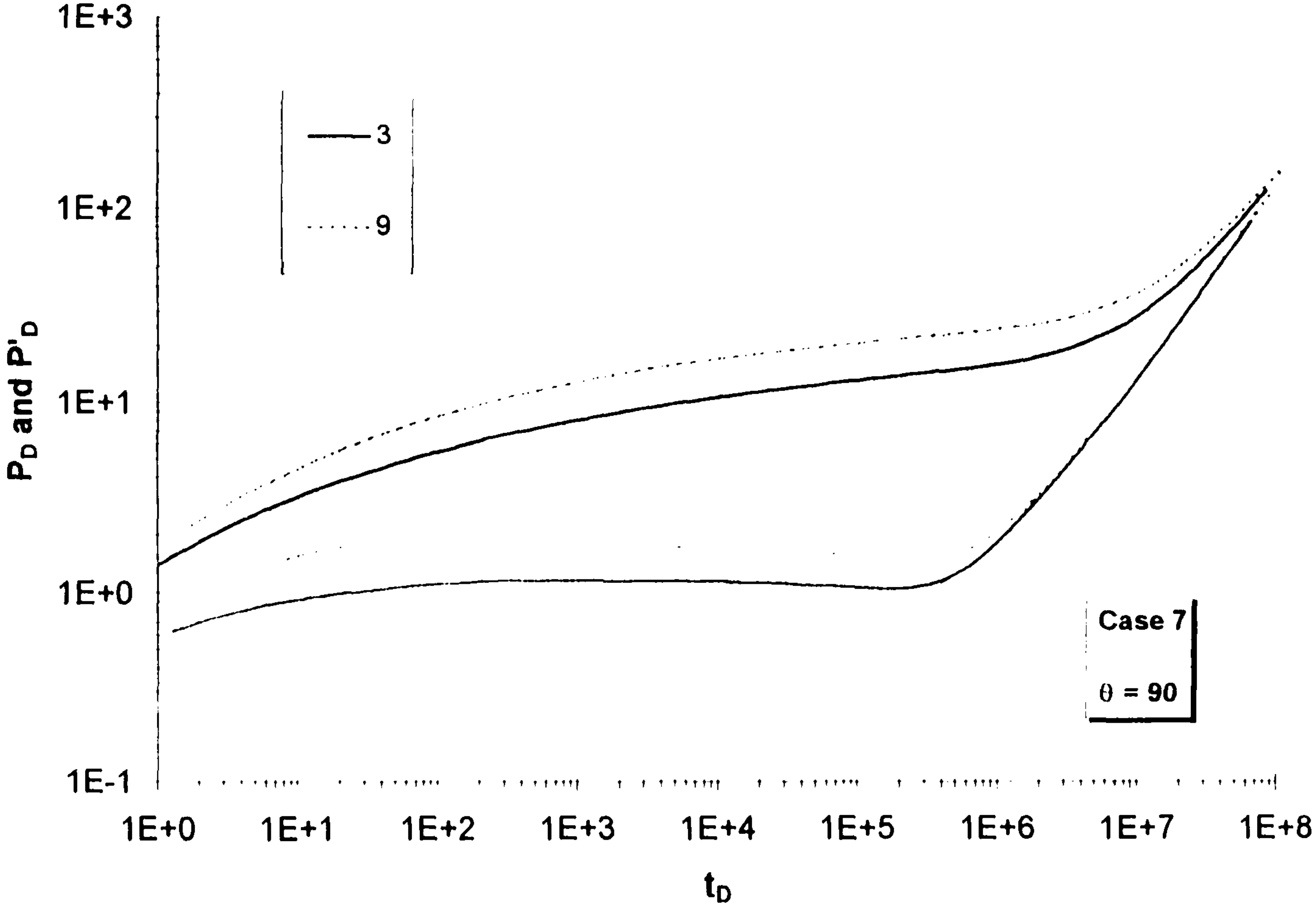

Figure 5.7.14 The Dimensionless Pressure and The Dimensionless Pressure Derivative

for Case 7.3 and 7.9

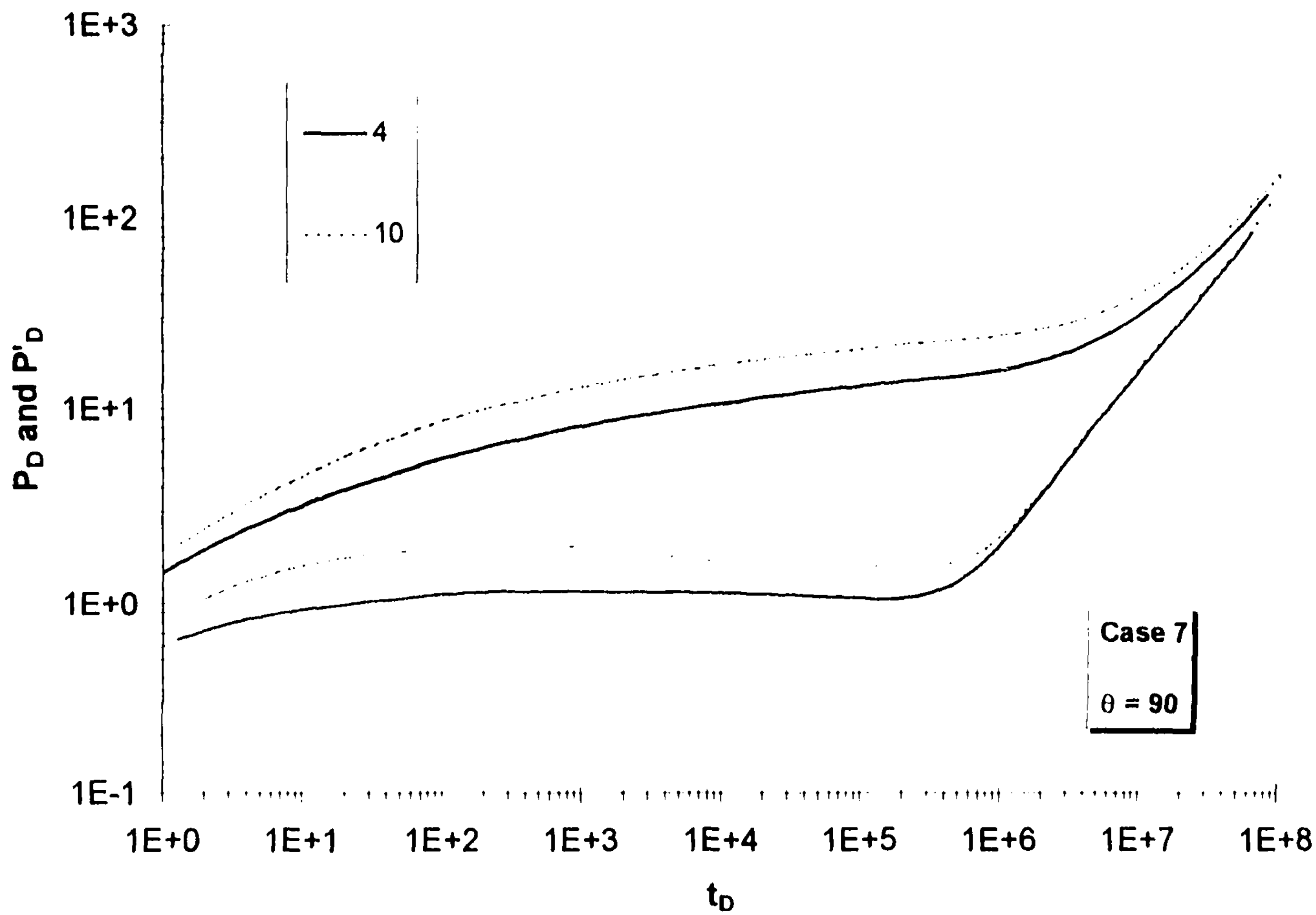

Figure 5.7.15 The Dimensionless Pressure and The Dimensionless Pressure Derivative

for Case 7.4 and 7.10

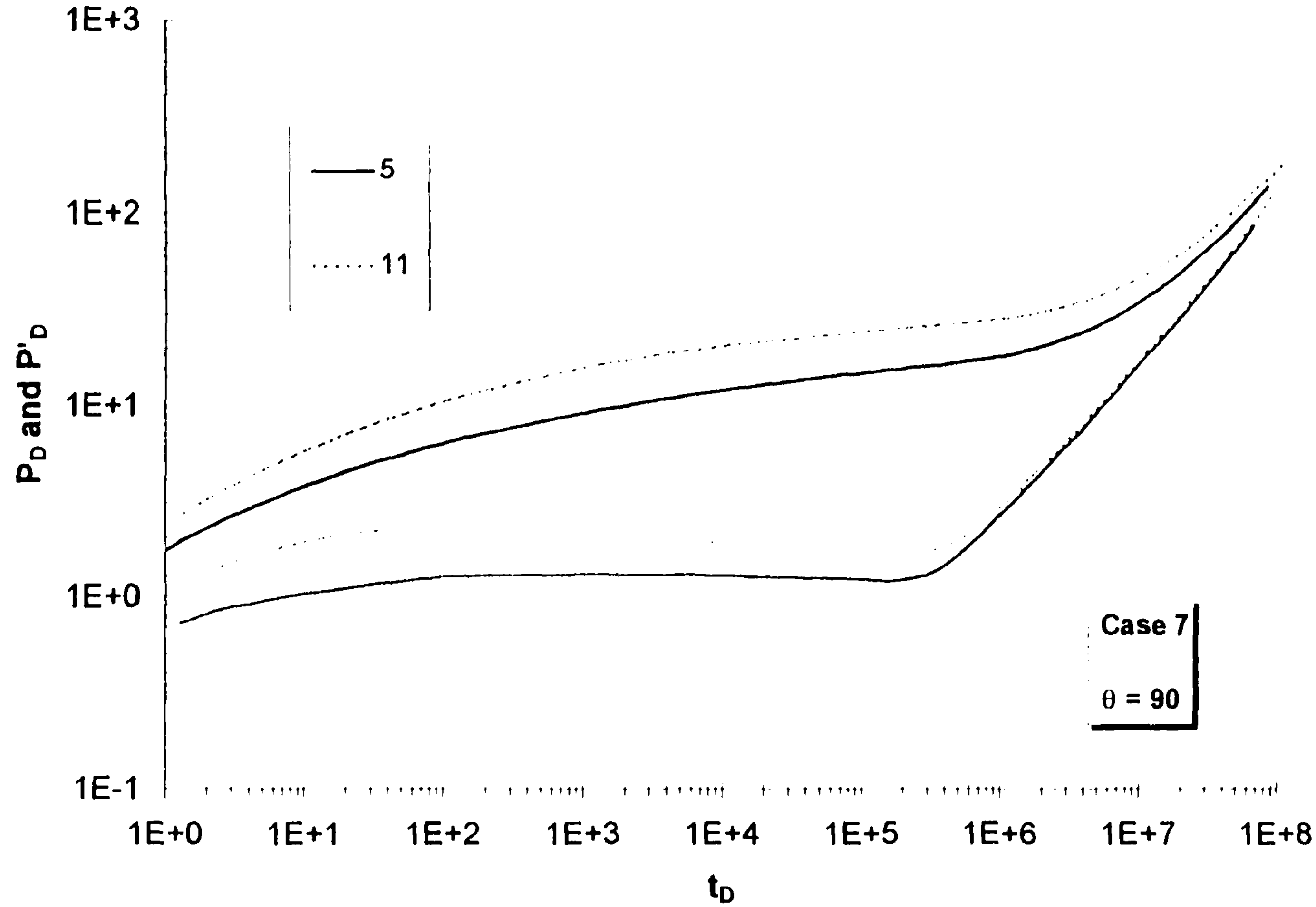

Figure 5.7.16 The Dimensionless Pressure and The Dimensionless Pressure Derivative

for Case 7.5 and 7.11

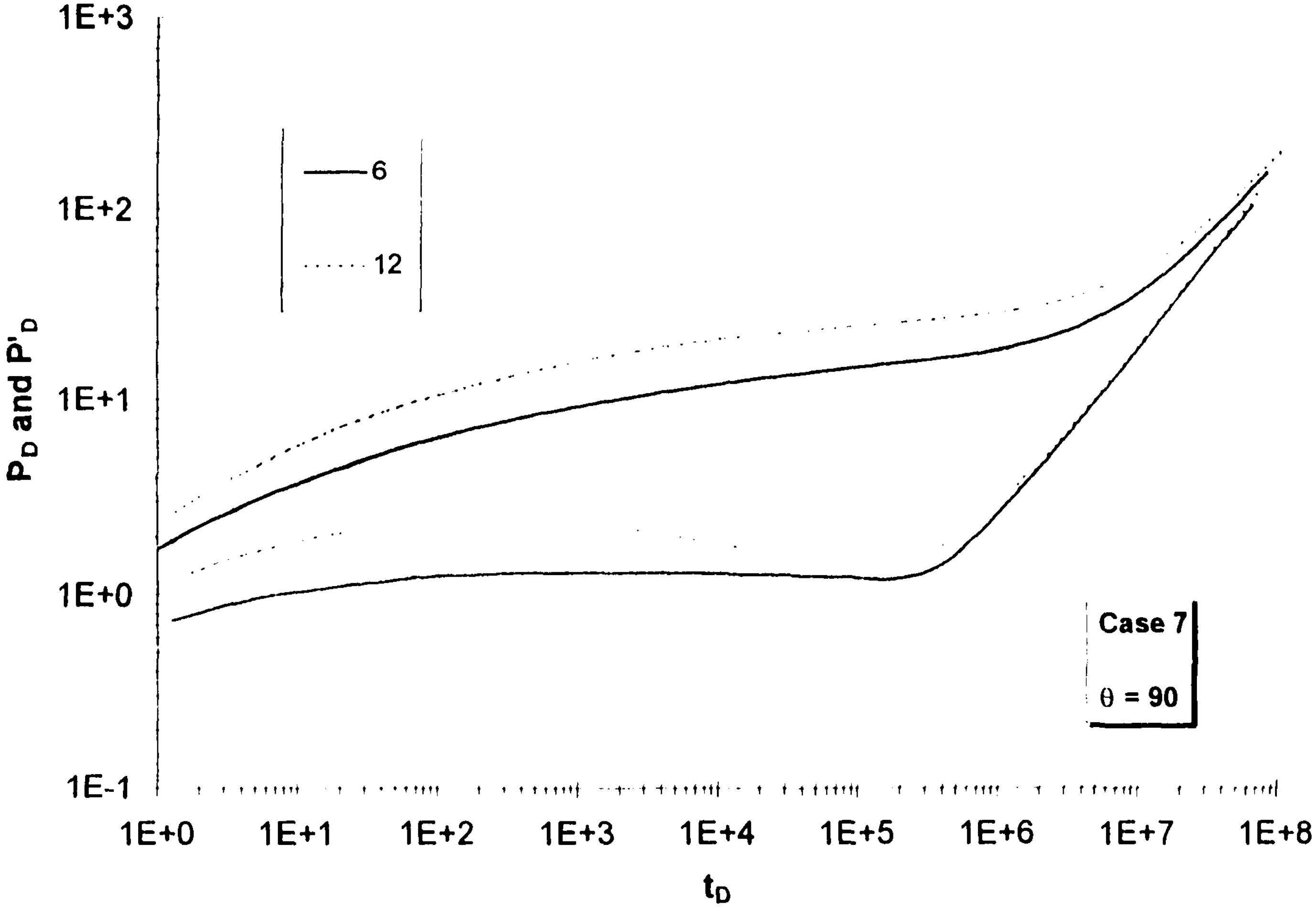

Figure 5.7.17 The Dimensionless Pressure and The Dimensionless Pressure Derivative

for Case 7.6 and 7.12

IMAGE EVALUATION TEST TARGET (QA-3)

150mm

6"

APPLIED IMAGE . Inc
1653 East Main Street
Rochester, NY 14609 USA
Phone: 716/482-0300
Fax: 716/288-5989